Copyright is owned by the Author of the thesis. Permission is given for a copy to be downloaded by an individual for the purpose of research and private study only. The thesis may not be reproduced elsewhere without the permission of the Author.

Applications of Multicomponent Metal-Organic Frameworks

A thesis presented in partial fulfilment of the requirements of the degree of

Doctor of Philosophy

in

Chemistry

at Massey University, Manawatū, New Zealand

Seok June Lee

2021

For 지현

Abstract

Multicomponent metal-organic frameworks (MOFs) comprise multiple organic ligands that are topologically distinct. Each organic ligand is precisely positioned in a highly ordered crystal lattice. These allow tunable pore environments induced by the predictable arrangement of chemical functional groups on multiple ligands. This study was mainly focused on utilising such benefit of multicomponent MOFs. First, a novel concept for asymmetric catalysis was implemented. Sequence-specific polymer synthesis by post-synthetically linking the two ligands in a framework was then covered. Both applications exhibited new approaches that had not been demonstrated in conventional chemical reactions. This study exhibits the possibility of multicomponent MOFs as a great platform for many applications.

Contributions

All the work in this thesis was completed by Seok June Lee

Except:

- Dr. Tian-You Zhou synthesised H_3hott, H_3hhtt, H_3hmtt, H_2bpdc-gua, H_2bdc-bnox and H_2bdc-iprox used in Chapter 3.
- Dr. Adil Alkaş synthesised H_3cbtt, H_3hhtt and H_3hmtt, and he also provided a few single-crystal structures used in Chapter 2.
- Joel Cornelio synthesised H_3hbtt, and he also provided a few single-crystal structures used in Chapter 2.
- Dr. David Perl synthesised H2bpdc-β_1 and -β_2 used in Chapter 7.
- Bernhard Auer synthesised H_3hmtt.
- Some preliminary experiments in Chapter 5 were conducted by Ruth Verbroekken under the supervision of Dr. Adil Alkaş.
- All ES-MS analyses were conducted by David Lun.
- SEM images in Chapter 5 were taken by Dr. Hui Yang.
- SEM images in Chapter 6 were taken by Yiming Zhang.
- Victoria-Jayne Reid synthesised H_3hhtt.
- Raman spectra was measured by Sam Brooke.

Acknowledgements

I would like to take the opportunity to thank the large number of people who have contributed to my PhD research and thesis. First, I would like to thank my supervisor Professor Shane Telfer for leading me into the chemistry world and providing me with this wonderful PhD opportunity. I do appreciate all your expert guidance and thoughtful mentoring on all matters throughout this PhD, from the big picture all the way to every single detail, even a tiny spelling mistake. Thank you for providing funding for me to attend conferences and workshops.

I would also like to thank my co-supervisor, Professor Geoff Jameson, for his much-valued advice, especially for crystallography. I also thank Dr. Tian-You Zhou for assisting in many ways, from organic ligand synthesis to much-valued advice concerning my catalysis work. I thank David Lun for his technical assistance and also for providing ES-MS data. I also thank Dr Pat Edwards for assisting with NMR experiments. I also thank Dr. Adil Alkaş for assisting with synthesis and for valuable comments and Joel Cornelio and Bernhard Auer for assisting in many ways. I also thank Dr. David Perl, Dr. Omid Taheri, Shikeale Harris, Heather Jameson, Ruth Verbroekken, Lara Kleine-Kleffmann, Nicholas Symon, Victoria-Jayne Reid, Dr. Ben Yin, Dr. John Clements, Simon Guery, Laurine Friche, Tim Craig, Nisansala Bandara and all other past Telfer group members for scientific discussions and technical assistance.

I would like to acknowledge the financial support from Massey University for a Doctoral scholarship and the School of Fundamental Sciences for fourth-year student fee funding. I also thank the SFS postgraduate travel fund for supporting me to attend a workshop in Como, Italy. I greatly thank the MacDiarmid Institute for organizing and supporting annual student and postdoc symposiums

I also thank SFS administration and technical staff for their great assistance during my PhD research and thesis writing.

I would like to take this opportunity to thank all of my friends and family, whose encouragement and support have helped me throughout this PhD study.

Finally, I would also like to thank my wife, Jihyun Choi, for her love and unlimited support. Her faith in me was most encouraging that enables me to come through this long journey.

Abbreviations

2-MI	2-Methylimidazolate
Bdc	Benzene-1,4-dicarboxylate
BET	Brunauer–Emmett–Teller
Bipy	4,4′-Bipyridyl
bnox	Benzyl oxazolidinone
Boc	Tert-Butyloxycarbonyl
Bpdc	[1,1'-Biphenyl]-4,4'-dicarboxylate
Btb	Benzene-1,3,5-tribenzoate
Btc	Benzene-1,3,5-tricarboxylate
Cbtt	Cyclobutyltruxene tricarboxylate
CSD	Cambridge Structural Database
DABCO	1,4-Diazabicyclo[2.2.2]octane
DEF	*N,N*-Diethylformamide
DMA	*N,N*-Dimethylacetamide
DMF	*N,N*-Dimethylformamide
DOT	2,5-Dioxidoterephthalate
FWHM	Full width at half maximum
Hbtt	5,5,10,10,15,15-hexabutyltruxene-2,7,12-tricarboxylate
Hhtt	5,5,10,10,15,15-hexahexyltruxene-2,7,12-tricarboxylate
HKUST	Hong Kong University of Science and Technology
Hmtt	5,5,10,10,15,15-hexamethyltruxene-2,7,12-tricarboxylate
Hott	5,5,10,10,15,15-hexaoctyltruxene-2,7,12-tricarboxylate
IAST	Ideal Adsorbed Solution Theory
Iprox	Isopropyl oxazolidinone
IRMOF	Isoreticular metal-organic framework
IUPAC	International Union of Pure and Applied Chemistry

MC-MOFs	Multicomponent metal-organic frameworks
MCP	Microporous coordination polymer
MIL	Matériaux de l'Institut Lavoisier
MOF	Metal-organic framework
MS	Mass spectroscopy
MTV-MOFs	Multivariate metal-organic frameworks
MUF	Massey University Framework
NDC	Naphthalene dicarboxylate
NMR	Nuclear magnetic resonance
NTB	4,4′,4″-Nitrilotribenzoate
NU	Northwestern University
PCN	Porous coordination network
PCP	Porous coordination polymer
phox	Phenyl oxazolidinone
PSD	Postsynthetic deprotection
PSE	Postsynthetic exchange
PSM	Postsynthetic modification
PVD	Pore Volume Distribution
PXRD	Powder X-ray diffraction
PyC	Pyrazole-4-carboxylate
RAI	Remote asymmetric induction
RCSR	Reticular Chemistry Structure Resource
SALE	Solvent assisted linker exchange
SALEM	Solvent-assisted linker exchanged material
SCXRD	Single-crystal X-ray diffraction
SEM	Scanning Electron Microscope
SUMOF	Stockholm University metal-organic framework

TGA	Thermogravimetric analysis
THF	Tetrahydrofuran
TLC	Thin layer chromatography
UiO	Universitetet i Oslo
UMCM	University of Michigan Crystalline Material
ZIF	Zeolitic imidazolate frameworks
ZMOF	Zeolite-like metal-organic framework

Publications and thesis structure

Publications relevant to this thesis

None

Additional publications

1. Macreadie, L. K.; Babarao, R.; Setter, C. J.; Lee, S. J.; Qazvini, O. T.; Seeber, A. J.; Tsanaktsidis, J.; Telfer, S. G.; Batten, S. R.; Hill, M. R. Enhancing Multicomponent Metal–Organic Frameworks for Low Pressure Liquid Organic Hydrogen Carrier Separations. *Angewandte Chemie International Edition* **2020**, *59*, 6090-6098.

2. Zhou, T.-Y.; Auer, B.; Lee, S. J.; Telfer, S. G. Catalysts Confined in Programmed Framework Pores Enable New Transformations and Tune Reaction Efficiency and Selectivity. *Journal of the American Chemical Society* **2019**, *141*, 1577-1582.

3. Lazaro, S. E.; Alkaş, A.; Lee, S. J.; Telfer, S. G.; Murray, K. S.; Phonsri, W.; Harding, P.; Harding, D. J. Abrupt spin crossover in iron(iii) complexes with aromatic anions. *Dalton Transactions* **2019**, *48*, 15515-15520.

4. Boonprab, T.; Lee, S. J.; Telfer, S. G.; Murray, K. S.; Phonsri, W.; Chastanet, G.; Collet, E.; Trzop, E.; Jameson, G. N. L.; Harding, P.; Harding, D. J. The First Observation of Hidden Hysteresis in an Iron(III) Spin-Crossover Complex. Angew. Chem. Int. Ed. 2019, 58, 11811-11815.

5. Zhou, C.; Longley, L.; Krajnc, A.; Smales, G. J.; Qiao, A.; Erucar, I.; Doherty, C. M.; Thornton, A. W.; Hill, A. J.; Ashling, C. W.; Qazvini, O. T.; Lee, S. J.; Chater, P. A.; Terrill, N. J.; Smith, A. J.; Yue, Y.; Mali, G.; Keen, D. A.; Telfer, S. G.; Bennett, T. D. Metal-organic framework glasses with permanent accessible porosity. Nat. Commun. 2018, 9, 5042.

Table of Contents

Chapter 1 Introduction

1.1. General introduction to metal-organic frameworks (MOFs)

1.1.1. Definition, terminology and nomenclature

The number of publications about new types of porous materials has exponentially grown since the late 20th century.[1] These materials are built from metals or metal clusters which behave as nodes and divergent organic ligands bridging the metal nodes, thereby forming multi-dimensional frameworks. The organic ligands in these materials are relatively rigid and generally possess anionic functional groups to bind to the positively charged metal nodes. The resulting frameworks have a higher void volume ratio compared to conventional porous materials, and such porosity is the fundamental property that allows these materials to be differentiated from other coordination compounds. In 2013, IUPAC released guidelines about the terminology, definition and classification with respect to these new class of porous materials due to the rapidly expanding related research field.[2]

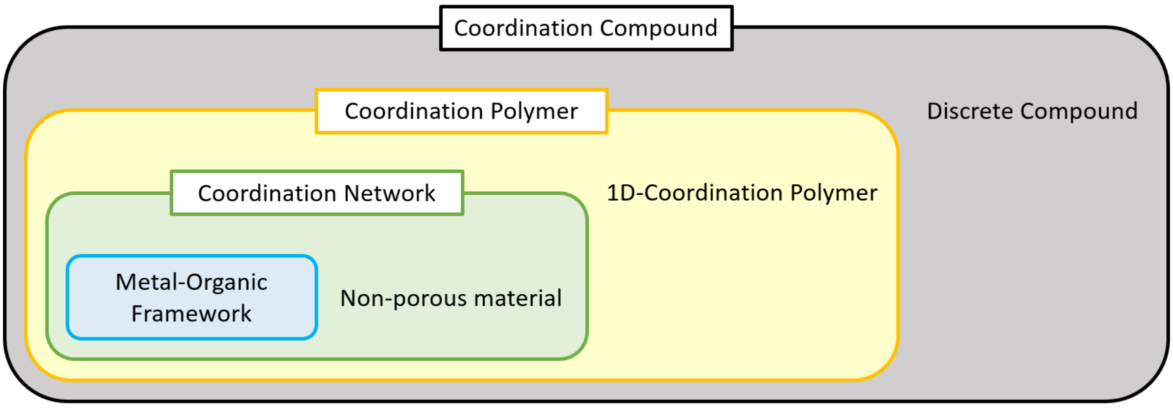

Term	Definition
Coordination Polymer	A coordination compound with repeating coordination entities extending in 1, 2, or 3 dimensions.
Coordination Network	A coordination compound extending, through repeating coordination entities, in 1 dimension, but with cross-links between two or more individual chains, loops, or spiro-links, or a coordination compound extending through repeating coordination entities in 2 or 3 dimensions.
Metal-Organic Framework	A metal–organic framework, abbreviated to MOF, is a coordination network with organic ligands containing potential voids.

Figure 1-1. The diagram (top) represents Coordination Compound family according to IUPAC classification, and the definition of subclasses of the Coordination Compound was tabulated (bottom).

According to the IUPAC recommendation 2013,[3] to call these new class of porous material MOFs (Metal-organic frameworks) is strongly recommended. However, some other abbreviations were used to call this material, such as microporous coordination polymers (MCP), porous coordination network (PCN), porous coordination polymer (PCP) and zeolite-like metal-organic frameworks (ZMOF). In this thesis, MOF will be used as the sole term to refer to these porous coordination networks. All materials initially reported with alternative terms will also be regarded as MOFs.

In general, a nickname (e.g. MOF-5[4] or PCN-777[5]) or an abbreviated formula (e.g. $Cu_3(BTC)_2$, BTC = benzene-1,3,5-tricarboxylic acid)[6] is used to refer to an individual MOF. Another widely accepted way to name a MOF is using the trivial name based on its place of origin followed by a number, such as MUF-77 (MUF = Massey University Framework),[7] HKUST-1 (HKUST = Hong Kong University of Science and Technology)[6] or UMCM-1 (UMCM = University of Michigan Crystalline Material).[8]

1.1.2. A brief history of MOFs

Of course, MOFs did not just appear one day; there was a lot of prior work before MOFs appeared. For instance, the description of porous coordination polymers first appears in 1989 by Richard Robson,[9] and the first publication containing 'metal-organic framework' in the title was reported in 1995 by Omar Yaghi.[10] However, it can be said that the history of MOF began in earnest with the iconic MOF-5 in 1999 by Omar Yaghi.[4] The design concept of MOF-5 is pretty simple but completely innovative. This idea came from the basic zinc acetate, which possesses octahedral geometry and had been known for decades. As shown in Figure 1-2, the capping ligand, acetate that coordinated on the supertetrahedron cluster was replaced with a bridging ligand, bdc (1,4-benzendicarboxylate). Thus, the combination of an octahedral node and linear bridging linkers allows the framework to expand indefinitely in all three dimensions.

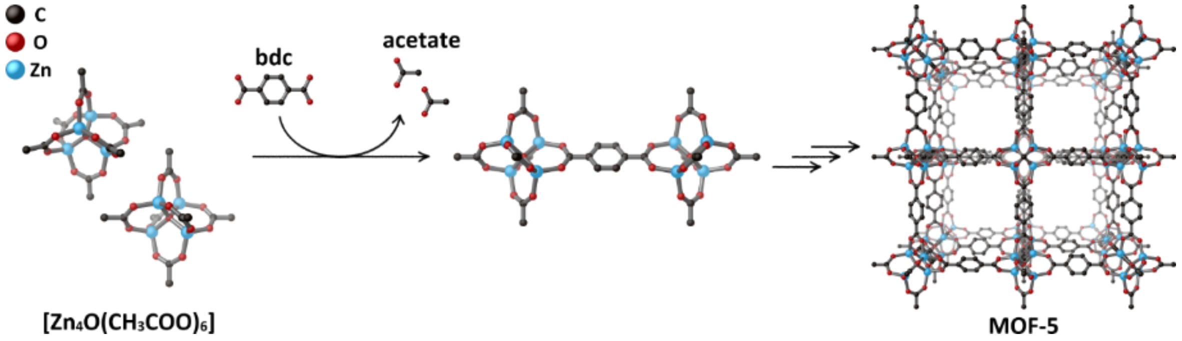

Figure 1-2. A schematic diagram of the derivation of MOF-5 from the basic zinc acetate complexes by replacing acetate with the bridging linker bdc.

The resulting structure possesses the following aspects that differentiate it from other materials. First, coordination between rigid bdc and Zn_4O cluster results in enhanced thermal and architectural stability of the framework. Second, the coordination network expands out three-dimensionally, resulting in a primitive cubic net (**pcu**) with a large void cavity. Last, the framework structure does not collapse or transform even after removal of the solvent molecules filling the void space and hence exhibits 'permanent' porosity.

The astonishing results from MOF-5 opened up the window for a new generation of porous materials which contain both metallic and organic properties with permanent porosity. The chemical environment of the pore can be modified depending on the functional groups on the organic linker backbones or by using different types of metals for the nodes. Furthermore, the incomparable size of void space, which had never been observed from any other porous materials, allows guest molecules to enter and interact with the surrounding. Hence, this new type of porous material became a hot topic in the field, and many research groups directed to study MOFs and their applications. Figure 1-3 clearly shows the rapid increase of interest from researchers since around 2000; the number of publications presented in the diagram is underestimated since other alternative terms for MOFs are used by many research groups. Gas storage,[11-12] gas separation[13] and catalysis[14] have been steady research topics ever since researchers first paid attention to their permanent and versatile porosity. Nowadays, broad research topics related to MOFs have risen in almost every field of chemistry, such as chemical sensors,[15] energy storage,[16] polymers,[17] membranes,[18] drug delivery,[19] water

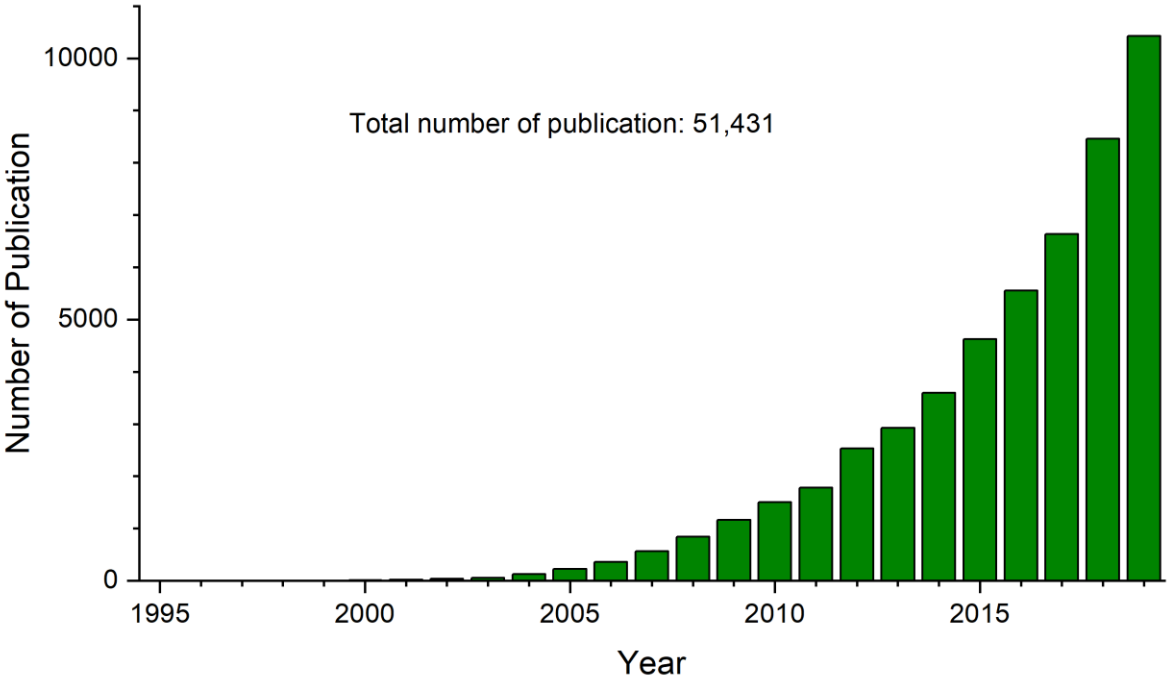

Figure 1-3. A histogram of the number of publications in each year retrieved by the search term 'metal-organic framework' in SciFinder.

remediation,[20] luminescent and photonic material,[21] magnetic[21] or electric[22] devices, and enzyme encapsulation.[23]

1.1.3. Building blocks and topology

As the name suggests, MOFs are composed of metals or metal clusters that behave as a node, and organic ligands, which bridge those nodes. The polynuclear complexes of metal ions and coordinating groups form a specific geometry which is referred to as secondary building units (SBUs), and this conceptual substructure is widely used to design or to analyse MOF structure. A few representative SBUs are depicted in Figure 1-4. The ZnN_4 arrangement is the most frequently observed single metal ion SBU adopted by zeolitic imidazolate frameworks (ZIF), one of the most common subclasses of MOFs.[24] The $M_2(COO)_4$ SBU is usually referred to as a paddlewheel due to its shape. Four carboxylates coordinate to two metal ions in the equatorial plane, and the axial positions of the SBU are occupied by solvent molecules or some nitrogen donor ligands that may bridge to the neighbouring SBU.[25] $M_4O(COO)_6$, as shown in MOF-5, is the most common SBU.[4] The M_4O^{6+} supertetrahedron cluster and six carboxylates form an octahedral geometry. The $M_3O_3(COO)_3$ cluster is the representative infinite rod shape SBU allowing 1D channels. 2,5-Dihydroxyterephthalate (dhbdc in Figure 1-5) in MOF-74 is commonly used to form such SBU because the extra coordinating oxygen atom on the hydroxy group is essential to build the cluster.[26] Open metal sites are readily obtainable by removing the solvent molecules that are usually required to initially form the cluster.[27] The $M_6O_4(OH_4)(COO)_{12}$ cluster is mostly seen in MOFs of the UiO series (UiO = Universitetet i Oslo), which is one of the most widely studied MOFs.[28] Because UiO frameworks are robust due to the high and dense connectivity of the SBU. They are also versatile due to their ability to form defects. Only a few examples are presented here,

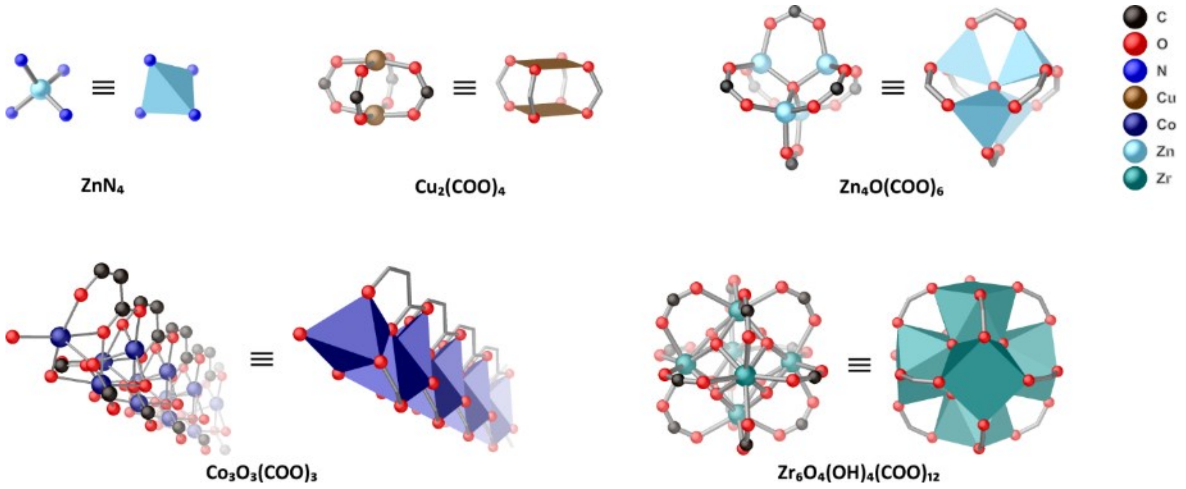

ZnN_4 $Cu_2(COO)_4$ $Zn_4O(COO)_6$

$Co_3O_3(COO)_3$ $Zr_6O_4(OH)_4(COO)_{12}$

Figure 1-4. A few representative secondary building units (SBUs) which were depicted with ball & stick and polyhedral models.

but there are even more SBUs because the majority of the metal atoms in the periodic table are used in MOF chemistry.[29]

Usually, two different types of organic ligands are used for MOF synthesis, carboxylate based ligand and N donor ligands. Although some neutral N donating ligands, like DABCO (1,4-diazabicyclo[2.2.2]octane) or 4,4'-bipyridine (Figure 1-5d), are used as building units, they are prone to defects in the form of missing ligands due to their weak bonds compared to the anionic ligands.[25] Also, their neutral charge allows them to be absent without affecting the overall charge in the framework. On the other hand, anionic functional groups, such as carboxylate or nitrogen heterocycles like imidazolate or tetrazolate, are a lot more advantageous over the neutral coordination groups. This is because the anionic ligand and

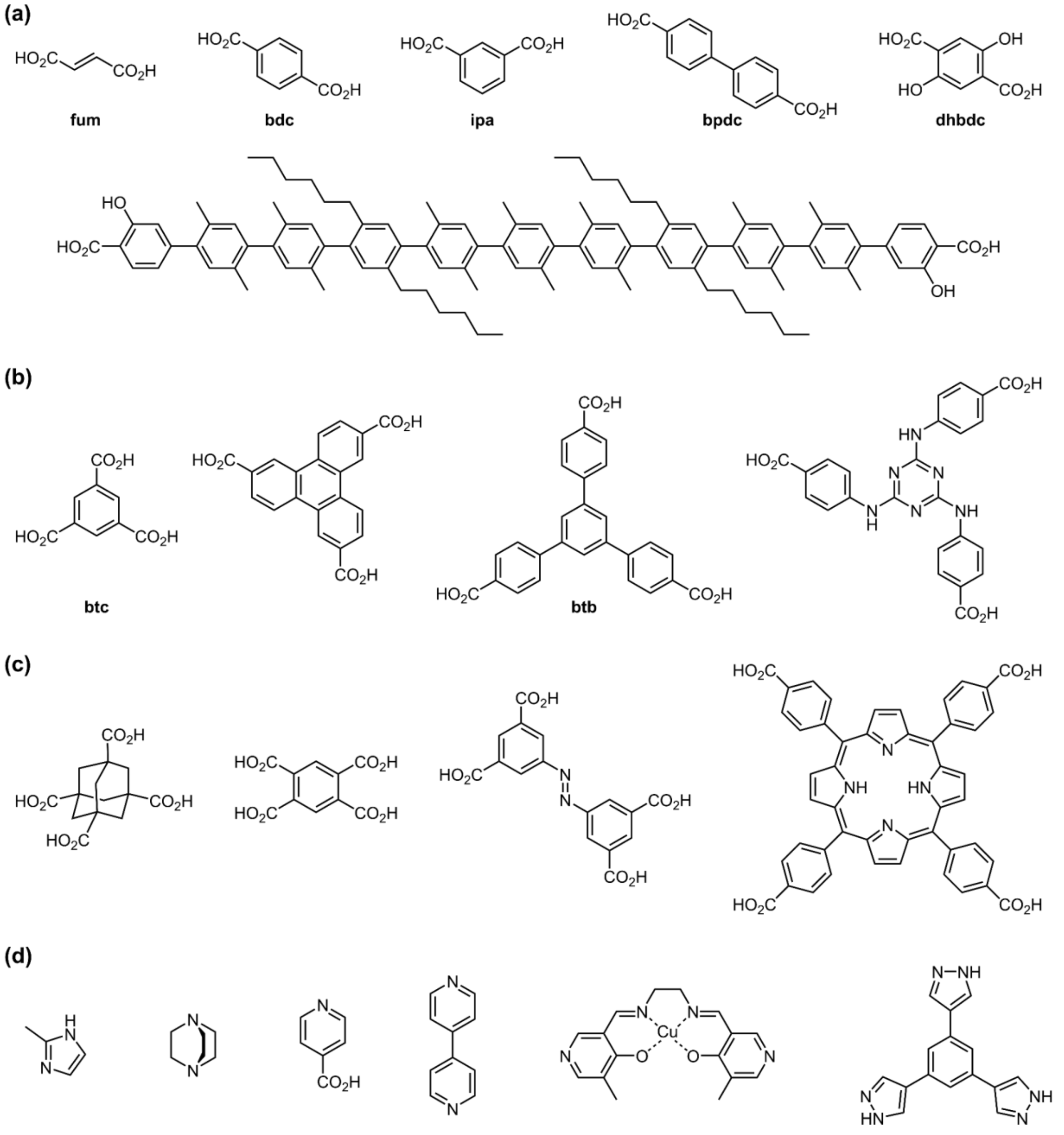

Figure 1-5. A few examples of (a) di-, (b) tri- and (c) tetra-topic organic linkers, and (d) nitrogen-based linkers.

cationic metal node form strong ionic bonds resulting in thermally, mechanically, and chemically robust frameworks. Moreover, such multi-dentate ligands prefer to develop a polynuclear cluster providing a fixed geometry and connectivity. Also, the cancellation of the charge from the cluster eliminates the need for counter ions.

Organic ligands bring great diversity and richness to the framework topology since they are amenable to modification; literally, an uncountable number of organic linkers can be designed and synthesised. A few examples of organic ligands are depicted in Figure 1-5. The chemical and physical properties of the MOF pore are mainly dictated by the organic linkers. Hence, designing and synthesising organic ligands is critical to implant the desired functionality to MOFs, but also the most challenging part because there are many factors to care about in designing organic linkers. The number of points of extension of the ligand most significantly affects the topology of the frameworks. However, a subtle change in other factors results in a structural change as well. For instance, in the simple ditopic carboxylate based ligands, the first row in Figure 1-5, there are a few variations between ligands such as length, directionality or offset. Such variations generally result in a different topology of the framework.

The number of possible topologies for MOF structure increases enormously depending on the combination of SBUs and ligands. It becomes even more complicated if the frameworks are composed of multiple classes of organic linkers. A systematic way to describe or to analyse the exponentially increasing MOF structures was demanded several years ago as there had been no such existing system. In 2008, O'Keeffe and other researchers suggested the RCSR code (RCSR = Reticular Chemistry Structure Resource) to refer to the underlying topology of a framework and constructed a database to facilitate reticular chemistry, http://rcsr.anu.edu.au.[30] The basic idea is to simplify the structure into a net consisting of vertices and edges and group the same kinds based on mathematical operations. Each group

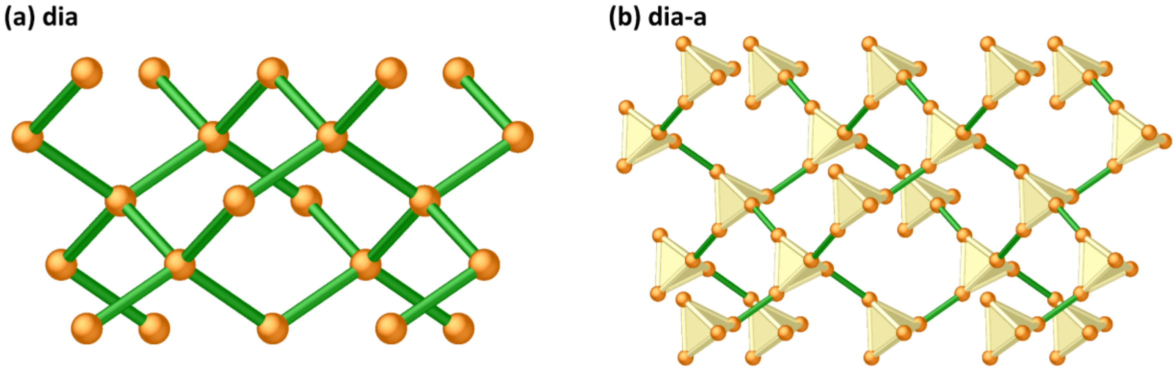

Figure 1-6. The two frameworks have the same diamond-like connectivity, so their topologies are represented with **dia**. However, the nodes in (b) are polynuclear augmented cluster, so the suffix '-a' was added to describe the augmented node.

is then denoted with a three-letter code. However, these three-letter codes are not intuitive due to the enormous number of topologies; only a few of them are acronyms relating to the geometrical shape of the network, such as **sod** for sodalite, **dia** for diamond or **qtz** for quartz. The code is written with the lower case and bold, and one or more extensions are followed after a hyphen if required. For instance, the two frameworks in Figure 1-6 have the same network connectivity as a diamond, so their topology is represented with **dia**. However, the nodes in Figure 1-6b are polynuclear (augmented) clusters, so the extra suffix '**-a**' was added to describe this distinctive feature.

To determine the topology of a MOF structure, a deep mathematical understanding of net geometry is required. Fortunately, a software package like ToposPro[31] provides useful and powerful functionalities for this purpose, or it can be done by simply uploading the crystal structure file into their web site (https://topospro.com) to obtain the topology.

1.1.4. Synthesis and activation of MOFs

As MOF chemistry draws increasing attention, the number of new MOF structures has exponentially increased, and various applications of MOFs have been introduced. Hence, different types of synthetic methods of MOF crystal have been developed to control their morphology or to incorporate with other types of materials depending on the applications. For instance, nano-sized MOF crystals are required for biomedical imaging[21] or drug release[19] and micro-sized MOF crystals are embedded into mixed matrix membranes for gas separation.[18] Conventional solvothermal synthesis is the most widely adopted synthetic method. Other methods, such as microwave-assisted, mechanochemical, electrochemical, spray-drying or sonochemical synthesis, have emerged.[32-33] Here, only solvothermal synthesis, which is directly related to this thesis, will be discussed.

MOF crystal formation is a reversible process under the laws of thermodynamics and governed by many factors, such as solvents, additives, stoichiometry between substances, pH, concentration, temperature, heating rate or duration. Even a subtle change can cause undesired crystal morphology or topologically different crystals. Since crystal formation is not a simple process and not fully understood, the trial and error approach is the most adopted method. A few amide solvents, like *N,N*-dimethylformamide (DMF), *N,N*-diethylformamide (DEF) or *N,N*-dimethylacetamide (DMA), are widely exploited as the primary solvent. Alcohols or water are often added. One reason for using these amide solvents is their incredible power to dissolve organic ligands and metal salts. However, there is another critical reason which is well depicted in Figure 1-7. The amide solvent molecule, for instance, DMF, is hydrolysed to produce formic acid and dimethylamine. The rate of

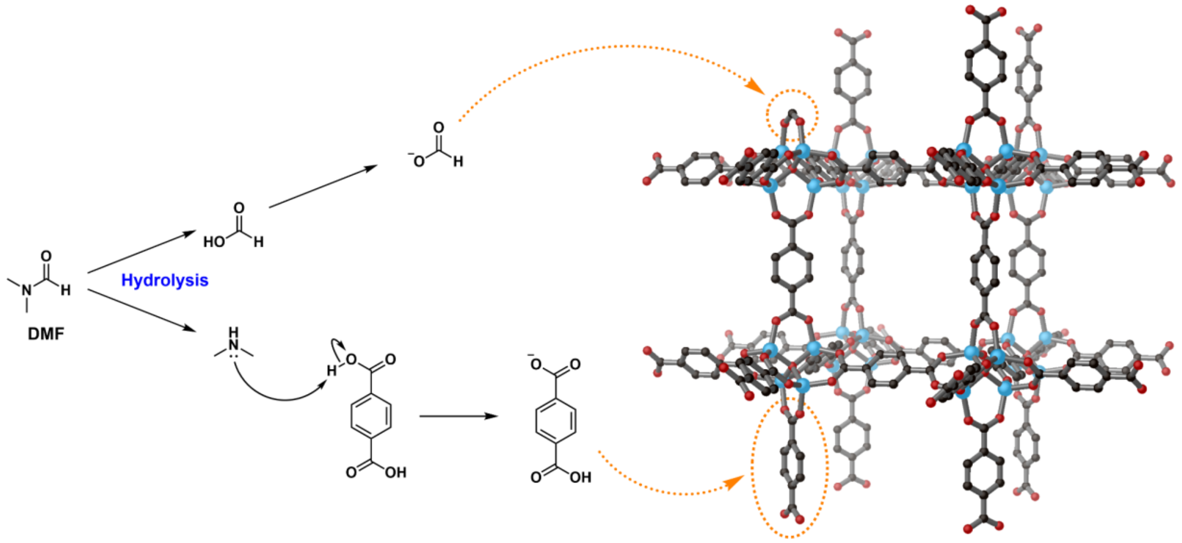

Figure 1-7. The process of DMF decomposition and the way how resulting formic acid and dimethylamine are utilised in MOF-5 crystal formation. Hydrogen atoms were omitted for clarity.

hydrolysis increases at an elevated temperature. The resulting dimethylamine deprotonates the carboxylic acid based ligand to form the carboxylate that allows the formation of a cluster with metal cations. The released formic acid is also deprotonated, and the formate also participates in the cluster formation. However, the formate lacks connectivity and is gradually replaced by multitopic linkers. The role of formate is to slow down the crystal formation, which enables to form a uniform and even crystalline structure. Such materials which control the speed of crystal formation or morphology of crystal are referred to as modulators. A few well-known materials, benzoic acid or acetic acid, are usually added to obtain large single crystals. Interestingly, 2-methylimidazole (2-MI) has also been reported as a modulator, but it helps to form nano-scaled crystals instead. According to Guo et al., the nucleation rate is boosted in the presence of 2-MI for various MOF syntheses, thereby forming a lot more nucleation seeds. Crystals then simultaneously grow on each nucleation seed by slowly replacing 2-MI with the desired ligands.[34]

Altering the synthesis temperature or pH of the reaction medium is another handle to control the crystal size or morphology. The rate of crystal formation generally increases at high temperature or higher pH, and vice-versa. In some cases, more than one type of metal ion or ligand are used to form a multivariate MOF or multicomponent MOF, which will be discussed in later sections. The ratio between substances is another essential factor in shaping the desired structure or in maintaining the aimed functionalities. Once MOF crystal formation is finished, it is highly recommended to replace the mother liquor with the same solvent used for the synthesis. This is because unreacted leftover materials sometimes form secondary phase crystals which are hard to separate, and the crystals are generally stable in synthesis solvent, which allows extended storage without deforming the crystal until further use.

Typically, the pores in an as-synthesised MOF are filled with unreacted organic ligands and solvents that generally have high polarity or high boiling point. Hence, the unwanted substances in the pore need to be cleared out to increase the accessible porosity and internal surface area through a series of processes referred to as activation.[35] Activation is an essential process to increase the desired performance of MOF, and the performance highly depends on how well the crystals are activated. Solvent exchange, which is generally followed by vacuum drying, is a widely exploited method for the activation of MOFs. The synthesis solvent, like DMF, generally has high polarity and boiling point and thereby not readily removable from the pore with conventional heating and vacuum methods. Therefore, the synthesis solvents are usually replaced with volatile solvents, such as acetone or CH_2Cl_2. Then, the MOFs are placed under a vacuum to empty the pores for further use.

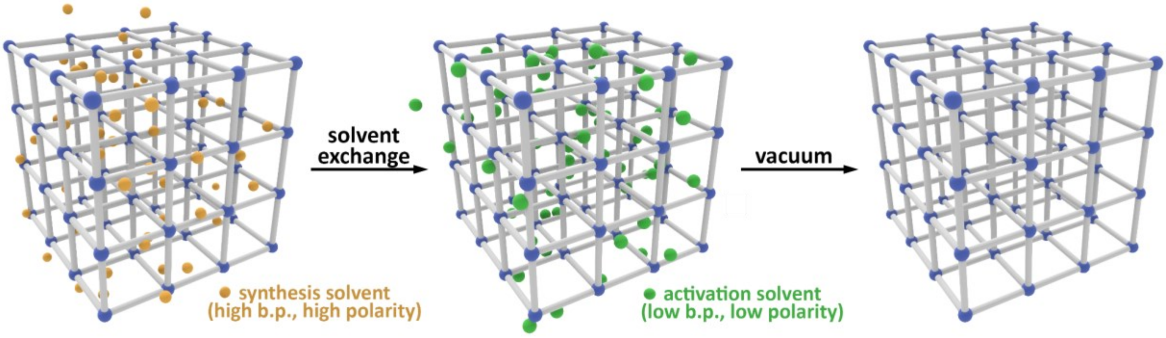

Figure 1-8. A schematic diagram of the activation process with solvent exchange and vacuum.

However, the solvent exchange process in MOFs is a lot different from that of other materials due to their relatively large inner pore volume. According to Matzger,[36] the entire exchange process usually occurs in seconds or minutes, rather than hours or days applied to conventional materials because small solvent molecules freely enter the large pores of MOF. Therefore, in the case of a MOF, the number of wash with the exchange solvent is a more important factor than how long it is soaked in the solvent. They also showed that the accessible pore volume significantly changes depending on the properties of the activation solvent. Therefore, choosing the right activation solvent, depending on the application, is critical. Often, a few steps of solvent exchange processes are required in some cases. For instance, it is impossible to exchange DMF with n-hexane directly due to their immiscibility. Hence DMF is first exchanged with CH_2Cl_2, then successively with n-hexane in this case. However, some MOF structures have been reported where the pores collapse upon solvent exchange or solvent removal.[37] In such cases, alternative activation methods can be applied, such as activation by supercritical CO_2 or freeze-drying.[38]

1.1.5. Postsynthetic modification

Not all ligands or metal ions can form the targeted structure, and this problem is generally caused by the presence of secondary functional groups on the ligand. The secondary functional groups are a non-structural component and added to the ligand to impart a specific chemical property to the pore. However, the chemical properties of the secondary functional groups are sometimes not compatible with the synthetic conditions required for the target structure. Postsynthetic modification (PSM) is a powerful and widely adopted method that provides a synthetic detour to the targeted structure when a direct synthesis is not available.[39] From a simple modification like adding a guest component or a functional group onto the organic linker to deformation of the entire structure by replacing structural components, PSM is very versatile and an extensively applied method in MOF chemistry.

1.1.5.1. Addition of guest components

MOFs have great expandability because any organic molecule possessing multiple coordination sites able to bridge metal nodes has the potential to be used as a linker. In this sense, many organic molecules with a specific functionality are utilised to implant such functionality into a framework. Organometallic compounds are versatile and widely used in catalysis, and many of the organic ligands can be incorporated into MOF synthesis by adding

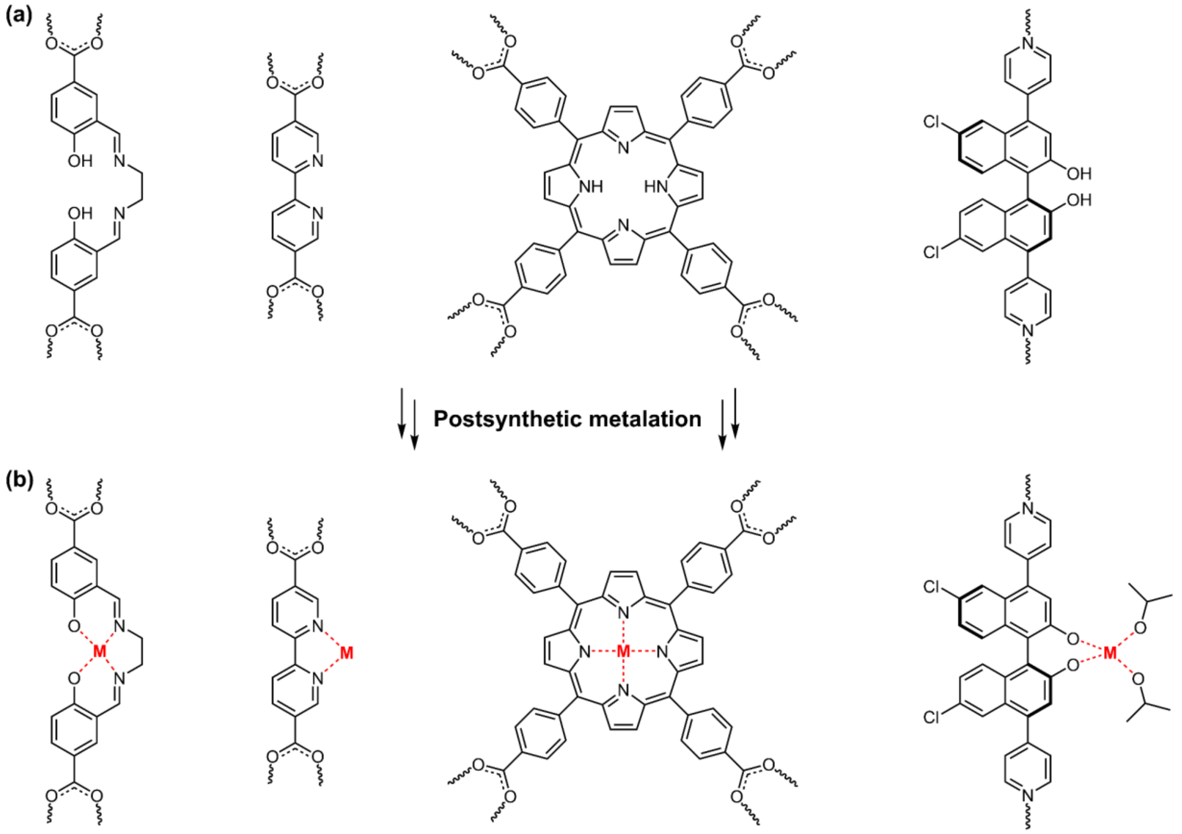

Figure 1-9. A few examples of ligands in various MOFs before (a) and after (b) postsynthetic metalation.

bridging coordination groups. However, such compounds have non-structural metal components which may interrupt MOF formation, so they are generally introduced to the framework after MOF synthesis. A few representative example ligands and their form after postsynthetic metalation are illustrated in Figure 1-9.[40-43] The general approach to synthesise the targeted MOF structure is straight forward and requires mild conditions. These ligands commonly possess non-structural coordination sites capable of chelating a metal centre but not hindering MOF formation. Once the desired MOF crystals are formed, they are separated, introduced to a concentrated metal salt solution, and soaked in the solution allowing the metal ions to bind to the chelating sites on the MOF ligands. Some additives, such as ligands and elevated temperatures, may also be required.

1.1.5.2. Implanting a functional group to the ligand backbone

Some secondary functional groups, such as carboxylic acid or nitrogen-containing groups that are favoured especially for catalysis, have strong coordination ability, so they interfere with MOF formation. In such cases, PSM is widely adopted to add the targeted functional groups forming a covalent bond to the ligand backbone. Alternatively, such functional groups can be shielded by a protecting group to mitigate their coordinating tendency. Hence, the desired MOF is constructed with a protected ligand, and then the protecting group is removed by PSM.

A series of MOFs derived from MIL-53(Al)-NH_2 (MIL: Matériaux de l'Institut Lavoisier) nicely represents the addition of a functional group employing covalent bond formation by a PSM process (Figure 1-10a).[44] The MIL-53(Al)-NH_2 framework was chosen for the base structure due to its chemical robustness and the versatile amino functional group on its bdc linker. It undergoes covalent bond formation with some reactive species introduced to its pores. Covalent bond formation between the bdc-NH_2 linker and incoming molecules was achieved under mild conditions (80 °C, 24 h in MeCN). The resulting framework showed catalytic activity for the methanolysis reaction of epoxides. This simple PSM procedure illustrated its efficacy to implant secondary functional groups, including reactive carboxylic acid. Furthermore, the cumbersome organic synthesis procedure to make each ligand was simplified.

In 2011, the Telfer group highlighted another creative approach to add a pendant group onto the ligand backbone using a protecting group (Figure 1-10b), which is termed postsynthetic deprotection (PSD).[45-46] They managed to embed a proline moiety into an IRMOF-10 framework (IRMOF: isoreticular MOF). Proline and pyrrolidine moieties are well recognised as potent organic catalysts for many reactions. However, the proline or pyrrolidine

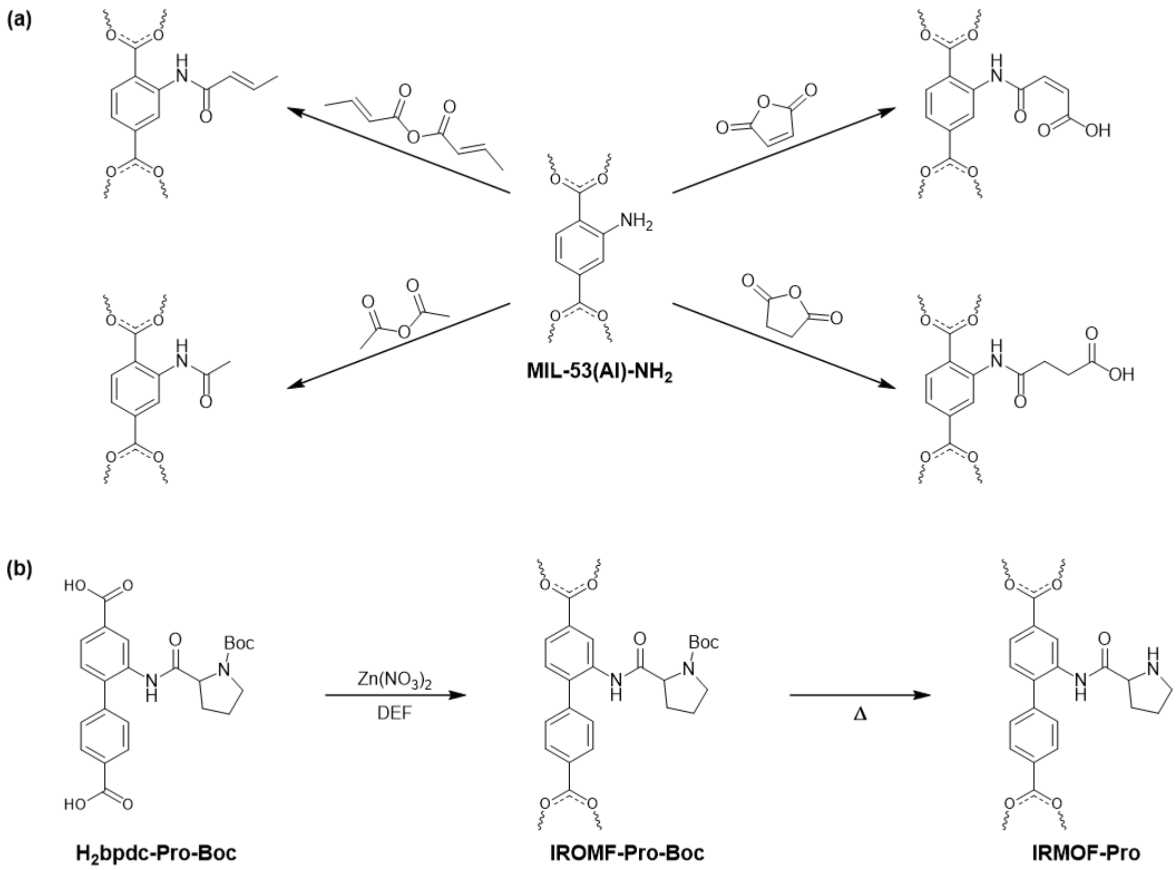

Figure 1-10. (a) Four different functional groups were added to the bdc-NH_2 ligand in MIL-53(Al)-NH_2 by forming a covalent bond through the PSM; (b) A brief scheme of PSD; IRMOF-Pro-Boc was synthesised from the Boc protected ligand, then the Boc group was removed by thermolysis to yield IRMOF-Pro.

containing ligands experience undesired processes during conventional MOF synthesis due to their Lewis basic nature. The nitrogen atom on the pyrrolidine ring can coordinate to the metal node hindering MOF formation or be protonated under the synthetic condition, thus removing its catalytic activity. They solved this problem by protecting the nitrogen atom of the proline moiety on the bpdc ([1,1'-biphenyl]-4,4'-dicarboxylic acid) ligand with a Boc (tert-butoxycarbonyl) group. After MOF synthesis, the activated crystals were then exposed to elevated temperatures (150-200 °C), and the Boc-protecting group was removed entirely from the framework by thermolysis. This approach also brought another benefit because of the large Boc protecting group. IRMOF-10 normally forms a doubly interpenetrating structure, which is known as IRMOF-9, due to its sizeable inner pore, but the concatenated structure formation was suppressed by the bulky protecting group.

1.1.5.3. Replacing structural components

Designing a new MOF is quite challenging due to its geometrical complexity in three-dimensions. Moreover, synthesising the designed structure is complicated since it is governed by unpredictable thermodynamics. A subtle change of any factor may cause a considerable difference in MOF formation. Thus, modifying a known framework to embed specific properties or to accomplish the desired functionality is often prefered. However, *de novo* synthesis with a similar replacement of metal ion or organic linker sometimes results in the same structure. Transmetalation or solvent-assisted linker exchange (SALE) is a generally adopted method in such cases in which the exchange of structural components can be achieved non-destructively. Transmetalation can be applied if the incoming metal ion has similar properties to the existing one. It can increase the stability of the MOF or introduce new chemical functionality. Song et al. demonstrated the feasibility of transmetalation and the stability and chemical property differences between the structures before and after transmetalation.[47] They prepared four isostructural MOFs, $M_6(BTB)_4(BP)_3$ (M = Zn(II), Co(II), Cu(II), and Ni(II), BTB = benzene-1,3,5-tribenzoate, and BP = 4,4′-bipyridyl), and the metal ion in each MOF was exchanged with other metal ions. The result illustrated that the metal ion that forms the thermodynamically more stable structure was not exchangeable with the ones forming the less stable structures. In contrast, the metal ion that forms a less stable structure was easily replaced with the ones constructing more stable frameworks. The stability order of the MOFs containing each of the four metal ions was well consistent with the trend in the Irving-Williams series, Cu(II) > Ni(II) > Co(II) ≈ Zn(II).

In 2012, Cohen's group reported impressive results known as a postsynthetic exchange (PSE).[48] They demonstrated that a structural component, either metal ion or ligand, was exchangeable with another one that was leached out from other crystal samples. For example, two isostructural MOF samples, MIL-68(In)-NH_2 and MIL-68(In)-Br, were prepared from 2-aminoterephthalic acid (bdc-NH_2) and 2-bromoterephthalic acid (bdc-Br), respectively. The two samples were then mixed in the same vial with solvent and incubated well below the synthesis temperature for a certain amount of time. Interestingly, both bdc-NH_2 and bdc-Br ligands were found in a single-crystal sample, which indicates that the bdc ligand leached out from a crystal and replaced another bdc ligand in another crystal.

In 2013, Farha's group reported a family of MOFs named SALEM (solvent-assisted linker exchanged material) that showed a fascinating structural transformation by SALE.[49] As depicted in Figure 1-11, a pillared-paddlewheel MOF was synthesised with two ligands, L0 and L1, and Zn(II). The linear linker, L1, has a relatively weak coordination bond to the paddlewheel cluster through the terminal N-donating pyridine so that it can be replaced by other N-donor ligands. However, they have demonstrated the complete structure change by using various lengths of linear pillars, L2 (8.795 Å), L3 (11.440 Å), L4 (13.527 Å) and L5 (16.511 Å). SALEM-5 was first prepared by exchanging L1 of the parent structure with L2, then L2 was further replaced by L3, L4, or L5 in order to form SALEM-6, SALEM-7 or SALEM-8, respectively. Complete ligand exchange was evidenced by ^{1}H NMR spectra of each

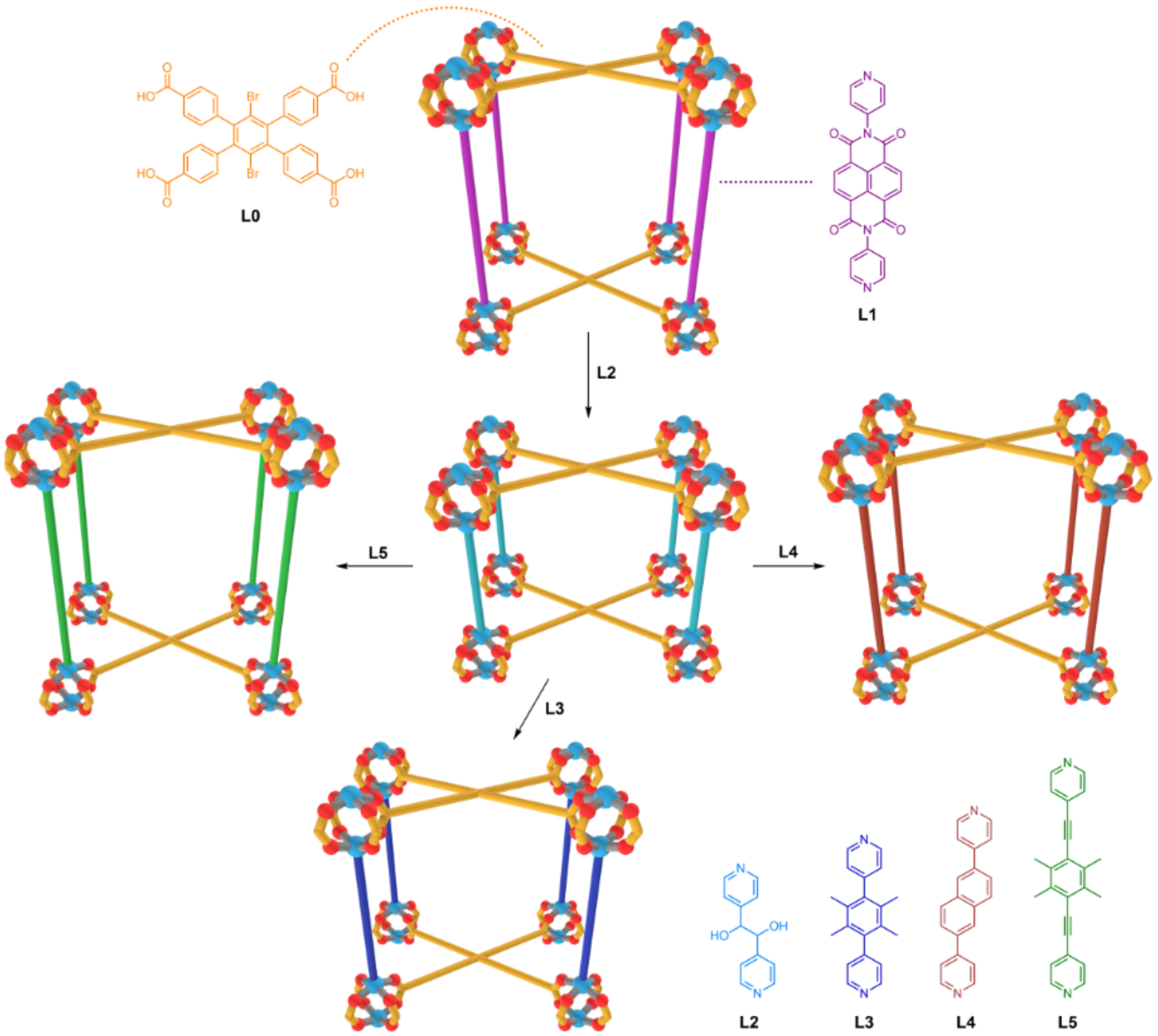

Figure 1-11. The parent structure was built from ligand L0 and L1 along with Zn(II). The linear ligand L1 was exchanged with L2, and then L2 was successively exchanged with L3, L4 or L5 by means of SALE. The blue sphere represents Zn.

digested MOF, and a morphological change of a single crystal during SALE was not observed by optical microscopy.

1.2. Diversity of MOFs

As discussed in the previous section, MOF structures are composed of two main building blocks, secondary building units (SBUs) and organic ligands. Although the SBUs are not physically separable from the frameworks, exploiting these conceptual structural components is merited in order to understand or to design new frameworks. For instance, the $Zn_4O(COO)_6$ SBU forms an octahedral geometry with six carboxylates extending in specific directions. Thus, the expected structure can be pictured as long as the same metal ions and carboxylate based ligands are used for MOF synthesis. The structural diversity of MOFs can be extended by utilising the various geometrical shapes of SBU and ligand assemblies, so pores with different sizes or shapes can be designed for specific purposes.

Moreover, an extensive range of chemical pendant groups can be added to decorate the ligand backbones surrounding such pores, thereby bringing chemical diversity into the pore environment.

1.2.1. Isoreticular chemistry in MOFs

Isoreticular chemistry is a simple but powerful and fundamental concept for designing MOF structures. The basic strategy is to replace a structural component of an existing MOF with a slightly modified building component but by retaining the same topology. The IRMOF (isoreticular metal-organic framework) series is a textbook example demonstrating the concept of isoreticular chemistry.[50] As depicted in Figure 1-12, the IRMOF series shares the same topology, primitive cubic unit (**pcu**), but is built from different linear ditopic carboxylate based ligands. These ligands can be divided into two, whether they have a different functional group(s) or a different length. This work clearly shows the fundamental principle of isoreticular chemistry in MOFs, which allows the systematic tuning of pore size and functionality. However, this isoreticulation is not the master key for designing a new structure since the interpenetrated structures can be formed as the void space grows sufficiently large to accommodate an additional net. For instance, a mutually interpenetrated structure was formed with the extended ligands (8–12 in Figure 1-12) when the concentration of ligands in the synthetic mixture is high. In some cases, the interpenetrated structure can be intentionally prepared and demonstrates a better performance for a specific use. However, interpenetration often occurs rather serendipitously and is hard to anticipate in the designing stage.[51]

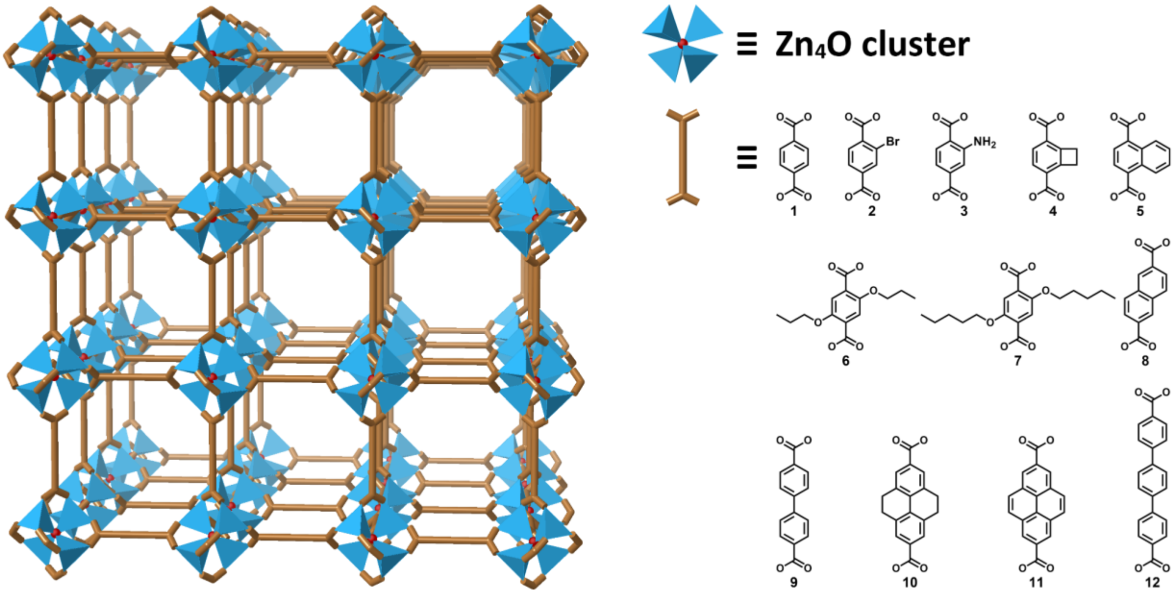

Figure 1-12. 3×3 Unit cell of IRMOF with **pcu** topology is shown on the left, and various linear organic ligands are depicted on the right. The ligands sharing the same backbone are presented with the same colour.

1.2.1.1. Physical diversity

Pore size is a readily controllable parameter that can be achieved by adjusting the ligand size. The IRMOF-74 series is built from ditopic linkers with various lengths. It is an iconic example of pore size control because the size of pores varies from 10 Å to 85 Å in diameter without any interpenetration.[52] The parent framework, MOF-74, was built from Zn(II) and DOT (2,5-dioxidoterephthalate) with the honeycomb type **etb** net topology (Figure 1-13b); the two *ortho*-hydroxyl functionalities on DOT play a crucial role in forming infinite SBUs, as shown in Figure 1-13c.[26] Therefore, all the ligands in this IRMOF-74 series have an *o*-hydroxyl group on each terminal benzoic acid moiety, and some of them possess alkyl groups on the phenyl rings in the middle to improve their solubility (Figure 1-13a). These IRMOF-74 materials have an exciting feature due to the wide range of pore apertures. For example, the pores in IRMOF-74-VII are large enough to be seen by electron microscopy, and the TEM image of IRMOF-74-IX showed the distinct honeycomb shape pores. Also, the size of this second-largest pore of IRMOF-74-IX was able to accommodate the green fluorescent protein (barrel structure with a diameter of 34 Å and length of 45 Å).

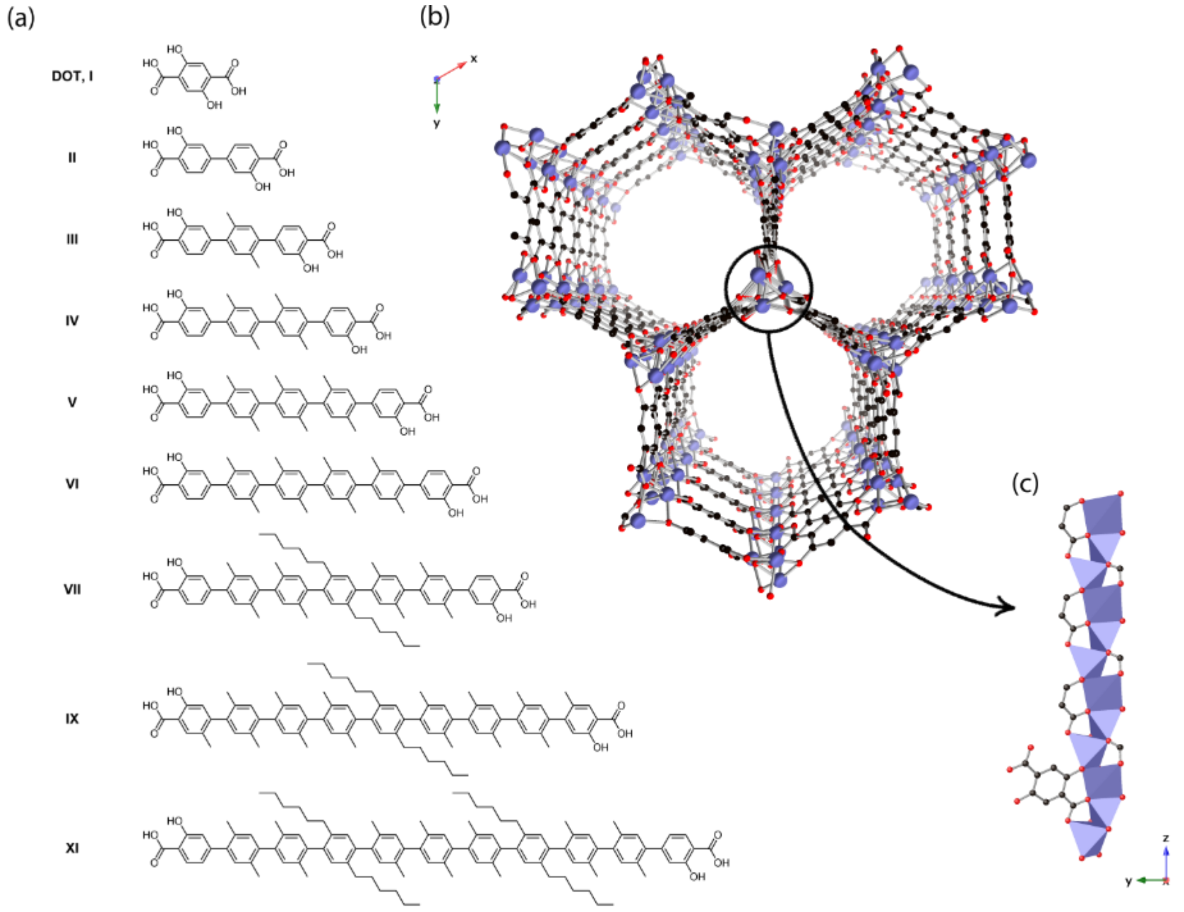

Figure 1-13. (a) Ditopic linear linkers to synthesise MOF-74 series; (b) ball and stick representation of MOF-74 structure indicating 1D channel pore; (c) the polyhedra model of a continuous SBU along the z-axis with a coordinating DOT ligand which illustrates how *o*-hydroxyl group cooperates with carboxylate to form the infinite SBUs.

The PCN-6x series is another example showing the physical diversity of pores keeping the same **rht-a** topology (Figure 1-14a).[53] Although the ligands, dendritic hexatopic carboxylate ligands with C_3 symmetry, exploited for this family of MOFs are geometrically a lot more complicated than the previous linear ones, the same isoreticular principle is applied. These carefully designed ligands, btei, ntei, ptei and ttei (Figure 1-14b), have slightly different length of arms, thereby forming various sizes of frameworks, PCN-61, -66, -68 and -610, respectively. The trend of the increased surface area of the MOFs match the increasing trend in pore sizes according to BET (Brunauer–Emmett–Teller[54]) calculations from N_2 adsorption measurement at 77 K. An impressively high H_2 uptake at 77 K for these three frameworks was also reported. It also followed the same trend, 73.2 $mg{\cdot}g^{-1}$, 66.5 $mg{\cdot}g^{-1}$ and 62.4 $mg{\cdot}g^{-1}$ for PCN-61, -66 and -68, respectively. However, the opposite trend was shown when the gravimetric capacity was converted to volumetric capacity by the crystal-density data, which indicates PCN-61 is advantageous for volume-limited application, such as fuel cells.[53]

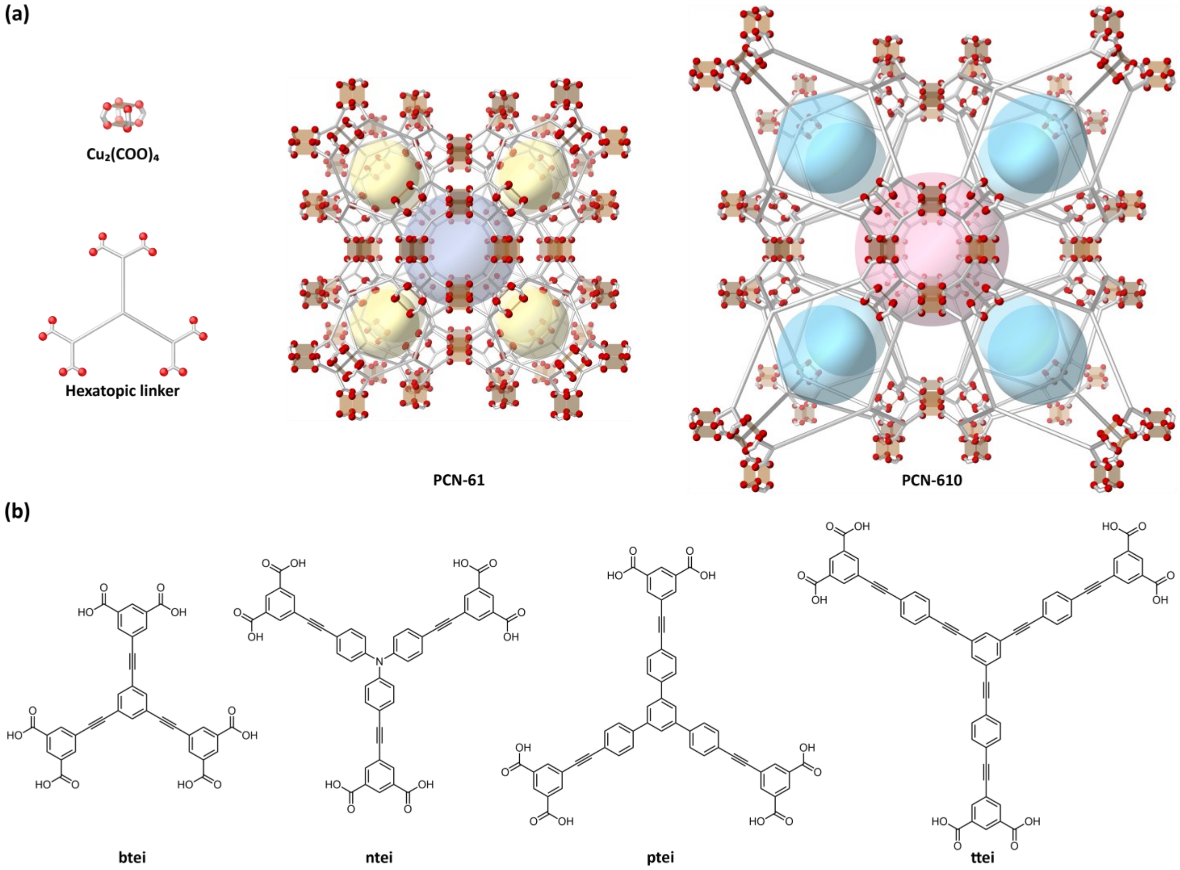

Figure 1-14. (a) The smallest (PCN-61 with btei) and largest (PCN-610 with ttei) frameworks in the PCN-6x series; (b) hexatopic linkers building PCN-6x series. The large spheres indicate void spaces in the frameworks.

1.2.1.2. Chemical diversity

In isoreticular MOFs, the size of the pores is mainly governed by the ligand geometry. In contrast, the chemical environment of pores can be altered by both organic ligands and metal ions. Such chemical modifications can occur by using topologically similar building units with different chemical properties, such as decorating with different secondary functional groups on the same ligand backbone or adapting different metal ions possessing similar coordination behaviour.

The isoreticular series of cobalt-adeninate bio-MOFs-11–14 demonstrated a dramatic enhancement of CO_2/N_2 selectivity and moisture stability by changing the aliphatic carbon chain length sticking into the pores.[55] The nitrogen-rich adenine was judiciously selected to enhance the interaction with CO_2 gas molecules. As depicted in Figure 1-15a, two N atoms, N4 and N5, in adeninate are free non-bonding atoms. On the other hand, N1 coordinates to the axial position of the cobalt paddlewheel SBU while N2 and N3 bridge the two cobalt atoms on the lateral position of the SBU (Figure 1-15b). Two carboxylate groups also participate in composing the paddlewheel SBU. These carboxylates were sourced from different cobalt salts, cobalt acetate, cobalt propionate, cobalt butyrate and cobalt valerate, which respectively form bio-MOF-11, -12, -13 and -14. The various lengths of alkyl chains attached to the α-carbon of the carboxylate extend into the channel space along with the free nitrogen N4 and N5, and they play a critical role in enhancing CO_2/N_2 separation and water stability. Figure 1-15c illustrates bio-MOF-12 with propionate; the alkyl chains depicted in orange show the pore filling behaviour. This channel blockage increases as the chain length grows. According to a gas adsorption study, the more the extension in the aliphatic chain, the

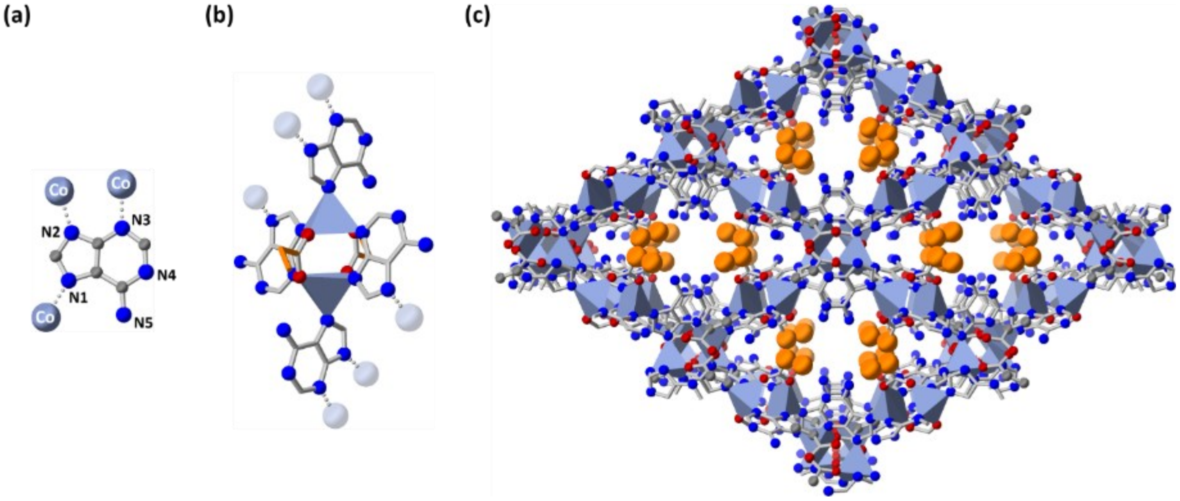

Figure 1-15. Bio-MOF-12, (a) non-bonding nitrogen atoms, N4 and N5 in adeninate; (b) each pair of propionate and adeninate coordinates on the equatorial position and another pair of adeninate coordinates on the axial position of the cobalt paddlewheel SBU through neutral nitrogen atom, N1; (c) the free nitrogen N4 and N5, and the carbon chains depicted in orange exposed to the channel space. Hydrogen atoms were omitted for clarity.

lesser the amount of N_2 isotherm uptake was observed at 298 K. In fact, a negligible amount of N_2 uptake was measured with bio-MOF-14, which has a valerate group. On the other hand, bio-MOF-14 shows a higher uptake of CO_2 due to the strong interaction between CO_2 molecules and the framework. A water stability test was also conducted by soaking each crystal samples in water for an hour, and bio-MOF-14 did not lose any crystallinity while bio-MOF-12 and -13 partially lost crystallinity or bio-MOF-11 wholly dissolved in water. Moreover, the CO_2 uptake capacity of bio-MOF-14 after soaking in water for 30 days was similar to the pristine material.

MOFs built from topologically distinct multiple organic linkers are denoted as MC-MOFs (multicomponent metal-organic frameworks), which will be discussed in the later section in detail. They generally possess several pores with diverse sizes and environments. Due to the topological difference of each ligand, the position of each ligand is determined during self-assembly, which allows us to predict the positions of chemical functional groups installed to each ligand in a pore. Therefore, the chemical environment of pores in MC-MOFs can be designed using various chemical pendants installed on separate ligands.

The isoreticular MUF-7 series is the first quaternary MOF built from three different organic ligands and one metal ion. MUF-7 series demonstrates designable and programmable pore environments.[56] As shown in Figure 1-16, three sets of ligands were prepared with two different versions, with or without a chemical pendant on the same backbone. Therefore, eight different frameworks were synthesised from either functionalised or non-functionalised ligands by exploiting the isoreticular principles. For instance, MUF-7a is built

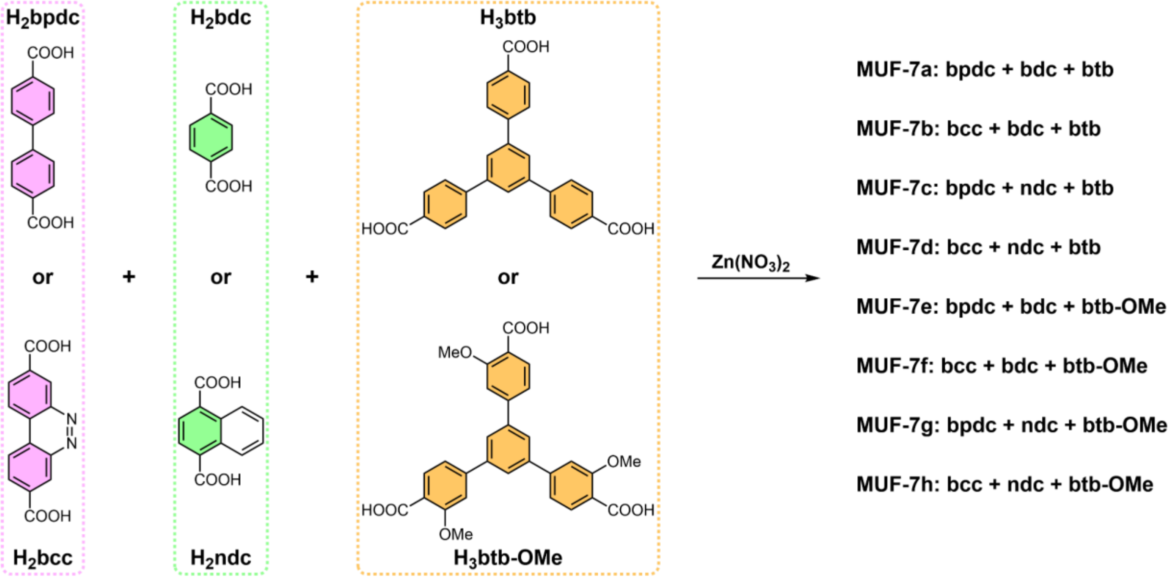

Figure 1-16. A schematic diagram of the syntheses of a MUF-7 series. Eight different MOFs which provide a distinct pore environment are synthesised from various combinations of the non-functionalised or functionalised version of each ligand set.

from all non-functionalised ligands (bpdc, bdc and btb), whereas MUF-7b is comprised of one functionalised ligand (bcc) and two non-functionalised ligands (bdc and btb).

All eight structures were confirmed to be identical by the PXRD (powder X-ray diffraction) and SCXRD (single-crystal X-ray diffraction) measurements, and no structural defects were noticed from the ^{1}H NMR spectrum of each digested MOF solution. However, interestingly, the pore size distributions of all eight frameworks varied based on the existence of pendant groups occupying pore spaces and such differences were reflected in the BET surface area of each MOF and its CO_2 uptake. According to the BET calculation from the N_2 isotherm measurement at 77 K, the lowest surface area was 3000 $m^2 \cdot g^{-1}$ for MUF-7f while the highest was 4480 $m^2 \cdot g^{-1}$ for MUF-7b. The CO_2 uptake (273 K, 1200 mbar) ranged from 30.3 $cm^3 \cdot g^{-1}$ (MUF-7a) to 58.8 $cm^3 \cdot g^{-1}$ (MUF-7h).

Utilising different metal ions can also change the chemical diversity of MOFs. The earlier example in the previous section (1.1.5.3) demonstrated that the stability of frameworks increased as Zn(II) was exchanged with Ni(II) or Cu(II) by a postsynthetic exchange process.[47] Alteration in chemical or thermal stability upon a change in metal ions is widely observed, for example, in trivalent metal ions, Cr^{3+}, Al^{3+} and V^{3+} in the MIL-53 series.[57] Another family of MOFs, LIFM-10 (LIFM: Lehn Institute of Functional Materials, Figure 1-17a) which was prepared from three different metal ions, Co(II), Cu(II) and Zn(II), and an organic linker H_2INOIA (1-oxidopyridin-1-ium-4-ylaminocarbonyl) was also reported that the stability of frameworks follows the trend of Irving-Williams series.[58] According to SCXRD measurements, the three frameworks have nearly identical unit cells, and their pore volumes are very close to each other. However, the subtle discrepancy induced by the different metal ions causes a vast divergence in BET surface areas and CO_2/CO selectivities (Figure 1-17b).

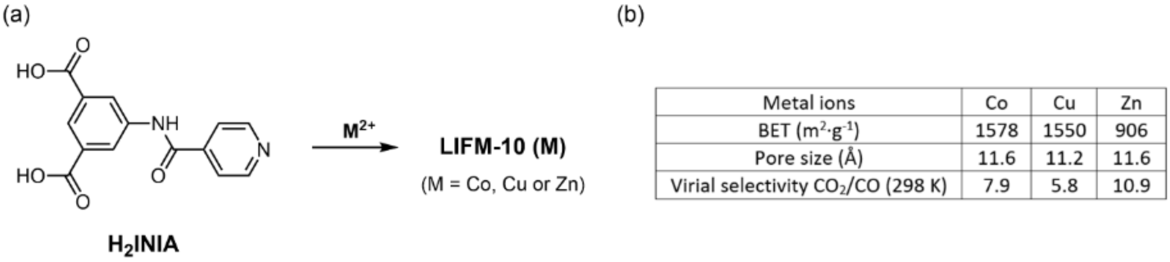

Metal ions	Co	Cu	Zn
BET ($m^2 \cdot g^{-1}$)	1578	1550	906
Pore size (Å)	11.6	11.2	11.6
Virial selectivity CO_2/CO (298 K)	7.9	5.8	10.9

Figure 1-17. (a) Brief scheme of formation of LIFM-10 series; (b) a few distinct properties of each MOFs composed of different metal ions.

1.2.2. Complexity and heterogeneity in MOFs

MOFs are a new type of material that does not exist in nature, and MOF chemistry is a fast-growing area and expanding its territory into real world applications. As it attracts the attention of many researchers, research topics have diverged, and the demand for specific functionalities and properties has grown. Above all, exploiting more diverse building blocks is a prominent and more accessible way to achieve such a demand. Therefore, the needs to make MOFs with more diverse building blocks are increasing. Designing and synthesising the MOFs is somewhat similar to making an object with the Lego® blocks. To make the desired model, of course, the more shape and colour of blocks you have, the easier it is to make. As the shape of Lego® blocks gets diverse, the complexity increases, thus the more diverse geometries are obtainable though not easier to achieve. On the other hand, as more colours of each block are allowed, the heterogeneity of blocks increases, and thereby the more details can be expressed. The same strategy is applied for MOF design and synthesis with an increased number of building blocks, increasing in complexity or in heterogeneity of building blocks.[59]

The majority of reported MOFs are binary MOFs which are composed of two building blocks, a single type of metal ion and an organic linker. MOFs made with more than two building blocks can be divided into two main categories. MOFs, built from geometrically and topologically different building blocks, are denoted as MC-MOFs (multicomponent MOFs), as discussed with MUF-7 (Figure 1-16). In contrast, MOFs made from building blocks, which are structurally identical but chemically different, are referred to as MTV-MOFs (multivariate metal-organic frameworks). For instance, the two ligands, bdc and bdc-Br, share the same backbone allowing them to be interchangeable within a framework since they have the same length and coordination geometry. Therefore, an MTV-MOF, comprised of both bdc and bdc-Br, can be built if both ligands were simultaneously used for MOF synthesis.

A critical difference between these two concepts is whether each building unit is arranged in order or in random in the framework. In other words, the different building blocks in MC-MOFs have different geometry, so their positions were determined by the entire network. On the contrary, the building blocks in MTV-MOFs possess the same structural feature, like bdc and bdc-Br, so there is no way to differentiate those building units. Thus, those building blocks would be randomly positioned in MTV-MOFs.

1.2.2.1. Multicomponent MOFs (MC-MOFs)

Compared to the binary MOFs, the number of MC-MOFs is relatively small; moreover, only a handful of MOFs are known to consist of four or more building blocks. It is because MOF formation is governed by many factors. Even with the simplest bdc ligand and the zinc ions which are known to form MOF-5, various topologies can be produced depending on the synthesis condition or many other factors, such as type of metal salt, synthesis solvent, pH, temperature, or presence of other additives.[60-66] Therefore, synthesising MC-MOFs is more challenging than synthesising the binary MOFs due to the increased complexity.

The study conducted by our group about MUF-8 and MUF-84 series well illustrates how delicate MC-MOFs formation is.[67] Both MUF-8 and MUF-84 series are composed of a tritopic linker, ntb (4,4',4''-nitrilotribenzoate), and various bdc derivatives, but their topologies are entirely different. Such a structural difference between the two frameworks was caused by the number of secondary functional groups on the phenyl ring of the bdc linker. MUF-8 is preferentially formed as more substituents are attached on the bdc linker, whereas the bare bdc or with one substituent form phase pure MUF-84, as depicted in Figure 1-18. Furthermore, the study shows that the ratio between the two organic ligands, ntb and bdc derivative, was a critical factor to control the MOF structure if a bdc derivative with two substituents was used.

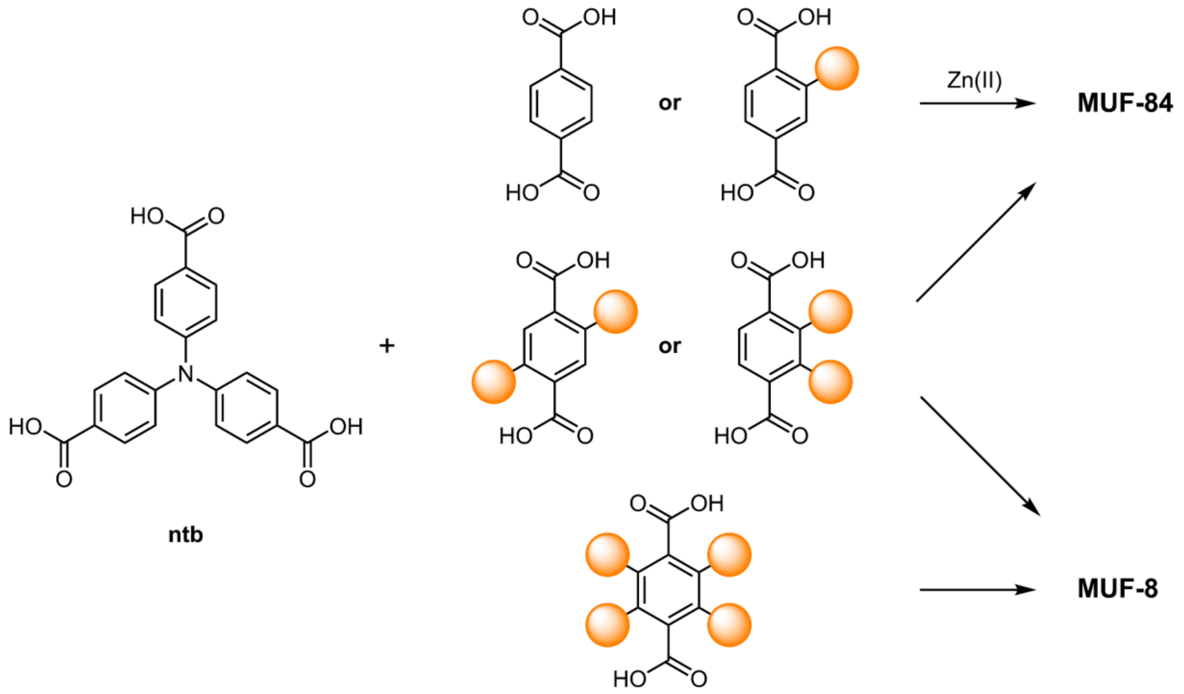

Figure 1-18. A schematic diagram of MUF-8 and MUF-84 synthesis.

Another major challenge for synthesising MC-MOFs is that there are multiple potential structures that can be formed by the subsets of building block combinations. For instance, as illustrated in Figure 1-19, MUF-7[56] is built from Zn_4O clusters and three topologically distinct ligands, bpdc, bdc and btb. However, each ligand can form its own MOF with the Zn_4O cluster resulting in IRMOF-10[50], MOF-5[4] and MOF-177[68], respectively. Also, two MC-MOF structures, SUMOF-4[69] (SUMOF: Stockholm University metal-organic framework) and UMCM-1[8] can be formed from the zinc cluster and two subset combinations, either bpdc and bdc or bdc and btb, respectively. This example clearly demonstrates how MC-MOF synthesis is challenging. Nevertheless, MUF-7 forms eventually by beating competing side products. This means that the MUF-7 structure is the thermodynamically favoured structure under these conditions.

The chemical environment of the pore in binary MOFs is reasonably simple due to its low complexity (Figure 1-19). In comparison, the complexity increases for the tertiary and quaternary MOFs. Their pore environments become more chemically and physically diverse. Besides, like MUF-7h in figure 1-16, multiple pendant groups can be introduced to bring a specific chemical environment to the pore in a controlled way, which cannot be achieved in the binary MOFs. For this reason, the demand for MC-MOFs is increasing, and its niche in the field is becoming sturdy despite the tough synthetic challenges.[70]

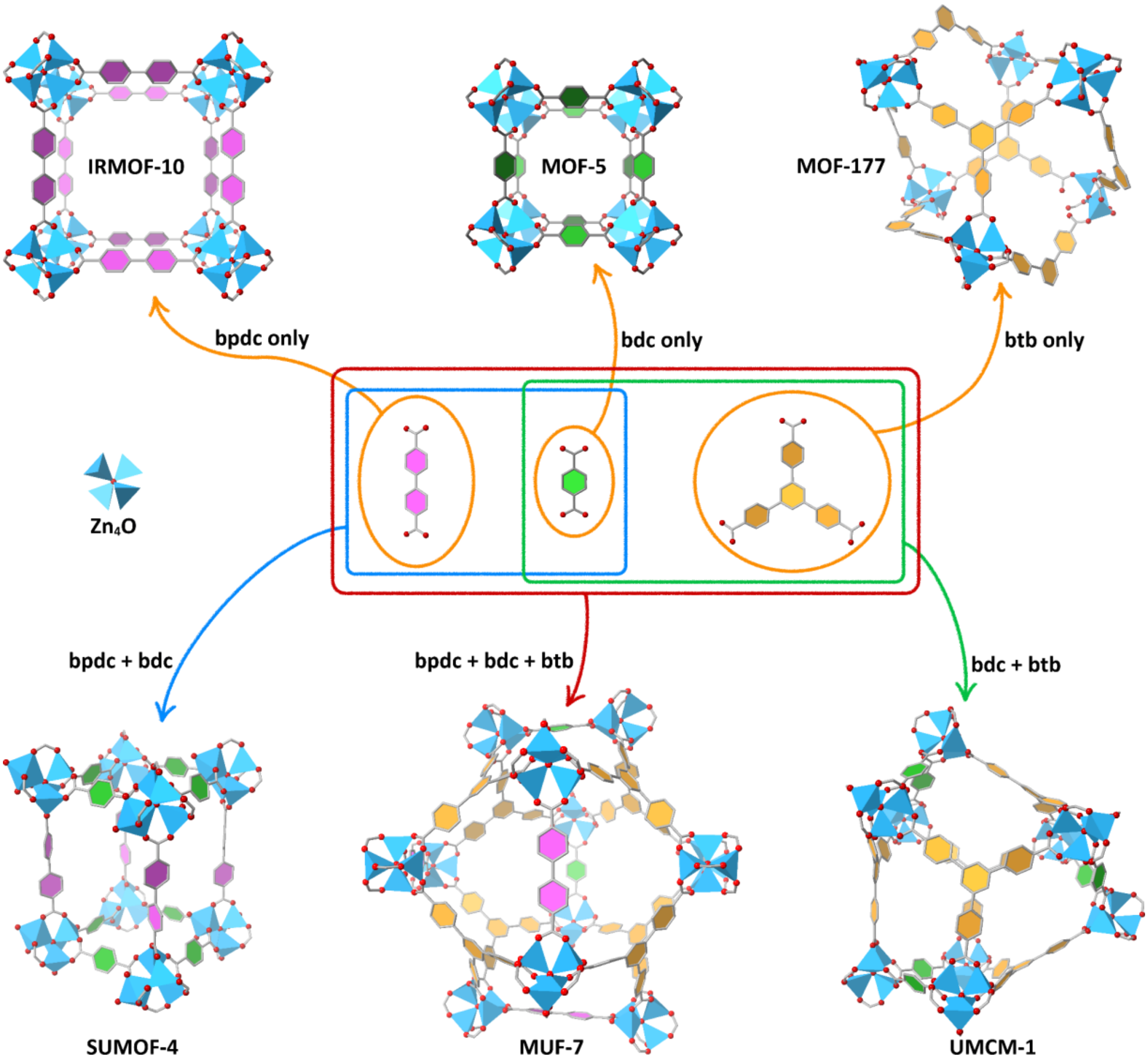

Figure 1-19. The various potential outcomes from the MUF-7 synthesis. Each ligand can form its own MOF as the orange arrows indicate, and two subsets of two ligands combination also form the distinct structure as indicated with blue and green arrows. MUF-7 can be formed only in the case of winning the competition among the potential MOF formations.

So far, FDM-8 combines the most building blocks in a one-pot synthesis, two inorganic components Zn(II) and Cu(II) and three organic linkers, bdc, 2,6-ndc (naphthalene-2,6-dicarboxylate), and PyC (pyrazole-4-carboxylate).[71] FDM-8 is isoreticular with MUF-7, possessing **ith-d** topology. The tritopic linker btb in MUF-7 was replaced with a complex of Cu(I) and PyC, which forms the planar three connected metalloligand. The linear bpdc was substituted by ndc. This example illustrates the strategy of how to expand complexity by replacing an organic component with a complex molecule.

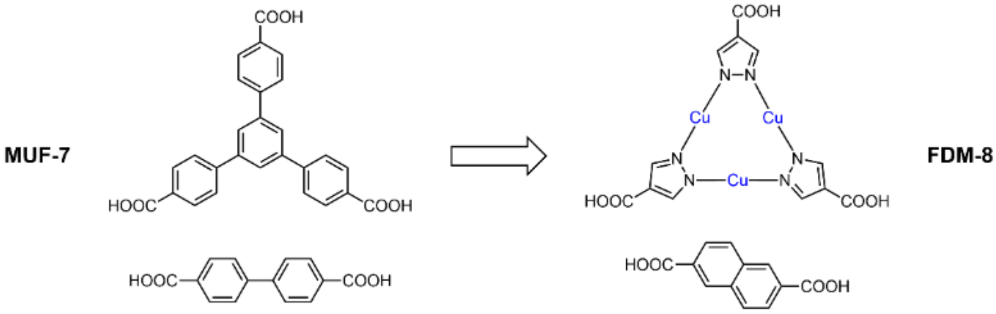

Figure 1-20. The tritopic btb in MUF-7 was replaced with the complex of Cu(I) and PyC, and the linear bpdc was replaced with a slightly shorter linker, ndc.

1.2.2.2. **Multivariate MOFs (MTV-MOFs)**

MTV-MOFs are built from the building blocks which have the same coordination geometry. Thus these compatible building blocks are randomly distributed in the framework and increase the homogeneity of the pore environment. MTV-MOF-5[72] and MTV-MOF-74[73] series are the representative cases of MTV-MOFs. MTV-MOF-5, as the name suggests, is isoreticular with MOF-5 and is built from two to nine different bdc derived linkers possessing various secondary functional groups. The bdc derived linkers are randomly distributed in the well ordered crystalline structure (Figure 1-21a) so that each pore has the chemical and physical properties from a large number of functional group combinations. Depending on the specific combination of the ligands, the resulting structure showed enhanced in CO_2/CO separation or BET surface areas compared to the parent MOF-5. Likewise, MTV-MOF-74 is an isoreticular analogue of MOF-74, and it accommodates up to ten different metal ions by the one-pot synthesis or PSE (Figure 1-21b). This work demonstrated that some trivalent metal ions like Ti^{3+}, V^{3+} or Cr^{3+}, or metal ions, such as Ca^{2+}, Sr^{2+}, Ba^{2+} or Cd^{2+}, which cannot be employed in the *de novo* synthesis, could be introduced to the framework via postsynthetic exchange.

As shown in the above two examples, MTV-MOF synthesis is relatively more straightforward than that of MC-MOFs, because the analogues of building units have structurally compatible properties which allow them to replace the existing ones in the parent structure by direct

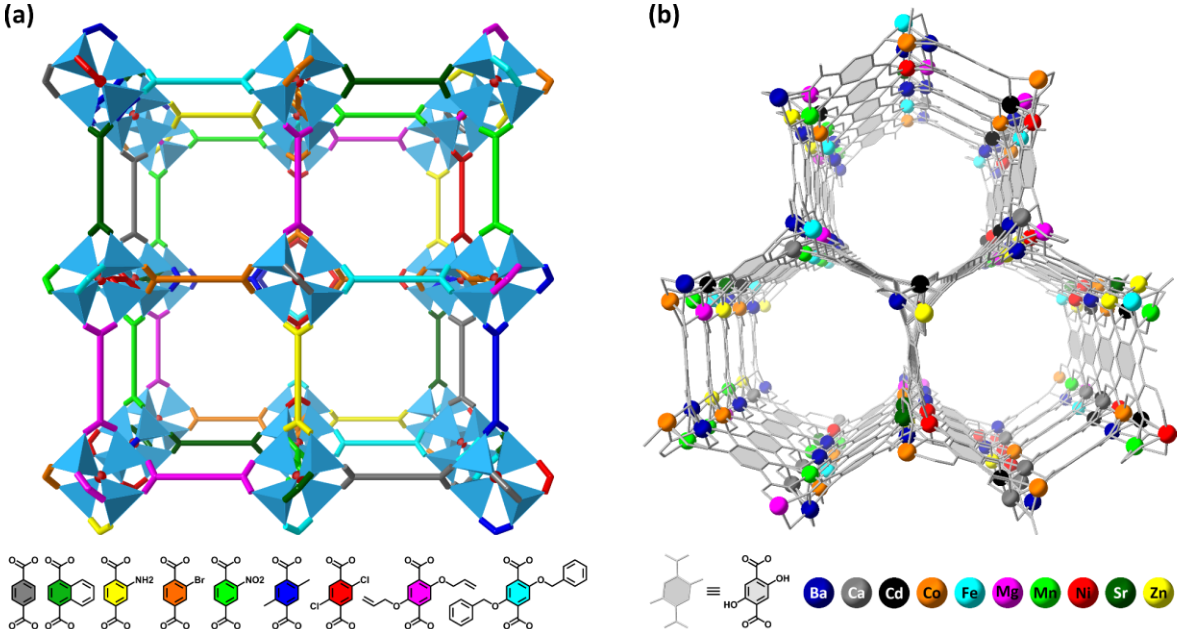

Figure 1-21. (a) MTV-MOF-5, which was built from nine different bdc derived linkers possessing a various functional group(s); (b) MTV-MOF-74, which consists of ten different metal ions.

synthesis or PSE. Therefore, enriching the chemical environment in the pore is readily achievable, which can accidentally lead to some good results through the ensemble of such diverse chemical moieties. However, increasing randomness is inevitable as the heterogeneity increases in the frameworks, which make it hard to expect the constant outcome at all times and to analyse the underlying mechanism for the obtained results.[74-75]

1.3. Application of MOFs

MOFs can be prepared as nanoscale powders through millimetre-sized single crystals. They possess an uncountable number of pores of various sizes, from Ångstrom- to micro-scale. This is the main reason why the area of MOF is proliferating, creating synergy with other chemistry fields. Compared to other conventional porous materials, the enormous porosity is the most distinct feature of MOFs. For this reason, the earlier application of MOFs was focused on what exploits such porosity, like gas storage or catalysis. As briefly mentioned about the applications of MOFs in the previous section (1.1.2), the collaboration with other areas of chemistry increases with ingenious ideas, such as making porous glass by melting MOFs or using MOF itself as a hypergolic fuel source.[76-77] A selection of some important applications of MOFs will be briefly introduced here.

1.3.1. Hydrogen storage and CO_2 capture

1.3.1.1. H_2 storage

Hydrogen, the most abundant element in the universe, is a clean energy source with a very high energy density. However, it is not easy to find real applications that exploit hydrogen as an energy source in our daily life. Probably, hydrogen vehicles, which operate using hydrogen fuel cells or by burning hydrogen in an internal combustion engine, are the only cases showing visible outcomes at present. The reason is that about 95 % of hydrogen production relies on the steam reforming of natural gas, which produces carbon dioxide as a byproduct. Also, the cost required to build infrastructure for utilising hydrogen as an energy source is enormously high compared to other energy sources. Furthermore, storing hydrogen requires high pressures and low temperatures, and the efficiency of the current hydrogen storage technology is yet not at a satisfactory level.[78]

Porous materials have been extensively studied to enhance the storage capacity of H_2. Physisorption in porous materials allows rapid uptake and release of H_2. MOFs are attracting great interest due to their controllable pore size and designable pore environment, which may enhance the interaction between H_2 and the adsorbent. Ever since H_2 uptake behaviour was first demonstrated by MOF-5, which presented 4.5 wt % at 77K and 1 atm,[79] many other studies have been conducted to increase the H_2 storage capacities with various approaches. The critical driving force in the physisorption is the dispersion forces between the adsorbate and adsorbent. Therefore, a comparable pore dimension to the kinetic diameter of the H_2 molecule (2.89 Å) is advantageous, which allows more interaction through dispersion force between H_2 molecules and the surroundings.

According to Schröder,[80] the total uptake of H_2 is related to the BET surface area and the pore volume. However, a larger pore size requires a higher pressure to store the same amount of H_2. Such trends were well demonstrated by the first three frameworks in the isoreticular NOTT-10x series (x = 0, 1, 2 and 3) (Figure 1-22). As the ligand length gets elongated, the pore diameter becomes larger (6.5 Å, 7.3 Å, 8.3 Å for NOTT-100, -101 and -102, respectively), thereby resulted in increased BET surface area and pore volume. However, the H_2 uptake at 1 bar, a low pressure, presented the opposite trend, which indicates the affinity of the H_2 molecule toward the framework gets increased as the pore size decreases. Based on these observations, they have calculated the optimum pore size that would provide increased interaction with H_2 gas molecules. Based on the calculation, L4 was prepared, and NOTT-103 was synthesised using L4. As expected, NOTT-103 showed enhanced H_2 uptake in both low and high-pressure ranges, and this was because of not only the optimised pore size but also

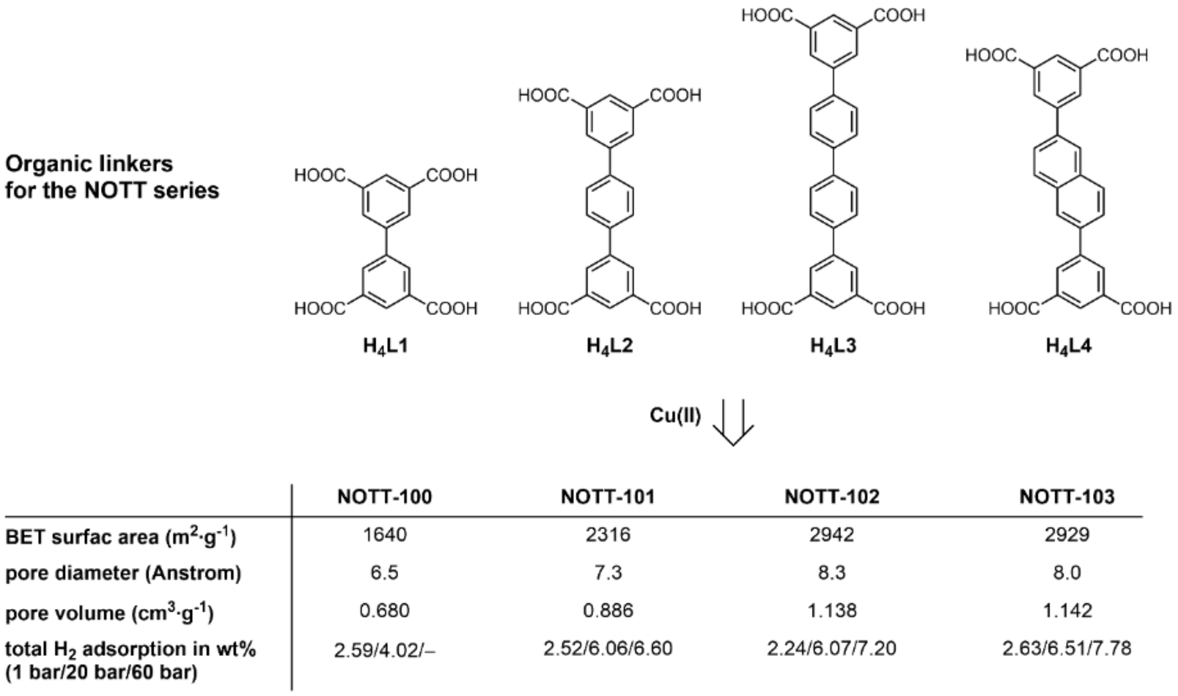

	NOTT-100	NOTT-101	NOTT-102	NOTT-103
BET surfac area ($m^2 \cdot g^{-1}$)	1640	2316	2942	2929
pore diameter (Anstrom)	6.5	7.3	8.3	8.0
pore volume ($cm^3 \cdot g^{-1}$)	0.680	0.886	1.138	1.142
total H_2 adsorption in wt% (1 bar/20 bar/60 bar)	2.59/4.02/–	2.52/6.06/6.60	2.24/6.07/7.20	2.63/6.51/7.78

Figure 1-22. NOTT-100, -101, -102 and -103 were prepared from the organic linker L1, L2, L3 and L4, respectively along with Cu(II). The BET surface area, pore diameter, pore volume and total H_2 adsorption in wt% of each framework were also presented.

the central functional group (naphthyl) which provide a stronger potential overlap to enhance adsorption of H_2 at low pressures.

Catenation is another strategy to control the pore size of the frameworks. Interpenetrated frameworks have widely been observed when the framework is built from elongated building blocks. It is due to the tendency of minimising the free space of the framework so that smaller pores are formed as a result. Therefore, judiciously designed interpenetrated structures can be used to improve H_2 uptake capacity.[11] PCN-6 (interpenetrated) and PCN-6' (non-interpenetrated) were prepared from 4,4′,4″-s-triazine-2,4,6-triyl-tribenzoate (isoreticular structure of the PCN-6x in Figure 1-14), and they are the right example demonstrating such an approach. According to Ma, the total H_2 adsorption capacity of the interpenetrated structure of PCN-6 could reach 8.7 wt % (77 K/50 bar), whereas the one of PCN-6' was 5.5 wt %.[81] Due to the long distance (21.4 Å) between opposite walls in PCN-6', the centre of the pore remained empty. However, catenation leads to closer distances between the walls, enhancing the interaction between pore walls and H_2 molecules, thus increasing the number of binding sites.

In addition to pore size control, generating open metal sites (coordinatively unsaturated sites at the metal or metal cluster) is another efficient strategy to enhance the H_2 uptake capacity. In some cases, the open metal sites can be readily generated by removing coordinated solvent molecules or neutral ligands at nodes. Such molecules are typically

Lewis basic and coordinate to a metal centre with a weak bond so that they can be removed by lowering pressure or mild heating.[25] Open metal sites result in strong interactions with H_2 molecules. As shown in Figure 1-13, MOF-74 possesses a hexagonal 1D-channel, and the synthesis solvent molecule coordinated to the exposed metal site to the channel space can be easily removed by mild activation condition. This consequently creates an open metal site alongside the channel space. Zhou et al. have demonstrated the binding trend between various divalent transition metal ions and the H_2 molecule in MOF-74.[82] Five different isoreticular MOF-74s were prepared from Mg(II), Mn(II), Co(II), Ni(II) and Zn(II), and open metal sites were generated. Then the relative strength of the interaction between M^{2+} and H_2 was investigated. Their result showed that the H_2 binding follows the trend of $Zn^{2+} < Mn^{2+} < Mg^{2+} < Co^{2+} < Ni^{2+}$, which matches the Irving-Williams series.

Another example from Suh's research group indicates a direct comparison between two identical frameworks with or without open metal sites.[83] The result showed that the framework with open metal sites possesses nearly twice larger heat of adsorption (11.60 $kJmol^{-1}$) compared to the one without open metal sites (6.53 $kJmol^{-1}$), indicating open metal sites provide stronger interactions with H_2 molecules.

1.3.1.2. CO_2 capture

The concern about greenhouse gases has been stiffly increasing. Especially CO2 emissions have exceeded the capacity that the ecosystem can manage, thus resulting in global warming. Therefore, the prosperity of human civilisation and the fate of the Earth's ecosystem relies on reducing atmospheric CO_2 level. Reducing CO_2 emissions has globally become the top priority of each government's environment policy. MOF chemistry, again, has found another niche related to such efforts to reduce carbon dioxide emission. This has been one of the most popular research topics regarding MOFs.[84-86] The basic principle of using MOFs as CO_2 capture material is pretty much similar to exploiting MOFs as H_2 storage material. However, due to the different physical and chemical properties of CO_2 and H_2, more diverse approaches are available, and the feasibility for the real applications is high.

Since the polar nature of a CO_2 molecule, a lot more extensive chemical functional groups can be employed compared to H_2 storage cases, such as Lewis basic N containing moieties or some polar functional groups. Amino-MIL-53(Al), which is the amine functionalised isoreticular structure of MIL-53(Al), is a good example showing the selective increase of CO_2 affinity by the simple addition of a small amine moiety to the ligand backbone.[87] The adsorption enthalpy of CO_2 nearly doubled from 20.1 $kJ{\cdot}mol^{-1}$ for MIL-53(Al) to 38.4 $kJ{\cdot}mol^{-1}$ for amino-MIL-53(Al). Those of ethane and propane only increased by 18.4 % and 14.1 %, respectively.

The Telfer group recently reported MUF-16 which is judiciously designed for CO_2 capture and separation from other gases.[88] MUF-16 is a simple binary MOF composed of Co(II) and m-isophthalate and possesses a one-dimensional channel comparable in size to a CO_2 molecule and is decorated with Lewis basic amine groups. Although the pore volume (0.11 $cm^3 \cdot g^{-1}$) and BET surface area (215 $m^2 \cdot g^{-1}$) are comparatively not high due to its narrow pore slits, the affinity toward CO_2 is much higher than other gases. According to the gas sorption measurement collected at 293 K and 1 bar (Table 1-1), the total uptake of CO_2 reaches nearly 50 $cm^3 \cdot g^{-1}$ and the curved plot shape indicates the pores are nearly saturated at 1 bar whereas those of other gases show a linear trend with much lower uptake. Furthermore, the selectivity for CO_2 from a given gas mixture, which was quantified by IAST (Ideal Adsorbed Solution Theory) calculation, demonstrated its superb separation performance compared to other reported MOFs. The experimental data also showed its high CO_2 separation performance from other gases, and the performance was well maintained after a few hundred cycles. MUF-16 well accomplished the basic strategies to design CO_2 capturing MOFs. It possesses the optimum pore size and proper functional groups to enhance the affinity toward the target molecule and successfully exhibited the efficacy of such strategies.

Table 1-1. Summary of gas adsorption data and IAST-calculated selectivities for the MUF-16 at 1 bar and 293 K.

Gas	Uptake ($cm^3 \cdot g^{-1}$)	CO_2 selectivity over selected gas	Ratio CO_2 / selected gas
CO_2	47.78	-	-
N_2	1.32	630	15 / 85
CH_4	1.20	6690	50 / 50
H_2	0.64	9690	20 / 80
C_2H_2	3.99	510	50 / 50
C_2H_4	3.17	600	50 / 50
C_2H_6	3.06	600	50 / 50
C_3H_6	5.35	260	50 / 50
C_3H_8	4.82	84	50 / 50

Zhou's group reported an interesting MOF, which shows a tunable affinity toward CO_2 by photochemical or thermal treatment.[89] PCN-123 is an isoreticular structure of MOF-5 and possesses azobenzene moiety on its bdc backbone. Although the performance of CO_2 uptake is not notably better than other MOFs, it demonstrated the controllable CO_2 uptake by reversible *trans-cis* isomerisation of azobenzene moiety. Phase pure PCN-123-*trans* was initially prepared from *trans*-azobenzene bdc under the controlled synthesis condition. As depicted in Figure 1-23, the reversible *trans* to *cis* or *cis* to *trans* isomerisation was conducted

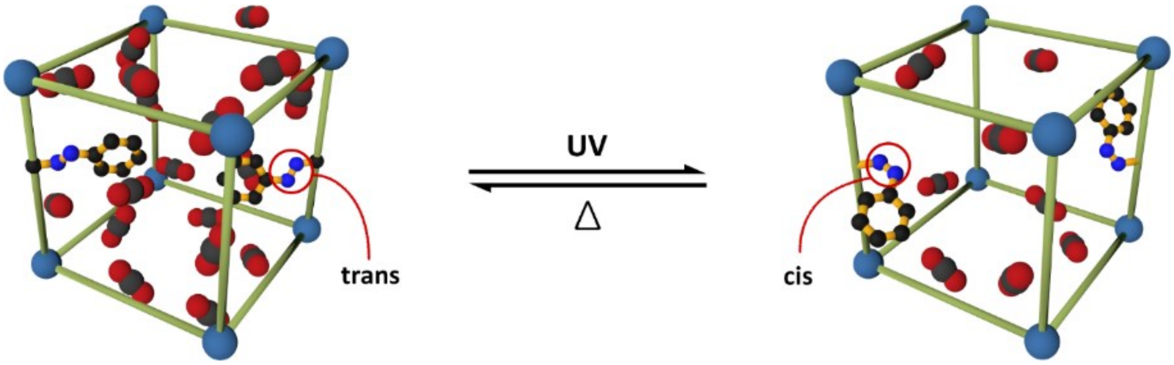

Figure 1-23. The conceptual diagram showing interchangeable azobenzene isomer moiety in PCN-123. Only two azobenzenes were presented without H atoms for the clarity.

by UV irradiation and heating, respectively. Then CO_2 adsorption isotherms were measured at 295 K and 273 K, and the results showed the CO_2 uptake with PCN-123-*cis* was about 50 % lower than that of PCN-123-*trans*, though no structural change or decomposition of the framework was observed. This study suggested a potential strategy to release a guest molecule under a particular circumstance.

According to Peyman et al., another interesting strategy to enhance CO_2 uptake was attempted.[90] The competition with water molecules is inevitable in the real environment for the CO_2 capturing application, and H_2O has a generally higher affinity to MOF pores due to its small size and higher polarity. FMOF-1 that has been armoured with hydrophobic CF_3 moiety was prepared, and its CO_2 adsorption isotherm was measured under different conditions. Surprisingly, the CO_2 uptake with water at 80 % relative humidity did not exhibit a notable difference from the CO_2 uptake of pure gas. Additionally, the water uptake was also successfully suppressed even at 30 bar.

1.3.2. **Catalysis**

MOFs can provide an excellent platform for catalysis. First of all, MOF catalysts are solid-state heterogeneous catalysts that provide advantages regarding product separation or catalyst recyclability. Second, they can integrate all different catalyst types, such as organocatalysts, metallic catalysts or metallorganic catalysts. Third, due to the crystallinity in MOF, they can provide a vast number of catalytically active sites which are periodically distributed through the entire framework. Fourth, the catalytic reactions are conducted in confined microenvironments provided by MOF pores. Therefore, more interactions from the various chemical pendants of the structural components surrounding the pores can be introduced.

On the contrary, there are some drawbacks with MOF catalysts, too. The reaction condition is limited due to the chemical stability of MOFs. For instance, not every MOF is stable in an aqueous medium or in specific pH ranges, meaning the limited reaction conditions. Furthermore, the target reactions occur in the pores, so the size of reactants or products must be small enough in order to diffuse through the pores. Otherwise, the framework will be clogged.

Due to the vast number and extensively diverse types of MOF catalysts, there are several ways to categorise MOF catalysts. In this section, MOF catalysts are categorised depending on where the catalytic activity is induced. Hence, they are categorised into mainly three categories, open metal sites on SBU, functionalised organic ligands or metalloligands. Additionally, some important applications in each category will be briefly introduced.

1.3.2.1. Open metal sites on SBU

Open metal sites are one of the most useful and multi-functional tools in MOFs.[91] Of course, they can also be utilised as a catalytic centre due to their high reactivity. Once open metal sites are generated using vacuum or heating, they can interact with the guest molecules entering the pore. Additionally, the surrounding environment caused by coordinated ligands can cooperate to induce chirality or regioselectivity to the reaction intermediate.

The paddlewheel SBU is one of the simplest SBUs, known to generate open metal sites on its axial positions (Figure 1-24a). The paddlewheel SBU comprises four btc (benzene-1,3,5-tricarboxylate) ligands with two Cu(II) ions in HKUST-1.[6] HKUST-1 is one of the most widely studied MOFs and commercially available as a catalyst because of its versatility obtained by easily attainable open metal sites. Therefore, an extensively wide range of organic reactions catalysed by HKUST-1 was reported.

For example, the cyanosilylation of benzaldehyde was reported by Kaskel et al. (Figure 1-24b).[92] Cyanosilylation is a convenient synthetic route to cyanohydrin, which is a versatile and important precursor to form other valuable functional groups. Since this study was one of the earlier works exploiting HKUST-1 as a catalyst, they demonstrated the crucial role of the open metal site for the catalytic capability rather than showing its catalytic efficacy. According to the results, the catalytic ability was decreased when the reaction medium was changed to THF (tetrahydrofuran), which can coordinate to the open metal site.

Corma et al. reported outstanding chemo- and diastereoselectivities of HKUST-1 for cyclopropanation reactions of alkenes with diazoacetates (Figure 1-24c).[93] Compared to other homogeneous catalysts or copper complexes, HKUST-1 displayed similar rates but higher selectivities and demonstrated high turnover numbers and superb recyclability. Especially the reactions of various alkenes with ethyl 2-phenyldiazoacetate resulted in almost diastereopure isomers. Moreover, with a dialkene substrate, 2,5-dimethyl-2,4-

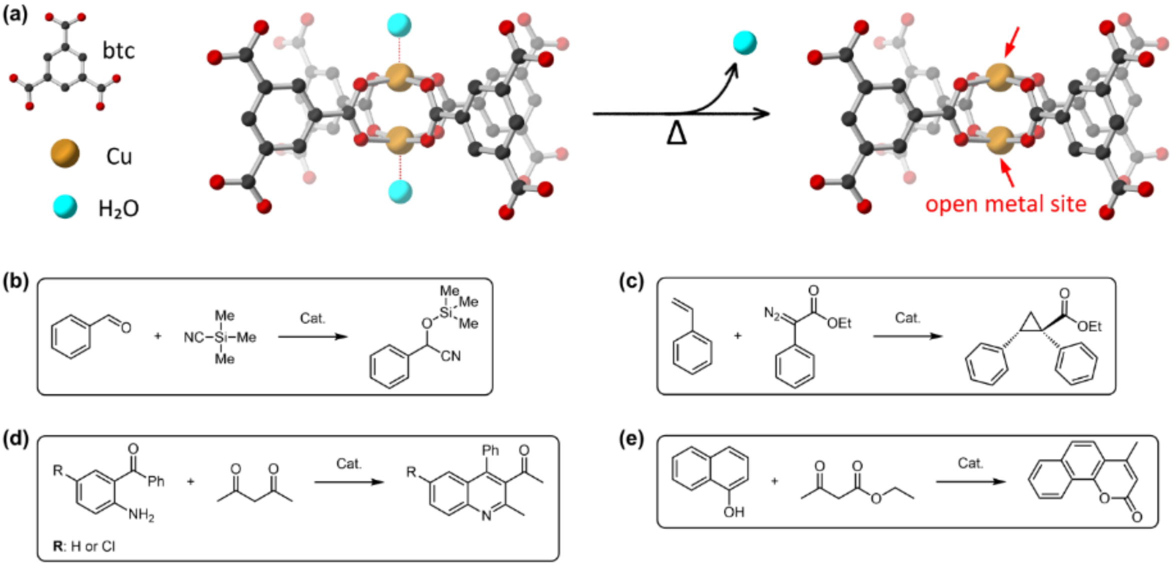

Figure 1-24. (a) A schematic diagram of inducing open metal sites on the paddlewheel SBU of HKUST-1; (b)-(e) a few example reactions which are catalysed by the activated HKUST-1.

hexadiene, ethyl diazoacetate exhibited exceptionally high chemo- and diastereoselectivities toward the *trans* isomer.

Čejka's research group demonstrated the excellent catalytic activity of HKUST-1 for the Friedländer reaction, which is generally catalysed by Lewis or Brønsted acids (Figure 1-24d).[94] HKUST-1 showed improved catalytic capability compared to existing catalysts for the formation of quinolone derivatives from 2-aminobenzophenone and ketone. They also exploited HKUST-1 to catalyse the Pechmann condensation of phenols and ethyl acetoacetate (Figure 1-24e).[95] This study investigated the catalytic activity of HKUST-1 composed of either Cu or Fe ions with three different phenol derived substrates, 3-hydroxy phenol, 2,3-dihydroxy phenol and naphthol. Also, they have compared the catalytic activity of HKUST-1 with a few large-pore zeolites.

1.3.2.2. Organic components on the ligand backbone

The catalytically active sites in organocatalysts (catalysts that consist of organic compounds) usually occupy a small portion in size. The catalytic capability is induced from the local acidity or basicity of the moiety. The majority of organocatalysts can be integrated into MOFs as a secondary functional group attached to a ligand backbone (e.g. bpdc-Pro in Figure 1-10b). Alternatively, the catalytically active sites can be mimicked with similar functional groups. For instance, some pyrrolidine containing moieties can replace proline if integrating proline into a MOF is not feasible.[96] The non-catalytically active sites do some other roles, such as enhancing solubility or stability of the catalyst in a specific reaction condition or cooperating with the catalytic centre, thereby enhancing various chemical selectivities depending on the reaction conditions. Such additional functionalities are sometimes unnecessary in MOF catalysts. Otherwise, it can be implemented by installing the additional functional groups in proximity on the same ligand backbone or neighbouring ligands if necessary.

MIL-101-SO_3H is a Brønsted acid catalyst prepared from monosodium 2-sulfoterephthalic acid and CrO_3 (Figure 1-25a).[97] Since MOF synthesis was carried under acidic condition, MOF crystals were synthesised as a mixture of sodium salt and acid form. The crystal was further treated with aqueous HCl to generate a more acidic catalyst by protonating the sulfonic acid moieties in MIL-101-SO_3H. The MIL-101-SO_3H crystal has both Lewis (Cr^{3+} in SBU) and Brønsted acidic (sulfonic acid on ligand) sites, and the catalytic capabilities of both sites were compared over the epoxide ring-opening reaction (Figure 1-25a). The parent framework (MIL-101) composed of bare bdc was also tested to investigate the catalytic activity of the Lewis acidic site. The results clearly showed superb catalytic activity of MIL-101-SO_3H as a Brønsted acid catalyst. The reaction was completed within 30 minutes with MIL-101-SO_3H, whereas MIL-101 demonstrated lower conversion and selectivity even after 48 hours. The result clearly indicates that the Brønsted acid moiety plays a crucial role in the epoxide ring-opening reaction. The durable stability and recyclability of the MIL-101-SO_3H were also confirmed after a few cycles of methanolysis of styrene oxide.

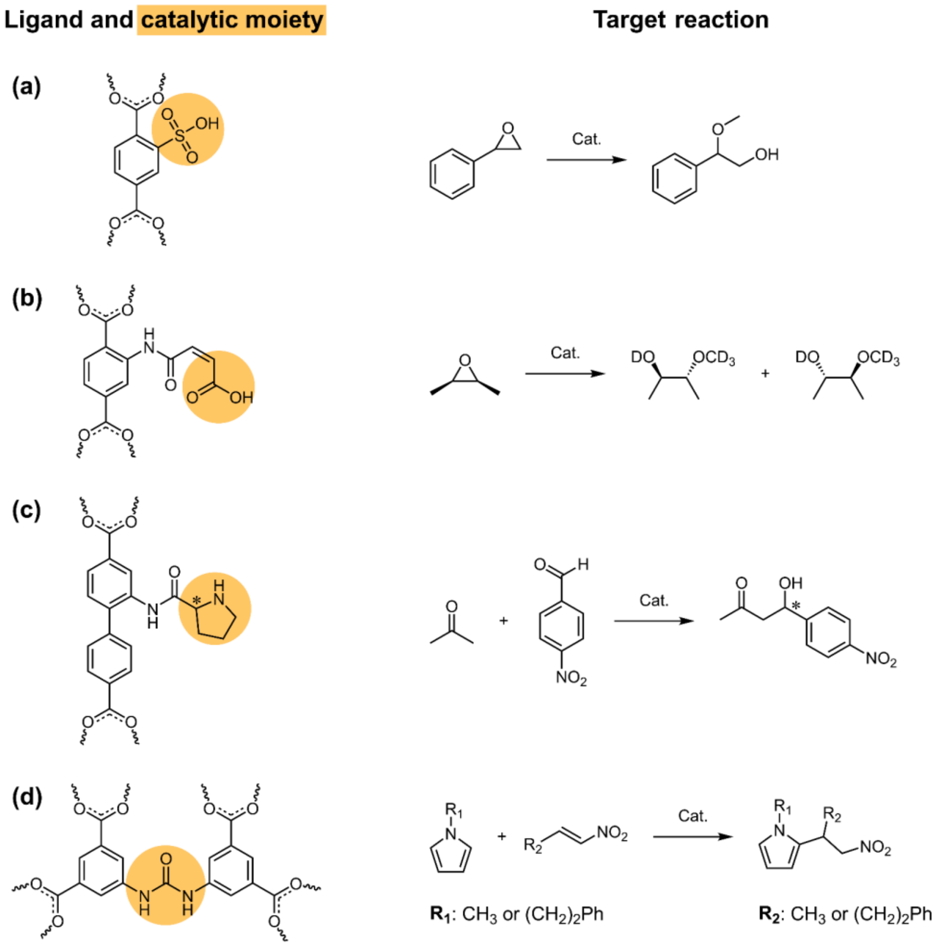

Figure 1-25. A few examples of organic linker possessing the catalytic functional groups which are depicted in yellow and the catalytic reactions conducted by each MOF catalysts.

Another methanolysis reaction of various epoxides, which was catalysed by a series of isoreticular MIL-53(Al)-NH_2, was demonstrated by Cohen's group (Figure 1-25b).[44] As depicted in Figure 1-10a, maleic anhydride was post-synthetically embedded to the bdc-NH_2 backbone, and the resulting framework was denoted as MIL-53(Al)-AMMal. Then its catalytic activity was demonstrated toward the methanolysis of *cis*-2,3-epoxybutane, cyclohexene oxide and styrene oxide substrates. Furthermore, the robust nature of MIL-53(Al)-AMMal allows restoration of the catalytic activity by treating with dilute HCl. The acid-treated crystal was then recycled several times without losing its catalytic power.

IRMOF-Pro[45] is another catalyst example prepared by PSM as already introduced in the previous PSM section (Figure 1-10b) along with the above MIL-53(Al)-NH_2 derivatives. The well-known organic catalyst unit, proline or pyrrolidine, is an optimum catalytic moiety to integrate into the MOF due to its relatively small size and strong catalytic activity. Incorporating proline moiety into the IRMOF-10 framework was managed through the PSM by utilising the Boc protecting group, as discussed before. Then its catalytic activity was explored with the aldol reaction of acetone and p-nitrobenzaldehyde (Figure 1-25c), and the proline unit was proved as the sole catalytic component by showing complete catalytic inactivity of IRMOF-Pro-Boc. However, this study left a few aspects which need to be improved since this was the very first case employing proline moiety into the MOF structure. The catalytic activity decreased upon recycling, and the enantioselectivity of IRMOF-Pro was not as good as the homogeneous proline catalyst.

John et al. reported NU-601 (NU: Northwestern University) composed of the judiciously designed ligand which incorporated the hydrogen donating catalyst moiety, urea, into the ligand backbone.[98] The original homogeneous thiourea catalyst[99] that inspires this study was known to possess a drawback such that the catalysts formed the self-assembled oligomers through the H-bonds leading to a potential decrease in catalyst capability. Thus they planned to exploit the MOF to fix the catalysts in separate enough positions not to interact with each other. As depicted in Figure 1-26, the thiourea was replaced with urea due to its stability issue during MOF formation, and carboxylic acids, which coordinate to SBU, took the place of CF_3. The prepared NU-601 from this urea containing ligand exhibited

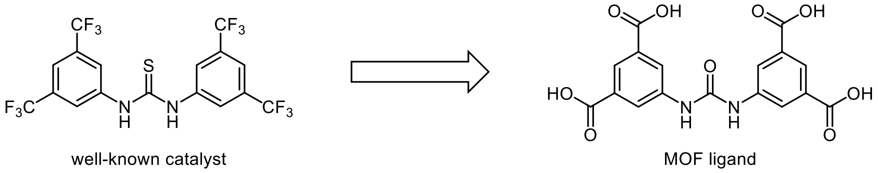

Figure 1-26. A designing scheme of urea containing ligand based on a well-known symmetrical thiourea catalyst.

catalytic activity well with the Friedel-Crafts reaction between pyrroles and nitroalkenes (Figure 1-25d). Although this study demonstrated the merit of adopting a MOF as a heterogeneous catalyst compared to a homogeneous catalyst, it also presented some limitations of a MOF catalyst. Significantly diminished yields were noted due to the limited pore size when large substrates were employed.

1.3.2.3. Metalloligands

As briefly introduced in the postsynthetic metalation section (Figure 1-9), many metalloligands are employed as heterogeneous catalysts in MOFs. For instance, porphyrin or salen complexes have been well known as a versatile homogeneous catalyst, and they can be transformed into building blocks for MOFs. Therefore, they can take advantage of the merits of heterogeneous catalysts exploiting MOF scaffold without losing their characteristics as catalysts.

1.3.2.4. Metalloporphyrin based MOFs

As depicted in Figure 1-27, various types and numbers of binding groups can be attached to the porphyrin component in order to be integrated into diverse MOF structures. Furthermore, the catalytic property of porphyrin derived MOFs can be tweaked depending on the porphyrin metal ions that can be integrated by direct synthesis or by transmetalation.

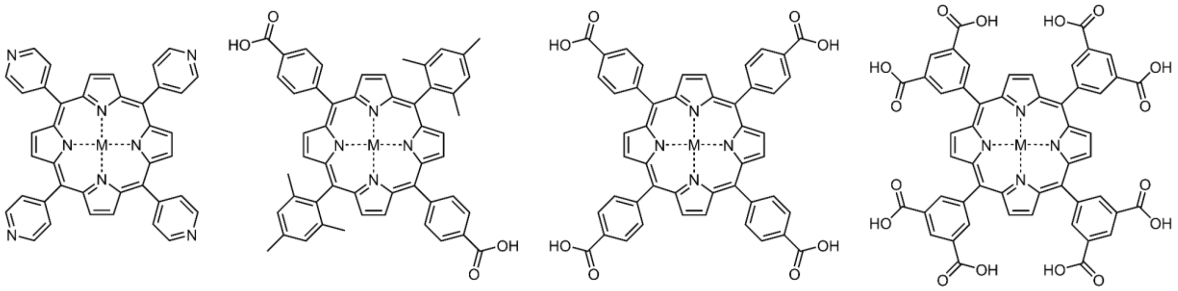

Figure 1-27. Various form of porphyrin derived ligands which possess different type and number of binding groups.

Shultz et al. explored the catalytic activity of metalloporphyrinic MOF, ZnPO-MOF, which was prepared as depicted in Figure 1-28a.[100] The Zn^{2+} ion occupies the free base site of the porphyrin ligand during MOF synthesis and provides Lewis acidic site for the catalysis reaction. The optimum distance between the two porphyrin layers (11.6 Å) in the frameworks plays a crucial role in this catalysis reaction, as shown in the reaction scheme in Figure 1-28b. Once the two complementary pairs of reactants coordinate to the Zn sites, the activated reactants will locate in close proximity due to the optimal conformation of the two porphyrin layers. Thus, the acyl transfer reaction between the two reactants occurs within the framework with a boosted reaction rate.

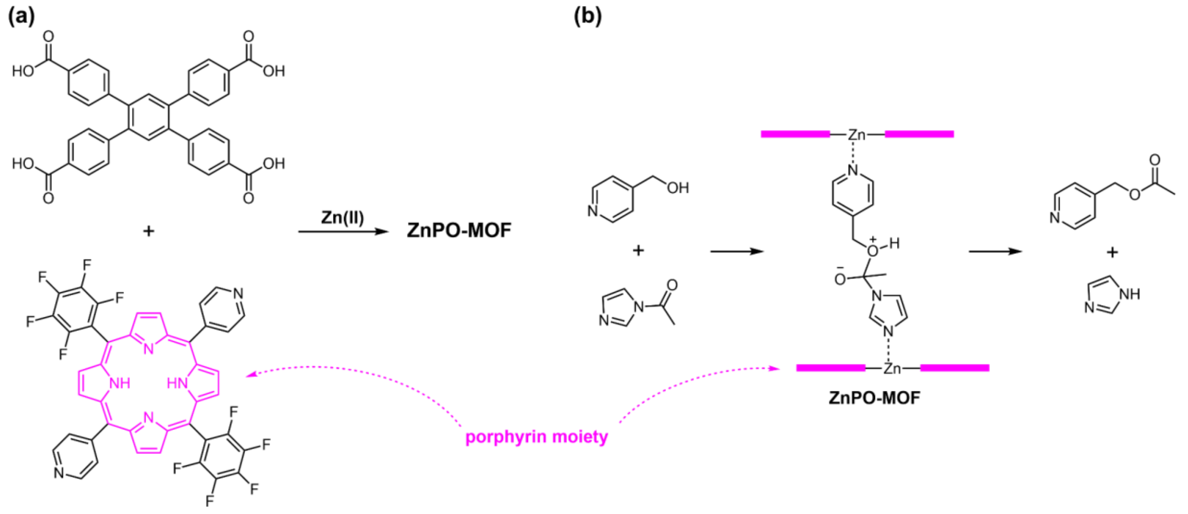

Figure 1-28. (a) A schematic diagram of ZnPO-MOF synthesis; (b) a proposed mechanism of the acyl-transfer reaction between pyridin-4-ylmethanol and N-acetylimidazole.

Another excellent metalloporphyrinic MOF catalyst, MMPF-3, was reported by Ma's group.[101] MMPF-3 was synthesised from a porphyrin-derived ligand and cobalt nitrate (Figure 1-28a). The Co(II) ion occupied the porphyrin centre during the course of MOF synthesis. The resulting structure presented a high density of porphyrin cobalt sites (5 Co atoms per nm^3) in the pore. The epoxidation of *trans*-stilbene (Figure 1-28b) using *tert*-butyl hydroperoxide as oxidant was carried out over the MMPF-3 along with other catalysts, including free Co-porphyrin ligand for control reactions. MMPF-3 demonstrated excellent catalytic activity in terms of both conversion and selectivity. Approximately 96 % of *trans*-stilbene was consumed in 24 hours, and the selectivity reached about 87 %. All the other control experiments showed much lower catalytic activity on the other hand. More impressively, this superb catalytic activity was sustained even after the eighth cycle of the reaction.

Figure 1-29. (a) A schematic diagram of MMPF-3 synthesis; (b) the epoxidation reaction of *trans*-stilbene catalysed by MMPF-3.

1.3.2.5. **Metallosalen-based MOFs**

Metallosalen struts have been extensively incorporated into MOFs because they can be transformed to bridging ligands by adding N donor (Figure 1-30 and Figure 1-31) or carboxylic acid groups (Figure 1-9). Metallosalen-derived catalysts are potent catalysts, especially for asymmetric reactions, because various chiral groups can be placed around the catalytic centre.[102-103] Thus, metallosalen-derived ligands can be integrated into MOFs with keeping their catalytic capability so that they can enhance their utility as a heterogeneous catalyst.

Hupp's research group reported an outstanding asymmetric catalyst.[104] As depicted in Figure 1-30a, the salen derived ligand, which has pyridyl groups as coordinating groups and contains Mn(III)-Cl, was used to form Cat-1 along with another ligand (bpdc) and Zn(II) ions. As a result, an interpenetrated framework possessing two channels was produced. The catalytic activity of Cat-1 was examined with asymmetric epoxidation of 2,2-dimethyl-2H-chromene with 2-(*tert*-butylsulfonyl)iodosylbenzene as an oxidant, as shown in Figure 1-30b rxn-1. The catalytic activity of the heterogeneous catalyst (Cat-1) was far more efficient than that of the control reaction conducted with the ligand itself as a homogeneous catalyst. The catalytic activity of the homogeneous catalyst was diminished over time because the catalyst was oxidised by other encountering catalyst molecules. Whereas in the case of Cat-1, all the catalytic units were well separated by the MOF scaffold and its catalytic activity remained constant. Although the enantioselectivity of Cat-1 (82 % ee) was slightly decreased compared to the one of homogeneous catalyst (88 % ee), this study presented how to utilise the MOF scaffold to improve the catalytic activity of homogeneous catalysts.

In 2011, the same group reported another Mn(III)-Cl-salen containing MOF catalyst, Cat-2, which possesses a non-interpenetrated structure by utilising the tetratopic linker, as depicted in Figure 1-30a. The catalytic activity of Cat-2 was examined with the same reaction, and the result was compared with Cat-1. The two catalysts showed different catalytic activities induced by the difference in crystal size of Cat-1 and Cat-2. Cat-1showed a greater catalytic activity at the beginning since the smaller Cat-1 crystal possesses greater external surface area than Cat-2. However, Cat-2 eventually demonstrated a higher catalytic activity as the substrate diffused through the catalyst pore over time.

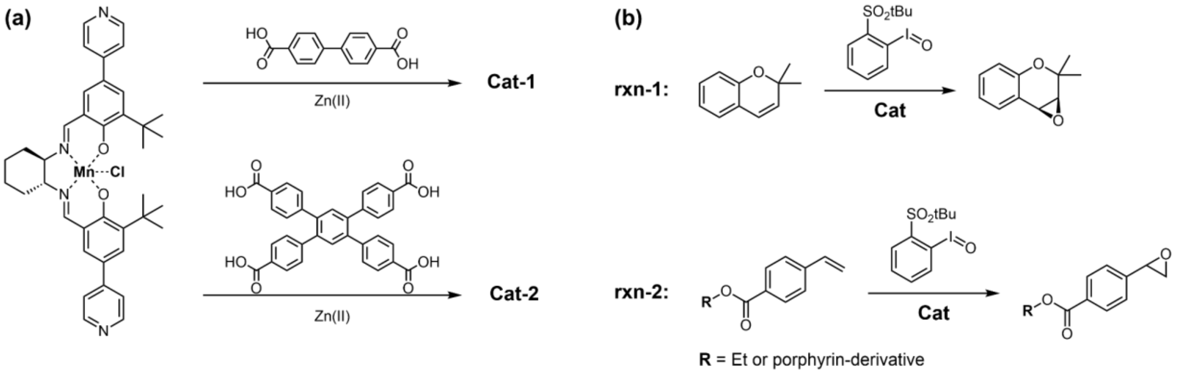

Figure 1-30. (a) A schematic diagram of syntheses of a few examples of MOF catalysts containing Zn(salen) derived ligand; (b) the reactions catalysed by the resulting catalysts.

Another example of two asymmetric Fe(salen) based MOFs, Cat-3(Zn) and Cat-3(Cd), were reported by Cui's research group, as shown in Figure 1-31a.[105] Due to the different orientation of the terminal pyridyl groups on each ligand, Cat-3(Cd) attained a larger cavity than Cat-3(Zn). This enhanced the catalytic activity of Cat-3(Cd) for asymmetric sulfide oxidation. Cat-3(Cd) resulted in a 94 % conversion with 100 % selectivity and 60 % ee of the sulfoxide after 8 hours. However, over-oxidation of sulfoxides to sulfones occurred over time, which dropped the chemoselectivity to 27 % after 30 hours while ee increased to 96 %. This can be explained by the kinetic resolution. This trend was also observed in the case of the homogeneous reaction with the free Fe(salen) ligand. Although the reaction rate catalysed by the homogeneous catalyst was higher, the heterogeneous catalyst demonstrated more conversion (94 % vs 78 %) with 100 % chemoselectivity.

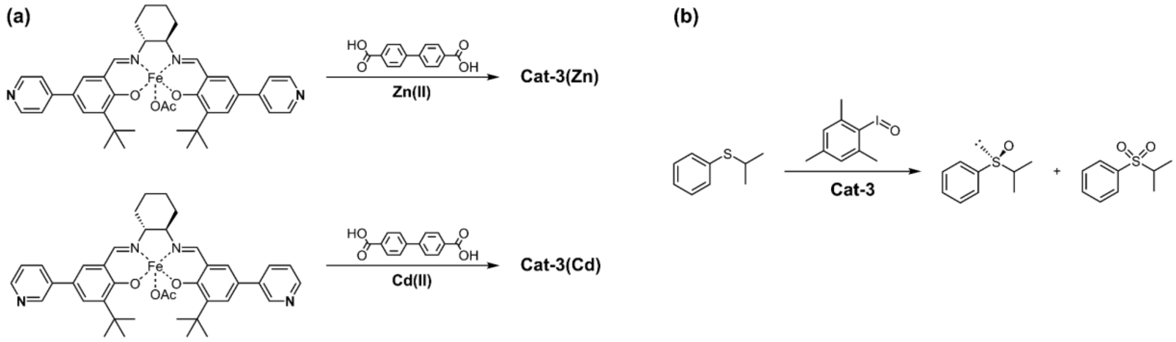

Figure 1-31. (a) A schematic diagram of syntheses of Cat-3(Zn) and Cat-3(Cd); (b) the asymmetric sulfide oxidation reaction catalysed by Cat-3s.

1.4. Introduction to selected experimental techniques

Many analytical techniques have been used to characterise MOFs. For instance, NMR (nuclear magnetic resonance) of the digested MOF sample is a critical analysis for MC-MOFs to prove the exact ligand ratios. Gas sorption is an essential technique to examine the porosity of materials and to figure out their surface area and pore volume. Also, X-ray crystallography is absolutely required to solve or to compare the structures of the frameworks. IR spectroscopy is widely used to detect specific chemical functionalities in the frameworks, and UV and fluorescence spectroscopies to observe light-induced properties. Electron microscopy is also regularly exploited to explore the morphology of MOF crystals. In fact, if it is extended to the applications of MOFs, almost all scientific instruments are utilised. In this chapter, a few of the most critical techniques and their basic principals to study MOFs will be introduced.

1.4.1. BET surface area calculation

The BET theory is a widely adopted method to calculate the surface area of porous materials. It is theoretically more appropriate for MOFs than Langmuir theory. This is because BET theory is based on multiple layers of absorbates formed on the adsorbent surface, while the Langmuir surface area is defined under the assumption of the monolayer formation on the surface, which is an ideal situation. Thus, the surface area calculated by BET theory is generally accepted as a standard.

The BET equation is defined as follows:

$$\frac{P/P_0}{v(1-P/P_0)} = \frac{1}{v_m C} + \frac{C-1}{v_m C}(P/P_0) \tag{1}$$

where v is the specific amount of the adsorbed gas at the relative pressure P/P_0, v_m is the monolayer capacity of the adsorbed gas, P is the gas pressure for the adsorbate in equilibrium with the porous material at each point of measurement, P_0 is the saturation pressure of a gas being adsorbed at the adsorption temperature, and C is the BET constant which is exponentially related to the energy of monolayer adsorption. The BET equation (1) can be plotted as a linear line, $\frac{P/P_0}{v(1-P/P_0)}$ against P/P_0 and then the two variables, v_m and C can be determined from the slope (a) and intercept (b). The BET surface area (A_{BET}) was then calculated by inserting the value for v_m into the following equation:

$$A_{BET} = v_m\ (cm^3g^{-1}) \times \frac{1\ (mol)}{22400\ (cm^3)} \times \sigma_0\ (\text{Å}^2) \times N_A(mol^{-1}) \times 10^{-20}\left(\frac{m^2}{\text{Å}^2}\right) \tag{2}$$

where N_A is Avogadro's constant, and σ_0 is the cross-sectional area of a N_2 molecule, which is 16.2 Å^2.

The four plots in Figure 1-32 are successive conversion processes to obtain the linear plot of the equation (1) from the raw N_2 adsorption data measured at 77 K according to the method presented by Snurr.[106] The raw N_2 adsorption data was converted to the plot of $v(1-P/P_0)$ against P/P_0, then the pressure range where values of $v(1-P/P_0)$ increasing with P/P_0 was selected, and then the selected range was converted to the plot of $\frac{P/P_0}{v(1-P/P_0)}$ against P/P_0. Then, a few data points, which fit a linear regression line, were chosen from near the point at which the N_2 gas adsorption reaches saturation. The Y-intercept of the regression line must have a positive value. The determined values for the slope and Y-intercept from the regression line are then used to calculate $v_m = \frac{1}{a+b}$ and $C = 1 + \frac{a}{b}$, and the value for v_m was plugged into the equation (2) in order to calculate the BET surface area.

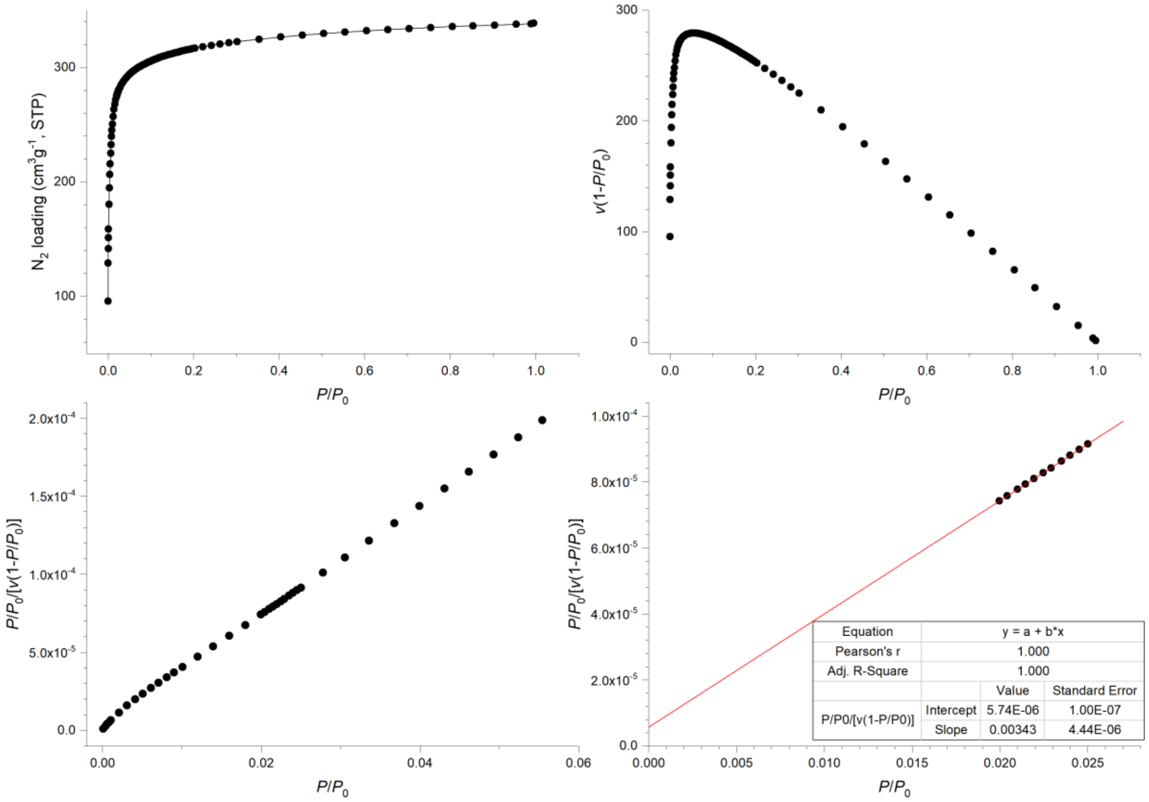

Figure 1-32. An example of N_2 adsorption at 77K and the plots resulted in successive data processing to obtain a linear regression line in order to get the variables for the equation (2).

1.4.2. X-ray crystallography

X-ray crystallography is a very complex subject to be dealt with in this short section. Thus, the basic principles of X-ray crystallography and the fundamentals of the apparatus will be briefly introduced.

1.4.2.1. The fundamental principles

The smallest and simplest repeating unit in a crystal is called a unit cell. The whole crystal is composed of a pack of unit cells that are stacked beside and on top of each other. Thus, solving a crystal structure means figuring out the exact structural information of all the contents in a unit cell. Often, the contents in a unit cell can be sub-divided into small fragments which are related to each other. The smallest fragment of such is referred to as the asymmetric unit. The entire unit cell can be reconstructed by applying the symmetry operations, such as rotation, reflection through mirror planes, inversion or translation, to the asymmetric unit (Figure 1-33 illustrates the relationship between the asymmetric unit, unit cell and crystal of MUF-77).

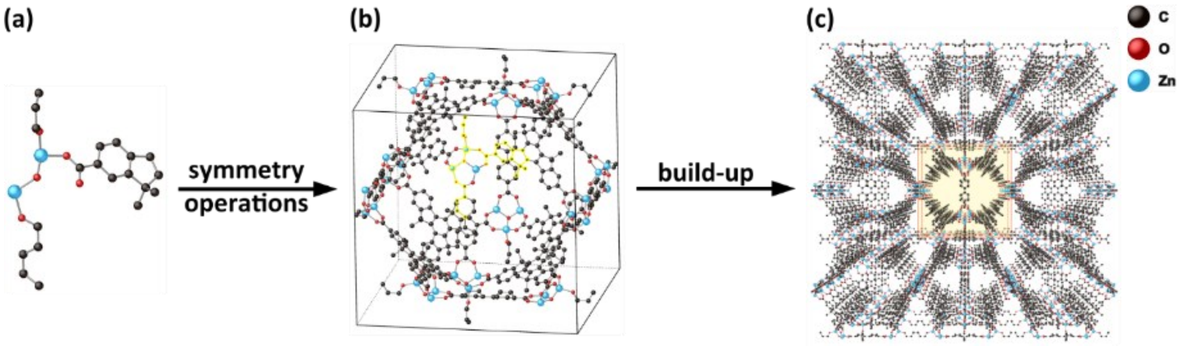

Figure 1-33. (a) The asymmetric unit; (b) the unit cell constructed from the asymmetric unit (highlighted in yellow) through symmetry operations; (c) a crystal which is a pack of unit cells (depicted yellow cube).

Any point in the crystal repeatedly appears due to a three-dimensional periodic arrangement of every component in a crystal, so the unit cell can arbitrarily be selected. However, the symmetrical arrangement of the cell contents must be considered to choose the best unit cell. The corner of the unit cell is referred to as a lattice point, and the neighbouring lattice points are described by vector translations. These vectors are denoted as $\vec{a}, \vec{b}$ and $\vec{c}$, and the angles between vectors are referred to as A, B and C for between $\vec{b}$ and $\vec{c}$, $\vec{a}$ and $\vec{c}$, and $\vec{a}$ and $\vec{b}$, respectively. Those six components, three vectors and three angles, are called unit cell parameters that describe fundamental features of a unit cell. A set of lattice points can sit on the same plane due to the periodicity, and the plane is named a lattice plane. Figure 1-34a illustrates two different lattice planes that are revealed depending on the crystal orientation. Each set of lattice planes is denoted by triple number codes (Miller indices), in round brackets

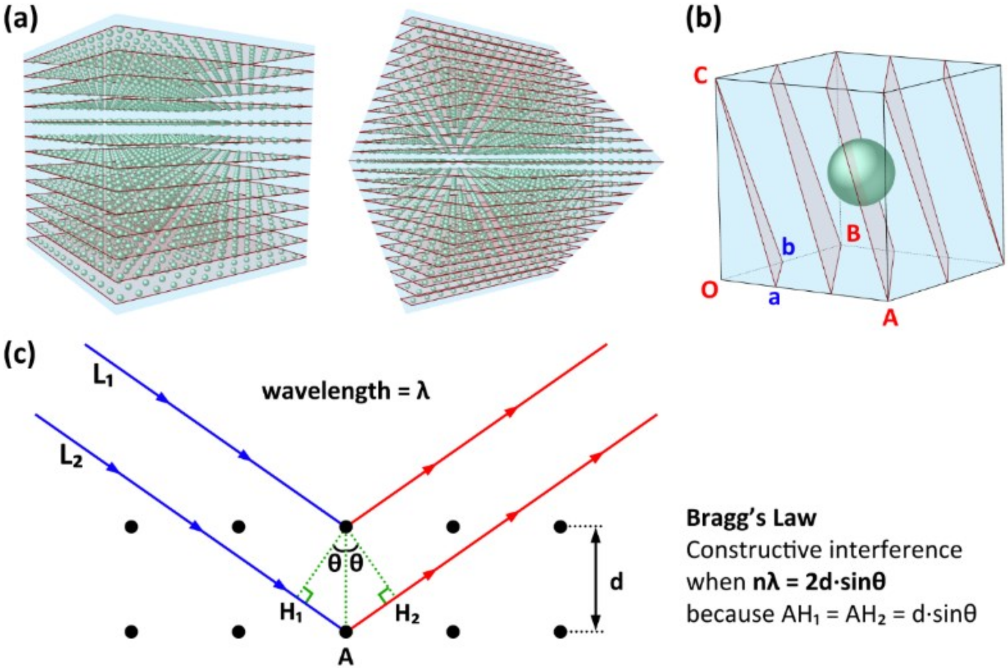

Figure 1-34. (a) Two different sets of lattice planes revealed in the different orientation of a crystal sample. (b) a unit cell sliced by a set of lattice planes (3, 2, 1); (c) a schematic diagram of reflected X-rays on two lattice planes in order to induce the Bragg's Law; the sphere represent a content in the unit cell.

as (h k l). A set of lattice planes are depicted in Figure 1-34b, and these parallel planes intersect the three edges (OA, OB and OC) of the unit cell. Therefore, each edge is evenly divided, and the slice length on each side can be displayed as a fraction. The denominator for each fraction will then be a number corresponding to h, k, and l. For instance, OA was divided into three pieces, and the length of each piece is 1/3 of the lengths of OA, so the denominator 3 becomes the number corresponding to h. Therefore, the set of lattice planes can be denoted (3, 2, 1) if the same method is applied to the remaining two edges.

When the X-ray beam hits the crystal sample, the majority of the X-ray beam penetrates the crystal and exits unchanged. However, a fraction of the X-ray beam is diffracted by the electron density of atoms. Since an X-ray is a type of electromagnetic wave, the scattered beams interfere with each other. The constructive interference only occurs when the incident and reflect rays fulfil Bragg's Law as depicted in Figure 1-34c. The two incident rays, L_1 and L_2, are reflected in a set of lattice planes separated by the length of d. However, the ray L_2 travelled more distance than L_1 by $AH_1 + AH_2$, which are equivalent to $2d{\cdot}\sin\theta$. Hence, if the value for $2d{\cdot}\sin\theta$ equals the multiple of the wavelength (λ), the reflected two rays will be in phase and will be identified as a spot on the detector. There are hundreds to tens of thousands sets of lattice planes in a crystal depending on the unit cell size, and the constructive interference occurs only with the sets of lattice planes that meet the condition of Bragg's Law. Figure 1-35 is a snapshot of the SCXRD (single-crystal X-ray diffraction) pattern, and there seem to be over a hundred diffraction spots on this image. Each spot represents the constructively interfering rays reflected on an individual set of lattice planes which fulfil Bragg's Law at this specific orientation of the crystal sample. A few diffraction points were indexed with the Miller indices, and a notable trend is shown. The spots indexed

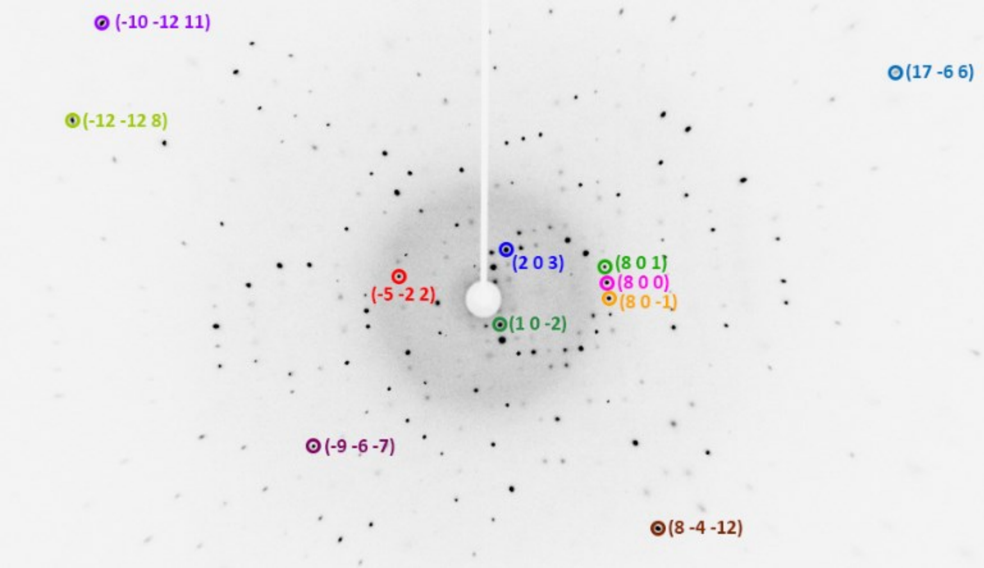

Figure 1-35. An example of the single-crystal X-ray diffraction pattern, a few of the diffraction spots are indexed with Miller indices.

with the higher the indices are further away from the beam centre. It was because the distance between two parallel lattice planes gets shorter as the indices increase, then the larger angle θ is required to satisfy Bragg's Law.

1.4.2.2. Single-crystal X-ray diffraction (SCXRD)

The previous example of a diffraction image shown in Figure 1-35 was taken while the crystal sample was rotated 1 ° around a specific axis. To precisely identify all the contents of a unit cell, hundreds of such images are measured while continuously changing the orientation of a crystal sample through rotation around various axes. Furthermore, the diffraction spots corresponding to higher indices enhance the resolution of the structure. So it is crucial to obtain as many diffraction spots of higher indices as possible to improve the quality of the crystal structure. The amount of data required to solve the structure profoundly depends on the crystal system. Generally, less data is required to solve the crystal structure of the higher symmetric system. Collecting more data is certainly advantageous, but it costs more time and other resources, so there is always a trade-off.

Once the data collection is finished, then the collected data is processed to calculate the indices for all the diffraction spots. The corresponding spot intensities on each image are integrated to produce a so-called hkl file. The unit cell parameters for the crystal sample are relatively easily determined by the positional information of each diffraction spots, and only a few images are required for that. However, the intensity of each diffraction spot contains much more information. Each set of lattice planes intersects a different portion of contents in the unit cell, so the electron density relative to each lattice plane is different depending on where it passes through the unit cell contents. Thus the corresponding spot intensity to the lattice plane is principally determined by the electron density belonging to the atoms on the lattice plane. For instance, if the unit cell parameters are accidentally identical for two different crystal samples which are prepared from different molecules, then the diffraction images collected from each sample at the same crystal orientation against the incident X-ray will show the same pattern of the diffraction spots. However, the spot intensity will be different since the contents in a unit cell are different.

To extract all the structural information of cell contents from the hundreds of spots on thousands of images is complicated work, but it is thankfully all done by computer software. The software package known as ShelX[107] is one of the most powerful and widely adopted software in the MOF field, and it calculates the types of atoms and their positions, based on the extra information provided, by complicated mathematical operations with Fourier transformation of each diffraction data. However, ShelX only provides a rough model of the

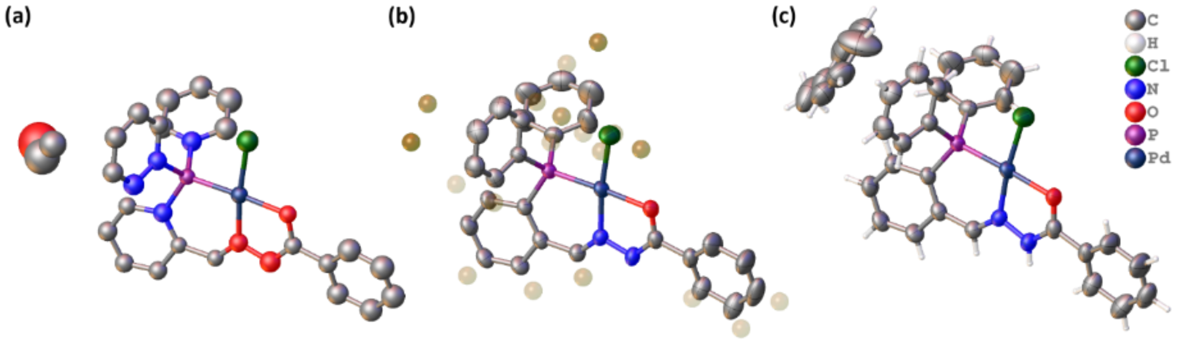

Figure 1-36. The step by step procedure refining the contents in the unit cell; (a) the initial coarse structure suggested by ShelXT; (b) the structure during the refinement procedure, brown spheres are local electron density suggested by the software; (c) the complete structure.

cell contents, thus requires a polishing process known as refinement. The ShelX also provides statistical information by comparing the spot intensities calculated from the current model with the collected spot intensities. Thus, decreasing the discrepancy between the two data sets and eventually finding the converging structure is the final goal of the refinement step.

Figure 1-36 illustrates the procedure of solving and refining crystal structure. The structure in Figure 1-36a is the coarse structure provided by the software after calculation with the collected raw data. The quality in the initial structure highly depends on the crystallinity of the sample and collected data quality. In this example, the suggested model is quite close to the final structure though a few atoms are assigned with the wrong element type, and the solvent molecule is not clear. If the molecular structure, formula, or solvents are known, it is not very difficult to modify the element types or local structures. Otherwise, other types of information are utilised in order to make a plausible guess and to refine the structure. In addition, what makes it more difficult to solve the crystal structure is disorder. Even more challenging are twinned structures. Successive iteration of the refinement is continued until the statistics converge within the acceptable range.

1.4.2.3. Powder X-ray diffraction (PXRD)

PXRD is a powerful, efficient, yet simple analysis technique to determine the structure of crystalline material. As discussed in the previous SCXRD section, diffraction appears as a spot when the ray encounters a lattice plane that obeys Bragg's law. However, if the diffraction was measured on a bulk crystal sample, then the resulting diffraction pattern appears as a set of concentric circles. These are denoted as Debye-Scherrer rings. Figure 1-37 well demonstrates the correlations between the numbers of crystals in a bulk sample and corresponding diffraction patterns. In the case of a single crystal depicted in Figure 1-37a, the diffracted spots seem like random scattering. However, as the number of crystals in a sample increases (Figure 1-37b), the diffracted spots appear to be a series of concentric

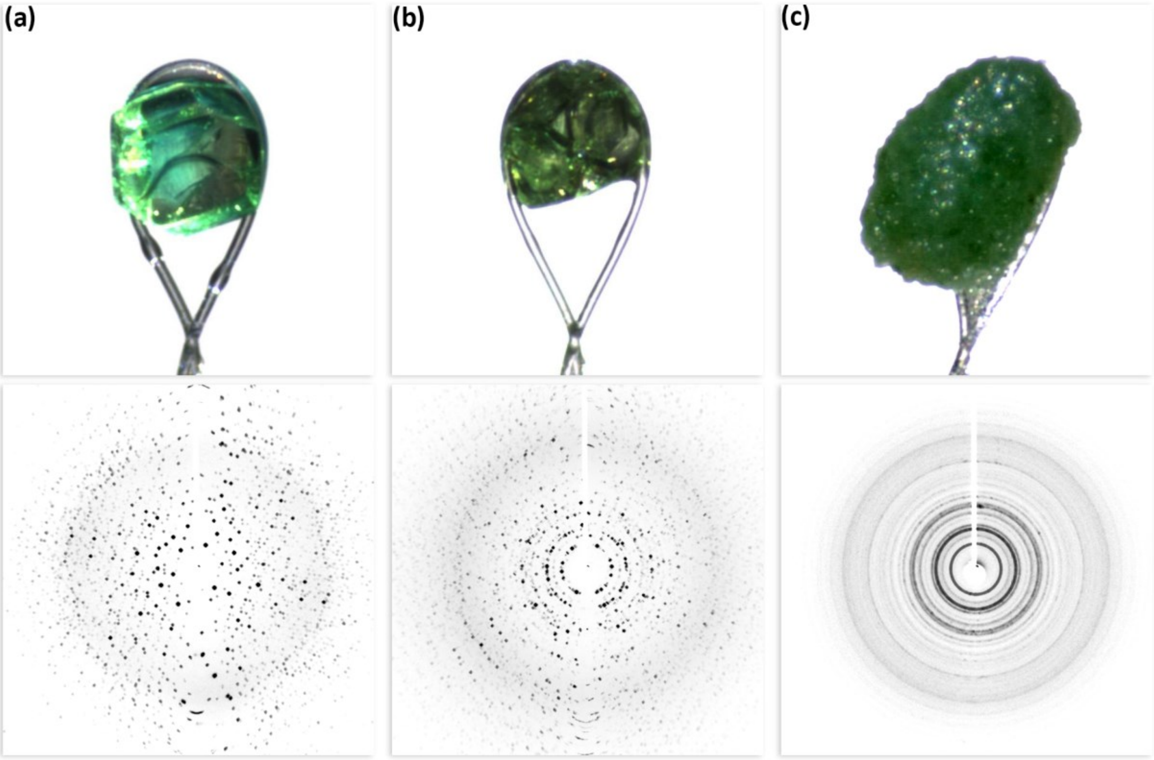

Figure 1-37. The difference in diffraction pattern with respect to the number of crystal sample; all three data collected with the same condition (scan width: 360 ° and exposure time: 60 secs). (a) a single crystal; (b) a few crystals; (c) ground crystals

circles. Eventually, the diffraction pattern is composed of complete concentric circles comprising hundreds of diffracted spots from the fine powdery crystal sample (Figure 1-37c).

Every single-crystal in a bulk sample is identical but randomly oriented with respect to the incident X-ray. Thus the spot reflected on a specific lattice plane of each single-crystal may or may not be presented depending on each crystal's orientation. However, due to the vast number of crystals in a bulk sample, some crystals produce a diffraction spot reflected on the same lattice plane. In that case, the angle of a reflected ray with respect to the penetrating X-ray will be the same for all corresponding single-crystals. However, the direction of reflected light will be all different due to the different orientation of individual crystal in a bulk sample. As a result, the diffraction spots belonging to the same lattice plane appears as a circle. The angle between the reflected ray and the incident ray is denoted as 2θ, and 2θ is determined by the distance between the two neighbouring parallel lattice planes. Therefore, if the two crystal samples have an identical diffraction pattern, they likely have the same crystal structure.

Once the PXRD pattern is collected, the intensities of all Debye-Scherrer rings are integrated and plotted against the angle 2θ (Figure 1-38a). Then, the resulting plot can be used to determine the structure of the measured sample by comparing it with other known ones. For example, many other MOFs can be formed during MUF-7 synthesis due to the competition between potential structures (Figure 1-19). In this case, the PXRD pattern produced from the synthesised MOF sample can be directly compared to the PXRD plots calculated from other possible structures, as depicted in Figure 1-38b. In this example, the PXRD pattern generated from the synthesised MOF matches the calculated pattern for MUF-7.

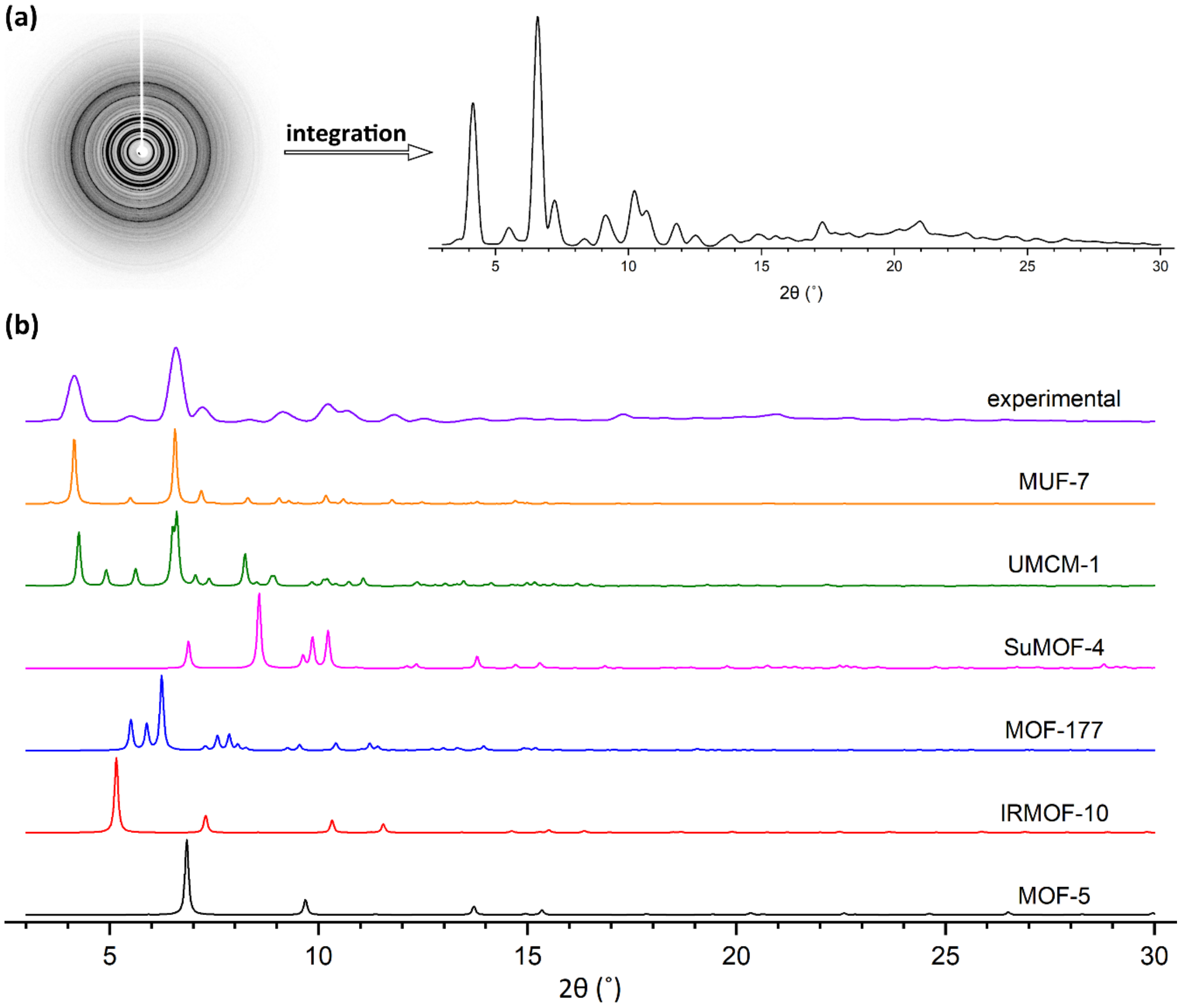

Figure 1-38. (a) An example of a converted 2D plot from a PXRD pattern; (b) the converted 2D plot (purple) matches the calculated pattern for MUF-7 (orange) among various potential PXRD patterns, strongly indicating the crystal sample is MUF-7.

Chapter 2 **MUF-7 vs MUF-77**

2.1. **Introduction**

MOF formation utilises relatively weak interactions between metal nodes and organic linkers. The bonds between building blocks are reversible, and forming and breaking bonds repeatedly occur during MOF synthesis until the thermodynamically favoured structure is formed. A subtle change in synthetic conditions, such as a small difference in synthesis temperature or a little variation in the ratio between substances, may affect MOF formation and lead to different structures. The structures in Figure 2-1 are all binary MOFs comprising two building blocks, a single type of node and linker. They show how diverse structures can be formed from the simplest building blocks, Zn(II) and bdc (benzene-1,4-dicarboxylate), and the number is surprisingly high. According to the Cambridge Structural Database (CSD), there are more than a hundred different structures when searched with the structure containing bonds between zinc (including zinc clusters) and bdc.

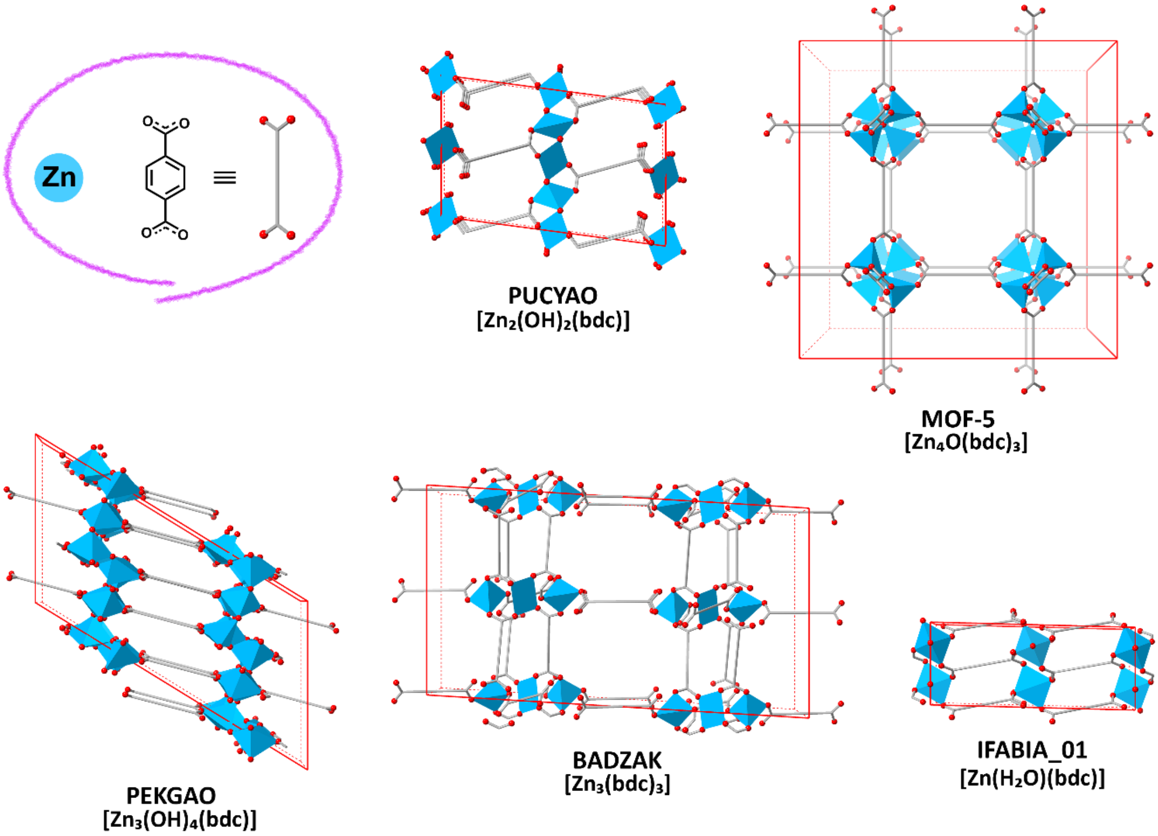

PUCYAO
[$Zn_2(OH)_2(bdc)$]

MOF-5
[$Zn_4O(bdc)_3$]

PEKGAO
[$Zn_3(OH)_4(bdc)$]

BADZAK
[$Zn_3(bdc)_3$]

IFABIA_01
[$Zn(H_2O)(bdc)$]

Figure 2-1. A series of MOFs composed of the simplest building blocks, zinc and bdc (in a purple circle), in [010] projection. Except for MOF-5,[4] the identifier was borrowed from CSD to refer to the unnamed structures (PUCYAO,[60] PEKGAO,[61] BADZAK[66] and IFABIA_01[108]); the red line indicates a unit cell.

Even such a simple combination of zinc and bdc gives rise to a wide range of frameworks depending on the synthetic conditions. Thus we can envisage that more complex outcomes would be obtained if the number of building blocks is increased. In the example above, the synthetic conditions, such as solvent, synthesis temperature and duration, source of metal ion or presence of other additives, determined the resulting MOF structure. However, more factors need to be taken into account for the MOF formation if the number of building blocks were increased.

For instance, Matzger's research group demonstrated the importance of other factors in MC-MOF (multi-component MOF) formation.[8] A series of UMCM-x (UMCM: University of Michigan Crystalline Material; x = 1, 2 and 4) composed of similar building blocks were used to demonstrate the role of these factors. As shown in Figure 2-2, each framework comprises each of geometrically identical tritopic and ditopic linkers. However, the resulting frameworks were governed by two main factors, so-called geometrical and statistical factors. The geometrical factor is the length ratio between tritopic and ditopic linkers (L_d/L_t where L_d = length of ditopic linker and L_t = length of tritopic linker), and the statistical factor is the feed ratio between the two linkers in the synthesis mixture.

The geometrical factor is critical in obtaining the desired framework. If a ligand, which is shorter or longer than the required length in a specific framework, was used for MOF synthesis, the entire framework will suffer from strain. If the difference is too much, the desired structure cannot be formed. Moreover, if the length ratio between the two linkers differs too much, like bpdc ([1,1'-biphenyl]-4,4'-dicarboxylate) and btb (benzene-1,3,5-

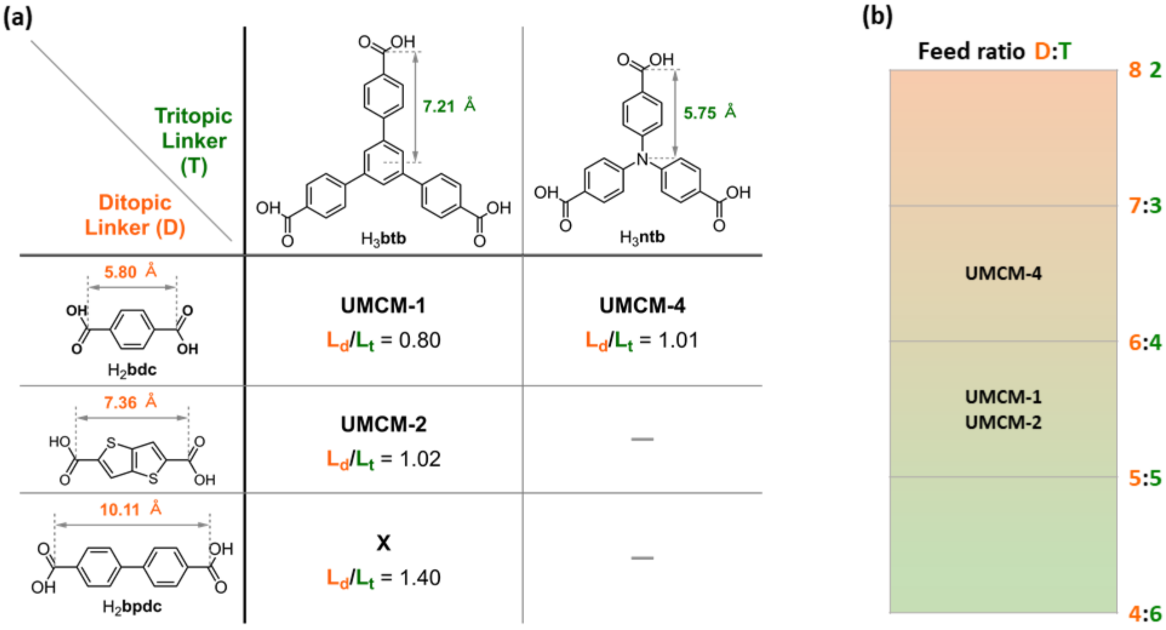

Figure 2-2. Five different UMCM series MOFs composed of a tritopic and a ditopic linker, and two different factors that determine the structure. (a) Geometrical factor, length ratios between ditopic and tritopic linkers; (b) statistical factor, feed ratios between the two linkers

tribenzoate) in Figure 2-2a, no framework comprising two ligands can be built. The statistical factor also plays an essential role in forming a pure phase framework because of their relative reactivities during crystal formation. Depending on the chemical property of each ligand, the rate of consumption of each ligand in MOF synthesis is different. As a result, one ligand can be depleted faster than the other, resulting in locally low concentration and eventually cause defect or disorder in the structure. Such different consumption rates can be compensated by adjusting the feed ratio in the synthesis mixture.

The two examples above show the challenges to find an optimum condition for the desired framework synthesis. They also evoke the complicated factors we need to consider for MOF synthesis, especially in case more than one organic linker is used. However, the two examples are relatively simpler cases than the MOFs that will be introduced and discussed in this thesis.

All the work reported in this thesis was designed and conducted based on two sister frameworks, MUF-7 and MUF-77,[7,56] which are composed of three topologically distinct organic linkers. Besides, the three linkers constructing both frameworks are almost identical. Thus, much more complex situations are associated with MOF formation than the two examples above. Sometimes, an unexpected framework is obtained, in other cases, two different phases grow in the same synthesis batch, or even both frameworks intergrow as a single crystal. Such uncertainty for the formation of two frameworks sometimes leads to unexpected results and thereby plays a crucial role in this thesis.

In this chapter, the architectural similarities and differences between the two frameworks, MUF-7 and MUF-77, will be explored. In addition, how the distinct structural features lead to different results in catalytic applications will be investigated through a few experiments.

2.1.1. The first quaternary multi-component MOF

As discussed in the earlier chapter (1.2.1.2), the isoreticular MUF-7 framework series was the first ever reported quaternary MC-MOF by the Telfer group in 2013.[56] MUF-7 is built from three topologically distinct organic linkers. The two linear linkers, bdc and bpdc, and one tritopic linker btb form a highly ordered crystal along with Zn_4O (Figure 2-3a). Since these linkers form a highly ordered network, the pores surrounded by these linkers are not all identical. According to the crystal structure, four different pores, one dodecahedral mesopore and three tetrahedral micropores, are formed in MUF-7 (Figure 2-3b). The dodecahedral mesopore (pore-I) has a diameter of 25 Å and is surrounded by all three linkers. Pore-I constitutes of three pairs of bdc and bpdc, which are facing each other across the pore, and eight btb linkers are connecting those linear linkers. This dodecahedral pore is slightly

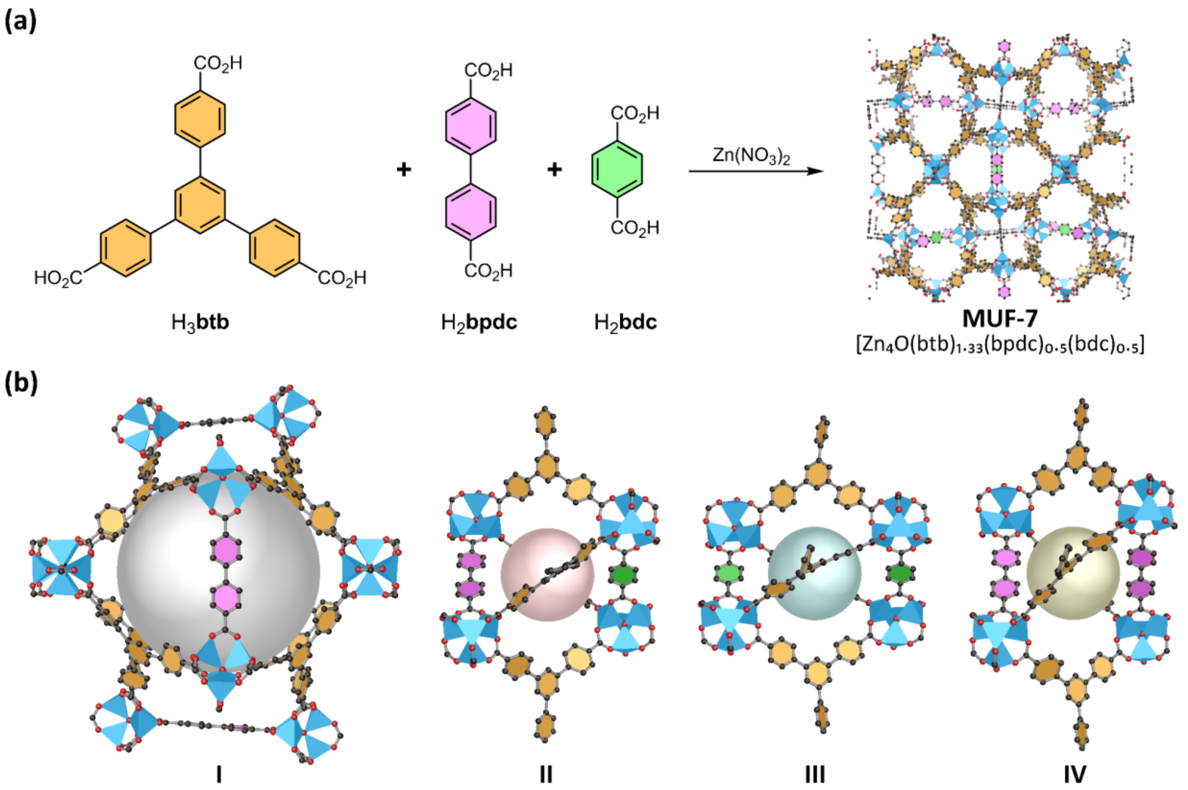

Figure 2-3. (a) Two linear and one tritopic linkers composing MUF-7; (b) four different pores in MUF-7; the spheres indicate the void spaces in each pore.

skewed, as depicted in the figure, due to the different lengths of two co-facial linear linkers. There are also three different types of tetrahedral micropores whose diameters are approximately 10 – 12 Å. These tetrahedral pores occupy the space between the mesopores, so the linkers consisting these small pores are all shared with the adjacent mesopores. All three tetrahedral pores are topologically identical; two linear linkers orthogonally face each other while four btb linkers connect these two linear linkers. However, each pore is composed of different linear linker pairs; either bpdc–bdc, bdc–bdc or bpdc–bpdc for pore-II, -III and -IV, respectively (Figure 2-3b). Hence, their pore sizes and environment are slightly different from each other.

2.1.2. A successor of MUF-7

In 2015, another isoreticular series of MC-MOFs, the MUF-77 series as a successor to MUF-7, was reported by the Telfer group.[7] The organic linkers composing MUF-77 are almost identical to those of MUF-7 (Figure 2-4a). Only a minor change is made to the tritopic linker while the two linear linkers remain the same. To compare with the btb of MUF-7, hmtt (5,5,10,10,15,15-hexamethyltruxene-2,7,12-tricarboxylate) is a more rigid and planar molecule since the peripheral phenyl rings cannot rotate with respect to the core. It is also more amenable to derivatisation with various functional groups at the 5, 10 and 15 positions.

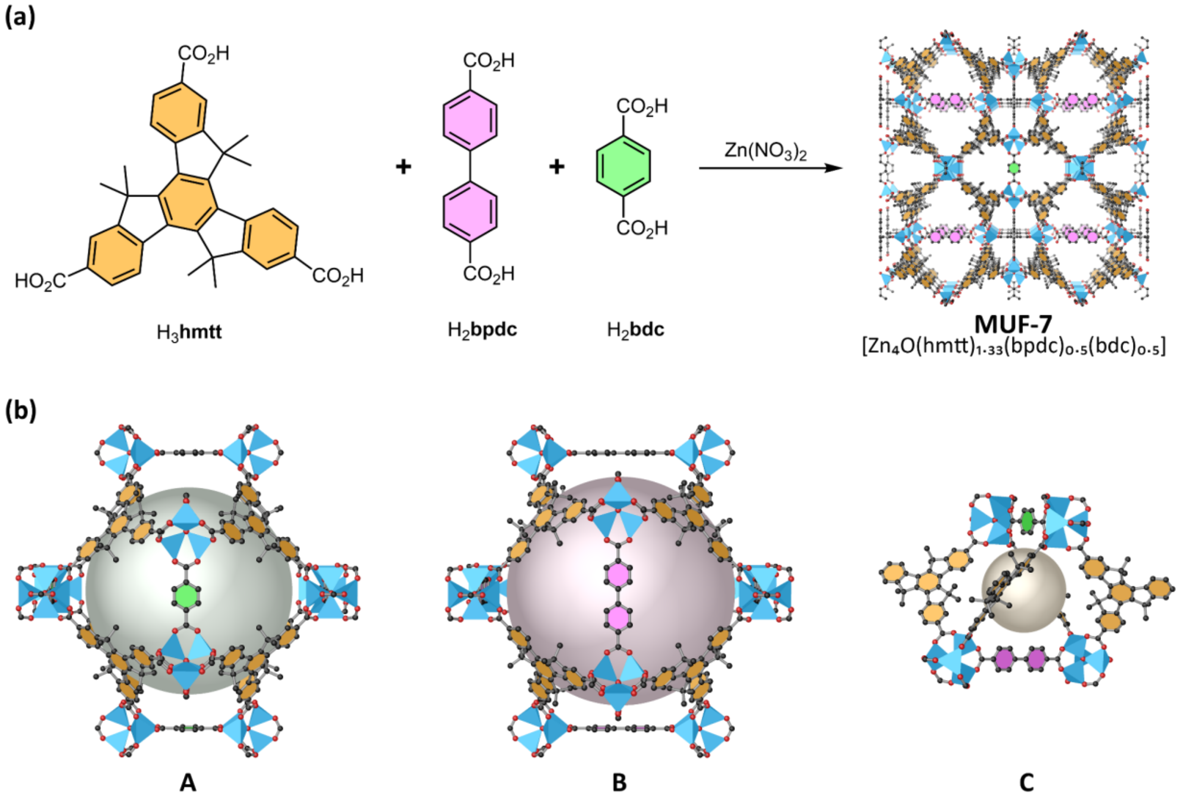

Figure 2-4. (a) Two linear and one tritopic linkers composing MUF-77; (b) three different pores in MUF-77; the spheres indicate the void space in each pore

Although btb and hmtt only differ in a minor way, several notable differences were observed in the resulting framework (the details of similarity and difference between the two frameworks will be discussed in the following sections). The most prominent structural change was seen in the pores. As depicted in Figure 2-4b, MUF-77 has two dodecahedral mesopores and one tetrahedral micropore. Two dodecahedral pores are composed of two ligands, either bdc and hmtt or bpdc and hmtt, thus being slightly different in size due to different dimension of bdc and bpdc. The tetrahedral pore is comprised of all three linkers. Unlike MUF-7, the three pairs of the linear linkers surrounding the dodecahedral pores are of the same kind. Therefore, they are parallel to each other, thereby allowing symmetrical pore shapes (pore-A and pore-B in Figure 2-4).

Apart from these structural differences, MUF-77 exhibits enhanced stability compared to MUF-7, especially against moisture, which allows more extensive applications, such as catalysis. Furthermore, MUF-77 is easier to synthesise because the rigid truxene derivatives exclude the formation of competing structures that are derived from flexible btb with other linkers. It is less likely affected by the ligand feed ratio or other synthesis parameters. Besides, a more diverse pore environment can be attained due to the expanded range of functional groups that can be embedded in the tritopic linker.

2.2. Isomerism of two frameworks

2.2.1. Similar but different

Two sister frameworks, MUF-7 and MUF-77, possess quite similar properties in many aspects, such as the synthesis conditions, the morphology of crystals (Figure 2-5). Especially, the crystal structures of the two frameworks share many common factors. For example, they both possess cubic unit cells and the same network topology of **ith-d**. Such similarities make it challenging to characterise whether the synthesised MOF is an isostructure of MUF-7 or MUF-77 and whether it is the sole phase. One of the most versatile analytical methods, ^{1}H NMR spectroscopy, which determines linker ratios, is not applicable in this case because both frameworks have the same linker ratios ([Zn_4O(tritopic linker)$_{1.33}$(bpdc)$_{0.5}$(bdc)$_{0.5}$]). Another standard characterisation method, PXRD, is not very reliable either. Figure 2-5 illustrates the calculated and experimental PXRD patterns of each structure. The difference in PXRD patterns of the two frameworks is hardly distinguishable unless carefully looked at them. The only notable differences between the two PXRD patterns are the tiny peaks presented in the yellow shaded boxes in Figure 2-5. The two small peaks at 3.5 and 5.5° for MUF-7 and the three little peaks at around 3, 5, and 6 ° for MUF-77 are the characteristic peaks that can differentiate the two frameworks. However, the peak at the low 2θ range (< 3 °) is not always

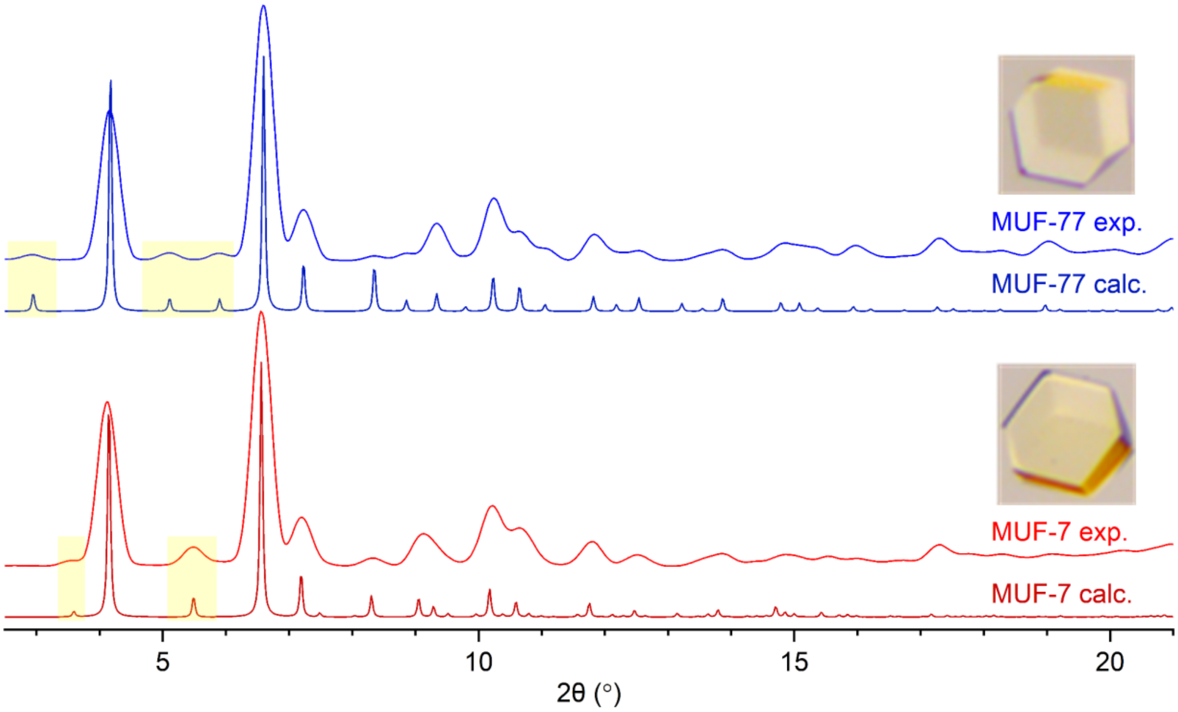

Figure 2-5. The calculated (calc.) and experimental (exp.) PXRD patterns of MUF-7 and MUF-77; the optical images of both crystals were also shown along with the corresponding PXRD pattern. The peaks inside the shaded boxes are the characteristic peaks which are used to differentiate the two different frameworks.

measurable due to the limitation of the X-ray apparatus in measuring at lower 2θ angles. Moreover, such tiny peaks cannot be distinguished if the diffraction has lower intensities or high background noise.

For these reasons, single-crystal X-ray diffraction is the most reliable characterisation method to determine the structure. Although they have quite a few common characteristics, the structural difference between the two frameworks is discernible. Most of all, MUF-7 has twice larger unit cell lengths than MUF-77. Figure 2-6a shows a single unit cell of MUF-7 (left) and a 2×2×2 supercell of MUF-77 (right), and their sizes are almost the same. The connectivity and positions of three organic linkers surrounding the zinc cluster are identical due to the identical network topology of the two frameworks. However, MUF-7 has a lower symmetry because of the different arrangement of the linear linkers, as discussed earlier, and this is prominently presented in Figure 2-6. Furthermore, MUF-7 is slightly larger than the MUF-77 supercell; they are drawn on the same scale, and the blue dashed line can be used to gauge the difference between the two frameworks. Such a subtle difference in unit cell length between them induces a slight peak shift in PXRDs; in Figure 2-5, most peaks belonging to MUF-7 are slightly shifted to a lower 2θ value compared to the ones of MUF-77.

Figure 2-6b is the simplified model of the two structures above, and the spheres in the circle of each framework indicate small pores which are aligned along the axis perpendicular to the presenting plane. Figure (c) illustrates the detailed arrangement of those small pores in each framework. As discussed above, there are three different small pores in MUF-7 due to the less symmetric arrangement of the two linear linkers. As a result, a pair of bdc and a pair of bpdc alternate and produce three different pores (pore-II, -III and -IV). On the other hand, the two linear linkers regularly alternate in MUF-77 and form only one type of pore-C, which is equivalent to the pore-II in MUF-7.

The two structures of MUF-7 and MUF-77 will be discussed throughout the entire thesis. Therefore, the two frameworks will be denoted with more intuitive and informative notations; from now on, the isoreticular structure of MUF-7 and MUF-77 will be referred to as type-L (L for larger & less symmetric unit cell) and type-S (S for smaller & symmetric unit cell).

(a) Type L ≡ isostructure of MUF-7 **Type S ≡ isostructure of MUF-77**

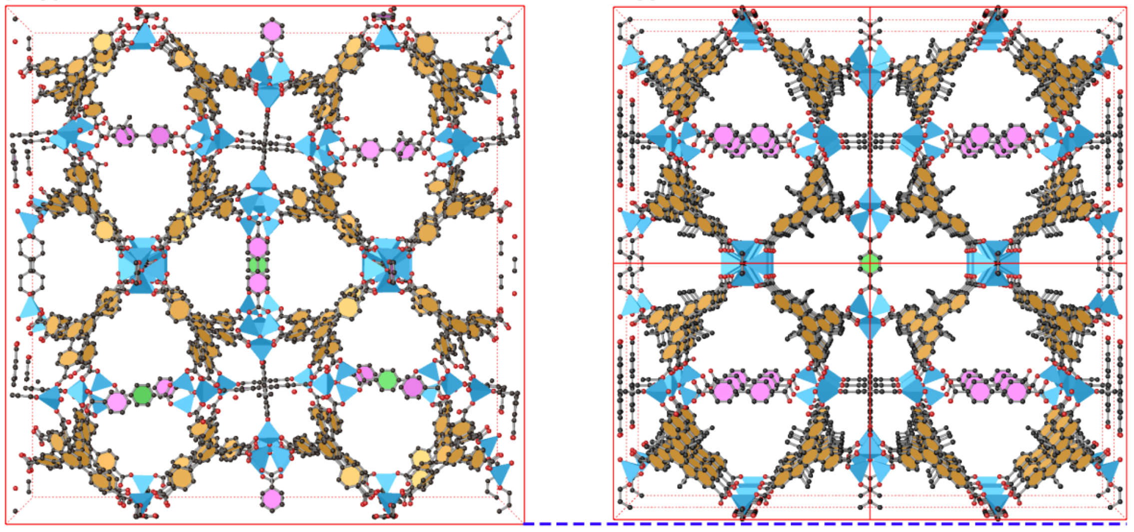

(b) simplified model

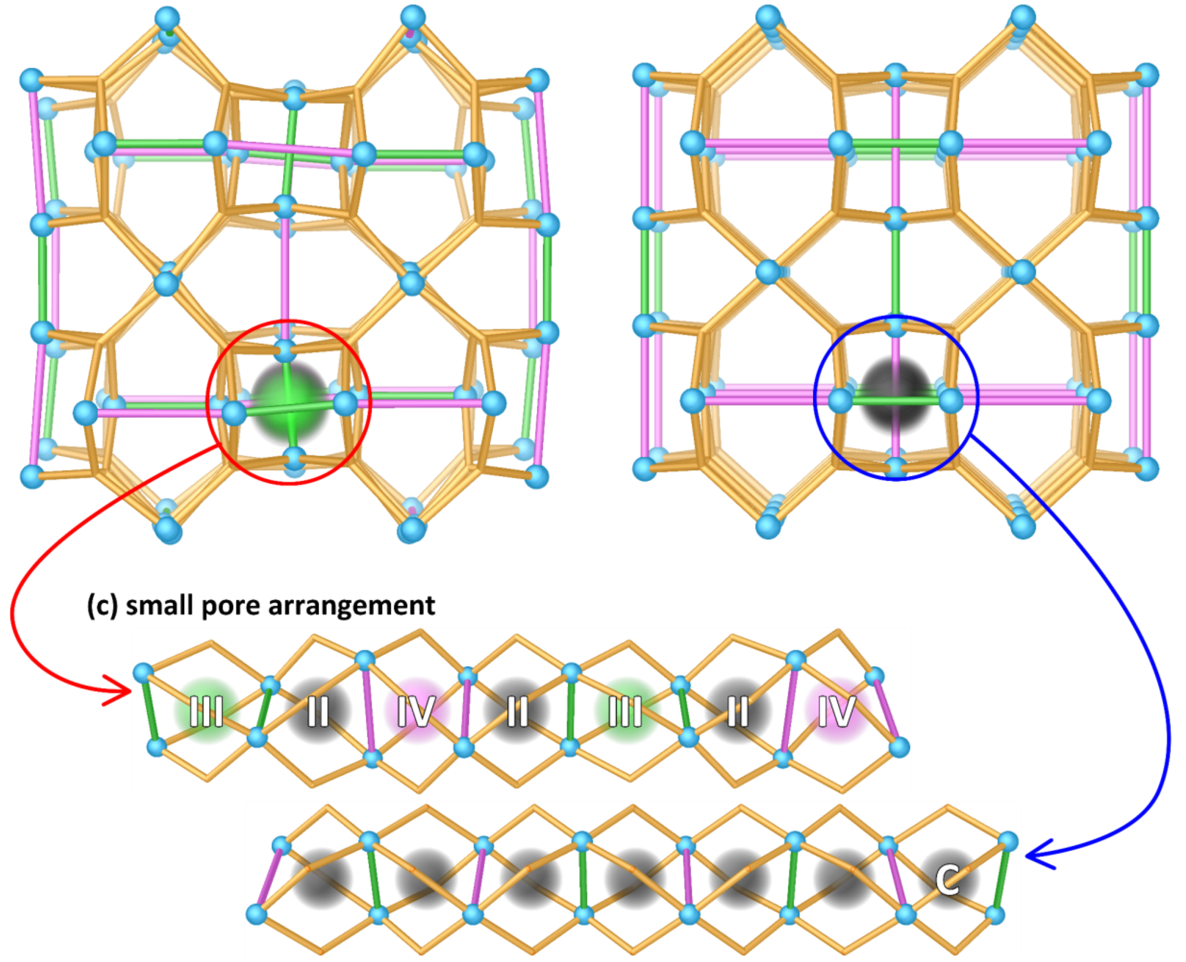

Figure 2-6. (a) The original model of a single unit cell of MUF-7 (Type L) and 2×2×2 unit cell of MUF-77 (Type S). The red line indicates a unit cell border, and the blue dashed line was drawn for an easier comparison for the size difference between the two unit cells. (b) The simplified model of each framework (c) Different arrangement of small pores from each framework.

2.2.2. Rule breakers

The difference between the two tritopic linkers, btb and hmtt (or other truxene derivatives), does not seem huge. Still, it is enough to cause significant structural differences considering that number of different structures formed from the bdc and zinc combination, which was introduced early in this chapter. According to our earlier studies on MUF-7 and MUF-77, the most apparent driving factor in determining the phase between the two frameworks during the MOF synthesis was the tritopic linker.[7,56,109-111] We regarded that the type-S framework is formed from the rigid truxene-derived linkers no matter what functional groups are installed on the bdc or bpdc linkers. We could not measure SCXRD for every crystal sample we had synthesised because it costs too many resources. Still, all the measured SCXRD data of the crystals synthesised from the truxene-derived linkers had corresponded with the type-S framework. Therefore, it was accepted as a solid trend that type-S frameworks are formed if truxene was used. However, as we expanded the ligand library by installing more various and complicated functional groups to the ligand backbones, the solid trend in type-S formation crumbled when some specific ligands combinations were used.

In this section, a few examples of rule-breakers will be presented and discussed. These example structures unexpectedly arose from the experiments for chapter 3 and 4, or they were found by our group lately.

2.2.2.1. Large functional groups

The type-L frameworks have been randomly and occasionally observed when bulky secondary functional groups are attached to the linkers. However, no clear relationship between the type or size of functional groups and the resulting frameworks has been found yet. Sometimes it happens with a single substituent on a specific ligand (Figure 2-7a), or a specific combination of multiple functional groups on each ligand cooperatively leads to the type-L framework (Figure 2-7b).

The H_2bdc-dpq (dpq: diphenylquinoxaline) derivatives shown in Figure 2-7a are one of the largest bdc derivatised molecules able to fit in type-L or -S. We highly expected that the type-S framework would be formed with the bdc-dpq linker because the bulky substituent would have less steric hindrance in the type-S framework. If the type-S framework were formed, the bdc linkers would not neighbour each other (Figure 2-6c), so the bulky functional group would occupy the entire pore space (pore-C). On the contrary, the two bdc linkers neighbour across pore-III in the type-L framework, and the two bulky substituents on them could experience a sterical hindrance if they both point toward pore-III and share the limited pore space.

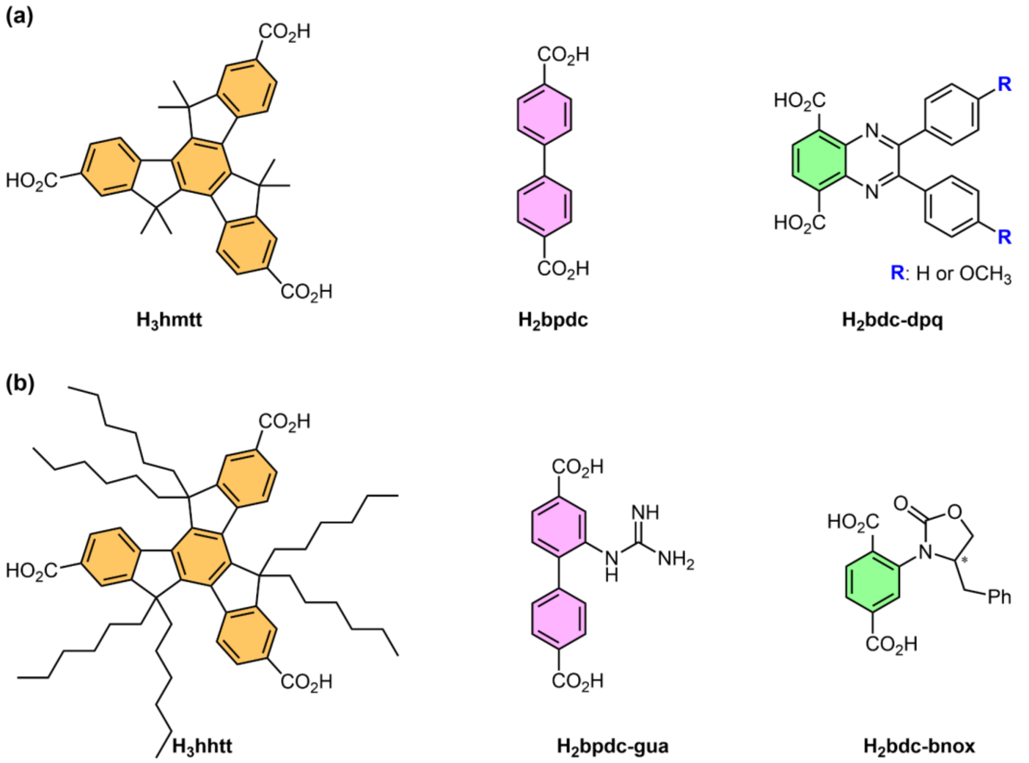

Figure 2-7. Two examples of linker combination which form the type-L frameworks, (a) the bdc derivative alone causes the type-L framework; (b) all three linkers cooperatively lead to the type-L framework.

Interestingly, the synthesised framework from the hmtt, bpdc and bdc-dpq combination (Figure 2-7a) was type-L. The structure obtained by SCXRD reveals the more exciting feature regarding the two dangling phenyl rings on the dpq moiety. It is rare that such a huge secondary functional group on a linear linker is clearly shown in the crystal structure because a high degree of disorder was generally found due to the rotational motion of the ligand backbone. Moreover, the two-terminal phenyl rings can also rotate freely by themselves. However, in this case, no disorder was found, and even the methoxy groups at the end of the terminal phenyl rings were explicitly positioned without any constraints or restraints. The reason was found from another view of the crystal structure why this specific linker combination forms a type-L framework and why no disorder was found in the dpq moiety.

According to the crystal structure, the dpq moieties on all the bdc linkers stretch toward pore-III, leaving pore-II empty (Figure 2-8a). Therefore, the four dangling phenyl rings from the two neighbouring bdc-dpq linkers interact with each other in pore-III and find a specific conformation. The close-up views (Figure 2-8b and c) of the two bdc-dpq-OMe linkers show that all four terminal phenyl rings are entangled by the edge-to-face π-π interactions, thus interlocking with each other. The distance between the H atom on a phenyl ring and the centroid of the conjugate phenyl ring is 3.00 Å, and the centroid to centroid of two rings is 5.05 Å, which are well coincident with the reported values.[112] The T-shape π-π interactions among four phenyl rings become a huge driving force for the two neighbouring dpq units to

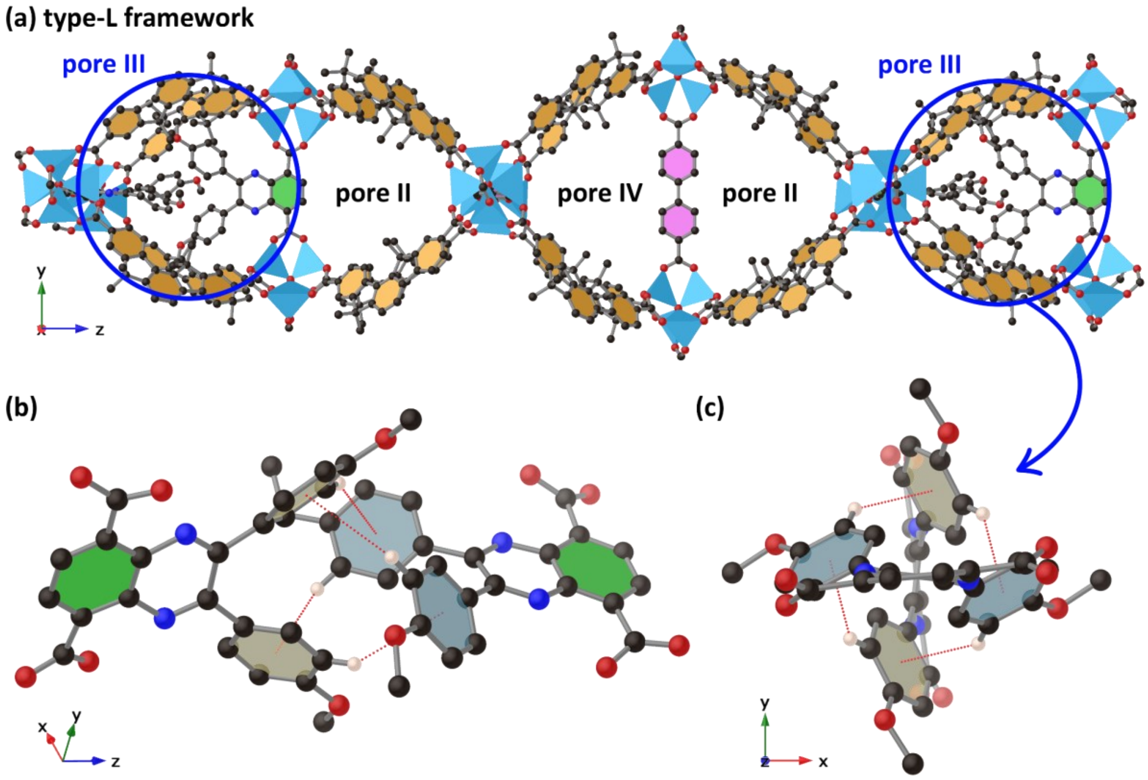

Figure 2-8. (a) The closely packed two diphenyl quinoxaline moieties in pore-III; (b) a close-up view of two bdc-dpq-OMe ligands in pore-III and (c) the close-up view through the z-axis, which well illustrates the mutually interlocking four phenyl rings through the edge to face pi stacking. Unnecessary H atoms were omitted for clarity; The phenyl rings that belong to different ligand were displayed in different colours.

stay in pore-III, thereby leading to the type-L framework.

Bdc-paq (paq: phenanthrenequinone, depicted in Figure 2-9) nicely contrasts the role of π-π interaction forming the type-L framework. The main difference is that the two terminal phenyl rings are no longer rotatable due to the single bond (depicted in red in Figure 2-9) between the two terminal phenyl rings. As a result, the entire bdc-paq turned into a rigid planar molecule and could not form the π-π stacking like bdc-dpq. Thus, the type-S framework is preferentially formed in this case in order to minimise the steric hindrance between the two bulky groups. This experiment strongly suggests that the formation of the type-L framework with bdc-dpq is hugely contributed by the π-π interaction between the two neighbouring bdc-dpq linkers.

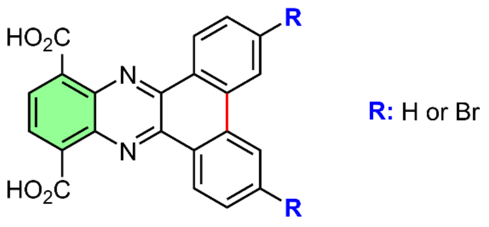

H_2bdc-paq

Figure 2-9. Two phenyl rings on dbp moiety are not rotatable due to the bridging bond (in red) connecting two rings.

The three ligands combination leading to the type-L framework is depicted in Figure 2-7b. In this specific case, all three functional groups are essential in forming the type-L framework. If any one of them is replaced with another compatible ligand, the probability of obtaining in the type-L framework gets lower, or phase pure type-S framework is formed. For instance, if the alkyl chain lengths on the truxene linker were changed, the type-S framework is more preferred over the type-L framework. In this case, the driving force to form the type-L framework is not figured out.

2.2.2.2. H_3cbtt (5,10,15-cyclobutyltruxene-2,7,12-tricarboxylate)

MUF-88, isostructural type-L framework, is formed from an interesting tritopic linker, cbtt (cyclobutyltruxene tricarboxylate).[113] The geometry and physical property of cbtt are a lot closer to hmtt rather than btb. However, it has been found that no matter with which linear ligands cooperate, it only produces the type-L frameworks so far. This result is a complete outlier considering the solid trend that the truxene derivatives form a type-S framework with the bare bdc and bpdc pair. Although we do not fully understand why cbtt exclusively forms the type-L framework, some interesting features were noted from the crystal structure.

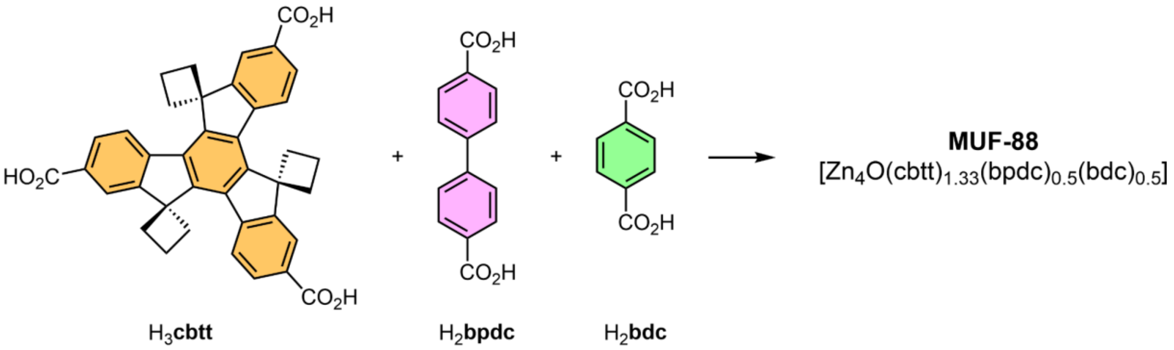

Figure 2-10. The tritopic linker, H_3cbtt forms only type-L frameworks no matter which the two linear linkers are.

The coordination geometry around the Zn_4O cluster with the four cbtt in the type-L framework or the four hmtt in type-S clearly shows a distinct characteristic of the two different frameworks. The coordination geometry of the two frameworks is depicted in Figure 2-11. The positions of all six linkers coordinating on the Zn_4O octahedral cluster are identical in both frameworks; each of the two linear ligands coordinates on the axial position of the cluster while the four tritopic linkers occupy the remaining equatorial positions. However, the symmetrical arrangement of the four tritopic linkers in type-L is changed. In type-S, the top view of four hmtt ligands shows two vertical mirror planes which are orthogonal to each other, and the side view exhibits the methyl groups all pointing downwards (Figure 2-11a). On the other hand, in type-L, one cbtt linker in the red circles is flipped, so the cyclobutyl ring on that cbtt linker points upwards while the others point downwards (Figure 2-11b). As a result, the elegant symmetry of type-S was diminished in type-L, and the framework turned into a body centred unit cell (space group: I-43d).

The difference between hmtt and cbtt is only three extra carbon atoms on each cyclobutyl

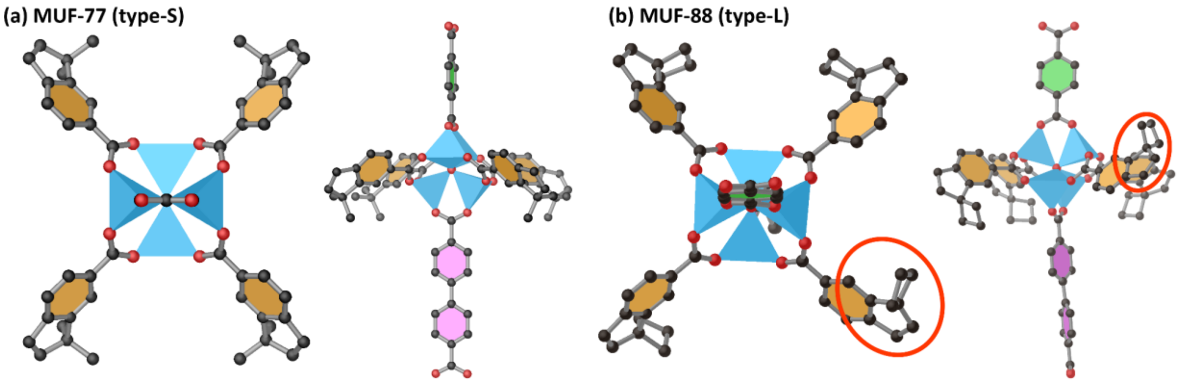

Figure 2-11. The top and side view of coordination geometry around zinc cluster of the two frameworks, (a) MUF-77 (type-S) and (b) MUF-88 (type-L).

ring of cbtt. The cyclobutyl group is not large enough to cause any type of inter-ligand interactions in the framework, which can cause structural change. Moreover, cbtt is not as flexible as btb linker. However, it is still mysterious why such a minor difference between hmtt and cbtt causes such structural change from type-S to type-L.

2.2.3. Both phases in a synthesis

2.2.3.1. Both phases in the same synthesis batch

As discussed above, a type-L framework was unexpectedly formed from the linker combination of hhtt, bpdc-gua and bdc-bnox (Figure 2-7b). However, if hmtt replaces hhtt in MOF synthesis, both type-L and -S frameworks occasionally appear in the same synthesis batch. As depicted in Figure 2-12a, the PXRDs clearly show that the experimental pattern (black) possesses all the characteristic peaks belonging to both type-L (red) and type-S (blue) at lower 2θ. The morphology of the synthesised crystals was not distinguishable between two phases (Figure 2-12b), which makes it difficult to figure out whether the two phases are grown together in a single crystal or two different phase pure crystals grow individually. Hence, twenty single crystals were randomly chosen, and thirty diffraction images were collected from each crystal sample to investigate their phases. As the example diffraction patterns indicate (Figure 2-12c and d), there is a notable difference between the two diffraction patterns. The diffraction spots belonging to type-L are more closely and tightly packed together due to the larger unit cell. After collecting diffraction data, the unit cell dimensions were calculated from the thirty diffraction images for each sample. According to the calculated unit cells, both type-L and type-S phases existed as a phase pure individual crystal in a single synthesis batch with almost one to one ratio (type-L/type-S = 11/9).

Based on the one to one ratio of both crystals from the synthesis batch, it is considered that the synthesis condition is optimum for both frameworks. As a result, it seems that a subtle

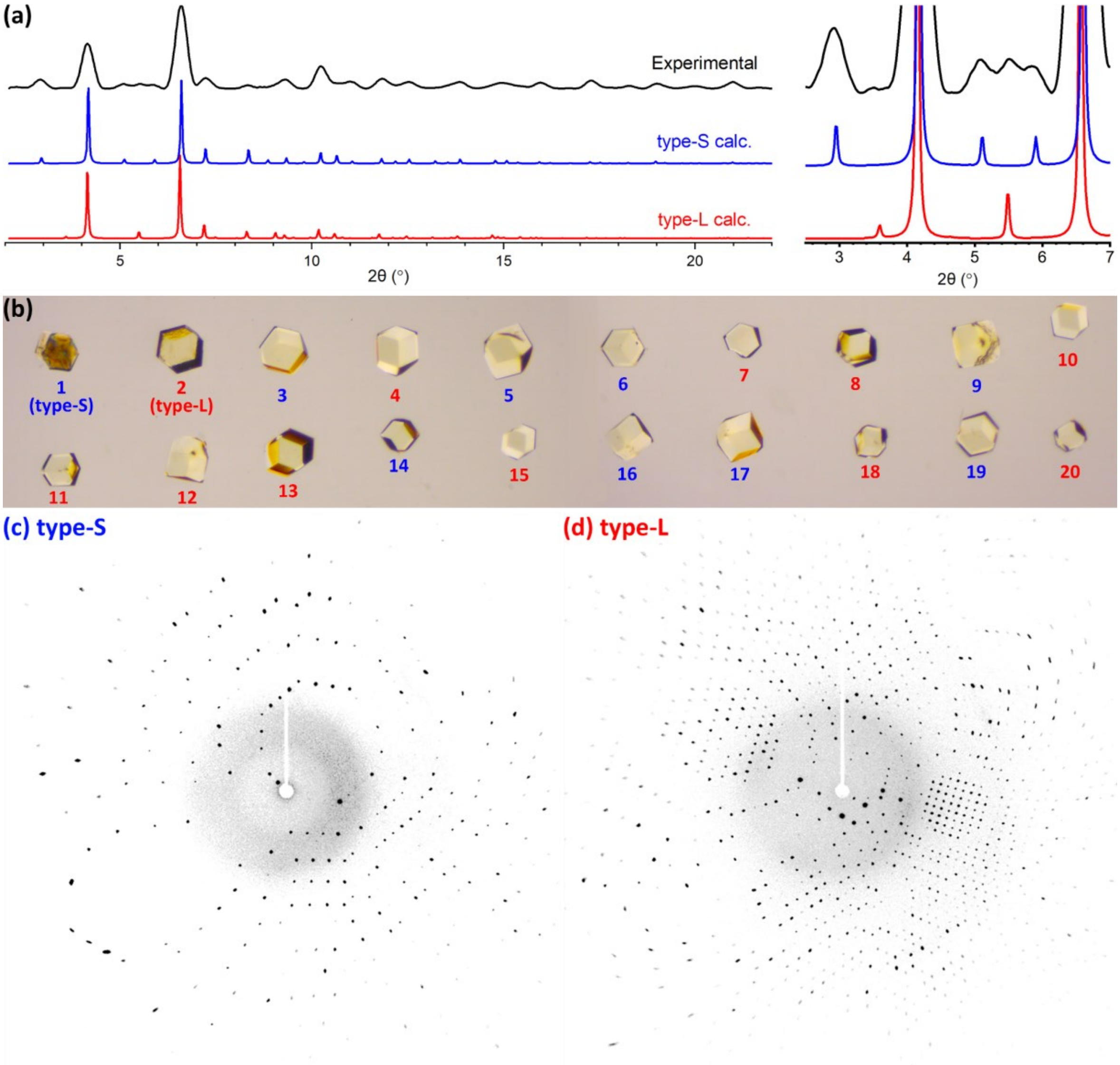

Figure 2-12. (a) PXRD pattern shows the characteristic peaks of both type-L and type-S; (b) Randomly selected twenty crystals from a single synthesis batch. The phase was determined by unit cell determination from thirty diffraction images of each crystal and was indicated using different colours (MUF-7: blue, MUF-77: red); an example diffraction pattern of (c) MUF-7 and (d) MUF-77.

difference in a local area in the synthesis vial caused different phase crystals. Thus, we planned to change the synthesis temperature to investigate the driving force of phase determination between type-L and type-S. Temperature control during crystal formation is a widely adopted method in order to regulate thermodynamic and kinetic factors in MOF synthesis to obtain different phase crystals.[114-115]

Three identical synthesis batches from the same ligand mixture (hmtt, bpdc-gua and bdc-bnox) were prepared, and each batch was kept at a different isothermal oven of 65 °C, 85 °C (the default synthesis temperature) or 105 °C. First of all, there were notable differences between the times required for crystal formation in each batch. A few crystals observable to the naked eye started forming after around 6 hours at 105 °C, while the other two batches

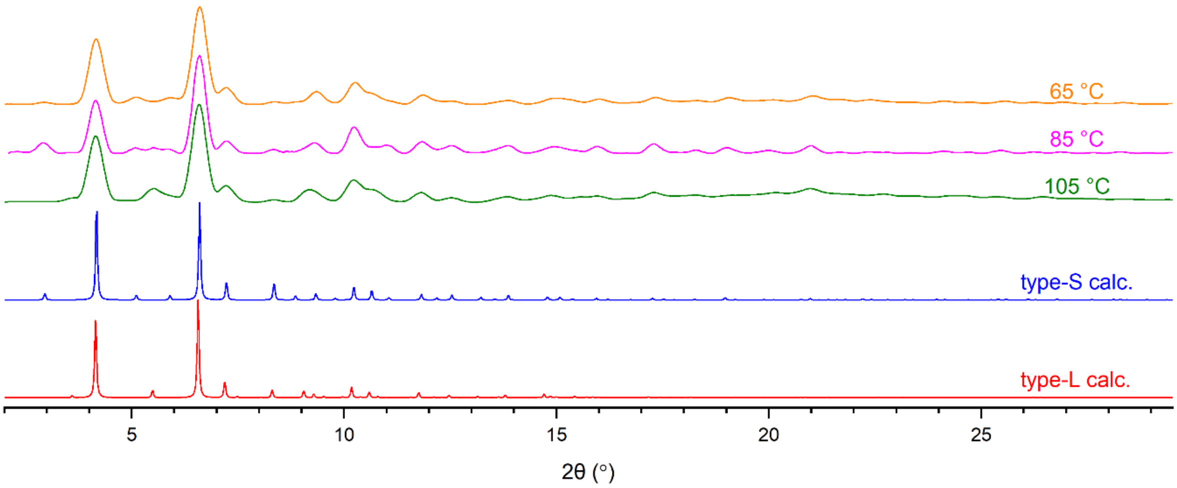

Figure 2-13. PXRD patterns collected from the crystal samples which were synthesised at the different temperature of 65, 85 and 105 °C.

took longer to get crystals, about 18 and 48 hours for 85 °C and 65 °C, respectively. After the crystals were fully grown, PXRD of a finely ground sample (20+ crystals) from each batch was collected. According to the PXRDs, type-S was dominating phase for the crystals synthesised at 65 °C while type-L seems the sole phase for the ones synthesised at 105 °C, and again, the ones synthesised at 85 °C were a mixture of the two phases (Figure 2-13).

The synthesis temperature variation obviously influenced the phase determination during crystal formation. Although it is hard to say a certain framework is thermodynamically or kinetically more favourable since many factors are involved in crystal formation, we can exploit the result that the type-L framework is likely formed at a higher temperature.

2.2.3.2. A single crystal composed of polycrystalline domains of the two frameworks

Both type-L and type-S crystals usually have the same morphology, prismatic polyhedron. However, irregularly shaped crystals sometimes were obtained, as shown in Figure 2-14a. Such irregularly shaped crystals are usually observed when a newly designed ligand is tested. The irregularly shaped crystal formation can be suppressed in most cases by adjusting the feed ratios between the ligands in the synthesis mixture. This suggests that the formation of the irregularly shaped crystals is caused by the changed reactivity of the new ligands. The change in ligand reactivity is caused by the different functional group installed on the ligand, and it will cause the ligand consumption rate. As a result, it leads to a relatively lower or higher local supply of a specific ligand, and eventually, to the local defects or disorder.[116] However, such defects caused by the uneven local concentration of a specific linker can be managed or minimised by adjusting linker feed ratios so that the regular prismatic shape crystal can be obtained.

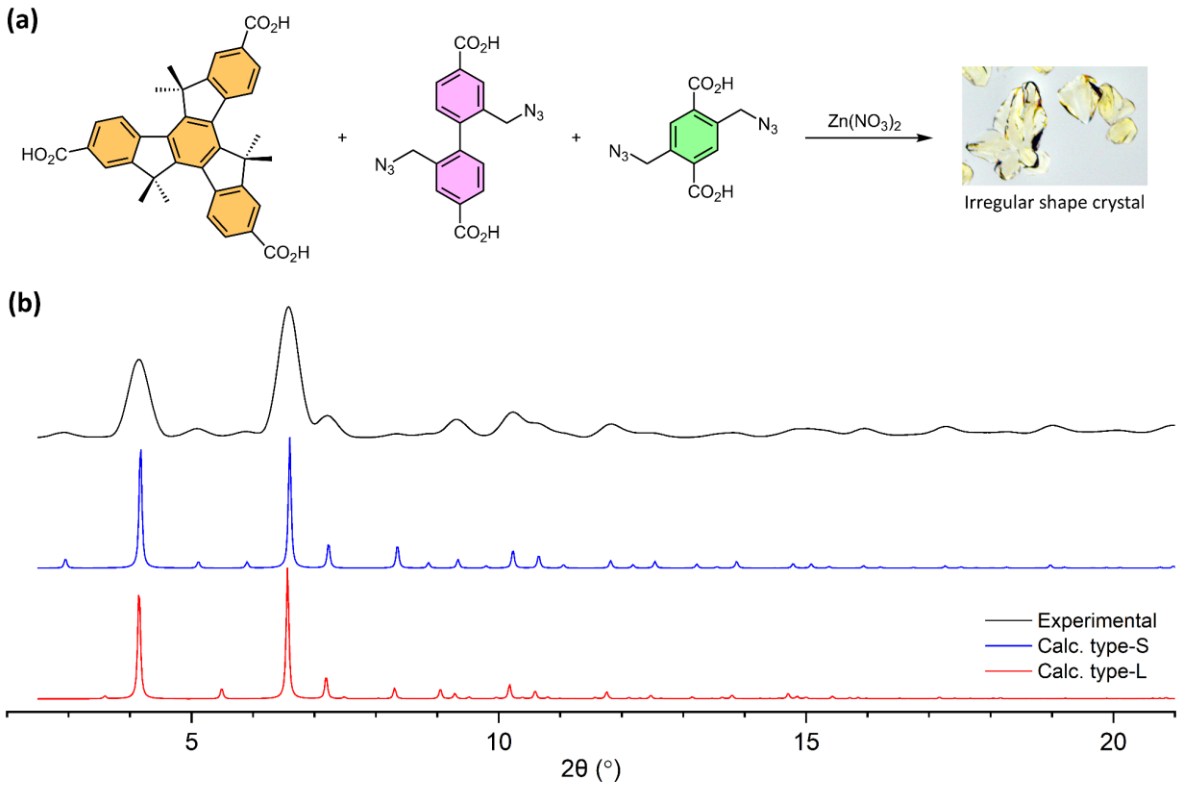

Figure 2-14. The optical microscopy image of the irregularly shaped crystals and the corresponding PXRD pattern which well match the calculated type-S diffraction pattern.

Although the morphology of the irregularly shaped crystal is a bit strange, it was a type-S framework according to the PXRD pattern (Figure 2-14b). Therefore, we had undoubtedly regarded it as the type-S framework and used it for a while. However, after noting that the trend between the tritopic linker and phase of the framework became obscure, we needed to make sure that the irregularly shaped crystal was type-S as the PXRD indicated.

Hence, a set of SCXRD data was collected from the irregularly shaped crystal, and the structure was solved. However, some interesting features were observed in the diffraction patterns. The SCXRD software determines a proper unit cell based on a few diffraction images before the main data collection. Then, the calculated unit cell is used to set up parameters for data collection, such as crystal orientation with respect to the incident X-ray, scan width (°) for each frame, the exposure time for each scan, and the number of total diffraction images to be collected. Furthermore, it can be used to integrate spot intensities after data collection. The number of diffraction images varies from hundreds to thousands, and each image contains tens to hundreds of diffraction spots, so the software integrates only the corresponding spots based on the calculated unit cell in order to save resources and time. For instance, Figure 2-15 illustrates the actual diffraction spots and calculated spots (appearing as circles) based on the calculated unit cells. Thus, the software only calculates the intensity of the diffraction spots enclosed in those circles.

According to the calculated unit cell, the irregularly shaped crystal was determined as type-

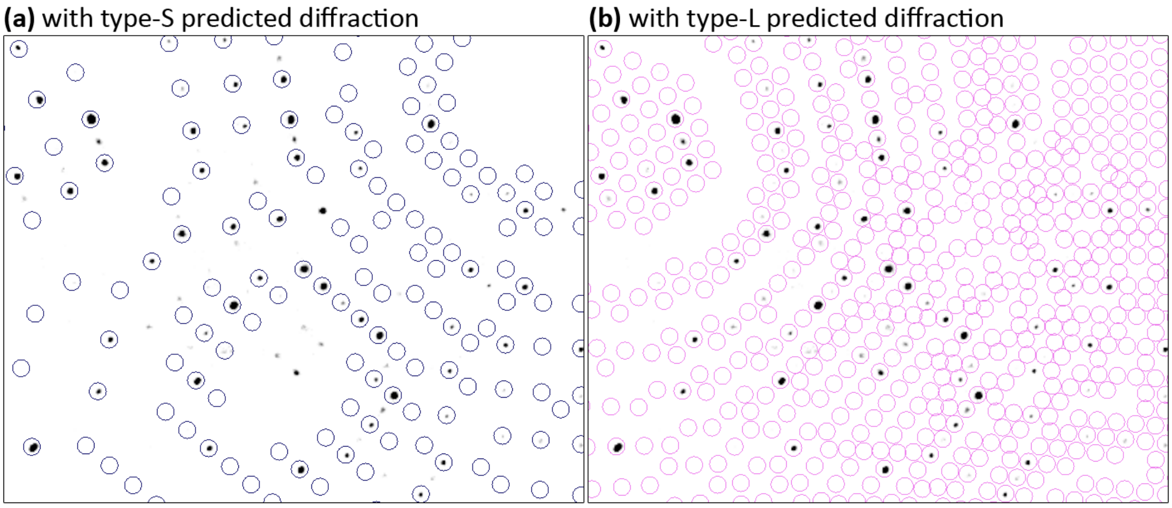

Figure 2-15. Both (a) and (b) are the same diffraction pattern, however, a few diffraction spots do not match the predicted ones for type-S, but match the predicted ones for type-L.

S. However, if the calculated spots for type-S are overlaid with the actual diffraction images, a few faint spots, which do not superimpose to the calculated ones, are observed (Figure 2-15a). Some of those spots are placed in between the two neighbouring predicted spots, indicating they might arise from a larger unit cell. Therefore, another unit cell calculation was conducted by changing the parameters to include those weakly diffracting spots as well. Interestingly, the resulted unit cell was one for the type-L framework. Both diffraction images, shown in Figure 2-15a and b, are identical, and the dark blue circles are the calculated spots based on the type-S unit cell while the pink ones are of type-L. The diffraction spots outside the dark blue circles are all enclosed in the pink circles, indicating that the actual structure could be the type-L framework.

However, the majority of the spots, not superimposing with the predicted diffraction spots, have relatively weaker intensity in general compared to the ones captured in the dark blue circle. Such intensity difference between the two groups might be simply caused by the cell contents in the crystal lattice. The cell content in the crystal lattice determines the spot intensity, while the unit cell dimension defines the position of the diffraction spots. Therefore, if the irregularly shaped crystal is a type-L framework with specific cell contents, such weak diffraction spots might be observed.

However, there is a more plausible explanation about the intensity difference between the two groups (inside vs outside dark blue circles) of diffraction spots. It seems that the two different domains of each framework coexist in the same crystal. According to Kim et al., two topologically different MOFs can seamlessly grow as a single crystal.[117] Although the two frameworks are composed of different organic linkers and have different network topologies, they share the same spatial arrangement of the metal nodes, which allows the epitaxial growth of one framework on another. In line with this, the two crystalline domains of type-L and type-S can grow together in a single crystal because they possess the same topology and are composed of identical organic linkers with the nodes of the same spatial arrangement.

If this is the case, we can make a hypothesis that both crystalline domains contribute to the highly intense spots, and the type-L crystalline domain contributes alone to the weak diffraction spots. It is because the unit cell of the type-L framework is almost the same size as the 2×2×2 supercell of the type-S framework (Figure 2-6a). Therefore, the majority of diffraction spots produced by the type-L crystalline domain will overlap with the ones diffracted from the type-S crystalline domain. However, the type-L framework diffracts more spots that the type-S framework can not diffract due to the size difference between their unit cells.

A set of experiments was designed to investigate further whether the spot intensity difference is induced by the two crystalline domains grown together in a single crystal (henceforth denoted as co-crystal). The two spot groups (inside vs outside type-S predicted circles in Figure 2-15a) have different spot intensities in general. Suppose the difference in spot intensities between the two groups is the general feature of the type-L frameworks comprised similar ligands (composed of light elements, such as C, H, O and N). In that case, the electron density in each crystal lattice would be similar, so the same trend should be observed in the other type-L frameworks because the spot intensity is determined by the electron density. Therefore the experiment was designed as follows.

A few spots from the two groups would be indexed and the corresponding spot intensities appearing in co-crystal, and then the other type-L frameworks would be compared with each other. If all spots have similar intensities, the difference between the two groups is then regarded as a general feature of the type-L framework. Otherwise, it can evidence that the co-crystal is composed of the two different domains of each framework.

The intensities of the indexed spots from each group in the co-crystal were calculated from the hkl file and compared with the ones calculated from three selected type-L frameworks (Figure 2-16a, refer to Appendix A for the experimental detail). The result is presented in Figure 2-16b, and it clearly contrasts differences in the spot intensities between co-crystal and the three tyle-L frameworks. The intensities labelled with a# (#: 0–9) are the ones outside circles (the intensity was contributed by only type-L subdomains), whereas the ones with b# are contributed by both type-S and the type-L phases. The spot intensities of the three type-L frameworks are almost identical for both groups. However, the co-crystal spot intensities are completely different from the other three type-L cases, especially the spot intensities of the group a of co-crystal is much lower than the others.

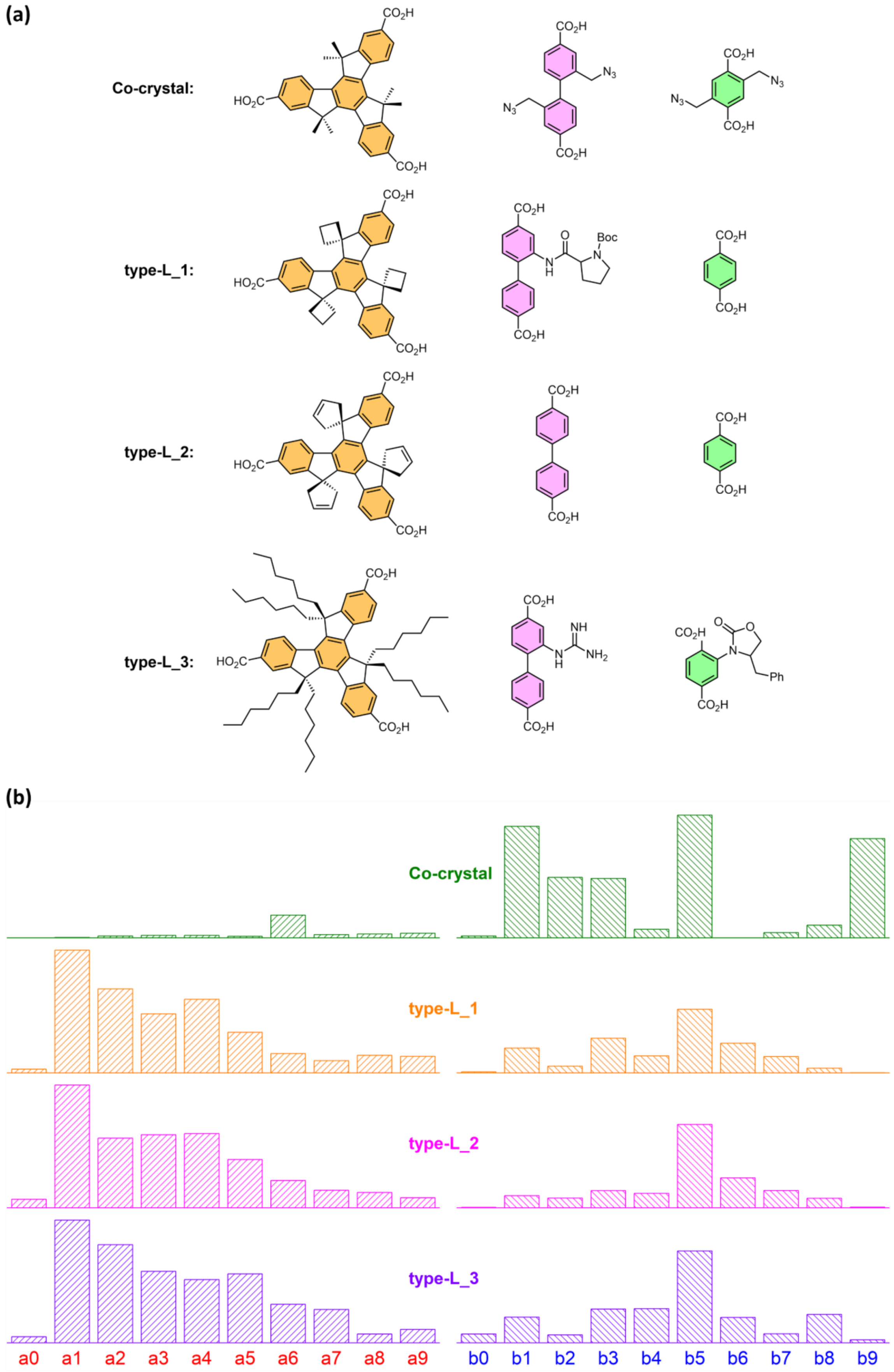

Figure 2-16. (a) The ligand combinations for the co-crystal and type-L_x frameworks; (b) the comparison of relative spot intensity between the two groups, a and b in each framework. There is a notable difference in the trends of spot intensities between co-crystal and the other three MUF-7 structures.

It is presumed that the two different framework domains grow together in a single crystal based on the result above. This is quite an unusual case since most of the crystal grows as phase pure type-L or type-S. Although this unusual co-crystal issue can be solved by adjusting the ligand feed ratio in the synthetic mixture, it evokes the importance of phase determination using SCXRD.

2.3. The difference in application

In this section, the catalytic activity between the type-L and type-S frameworks will be compared and discussed. Farha's research group clearly demonstrated the framework-topology-dependent catalytic activity of several different frameworks.[118] However, those frameworks comprised different building blocks, and the structural difference between the frameworks was significant. In this experiment, we examine how the minor structural difference between the type-L and type-S frameworks influences their catalytic activity. Aside from the minor structural difference caused by the two linear ligands arrangement in the two frameworks, the other structural differences influencing the catalysis need to be eliminated or reduced as much as possible.

In order to induce the two different structures, some form of change must be made to either synthesis conditions or the building blocks. However, changing synthesis conditions cannot guarantee building the desired structure. On the other hand, the two different frameworks can deliberately be synthesised by using different tritopic linkers. As introduced in the previous section, so far, cbtt has exclusively formed the type-L framework regardless of the other two linear ligands. Thus, if we install a catalyst unit to the type-S framework comprising hmtt, then its sister type-L catalyst can be prepared by using cbtt instead of hmtt.

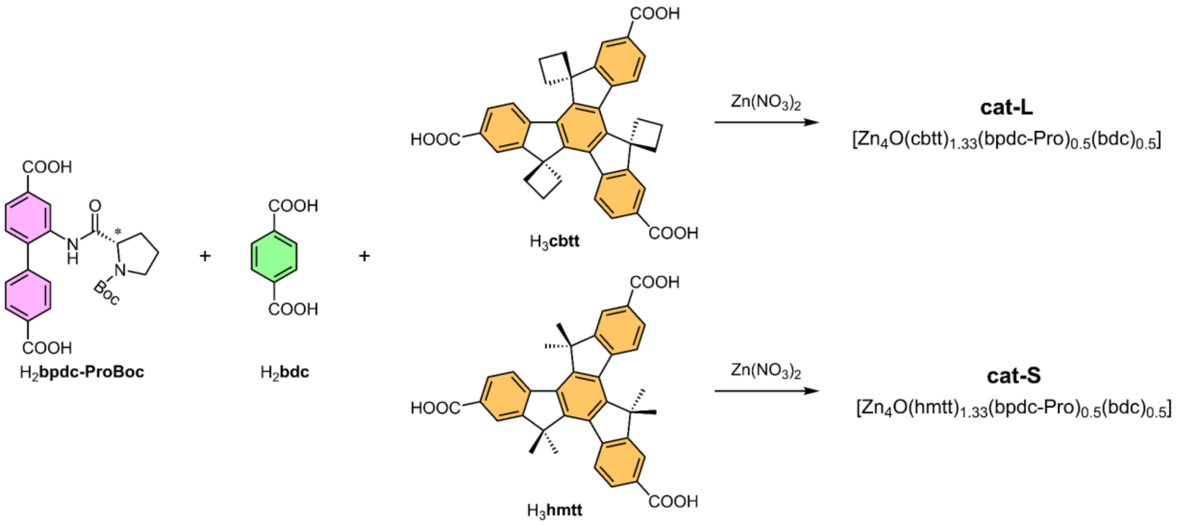

Figure 2-17. A schematic diagram of cat-L (type-L) and cat-S (type-S) syntheses.

In this case, the difference between the two frameworks will be minimised since the methylene bridge to form a cyclobutyl ring in cbtt is the only difference between the two frameworks. Therefore, the two catalysts, cat-L (type-L framework) and cat-S (type-S framework), were prepared using cbtt and hmtt, respectively, together with bpdc-Pro and bdc (Figure 2-17). The chemical make-up of the two frameworks does differ (cbtt vs hmtt), but we assume that this does not greatly influence the catalytic activity. In this way, the difference in the inherent catalytic activity of cat-L and cat-S can be assessed.

2.3.1. **Experiments**

We chose bpdc-Pro and aldol reaction respectively for the catalyst group and the target reaction for several reasons. The catalytic capability of bpdc-Pro in the type-S framework for aldol reaction has been well established from our previous works.[109] Due to the chirality of the catalytic prolinyl moiety installed to bpdc, the aldol reaction of aldehyde-derived substrates and acetone will be enantioselectively catalysed. Therefore, we can investigate how the structural difference between the type-L and type-S frameworks influences the enantioselectivity of the two frameworks by monitoring the enantiomeric excess of the aldol product catalysed by each catalyst.

2.3.1.1. **Catalyst preparation**

The prolinyl group is a very versatile catalyst, but it inhibits MOF formation if placed directly on a linker. Therefore, a Boc protecting group is first used then cleaved in a postsynthetic step by thermolysis (Figure 2-18a).[45] Cat-L ($[Zn_4O(cbtt)_{1.33}(bpdc\text{-}Pro)_{0.5}(bdc)_{0.5}]$) and cat-S ($[Zn_4O(hmtt)_{1.33}(bpdc\text{-}Pro)_{0.5}(bdc)_{0.5}]$) were both prepared using this method (Figure 2-17). However, an undesired side reaction involving thermolysis of the cyclobutyl group coincided with the thermolysis of the Boc protecting group. The cyclobutyl group on the cbtt ligand is known to decompose to a vinyl group upon heating (Figure 2-18b).[113] According to the TGA (Thermogravimetric analysis) study, the thermolysis of the Boc group occurs at 150 – 200 °C, while cyclobutyl decomposition occurs at 220 – 280 °C.[45,113] Therefore, the thermolysis temperature (180 °C) was carefully chosen but partially decomposed cyclobutyl groups were observed in the ^1H NMR spectrum of cat-L after heating (Appendix A.3). Although the vinyl group is not catalytically active for the aldol reaction, we ran a control experiment to show that the decomposed cbtt linker does not affect the target aldol reaction. For a control reaction, MUF-88 ($[Zn_4O(cbtt)_{1.33}(bpdc)_{0.5}(bdc)_{0.5}]$) (Figure 2-10) was used and processed with the same procedures to the other catalysts. After thermolysis with MUF-88, approximately the same portion of the vinyl group will be produced by the thermal decomposition of the cyclobutyl ring. If the thermalised MUF-88 did not show any catalytic activity, we could regard that the catalytic performance presented by cat-L is induced only by the deprotected prolinyl group.

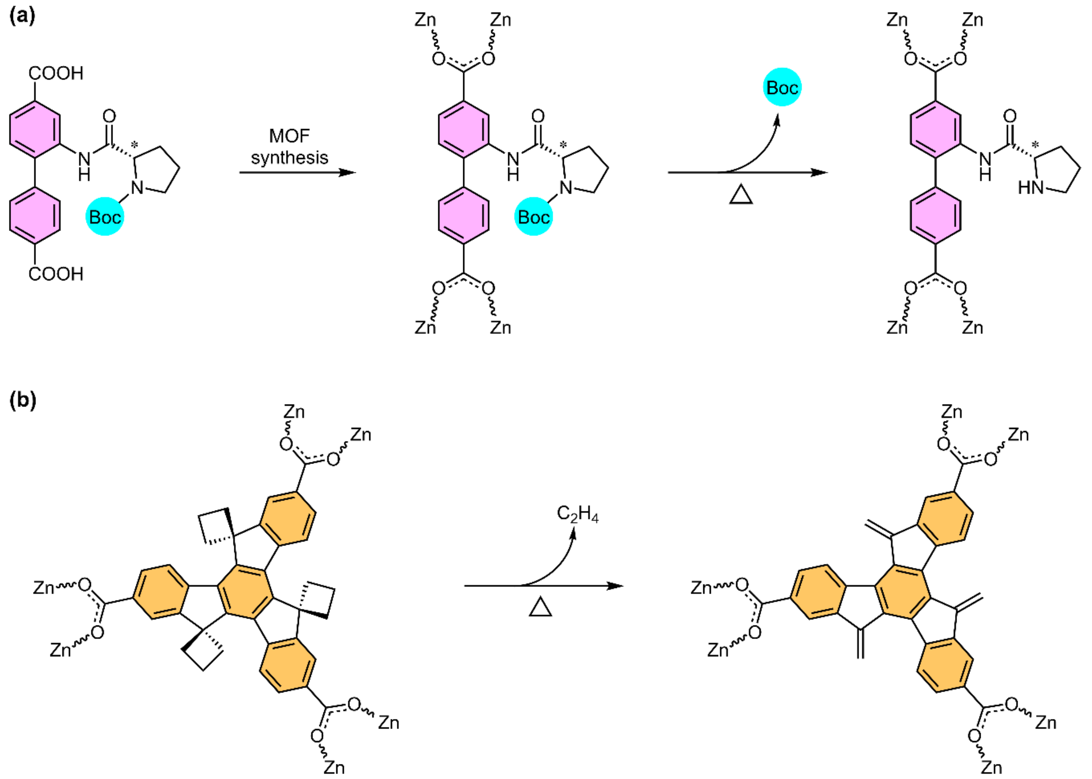

Figure 2-18. (a) General procedure of MOF synthesis with the prolinyl group, initially protected by a Boc groups, as a secondary (catalytic) functional group; (b) the schematic diagram showing the thermal decomposition of a cyclobutyl ring to a vinyl group on the cbtt linker upon heating.

2.3.1.2. **Catalysis**

All three crystals, cat-L, cat-S and MUF-88 (control), were prepared with the identical activation method (heated to 180 °C for three hours using a TGA apparatus). Then, they were tested as a catalyst for the aldol reactions of various aldehyde substrates and acetone. The stock solution (35 mM) for each reaction was prepared beforehand by dissolving the aldehyde substrate in an acetone/water mixture (4:1 v/v). The stock solution was introduced to the activated crystals (approximately 5 mg, 10 % catalyst loading with respected to the aldehyde substrate), and then the reaction mixtures were kept at ambient temperature for one day. After each reaction, the crystals were recycled for the next reaction. Once all the stock solutions were catalysed, the first reaction stock was catalysed again to examine the catalytic activity of the crystals. Both cat-L and cat-S showed the same reaction rate and ee.

Eight different aldehyde substrates were tested (Figure 2-21), but only five of them were catalysed by the prepared catalysts, and they are presented in Figure 2-19. The resulting chiral products were analysed by HPLC equipped with a chiral column. The HPLC chromatograms of the five different reactions with all three catalysts (cat-L, cat-S and MUF-88) are presented in Figure 2-20. The corresponding aldehyde substrate for each set of

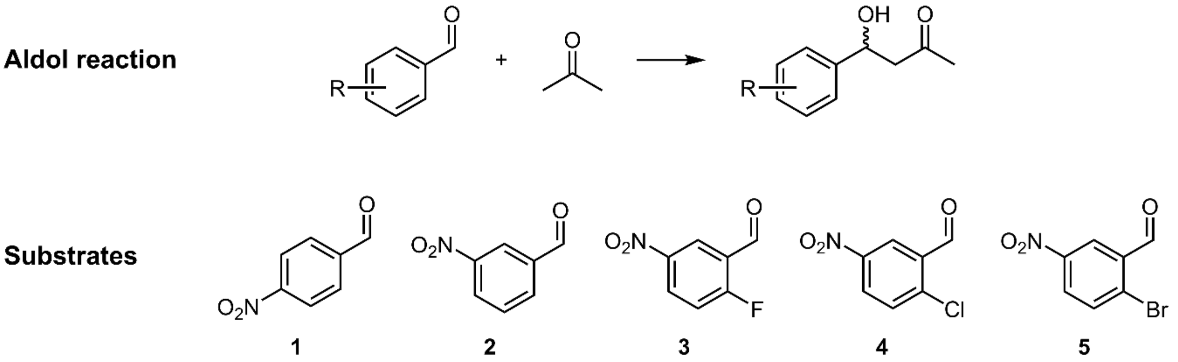

Figure 2-19. Aldol reactions with five different aldehyde substrates were catalysed by the two catalysts.

reactions and the resulting ees are also displayed with the HPLC chromatograms.

The activities of the MOF catalysts differ for each substrate. For instance, the 2-chloro-5-nitrobenzaldehyde substrate was completely consumed by both cat-L and cat-S (entry 4), while only a small amount of 4-nitrobenzaldehyde was consumed during the same reaction time (entry 1). On top of that, the enantioselectivities of both cat-L and cat-S showed a similar trend with respect to the substrates. Both catalysts show high enantioselectivity for the 2-x-5-nitrobenzaldehyde substrates (x = F, Cl, and Br). Slightly higher ees were obtained as the size of the halogen group increased. However, cat-L presents higher enantioselectivity

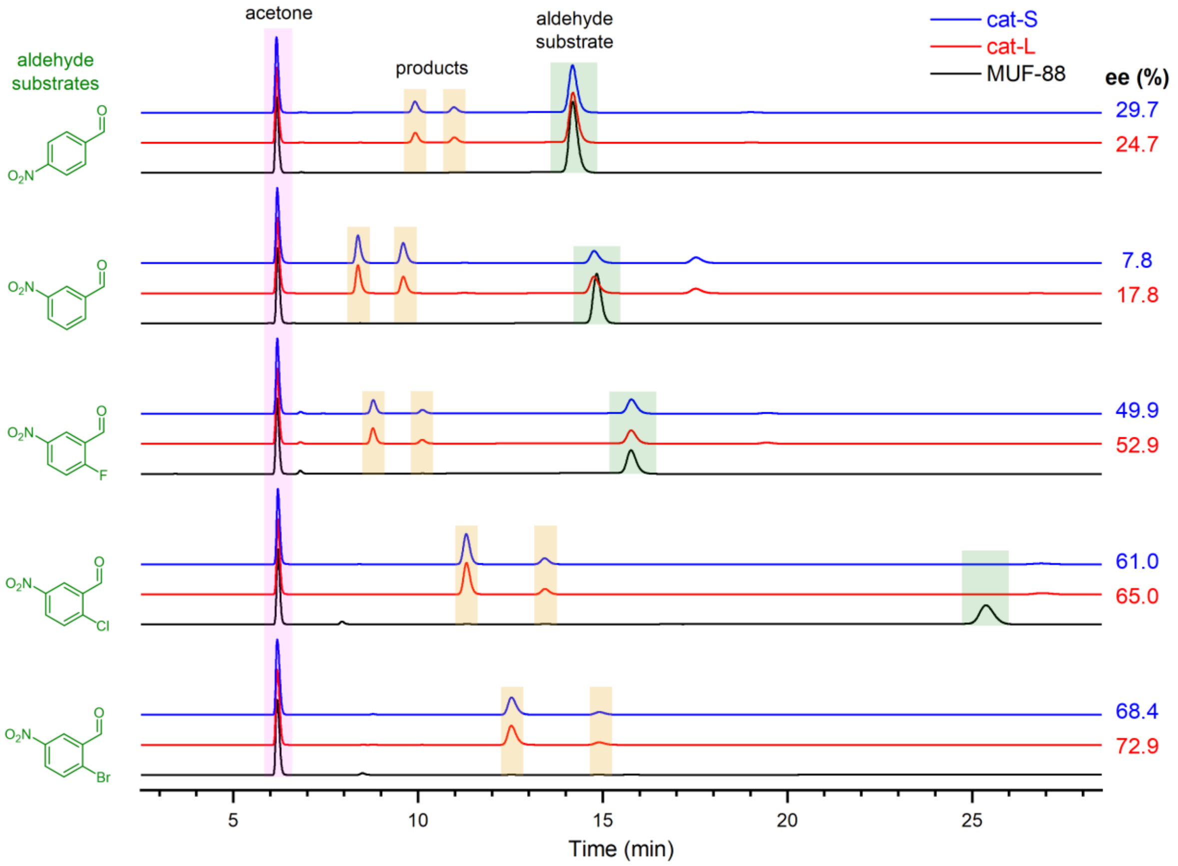

Figure 2-20. HPLC chromatograms of aldol reactions of five aldehyde substrates. The product peaks were shaded with light orange, and the corresponding ees, calculated from the peak areas, for each catalyst were also presented on right. The un-assigned peaks belong to the dehydrated aldol product.

with the aldehyde substrates having the nitro group at the meta position (2, 3, 4 and 5 in Figure 2-19). On the other hand, the type-S catalyst resulted in a higher ee only with substrate 1.

Although unexpected cbtt decomposition during the activation process added another variable and prevented the direct comparison of the catalytic performance of the two different frameworks, it was revealed that the decomposed cbtt did not affect the catalysis according to the control experiment. The result shows that the difference in ee caused by the two frameworks is not significant. The two frameworks also maintained their catalytic activity and crystallinity (Figure 2-22) even after eight recycles in the aqueous medium (20 %). This was an amazing result since the type-L framework was regarded as a fragile and sensitive framework. However, the type-L framework comprised truxene derived linker instead of btb shows similar stability to the type-S framework under the same condition. Here, the type-L framework presented as great potential as the type-S framework as a catalysis platform.

2.4. Conclusion

In this chapter, type-L and type-S frameworks were introduced, and their properties were discussed. The two frameworks are built from similar building blocks and possess identical network topology (**ith-d**). Therefore, the two frameworks possess similar external properties which make it difficult to distinguish one from another. The phase determination between type-L and type-S requires much attention to determine the phase of crystals. SCXRD must be used to differentiate them if unsure. Meanwhile, the arrangement of the two linear linkers slightly differs in the two frameworks, resulting in different pore shapes and chemical environment.

Based on our a few years of practical experience, it had been recognised that the btb derivatives form the type-L framework, while truxene derivatives form the type-S framework. However, we discovered a few exceptions to this rule as exampled above. The two different crystal types can grow together as a co-crystal, or both types of individual crystals can be formed in the same synthesis batch. These previously unobserved (or overlooked) results are noteworthy because it plays a critical role to rewrite our hypothesis which will be discussed in the later chapters.

As the experimental results showed, both frameworks exhibited a brilliant potential as a platform for catalysis. Although they showed slightly different performance inducing the enantioselectivity, the difference was minor, and both showed over 70 % ees with some selected substrates. Both type-L and type-S frameworks comprise three organic linkers which can be equipped with a wide range of functional groups. Further research is required to take advantage of these two powerful frameworks at will. Especially, synthesising pure phase of each framework with the desired combination of ligands is the urgent task.

2.5. Experimental section

2.5.1. General procedures

All starting materials and solvents were used as received from commercial sources without further purification unless otherwise noted. H_3hmtt[7], H_3cbtt[113] and H_2bpdc-Pro-Boc[45] were prepared via literature procedures.

NMR spectra were recorded at room temperature (unless otherwise noted) on Bruker-500 Avance instruments, with the use of the solvent proton as an internal standard.

High-performance liquid chromatography (HPLC) was carried out using a Thermo Fisher Dionex Ultimate 3000 system equipped with a UV detector, and chiral separation was conducted by using Phenomenex chiral column, LUX-Amylose-1.

All powder X-ray diffraction measurements were carried out on either Rigaku Spider or Bruker D8 Venture. Rigaku Spider X-ray diffractometer is equipped with CuKα radiation (Rigaku MM007 microfocus rotating-anode generator), monochromated and focused with high-flux Osmic multilayer mirror optics and a curved image plate detector. Bruker D8 Venture diffractometer is equipped with CuKα radiation with a diamond microfocus X-ray source and a Photon III 28 detector. The samples were solvated with DMF prior to and during measurements. The two-dimensional images of the Debye rings were integrated with 2DP or Diffract Eva to give 2θ vs I diffractograms. Predicted powder patterns were generated from single-crystal structures using Mercury.

All single-crystal X-ray diffraction measurements were carried out on Bruker D8 Venture, and the measurement temperature was controlled using Oxford Cryostream if required. Bruker APEX 3 was used to collect and process data, and the structure was solved and refined using the Shelx package[107,119] under Olex2[120]. The crystal samples were solvated in n-octane and mounted on a nylon loop using Fomblin oil in most cases.

2.5.2. Aldol reaction

2.5.2.1. MOF synthesis (1 mL scale)

Table 2-1. The substances and required amount for MOF syntheses

	type-S	type-L	MUF-88
$Zn(NO_3)_2.6H_2O$ (mg)	16.5	16.5	16.5
tritopic linker (mg)	hmtt: 2.2	cbtt: 2.0	cbtt: 2.0
H_2bpdc-pro-Boc (mg)	2.4	2.4	H_2bpdc: 1.3
H_2bdc (mg)	1.3	2.0	1.3
benzoic acid (mg)	8	8	8
H_2O (mL)	0.05	0.05	0.05
DEF (mL)	1	1	1

All the substances, as described in Table 2-1, was placed in a 4 mL vial, and the vial was briefly sonicated and placed in an isothermal oven at 85 °C overnight. The crystal (approx 3 mg) is washed with fresh DMF two times and kept in fresh DMF until further use.

2.5.2.2. Catalyst activation

The crystals were washed with CH_2Cl_2 four times, and the solvent was removed. Then the crystal was heated to 180 °C for 12 hours under vacuum to remove the Boc protecting group. After removing from the heat and vacuum, the crystal was solvated in acetone until further use. Its ^1H NMR spectrum was measured to confirm the complete removal of the Boc protecting group.

2.5.2.3. Aldehyde stock solution (35 mM) preparation

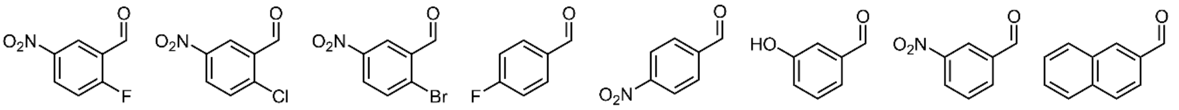

1 2 3 4 5 6 7 8

Figure 2-21. Eight different aldehyde substrates for aldol reaction

Each aldehyde substrate (70 μmol, sample masses are in the table below) in Figure 2-21 was dissolved in a mixture of acetone (1.6 mL) and water (0.4 mL) and kept at ambient temperature until use.

#	1	2	3	4	5	6	7	8
mass(mg)	11.8	13.0	16.1	8.7	10.6	8.6	10.6	10.9

2.5.2.4. General catalysis procedure

Solvated crystals (approx. 5 mg) in acetone were transferred to a 1.5 mL HPLC sample vial and the solvent was removed by decantation and using a glass capillary tube, and then the aldehyde stock solution (0.5 mL) was added to each vial. The amount of added aldehyde solution was adjusted to give a ratio of prolinyl groups-to-aldehyde of approximately 10 mol%. The reaction mixture was allowed to stand at ambient temperature for a day. 1.0 μL of the supernatant was subjected to HPLC and analysis was carried out under the following conditions: Lux amylose-1 column; mixed solvent of CH_3CN and deionized water (55:45 v/v); flow rate of 0.5 mL/min. Products were detected according to their absorption of 254 nm UV light. The ee value of each reaction is reported based on the excess of the enantiomer with the shorter retention time.

2.5.2.5. PXRDs

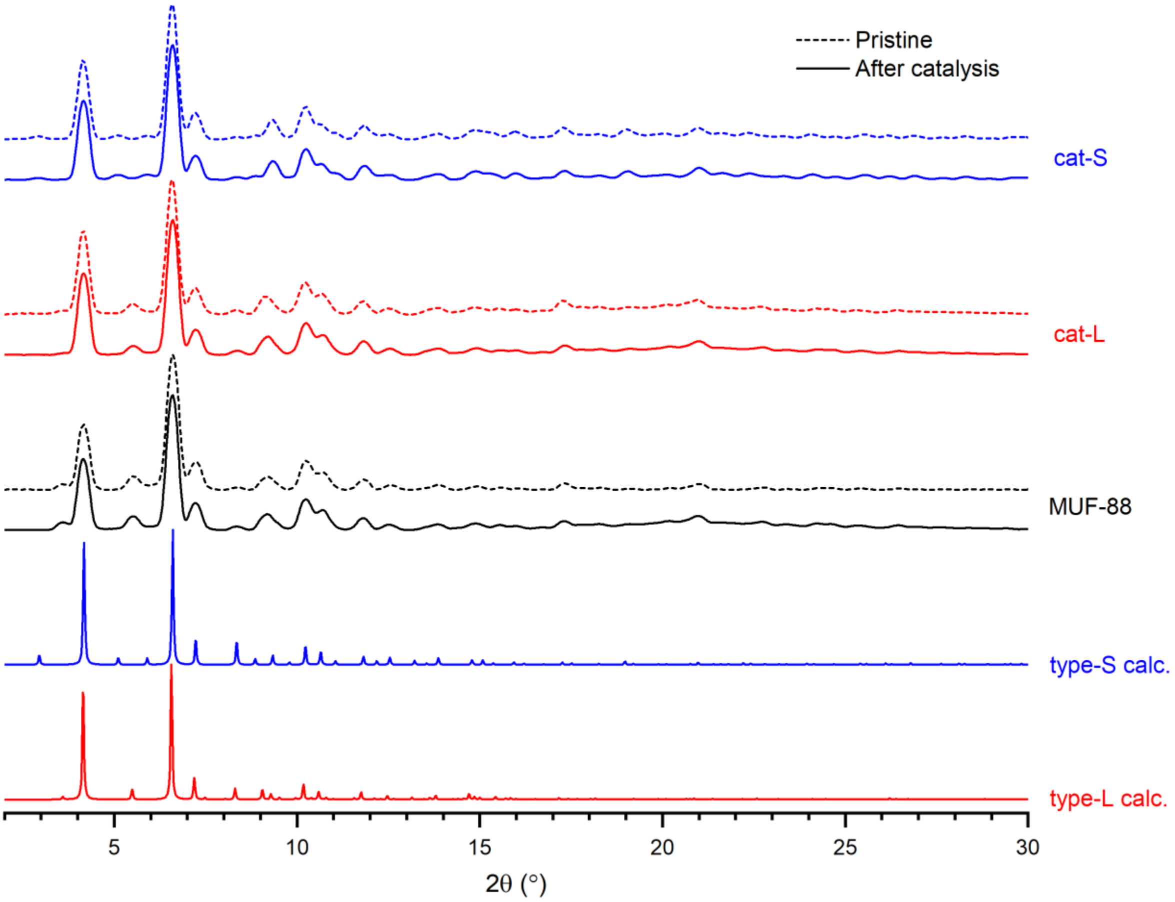

Figure 2-22. PXRD patterns of the three crystal samples used for the aldol catalysis reaction. The two sets of PXRD patterns indicate that the crystallinity was not lost for all samples after the aldol reaction and the eight times recycling experiments.

Chapter 3 Remote asymmetric induction – Part 1

3.1. Introduction

Chirality is a fundamental property of living organisms since their basic building blocks, such as amino acids and sugars, are asymmetric.[121] A chiral molecule and its mirror image are referred to as a pair of enantiomers. They are not superposable due to their different spatial arrangements. Although chiral chemistry itself has long been recognised, its importance has been highlighted relatively recently after artificial chemical compounds began to be used in medicine.[122] Since then, to obtain enantiomerically pure compounds has been regarded as most important for synthetic chemists. There are two main ways to obtain a chiral compound. One is separating the desired enantiomer from an equimolar (racemic) mixture of the two enantiomers. In this case, the maximum yield is 50 %, so it is economically ineffective. On the other hand, asymmetric catalysts can be used to synthesise the desired enantiomer. Asymmetric catalysts have enantioselectivity so that the desired enantiomer is preferentially more produced. Hence, exploiting asymmetric catalysts has become efficient and effective, provided that the catalyst produces satisfactorily high enantioselectivity.[123]

Nature has demonstrated an elegant solution to the synthesis of enantiopure compounds by using enzymes. Enzymes catalyze many important biological transformations. The catalytic pockets in enzymes are precisely crafted from the various functional groups installed on the folded peptide backbones. They provide superb substrate recognition and deliver high enantioselectivity.[124] For this reason, mimicking enzymes is one of the good strategies for designing asymmetric catalysts. In this case, the specific arrangement of functional groups surrounding the catalytic centre in close vicinity is crucial.[125-128] These functional groups non-covalently interact with a substrate and lead the substrate to the desired conformation during the transition state. This allows another reactant to approach from a specific direction relatively easily so that one enantiomer becomes the preferred product over another.

3.1.1. Conventional asymmetric MOF catalysts

MOFs have excellent potential as catalysts (section 1.3.2), and they can also be applied to asymmetric catalysts. The most straight forward method of preparing asymmetric MOF catalysts is integrating asymmetric organic catalyst moieties into a framework. For instance, some small chiral organic catalysts (e.g. prolinyl) can be attached to the organic linker backbones and incorporated into the framework.[45,129] Additionally, some chiral organic molecules, such as salen or some atropisomers like BINOL/BINAP derivatives, can be directly incorporated into frameworks as a ligand (Figure 1-9).[40,104-105,130] Once these organic linkers are integrated into a MOF, metallation is generally followed with the desired metal ion, which sits on the chiral organic linkers and functions as an asymmetric catalyst.

Alternatively, MOF catalysts can be prepared using achiral organic linkers. In this case, the chiral structures of MOFs, such as the helical structure, provide enantioselectivity. Duan et al. suggested a novel strategy of growing MOF crystal with a chiral space group employing a judiciously controlled crystallisation method.[131-133] They have exploited a few different prochiral organic linkers that crystallise with a chiral space group induced from a helical motif. Those prochiral organic linkers spontaneously grow racemic mixtures. However, homochiral MOF crystals were produced when a chiral adduct was added to the synthetic mixture. The chiral adducts used for the MOF synthesis were not incorporated into the MOF scaffold.

For instance, they have reported a homochiral MOF Ce-MDIP synthesised from Ce(III) and the prochiral organic linker, methylenediisophthalic acid (H_4MDIP), in the presence of the chiral adduct, *d*-pyrrolidine-2-yl-imidazole (PYI) (Figure 3-1).[131] In Ce-MDIP, an open metal site can be generated on the Ce node by removing a coordinated labile water molecule. Then it was served as Lewis acidic site to catalyse cyanosilylations.

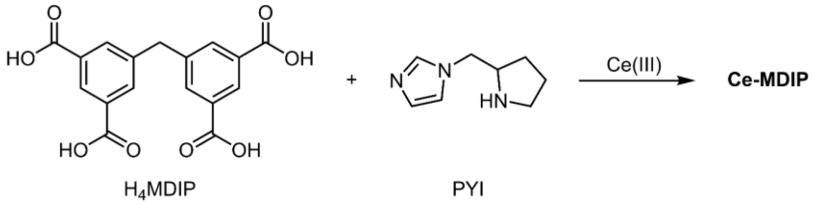

Figure 3-1. A schematic diagram of Ce-MDIP synthesis, PYI was not integrated into Ce-MDIP

3.1.2. The prior study of type-S (MUF-77 derived) catalyst

A series of asymmetric MUF-77 (type-S framework) catalysts were reported in 2017.[109] In this study, the well-known chiral catalyst, *l*-proline, was incorporated into MUF-77, and its catalytic activity was tested under various conditions for an aldol reaction. As depicted in Figure 3-2a, the prolinyl moiety was attached to either bpdc or bdc backbone to form bpdc-pro or bdc-pro, respectively. Another set of linkers (modulators) were also prepared to modulate the chemical environment surrounding the catalyst centre (Figure 3-2b). A series of type-S catalysts were then prepared using bpdc-pro or bdc-pro together with various combinations of other linkers. The prepared type-S catalysts were then used to investigate how such diverse chemical environments surrounding the catalytic centre influence the

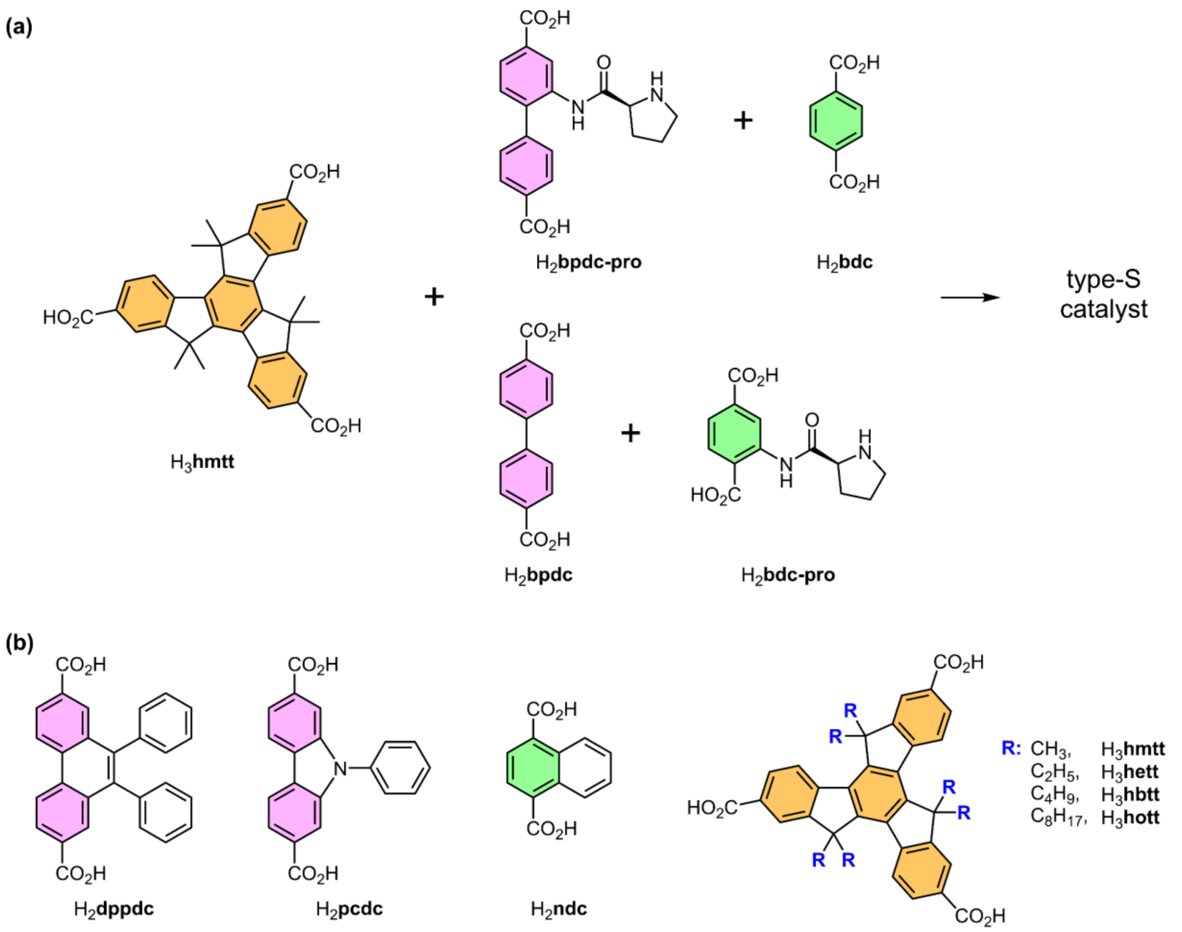

Figure 3-2. (a) A schematic diagram of MUF-77 catalyst synthesis, the chiral catalytic auxiliary prolinyl group was installed onto either bpdc or bdc. (b) various modulating groups were exploited to bring divergent chemical environments to the catalytic pocket.

enantioselectivity of the aldol product and reaction rate.

The results from each catalyst prepared with different linker combinations were tabulated in Table 3-1. Depending on the catalyst and modulator combinations, the reaction rate and the enantiomeric excess (ee) notably changed. Since the modulators vary in size, which affects the diffusion rate of the reaction substrates through the MOF pores, the change in the reaction rate is understandable. However, the hugely diverged enantioselectivity, even reversed in some cases, is mysterious and hard to be elucidated. The prolinyl group is the sole asymmetric component that induces chirality to the reaction substrates during the transition state. Both prolinyl moieties installed on either bdc or bpdc have the same chirality. Therefore, some degree of change in ee was understandable as a reasonable result due to the slightly different surrounding environment of the catalyst. However, the reversed ee was an unexpected result. This clearly indicates that the environment surrounding the catalyst centre can become more influential than the chiral source to induce the chirality of a product in some cases. The various pore environments caused by different ligand combinations and the corresponding catalysis results affected by such environment change are presented in Table 3-1

Table 3-1. The result from Aldol reaction of acetone and *p*-nitrobenzaldehyde catalyzed by MUF-77 analogues comprised of various linker combinations

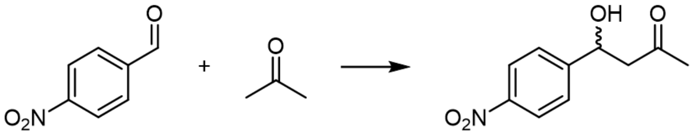

#	**catalyst linker set**			**ee (%)**	**k_{obs}***
1	bdc-Pro	bpdc	hmtt	−3.9 ± 0.6	0.74 ± 0.03
2	bdc	bpdc-Pro	hmtt	19.2 ± 1.1	0.52 ± 0.03
3	bdc-Pro	bpdc	hett	−3.9 ± 0.6	0.69 ± 0.04
4	bdc	bpdc-Pro	hett	17.0 ± 1.0	0.32 ± 0.02
5	bdc-Pro	bpdc	hbtt	4.2 ± 0.6	0.62 ± 0.02
6	bdc	bpdc-Pro	hbtt	18.3 ± 2.6	0.15 ± 0.01
7	bdc-Pro	bpdc	hott	1.8 ± 0.3	0.42 ± 0.02
8	bdc	bpdc-Pro	hott	15.7 ± 2.1	0.11 ± 0.01
9	ndc	bpdc-Pro	hmtt	24.2 ± 1.4	0.50 ± 0.02
10	ndc	bpdc-Pro	hbtt	18.1 ± 1.1	0.16 ± 0.01
11	ndc	bpdc-Pro	hott	19.1 ± 1.1	0.13 ± 0.01
12	bdc-Pro	pcdc	hmtt	−10.3 ± 1.4	0.052 ± 0.003
13	bdc-Pro	dppdc	hmtt	−26.5 ± 1.6	0.27 ± 0.01

* Observed rate constant based on the consumption of p-nitrobenzaldehyde with units of $L{\cdot}mol^{-1}{\cdot}day^{-1}$

However, the experiment results presented above did not give an intuitive interpretation of how the ee was affected. For instance, the enantioselectivity was reversed by simply switching the location of the prolinyl group from bpdc to bdc backbone (entry 1 vs 2 Table 3-1). Therefore, a more straightforward system is required to interpret experimental results and to design to improve the enantioselectivity.

In this sense, we introduce a new concept for asymmetric MOF catalysis. The two functions of an asymmetric catalyst, catalysis and asymmetric induction, are assigned to the separate organic linkers. Hence, an achiral catalyst moiety that produces a racemic mixture by itself will be incorporated into MOF (Figure 3-3a). It would then be more feasible to understand how modulators influence enantioselectivity upon introducing them to the framework. For modulators, various chiral components which do not have catalytic activity will be used. Thus, a chiral modulator can influence the enantioselectivity from the remote site during the transition state but alone cannot catalyse the reaction (Figure 3-3b and c). Hereafter, this novel concept catalyst will be denoted as a remote asymmetric induction (RAI) catalyst, which well describes the unique feature of this catalyst.

As far as we recognise, the RAI catalyst is a novel concept of catalyst and has not been observed in any other MOF catalyst. Even if we expanded the search area to the general

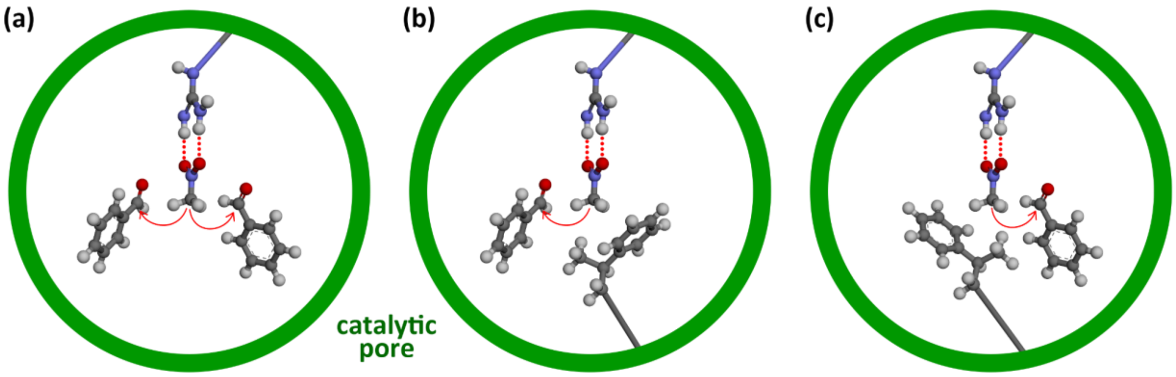

Figure 3-3. A schematic diagram of the RAI catalyst concept. (a) A racemic mixture is produced without a chiral modulator; (b, c) a certain enantiomer is preferrentially produced depending on the chirality of the introduced chiral modulator. The green circles indicate a pore space and no reaction mechanism is involved.

chemistry field, it was difficult to find a catalyst of a similar concept. Although there are several asymmetric catalysts inducing the chirality from the remote sites,[127,134-135] the catalytic centre and chiral motifs are in the same molecule. On the contrary, in the case of the RAI catalyst, the multiple functional groups were installed in the separate molecule then they incorporated into the same framework to propagate chirality together during the catalysis. The RAI catalyst concept is a superb example of exploiting the advantages of MC-MOFs. All the building components in the MC-MOFs are precisely located in the frameworks, allowing us to envisage the environment of the pore space. Thus, we can design specific cooperation among the functional groups attached to each organic linker.

The RAI catalyst was initially designed based on the hypothesis induced from the type-S framework since the truxene derived tritopic linkers, which we believed exclusively forming the type-S framework, were used. Moreover, the strategies to increase enantioselectivity were developed and attempted based on this hypothesis. However, as was introduced in the previous chapter, we discovered that the type-L frameworks were also unexpectedly formed with specific ligand combinations, and this was overlooked until the majority of experimental data were collected. Therefore, the experimental works designed and conducted based on our initial hypothesis will be presented in this chapter. Then, the interpretations of the experimental results using the initial and new hypotheses will be discussed in detail in the following chapter.

3.2. Experiments and Results

3.2.1. Initial hypothesis

The result presented in Table 3-1 shows that all three organic linkers cooperate to influence the reaction outcome. The MOF catalysts used in the experiment above were a type-S framework according to the crystal structure and PXRD data. As discussed in the previous chapter, only the small tetrahedral pore (pore-C in Figure 2-4) in the type-S framework provides a space where two linear linkers can interact with each other. The other two mesopores are composed of either hmtt and bdc (pore-A) or hmtt and bpdc (pore-B), indicating that cooperation between bpdc and bdc cannot occur in those two mesopores.

Based on the observation above, it seemed that the reaction that occurred in pore-C mainly contributes to the corresponding enantioselectivity. Thus, we hypothesised that the reaction happening in pore-C plays a crucial role in asymmetric catalysis. Therefore, the majority of the following experimental works were designed and conducted based on this hypothesis. The scheme to design and develop the RAI catalyst is described below:

- Search for the suitable achiral organic catalyst and target reaction, which can be applied to the type-S framework.
- Incorporate the selected catalyst to the type-S framework by installing them to one of the linkers
- Check the integrated catalyst unit is still functioning for the target reaction within the framework
- Install a range of different chiral modulating groups and screen them for the chiral induction
- Tweak the reaction parameters to enhance the enantioselectivity of the RAI catalyst.

3.2.2. Catalyst design

The three linkers in the type-S framework can be readily functionalised with various chemical groups, and the susceptible positions to attach functional groups are denoted with coloured balls in Figure 3-4a. The functional groups could interact in the small pore, as shown in Figure 3-4b. It is presumed that the functional groups on the linear linkers would point to the centre of the pore-C most of the time. The rotational barrier due to the π-conjugation along the linear linkers helps to keep low dihedral angles between the phenyl ring and carboxylate.[136-138] Such a low dihedral angle range has been well observed through various single-crystal structures of the type-S frameworks.[7]

On the other hand, the functional groups on the truxene derivatives tend to diverge orthogonally to the planar body of truxene in order to minimise the steric hindrance between the two functional groups branching out from the same position.[7] Therefore, the functional groups on the linear linkers will probably have a higher chance to locate within pore-C than the ones on the tritopic linker. Figure 3-4b demonstrates that the functional groups on the linear linkers are touching the ball, indicating the pore space. On the other hand, the functional groups on the tritopic linker are diverging away from the truxene linker, not pointing to the centre of the pore. For this reason, we determined to install the catalyst unit and the chiral modulating groups on to the linear linkers to induce more interaction between them in pore-C.

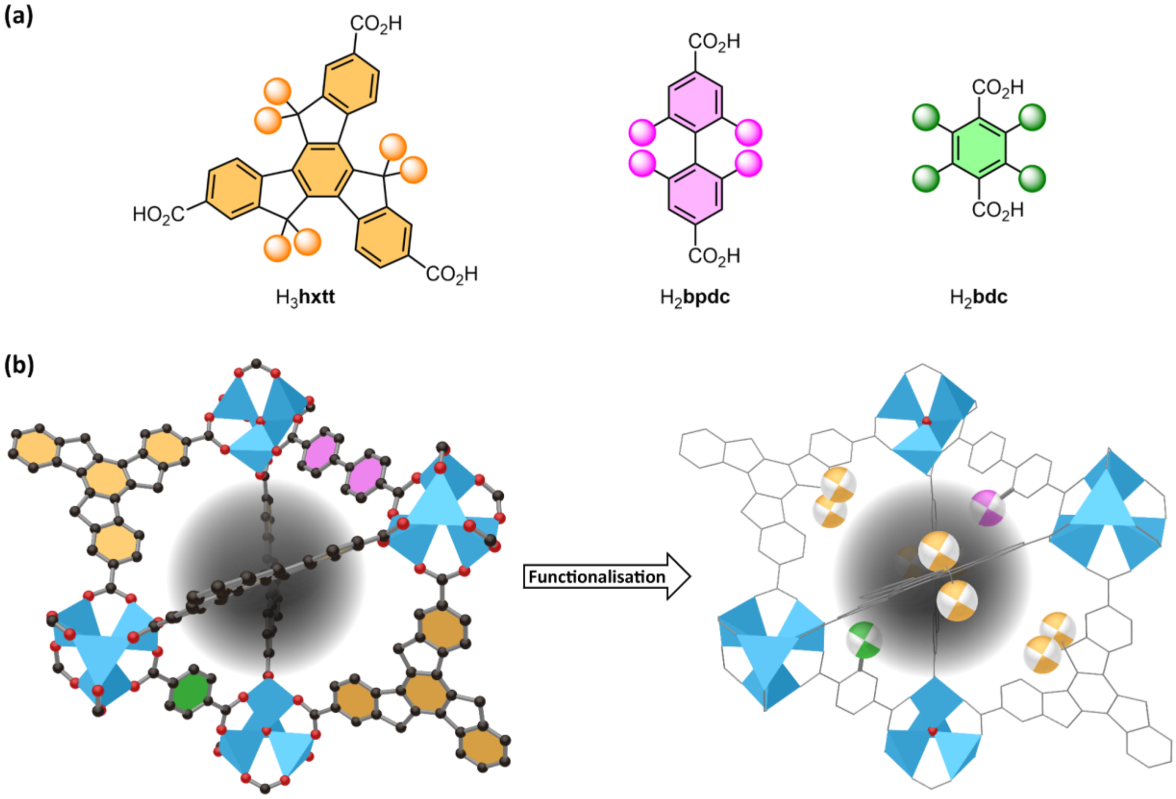

Figure 3-4. (a) Three organic linkers of the type-S framework, the coloured balls indicate the possible positions to add functional groups; (b) the ligand arrangement surrounding pore-C and a schematic illustration of the functional groups attached to the linkers. Shaded area indicates the pore space.

3.2.3. Screening with homogeneous catalyst and MOF catalyst

The well-known organic catalysts are generally composed of N-containing motifs, such as amine, urea or heterocyclic rings.[139] Thus, a few bpdc derivatives, which comprised the same or similar functional group to those organic catalysts, were selected from our ligand library, as illustrated in Figure 3-5a. They were all attached to the bpdc backbone because bpdc is more facile for derivatisation with functional groups and causes less trouble during MOF formation than bdc derivatives. Provided that these N-containing motifs are attached to bdc, the distance between the nitrogen atom and carboxylate groups are too close. Therefore, unwanted side reaction can occur during ligand synthesis like cyclisation, or the nitrogen atom could inhibit the desired MOF synthesis.

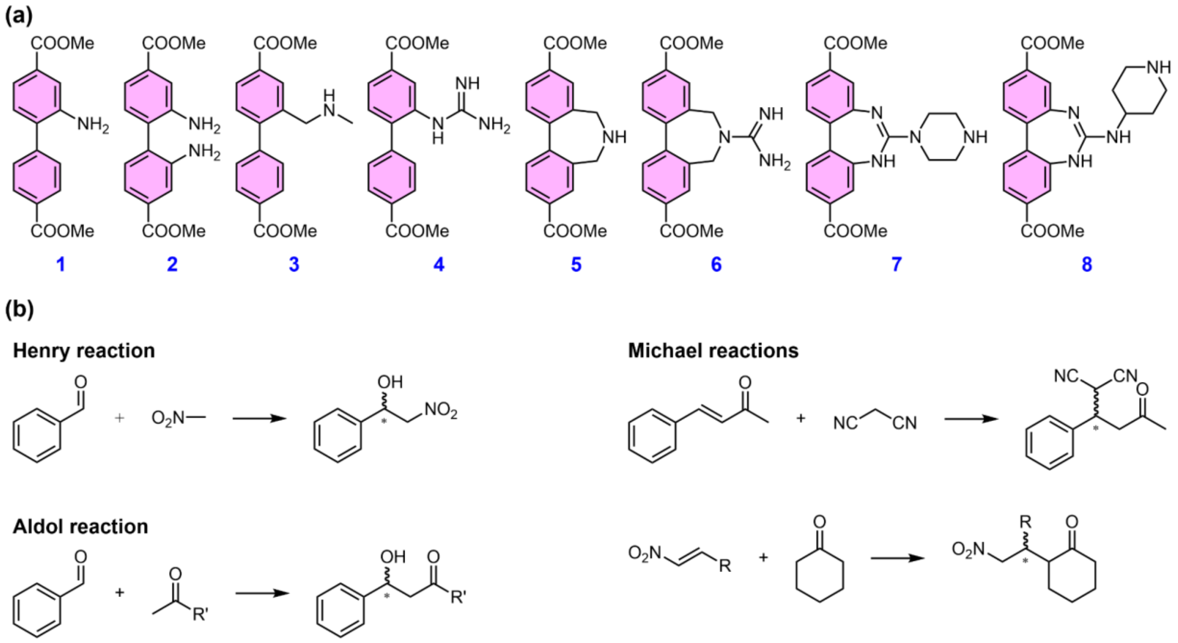

Figure 3-5. A few examples of (a) achiral catalysts installed to Me_2bpdc for the homogeneous catalysis test reactions and (b) the target asymmetric reactions

The selected bpdc derivatives were tested for a few known reactions (Figure 3-5b). The ester form of each bpdc derived molecule was first tested as a homogeneous catalyst before incorporation into the framework. The catalytic activity of each homogeneous catalyst was monitored using TLC (thin layer chromatography), and then corresponding acids were used for MOF synthesis if they show good catalytic performance. Once the selected bpdc derivative was successfully incorporated into the type-S framework, the corresponding MOF catalyst is also tested for the same reaction heterogeneously.

According to the screening results, Henry reaction showed some prominent progress with guanidine derivatives (4, 6, 7 and 8 in Figure 3-5). The guanidine or similar motifs like urea or thiourea are the well-recognised catalysts for Henry reactions.[140-141] Especially, 4 (bpdc-gua) showed better catalytic activity than others, thus was selected as the best candidate for Henry reaction. Therefore, the type-S framework was synthesised with H_2bpdc-gua, H_2bdc and H_3hmtt (Figure 3-6a). Bpdc-gua was successfully incorporated into the type-S framework, and the resulting achiral catalyst was denoted as achiral-cat ([$Zn_4O(hmtt)_{1.33}(bpdc\text{-}gua)_{0.5}(bdc)_{0.5}$]). The achiral-cat was then tested for the Henry reaction of m-nitrobenzaldehyde and nitromethane (Figure 3-6b). Approximately 2-3 mol %[a] catalyst was introduced to the reaction mixture, and the reaction was conducted at ambient

---

[a] The percentage of catalyst is the ratio of the guanidine moieties in the given amount of the type-S framework with respect to the amount of aldehyde substrate in the reaction mixture. The desolvated crystal loses the catalytic activity, preventing from measuring the precise mass of catalyst beforehand. Therefore the mass of crystal was once measured with a sacrificed batch, and the catalyst loading was estimated based on it.

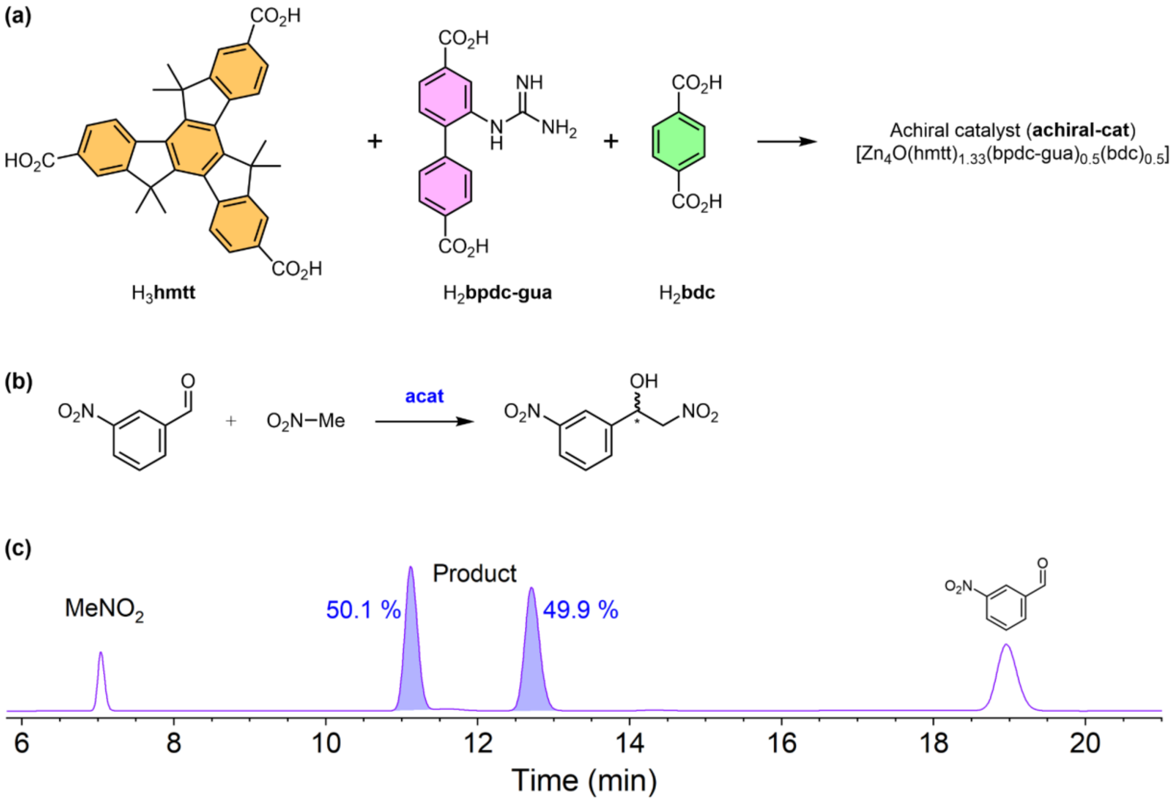

Figure 3-6. The schematic diagrams of (a) catalyst synthesis from bpdc-gua, bdc and hmtt; (b) the target Henry reaction; and (c) HPLC chromatogram of the reaction mixture after catalysis.

temperature for three days. The reaction mixture was then analysed by HPLC chromatogram using the chiral column to separate the two enantiomeric products (Figure 3-6c). An equimolar mixture of two enantiomeric products was detected based on the peak areas, and MS (mass spectroscopy) confirmed that the compounds belong to the two peaks are the right Henry products.

The enantiomeric excess (ee) was calculated by Equation 1 regardless of the absolute chirality of the product. Equation 1 is used throughout the entire thesis for the ee calculations.

$$ee\ (\%) = \frac{enantiomer\ A - enantiomer\ B}{enantiomer\ A + enantiomer\ B} \times 100 \qquad \text{Equation 1}$$

Where enantiomer A is the product that belongs to the peak comes out first in HPLC chromatogram, and enantiomer B is the one that comes out later.

3.2.4. **Chiral induction**

Achiral-cat demonstrated its catalytic activity for the Henry reaction, and the catalysed Henry product was determined as a racemic mixture. Hence, we turned our focus on exploring the chiral modulators that would cooperate with the bpdc-gua and induce chirality to the product. A chiral modulator must meet a few conditions to be incorporated into the RAI catalyst. First, they should not have any catalytic capability for the target reaction. Second, they should not inhibit MOF formation. Third, they should be a proper size to

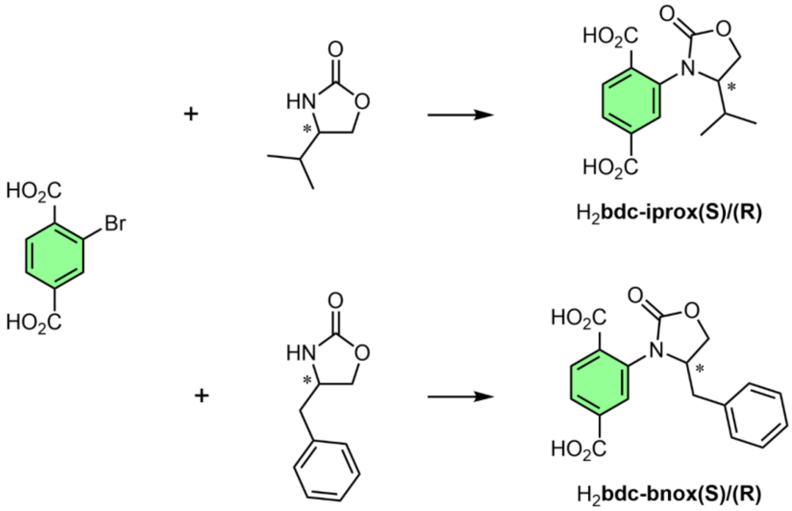

Figure 3-7. A schematic diagram for modulator synthesis. 2-bromo bdc was coupled with chiral isopropyl oxazolidinone or benzyl oxazolidinone moiety.

cooperate with the catalyst moiety from proximity but not too big to hinder the diffusion of the reactants and products. Lastly, they should have a feasible synthesis route to be attached to the bdc backbone.

The tritopic linker was not considered as a platform for chiral modulator installation. Six chiral modulating groups would then be attached to each truxene linker if chiral modulators were installed. Hence, the outnumbered bulky functional groups might cause diffusion issues for reactants and products. Moreover, too many chiral modulators will hinder a straightforward interpretation of experimental results. On the contrary, the influence from one chiral modulator attached to the bdc backbone is more intuitive.

A few oxazolidinone derivatives were chosen for a chiral modulating group because their usage as a chiral component in a MOF was successfully demonstrated. According to Hoffmann et al., the asymmetric bdc-oxazolidinone derivatives were successfully incorporated into the UMCM-1 framework and demonstrated their usage for chiral separation.[142-143] The size of oxazolidinone derivatives seems optimum considering the cooperation with bzzpdc-gua in pore-C. Moreover, it can easily be attached to the bdc backbone by a coupling reaction with 2-bromo bdc (Figure 3-7).

Four different bdc modulators were prepared from both enantiomers of 5-isopropyl oxazolidinone (bdc-iprox(R)/(S)) and 5-benzyl oxazolidinone (bdc-bnox(R)/(S)), and they were well integrated into the type-S framework along with hmtt and bpdc-gua. Their enantioselectivity was then tested for the Henry reaction of m-nitrobenzaldehyde and nitromethane, and the products were analysed comparing with a few control reactions conducted under the same condition. As described in Table 3-2, seven different type-S frameworks were prepared with the corresponding ligand combinations. Each framework

Table 3-2. The ligand combination in MUF-77 analogues used as catalyst or controls for the Henry reaction.

#	Ligand combination	Note	ee (%)
1	hmtt + bpdc + bdc	control – parent MUF-77 framework	0
2	hmtt + bpdc + bdc-bnox(r)	control – modulator only	0
3	hmtt + bpdc-gua + bdc	control – catalyst only	0.2
4	hmtt + bpdc-gua + bdc-iprox(s)		-2.1
5	hmtt + bpdc-gua + bdc-iprox(r)		1.7
6	hmtt + bpdc-gua + bdc-bnox(s)		-4.1
7	hmtt + bpdc-gua + bdc-bnox(r)		1.2

was tested for the Henry reaction, and the products were analysed by HPLC (Figure 3-8).

The first three entries were carried out as control experiments. According to the HPLC analyses, the first entry exhibits no product peaks, indicating that there is no spontaneous reaction going and no catalytic activity of the parent MOF. No product peak was found on the second entry either, which means that the modulator has no catalytic capability on Henry reaction. Entry 3 showed that no notable enantioselectivity was induced to the Henry product without any chiral modulator. The three control experiments evidenced that the reaction is not spontaneous, the modulator does not catalyse the target reaction, and a racemic mixture was produced when no chiral modulator was used.

The next four entries (4-7) were conducted to investigate the capability of the four prepared chiral modulators to induce enantioselectivity. According to the HPLC chromatogram in Figure 3-8, entry 4-7 showed notable ee changes. Although the absolute values for ee were not very significantly high, the sign of ee was coincident with the chirality of the modulators. Both bdc-bnox(S) and bdc-iprox(S) produced negative ees, and positive ees were induced by

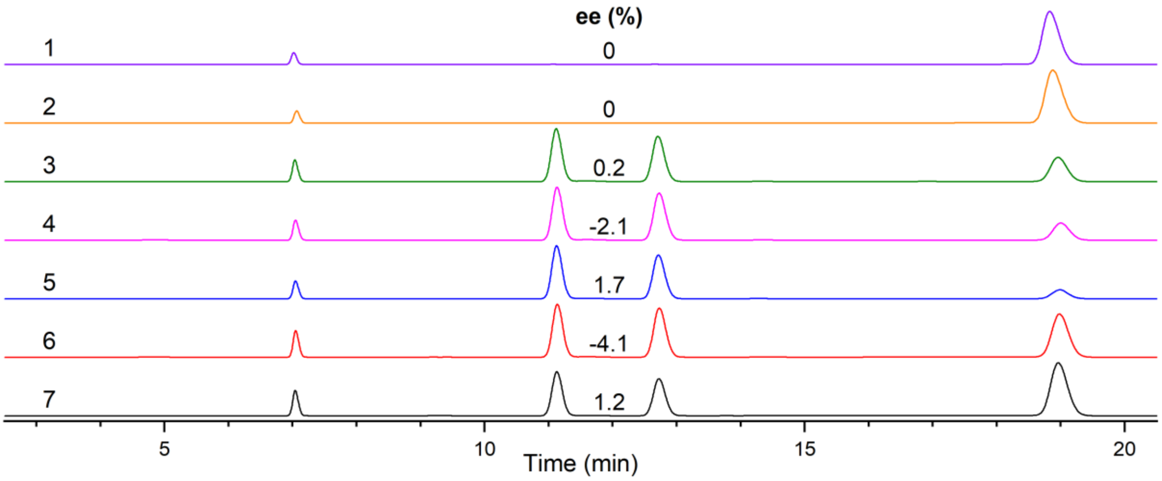

Figure 3-8. The normalised HPLC chromatograms for Henry reaction of m-nitrobenzaldehyde and nitromethane with the prepared catalysts, includling the controls. The corresponding ee calculated by the integration of the two enatiomeric product peaks were shown with the chromatograms.

the (R) type modulators. This clearly shows that the chirality on the modulator influences the enantioselectivity during catalysis.

3.3. Enhancing enantioselectivity

The catalysis result shown in Figure 3-8 successfully demonstrates that the RAI catalyst model functions as designed. However, there are far more things to do to increase the enantioselectivity of the RAI catalyst to be used for practical applications. In this section, the parameters which were changed to improve the RAI catalyst and how the changed parameter influenced the enantioselectivity will be discussed.

3.3.1. Various aldehyde substrates

The aldehyde substrates for the Henry reaction were judiciously chosen based on a few conditions. Above all, the size of a molecule was first considered since both reactant and product need to diffuse through the framework freely. The type and position of functional groups on the aldehyde substrate also need to be considered. The conformation of an aldehyde substrate in a catalytic pore highly depends on the interaction with the functional groups of the surrounding. Therefore a certain aldehyde substrate would better fit in the

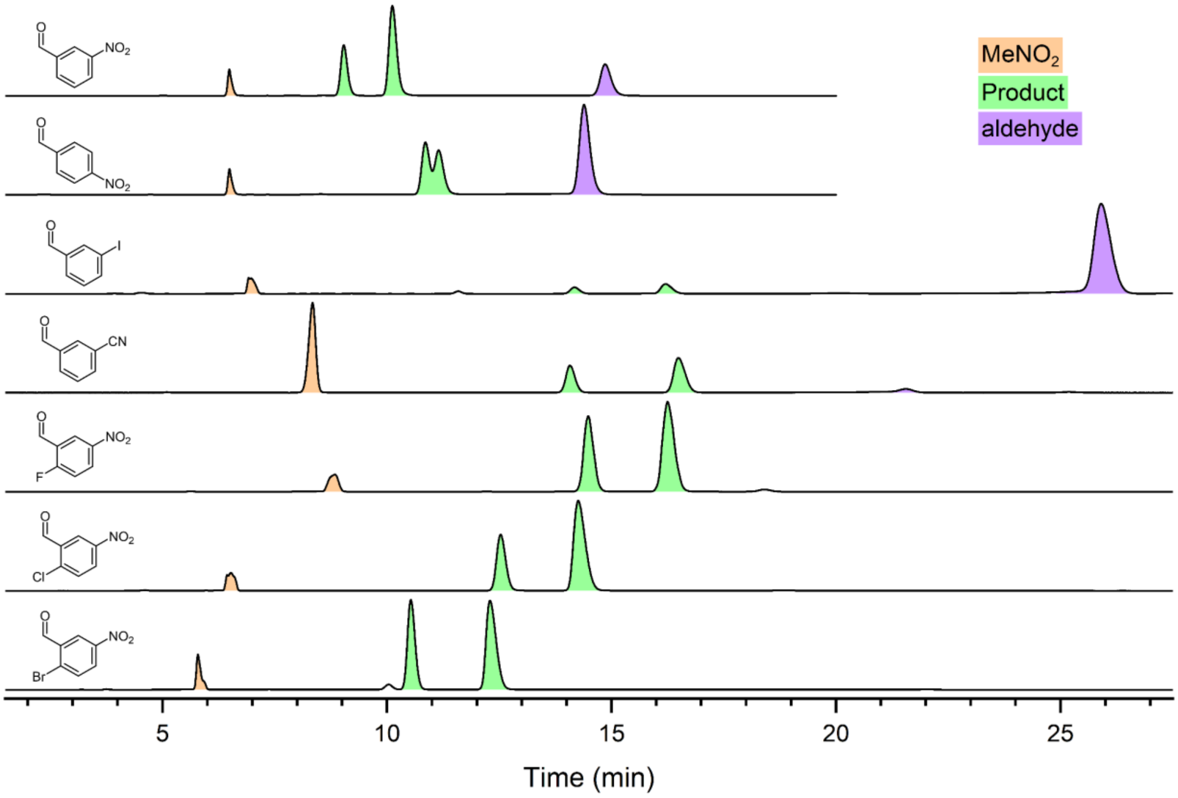

Figure 3-9. HPLC chromatograms of Henry reactions with a few selected benzaldehyde substrates. The reactions with 3-nitrobenzaldehyde derivatives showed particularly high conversion (the benzaldehyde peaks were very small or completely disappeared). The HPLC conditions all vary and presented in **Table 3-3**.

catalytic pore with a proper conformation during the transition state so that the catalyst and modulator can efficiently influence delivering asymmetric induction. Lastly, UV detectable aldehydes were considered for a more straightforward analysis so that the reaction medium can be directly injected to HPLC equipped with a chiral column and UV/Vis detector.

Although more than 30 aldehyde reaction substrates were screened (Figure 3-22), the catalytic activity of the RAI catalyst was observed with only a few of them. Interestingly, the aldehyde substrates, which shows a comparatively high consumption rate and enantioselectivity, were all m-nitrobenzaldehyde derivatives (Figure 3-9). We first thought that the electron-withdrawing nitro group helped to enhance the reactivity of the aldehyde substrates so that the nucleophilic nitromethane readily attacks the carbonyl carbon. However, the other two nitrobenzaldehyde substituted at ortho or para position did not show much progress, especially o-nitrobenzaldehyde showed little product peaks. In addition, other benzaldehyde substrates which possess a substituent (CN, CF_3, Br or I) at the meta position did not present as good result as m-nitrobenzaldehyde derivatives. The two meta-functionalised benzaldehyde with CF_3 and Br were not even presented in Figure 3-9 since they showed little product. Only m-cyanobenzaldehyde presented relatively good ee (-22 %) and reaction rate.

It seems that m-nitrobenzaldehyde derivatives interact with the catalyst and modulator groups in a specific way, resulting in a faster reaction rate and relatively higher enantioselectivity than other substrates. Thus, most experiments were conducted with the nitrobenzaldehyde derivatives, especially 2-chloro-5-nitrobenzaldehyde as a standard substrate.

3.3.2. **Solvent effect**

In a solvent-assisted chemical reaction, the type of solvent is critical.[144] Changing the reaction medium with various solvents is also an efficient way to adjust reaction conditions. Hence, a range of solvents was judiciously selected regarding their chemical properties, such as protic vs aprotic, polarity or size. A few solvents, such as DMF (N,N'-dimethylformamide) or DEF (N,N'-diethylformamide), which are catalytically active, were omitted. The halogenated solvents, such as CH_2Cl_2 or $CHCl_3$, were also omitted from the list since their high densities make the crystals float on the surface of the reaction medium. The catalyst needs to be immersed in the reaction medium to demonstrate its catalytic activity adequately.

Cat-1s ($[Zn_4O(hhtt)_{1.33}(bpdc\text{-}gua)_{0.5}(bdc\text{-}bnox(S))_{0.5}]$) was prepared, as shown in Figure 3-10a, and cat-1s was used as a standard catalyst for most experiments. Fifteen different

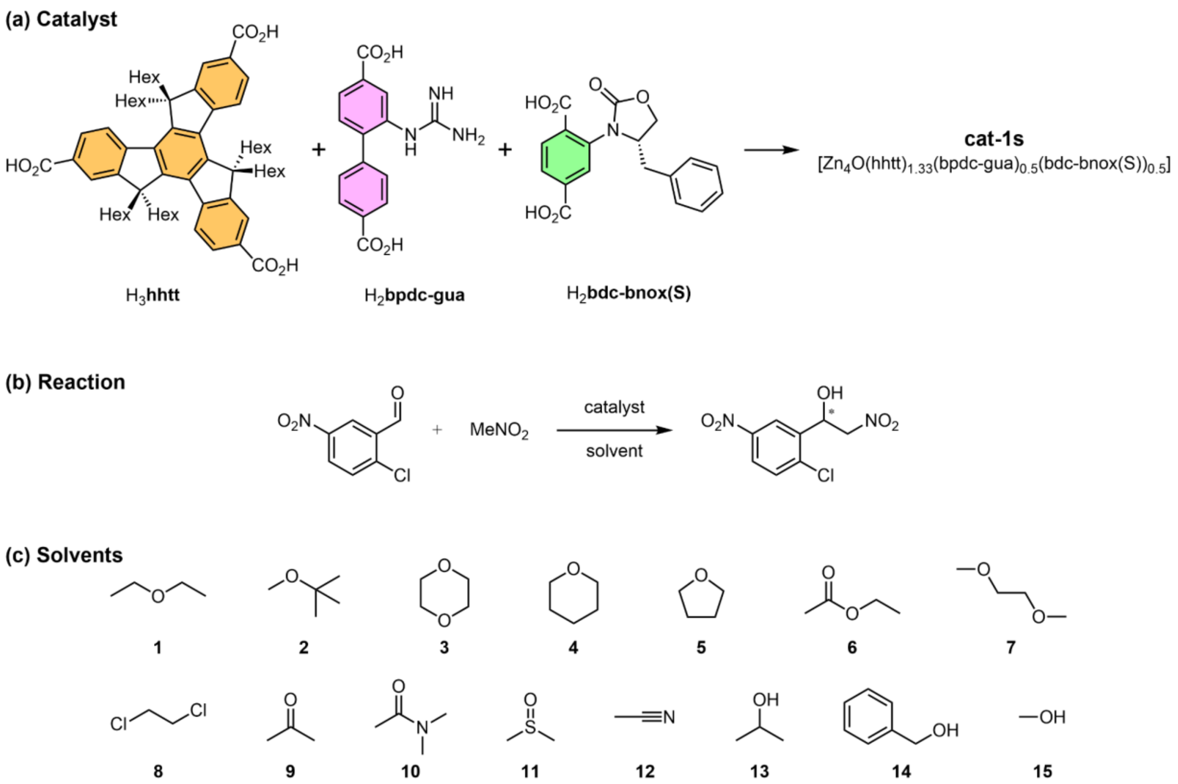

Figure 3-10. (a) A schematic synthesis diagram of cat-1s ([$Zn_4O(hhtt)_{1.33}(bpdc\text{-}gua)_{0.5}(bdc\text{-}bnox(S))_{0.5}$]); (b) the target Henry reaction; (c) fifteen different solvents tested for the target reaction.

reaction stock solutions of the standard Henry reaction (Figure 3-10b) were then prepared with the same concentration (35 mM) using each of the selected solvents shown in Figure 3-10c. Each reaction stock solution (0.6 mL) was then introduced to an approximately equal amount (ca. 3 mg) of cat-1s in an HPLC vial, and the reactions were carried out at ambient temperature simultaneously.

The supernatant of each vial was analysed using HPLC after two days, and the chromatograms were depicted in Figure 3-11 with the corresponding ees. The result clearly shows that dioxane provides an outstanding environment for the catalyst and modulator units to induce high enantioselectivity. However, a few similar solvents to dioxane in terms of the chemical and physical properties show much lower efficiency, especially tetrahydropyran (entry 4).

The experiment above demonstrates that the reaction rate is highly dependant on the reaction medium as well. For instance, all aldehyde substrate was consumed in dimethyl sulfoxide (entry 11), while no or very little catalytic activity was noted with acetonitrile (entry 12). Another interesting observation is noted with 1,2-dimethoxyethane (entry 7). Although the reaction rate was comparatively slower than the others, the enantioselectivity was reversed. All alcoholic solvents were revealed as not a good reaction medium for the Henry reaction since there was a high degree of background reaction, producing a large amount of side products (entry 13, 14 and 15; due to the intense peak of benzyl alcohol, all other peaks appear small in entry 14).

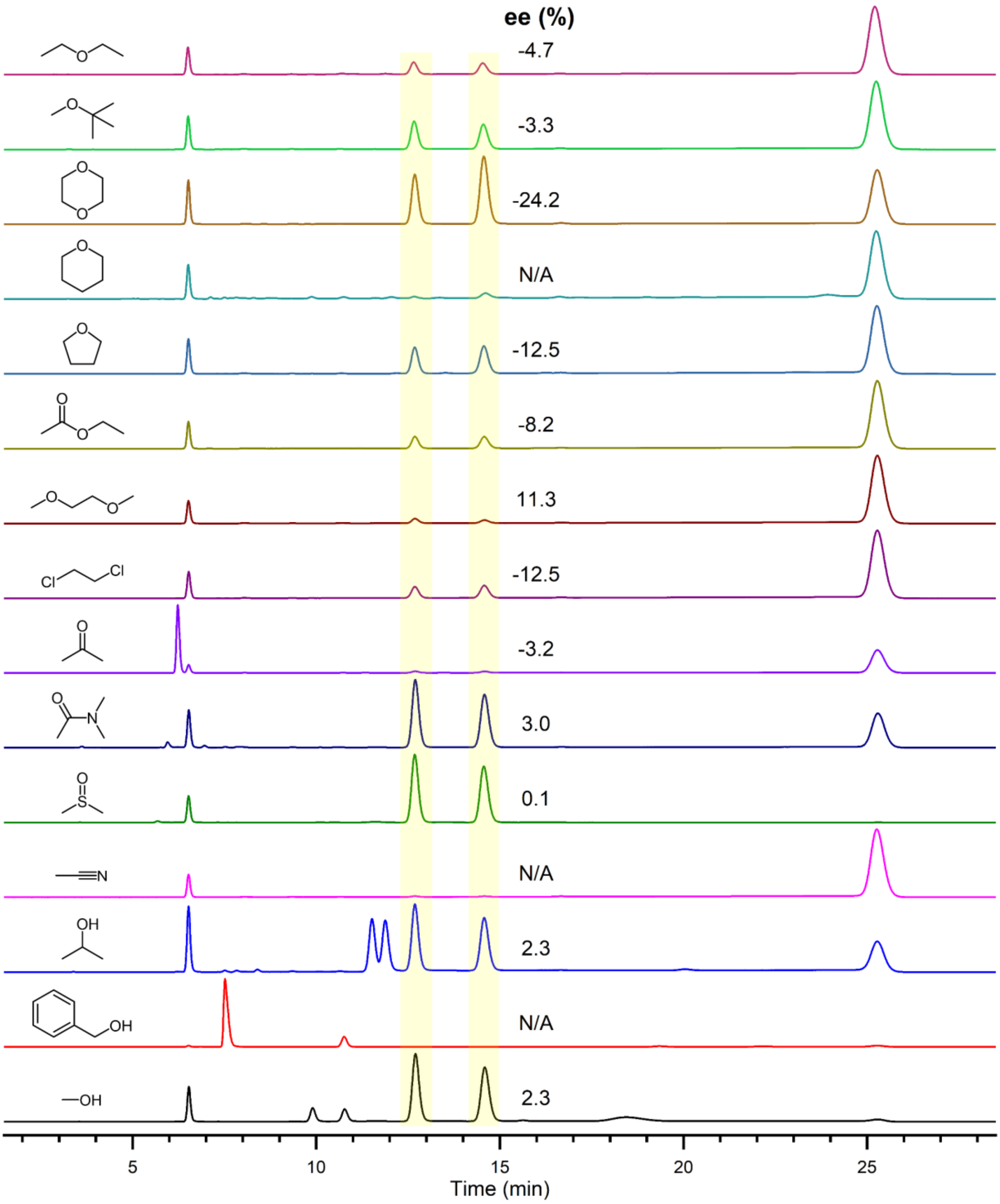

Figure 3-11. HPLC analyses for the products catalysed by the same RAI catalyst in 15 different reaction medium. The two product peaks were highlighted with yellow and the corresponding ee was written along with each chromatogram.

3.3.3. Chiral modulators

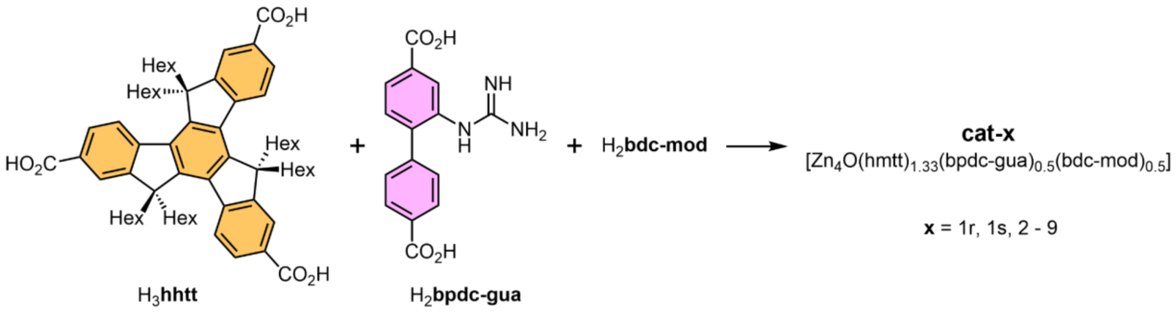

Figure 3-12. A schematic diagram of catalyst preparation to test various modulator groups. The prepared catalysts were denoted as cat-x, where x is the number for each bdc derived modulator.

Needless to say, the chiral modulating group is the core feature of the RAI catalyst. The chiral motif on the modulator directly cooperates with the achiral catalyst and interacts with the reaction substrates during the transition state to induce the chirality. The preliminary results clearly showed that the guanidine moiety itself does not have any enantioselectivity without the chiral modulator (entry 2 in Figure 3-8). Therefore, designing the chiral modulator is a crucial task of this project.

The oxazolidinone moieties have already demonstrated their capability to induce enantioselectivity. Therefore, we decided to test more oxazolidinone derivatives instead of testing new chiral functional groups. As depicted in Figure 3-12, a series of RAI catalysts (cat-x, where x refers to the bdc-derived chiral modulator's number) was prepared using the same ligand combination except for the chiral modulator in order to weigh correctly an influence caused by the tested chiral modulator only.

3.3.3.1. Size and position

As introduced in the previous section (3.2.4), two enantiomeric pairs of modulators, bdc-bnox(R)/(S) and bdc-iprox(R)/(S), were tested for the preliminary experiment. Adding on these four modulators, two other modulators, H_2bdc-4-phox(R) and H_2bdc-5-phox(R) (phox: phenyloxazolidin-2-one), were designed and synthesised to test a few parameters. As

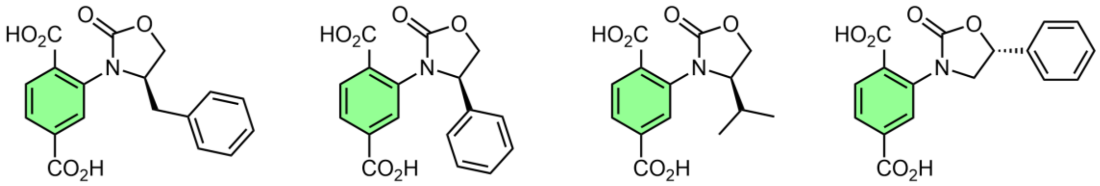

	1r. H_2**bdc-bnox(R)**	**2.** H_2**bdc-4-phox(R)**	**3.** H_2**bdc-iprox(R)**	**4.** H_2**bdc-5-phox(R)**
ee (%)	25.8	11.6	13.0	-21.2

Figure 3-13. How the two parameters, size (1 vs 2 vs 3) and position (2 vs 4) of chiral motif, affect inducing enantioselectivity will be investigated using these four modulators.

depicted in Figure 3-13, the first three modulators have functional groups in different sizes as a chiral motif. These will allow us to investigate how the size of a chiral motif (benzyl vs phenyl vs isopropyl) influences the enantioselectivity. The influence caused by the different positions of the chiral motif can also be studied by comparing the two modulators, 2 and 4.

The ee produced by each chiral modulator were depicted in Figure 3-13. The first three chiral modulators show an interesting result. The largest benzyl group of 1r induced the highest enantioselectivity. The ee produced by 1r is nearly twice larger than those induced by the other two. However, the smallest isopropyl group of 3 induced higher enantioselectivity than the phenyl group of 2. It does not clearly seem that the size of a chiral motif affects enantioselectivity much. The benzyl group possesses more degree of freedom due to its flexibility than the other two, allowing the chiral motif to point in various directions. This suggests that the influence on the enantioselectivity could be rather affected by the directionality of the chiral motif than the size. The high ee, induced by 4 and comparable to that of 1r, also supports such reasoning. Both 2 and 4 have the same phenyl group as a chiral motif but in a different position. Thus, the phenyl ring of 4 is almost orthogonally stretched out from the bdc backbone, and this allows 4 to cooperate with catalyst moiety in closer proximity.

3.3.3.2. Extending out from the bdc backbone

All the oxazolidinone moieties of the chiral modulators introduced above are directly attached to the bdc backbone through the C-N bond. As a result, the oxazolidinone moiety lacks mobility except for the rotational motion around the C-N bond. Moreover, the rotational motion of the oxazolidinone moiety is constricted due to the steric hindrance between the oxazolidinone and bdc carboxylate. According to the simple 3D modelling as illustrated in Figure 3-14a, the two atoms, O1 and C1, on the oxazolidinone moiety touch O2 on the

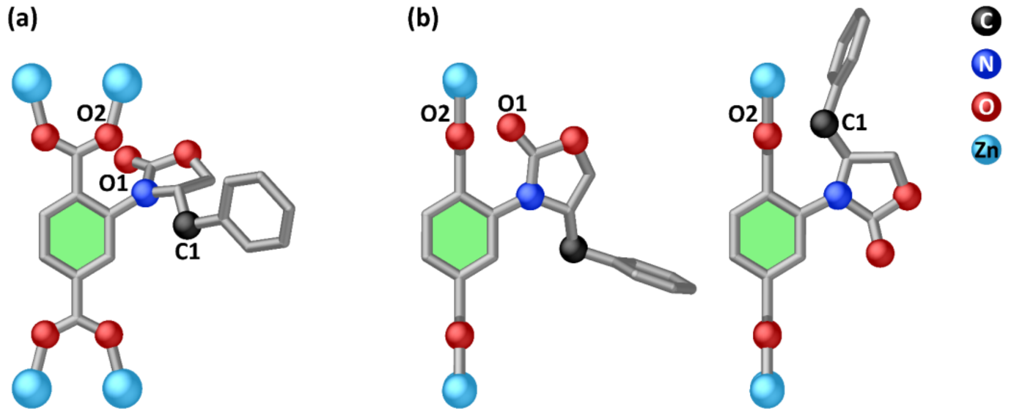

Figure 3-14. (a) When the dihedral angle between carboxylate and phenyl ring of bdc is zero, O1 and C1 on bnox could almost touch O2 while the oxazolidinone moiety is spinning around the C-N bond; (b) O1 and C1 are still too close to the Zn node even if the dihedral angle is 90°.

carboxylate of the bdc backbone while bnox revolves around the C-N bond. Even if the dihedral angle between the bdc phenyl ring and carboxylate group in bdc was set to 90° to minimise steric hindrance, O1 and C1 approach too close to the zinc cluster (Figure 3-14b). Therefore, the conformation of the oxazolidinone moiety is considered to be limited due to such steric hindrance.

As discussed in the previous section, the directionality of the chiral motif seems to play a critical role in asymmetric induction. Therefore, we hypothesised that if we add a methylene bridge between the bdc backbone and the oxazolidinone moiety, it can solve the problem caused by the limited rotational motion of oxazolidinone moiety. On top of that, it could also bring a benefit concerning the directionality of the chiral motif. Therefore, two modulators shown in Figure 3-15 were prepared using a coupling reaction between 2-bromomethyl terephthalic acid and oxazolidinone derivatives.

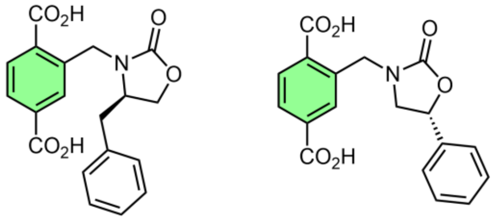

	5. H_2**bdc-mebnox(R)**	**6.** H_2**bdc-me-5-phox(R)**
ee (%)	(r): 3.2	(r): -1.2

Figure 3-15. The extended version of chiral modulators; a methylene group was inserted as a spacer between the bdc backbone and oxazolidinone moiety.

Two RAI catalysts were prepared using the two new modulators, 5 and 6, and they were tested for the enantioselectivity with the standard Henry reaction. However, the corresponding enantioselectivities from these two chiral modulators were significantly lower, indicating that the modulator units did not behave as expected. We tried to find the answer to this unexpected result from the equilibrium geometry of the modulator using computer simulation. Due to the complexity of the type-S framework, uncoordinated free acids were used for the calculation. Although the computer-simulated model of a free ligand cannot represent the conformation of the ligand integrated into the framework, it will be useful to understand the equilibrium conformation of the ligand in the framework. Therefore, the equilibrium conformers of 5 and 6 were simulated using the density functional theory (DFT) calculations. The calculation was computed using Spartan software at the B3LYP level of theory with the 6-31G* basis set.

According to the computer simulation, the equilibrium conformations of both 5 and 6 were not close to the ideal geometry to cooperate with the catalyst unit in the pore (Figure 3-16). Figure 3-17 shows the usual conformations of bpdc and bdc backbones in pore-Cs. Therefore,

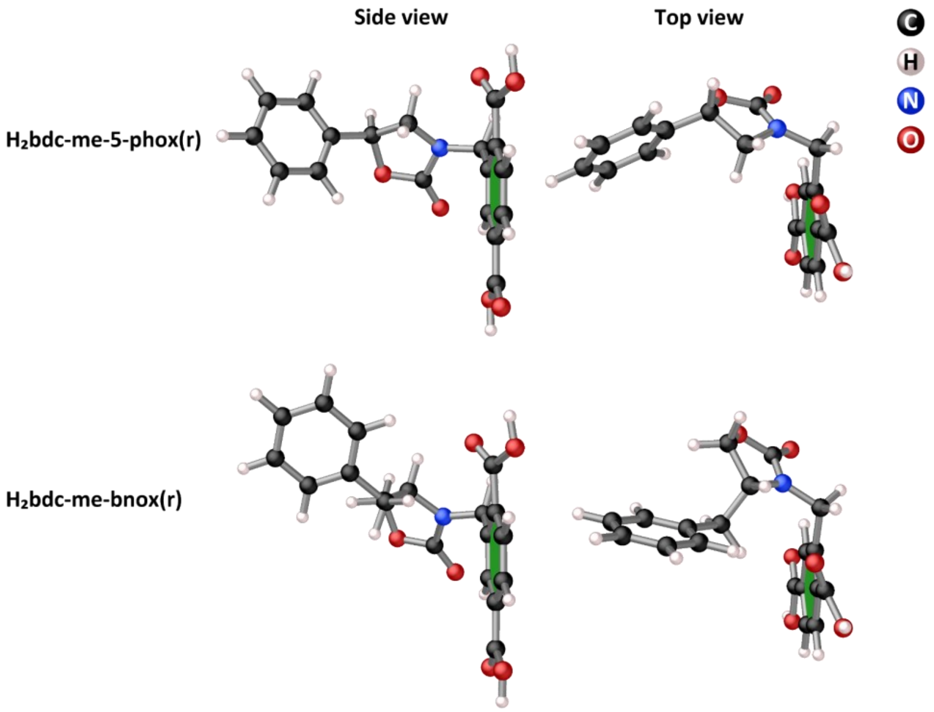

Figure 3-16. The optimised geometry of the two bdc derived chiral modulators at an equilibrium level. Both top view and side view clearly show the chiral motif on the oxazolidinone moiety stretching out close to an orthogonal direction to the planar of bdc.

the direction of the functional groups attached to those backbones is important if they need to interact in pore-C. If both bdc phenyl ring and functional groups were laid on the same plane, they would have a high probability of interacting in pore-C. However, the two oxazolidinone moieties on 5 and 6 shown in Figure 3-16 almost orthogonally stretch out to the planar of the bdc molecule.

As mentioned above, the equilibrium geometry calculated with the free ligand does not represent the actual conformation of them in the framework. Moreover, the arrangement of the functional groups in the pore dynamically changes depending on the solvent and guest molecules in proximity and many other variables. Hence, we do not overinterpret the simulation result, but we presume that this could be one plausible reason why they induced low ees.

3.3.3.3. Mono- vs di-substituted bdc

All the bdc-derived modulators introduced so far were mono-functionalised. In this case, we can envisage four different simplified environments in pore-C with respect to the arrangement of the catalyst and chiral modulator. Pore-C can be occupied by both catalyst and modulator, either catalyst or modulator, or by none. For instance, four successive pore-Cs are presented in Figure 3-17a, and each pore represents four different plausible pore environments depending on the orientation of catalyst and modulator units. The red sphere indicates the pore occupied by both catalyst and modulator, whereas the blue sphere refers

(a) mono-functionallised bdc

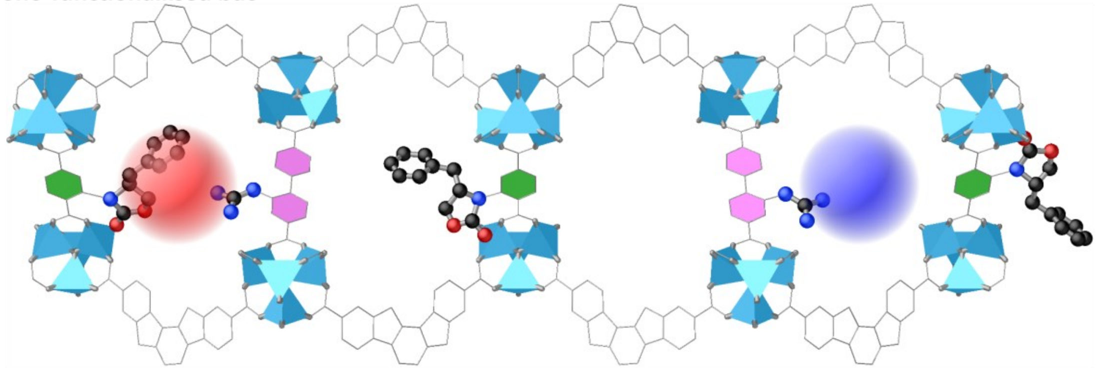

(b) bi-functionallised bdc

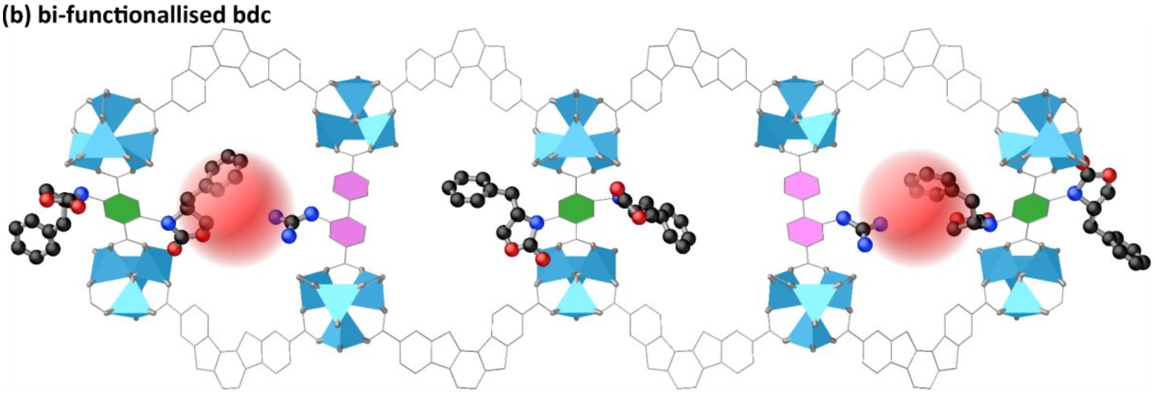

Figure 3-17. Simplified models of the successive pore-Cs in a row with different pore environments induced by (a) mono-functionalised bdc or (b) bi-functionalised bdc. The red spheres indicate the pore space occupied by both catalyst and modulator units, whereas the blue sphere represents the pore space occupied by the catalyst unit only.

to the pore space occupied by the catalyst alone. The former is the desired situation that contributes to enhancing the enantioselectivity of the RAI catalyst. On the other hand, a racemic mixture would be produced in the latter case, and the ee produced by the entire catalyst will be diluted.

On the contrary, the catalyst unit can always be paired with the modulator in pore-C if a bi-functionalised bdc ligand replaces the mono-functionalised one. Figure 3-17b demonstrates that all the catalyst units can cooperate with a modulating group if the bi-functionalised bdc ligand is recruited. Such simplified models cannot reflect the actual dynamic pore environments during the catalysis. However, we can expected that adding one more modulator moiety will probably increase the desired interaction between the catalyst and chiral modulator.

As shown in Figure 3-18, the bi-functionalised bdc (7) was prepared with bnox(S), and the corresponding ee was compared with the one induced by mono-substituted one (1s). However, unfortunately, the result caused by the bi-functionalised bdc did not work as expected, though the result was quite interesting. The first prominent result is the reversed enantioselectivity, although both modulators have the same chirality. Furthermore, the magnitude of ee produced by the di-substituted modulator is much smaller than the one

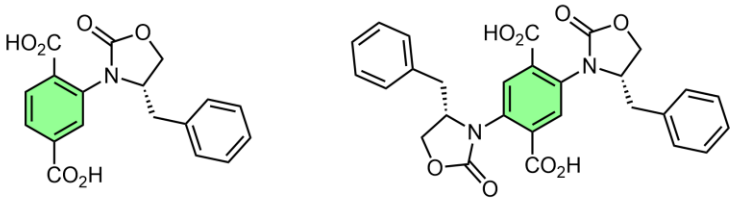

	1s. H$_2$**bdc-bnox(S)**	**7.** H$_2$**bdc-(bnox(S))$_2$**
ee (%)	-22.3	7.4

Figure 3-18. Mono- vs bi-functionalised bdc modulator with bnox(s) and the corresponding ee induced by RAI catalyst prepared from each modulator.

induced by the mono-substituted one.

Indeed, the bi-functionalised modulator did not behave as we designed. It is thought that this unexpected result is related to the rotational barrier of the phenyl ring of the bdc linker. According to Pakhira et al., the rotational barrier of the central phenyl ring in bdc is lowered as the number of substituents attached to the bdc increases or the size of the substituent becomes large.[137-138] The bare bdc molecule is fully conjugated through the π-bond, thus has a relatively high rotational barrier and prefers planar geometry. However, as the number or size of the substituents on the bdc increases, the steric hindrance between the carboxylate and substituents grows as well, resulting in lowering the rotational barrier. Similarly, the dihedral angle between the bdc phenyl ring and the carboxylate group at the equilibrium geometry also gets larger to minimise the steric hindrance.

The bnox moiety is almost the same size as the bdc backbone, and it causes a lot greater steric hindrance than simple substituents (CH_3 or Br) presented in Pakhira's work. Thus, it is expected that the rotational barrier of a bdc phenyl ring would get lower if two bnox moieties were installed to bdc. In addition, the dihedral angle of the bdc phenyl ring with respect to the carboxylate groups is also expected to become large. As a result, the desired interaction between the catalyst and chiral modulator was unlikely encouraged.

3.3.3.4. Various alkyl chains on truxene

We have noted another variable influencing the ee from our previous work presented in section 3.1.2 ; different ees were observed upon changing the alkyl chain length on a tritopic linker. Therefore, four different alkyl chains were introduced to the framework using H$_3$hmtt, H$_3$hbtt, H$_3$hhtt and H$_3$hott (Figure 3-19). The resulting catalyst was then denoted as cat-x ([Zn$_4$O(hxtt)$_{1.33}$(bpdc-gua)$_{0.5}$(bdc-bnox(S))$_{0.5}$], where x = m, b, h or o referring to methyl, butyl, hexyl or octyl, respectively). The influence caused by the different alkyl chain lengths was then investigated.

An approximately equal amount (ca. 3 mg) of each catalyst (cat-m, -b, -h or -o) was

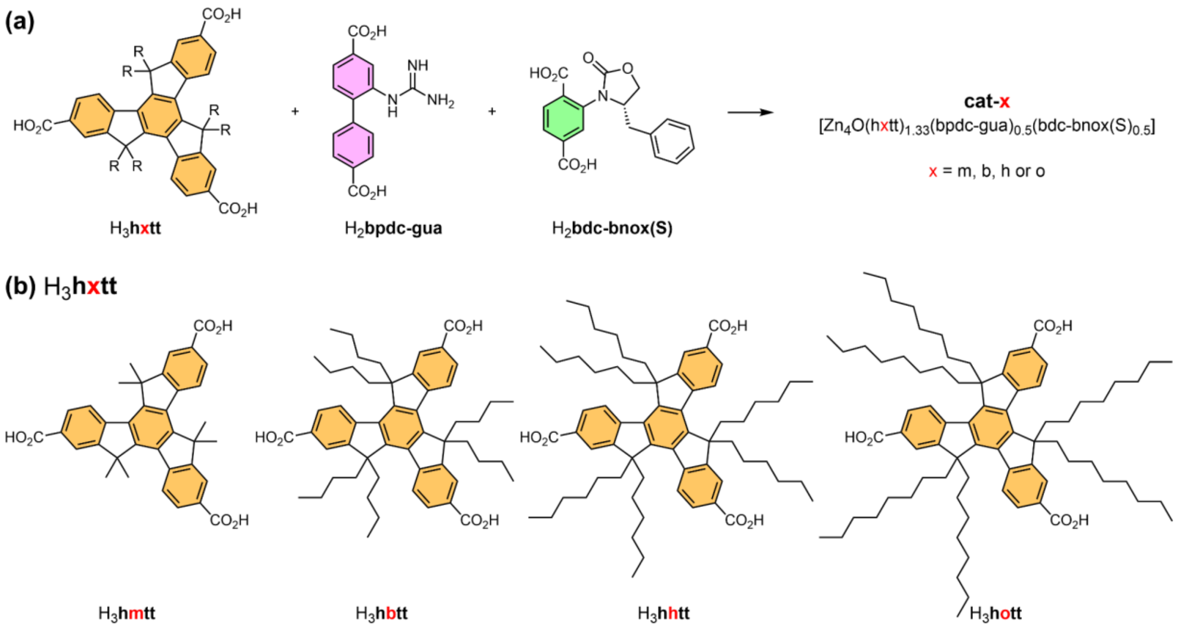

Figure 3-19. (a) A schematic diagram of catalyst preparation with the truxene derivatives for testing their influence on ee; (b) four different truxene derivatives tested

introduced to the standard Henry reaction stock solution of 2-chloro-5-nitrobenzaldehyde and nitromethane (35 mM, 0.6 mL). The four reactions were carried out simultaneously at room temperature for two days. The supernatant from each vial was then analysed using HPLC, and the chromatograms were presented in Figure 3-20.

Surprisingly, it was revealed that changing the alkyl chain length on truxene is the most influential parameter among many others. The enantioselectivity induced by cat-h is incomparably higher than those induced by other catalysts. However, there was no intuitive relationship between the chain lengths and the corresponding enantioselectivity. The same experiment was repeated several times with newly synthesised crystals to confirm the reproducibility of each catalyst. However, not much difference was noted compared to the ones presented in Figure 3-20. We have developed two hypotheses to explain such unpredicted result presented above as we were conducting more experiments and collecting more data. The interpretation of the experimental result based on the two hypotheses will be discussed in detail in the next chapter.

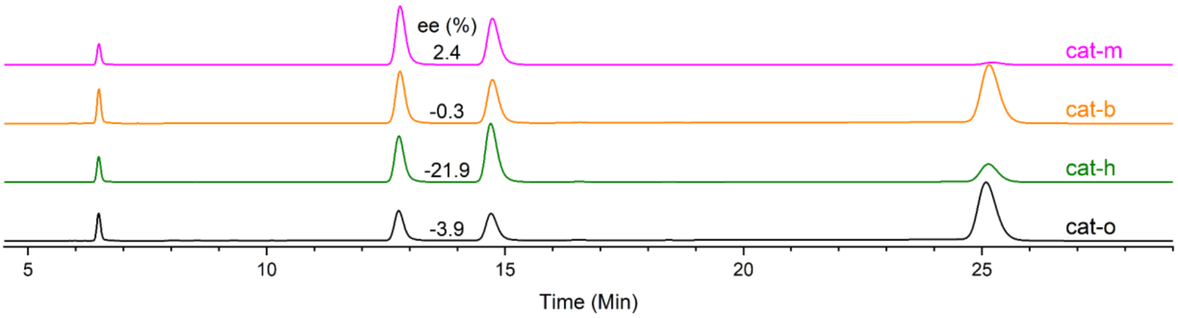

Figure 3-20. HPLC chromatograms and the corresponding ee of the catalysed reactions by RAI catalysts composed of different tritopic linkers

3.4. Conclusion

In this chapter, we have introduced a new concept asymmetric catalyst. Unlike conventional asymmetric catalysts, the two different functions (catalysis and asymmetric induction) were performed by a separate component. The experimental results presented that the catalyst unit alone could not induce any enantioselectivity, and the chiral modulator alone could not catalyse the reaction. It only worked as an asymmetric catalyst when the two components were presented in the same framework.

We have demonstrated such a novel concept of asymmetric catalysis using bpdc-gua as a catalyst and various bdc derivatives as a chiral modulator. The catalytic performance then tweaked by changing various parameters, and a surprisingly enhanced result was obtained under some specific conditions. In the following chapter, it will be discussed how those parameters influenced the catalytic performance. Moreover, the right direction to enhance the capability of the RAI catalyst will be discussed and suggested.

3.5. Experimental section

Syntheses and ^{1}H NMR data are presented in Appendix B.

3.5.1. General procedures

All starting materials and solvents were used as received from commercial sources without further purification unless otherwise noted. H_3hxtt[7] and the chiral modulators (H_2bdc-oxazolidinone derivatives)[142] were prepared via literature procedures.

Column chromatography was carried out on silica gel (grade 60, mesh size 230-400, Scharlau).

NMR spectra were recorded at room temperature (unless otherwise noted) on Bruker-500 Avance instruments, with the use of the solvent proton as an internal standard.

High-performance liquid chromatography (HPLC) was carried out using a Thermo Fisher Dionex Ultimate 3000 system equipped with a UV detector, and chiral separation was conducted by using Phenomenex chiral column, LUX-Amylose-1.

All powder X-ray diffraction measurements were carried out on either Rigaku Spider or Bruker D8 Venture. Rigaku Spider X-ray diffractometer is equipped with CuKα radiation (Rigaku MM007 microfocus rotating-anode generator), monochromated and focused with high-flux Osmic multilayer mirror optics and a curved image plate detector. Bruker D8 Venture diffractometer is equipped with CuKα radiation with a diamond microfocus X-ray source and a Photon III 28 detector. The samples were solvated with DMF prior to and during measurements. The two-dimensional images of the Debye rings were integrated with 2DP or Diffract Eva to give 2θ vs I diffractograms. Predicted powder patterns were generated from single-crystal structures using Mercury.

All single-crystal X-ray diffraction measurements were carried out on Bruker D8 Venture, and the measurement temperature was controlled using Oxford Cryostream if required. Bruker APEX 3 was used to collect and process data, and the structure was solved and refined using the Shelx package[107,119] under Olex2[120].

3.5.1.1. PXRD

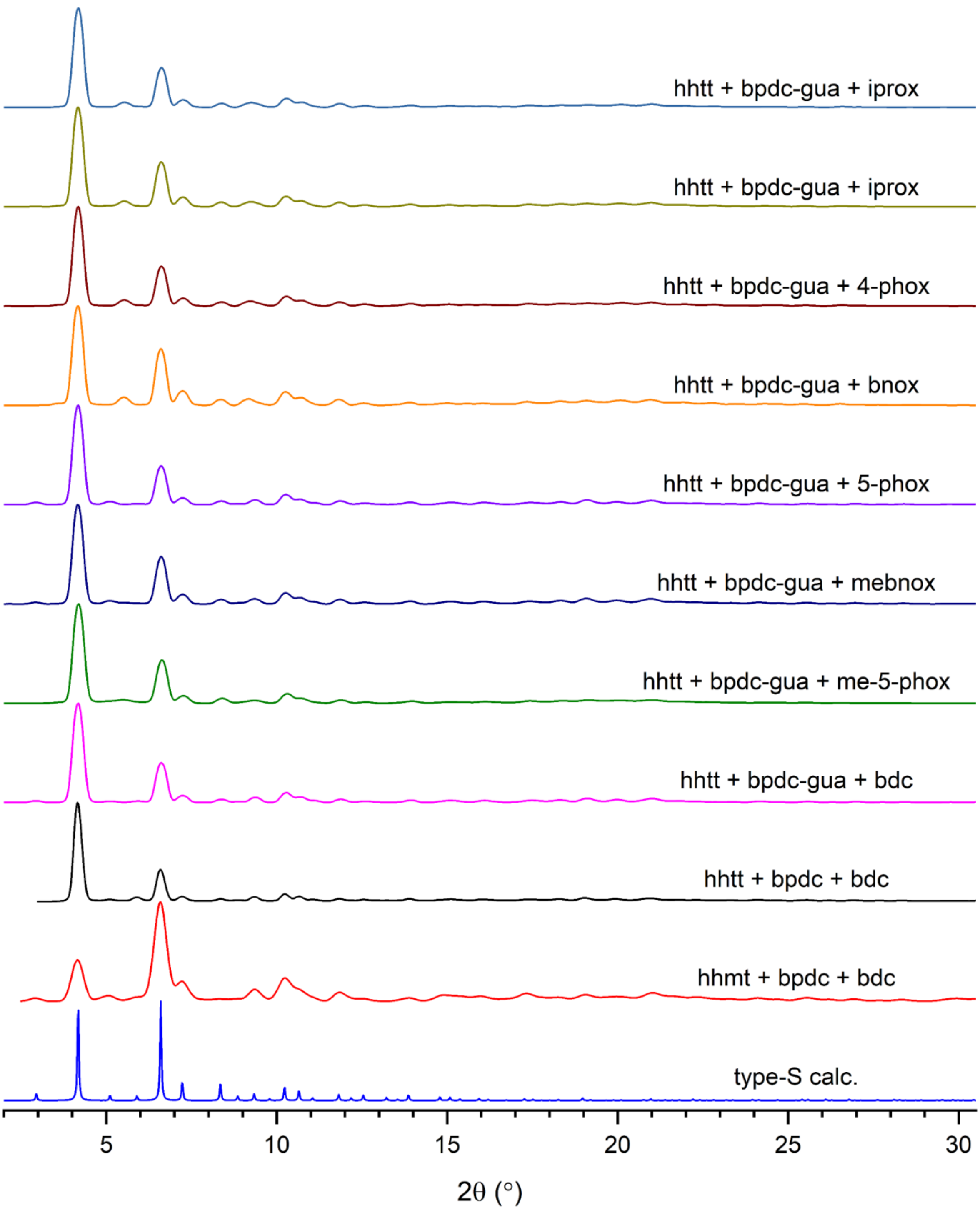

Figure 3-21. PXRD plots for the crystal samples used in this chapter.

3.5.2. Henry reaction and HPLC analysis

3.5.2.1. General reaction procedure

Approximately 2-3 mg of catalysts were placed in a 1.5 mL HPLC sample vial, and the crystals were washed with dioxane (×3) before use. The residual solvent was removed using a glass capillary tube, and then the reaction stock solution (0.6 mL) was introduced to the vial. The reaction mixture was kept at room temperature for two days before analysis. 1.0 μL of the supernatant was subjected to HPLC, and analysis was carried out under the following conditions: Lux amylose-1 column; mixed solvent of CH_3CN and deionized water (55:45 v/v); flow rate of 0.5 ml/min. Products were detected according to their absorption of 254 nm UV light. The ee value of each reaction is calculated based on Equation 1.

3.5.2.2. Standard reaction stock (35 mM) preparation

2-Chloro-5-nitrobenzaldehyde (130 mg, 0.7 mmol, 1 eq.) was dissolved in dioxane (18 mL) and $MeNO_2$ (1.88 mL, 35 mmol), and the mixture was kept at room temperature until use. No background reaction was observed for a few months.

3.5.2.3. Stock preparation for solvent screening experiment (for section 3.3.2)

The concentrated reaction stock was prepared as followed. 2-chloro-5-nitrobenzaldehyde (260 mg, 1.40 mmol) was dissolved in nitromethane (3.75 mL, 50 eq.). Then the concentrated stock solution (0.1 mL) was diluted with an appropriate solvent (0.9 mL) to make a reaction stock solution (35 mM).

3.5.2.4. Various aldehyde substrates

Approximately 30 different aldehyde substrates were screened to test the RAI catalyst for Henry reaction with nitromethane, as illustrated in Figure 3-22. The identical reaction condition was applied for all reactions; the same concentration of the reaction stock solution, approximately the same amount of catalyst, which comprised of hhtt + bpdc-gua + bdc-bnox(S), and the same reaction time (2 days).

However, only a few of them were relatively well catalysed, so the analyses data and chromatograms of selected substrates were presented in Table 3-3.

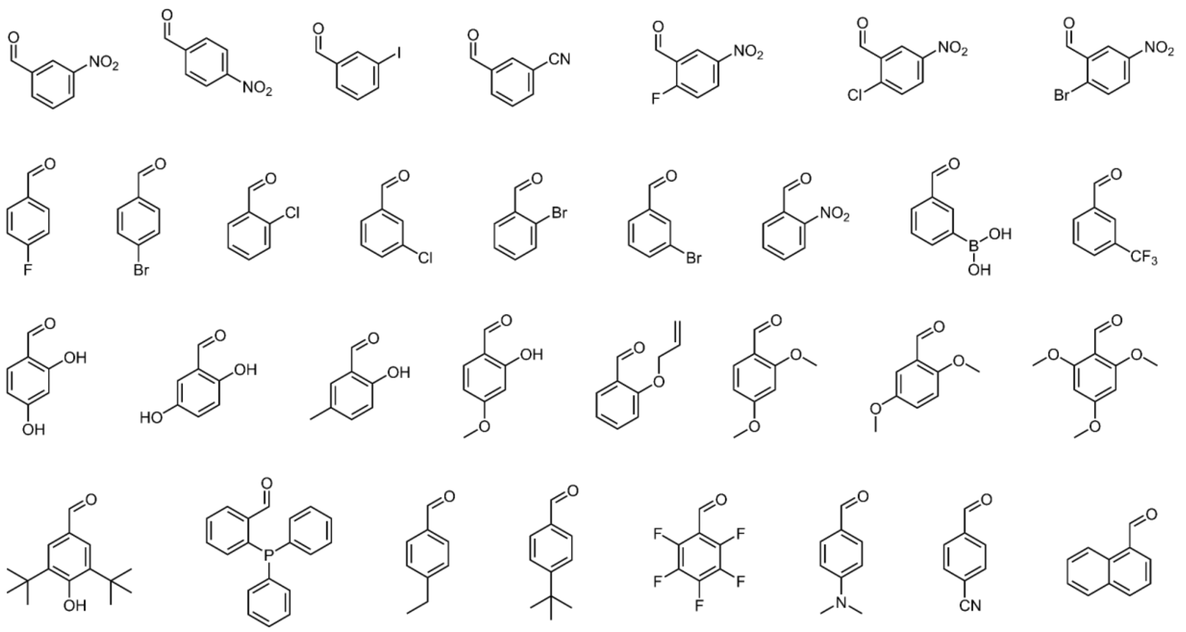

Figure 3-22. Aldehyde substrates for Henry reaction to test RAI catalysts

Table 3-3. The aldehyde substrates relatively well catalysed by the RAI catalysts were presented with their HPLC analysis condition and the corresponding ee.

#	Substrate	HPLC condition				ee (%)
		Eluent			Detection wavelength (nm)	
		MeCN (%)	H_2O (%)	Rate (mL/min)		
1	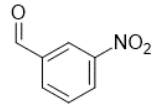	55	45	0.5	254	-34.7
2	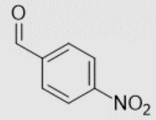	55	45	0.5	254	2.3
3	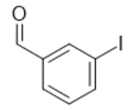	55	45	0.5	254	-28.3
4	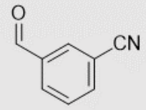	40	60	0.5	280	-22.9
5	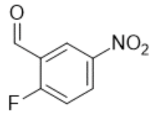	50	50	0.5	254	-17.5
6	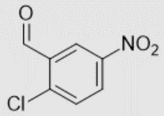	55	45	0.5	254	-25.7
7	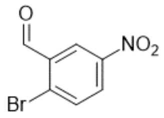	60	40	0.55	254	-13.4

3.5.2.5. HPLC chromatograms of the Henry reaction catalysed by cat-1 – 7 (section 3.3.3).

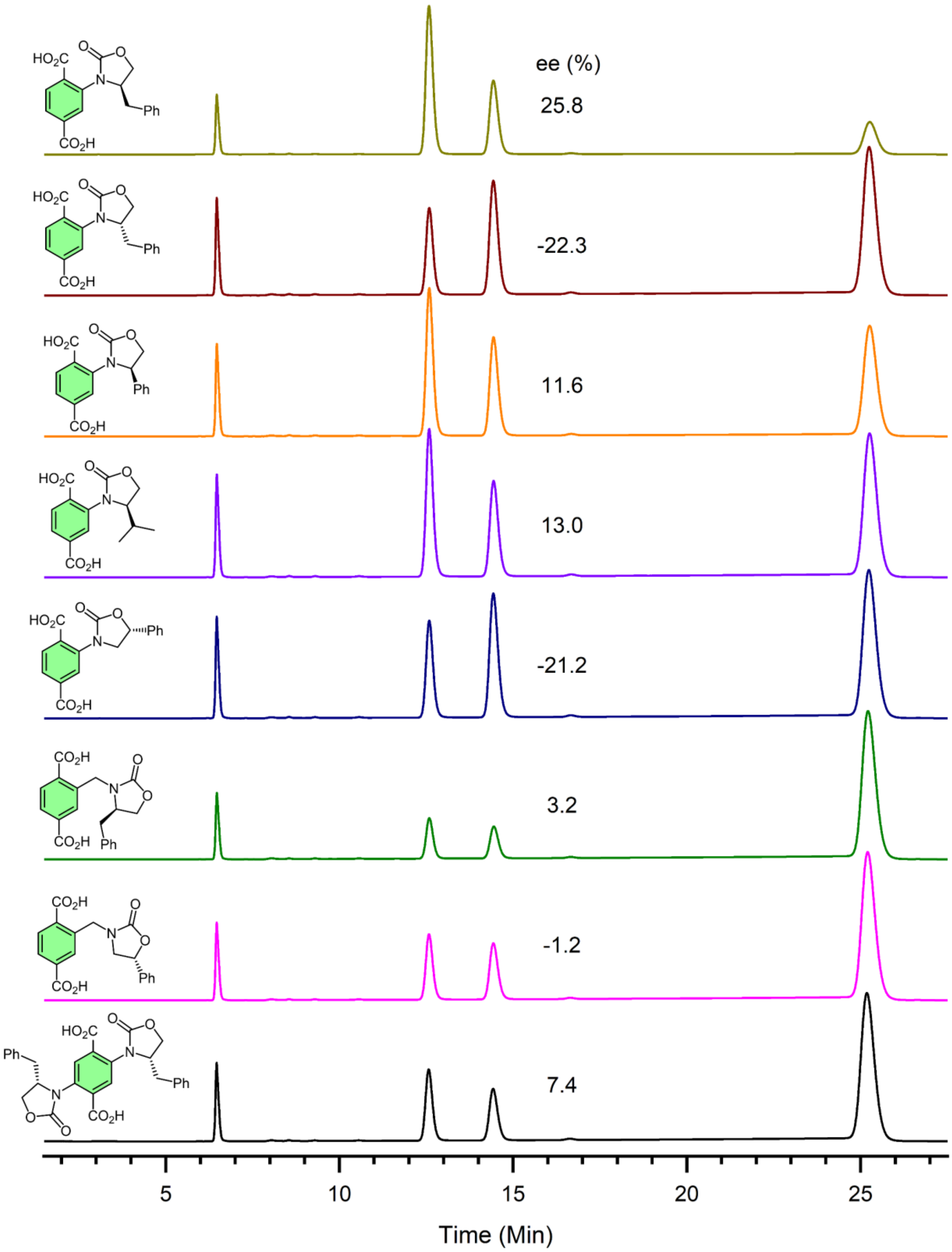

Figure 3-23. HPLC chromatograms with the corresponding ee which induced various chiral modulators, 1–7.

Chapter 4 Remote asymmetric induction – Part 2

Chapter 3 was mostly focused on developing the RAI catalyst and what experiments were conducted to deliver and enhance the enantioselectivity. In this chapter, those experiment results will be interpreted and discussed based on two different catalyst models. In addition, some experiments that were further conducted to investigate the catalyst model and increase the enantioselectivity will be introduced and discussed.

4.1. Developing the RAI catalyst model

The first MUF-7 series (type-L) discovered in 2013 has very interesting features.[56] However, the framework comprised of btb is poorly stable and has difficulty producing phase pure crystals due to the various competing frameworks. Such drawbacks make it hard to be studied further and be used in practical applications. On the other hand, the MUF-77 series (type-S) synthesised from truxene derivatives has improved properties in many different aspects,[7] allowing us to investigate further this material under various conditions. We have noted that the type-S framework has great potential as an excellent catalysis platform. A wide range of chemical functional groups can be incorporated into the framework, and pore-C provides space where all these functional groups can interact with each other along with the entering guest molecules. During a few years of research on various topics using type-S frameworks in our group, all the experimental data and observations had exhibited a clear trend.

'A type-S framework was formed when a truxene derivative was used as the tritopic linker.'

Such a trend was also presented in other catalysis projects using type-S frameworks. Thus we have developed a hypothesis that the interaction between functional groups attached to the linkers occurring in pore-C plays a significant role in adding particular functionalities to the catalyst, such as enantioselectivity or chemoselectivity. [109,111] We took it for granted that the MOF catalysts used for this RAI catalyst were also type-S frameworks since they comprised truxene derivatives. Hence, the same hypothesis was also initially used to interpret the experimental data from the RAI catalysis.

4.1.1. Pore-C model

As discussed in Chapter 3, the RAI catalyst was inspired by the reported work in 2017 (section 3.1.2).[109] In this work, various combinations of the functional groups attached to the three linkers were systematically tested, and the results demonstrated the apparent

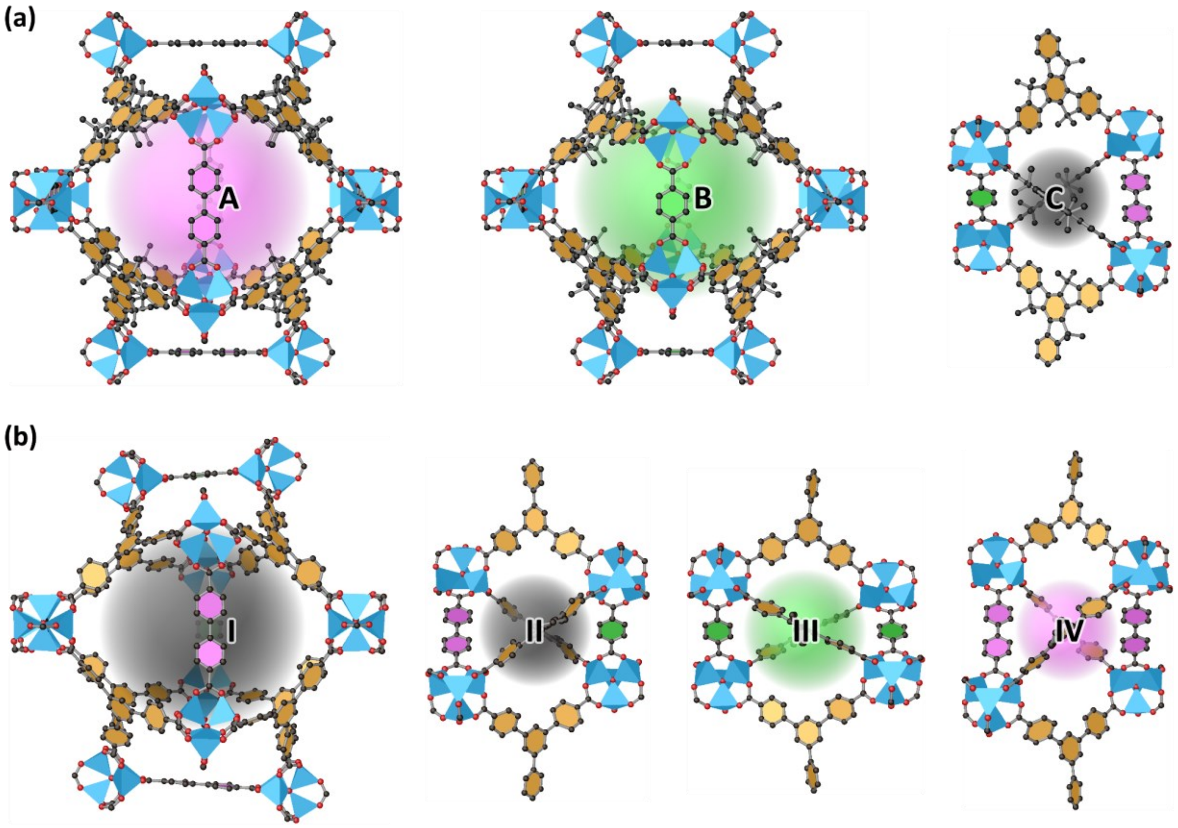

Figure 4-1. (a) Three different pores, A, B and C in the type-S framework; (b) four different pores, I, II, III and IV in the type-L framework. The pore-colours indicate the ligand combination which surrounding the pore; pink – bpdc and tritopic, green – bdc and tritopic, and black – all three.

cooperation between those, influencing the reaction outcomes. The single-crystal structure and the PXRD patterns identified that all of the catalysts used in this work were type-S. Therefore, it is a plausible and logical interpretation that the reaction occurring in pore-C mostly contributed to the enantioselectivity of the catalyst since pore-C is the only space defined by all three linkers. On the contrary, the catalyst units can also occupy the larger pore due to the rotational motion of the ligand backbone and carry out catalysis. However, no interaction between the catalyst and modulator is expected in this case because the large pores are surrounded by either bpdc and truxene (pore-A in Figure 4-1a) or bdc and truxene linkers (pore-B). As a result, the desired interaction between bdc and bpdc linkers does not occur in pore-A and pore-B, so that the racemic product catalysed in these pores will decrease the enantioselectivity of the RAI catalyst.

The MOFs used for the RAI catalysis resemble those used in the previous work in many aspects, especially they all comprised of the truxene derivatives. Therefore, we naturally regarded that the same type-S framework would be used for the RAI catalysis because they were all synthesised from the truxene-derived ligands. Thus, the priority to increase the enantioselectivity of the RAI catalyst was focussed on inducing stronger interactions between the catalyst and chiral modulator units together with the reactants in pore-C. For that reason, various parameters were changed and tested, such as modulators, solvents and reaction substrates based on the inherited model (pore-C model).

4.1.2. **Changing direction**

However, as introduced in Chapter 2, a remarkable discovery that steered the entire project in a different direction was observed. It was revealed that the type-L framework could also be formed from truxene derivatives. After that, all the structural information was carefully investigated again, and it turned out that many of these RAI catalysts that produced impressive ee values were actually type-L.

All this confusion was caused by the moisture-sensitive crystals causing the poor SCXRD data quality. The crystal samples were decomposed during SCXRD data collection due to the hydrophilic guanidine moiety in the RAI catalyst so that we could not solve the crystal structure. Also, the characteristic peaks, which can be used to differentiate the two frameworks, in PXRDs were not carefully investigated due to their low intensity (Figure 4-2). Above all, we had too much relied on the trend developed by our long experience and observations, which is the type-L framework is not likely formed from the truxene-derived linkers. However, the crystal structure was finally solved with improved techniques together with a powerful new X-ray diffractometer. The solved structure was obviously the type-L framework, although it did not clearly show the secondary functional groups due to their positional and rotational disorders.

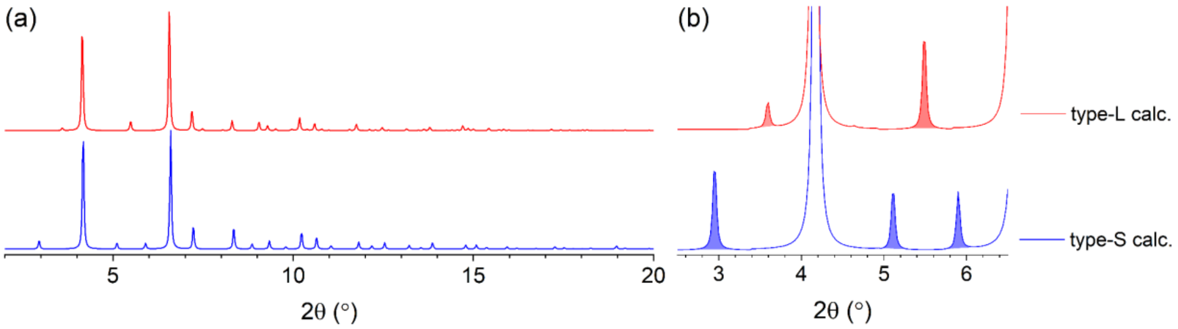

Figure 4-2. (a) The calculated PXRD patterns of type-L and type-S framework; (b) the characteristic peaks (shaded) appearing at low 2θ range were zoomed.

When it was first noted that some of the RAI catalysts were actually the type-L framework, we regarded it as an unwanted phase which we should avoid. We still thought that pore-C in the type-S framework plays a crucial role in inducing enantioselectivity. The type-L framework would work with only 50 % of the efficiency of the type-S framework because only half of its small pores are pore-II, which is equivalent to pore-C (Figure 4-1). However, as we carefully investigated the old data and collected more evidence, we actually found that it flowed in the opposite direction.

All the experimental results were re-examined to check the relationship between the framework phase (type-S vs type-L) and the corresponding ee. According to the experimental result, which will be discussed in detail later, the ees produced by the type-S frameworks were relatively low, indicating that pore-C was actually ineffective in generating chirality in the product. In contrast, all the type-L catalysts produced relatively higher ees regardless of the modulator type. This indicates that the pore-C model is not the right model for the RAI catalyst, and our approach to obtain high enantioselectivity rested on incorrect assumptions.

4.1.3. Pore-I model

Now, another model is required to replace the pore-C model so that we can elucidate our experimental results and design and plan further experiments. Approximately one unit cell of the type-S framework is depicted in Figure 4-3a. Two large dodecahedral pores neighbour each other, and the corner-sharing three tetrahedral pores are located in between the two large pores. As the colour of the pores indicates, the larger pores are surrounded by two

(a) Type-S

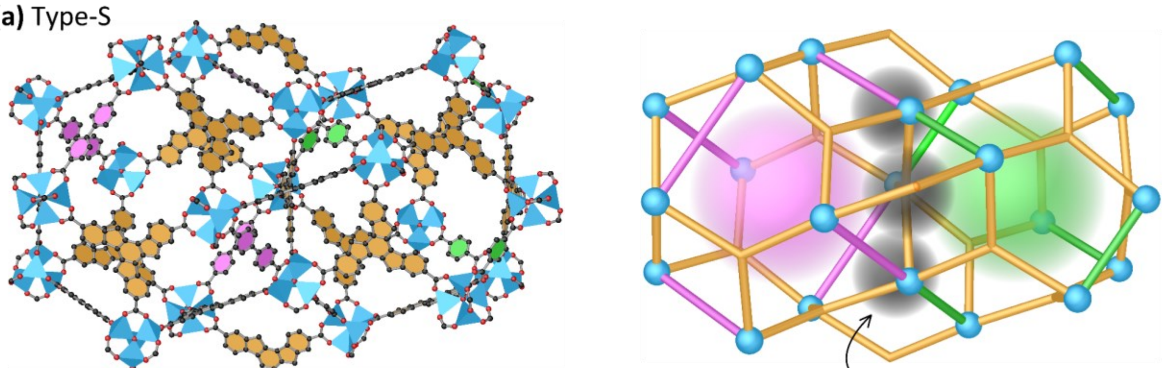

(b) Type-L

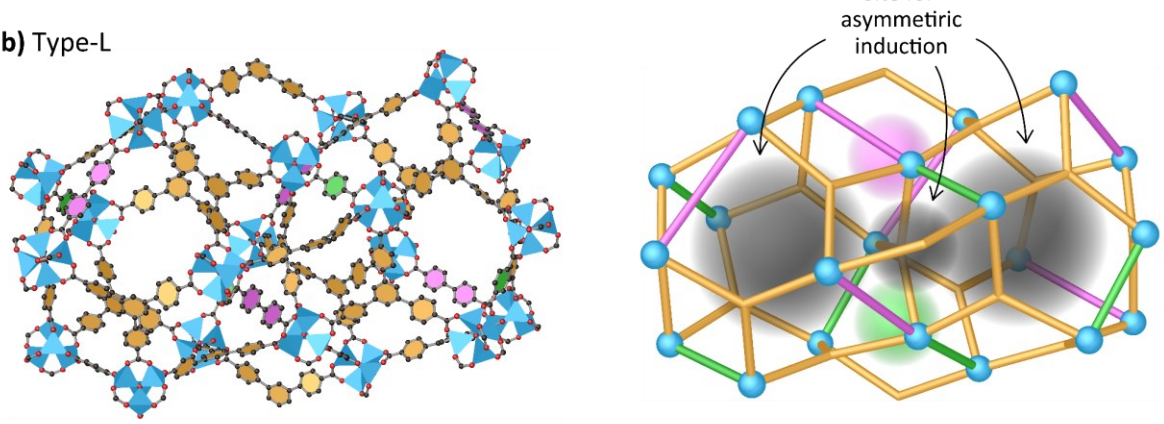

Figure 4-3. (a) Approximately one unit cell of the type-S framework (left) and its simplified model with three different pores (right); (b) the type-L framework of the same size for easier comparison with the type-S framework. The large sphere indicates pores and the colour denotes the surrounding linker combinations; pink – bpdc and tritopic linker, green – bdc and tritopic linker, and black – all three linkers. All the secondary functional groups and hydrogen atoms were omitted for clarity.

linkers, whereas the small pores comprise all three linkers. On the other hand, the proportion of the small pore defined by all three linkers is low in the type-L framework (Figure 4-3b). However, in this case, the large dodecahedral pores (pore-I) are defined by all three linkers. We hypothesise that pore-I provides a suitable environment for the cooperation of all three linkers. Thus, the desired interaction between the catalyst unit and the modulator (together with the reactants) can occur in pore-I of the type-L framework. We need not invoke the involvement of the small tetrahedral pores. Notably, this kind of pore (pore-I) is absent from the type-S framework, consistent with the low observed ee.

If we look into pore-I in further detail, three pairs of bpdc and bdc, which are facing each other across the pore, surround the pore-I (Figure 4-4a). The distance between the two facing linkers (e.g. α and iii) is too far (~ 30 Å from the centroid to centroid) to interact with each

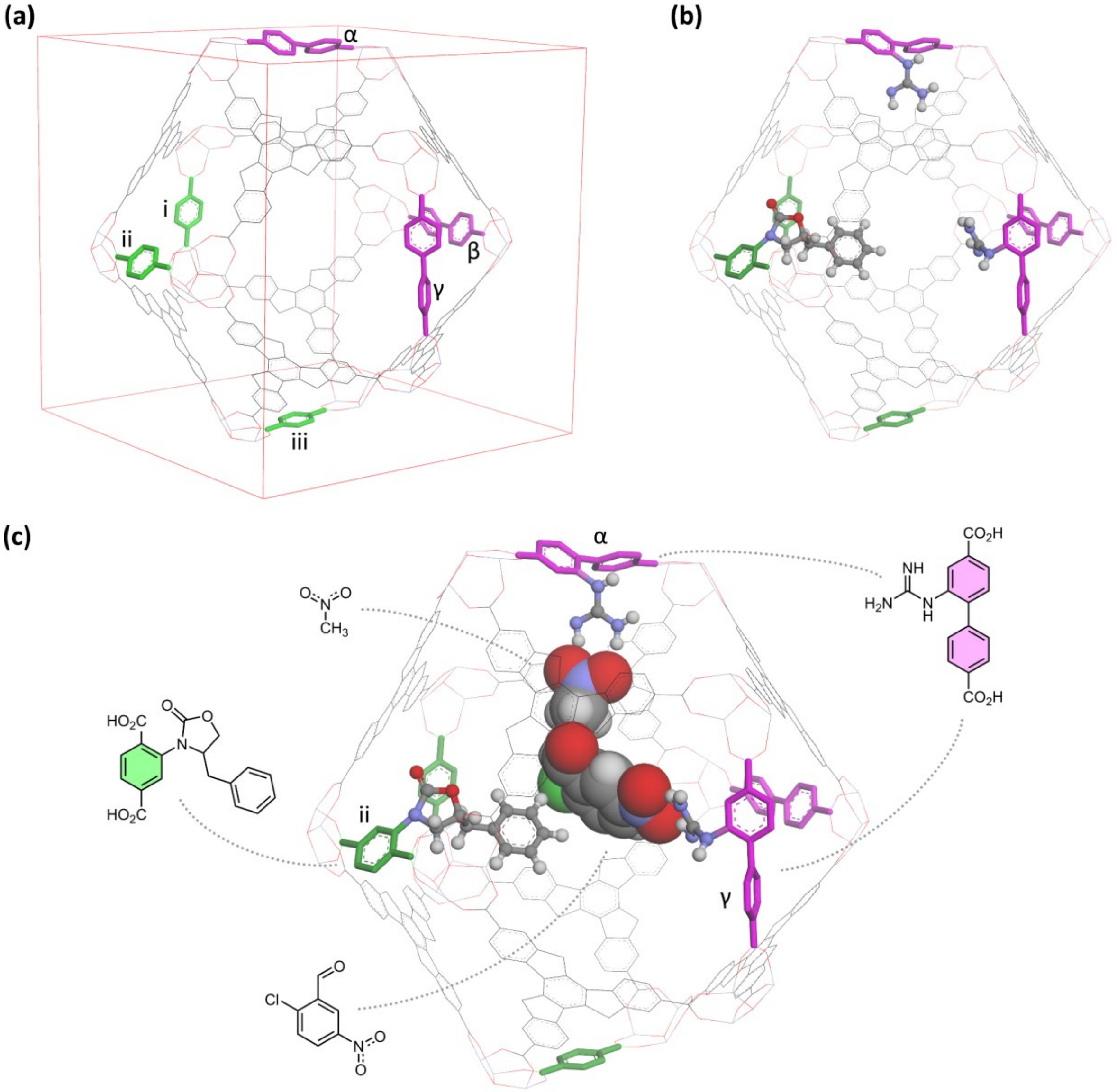

Figure 4-4. (a) The spatial arrangement of bpdc and bdc backbone in pore-I of the type-L framework; (b) a plausible conformation of the catalyst and chiral modulator; (c) likely interactions between catalyst, modulator and reactants.

other. However, the two linear inkers also orthogonally neighbour each other (e.g. γ and iii), and in this case, the distance between them is not very far. Moreover, when the functional groups attached to those linkers, the distance between them is close enough to interact with the substrate molecules (Figure 4-4b). The snapshot shown in Figure 4-4c was manually modelled to visualise how catalyst and modulator units might interact with the reactants in pore-I. The arrangement of all the components was judiciously determined regarding their chemical properties. It seems the desired interaction between the functional groups could occur in pore-I according to this model. Moreover, we could expect more than one catalyst or modulator groups working together. For instance, the two guanidine moieties attached to α and γ interact with the reactants by forming hydrogen bonds with the nitro group of nitromethane and nitrobenzaldehyde in Figure 4-4c. This new catalyst model with pore-I of the type-L framework seems appropriate and chemically sensible.

Two different catalysis models are now proposed. The desired interaction between catalyst and modulator could occur in pore-C of the type-S framework (pore-C model) or in pore-I of the type-L framework (pore-I model). In the rest of this chapter, the two different catalysis models will be used to interpret the experimental results exhibited in Chapter 3. The two different interpretations will then be discussed and compared to each other.

4.2. Interpretation of the experiment results with the two different models

4.2.1. Various modulators

In section 3.3.2, eight different chiral modulators (1r, 1s, 2–7 in Figure 4-5b) were tested, and the corresponding ees were compared to each other. Although the experiment was designed to see the trend between the size and shape of modulator groups and corresponding ees, the diverse ees seem more related to the crystal phases (type-L vs type-S), which arise from the specific linker combinations. Thus, the relationship between the modulator, phase and ee was reinvestigated. Two other modulators (8 and 9) were also examined (Figure 4-5b).

The phase of each catalyst sample was determined using the PXRD pattern (Figure 4-5c). Some PXRD patterns clearly have the characteristic peaks of either the type-L or type-S framework. The type-L catalysts (cat-1, -3, -4 and -7) possess higher ee than the type-S catalysts (cat-5 and -6). On the contrary, both phases appear in cat-2, -6 and -9. However, cat-2 has intenser characteristic peaks of type-L than cat-6 and -9, indicating that more type-L portion is present in cat-2, thus having higher ee than 6 and 9 as a result.

(a) Catalyst syntheis

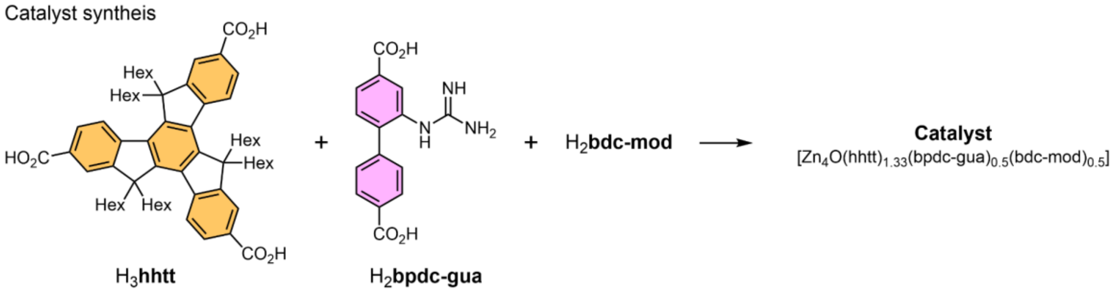

(b) H$_2$**bdc-mod**

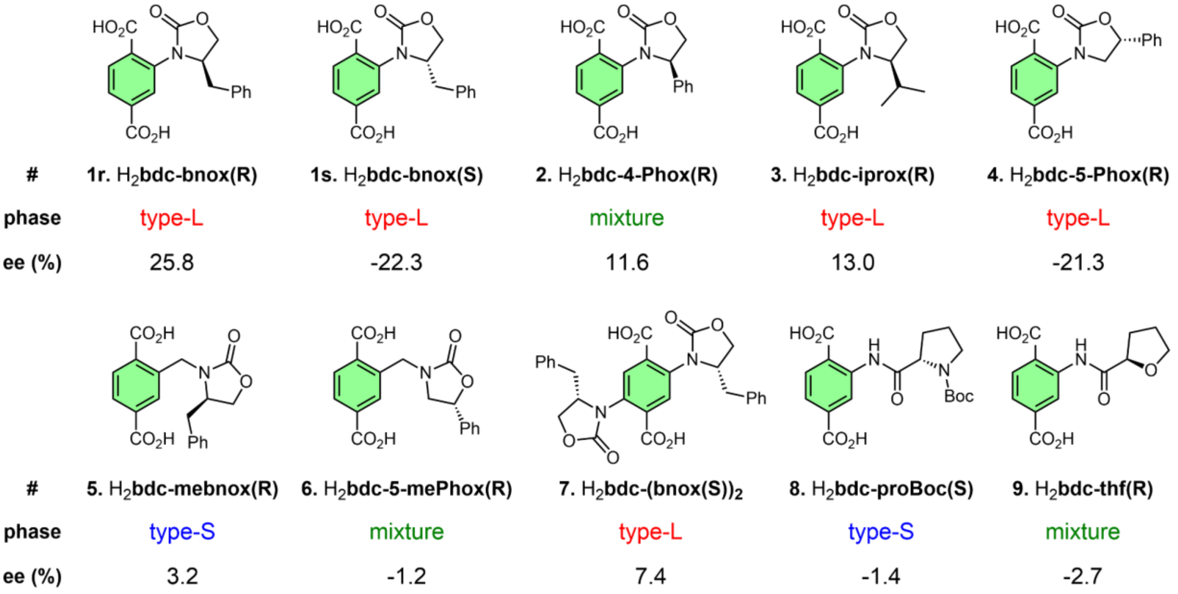

#	1r. H$_2$bdc-bnox(R)	1s. H$_2$bdc-bnox(S)	2. H$_2$bdc-4-Phox(R)	3. H$_2$bdc-iprox(R)	4. H$_2$bdc-5-Phox(R)
phase	type-L	type-L	mixture	type-L	type-L
ee (%)	25.8	-22.3	11.6	13.0	-21.3

#	5. H$_2$bdc-mebnox(R)	6. H$_2$bdc-5-mePhox(R)	7. H$_2$bdc-(bnox(S))$_2$	8. H$_2$bdc-proBoc(S)	9. H$_2$bdc-thf(R)
phase	type-S	mixture	type-L	type-S	mixture
ee (%)	3.2	-1.2	7.4	-1.4	-2.7

(c) PXRDs

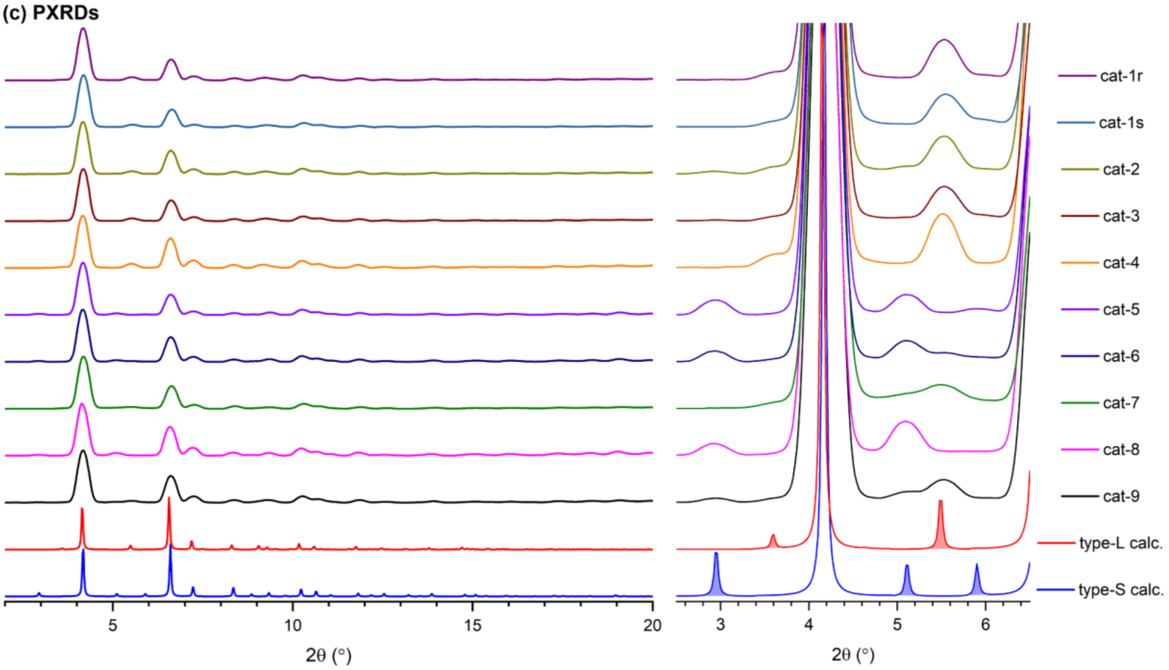

Figure 4-5. (a) A schematic procedure of the catalyst synthesis using various bdc derived chiral modulators; (b) ten different modulators and the corresponding crystal phase and ee were also presented with each ligand; (c) PXRD patterns of the catalysts prepared from various modulators.

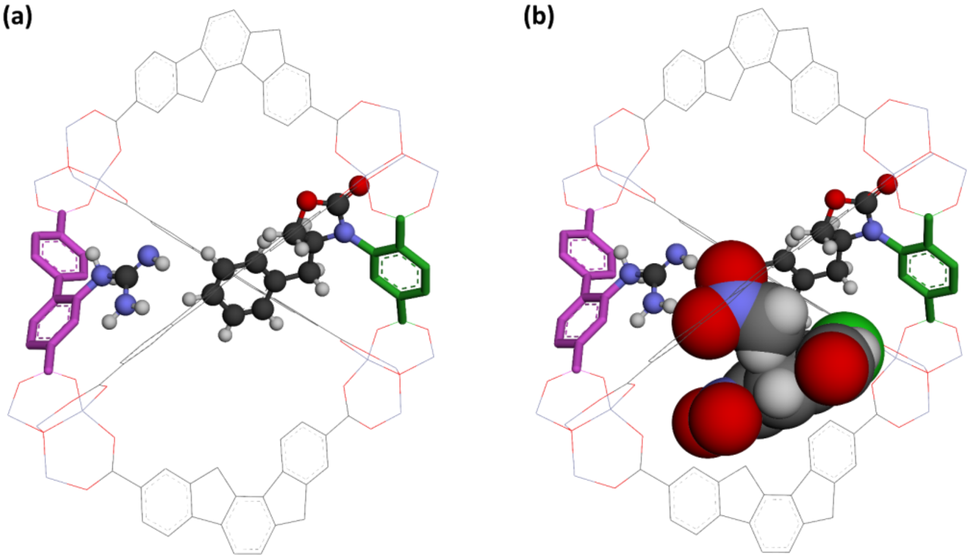

Figure 4-6. (a) Simplified spatial arrangement of catalyst and modulator units in pore-C of cat-1r; (b) the reactants (2-chloro-5-nitrobenzaldehyde and $MeNO_2$) were added to pore-C.

A simple 3D model of pore C provides a clue why low ees were obtained from the type-S catalysts (Figure 4-6). The interaction between the guanidine catalyst unit and the chiral modulator in pore-C was studied, and their spatial arrangement was modelled with a typical substrate. However, a simple ball and stick model indicates that pore-C is already crowded only with the catalyst and modulator units placed in pore-C (Figure 4-6a). Moreover, if the two reactants were added in pore-C, it is certainly overpopulated (Figure 4-6b), especially when this is compared with Figure 4-4c; the solvent molecule, dioxane, is not even considered. Hence, there is a high chance that the expected interaction between the catalyst and modulator in pore-C cannot actually occur easily.

4.2.2. Various alkyl chains on the tritopic linkers

Another parameter that dramatically improved the enantioselectivity was the alkyl chains on the truxene linker. Four catalysts, comprised different truxene derivatives possessing different alkyl chains (methyl, butyl, hexyl or octyl), were tested (Figure 4-8a). However, the result was not straightforward to interpret because no trend was found between the alkyl chain length and the corresponding ee. The hexyl chain on hhtt demonstrated enhanced performance while methyl, butyl and octyl did not.

We first tried to elucidate this result based on the alkyl chain conformation in the crystal lattice when it was first discovered. The behaviour of the hexyl chain in the type-S framework is well illustrated in the reported structure (CCDC 1885842);[111] three pairs of hexyl chains orthogonally stretch out from the planar truxene body. We thought that the conformation shown in the crystal structure is a lower energy state of the hhtt molecule minimising steric hindrance between two hexyl chains branched out from the same carbon atom. Such behaviour of the alkyl chains on the truxene is also exhibited in the crystal structure of the organic molecule, Br_3hht, which is the intermediate material during the H_3hhtt synthesis (Figure 4-7a). There is undoubtedly a limitation in using the crystal structures to envisage the arrangement of the hexyl chains during catalysis. The long alkyl chains are flexible, and their conformation is highly affected by the solvent and guest molecules which dynamically move around. Hence, we cannot simply picture their behaviour in the framework based on a few snapshots.

However, such tendency of the hexyl chains on the truxene linkers is well demonstrated in another set of experiments (section 4.5.1.2). Three different SCXRD data of a type-S crystal sample, prepared from hhtt, bpdc and bdc ($[ZnO_4(hhtt)_{1.33}(bpdc)_{0.5}(bdc)_{0.5}]$), were collected at 173, 273 and 333 K. It was expected that modelling the hexyl chains would become more difficult as the measurement temperature increases because of the random motion of each chain caused by the increased thermal energy. However, the consistent conformation of the hexyl chains was shown in all three crystal structures. Although the overall ellipsoid sizes get slightly larger due to the thermal motion of each atom, the first three atoms branching out from the truxene plane were clearly shown that they are orthogonally stretching out even at 333 K. The result indicates the strong tendency of the hexyl chains orthogonally stretching out from the plane of truxene. Therefore, we might be able to assume that the majority of the hexyl chains would behave as they shown in the crystal structures.

Provided that the assumption made above is valid, we can envisage the conformation of the hexyl chains in the framework. In both type-L and type-S frameworks, the eight hhtt ligands

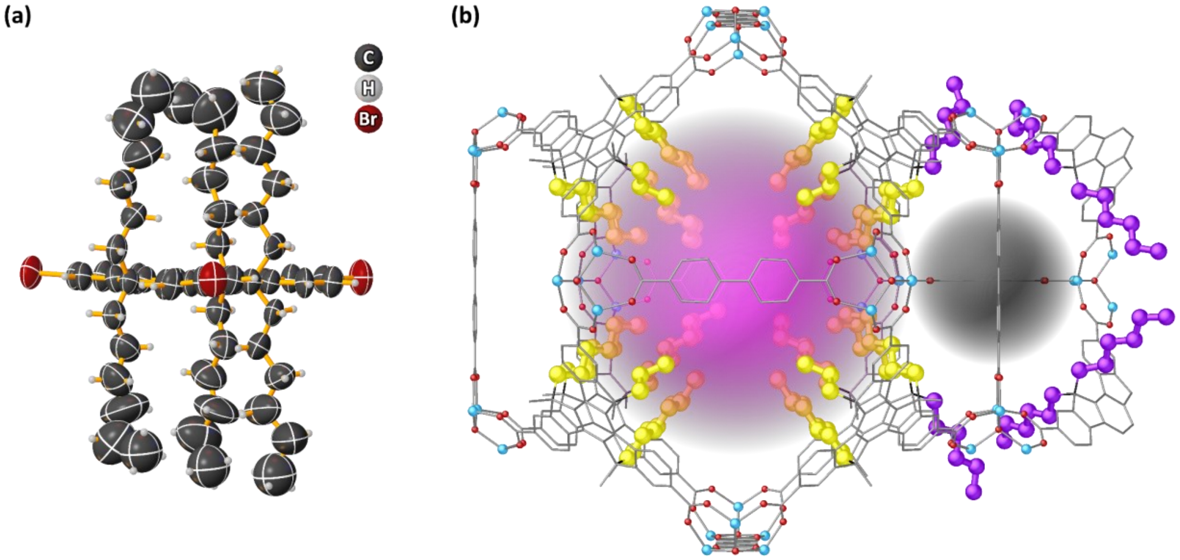

Figure 4-7. (a) The crystal structure of Br_3htt showing the orthogonally evolving hexyl chains from the planar of truxene; (b) the schematic diagram of the two different pores and arrangement of the hexyl chains stretching out from the truxene linkers surrounding the pores.

are allocated around the large dodecahedral pore as if they were wrapping the pore space using the planar truxene body. On the contrary, the small tetrahedral pores are surrounded by the edge of four truxene bodies. As a result, the long hexyl chains direct into the centre of the dodecahedral pores like a micelle, while the tetrahedral pore spaces remain free from the hexyl chains. The contrast of the two pores is well illustrated in Figure 4-7b. The hexyl chains coloured with yellow all point toward the centre of pore A, while the purple chains do not enter inside pore-C, providing a room for the functional groups and guest molecules to interact together.

Before we developed the pore-I model, we tried to understand and explain the experimental results using the alkyl chain conformations. As depicted in Figure 4-7b, pore A is congested by the hexyl chains from surrounding truxene linkers so that the reactants are pushed away by those chains to relatively roomy pore-C. Therefore, the desired interaction between the catalyst, modulator and guest molecules presumably more occurs when hhtt was employed.

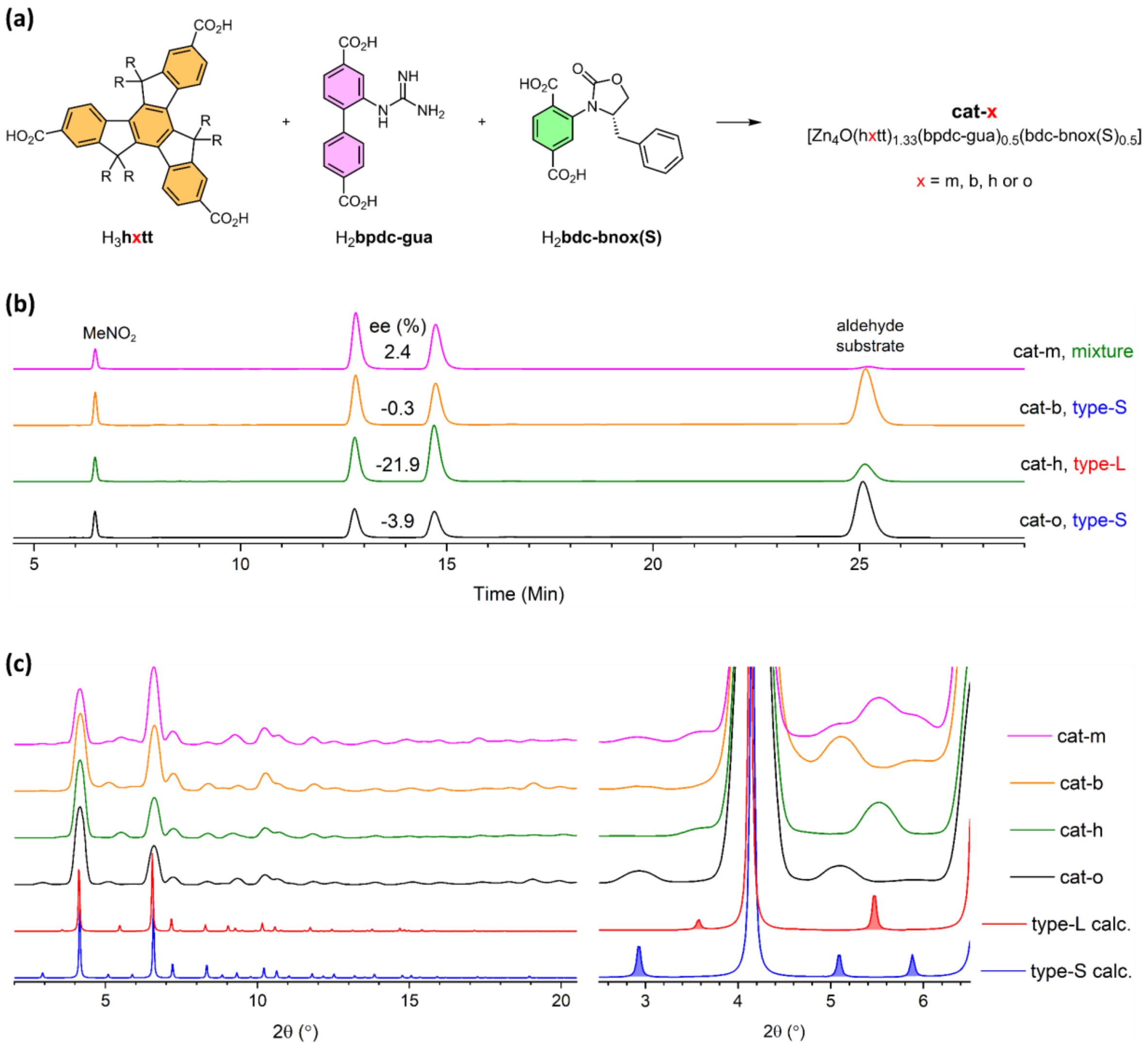

Figure 4-8. (a) Four different truxene derivatives with alkyl chains in different lengths; (b) HPLC chromatograms catalysed by the crystals; (c) PXRD patterns for the crystals synthesised from the truxene derivatives

However, this does not clearly explain the trend of ee with respect to the chain lengths (Figure 4-8b). We thought that the methyl and butyl chains are not long enough to influence the behaviour of the reaction components as the hexyl chains do. On the contrary, cat-o comprised of hott must show a similar or higher degree of enantioselectivity because it has a longer chain that can induce more influence. First, we thought that the octyl chain was too long so that it could inhibit the diffusion of the reactants and products through the pores. As a result, the proportion of the reaction catalysed on the surface of cat-o is high, resulting in a dilution of the entire enantioselectivity.

However, the reasoning about the experimental result above can be differently elucidated by the pore-I model. According to the PXRDs in Figure 4-8c, there is a noticeable structural difference between the four catalysts. The zoomed-in PXRD plot on the right-hand side clearly indicates that phase pure type-L framework was formed from hhtt, while the other three truxene derivatives produce the type-S framework (hbtt and hott) or a mixture of the two (hmtt). The reason why hhtt exclusively forms the type-L framework is unknown, but the relationship between the phase of crystal and corresponding ee is apparent. Moreover, the result is consistent with the outcomes produced by the experiments with the various modulators discussed in the previous section (4.2.1).

Although the two catalyst models agree with the experimental result to some extent, there is a conflict between the two models. In the pore-C model, the optimised length of the hexyl chain is the key to inducing higher enantioselectivity compared to the other alkyl chains. In comparison, the type-L framework itself is the critical feature in the case of the pore-I model. However, the pore-I model cannot clearly explain the disturbance caused by the hexyl chains to the catalysis. Based on the single-crystal structure, the long hexyl chains point to the pore centre, resulting in less room for the reaction components, thus hindering the desired reaction occurring in the pore-I.

Therefore, another experiment was designed to determine the better model between the two. If the two different phases, type-L and type-S, can be formed from hhtt, then we can easily find the answer to the question by comparing the resulting ees from the two frameworks. In other words, the type of framework is the critical factor for enhancing the enantioselectivity if the type-L framework produces a higher ee. On the other hand, the hexyl chains of hhtt play a critical role in inducing the enantioselectivity if the type-S framework results in high ee.

According to the previous experiment, the type-S framework tends to be formed at a lower temperature while the type-L framework forms at a higher temperature. Hence, three different catalysts, cat-t ($[ZnO_4(hhtt)_{1.33}(bpdc\text{-}gua)_{0.5}(bdc\text{-}bnox(S))_{0.5}]$) (t = 75, 85 or 95), were prepared from the identical synthesis batches at three different temperatures of 75, 85 and 95 °C (Figure 4-1a). As a result, both type-L and type-S frameworks were obtained as planned; the type-S framework was formed from the batch prepared at 75 °C while the type-L framework was obtained from 85 and 95 °C (cat-75: type-S, cat-85 and -95: type-L). Then, the Henry reaction of 2-chloro-5-nitrobenzaldehyde and nitromethane was catalysed by each of the prepared catalysts under the same condition with approximately the same amount of catalyst loading. The reaction mixtures after catalysis were analysed with HPLC, and the resulting chromatograms exhibited two clear outcomes. The enantioselectivities induced by those catalysts were increased as the synthesis temperature increased; -7.7, -16.8 and -20.4 % of ees were obtained from cat-75, cat-85 and cat-95, respectively. In addition, the reaction rates caused by the three catalysts were apparently different. Based on the

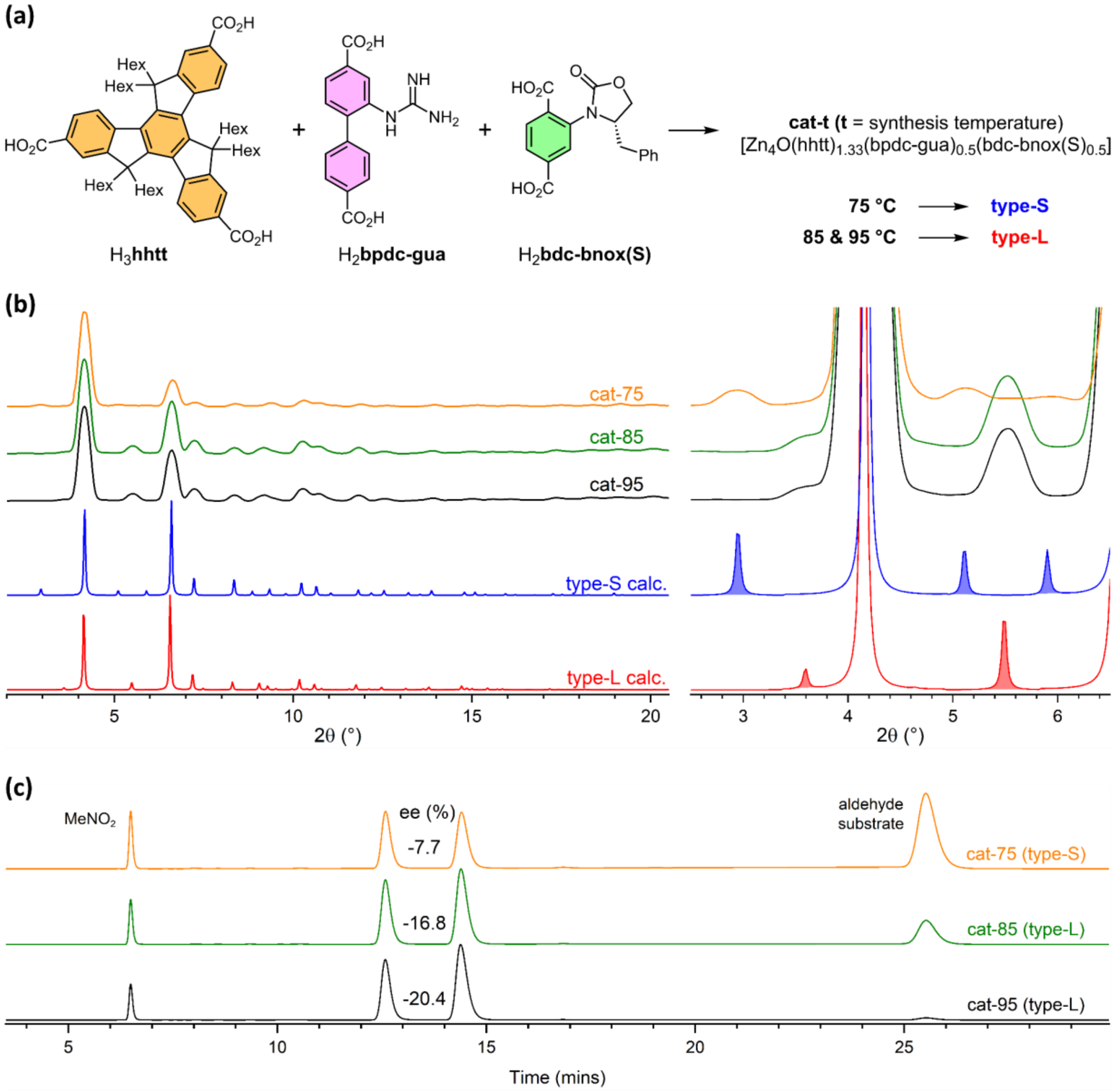

Figure 4-9. (a) A schematic diagram of catalyst syntheses at different temperatures; (b) the PXRD patterns of the three catalysts synthesised at 75, 85 and 95 °C; (c) the HPLC chromatograms of the Henry reaction products catalysed by those three catalysts, the corresponding ee for each reaction was presented.

consumption of the aldehyde substrate (the peak at 25 - 26 min), the catalyst performance was also increased as their synthesis temperature increases. Therefore, it seems that the pore-I model is highly likely the right catalysis model for the RAI catalyst.

The experimental result above also suggests a hint on how to improve the performance of the catalyst. Both cat-85 and cat-95 are type-L according to the PXRD patterns. However, cat-95 shows better performance with respect to both enantioselectivity and reaction rate. PXRD is a simple yet powerful characterisation method to determine the crystal structure of the bulk sample, but it has a limitation in this case. The problem with PXRD is that some weak diffractions produced by a minor phase of crystals are overlooked as the peak intensity of the PXRD pattern is an average value diffracted from all individual crystals.

Therefore the difference in catalysis performance between cat-85 and cat-95 can be elucidated as follows. Although it is not clear whether the type-S phase exists as separate crystals in small numbers or grows together in a single crystal with the type-L framework as a small portion, the catalyst prepared at 85 °C likely contains more of the type-S character than the one prepared at 95 °C. Hence, the key to improving the RAI catalyst performance is to synthesise the phase pure type-L catalyst.

4.3. Further tweaks to enhance enantioselectivity

The RAI catalyst has demonstrated its novel way of asymmetric induction, and the best ee obtained was approximately ±25 %. However, the ee was not consistent each time the experiment was repeated and varied between around 15 % and 25 %, even though every single step of the experimental procedures was carried out in the same way with the same catalyst. However, an interesting trend was noted, which could give a clue about the reason behind the non-consistent ee.

The catalytic activity of the RAI catalyst was usually well maintained after a few cycles of reuse, so it was generally recycled a few times. Interestingly, it was noted that the ee was gradually increased bit by bit each time the crystal is recycled in most of the cases. It is considered that residual solvent molecules, DEF from synthesis or DMF from washing, remain in the pore and function as a racemic catalyst, and they gradually washed out upon each recycle. According to the previous experiment, it was observed these amide solvents, DMF or DEF, quite actively catalyse the Henry reaction. Alternatively, it could be due to the trace amounts of uncoordinated bpdc-gua ligands remainng in the pore.

Another exciting observation was also noted when pH in the reaction medium was adjusted by adding some organic acids or bases, such as formic acid, acetic acid, or triethylamine. It was observed when a small amount of acid (1 % v/v) was added to the reaction mixture the corresponding ee was increased by approximately 5 %. Moreover, no background catalytic activity was observed with these acids. On the contrary, the organic base behaved as a very efficient catalyst for the Henry reaction, and even the trace amount diluted the enantioselectivity.

Based on the two observations above, a few different activation methods were examined, such as using various washing solvents in different ways or applying acid treatment for the catalyst activation process. According to a few washing tests for the catalyst activation, acetone was chosen as the most efficient washing solvent. Thus, two different acid treatment methods were tested combining with acetone wash.

First, three different catalyst samples were prepared by dividing the approximately equal amount of crystals into each vial from one synthesis batch of [$Zn_4O(hhtt)_{1.33}(bpdc\text{-}gua)_{0.5}(bdc\text{-}bnox(S))_{0.5}$]. Then each sample was treated as described below.

#	Washing	Reaction mixture
Sample 1	regular washing*	normal
Sample 2	soaked in the mixture of acetic acid and acetone (5 % v/v) for three hours before regular washing	normal
Sample 3	regular washing	acetic acid was added (1 % v/v)

*** Crystals were successively washed with acetone (×3) and dioxane (×3), and solvents were removed using a glass capillary tube.**

Sample 1 was prepared for a control experiment, and two different acid treatments were tested with Sample 2 and 3. Sample 2 was treated with an acidic solution before catalysis, whereas an acid was added to the reaction mixture for Sample 3. Then, the washing processes were simultaneously conducted on all three samples after acid treatment for Sample 2. The reactions were then carried out at the same time under the same condition. The reaction mixtures were analysed with HPLC after two days, and the resulting chromatograms (the green chromatogram, the top one for each sample) were presented in Figure 4-10.

The results clearly showed that the acid-treated catalysts resulted in better enantioselectivity compared to the control (Sample 1). Furthermore, no catalytic activity was observed from acetic acid according to the control experiment (the chromatogram with a black line in Figure 4-10). However, the reaction rate of Sample 2 was a lot slower than the other two, and the areas underneath the product peaks were almost negligible. Therefore, the ee produced by Sample 2 was not very reliable. Sample 2 was originally intended to be soaked in the acid solution overnight, but it was removed from the acidic solution after three hours

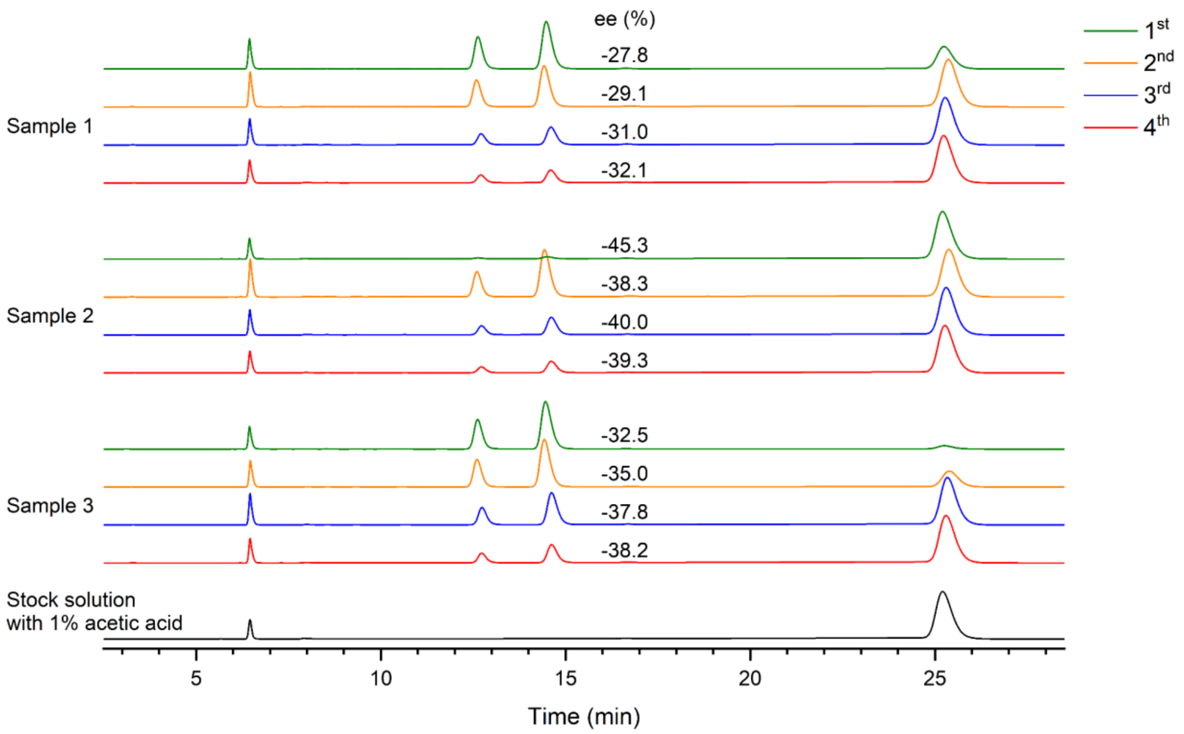

Figure 4-10. HPLC chromatograms for the reactions catalysed by three different catalysts which treated in different ways and recycled three times. No catalytic activity of acetic acid was observed (bottom black chromatogram).

since the crystal starts losing transparency. The slow reactivity of Sample 2 was probably caused by some defect generated by the too harsh acidic condition.

However, interestingly, the reactivity of Sample 2 was revived when it was reused for the next run. All three catalysts were recycled to examine whether the discrepancy among the enantioselectivities of all three samples presented in the first run is maintained if the catalysts were recycled. For the recycling experiment, the crystals were briefly rinsed with acetone (×3) and dioxane (×3), and the usual reaction stock was used for all three catalysts. The result shows (Figure 4-10) that the enantioselectivity of Sample 2 slightly dropped compared to the first run, but it still shows the best enantioselectivity. Also, the difference in ee between Sample 1 and 3 presented in the first run was maintained almost the same for the second run, indicating that the change applied to Sample 3 caused by acid treatment during the first run was not diluted by washing. The catalysts were recycled two more times, and the recycling experiment was stopped because it was noted that they were losing catalytic activity (the product peaks get smaller in all cases).

The produced ees by all three samples over the four successive runs with the recycling experiments were plotted in Figure 4-11. The ee from the first measurement with Sample 2 was omitted since the calculated ee was not reliable due to the low amount of the products. The ees produced by Sample 1 and 3 increased gradually over the recycling experiments. Based on the trend of ees produced by Sample 2 and 3, which were treated with acetic acid,

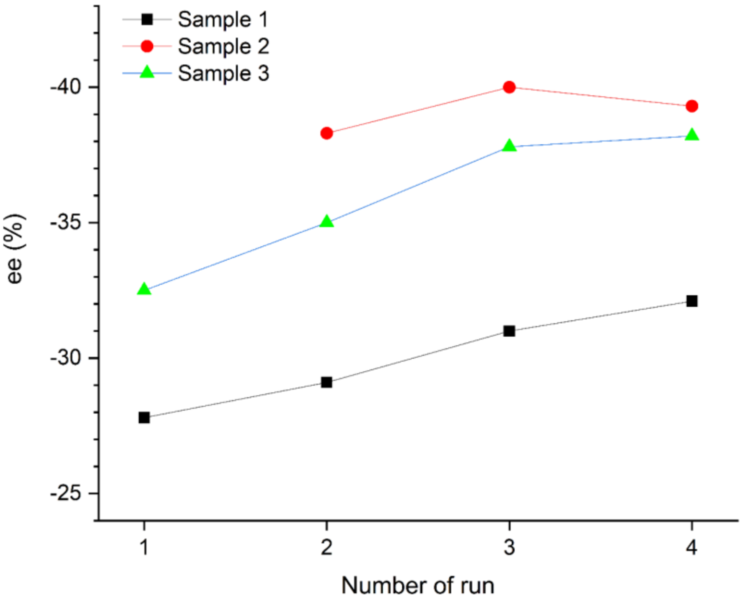

Figure 4-11. The ees produced by Sample 1-3 over the recycling experiments were plotted. The ee for the first run of Sample 2 was omitted due to its unreliable data caused by too slow catalysis.

the maximum ee to which the acid-treated catalyst can reach is regarded as approximately -40 %. The ees generated from the recycled Sample 2 did not change much, ranging between -38 and -40 %. Moreover, the ee produced by Sample 3 is drawing a plateau converging at about -40 %.

According to the experiment above, the effect introduced by acid treatment and recycling the catalysts boosted the enantioselectivity up to 40 %. The gradual increasing ee seems to be caused by some washable racemic catalysts, such as DMF, DEF or uncoordinated bpdc-gua. Figure 4-11 clearly demonstrates that the more crystal was recycled, the more such racemic catalysts washed away. Hence, a few different washing protocols were tried to obtain a high ee in the first run, but none of them has shown a promising result.

4.4. **Conclusion**

Through chapter 3 and 4, the novel concept of the asymmetric catalyst was introduced. Such a novel concept was achievable because of the two multi-component platform, the type-L and type-S frameworks. The type-S framework demonstrated its incredible potential as the designable catalyst accommodating multiple functional groups in our previous works. In this work, we discovered that the type-L framework could also provide a stable and sustainable environment to be utilised in many ways. This brought the unused and forgotten framework (type-L frameworks) a new life as an emerging catalyst platform. The Type-L framework not only provides a larger space (pore-I) for catalytic reactions but also allows more than one functional group of the same kind to cooperate in this space.

The RAI catalyst presented in this chapter demonstrated catalytic activity and the enantioselectivity for the Henry reaction of nitrobenzaldehyde derivatives and nitromethane. However, it still requires much work to be improved. Obtaining the pure phase framework from a particular linker combination and washing out undesired impurities that work as a racemic catalyst from the catalysis pore are the most urgent targets to solve. Despite all, the RAI catalyst suggested a novel way to transfer the desired chirality during the catalysis. Also, it has much potential to be enhanced and eventually acknowledged as a new branch of the asymmetric catalyst in the near future.

4.5. Experimental section

4.5.1. X-ray crystallography

All cif files are available through the link provided below.

https://drive.google.com/drive/folders/1mEMRFRL3ME5N6OtzIjeEWkluLPOIArSg?usp=sharing

4.5.1.1. SCXRD of cat-1s

Due to the moisture-sensitive guanidine unit, the crystal samples of cat-1s ([$Zn_4O(hhtt)_{1.33}(bpdc\text{-}gua)_{0.5}(bdc\text{-}bnox(S))_{0.5}$]) were quickly decomposed during data collection. Hence, a crystal sample was captured in a sealed glass capillary tube with the reaction mixture, as depicted in Figure 4-12 (various solvents were tested later for better data). A decent quality of SCXRD data was collected, which is enough to see all the ligand backbones in the type-L framework. However, all the guanidine and oxazolidinone moieties could not be solved due to their disorders.

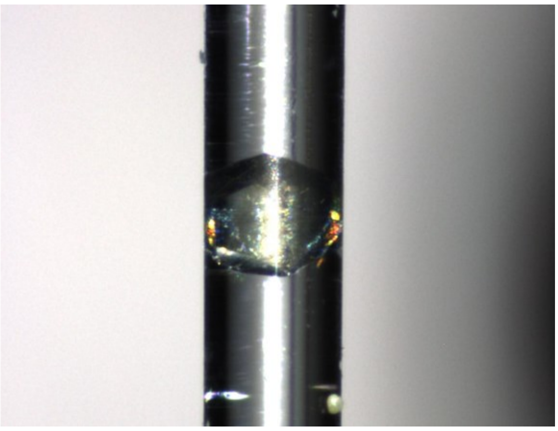

Figure 4-12. A crystal sample in a sealed capillary tube with the reaction medium.

4.5.1.2. [$Zn_4O(hhtt)_{1.33}(bpdc)_{0.5}(bdc)_{0.5}$] at different temperature

A single crystal sample of [$Zn_4O(hhtt)_{1.33}(bpdc)_{0.5}(bdc)_{0.5}$] was mounted on a nylon loop with Fomblin® Oil. Three different sets of SCXRD data was successively measured with the same crystal sample at 173, 273 and 333 K. The resulting structures were depicted in Figure 3 22. Although the shapes of the ellipsoids (C11, C12 and C13) became much larger at 333 K, the chains still orthogonally diverging out from the plane of the truxene body.

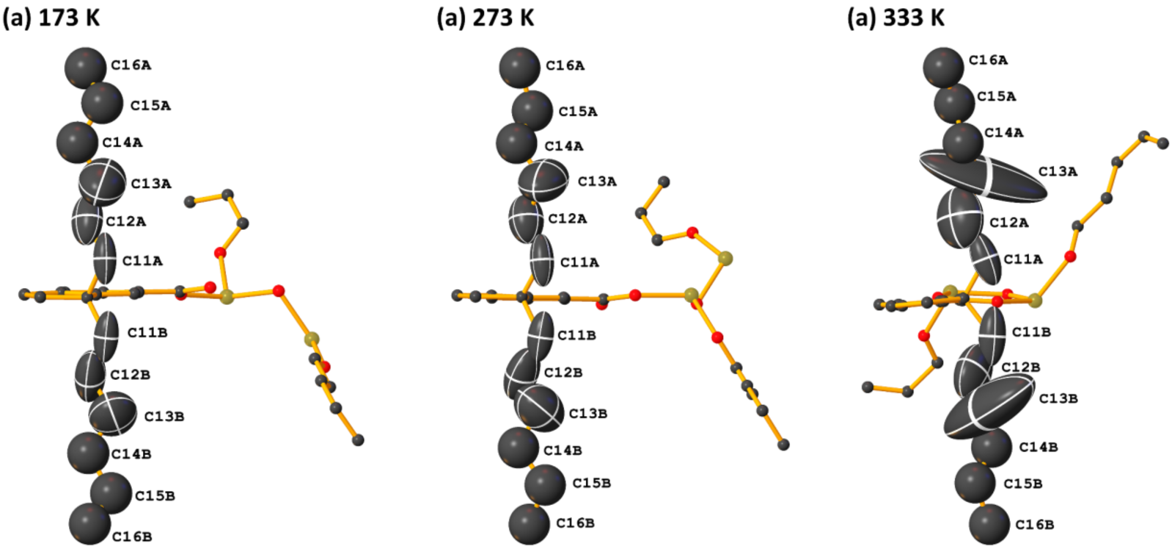
(a) 173 K (a) 273 K (a) 333 K

Figure 4-13. The asymmetric unit cell of [$Zn_4O(hhtt)_{1.33}(bpdc)_{0.5}(bdc)_{0.5}$] at three different temperatures (173, 273 and 333 K).

Table 4-1. Summary of X-ray crystallography data collection and refinement details of the selected single-crystal structures.

Identification code	Br_3hht	cat-1s	hhtt_173K	hhtt_273K	hhtt_333K
Empirical formula	$C_{63}H_{87}Br_3$	$C_{99}H_{121}O_{13}Zn_4$	$C_{99}H_{122}O_{13}Zn_4$	$C_{99}H_{122}O_{13}Zn_4$	$C_{99}H_{122}O_{13}Zn_4$
Formula weight	1084.05	1780.43	1781.44	1781.44	1781.44
Temperature/K	286	293	173	273	333
Crystal system	monoclinic	cubic	cubic	cubic	cubic
Space group	$P2_1/c$	I-43d	Pm-3	Pm-3	Pm-3
a (Å)	12.8931(13)	59.604(2)	29.8592(3)	29.8639(3)	29.8469(3)
b (Å)	18.2277(17)	59.604(2)	29.8592(3)	29.8639(3)	29.8469(3)
c (Å)	25.559(2)	59.604(2)	29.8592(3)	29.8639(3)	29.8469(3)
α (°)	90	90	90	90	90
β (°)	91.691(4)	90	90	90	90
γ (°)	90	90	90	90	90
Volume ($Å^3$)	6004.1(10)	211748(23)	26621.6(8)	26634.2(8)	26588.7(8)
Z	4	48	6	6	6
$\rho_{calc}g$ (cm^3)	1.199	0.67	0.667	0.666	0.668
μ (mm^{-1})	2.74	0.863	0.859	0.858	0.86
F(000)	2280	45072	5640	5640	5640
Crystal size (mm^3)	0.5 × 0.5 × 0.3	0.5 × 0.4 × 0.4	0.4 × 0.3 × 0.3	0.4 × 0.3 × 0.3	0.4 × 0.3 × 0.3
Radiation	CuKα (λ = 1.54178)	CuKα (λ = 1.54178)	CuKα (λ = 1.54178)	CuKα (λ = 1.54178)	CuKα (λ = 1.54178)
2Θ range for data collection (°)	5.956 to 108.476	3.63 to 129.394	4.184 to 152.58	4.184 to 152.506	4.186 to 152.774
Resolution range for refinement	0.95	0.85	0.79	0.79	0.79
Index ranges	$-13 \le h \le 13$ $-19 \le k \le 19$ $-26 \le l \le 26$	$-69 \le h \le 63$ $-53 \le k \le 36$ $-69 \le l \le 45$	$-33 \le h \le 30$ $-37 \le k \le 24$ $-35 \le l \le 28$	$-33 \le h \le 31$ $-24 \le k \le 37$ $-28 \le l \le 35$	$-24 \le h \le 37$ $-27 \le k \le 35$ $-33 \le l \le 31$
Reflections collected	68786	319038	66890	67509	67887
Tmin/Tmax	0.7521/0.6082	0.7525/0.3668	0.7540/0.6273	0.7540/0.6335	0.7540/0.6233
Independent reflections	7335 R_{int} = 0.0656 R_{sigma} = 0.0451	29554 R_{int} = 0.0837 R_{sigma} = 0.0432	9797 R_{int} = 0.0500 R_{sigma} = 0.0295	9810 R_{int} = 0.0464 R_{sigma} = 0.0305	9804 R_{int} = 0.0482 R_{sigma} = 0.0308
Data/restraints/parameters	7335/421/919	29554/642/778	9797/12/235	9810/12/235	9804/12/231
Goodness-of-fit on F^2	1.346	1.023	1.43	1.406	1.444
Data completeness	1	0.99	1	1	1
Final R indexes [I>=2σ (I)]	R_1 = 0.0935 wR_2 = 0.2974	R_1 = 0.0451 wR_2 = 0.1217	R_1 = 0.0966 wR_2 = 0.3066	R_1 = 0.1004 wR_2 = 0.3036	R_1 = 0.1061 wR_2 = 0.3150
Final R indexes [all data]	R_1 = 0.1082 wR_2 = 0.3183	R_1 = 0.0540 wR_2 = 0.1260	R_1 = 0.0977 wR_2 = 0.3086	R_1 = 0.1021 wR_2 = 0.3066	R_1 = 0.1086 wR_2 = 0.3193
Largest diff. peak/hole (e $Å^{-3}$)	0.34/-0.61	0.31/-0.28	1.63/-1.81	1.76/-1.86	1.54/-1.81

Chapter 5 **Postsynthetic inter-ligand coupling reaction**

5.1. **Introduction**

As introduced in Chapter 1 (section 1.1.5), postsynthetic modification (PSM) is an approach to introduce a specific chemical or physical properties when it is not available through direct synthesis.[145] PSM is a versatile and matured tool in MOF chemistry and is widely used when the desired properties cannot be incorporated into the framework directly. Adding a specific functionality using PSM is usually achieved by making a covalent bond between a guest component and a MOF strut. In this chapter, new functionality will be introduced by PSM reaction in an MC-MOF without adding any guest component.

In the type-S framework, the two linear linkers, bpdc and bdc derivatives, are precisely located in the framework. They alternate along the three crystallographic axes: -bdc-bpdc-bdc-bpdc- (Figure 5.1a). Our aim is to use a PSM reaction to make a covalent bond between

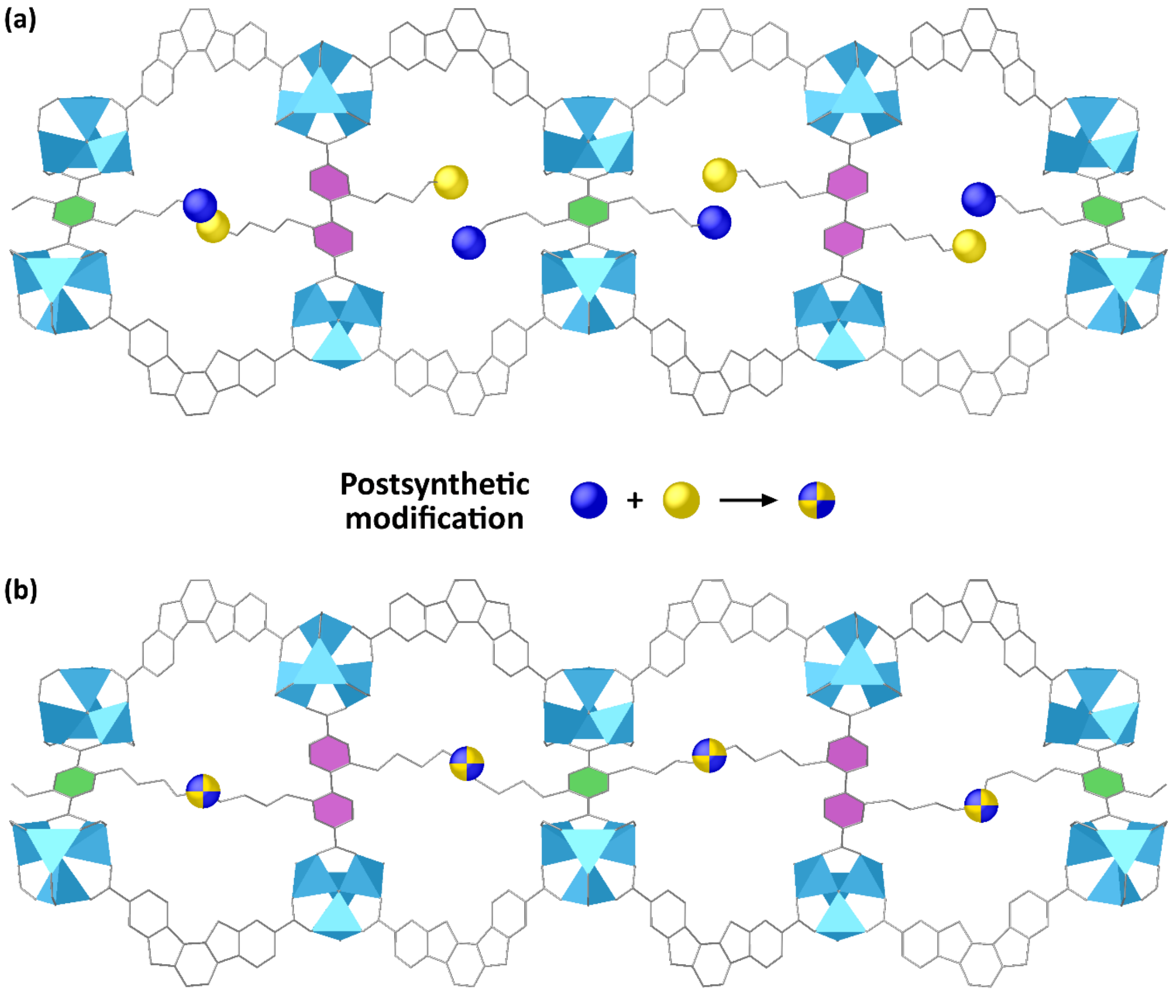

Figure 5-1. A schematic diagram of alternating bpdc and bdc which were equipped with functional groups shown as blue and yellow balls in the type-S framework (top); and the new functional group formed using the post-synthetic modification reaction (bottom).

each bdc and bpdc linker once they are assembled into the framework (Figure 5.1b). For this to be feasible, the two linkers must be equipped with chemical functional groups that can react with one another. In this way, we can precisely introduce a new functionality at a specific site in MOF using PSM reaction, even without using a guest component. This highlights the utility of MC-MOF and the importance of the MOF scaffold.

In addition, another utility of the MOF scaffold will be demonstrated. If each linear linker is equipped with two functional groups of the same kind, which diverge from the linker backbone (as in Figure 5-1a), the alternating bpdc and bdc ligands will become linked into a linear polymer (Figure 5-1b). The polymer chain theoretically can grow the size of MOF in this way. On the contrary, synthesising a linear long polymer chain would be difficult if the same polymerisation reaction occurs with free monomers in a solution. The polymer chain has a higher chance to end up as a macrocycle molecule as the chain grows due to the two mutually reactive functional groups on each end.

5.1.1. **Azide-alkyne click reaction**

The two functional groups installed on the linear linkers must meet a few conditions. First, they should not interfere with the desired MOF synthesis. Second, their coupling reaction must be triggered by an external stimulus. If it occurs spontaneously, the two linear ligands could be crosslinked resulting in the formation of an unwanted polymer chain before the MOF formation. Third, the external stimulus to trigger the crosslinking PSM reaction should not harm the framework. For instance, if the PSM reaction requires strongly acidic or basic conditions, the framework will decompose.

Azide and alkyne functional group pair is one of the promising candidates. These two functional groups can be coupled, forming a triazole ring with a Cu(I) catalyst under mild conditions, known as Huisgen [3+2] cycloaddition or simply as a 'click' reaction.[146] The azide-alkyne cycloaddition reaction (hereafter referred to as click reaction) is a versatile tool widely utilised and is proven safe and facile for the PSM reaction of MOF chemistry by many other researchers.[147-152]

Alternatively, the azide-alkyne coupling reaction can be triggered by heating. Hema et al. reported a crystalline material that is composed of a sugar molecule equipped with both azide and alkyne. The two functional groups are close vicinity in a crystal lattice, and the cycloaddition reaction was carried out when heating (90 °C) was applied to the crystal[153]. Even a spontaneous azide-alkyne click reaction at room temperature was also reported with similar crystalline material.[154] However, in this specific case, the two functional groups are not just close to each other (3.2–3.7 Å) but also arranged with a right reactive orientation in the crystal lattice. Such heat-driven azide-alkyne click reaction is also well demonstrated in MOF chemistry, which will be introduced in detail in the next section.[155] Therefore, heating can be another option for triggering the azide-alkyne cyclisation reaction between the two bpdc and bdc derivatives of the type-S framework.

5.1.2. Inter-ligand coupling reactions

PSM reactions that covalently link the ligands in a framework has been reported by others.[150,155-157] In these studies, the PSM crosslinking reactions were carried out in MOFs built from just a single type of organic linker (the same ligand backbone with different chemical pendant). The coupling reaction will occur between two adjacent linkers and result in unpredictable outcomes. For instance, Richardson and coworkers reported a PSM reaction in an IRMOF-9 type framework (Figure 5-2).[155] IRMOF-9 is an interpenetrated structure of two identical frameworks of a cubic lattice composed of bpdc and Zn_4O cluster ($[Zn_4O(bpdc)_3]$). Due to the interpenetrated frameworks, the distance between the two bpdc linkers of each framework is close (~4 Å) enough to interact if they were equipped with proper functional groups. They introduced a pair of bpdc derived linkers (A and B in Figure 5-2) into IRMOF-9, and the PSM reaction was triggered by heating to link two adjacent A and B. However, both A and B were randomly distributed in the framework because they have the same backbone. As a result, the target azide-alkyne cyclisation reaction is observable only if A and B neighbour each other through the interpenetrated frameworks.

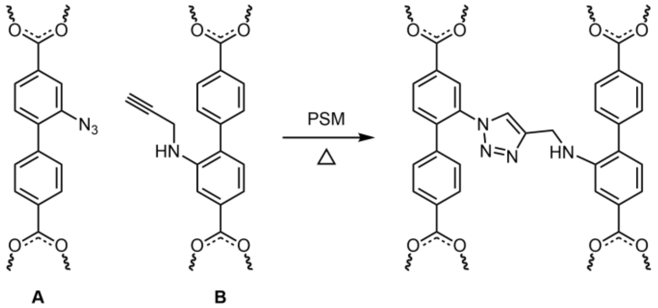

Figure 5-2. The heat-driven inter-linker PSM conducted in IRMOF-9 derived framework.

They also reported that the click reaction between A and B spontaneously occurred during MOF synthesis. Although the proportion of the linked A and B during MOF synthesis was low, it made us concerned since both azide and alkyne groups are presented in our MOF synthesis as well. However, it seems that such *in situ* click reaction occurred after A and B were integrated into the framework. It was because the same type of reaction was not observed if the two functional groups are apart from each other in the crystal lattice.[152] The distance between the two linkers used in our study (15 Å) is much farther than that of A and B in

IRMOF-9. Moreover, the chance that the two functional groups align in the reactive orientation would be very low since the two functional groups were attached to the linker backbones with long and flexible alkyl chains. Therefore, such in situ click reaction during MOF synthesis would not occur in our system.

Another example of the crosslinking reaction in a MOF was reported by Sada's research group in 2013.[156] In this work, three different MOFs were prepared using the organic linkers bi-functionalised with two azide groups (Figure 5-3). The guest molecule equipped with multiple diverging alkynes was then introduced to the frameworks, and the PSM reaction was carried out with a Cu(I) catalyst to form a polymerised network. The resulting polymer was sustained as a form of a gel even after etching the metal components. However, the linkers in the resulting network would be inhomogeneously linked since there is no way to regulate the reaction between the linker and guest. For instance, some azide groups can be clicked with a separate individual guest molecule and remained unlinked.

Unlike the two examples above, a controlled inter-ligand click reaction between azide and alkyne will be demonstrated in this chapter. The critical difference from the two examples above is utilising a multi-component MOF. Each functional group will be attached to a different linker, and each linker will be precisely located using a MOF scaffold. Therefore, the inter-ligand click reaction will occur at an exact site with a designed direction in a crystal lattice.

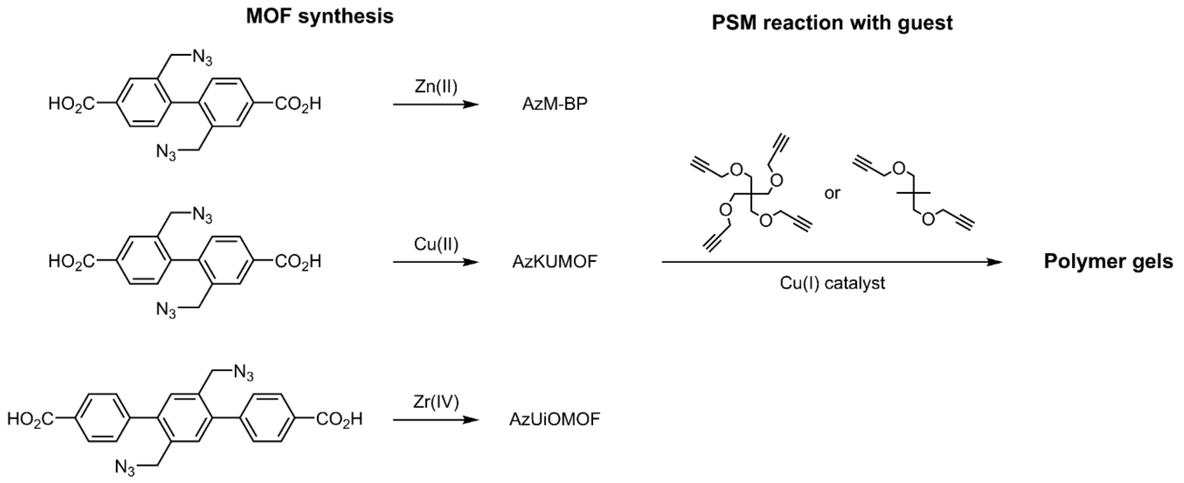

Figure 5-3. The schematic diagram of inter-ligand polymerisation with guest molecules

5.2. Result and discussion

5.2.1. Ligand design

To achieve the PSM reaction between azide and alkyne functional groups in the type-S framework, the two functional groups must be in close proximity. According to the crystal structure, bpdc and bdc orthogonally facing each other across pore-C (those depicted in Figure 5-1), and their distance is approximately 15 Å (from the centroid to centroid). It seemed that approximately 9-10 atom long-chain likely fit the space between the bpdc and bdc backbones according to the 3D model. Therefore, the bpdc derived linker decorated with two azide groups (L1[158]), and its complementary pair bdc derived linker (L2) were designed (Figure 5-4a). L2 was prepared with a simple coupling reaction between 2,5-dihydroxy terephthalic acid and 1-chlorohex-5-yne. However, it turned out that the chain length was slightly shorter than required, resulting in stress in the framework followed by a low degree of polymer chains. Therefore, another bdc derivative, L3 equipped with a slightly longer alkyne chain (octyne), replaced L2 later.

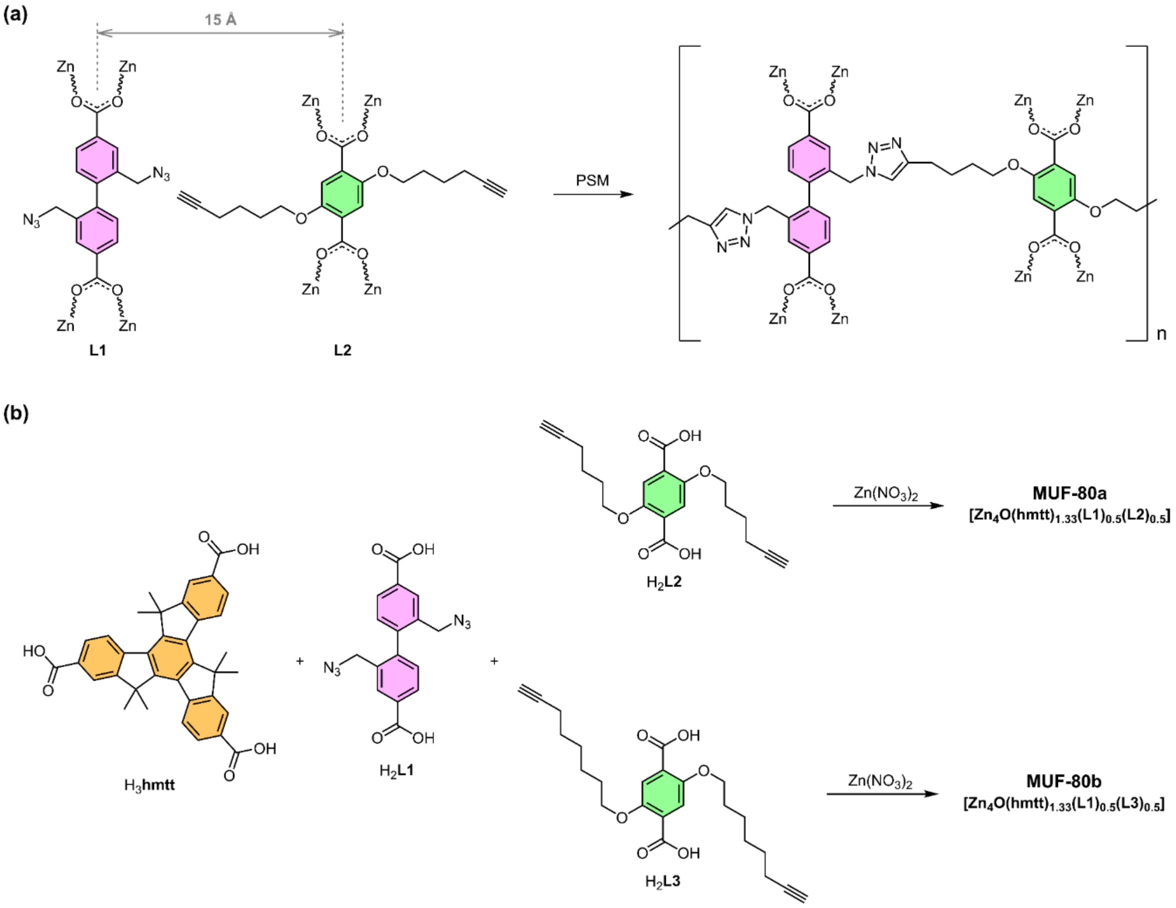

Figure 5-4. (a) The conceptual diagram of before and after the inter-ligand azide-alkyne click reaction between the two linear ligands L1 and L2 in the type-S framework; (b) Two different sister frameworks , MUF-80a and MUF-80b, were synthesised from hmtt, L1, zinc nitrate and respectively L2 or L3.

In this chapter, the two sister type-S frameworks, MUF-80a and MUF-80b, respectively comprised L2 or L3 (Figure 5-4b), will be used to demonstrate inter-ligand crosslinking PSM reaction. The majority of experiments were carried out using MUF-80a at first, but they were repeated later using MUF-80b to obtain a higher degree of polymer chain by reducing the stress applied to the framework after PSM reaction.

5.2.2. Post-synthetic modification reaction with MUF-80a

Click reaction in MOFs is generally monitored using two facile and straightforward characterisation methods, IR and ^{1}H NMR spectroscopies. The intense and sharp peak at 2100 cm^{-1} in the IR spectrum is the characteristic azide peak, so that reduction in azide peak can evidence the completion of the click reaction. In addition, the terminal alkyne peak (C≡C) also appears at around 2100 cm^{-1} with a lot weaker intensity. Thus, the peak around 2100 cm^{-1} is a good indicator showing the progress of azide-alkyne click reaction regardless of its origin. ^{1}H NMR of a digested framework is also a suitable characterisation method, and it enables us to determine qualitatively and quantitatively the progress of PSM reaction. The reduction of the terminal alkyne proton peak at around 2.7-2.8 ppm and the new peak for the azide proton around 7.7-8.0 ppm are usually used as good indicators in this work.

However, some side reactions, such as azide decomposition due to high temperature, can also lead to a peak intensity reduction in the IR spectrum. Furthermore, using ^{1}H NMR spectroscopy to detect the aforementioned peaks (the triazole and alkyne protons) would not be available either in this work because the peaks belonging to L1 and L2 would be broadened after polymerisation due to the different degrees of the polymer chain. Such broadened peaks are generally regarded as a good sign of polymerisation. However, partially and unevenly decomposed ligands due to the harsh reaction condition can also cause such broadened peaks in ^{1}H NMR spectroscopy. Hence, using these two techniques must be proved as a valid characterisation method in this particular work.

For this reason, a control experiment was prepared to prove the validity of the two characterisation methods. Two different type-S frameworks were prepared using either L1 or L2, and then the PSM click reaction was carried out with a guest molecule. In this way, any change in L1 or L2 after PSM reaction with the guest will be identified by ^{1}H NMR. The reliability of the IR spectrum is then established if both analyses were conducted in pairs for the same samples.

Hence, the two frameworks, MUF-80a-1 ([$Zn_4O(hmtt)_{1.33}(L1)_{0.5}(bdc)_{0.5}$]) and MUF-80a-2 ([$Zn_4O(hmtt)_{1.33}(bpdc)_{0.5}(L2)_{0.5}$]) were synthesised using either L1 or L2, respectively

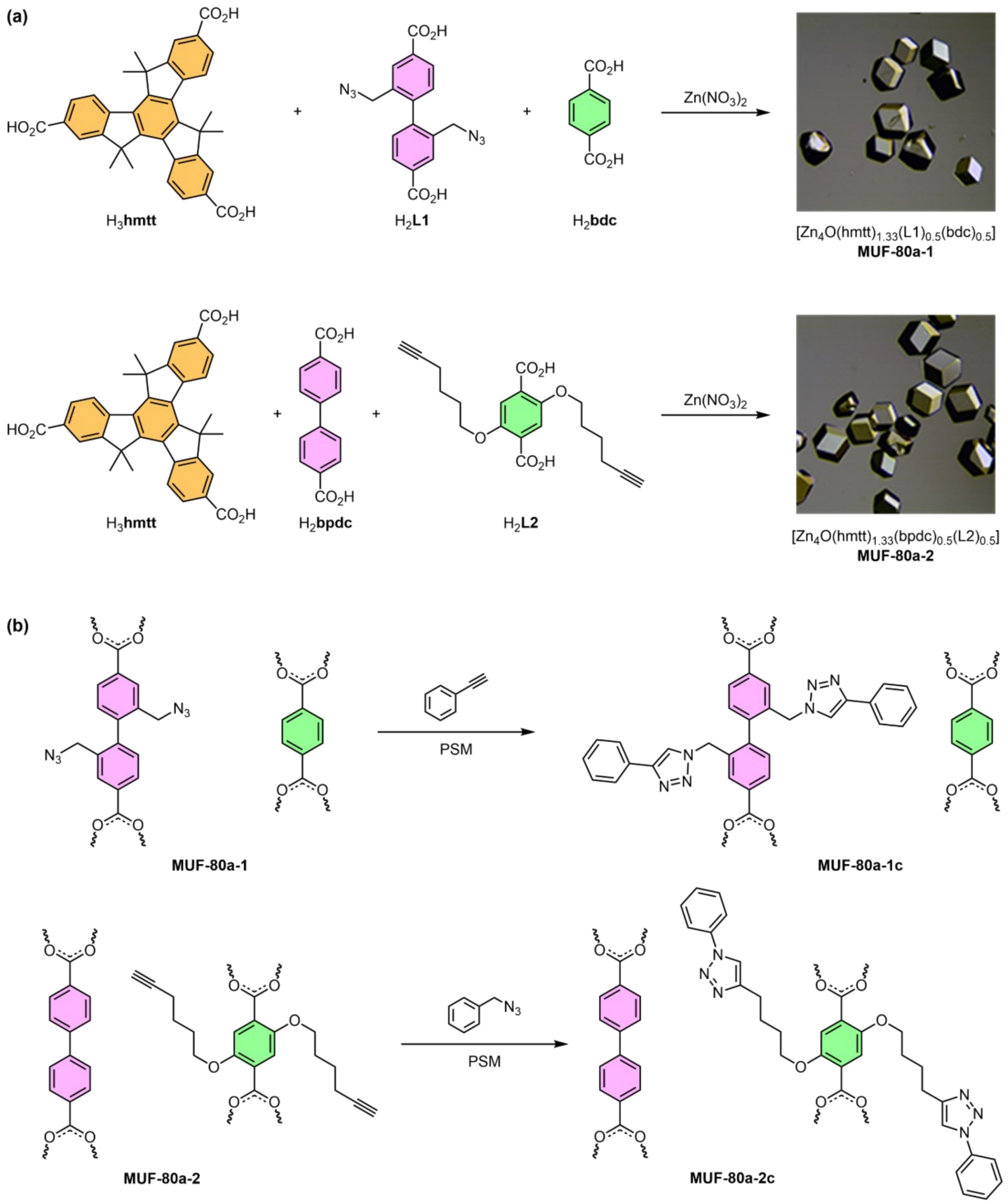

Figure 5-5. (a) A schematic diagram of MUF-80a-1 and -2 syntheses; (b) the PSM click reactions between the linkers in the frameworks and guest molecules.

(Figure 5-5a). The resulting crystals were confirmed as the desired frameworks (type-S) based on PXRDs and ^{1}H NMR and IR spectroscopies. Then post-synthetic click reaction was carried out with MUF-80a-1 and phenylacetylene or MUF-80a-2 and benzyl azide (Figure 5-5b) to produce MUF-80a-1c[b] and MUF-80a-2c, respectively. The click reaction was conducted with microwave heating at 100 °C for 1.5 hours. Approximately 5 mg of crystal sample was solvated in acetonitrile with an excess amount of guest molecule and catalyst.

---

[b] The framework after PSM reaction was denoted with the postfix c, indicating clicked or connected.

CuI·P(OEt)$_3$ was selected as a catalyst due to its good solubility in organic solvents. After completion of the reaction, MUF-80a-1c and MUF-80a-2c were then analysed using the same analysis methods used for the pristine samples, and the results were compared to each other.

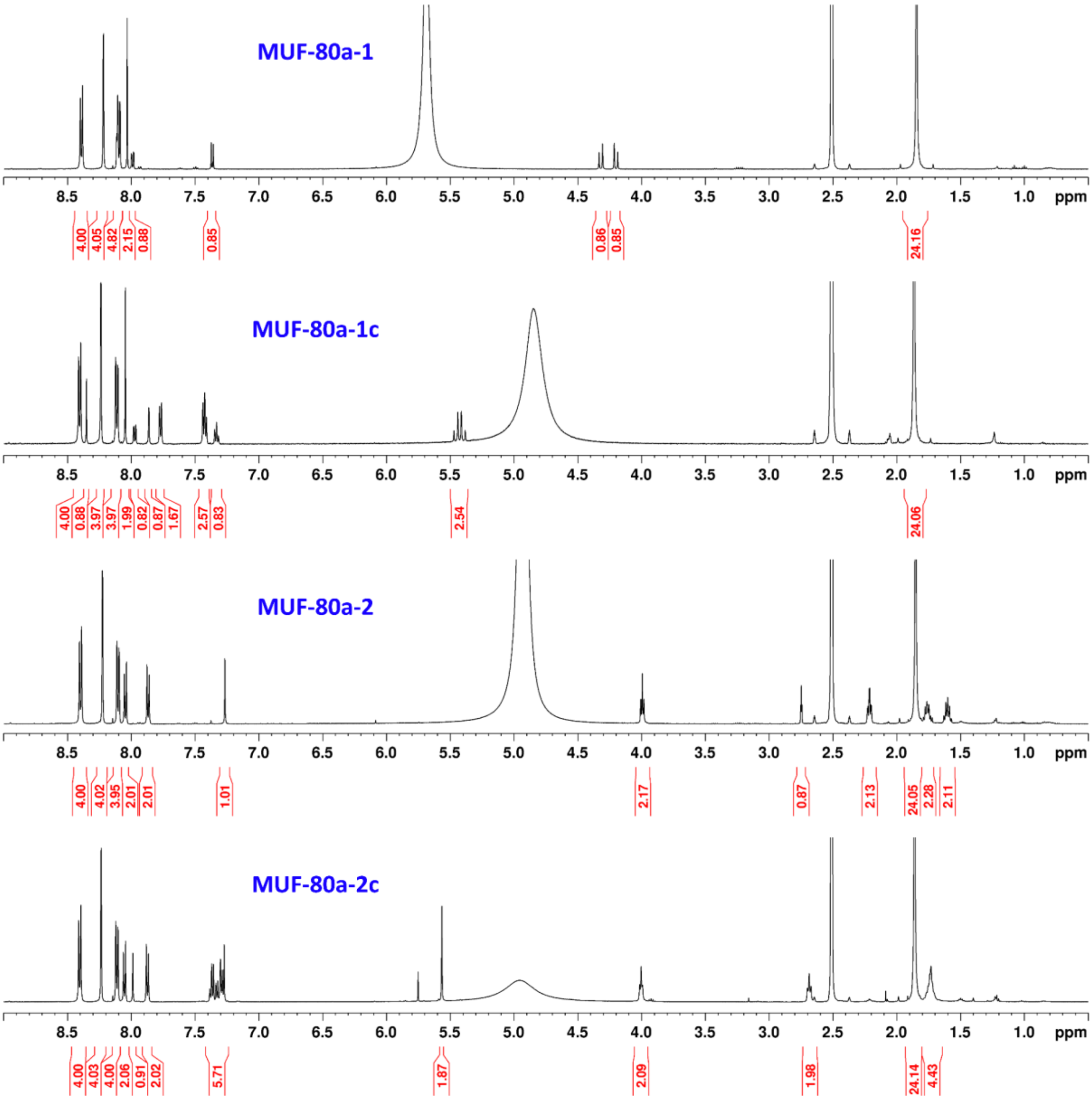

Figure 5-6. ^{1}H NMR of the frameworks before and after the click reaction with the guest molecules for the control experiment.

^{1}H NMR spectra (Figure 5-6, refer to Appendix C for detailed NMR spectroscopies) clearly showed the added functional groups. The distinct change between MUF-80a-1 and MUF-80a-1c is the chemical shift of the methylene (CH$_2$). Due to the triazole formation resulting from the click reaction, the peaks for the bridging methylene between the bpdc backbone and azide were shifted from 4.3 ppm to 5.4 ppm.[159] The bridging methylene peak (at 5.6 ppm in MUF-80a-2c) can also be used to evidence the newly added benzyl azide to MUF-80a2. Both MUF-80a1-c and MUF-80a2-c also shows the peaks (7.2–7.5 ppm) corresponding to the added phenyl ring from phenylacetylene or benzyl azide, respectively. The sharp peak at around 7.9 ppm in both MUF-80a-1c and MUF-80a-2c also indicates the triazole proton.

According to the PXRDs (Figure 5-7a), the crystallinity of the two samples remained the same after the PSM reaction, indicating the reaction condition did not harm the crystalline structure of the two frameworks. The PXRD patterns for each framework before and after the click reaction are almost identical and match the calculated type-S PXRD pattern. The IR spectrum (Figure 5-7b) was revealed only useful to monitor the azide peak appearing at 2100 cm^{-1}. Using the characteristic acetylene peaks (C≡C at 2100 C≡C–H at 3400 cm^{-1}) was not valid (MUF-80a-2 vs MUF-80a-2c) due to their weak intensities.

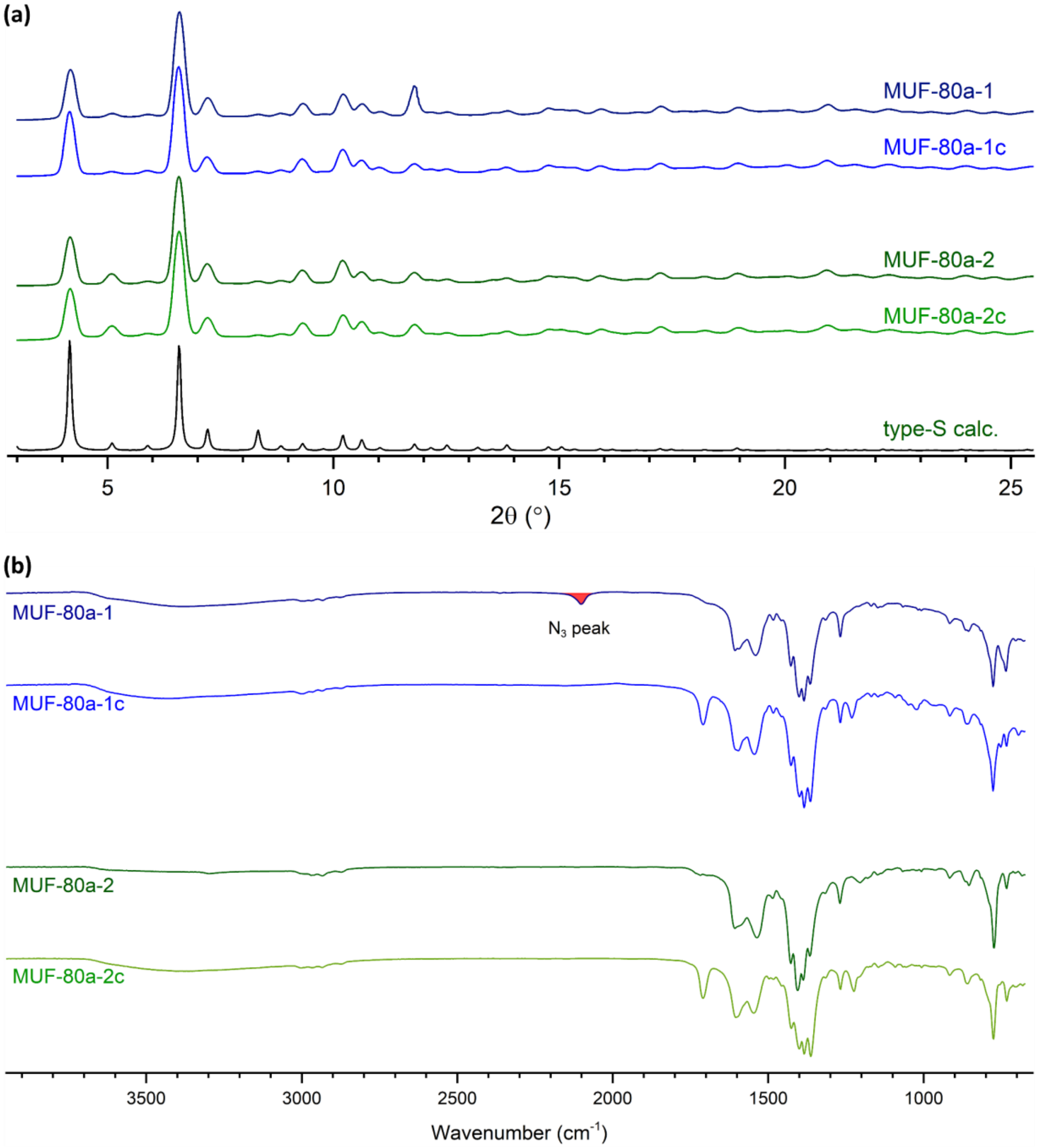

Figure 5-7. (a) PXRD patterns and (b) IR spectrascopies of the frameworks before and after the click reaction with the guest molecules for the control experiment.

The control experiment successfully demonstrated that the desired reaction was carried out within the type-S framework and the validity of the characterisation methods. Therefore, inter-ligand azide-alkyne click reaction between the two linkers, L1 and L2, was carried out as the next target. First, MUF-80a ([Zn$_4$O(hmtt)$_{1.33}$(L1)$_{0.5}$(L2)$_{0.5}$]) was synthesised from both L1 and L2 together with hmtt and zinc nitrate (Figure 5-8a). The PXRD pattern shows that every single peak coincident with those of the calculated type-S PXRD pattern, indicating MUF-80a is an isoreticular type-S framework (Figure 5-8b). ^{1}H NMR of the digested MUF-80a crystal sample also confirms the presence of both L1 and L2 together with hmtt in MUF-80a (Figure 5-8c).

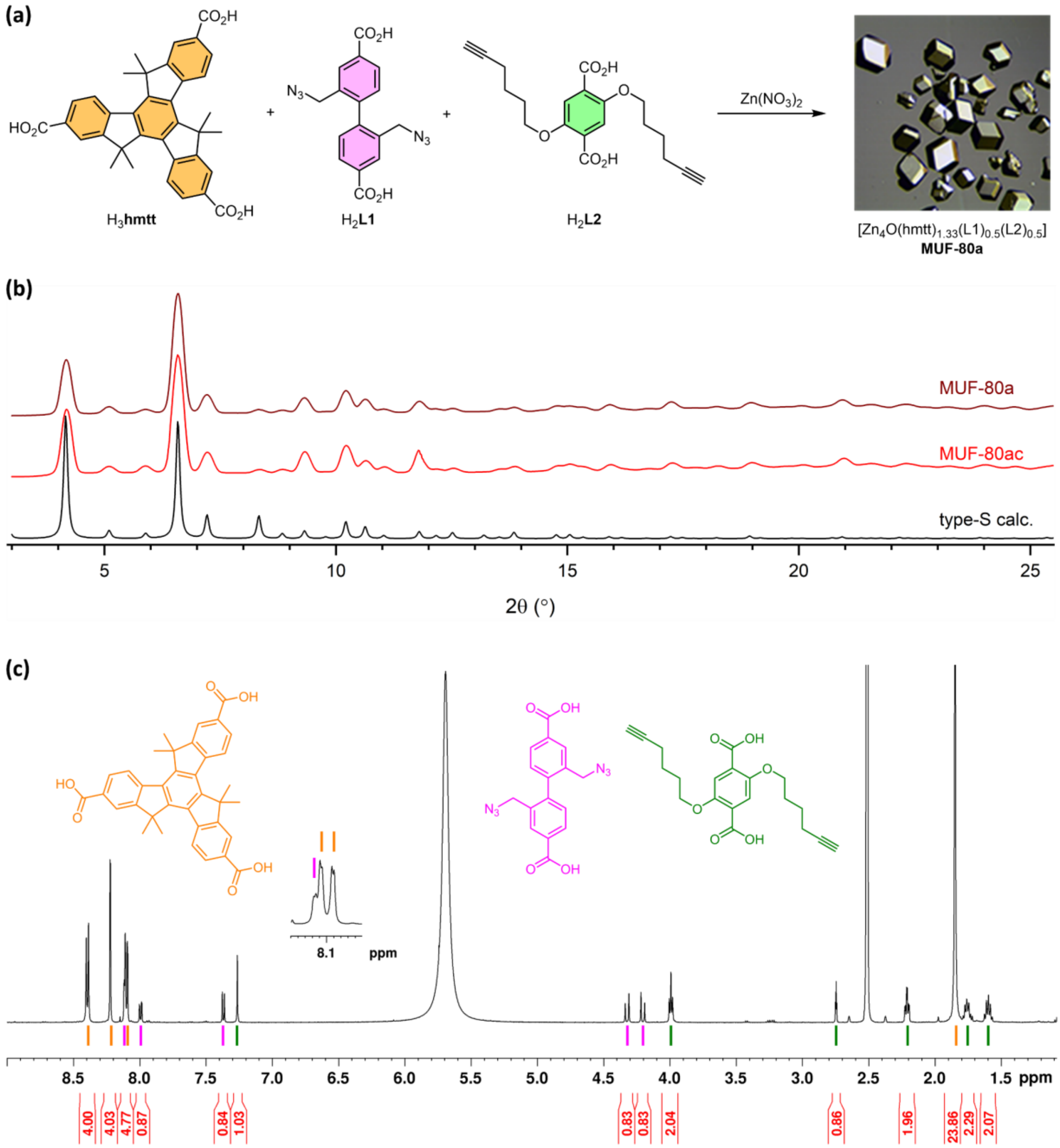

Figure 5-8. (a) A schematic diagram of MUF-80a synthesis; (b) PXRD patterns before and after the click reaction with MUF-80a; (c) ^{1}H NMR spectrum of the digested MUF-80a sample in DMSO-d6/DCl mixture.

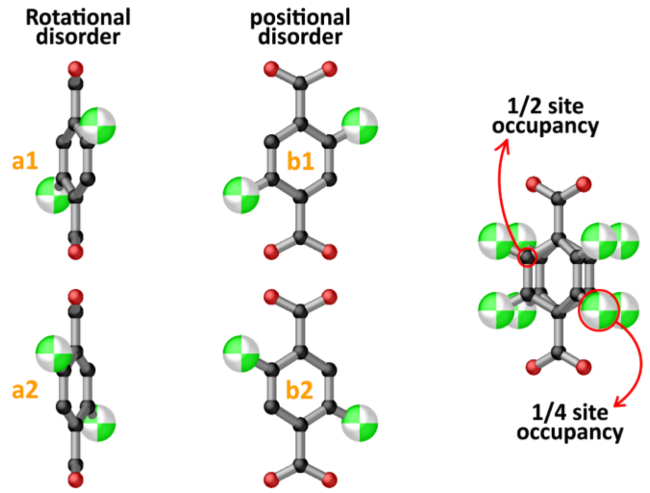

Figure 5-9. The 2,5-functionalised bdc illustrates the rotational and positional disorders of the side groups attached to the bdc backbone in a crystal lattice.

SCXRD data was also used whether the prominent change before and after click reaction is observable in the crystal structures. However, using the crystal structure has a limitation due to the low site occupancies of the atoms on the side chains. Figure 5-9 illustrates simplified bdc molecules in a crystal lattice and the two different disorders. The rotational disorder is caused by the rotational motion of the phenyl ring on bdc. The functionalised bdc molecule prefers non-zero dihedral angles between the functional groups and carboxylates to minimise the steric hindrance.[137-138] For this reason, the functionalised bdc linkers are generally shown as the two possible geometries (a1 and a2 inFigure 5-9).

The positional disorder of the attached functional group(s) would be observed depending on the number of functional groups of the same kind on a bdc molecule. The functional group will be seen on all available sites regardless its number and positions due to the random orientation of the linear linker backbone in the framework. For instance, the bdc molecule in the example above was functionalised with two same pendants at 2 and 5 positions (b1). However, the bdc backbone can be incorporated into the framework upside down, like b2. Therefore, the functional group will appear at all four positions in bdc with a half probability.

In this particular example, the bdc linker has both rotational and positional disorder. As a result, the carbon atoms on the phenyl ring and the functional groups will appear in several different positions with low site occupancies. Each of four carbon atoms on bdc rings will appear in two different positions with a half site occupancy due to the rotational disorder. On the other hand, each functional group on the bdc linker will appear in four different sites with one-fourth site occupancy because both rotational and positional disorder is applied.

To make matters worse, if the functional group itself, attached to the linker backbone, is flexible, the individual atoms in such a functional group will be shown in multiple places in the crystal lattice with a much lower probability. For this reason, the crystal structures presented in this study do not show the absolute structure, especially with respect to the flexible chains.

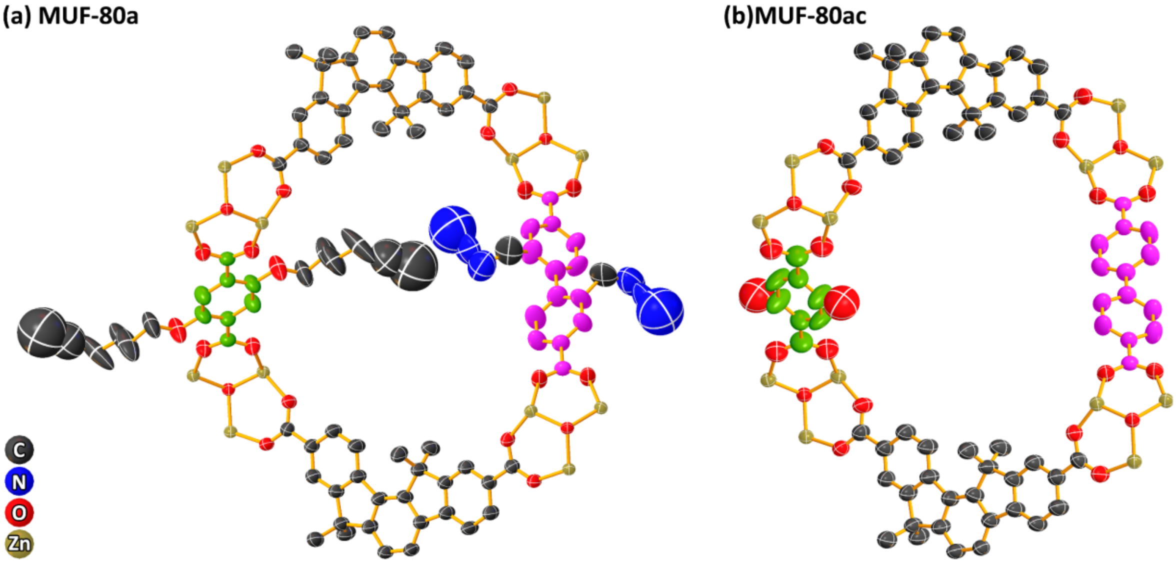

Figure 5-10. The crystal structures of (a) MUF-80a and (b) MUF-80ac are presented with one model among four disordered ones. The bdc and bpdc backbones were coloured green and pink, respectively.

The crystal structure of MUF-80a was solved from SCXRD data. Every single atom on the flexible chains was successfully modelled, and the data converged to the model with good statistics (Table 5-4).

The reaction condition used for the control experiments could not complete the polymerisation, and it turned out a harsher condition was required for the inter-ligand click reaction within MUF-80a. It can be elucidated that the probability of the valid collision between azide and alkyne became lower due to the equimolar ratio of the two groups. In contrast, the click reaction used in the control experiment was carried out with an excess amount of guest molecules. Therefore the azide-alkyne click reaction in MUF-80a required a higher temperature and a more extended reaction time to complete the PSM reaction (140 °C, 3 hours).

The completion of the reaction was determined using IR spectroscopy. However, the azide peak reduction was also caused by thermal decomposition due to the harsh reaction condition.[160] For this reason, the same reaction was carried out with MUF-80a1 ($[Zn_4O(hmtt)_{1.33}(L1)_{0.5}(bdc)_{0.5}]$) as a control experiment. If MUF-80a-1 also loses the azide peak, it will indicate the azide decomposition since there is no alkyne to react with azide in MUF-80a-1. As indicated in Figure 5-11, the azide peak reduction was observed only with MUF-80ac, and this explains that the azide group was consumed to form triazole rings with its adjacent alkyne group.

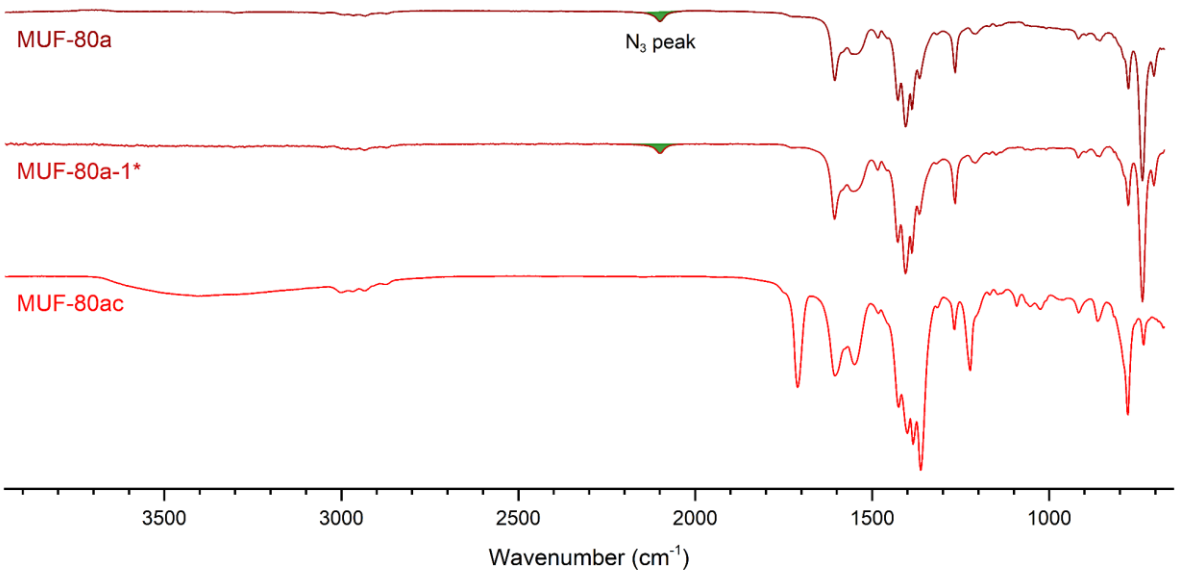

Figure 5-11. The IR spectra of MUF-80a, MUF-80a-1* and MUF-80ac. The azide peak disappeared in MUF-80ac spectrum. MUF-80a-1* refers to the crystal sample after heating.

The SCXRD data was also collected with MUF-80ac. It was expected to see the chain containing a triazole ring and linking L1 and L2 across pore-C. Since even the flexible chains were visible in the crystal structure of MUF-80a, we thought that the comparatively immobile linked chain could have more probability to be seen. However, only the oxygen atoms attached directly to bdc was observable among the atoms in the chain (Figure 5-10b).

The ^{1}H HMR spectrum of MUF-80ac (Figure 5-12) was first regarded as the evidence of click reaction between L1 and L2 because the peaks belonging to the linear linkers seemed broadened, especially in the aromatic region. However, the peaks look like a cluster of spikes rather than broadened smooth curves, and notably, the peak at 7.3 ppm belonging to bdc remained still sharp.

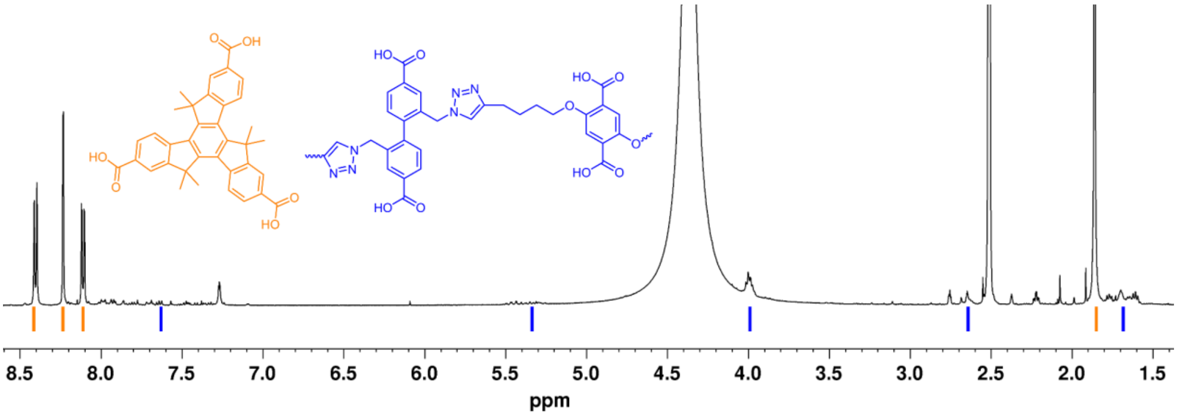

Figure 5-12. ^{1}H HMR spectrum of MUF-80ac.

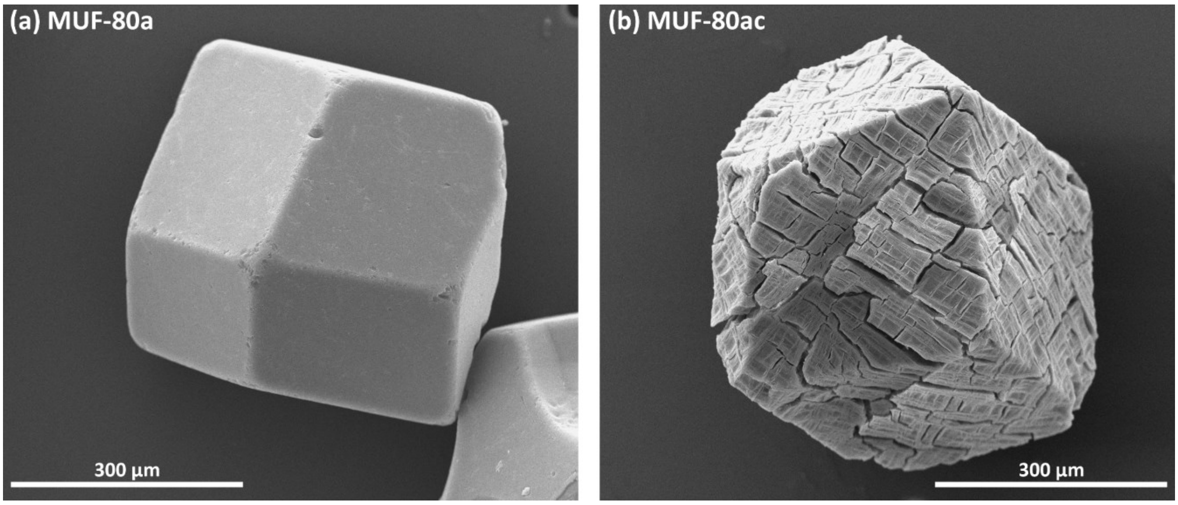

Figure 5-13. SEM images of MUF-80a and MUF-80ac, before and after PSM reaction, respectively

A plausible reason for the strange results from the crystal structure and ^{1}H NMR was found from the scanning electron microscopy (SEM) image of MUF-80ac. The two crystal images in Figure 5-13 clearly contrast the physical change after the click reaction. The smooth surface of MUF-80a turned like a dry turtle shell after the click reaction. This indicates that the crystal underwent stress during the course of the click reaction.

The data from gas physisorption isotherm experiments are also coincident with the morphology change of the two crystal samples. According to BET surface area calculation based on N_2 adsorption at 77 K, the surface area of MUF-80a (2900 $m^2 \cdot g^{-1}$) reduced after the click reaction (2430 $m^2 \cdot g^{-1}$). Since there was not much change regarding the cell contents between MUF-80a and MUF-80ac, the surface area was expected to be comparable. The pores in MUF-80a seems partially collapsed due to the stress during the click reaction, as the morphology change in MUF-80ac crystals indicates.

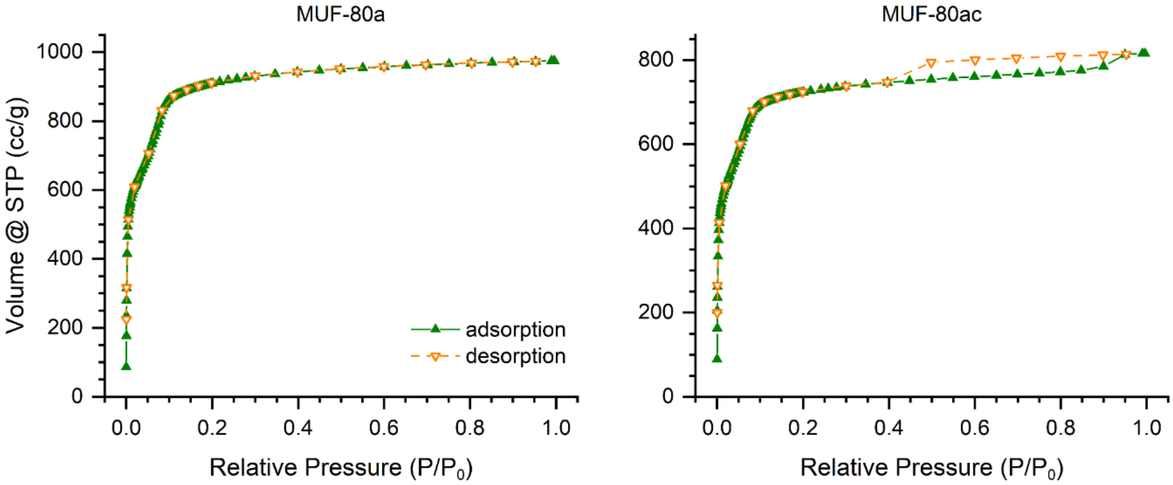

Figure 5-14. Two plots of N_2 physorption isotherm at 77K for before and after azide-alkyne click reaction.

Furthermore, the adsorption and desorption curves of MUF-80ac are slightly different from those of MUF-80a. This change seems related to the morphology change after the click reaction. As shown in Figure 5-14, the N_2 gas adsorption isotherm at 77 K exhibits a stepwise increase. The first steep rise at the beginning indicates the monolayer formation of the absorbate molecule, while the second rise is associated with the multilayer formation of absorbate in the mesopores. However, the slight rise in the adsorption curve at the very end of the plateau and the hysteresis loop appears in the MUF-80ac plot. These are the characteristic sorption profile of the capillary condensation in mesopores and often found with aggregated crystals of zeolites, some mesoporous zeolites, or micro-mesoporous carbons.[161] In this case, such capillary condensation occurs in the cracks of the MUF-80ac crystals and indicates that the partial structural collapse happened to the bulk sample.

The experimental results suggest that the click reaction between L1 and L2 likely carried out. However, the incomprehensible experimental results, like crystal structure and ^{1}H NMR, and the morphology change after the click reaction imply something went wrong. Based on all these results and observations, we have deduced that the chain linking L1 and L2 after the click reaction is too short. Therefore, the stress over the crosslinked polymer accumulates as the degree of polymerisation increases and eventually causes partial structural collapse. The simulated 3D model was investigated in detail, and it was revealed that the bond lengths between the atoms composing the chain were longer than the usual bond lengths, indicating it is under stress (Figure 5-15).

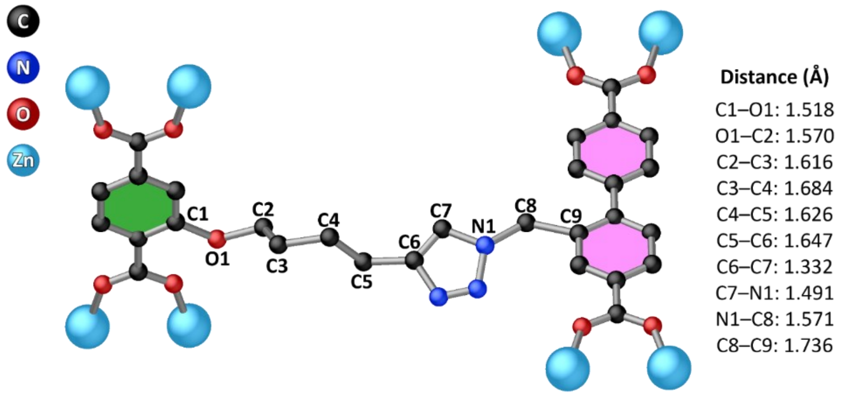

Distance (Å)

C1–O1: 1.518
O1–C2: 1.570
C2–C3: 1.616
C3–C4: 1.684
C4–C5: 1.626
C5–C6: 1.647
C6–C7: 1.332
C7–N1: 1.491
N1–C8: 1.571
C8–C9: 1.736

Figure 5-15. A simulated triazole containing alkyl chain by 3D modelling software after inter-ligand cross-linking click reaction between the two ligands, L1 and L2. The position of L1 and L2 backbones are fixed at proper positions with a similar arrangement to the geometry in the crystal lattice. The bond lengths between atoms composing the chain were longer than normal, indicating the chain length is not long enough to fill the gap between L1 and L2.

5.2.3. Post-synthetic modification reaction with MUF-80b

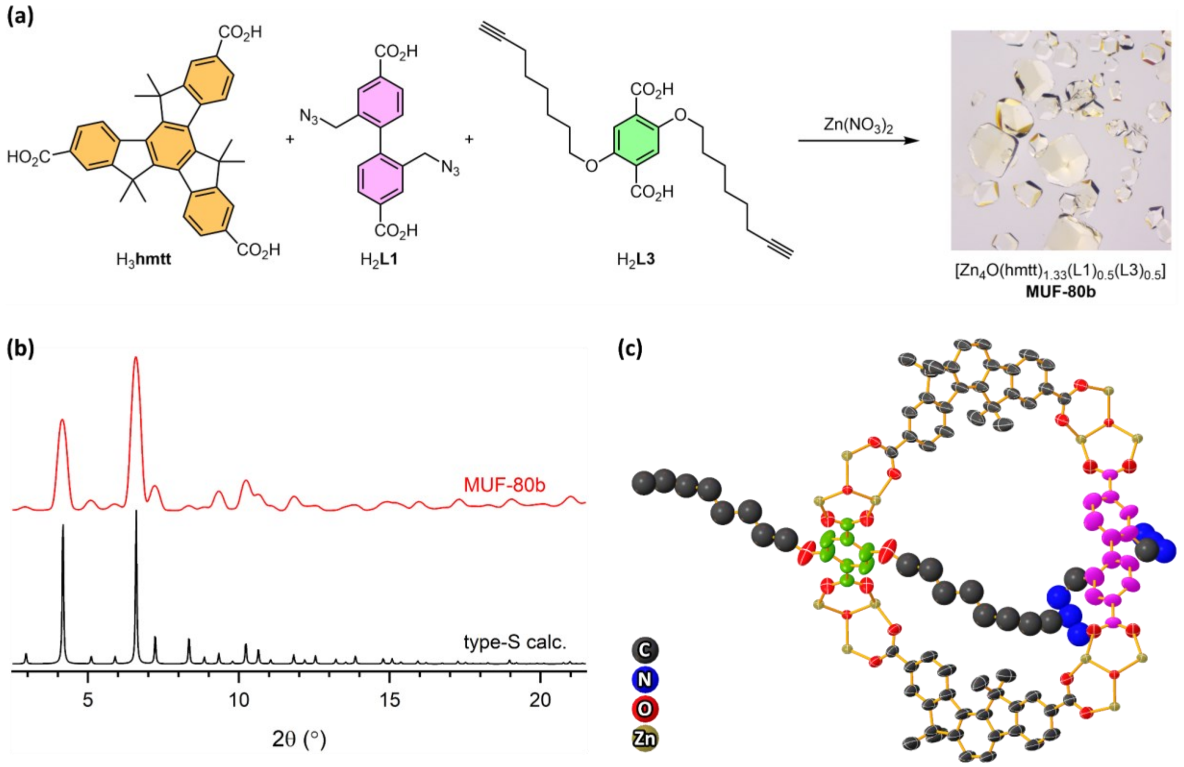

Figure 5-16. (a) A schematic diagram of MUF-80b synthesis; (b) PXRD pattern and (c) crystal structure of MUF-80b.

The new bdc derivative (L3) decorated with a longer alkyne chain was prepared to correct the chain length problem presented with MUF-80ac. MUF-80b was then synthesised using L1 and L3 (Figure 5-16a). The resulting crystal was characterised with the same methods used for MUF-80a. According to the PXRD pattern, MUF-80b is an isoreticular type-S framework. The crystal structure also supports that all the components were integrated into the type-S framework. Therefore, the click reaction was carried out with MUF-80b.

Since all the reaction condition and analysing methods were previously established with MUF-80a, they were applied straightly to MUF-80b. It was expected that the target click reaction occurs relatively easily compared to MUF-80a because the alkyne chain is extended further, resulting in a higher probability to have the desired reaction orientation. Therefore, two additional azide-alkyne cyclisation reaction methods, which failed with MUF-80a previously, were tested. Another well-known catalyst for azide-alkyne click reaction, CuBr, was tested, and the solid-phase thermal coupling reaction between azide and alkyne was also tested. The former reaction condition applied to MUF-80a was also slightly modified to a milder condition to avoid damaging the crystal samples. Therefore, three different azide-alkyne coupling reaction methods were tested in total.

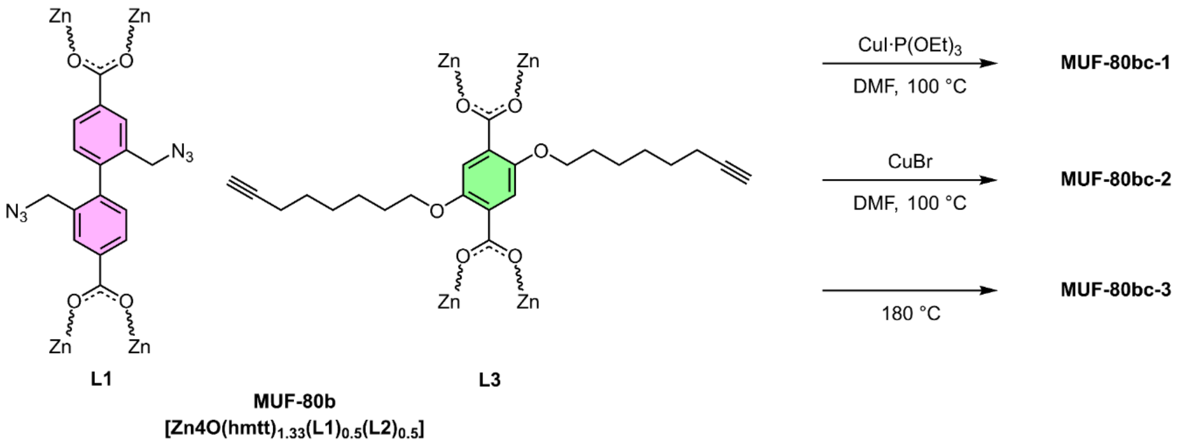

Figure 5-17. A schematic diagram showing three different ways to crosslink L1 and L3 with different PSM reactions, exploiting catalysts or heating to trigger the azide-alkyne cyclisation reaction

The three PSM reactions were conducted as described below.

I. MUF-80b (approximately 40 mg) and CuI·P(OEt)$_3$ solution (1 mL, 140 mM in DMF) were placed in 20 mL vial, and the vial was kept in an isothermal oven of 100 °C for three days. The catalyst solution was refreshed after one day. After cool down, the crystals were washed with DMF and CH_2Cl_2 several times. The resulting crystal was denoted as MUF-80bc-1

II. MUF-80b (approximately 34 mg) and saturated CuBr solution (1 mL in DMF) were placed in a 20 mL vial, and the vial was kept in an isothermal oven of 100 °C for three days. The catalyst solution was refreshed after one day. After cool down, the crystals were washed with DMF and CH_2Cl_2 several times. The resulting crystal was denoted as MUF-80bc-2

III. MUF-80b crystals (approximately 35 mg) was transferred to a gas adsorption sample cell, and the sample was heated to 180 °C for 24 hours. The resulting crystal was denoted as MUF-80bc-3

All three frameworks after the PSM reaction were then analysed with the same characterisation methods, and their analyses results were compared with each other. IR spectroscopy was first used to determine the completion of the reaction. The characteristic azide peak that appeared at 2100 cm^{-1} in MUF-80b disappeared in all three cases, indicating the desired azide-alkyne click reaction occurred (Figure 5-18c).

The notable changes were observed in the colour of crystal samples (Figure 5-18a). Although the colour of MUF-80bc-3 remained unchanged, the other two (MUF-80bc-1 and -2) changed to greenish-yellow. The two crystal samples underwent a copper catalysed azide-alkyne click reaction, so it seems that the colour change was probably caused by the transmetalation between the copper ion and zinc ion in the framework.

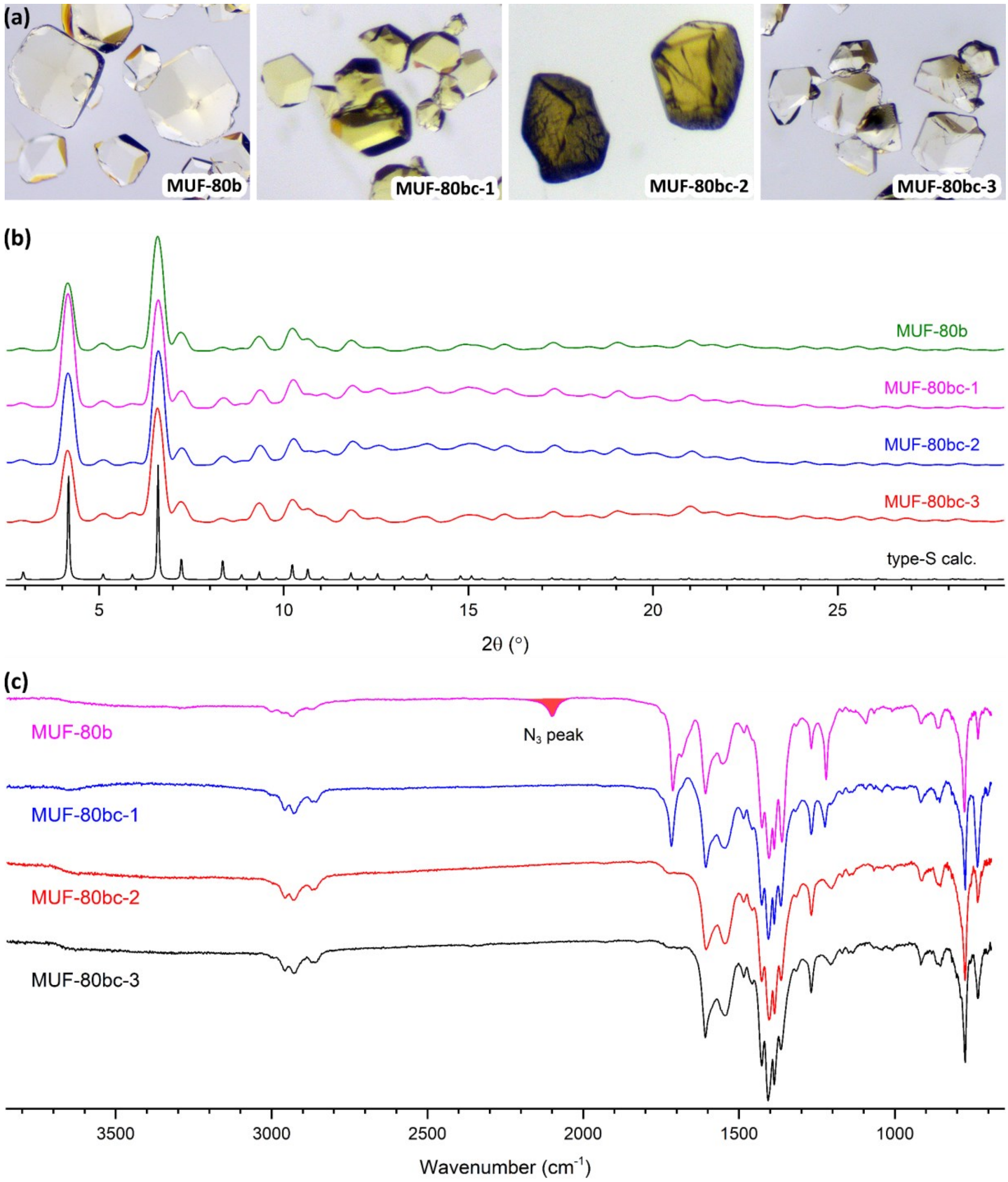

Figure 5-18. IR spectra of MUF-80b, bc-1, bc-2 and bc-3. The azide peak at 2100 cm^{-1} of MUF-80b was disappeared after PSM click reaction in all three cases.

The PXRDs measurements for all three frameworks after the PSM reaction show the crystallinity was well maintained (Figure 5-18b). Compared to the PXRD pattern of MUF-80b, the shapes and intensities of every single peak remained almost identical.

The single-crystal structures of all three samples after the PSM click reaction were solved, and the structure of MUF-80bc-3 is depicted in Figure 5-19 (the structure of the other two frameworks are the same). The triazole containing alkyl chain linking bpdc and bdc backbones was solved in all three frameworks after the PSM reaction. Although the crosslinked chain required more restraints to be properly modelled, the SCXRD data clearly indicated electron density peaks between the two ligands. Moreover, the SCXRD data converged to the single-crystal structure modelled with the triazole containing chain with low statistical errors (section 5.4.3.1).

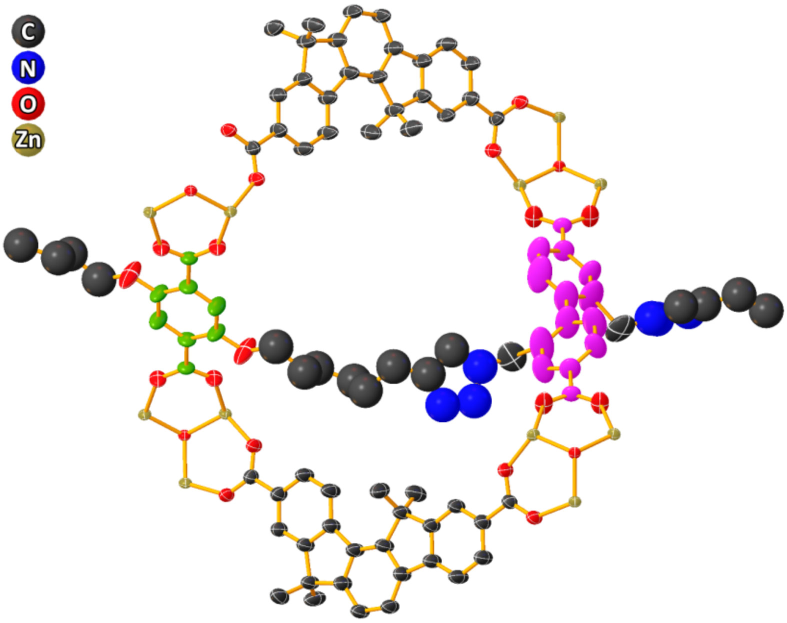

Figure 5-19. The crystal structure of MUF-80bc-3. The triazole containing crosslinked alkyl chain which connects L1 and L3 is properly solved.

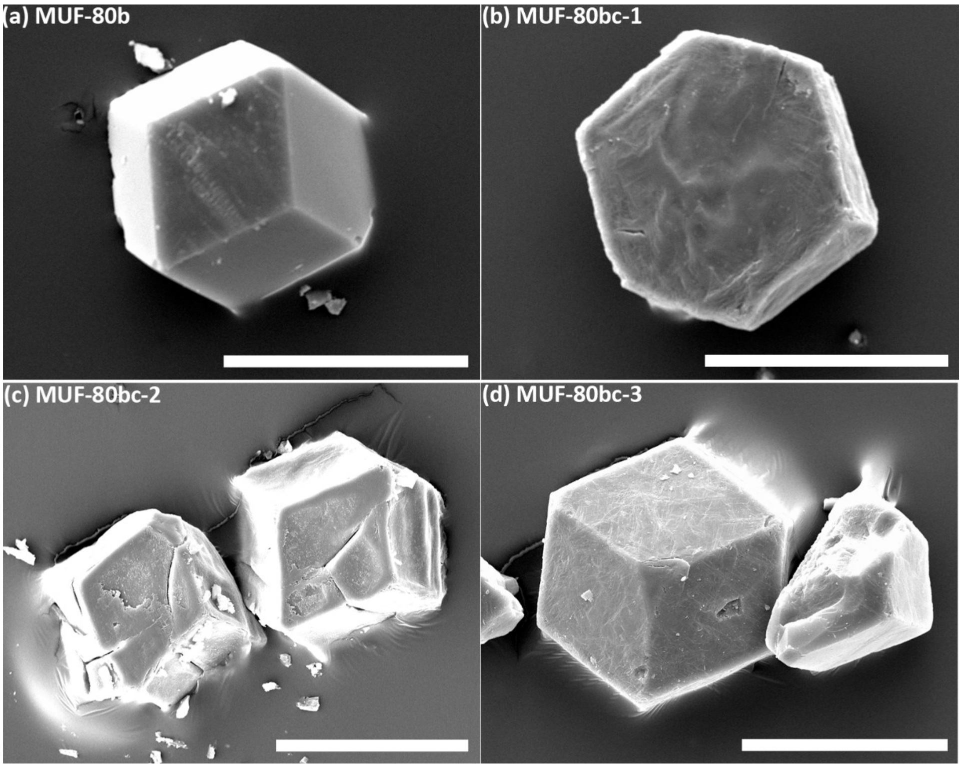

Figure 5-20. SEM images of MUF-80b and its derivatives after PSM reaction; the scale bar is equivalent to 200 µm

SEM images of all four samples were collected (Figure 5-20), and they contrast the morphology change before and after the PSM reaction. The smooth crystal surface of MUF-80b became rough in all three cases, and some cracks were noted. Although the MUF-80bc-2 crystal samples had deep cracks, all three crystal sample after the PSM reaction did not seem to have much stress during the reaction compared to MUF-80ac.

^{1}H NMR spectra also show that the azide-alkyne click reaction was conducted in all three samples. As depicted in Figure 5-21, ^{1}H NMR spectra of the four samples before and after the PSM reaction were stacked (refer to Appendix C for the detailed spectra data). First, peak shifts were noted after the reaction. The peaks around 4.2 ppm in the MUF-80b spectrum corresponded to the bridging methylene that connects bpdc and azide group shifted to 5.3 ppm after forming the triazole ring. The aromatic peaks belong to bpdc shifted, too. The newly produced peak at around 8.0 ppm, which corresponds to the triazole proton, indicates the formation of the triazole ring after the azide-alkyne click reaction, though it is rarely seen in the MUF-80bc-3 spectrum. The peak shifts of the long alkyl chains on L3 are also a prominent feature after the reaction. Second, the sharp peaks belong to L1 and L3 in MUF-80b became slightly broadened, while the peaks belong to hmtt remained still sharp. Especially, the peaks for the long alkyl chains on L3 get broadened notably.

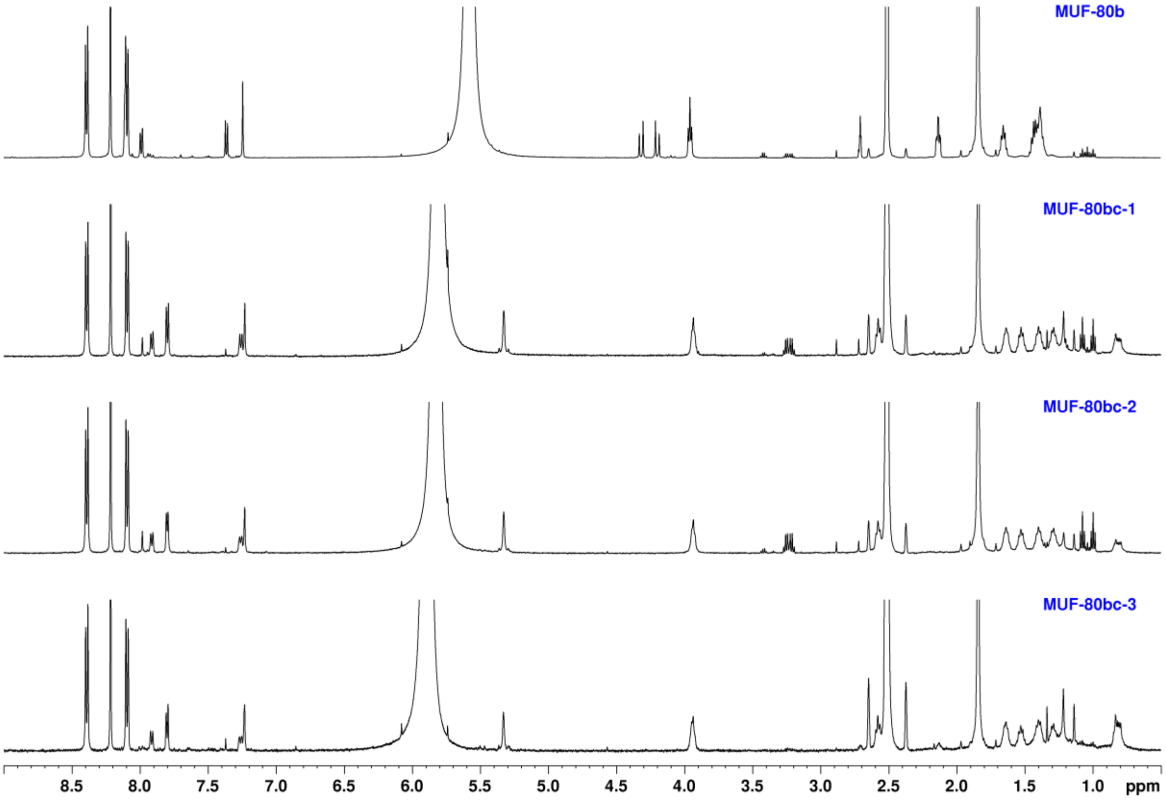

Figure 5-21. The stacked ^{1}H NMR spectra of MUF-80b and its derivatives after the PSM reaction for an easier comparison. The multiplets appearing at 3.2 ppm were because of the contaminated samples.

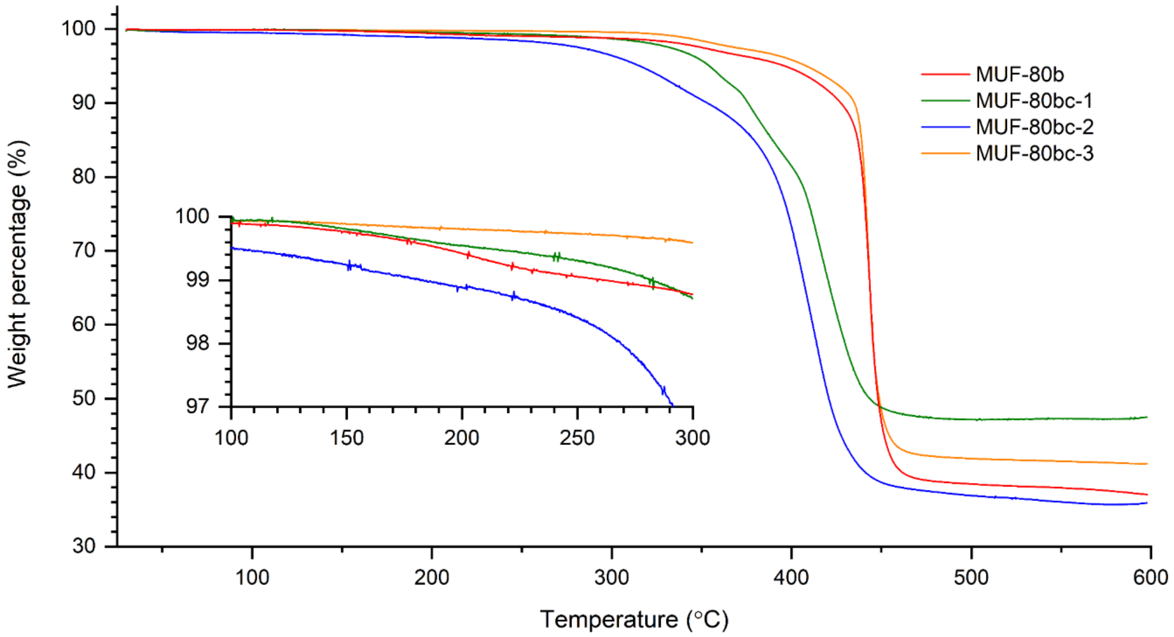

Figure 5-22. TGA plots of MUF-b and its derivatives after PSM. The mass loss at around 200 °C due to azide decomposition in MUF-80b is shown in the inset plot.

The thermogravimetric analysis (TGA) was also performed with all samples before and after the PSM reaction, and the weight change vs temperature plot is presented in Figure 5-22. According to the TGA plots, the thermal stability of the crystal samples which reacted with copper catalysts was reduced significantly. The weight loss of MUF-80bc-1 and MUF-80bc-2 begins at around 320 °C and 250 °C, respectively. On the other hand, Both MUF-80b and MUF-80bc-3 are quite stable up to 350 °C. Notably, a small weight loss with MUF-80b observed at around 200 °C in the inset graph, indicating the thermal decomposition of the azide group, and this does not appear in the other three cases.

The gas adsorption and desorption isotherms for various gases were measured with the crystal samples before and after the PSM reaction to identify any chemical or physical changes. First, the surface area and total pore volume were calculated based on the N_2 adsorption isotherm measurements at 77 K, and the results were tabulated in Table 5-1. The experimental data of MUF-80a and MUF-80ac were also tabulated together for comparison. Both surface area and total pore volume of all MUF-80b series were slightly reduced compared with MUF-80a, which corresponds with increased volume of the cell contents due

Table 5-1. BET surface areas and total pore volume of MUF-80a and MUF-80b before and after the PSM azide-alkyne cyclisation reaction.

	MUF-80a	**MUF-80ac**	**MUF-80b**	**MUF-80bc-1**	**MUF-80bc-2**	**MUF-80bc-3**
Total pore volume ($cc{\cdot}g^{-1}$)	1.508	1.214	1.428	1.425	1.416	1.459
BET surface area ($m^2{\cdot}g^{-1}$)	2900	2430	2720	2810	2760	2800

to the elongated alkyne chain of L3. However, the azide-alkyne cyclisation reaction in MUF-80b did not cause much change regarding both surface area and total pore volume, whereas they both were significantly reduced in the cases of MUF-80a and MUF-80ac. These indicate that the partial pore collapse, which presented in MUF-80ac, did not appear in MUF-80bc-1, -2 and -3.

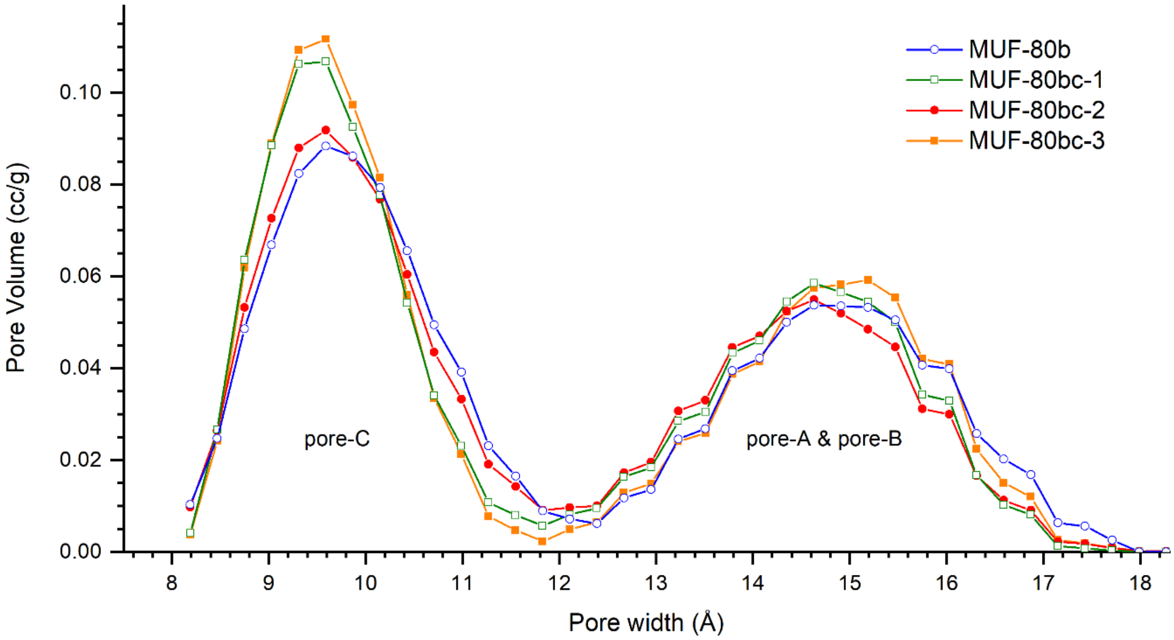

Figure 5-23. Overlaid plots of pore volume distribution of MUF-80b and its derivatives for an easier comparison after the PSM click reaction.

Pore size distributions (PSD) for all the samples before and after the PSM reaction were also calculated with a DFT method based on N_2 adsorption isotherm at 77 K data. The PSD data are plotted using the symbol and line graph for better comparison instead of the conventional column graph (Figure 5-23). The first peak around 8-11 Å corresponds to the PSD of pore-C, while the second peak around 15 Å indicates the PSD of pore-A and pore-B. Regarding the PSD of pore-A and pore-B, no notable difference was observed between all four samples. On the other hand, the PSD of pore-C in MUF-80bc-1 and -3 got narrower and higher than that of MUF-80b. The change indicates that the sizes of pore-Cs in these two frameworks became more uniform over the entire frameworks. The flexible functional groups installed on L1 and L3 dynamically behave in MUF-80b. However, if these functional groups were tied together after the reaction, they became relatively immobile. Therefore, the pore size variation caused by the freely moving functional groups diminishes after they are tied together. Thus, based on the PSD results, the desired reaction occurred more in MUF-80bc-1 and -3 than MUF-80bc-2.

The Gaussian fits of the pore-C peak in the PSD plots for all four samples also agree with the observation above (Table 5-2 and section 5.4.3.2.4). According to the statistical values from the Gaussian fits, the total pore volume and the average size of pore-C (the area underneath and the centre of the Gaussian fit, respectively) did not change much after the PSM reaction. However, the FWHMs (full width at half maximum) for MUF-80bc-1 and -3 notably decreased, meaning that the size of pore-C of MUF-80bc-1 and -3 became uniform due to the inter-ligand cross-linkage between L1 and L3.

Table 5-2. The calculated values for the average pore width and FWHM of the pore-C using Gaussian fits.

	MUF-80b	**MUF-80bc-1**	**MUF-80bc-2**	**MUF-80bc-3**
Average pore width (Å)	9.77	9.57	9.69	9.58
FWHM (Å)	2.08	1.71	1.99	1.65

The isosteric heats of adsorption (Q_{st}) for various gases were also determined using the Virial fits with the adsorption isotherm data measured at two different temperatures, 273 and 293 K.[162] Q_{st} is the amount of heat released upon an adsorbate molecule being adsorbed to the solid adsorbent surface and widely adopted to gauge the interaction between adsorbate-adsorbent pair. The calculated Q_{st} values of four different gases (CH_4, CO_2, C_2H_4 and C_2H_6) with all four frameworks were tabulated in Table 5-3. The result shows that the Q_{st} values for all adsorbate gases increased after the PSM click reaction. In other words, the affinities of the framework toward these adsorbate molecules increased after triazole forming click reaction. It was understood that the interactions between triazole and the adsorbates were stronger than the azide-alkyne pair and adsorbates. In the case of methane, the Q_{st} values increased more than three times with MUF-80bc-1 and -3.

Table 5-3. The isosteric heats of adsorption of CH_4, CO_2, C_2H_4 and C_2H_6 at zero loading in kJ·mol^{-1}.

	MUF-80b	**MUF-80bc-1**	**MUF-80bc-2**	**MUF-80bc-3**
CH_4 (kJ·mol^{-1})	2.40	7.51	4.33	8.33
CO_2 (kJ·mol^{-1})	15.19	16.97	16.19	15.78
C_2H_4 (kJ·mol^{-1})	16.19	18.40	18.98	17.43
C_2H_6 (kJ·mol^{-1})	17.59	18.81	19.58	19.35

5.3. Conclusion

In this chapter, the inter-ligand azide-alkyne coupling reaction was demonstrated post-synthetically. The first attempt using L2 was not very satisfied due to the slightly short chain length of L2. However, a satisfactory result was obtained once L3, which equipped a longer functional group, replaced L2. The desired azide-alkyne click reaction was well performed in two different ways, using a copper catalyst or heating. The various experimental results indicate that the chemical and physical properties of MOFs were altered in both cases.

This work demonstrated introducing a new functionality using PSM reaction without any guest molecules. Unlike the previously reported works, the desired reaction was carried out in a regulated manner using an MC-MOF scaffold. In addition, a polymer chain consists of alternating bpdc and bdc was produced as a product. This suggests that using MOF scaffold can be a novel way of polymer synthesis, which are not achievable in a conventional solvent assisted reaction.

5.4. Experimental section

Syntheses, gas physorption and ^{1}H NMR data are presented in Appendix C.

5.4.1. General procedure

All starting materials and solvents were used as received from commercial sources without further purification unless otherwise noted. H_2L7 (2,5-bis(azidomethyl)terephthalic acid) was prepared with the known procedure.[163]

Column chromatography was carried out on silica gel (grade 60, mesh size 230-400, Scharlau).

NMR spectra were recorded at room temperature (unless otherwise noted) on Bruker-500 Avance instruments, with the use of the solvent proton as an internal standard, and the collected data was processed with TopSpin software.

The IR spectroscopy data were collected using ThermoFisher Nicolet 5700 equipped with Smart iTR™ Attenuated Total Reflectance (ATR) Sampling Accessory and processed with OMNIC™ Specta Software.

All powder X-ray diffraction measurements were carried out on either Rigaku Spider or Bruker D8 Venture. Rigaku Spider X-ray diffractometer is equipped with CuKα radiation (Rigaku MM007 microfocus rotating-anode generator), monochromated and focused with high-flux Osmic multilayer mirror optics and a curved image plate detector. Bruker D8 Venture diffractometer is equipped with CuKα radiation with a diamond microfocus X-ray source and a Photon III 28 detector. The samples were solvated with DMF prior to and during measurements. The two-dimensional images of the Debye rings were integrated with 2DP or Diffract Eva to give 2θ vs I diffractograms. Predicted powder patterns were generated from single-crystal structures using Mercury.

All single-crystal X-ray diffraction measurements were carried out on Bruker D8 Venture, and the measurement temperature was controlled using Oxford Cryostream, if required. Bruker APEX 3 was used to collect and process data, and the structure was solved and refined using the Shelx package[107,119] under Olex2[120]. The crystal samples were solvated in n-octane and mounted on a nylon loop using Fomblin oil in most cases. Alternatively, if moisture sensitive, a single crystal was completely sealed in a glass capillary during the measurement.

Thermogravimetric analyses were performed on a TA Instruments Q50 instrument.

5.4.2. Post-synthetic click reaction

MUF-80a-1c MUF-80a-1 (approximately 5 mg), phenylacetylene (4 µL, approximately 10 eq.) and CuI·P(OEt)$_3$ solution (1 mL, 10 mM in acetonitrile) were placed in 10 mL microwave vial, and the vial was heated to 100 °C for 90 minutes with a microwave. After cooling down to room temperature, the crystals were washed with acetone then CH_2Cl_2 several times and kept in fresh CH_2Cl_2 for further use.

MUF-80a-2c MUF-80a-2 (approximately 5 mg), benzylazide (4 mg, approximately 10 eq.) and CuI·P(OEt)$_3$ solution (1 mL, 10 mM in acetonitrile) were placed in 10 mL microwave vial, and the vial was heated to 100 °C for 90 minutes with a microwave. After cooling down to room temperature, the crytals were washed with acetone then CH_2Cl_2 several times and kept in fresh CH_2Cl_2 for further use.

MUF-80ac MUF-80a (approximately 5 mg) and CuI·P(OEt)$_3$ solution (1 mL, 10 mM in acetonitrile) were placed in 10 mL microwave vial, and the vial was heated to 140 °C for 3 hours with a microwave. After cooling down to room temperature, the crystals were washed with acetone then CH_2Cl_2 several times and kept in fresh CH_2Cl_2 for further use.

MUF-80bc-1 MUF-80b (approximately 40 mg) and CuI·P(OEt)$_3$ solution (1 mL, 140 mM in DMF) were placed in 20 mL vial, and the vial was kept in an isothermal oven of 100 °C for three days. The catalyst solution was refreshed after one day. The crystals were washed with DMF with sonication then CH_2Cl_2 several times and kept in fresh CH_2Cl_2 for further use.

MUF-80bc-2 MUF-80b (approximately 34 mg) and saturated CuBr solution (1 mL in DMF) were placed in 20 mL vial, and the vial was kept in an isothermal oven of 100 °C for three days. The catalyst solution was refreshed after one day. The crystals were washed with DMF with sonication then CH_2Cl_2 several times and kept in fresh CH_2Cl_2 for further use.

MUF-80bc-3 Solvated MUF-80b crystals (approximately 35 mg) in hexane was transferred to a gas adsorption sample cell. After removing the solvent by decantation, the sample was heated to 180 °C for 24 hours. The resulting sample was directly used for gas adsorption measurements. The crystals were washed with DMF with sonication then CH_2Cl_2 several times and kept in fresh CH_2Cl_2 for further use.

5.4.3. Analyses

5.4.3.1. SCXRD (Single-crystal X-ray diffraction)

All cif files are available through the link provided below.

https://drive.google.com/drive/folders/1mEMRFRL3ME5N6OtzIjeEWkluLPOIArSg?usp=sharing

Table 5-4. Summary of X-ray crystallography data collection and refinement details of MUF-80a, ac, b, bc-1, bc-2 and bc-3

Identification code	MUF-80a	MUF-80ac	MUF-80b	MUF-80bc-1	MUF-80bc-2	MUF-80bc-3
Empirical formula	$C_{66}H_{51}N_3O_{14}Zn_4$	$C_{59}H_{40}O_{14}Zn_4$	$C_{68}H_{55}N_3O_{14}Zn_4$	$C_{68}H_{55}N_3O_{14}Zn_4$	$C_{68}H_{55}N_3O_{14}Zn_4$	$C_{68}H_{55}N_3O_{14}Zn_4$
Formula weight	1371.58	1234.39	1399.63	1399.63	1399.63	1399.63
Temperature (K)	110	110	294	280	123	123
Crystal system	cubic	cubic	cubic	cubic	cubic	cubic
Space group	Pm-3	Pm-3	Pm-3	Pm-3	Pm-3	Pm-3
a=b=c (Å)	30.0100(3)	29.9819(5)	29.8804(3)	29.8509(3)	29.935(3)	29.9568(3)
α=β=γ (°)	90	90	90	90	90	90
Volume (Å^3)	27027.0(8)	26951.2(13)	26678.4(8)	26599.4(8)	26826(8)	26883.5(8)
Z	6	6	6	6	6	6
ρ_{calc}g (cm^3)	0.506	0.456	0.523	0.524	0.52	0.519
μ (mm^{-1})	0.797	0.774	0.812	0.814	0.807	0.805
F(000)	4200	3756	4296	4296	4296	4296
Crystal size (mm^3)	0.5 × 0.5 × 0.4	0.5 × 0.5 × 0.4	0.4 × 0.4 × 0.2	0.3 × 0.3 × 0.2	0.5 × 0.5 × 0.3	0.3 × 0.3 × 0.2
Radiation	CuKα (λ = 1.54178)	CuKα (λ = 1.54178)	CuKα (λ = 1.54178)	CuKα (λ = 1.54178)	CuKα (λ = 1.54184)	CuKα (λ = 1.54178)
2Θ range for data collection (°)	4.164 to 144.032	13.206 to 124.712	4.182 to 152.248	5.128 to 152.71	5.114 to 153.226	5.11 to 152.046
Resolution range for refinement (Å)	0.81 to ∞	0.87 to 8.0	0.79 to ∞	0.79 to ∞	0.79 to ∞	0.79 to ∞
Index ranges	$-19 \le h \le 36$ $-36 \le k \le 36$ $-25 \le l \le 22$	$-34 \le h \le 23$ $-26 \le k \le 31$ $-26 \le l \le 32$	$-37 \le h \le 33$ $-30 \le k \le 27$ $-31 \le l \le 36$	$-22 \le h \le 27$ $-33 \le k \le 37$ $-35 \le l \le 25$	$-32 \le h \le 37$ $-27 \le k \le 30$ $-37 \le l \le 22$	$-37 \le h \le 26$ $-15 \le k \le 35$ $-27 \le l \le 37$
Reflections collected	66646	60717	166119	96116	74687	124896
Tmin/Tmax	0.576/1.000	0.511/1.000	0.663/0.754	0.634/0.754	0.593/0.754	0.667/0.754
Independent reflections	9377 R_{int} = 0.0588 R_{sigma} = 0.0486	7603 R_{int} = 0.0718 R_{sigma} = 0.0519]	9782 R_{int} = 0.0279 R_{sigma} = 0.0123	9789 R_{int} = 0.0373 R_{sigma} = 0.0174	9883 R_{int} = 0.0355 R_{sigma} = 0.0255	9878 R_{int} = 0.0286 R_{sigma} = 0.0150
Data/restraints/parameters	9377/41/303	7603/7/213	9782/25/249	9789/36/249	9883/36/249	9872/36/249
Goodness-of-fit on F^2	1.151	1.135	1.147	1.13	1.051	1.079
Data completeness	0.994	0.997	0.991	0.992	0.989	0.991
Final R indexes [I>=2σ (I)]	R_1 = 0.0524 wR_2 = 0.1360	R_1 = 0.0533 wR_2 = 0.1654	R_1 = 0.0600 wR_2 = 0.1897	R_1 = 0.0575 wR_2 = 0.1877	R_1 = 0.0509 wR_2 = 0.1538	R_1 = 0.0468 wR_2 = 0.1472
Final R indexes [all data]	R_1 = 0.0818 wR_2 = 0.1629	R_1 = 0.0652 wR_2 = 0.1739	R_1 = 0.0639 wR_2 = 0.1955	R_1 = 0.0657 wR_2 = 0.1968	R_1 = 0.0584 wR_2 = 0.1605	R_1 = 0.0499 wR_2 = 0.1507
Largest diff. peak/hole (e Å^{-3})	0.42/-0.60	0.46/-0.41	0.64/-0.68	0.47/-0.37	0.49/-0.57	0.77/-0.56

5.4.3.2. **Gas adsorption**

The crystal samples were rinsed with CH_2Cl_2 and n-hexane several times, and the samples were transferred to the sample cell with n-hexane. After removing n-hexane by decantation, the sample was activated at 80 °C under vacuum for 20 hours.

Only selected data were presented as examples. Please see Appendix C for the full data collection.

5.4.3.2.1. N_2 adsorption at 77 K data and BET plots

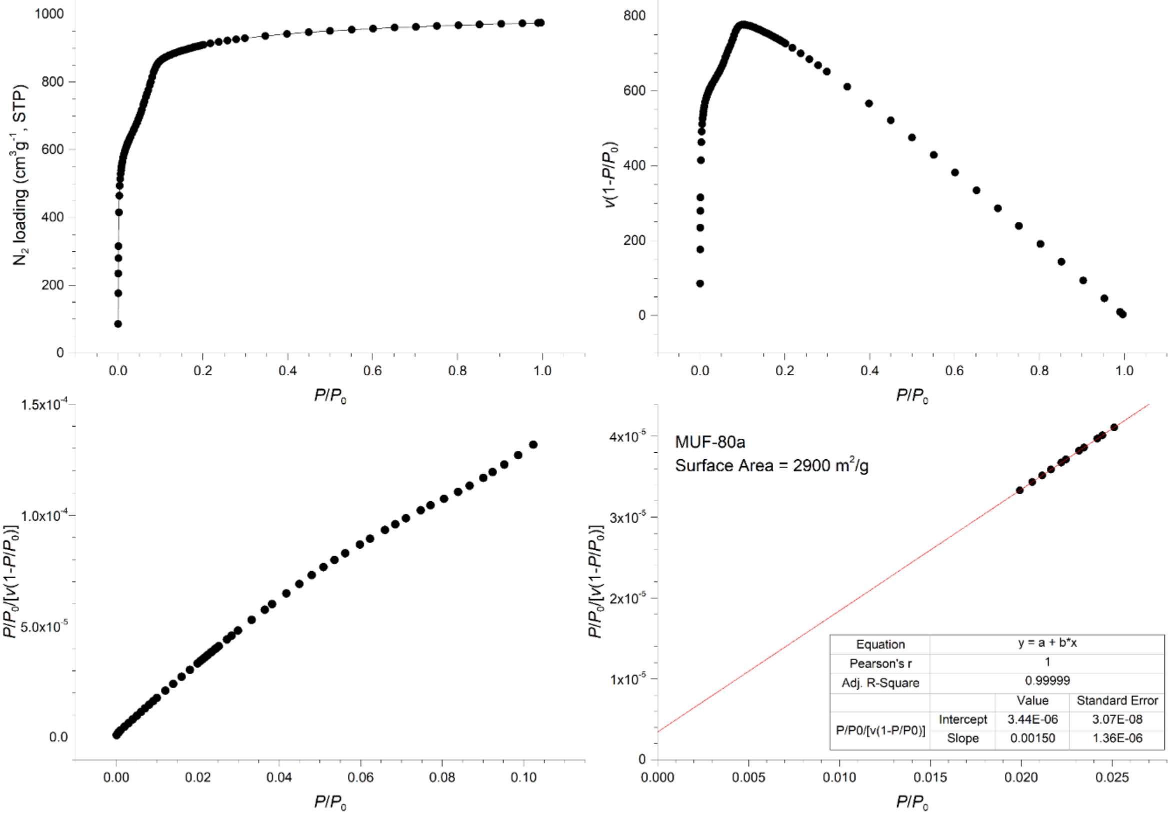

MUF-80a
Surface Area = 2900 m²/g

Equation	y = a + b*x		
Pearson's r	1		
Adj. R-Square	0.99999		
		Value	Standard Error
P/P0/[v(1-P/P0)]	Intercept	3.44E-06	3.07E-08
	Slope	0.00150	1.36E-06

Figure 5-24. N_2 adsorption isotherm at 77 K and BET surface area plots for MUF-80a.

5.4.3.2.2. Physisorption of various gases at 273 and 293 K

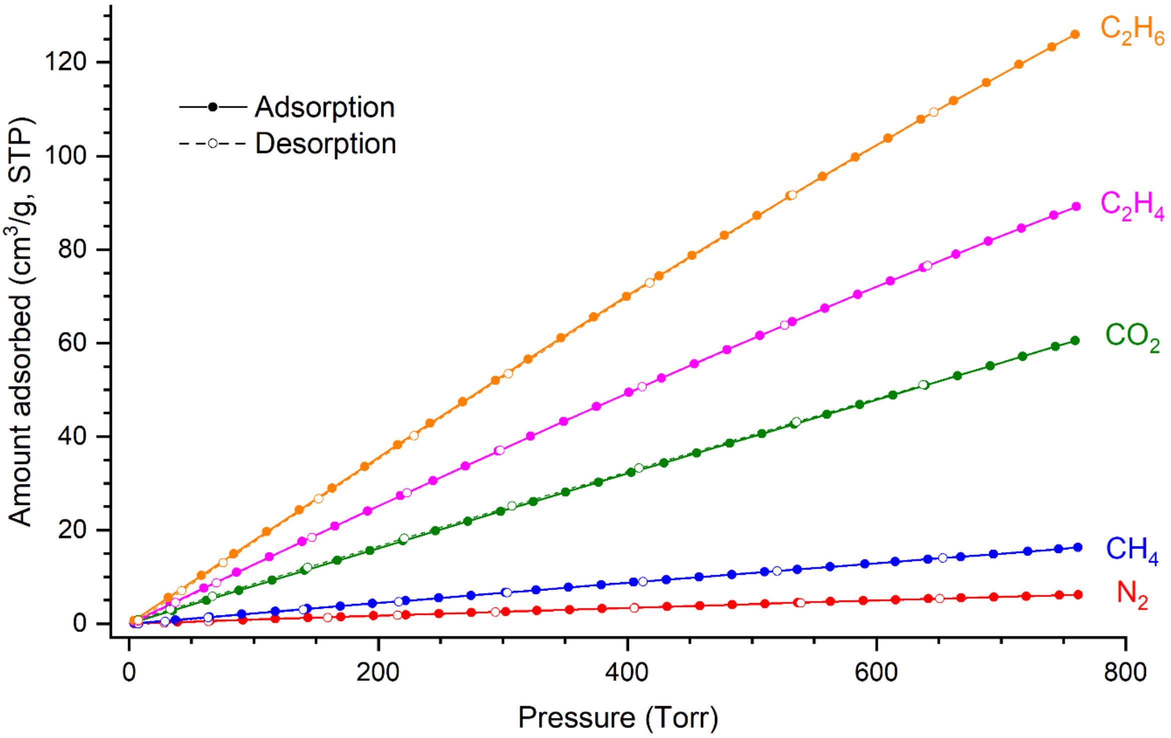

Figure 5-25. Gas adsorption and desorption isotherms of MUF-80a at 273 K.

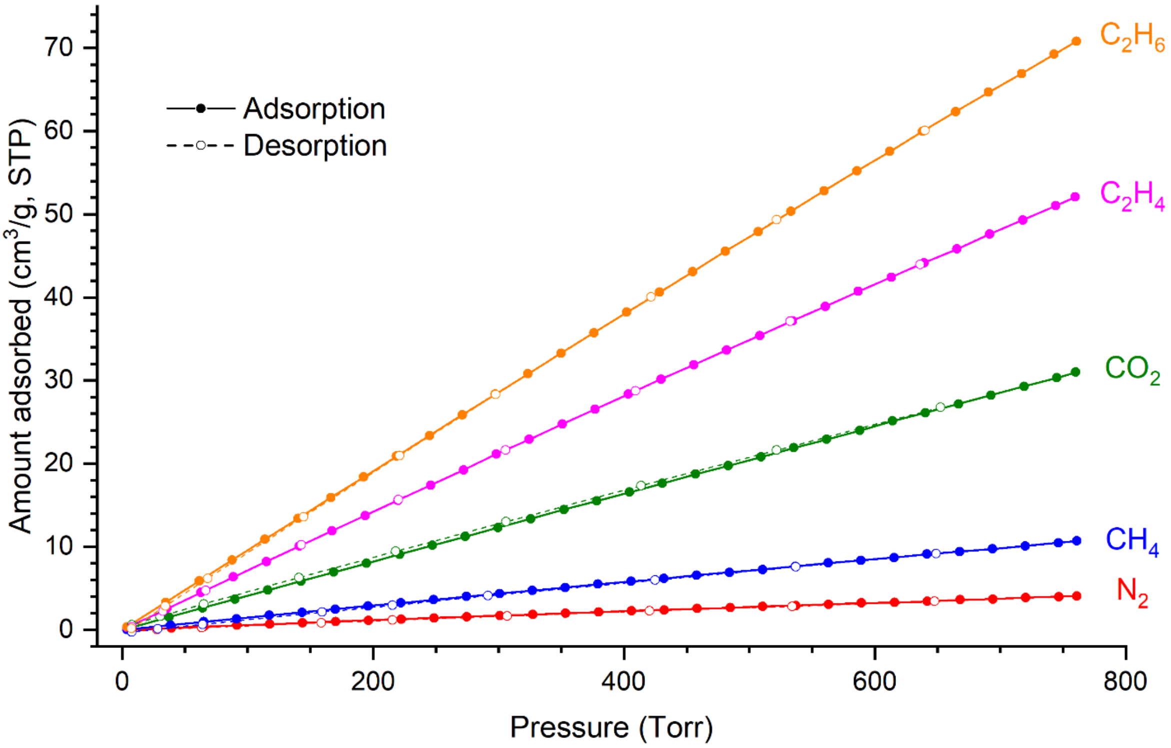

Figure 5-26. N_2, CH_4, CO_2, C_2H_4 and C_2H_6 adsorption and desorption isotherms at 293 K of MUF-80a.

5.4.3.2.3. Isosteric heat of adsorption (Q_{st}) calculations[164]

N_2, CH_4, CO_2, C_2H_4, and C_2H_6 adsorption isotherms at two different temperatures (273 K and 293 K) were used to calculate isosteric heat of adsorption[c]. In each case, the data were fitted by using the Virial equation.

$$\boldsymbol{lnP = lnN + \frac{1}{T}\sum_{i=0}^{m} a_i N^i + \sum_{i=0}^{n} b_i N^i}$$

where P is the pressure expressed in torr, N is the amount adsorbed in cm^3/g, T is the temperature in K, a_i and b_i are virial coefficients, and m and n represent the number of coefficients required to adequately describe the isotherms (m = 1, n = 0 were used since more coefficients didn't improve overall fit). Then the fitted parameters a_0 to a_m from the virial equation are used in the following equation:

$$\boldsymbol{Q_{st} = -R\sum_{i=0}^{m} a_i N^i}$$

Please, refer to Appendix C to see the individual plot of uptake vs lnP and Virial fitting.

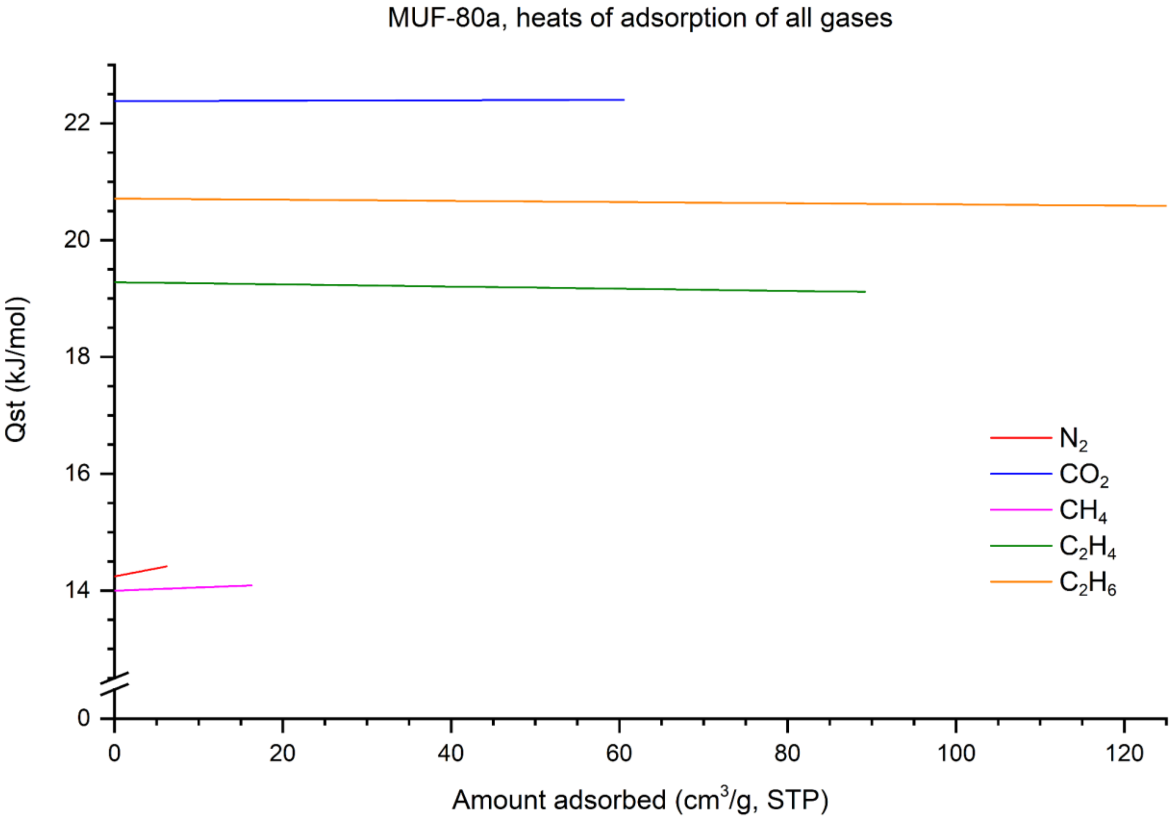

Figure 5-27. Isosteric heats of adsorption for MUF-80a plotted as a function of uptake.

---

[c] The Q_{st} calculation for N_2 was not included in some cases, since N_2 adsorption data did not fit well the Virial fitting.

5.4.3.2.4. Pore size distributions

The pore size distribution was calculated by Quantachrome VersaWin software based on N_2 physisorption isotherms data at 77 K using DFT method with a model of 'N$_2$ at 77 K on carbon (slit/cylindr./sphere pores, QSDFT adsorption branch)'.

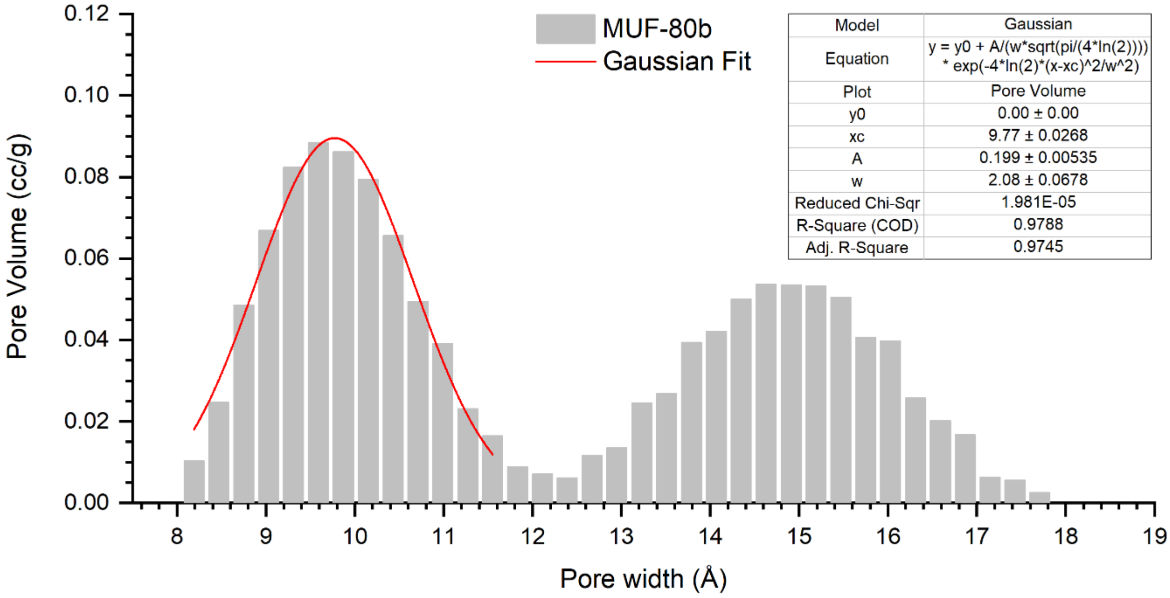

Model	Gaussian
Equation	y = y0 + A/(w*sqrt(pi/(4*ln(2)))) * exp(-4*ln(2)*(x-xc)^2/w^2)
Plot	Pore Volume
y0	0.00 ± 0.00
xc	9.77 ± 0.0268
A	0.199 ± 0.00535
w	2.08 ± 0.0678
Reduced Chi-Sqr	1.981E-05
R-Square (COD)	0.9788
Adj. R-Square	0.9745

Figure 5-28. Pore volume distribution plot of MUF-80b and the Gaussian fit for pore-C

Chapter 6 **Sequence-specific polymerisation using a MOF scaffold**

6.1. Introduction

In Chapter 5, the inter-ligand crosslinking PSM reactions were demonstrated with the type-S framework. As a result, polymer chains consisting of alternating bpdc and bdc units were produced. However, the polymer chain produced by the PSM reaction could, in principle, be directly synthesised without the aid of the framework scaffold. This is because the bpdc and bdc units have mutually reactive functional groups, so each linker can only react with its partner and not another copy of itself. For instance, in MUF-80b, the two linkers (L1 and L3) are decorated with azide and alkyne functional groups, respectively. Therefore they can be polymerised to form sequence-specific -ABAB- type polymer chains if the triazole forming click reaction carried out with these two free ligands (Figure 6-1a). In this case, the main advantage of using the MOF scaffold is to control the length of the polymer chain by the linear allocation of monomers. The framework prevents the formation of macrocyclic rings by the coupling reaction.

On the other hand, if two monomers are functionalised with the same chemical group that can be covalently linked by a homo-coupling reaction, the sequence of the two monomers in the resulting polymer chain would be random (Figure 6-1b). In this case, the MOF scaffold ensures that the polymer chain has a specific sequence. Bpdc and bdc alternate along the three crystallographic axes in the type-S framework, and a pair of bpdc and a pair of bdc

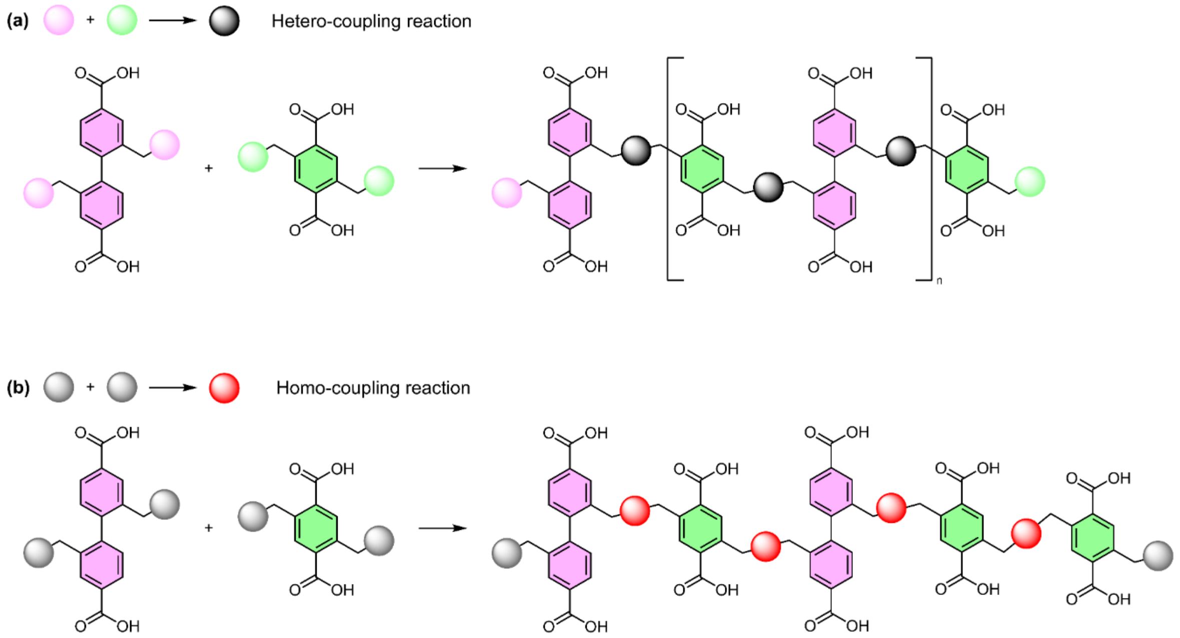

Figure 6-1. A schematic diagram of polymerisation with (a) hetero-coupling or (b) homo-coupling.

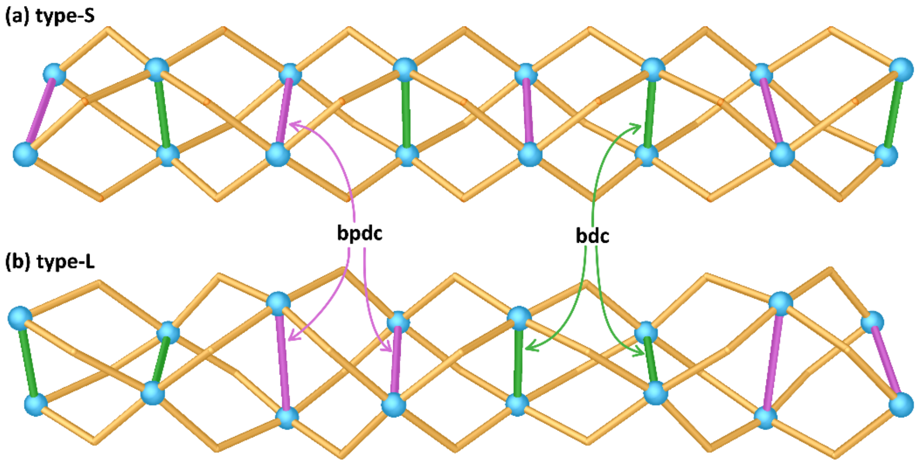

Figure 6-2. A schematic diagram showing the arrangement of the two linear linkers, bpdc and bdc, (a) bpdc and bdc alternate; (b) each pair of bdc and bpdc alternate.

alternates in the type-L framework (Figure 6-2). Therefore, -ABAB- or -AABBAABB- type polymer chains, which cannot be synthesised in a homogeneous reaction with free monomers, can be produced using either the type-S or type-L framework as a scaffold.

Similarly, a guest-mediated polymerisation can take advantage of using MOF scaffold to produce sequence-specific polymers. If two different monomers were equipped with the same functional groups and were indirectly linked using a guest molecule, the sequence of the two monomers would be random in resulting polymers. However, sequence-specific polymers can be obtained if they were precisely arranged in a MOF scaffold (Figure 6-3)

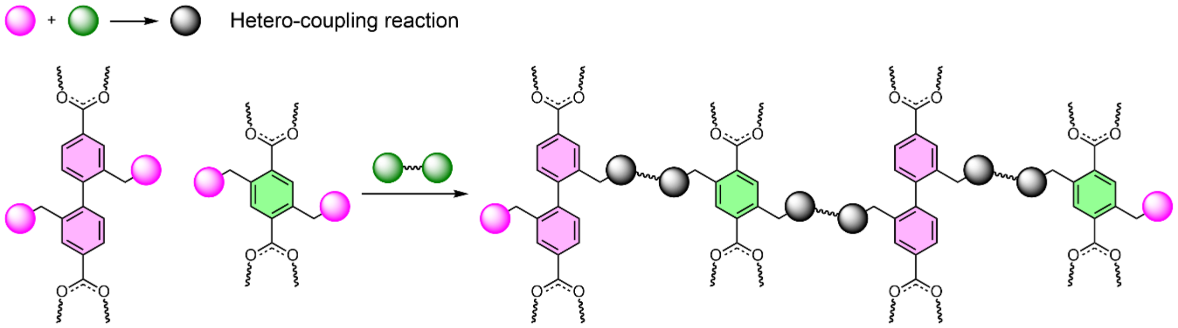

Figure 6-3. The concept of synthesising the sequence-specific polymer using a guest molecule to link the bpdc and bdc derivatives equipped with the same functional group.

6.2. Result and discussion

6.2.1. Ligand and experiment design

Since the polymerisation is post-synthetically achieved in a framework, the polymerisation reaction must not spontaneously occur during MOF synthesis. The functional groups should not inhibit MOF formation, either. In that sense, three different chemical functional groups

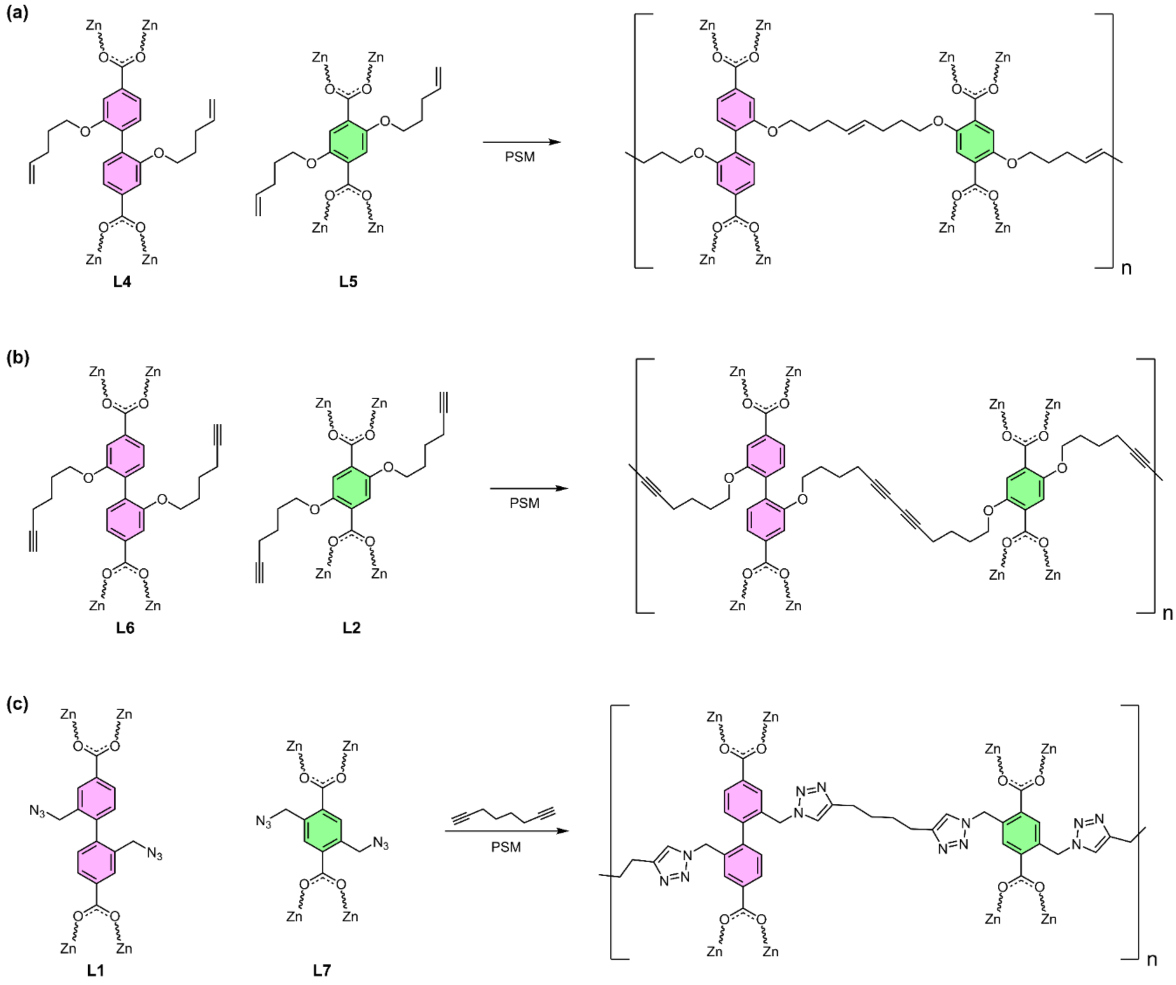

Figure 6-4. A few examples of coupling reactions between the bpdc and bdc derivatives equipped with the same functional group in the type-S framework using (a) alkene metathesis reaction, (b) alkyne-alkyne Glaser coupling or (c) guest mediated azide-alkyne click reaction.

were chosen. The first two cases in Figure 6-4 utilise the direct homo-coupling reactions. Both linear linkers, bpdc and bdc, are equipped with the same functional group, either alkene (Figure 6-4a) or alkyne (Figure 6-4b). Once they are incorporated into a framework, they will be covalently linked by postsynthetic modification reaction using external stimuli, such as catalyst or heat. In contrast, the third one uses a different approach to polymerise two monomers. Although both bpdc and bdc are also functionalised with the same group (azide), they will be indirectly linked using a hetero-coupling reaction with a guest molecule. In this case, the guest component possesses two terminal alkynes and will bridge the two linear linkers exploiting the postsynthetic azide-alkyne click reaction.

In either case, whether the guest component is involved, a random sequence of polymer chain would be formed if conventional polymerisation methods were used. Therefore, these three candidates could successfully demonstrate the novel way of the sequence-specific polymer synthesis using MOF scaffold.

6.2.1.1. Alkene-alkene coupling reactions

Alkene (or olefin) is one of the best candidates for the homocoupling reaction because its chemistry for bridging two components has long been recognised and well established with thousands of applications and various reaction mechanisms.[165-167] The two terminal alkenes can be coupled using alkene metathesis,[168] dimerisation[169] or [2+2] cycloaddition reaction (Figure 6-5).[170] These reactions are often triggered by external stimuli like catalysts or light, making olefins a candidate for the PSM homocoupling reaction in MOFs.

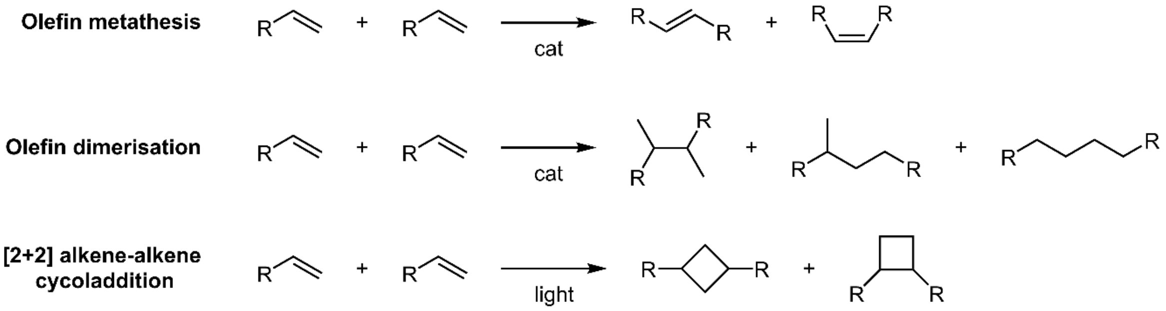

Figure 6-5. A few examples of olefin homo-coupling reactions.

First, the two organic ligands, L4 and L5, were prepared using the reaction between 2,5-dihydroxy terephthalic acid or 2,2'-dihydroxy-[1,1'-biphenyl]-4,4'-dicarboxylic acid and 1-bromopent-4-ene (Figure 6-6). Then they were used for MOF synthesis together with hmtt and zinc nitrate. According to the PXRD (Figure 6-7a), the resulting framework was determined as an isostructural type-S framework, and it is denoted as MUF-80c ($[Zn_4O(hmtt)_{1.33}(L4)_{0.5}(L5)_{0.5}]$). The crystal structure clearly shows the two pentene units attached to the bdc backbone (depicted in green) and bpdc backbone (depicted in pink) (Figure 6-7b). The sharp multiplets (5.5 – 6 ppm) belonging to the terminal alkene in the ^{1}H NMR spectrum of the digested MUF-80c evidences that the terminal alkenes remained intact after MOF formation. (Figure 6-9).

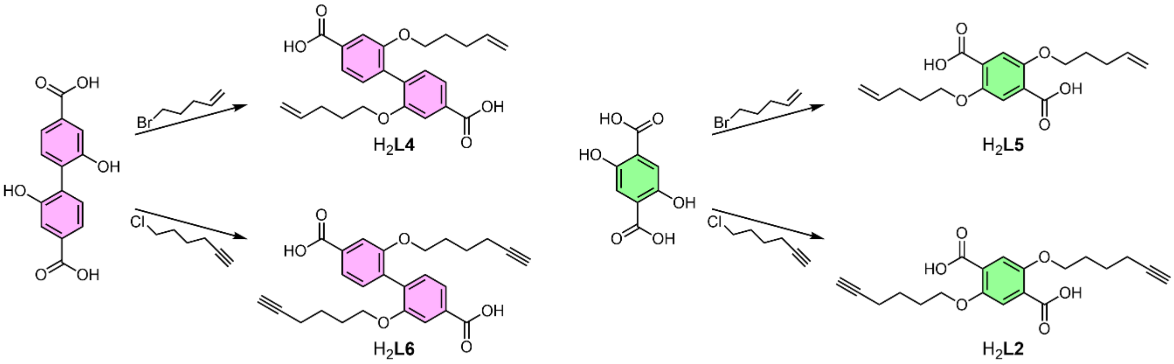

Figure 6-6. A schematic diagram of ligands syntheses for the postsynthetic polymerisation utilising homo-coupling reaction.

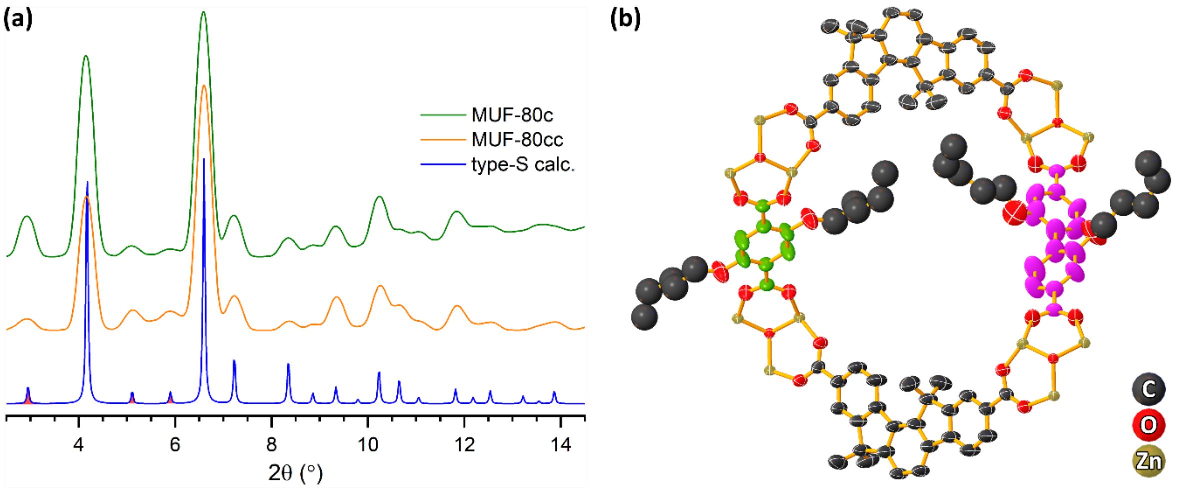

Figure 6-7. (a) PXRD pattern of MUF-80c, MUF-80cc and the calculated type-S framework (the characteristic peaks were filled with red); (b) crystal structure of MUF-80c, pentene chains were modelled with the ball-and-stick model.

Since olefin coupling can be performed using a few different chemical reactions, all the available methods were tested. First, olefin metathesis exploiting Grubbs 2nd generation catalyst (G2C, Figure 6-8) was tested. G2C is a very efficient and versatile catalyst for olefin metathesis due to its tolerance against many chemical functional groups on the alkene substrate and compatibility with a wide range of solvents.[171-173] Therefore, many inter- and intramolecular alkene metathesis reactions using G2C are well developed. As shown in Figure 6-5, both trans and cis isomers are produced as a product of metathesis reaction using ruthenium catalysts.[174-175] However, investigating stereochemistry between trans and cis is not our interest since our goal is synthesising a high degree of polymers comprised the two linear linkers.

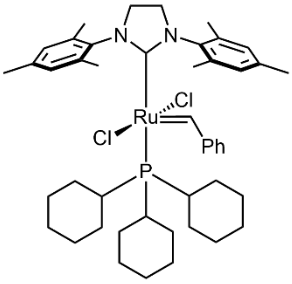

Figure 6-8. Grubbs 2nd generation catalyst (G2C).

Before G2C was directly applied for the postsynthetic inter-ligand olefin metathesis in MUF-80c, a test reaction was performed with styrene to examine the catalytic activity of G2C and establish suitable reaction conditions. The metathesis reaction with styrene was carried out at ambient temperature with less than 1 % of catalyst. The reaction mixture solidified within one hour, and ^{1}H NMR confirmed that the metathesis was nearly complete. Subsequently, the reaction was carried out on MUF-80c itself to connect the bdc and bpdc ligands by metathesis. An increased amount of G2C (approximately 80 % of the catalyst with respect to the number of alkene groups in the MUF-80c sample) was used for three days at room temperature. However, no reaction was observed according to the ^{1}H NMR spectrum of the digested MOF sample (the peaks belonging to the terminal alkenes were still sharp).

It was thought that the bulky G2C struggled to diffuse through the pores in the type-S framework. Therefore, harsher reaction conditions were applied to increase the performance of G2C for the alkene metathesis reaction with MUF-80c. A microwave was used to carry out the metathesis reaction if heating is required since it is facile for a small scale reaction (1-2 mg of MUF-80c). Notable reaction progress was observed according to ^{1}H NMR spectra of the digested MUF-80c and MUF-80cc[d] (Figure 6-9). The alkene metathesis reaction was partially carried out after heating at 80 °C for 18 hours. The most prominent change appears with the peaks belonging to the CH group (5.5 – 6 ppm) and CH_2 (4.8 – 5 ppm) of the terminal alkenes. The intensity of those peaks was reduced to half, and the new peaks were produced at 5 – 5.5 ppm. Moreover, the peaks were slightly broadened, and new peaks were generated at both aromatic and aliphatic regions. This indicates that the metathesis reaction partially occurred with MUF-80c, and approximately a half number of alkenes were reacted based on the peak integrals of the remaining unchanged peaks.

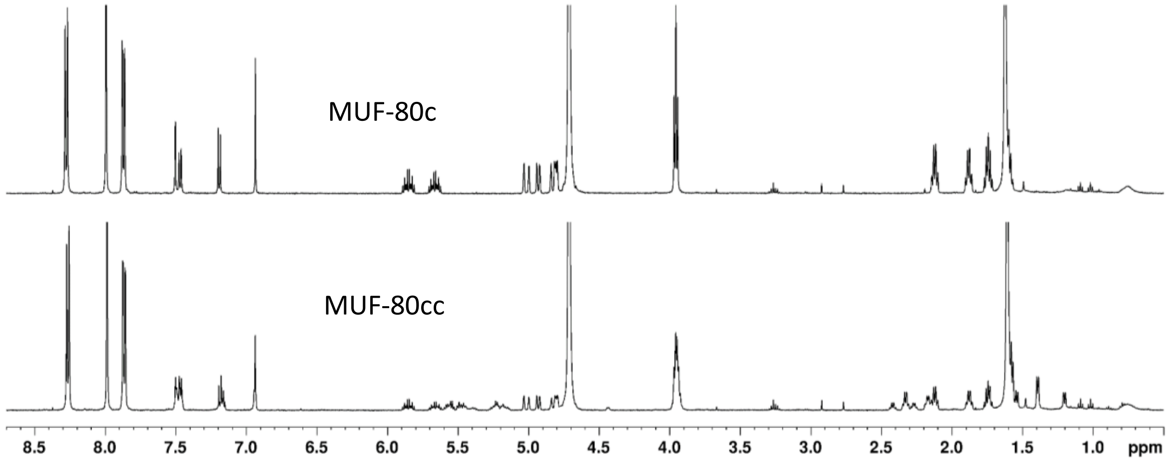

Figure 6-9. ^{1}H NMR spectra of MUF-80c and MUF-80cc.

However, the alkene metathesis reaction within MUF-80c did not further progress to completion even though harsh reaction conditions were applied. The reason why the reaction progress stops at a certain point is considered as follows. The alkene metathesis reaction is supposed to begin in the outmost crystal lattice as the G2C diffuse slow from outside due to its large size. However, the metathesis reaction rate would be slowed down as the reaction progresses. After the metathesis reaction, the linked chain will slow down the working catalyst molecules diffusing through the pores since the pore-C is divided by the linked chain. Or, catalyst units could be locked in the pores in the worst case. Furthermore, significantly more alkyl chains are produced by the coupling reactions, the barrier for a fresh catalyst to

---

[d] The suffix c was used to refer to the crystal samples after click reaction indicating 'clicked' or 'connected' in chapter 5. However, the same notation is used here to refer the crystal samples after polymerisation reaction as a meaning of 'connected', instead of introducing a new notation.

enter the MUF-80c crystal increases, and the reaction rate will drop.

Although the alkene metathesis reaction using G2C has a limit due to its size, positive outcomes were observed. Hence, other alternative reaction mechanisms using a smaller catalyst or no catalyst were sought for the alkene homo-coupling reaction. Quite a few reactions were tested after literature research, but none of them was successful. For instance, $W(CO)_6$, another reported catalyst for the olefin metathesis under UV radiation in CCl_4,[176-177] zirconocene with MAO (methylalumoxane) for the olefin dimerisation reaction,[178-179] or [2+2] cyclisation reaction using UV radiation or heating were tested.[180] However, none of them exhibited any sign of progress in the coupling reaction, so this approach was abandoned.

6.2.1.2. **Alkyne-alkyne coupling reactions**

The homo-coupling reaction of the two terminal alkynes to form a dialkyne, known as a Glaser coupling reaction, has long been recognised and extensively used.[181-183] The slightly modified versions of this reaction were also well known as the Eglinton reaction or Hay coupling reactions.[184] These alkyne-alkyne coupling reactions utilise copper catalysts with oxidants (usually O_2 gas) if necessary, and the reaction conditions are relatively mild. Therefore, they are suitable for the postsynthetic polymerisation reaction within MUF-77 frameworks.

Bdc derivatives with terminal alkynes (L2 and L3) were already introduced and used in Chapter 5, so only the bpdc derivative with terminal alkyne needed to be synthesised. Hence, H_2L6 in Figure 6-4b was prepared by the coupling reaction of 2,2'-dihydroxy-[1,1'-biphenyl]-

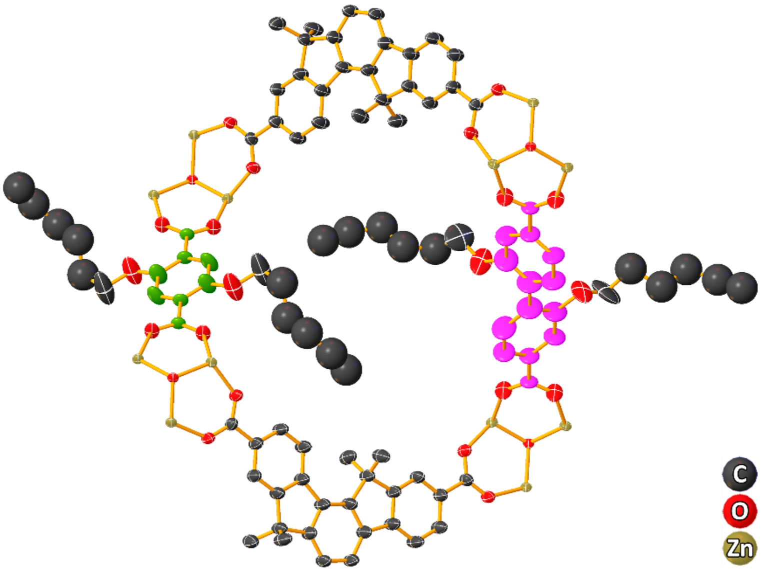

Figure 6-10. The crystal structure of MUF-80d. The hexyne chains, which are attached to bdc backbone (green) and bpdc backbone (pink), are clearly shown.

4,4'-dicarboxylic acid and 1-chlorohexa-5-yne (Figure 6-6). H_2L6 successfully formed a prismatic crystal together with L2, hmtt and zinc nitrate. The resulting framework, MUF-80d ($[Zn_4O(hmtt)_{1.33}(L6)_{0.5}(L2)_{0.5}]$), was determined as an isostructural type-S framework with PXRD (Figure 6-11b) and the presence of L2 and L6 in the framework were confirmed with ^{1}H NMR (Figure 6-12a). The long alkyl chains decorated with the terminal alkyne on both L2 and L6 were also shown in the single-crystal structure. Some atoms on the alkyl chains were modelled with the ball and stick model since they have a huge degree of freedom, and a few restraints were also applied due to their flexibility and positional disorders (Figure 6-10).

Once the structural integrity of MUF-80d was confirmed with the presence of both L2 and L6, suitable alkyne-alkyne homo-coupling reaction conditions were searched. Since the long history and extensive study of Glaser coupling, there are a wide variety of modified reaction conditions.[183] However, the postsynthetic alkyne-alkyne coupling reaction needs to occur between two immobile alkyne chains in a constricted space of the type-S framework. Therefore, the catalyst needs to be soluble in the reaction medium (non-aqueous) and small enough to diffuse freely through the framework. For this reason, we decided to use a copper complex composed of Cu(I) salt and N-donor ligands. This type of reaction is well acknowledged as Glaser-Hay coupling, and TMEDA (*N,N,N',N'*-tetramethyethylenediamine) is the most widely used ligand for a copper catalyst preparation.[185-186] Based on the test reaction with phenylacetylene, the results were nearly the same when TMEDA or DMEDA

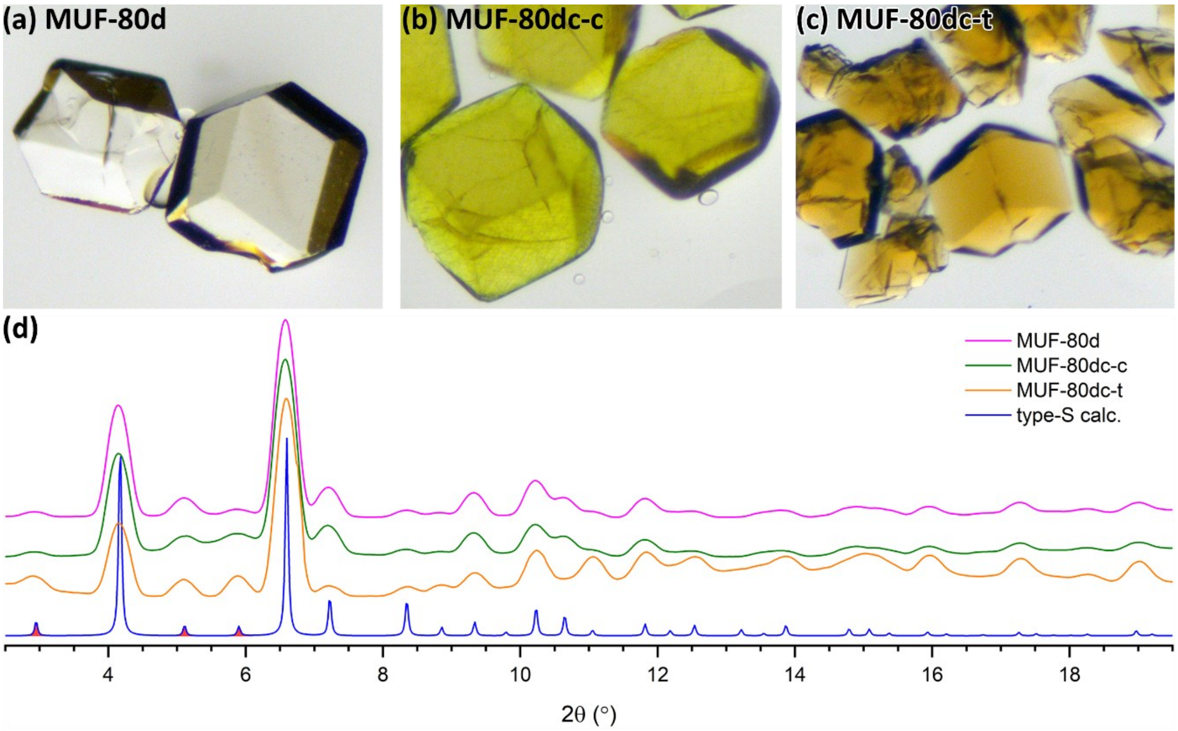

Figure 6-11. (a-c) The optical microscopy images of MUF-80d and its derivatives; (d) PXRD patterns of MUF-80d and derivatives after polymerisation reaction. The charateristic peaks of type-S framework were filled with red.

(*N,N'*-dimethylethylenediamine) was used, so DMEDA was used for the rest of the reactions due to its smaller size.

A test reaction with phenylacetylene was conducted homogeneously under mild conditions (in acetone with 5 mol % catalyst at room temperature), and more than 90 % of starting material was consumed to form a dimer within five hours (section 6.4.2.2). However, nothing happened when the same conditions were applied to MUF-80d, even with a higher catalyst loading and extended reaction time (3 days). Hence, various modified reaction conditions were tested for the postsynthetic alkyne homocoupling reaction in MUF-80d, and one of the reactions conducted with microwave showed some positive sign of polymerisation.

The reaction was carried out in DEF to reach a higher temperature, and O_2 gas was bubbled through before the microwave vessel was capped, and the reaction mixture was heated to 150 °C for 3 hours with a microwave. The crystal after alkyne-alkyne coupling reaction using catalyst was denoted as MUF-80dc-c. The sharp peaks in the PXRD patterns of the MUF-80dc-c bulk sample indicate the crystallinity was well maintained even after the reaction under harsh condition (Figure 6-11b). However, the colourless crystal turned into intense green, indicating transmetalation occurred within the framework. That is, the zinc(II) ions of the framework were replaced by copper(II) (Figure 6-11a).

The ^{1}H NMR spectrum collected with the digested MUF-80dc-c clearly showed a positive sign of polymerisation (Figure 6-12b). Since different NMR solvent used for the MUF-80dc-c

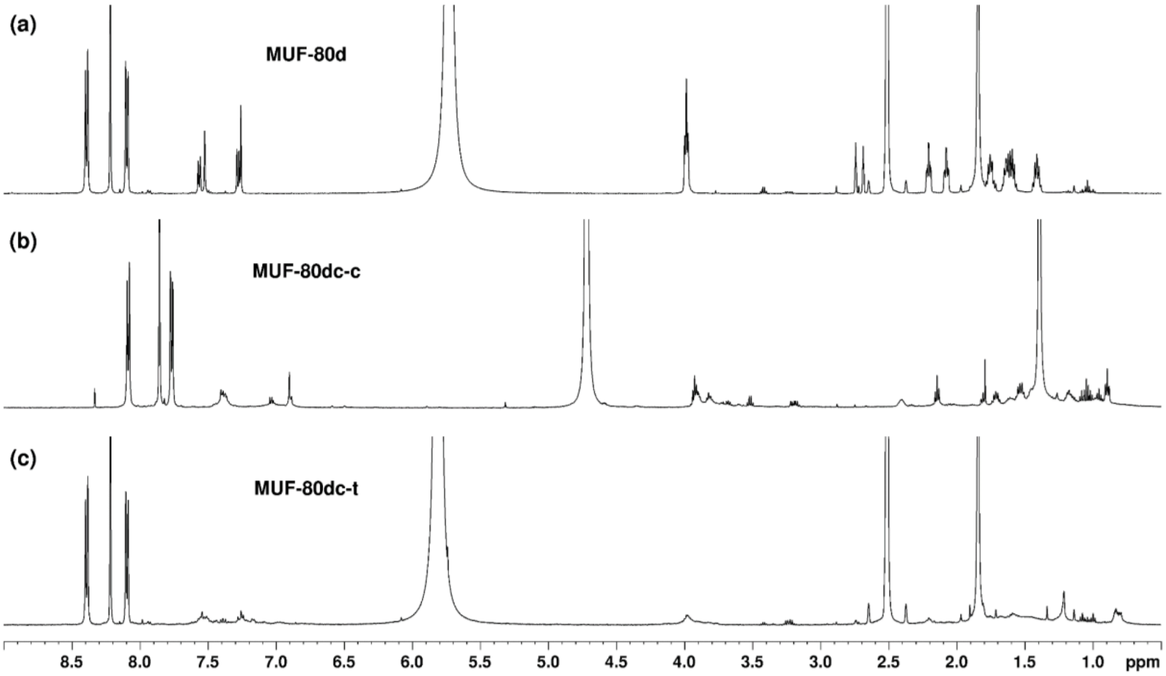

Figure 6-12. ^{1}H NMR spectra of (a) MUF-80d, (b)MUF-80dc-c, after Glaser coupling reaction and (c) MUF-80dc-t, coupled by heating. The NMR samples were prepared by dissolving crystals in either DMSO-*d6*/DCl mixture (for a and c) or NaOD/D_2O mixture (for b).

sample, the direct comparison between MUF-80d (Figure 6-12a) and MUF-80dc-c is not available. The peaks belonging to L2 and L6 became broadened while the peaks belonging to hmtt still remained sharp. This indicates that the desired coupling reaction between L2 and L6 occurred and produced a different degree of polymer chains which caused the peak broadening. However, some portions of sharp peaks still remain, which indicate the alkyne-alkyne coupling reaction was not fully carried out in all available sites. Thus, the harsher reaction conditions were applied by adjusting catalyst loading, temperature, or duration of the reaction, but not much improvement was achieved. On the other hand, the peaks belonging to L2 and L6 were broadened more in a few cases, but the crystals turned to opaque, and the crystallinity was lost in such cases.

Meanwhile, an alternative alkyne-alkyne coupling reaction method was tested. According to Peng *et al.*, intramolecular [2+2] thermal cycloaddition reaction was carried out between the two alkyne groups in proximity, resulting in cyclobutadiene.[187] Although the product containing cyclobutadiene could not be isolated due to its unstable and highly reactive nature, its presence was proved by a trapping experiment with cyclopentadiene derivatives to produce a Diels-Alder adduct (Figure 6-13). The key to the alkyne-alkyne [2+2] thermal cycloaddition is the close proximity with a reactive conformation between the two alkynes.

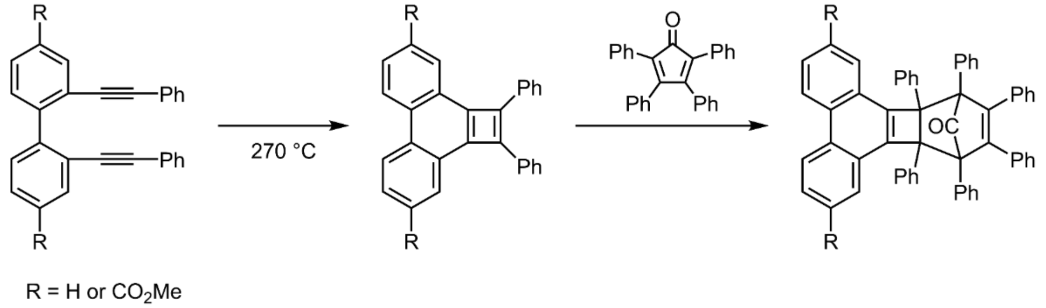

Figure 6-13. A schematic diagram of intramolecular alkyne-alkyne [2+2] cycloaddition; the formation of cyclobutadiene species was proved with a trapping experiment with cyclopentadiene derivatives to give rise to the Diels-Alder adduct.

Considering the distance between the two linear linkers (L2 and L6) in MUF-80d and the length of alkyne chains on them, such a reactive orientation seems feasible in MUF-80d. The crystal structure of MUF-80d also shows that the two alkynes can be in proximity (Figure 6-10). Furthermore, the thermal stability of the framework was well maintained up to almost 400 °C according to TGA analysis (Figure 6-14). Therefore, a milligram-scale thermal coupling reaction was carried out with MUF-80d using the TGA apparatus. Due to the instability of desolvated MUF-80d crystal, a solvated crystal sample in n-hexane was directly heated to a target temperature under N_2 flow and held at the temperature for a while. After

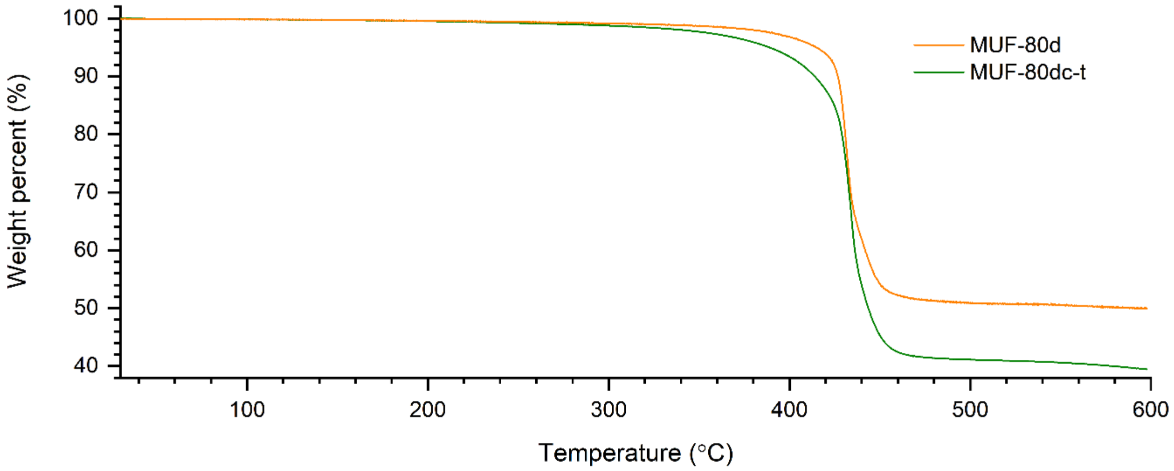

Figure 6-14. TGA analyses of MUF-80d and MUF-80dc-t after the alkyne-alkyne [2+2] thermal cycloaddition reaction.

heating, the crystal sample was then digested in the NMR solvent, and the polymerisation reaction progress was determined using the peak shapes and positions in the ^{1}H NMR spectrum. After a few test reactions, peak broadening was observed when the crystal was heated to 300 °C for 3 hours (Figure 6-12c); the crystal after the thermal coupling reaction was denoted as MUF-80dc-t. The PXRD indicated that the crystallinity remained intact, though the colour of the crystal changed to intense orange (Figure 6-11c and d).

According to the crystal structure of MUF-80dc-t, the presence of alkyl chains on L2 and L6 was evidenced (Figure 6-15). The first five carbon atoms (C44 – C48) attached to the bdc backbone and the first three carbon atoms (C26 – C28) on the bpdc backbone were relatively easily assigned. The rest of the atoms on the chains were then assigned by applying the solvent mask (in Olex2[120] software) for the refinement process. The electron density in void space is ignored if the solvent mask is applied (the solvent mask is usually used to hide solvent molecules that are unknown or hard to assign properly, and the error between the collected data and structure gets lowered). Therefore, only the electron density in the proximity of the existing structure is shown. As a result, the weak electron density, which corresponds with the carbon atoms on the rest of the chain, became visible so that they could be assigned.

The SCXRD data was converged with the presented structure in Figure 6-15. However, an interesting feature was noted regarding the arrangement of the four carbon atoms (the two terminal carbon atoms of each chain, labelled as C30, C31, C48 and C49). The structure suggests that the cyclobutadiene could be a product of the thermal coupling reaction of the two terminal alkynes, as the possible reaction mechanism indicated in Figure 6-15. However, cyclobutadiene is known as impossible to be isolated due to its strong reactivity.[188-189] Even though it is formed, side reactions could happen during sample handling, like reacting with

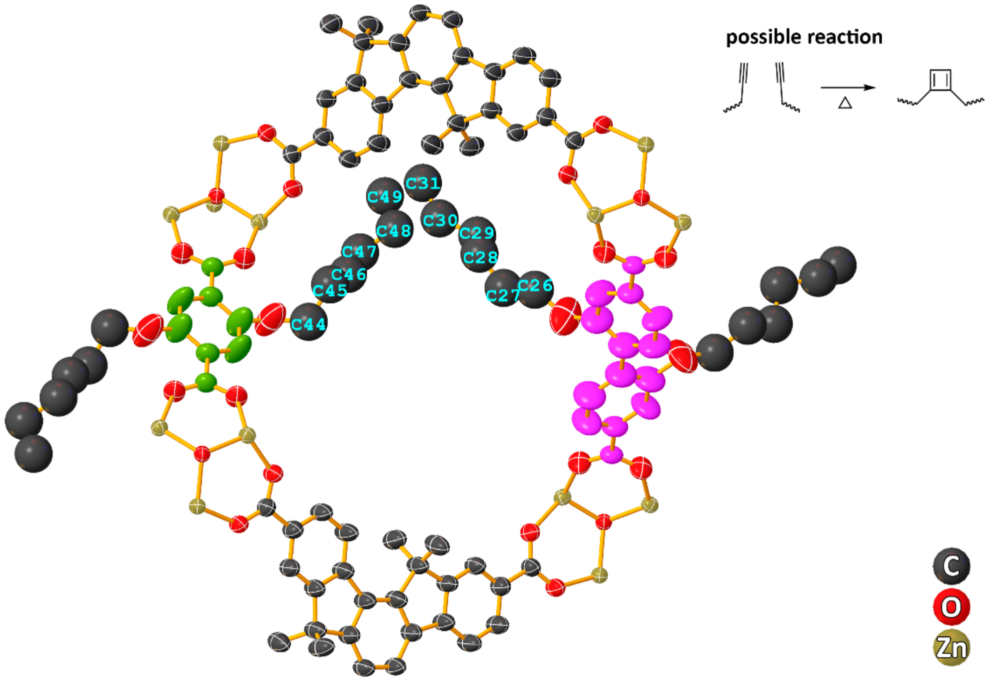

Figure 6-15. Crystal structure of MUF-80dc-t. The cyclobutadiene consisting of C30, C31, C48 and C49 was modelled based on the arrangement of those carbon atoms.

atmospheric moisture. Therefore the chains were left unconnected as they appeared even though the two terminal atoms of each chain were in close proximity as if they were connected because the exact product is unknown. Nevertheless, based on the crystal structure, cyclobutadiene is our best approximation for the functional group linking the two alkyl chains. Other characterisation methods must be carried out to identify the real functional group.

Gas physisorption measurement experiments were carried out with a bulk sample of MUF-80d before and after thermal coupling reaction. A set of gas physisorption measurements with various gasses was carried out with a fresh MUF-80d sample. The same sample was then directly heated using the gas sorption instrument, and another set of gas physisorption experiments was straight carried out. The sorption sample cell was heated to 300 °C over 24 hours, and the crystal sample was carefully handled to minimise exposing to the atmosphere.

Based on the N_2 adsorption isotherm measurement at 77 K, the total pore volume and BET surface area were calculated, and the results were presented in Figure 6-16a. The isotherm curves of both frameworks were nearly identical regarding the total uptake and shape. As a result, they both have almost identical total pore volume and BET surface area values. The pore size distributions (PSD) of pore-C in each framework were also calculated using DFT methods (Figure 6-16b). Since it is also calculated from the N_2 adsorption data at 77 K, the PSD of MUF-80d did not change much after the thermal coupling reaction.

(a)

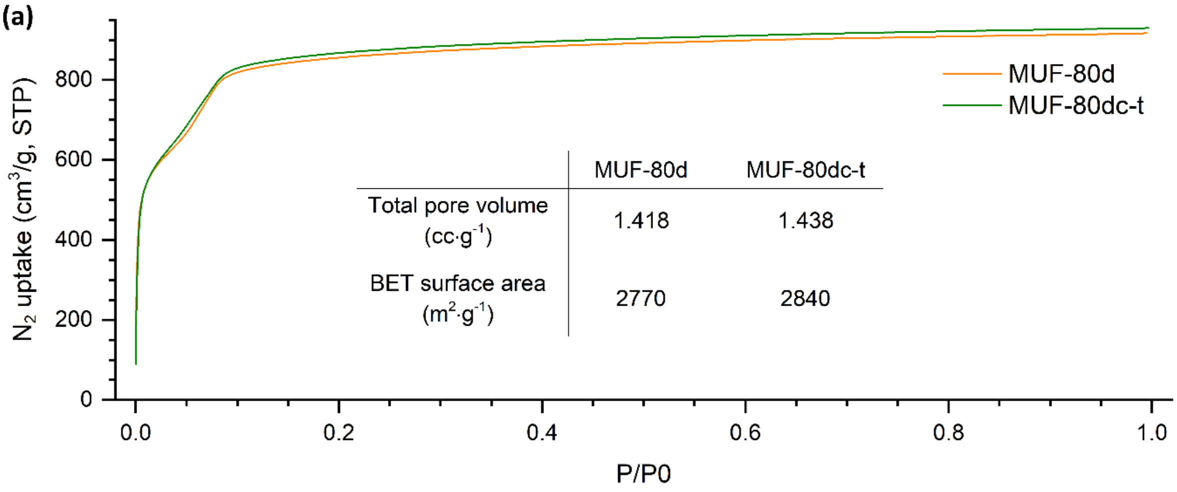

	MUF-80d	MUF-80dc-t
Total pore volume ($cc{\cdot}g^{-1}$)	1.418	1.438
BET surface area ($m^2{\cdot}g^{-1}$)	2770	2840

(b)

	Position of centre (Å)	FWHM (Å)	Area
MUF-80d	9.82	2.16	0.209
MUF-80dc-t	10.2	2.16	0.211

(c)

	CH_4 (kJ·mol^{-1})	CO_2 (kJ·mol^{-1})	C_2H_4 (kJ·mol^{-1})	C_2H_6 (kJ·mol^{-1})
MUF-80d	12.2	19.8	17.0	19.9
MUF-80dc-t	10.4	17.1	18.8	20.1

Figure 6-16. (a) N_2 adsorption isotherm at 77K and the total pore volume and BET surface area of MUF-80d and MUF-80dc-t;(b) the pore size distributions of pore-C in each framework; (c) The isosteric heats of adsorption of CH_4, CO_2, C_2H_4 and C_2H_6 at zero loading in kJ·mol^{-1}.

In addition, various gas adsorption isotherms at 273 and 293 K were measured with both frameworks. The heats of adsorption (Q_{st}) for the selected gasses were then calculated based on these adsorption data. The Q_{st} values did not change much after heating, indicating that the affinity toward the corresponding adsorbate remained almost the same after the thermal coupling reaction (Figure 6-16c).

The results from various analyses, especially ^{1}H NMR and IR spectroscopy, of MUF-80dc-t indicate some form of change definitely occurred after thermal coupling reaction. However, the type of product resulted from the alkyne-alkyne thermal coupling reaction is unclear. Although cyclobutadiene is known as a product, and the crystal structure also shows a similar structure to cyclobutadiene, it is unlikely to be the product due to its high reactivity. Other experiments were conducted to figure out the functional group linking the two chains. Raman spectroscopy was used to see any information about the functional group, but the signal was too weak, and the framework produced too much noise since it is fluorescent. Bromination of alkene was also tried just in case cyclobutadiene is presented in the framework. A crystal sample was soaked in a dilute Br_2 solution for a few hours, and SCXRD was then measured to see if Br atoms are presented in the framework. The Br atoms could be easily detected in a crystal structure due to their high electron density if the bromination reaction occurred. However, this experiment did not work, either.

6.2.1.3. **Guest-mediated coupling**

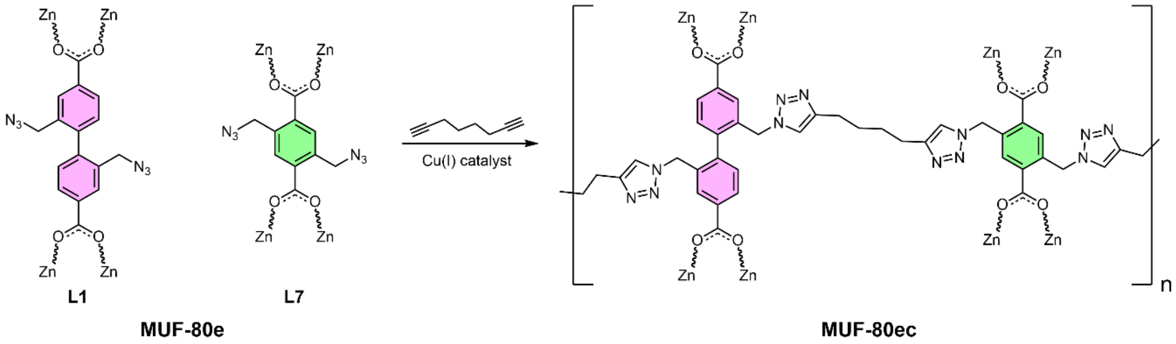

Figure 6-17. A schematic diagram of guest-mediated coupling reaction utilising the azide-alkyne click reaction.

The first two polymerisations utilised the direct homocoupling reaction between the two alkenes or alkynes. Unlike these two experiments, a guest molecule will be utilised to couple the two linear linkers in this section (Figure 6-3). The inter-ligand azide-alkyne click reaction is exploited again, as its application was successfully demonstrated in the type-S framework in Chapter 5. As shown in Figure 6-17, the two linear linkers are equipped with two azides, and they are linked using azide-alkyne click reaction with a guest molecule functionalised with two terminal alkynes.

The azide equipped bdc derived linker, H_2L7, was prepared by a simple substitution reaction of 2,5-bis(bromomethyl)terephthalic acid with sodium azide.[163] It was then paired with H_2L1, which was already introduced in chapter 5, to form a framework together with hmtt and zinc nitrate. The resulting crystal was named MUF-80e ($[Zn_4O(hmtt)_{1.33}(L1)_{0.5}(L7)_{0.5}]$) and analysed using various characterisation methods.

X-ray diffraction was used to determine the structure of as-synthesised MUF-80e. PXRD proved that MUF-80e is a type-S framework since it shows all the characteristic peaks of the type-S framework (Figure 6-18a). The crystal structure also clearly shows both L1 and L7, equipped with two azide moieties, were incorporated into the type-S framework (Figure 6-18b). The presence of both L1 and L7 with an equimolar ratio was also evidenced with the ^1H NMR spectrum (Figure 6-21). The IR spectrum of MUF-80e possesses an intense peak at 2100 cm^{-1} which emanates from the azide group.

1,7-Octadiyne was selected as a complementary pair guest molecule due to its optimum

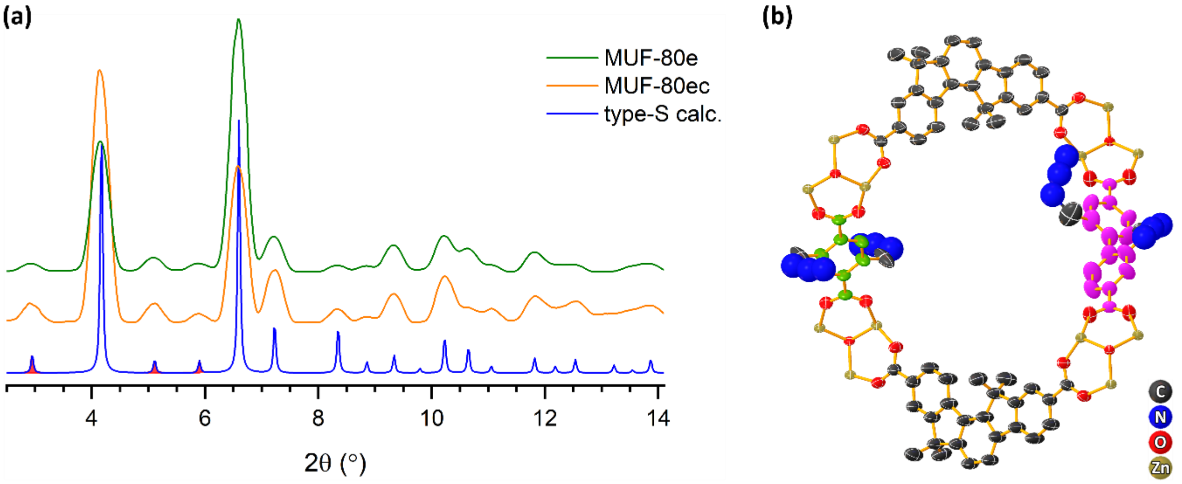

Figure 6-18. (a) PXRD patterns of MUF-80e and MUF-80ec; the characteristic peaks of type-S framework are filled with red. (b) The crystal structure of MUF-80e; two pairs of azide groups attached to each linear linker are clearly shown.

length to link L1 and L7 in MUF-80e. However, unlike the azide-alkyne click reaction between L1 and L3 exhibited in Chapter 5, polymerisation using a guest molecule has more potential factors which prevent increasing the degree of polymerisation. Theoretically, the length of the polymer chain composed of L1 and L3 is limited by the crystal size if the ligands were pure and the framework was built without disorders or defects. The two linkers, L1 and L3, are alternating along the crystallographic axes and functionalised with complementary chemical groups. Thus, the coupling reaction between L1 and L3 could be carried out in all available sites if the reaction conditions were met.

In contrast, the degree of the polymerisation reaction is highly dependent on a few parameters in the case of MUF-80e, such as the number of guest molecules or reaction rate. For instance, the two azide groups facing each other in pore-C could be linked or remain free. Alternatively, they could each be linked with a separate individual guest molecule if the number of guest molecules in their proximity is high (Figure 6-19). This reaction would not result in polymerisation. Moreover, even if the optimum amount of guest molecule was

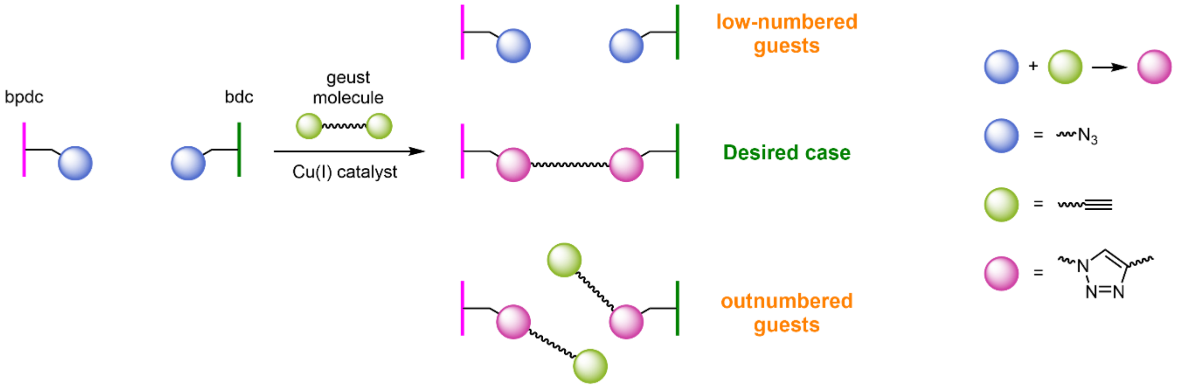

Figure 6-19. Schematic visualisation of the three different outcomes from the guest mediated coupling reaction.

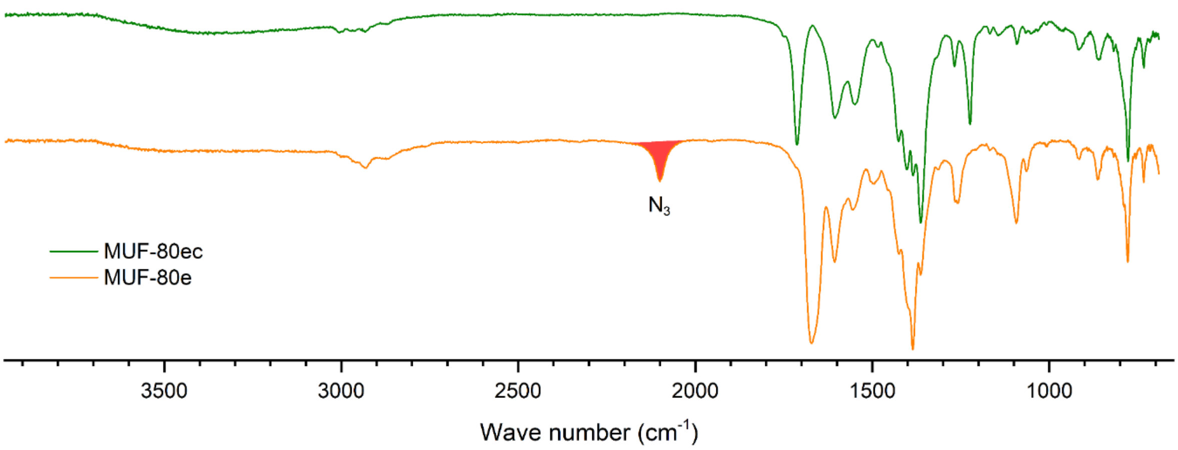

Figure 6-20. IR spectra of MUF-80e and MUF-80ec. The characteristic peak belonging to azide were disappeared after the azide-alkyne click reaction.

introduced, the two azide groups in the same pore can be clicked with a separate alkyne guest. Therefore, the amount of catalyst and controlling the reaction rate is also essential.

Various reaction conditions were therefore tested for the azide-alkyne click reaction between MUF-80e and 1,7-octadiyne. The reactions were conducted with different loading of the octadiyne guest and catalyst, and the completion of the reaction was monitored using IR spectroscopy (Figure 6-20). The optimum reaction condition was found after several trials. The MUF-80e crystal samples were soaked in a mixture of dioctyne and DMF solution (10 % v/v) for an hour at 60 °C. Then, CuI·P(OEt)$_3$ solution in DMF (approximately 2.5 eq. per azide) was added as a catalyst after removing the dioctyne solution by decantating. The reaction vessel was then placed in an isothermal oven of 100°C overnight. The crystal after the reaction, MUF-80ec, was then analysed with various characterisation methods, and the results before and after the azide-alkyne click reaction were compared.

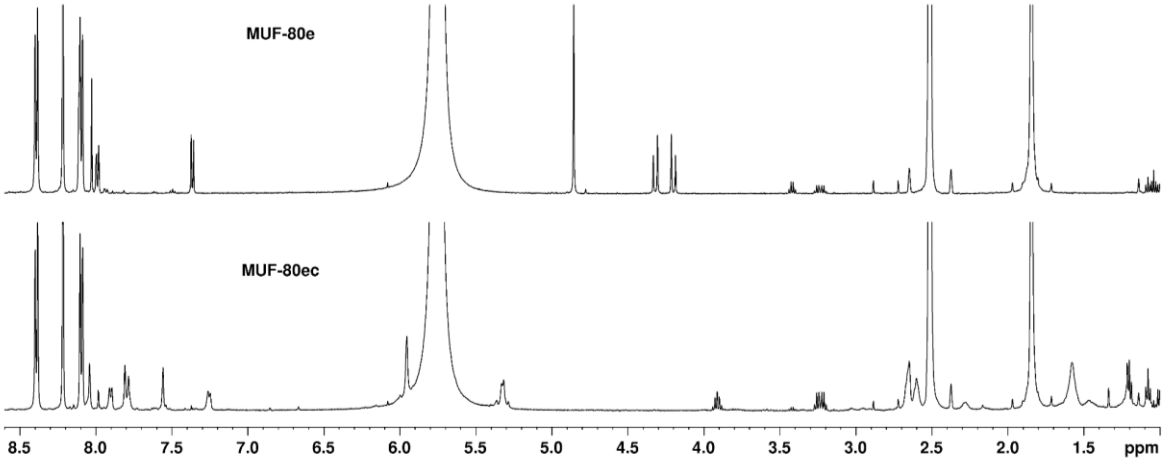

Figure 6-21. The ^{1}H spectra of MUF-80e and MUF-80ec. The sharp peaks of the bridging methylene (4 – 5 ppm) were shifted to (5 – 6 ppm) and the peaks belonging to L1 and L7 were slightly broadened after the click reaction with guest molecule.

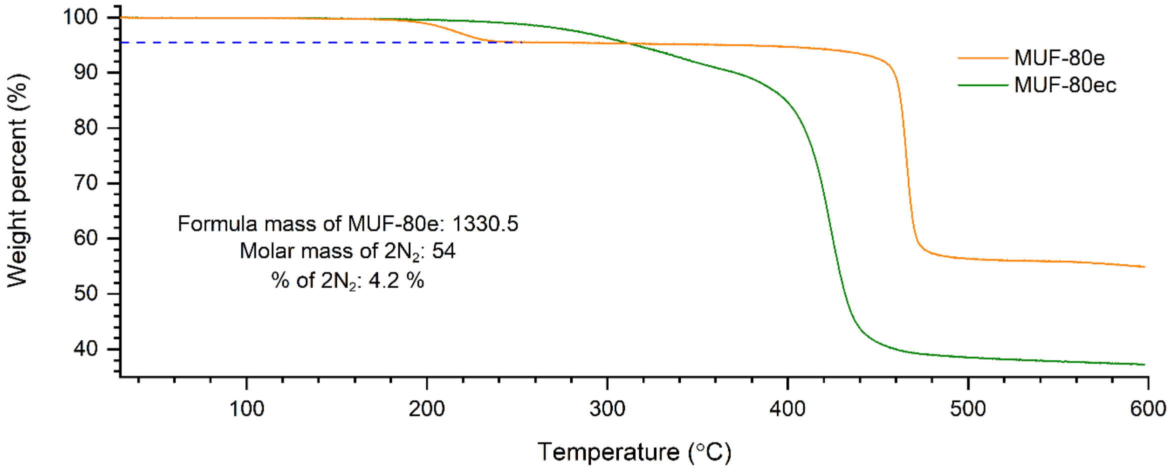

Figure 6-22. TGA analyses of MUF-80e and MUF-80ec after the azide-alkyne click reaction with the guest component, dioctyne.

The differences in the ^{1}H NMR spectra of MUF-80e and MUF-80ec clearly indicated that the azide-alkyne click reaction occurred with the octadiyne guest (Figure 6-21). The peaks belonging to L1 and L7 in the aromatic area of digested MUF-80e are all shifted in MUF-80ec, and the peaks belonging to the methylene group around 4-5 ppm all moved to 5-6 ppm.[159] Moreover, the newly formed broad aliphatic peaks at 1.6 and 2.6 ppm is evidence of the newly added bridging alkyl chain between the two triazole units.

The TGA analysis is also useful in this case to show the completion of the azide-alkyne click reaction (Figure 6-22). Since both bpdc and bdc were equipped with two azide groups, the weight percentage of losing N_2 by thermolysis of the azide group is relatively large (4.2 weight %) and explicitly shown in the TGA analysis. Two N_2 gas molecules are thermalised from L1 and L7 from each formula unit of MUF-80e ($[Zn_4O(hmtt)_{1.33}(L1)_{0.5}(L7)_{0.5}]$), and the weight loss at around 200 °C in the TGA plot of MUF-80e coincide with the mass percentage of two N_2 gas molecules being lost from each formula unit. On the other hand, no weight loss due to azide thermolysis evident in MUF-80ec (Figure 6-22). However, the gradual weight loss was seen from approximately 200 °C, indicating the overall thermal stability was decreased. It is thought that the decrease in thermal stability of MUF-80ec was probably caused by the stress during the azide-alkyne click reaction.

The MUF-80ec crystal images from both optical microscope and SEM (Figure 6-23) show that the crystal samples possess deep cracks and small holes on the crystal, which also exhibits that the crystal samples received stress during the azide-alkyne click reaction. However, the PXRD pattern (Figure 6-18a) shows that the crystallinity was well maintained despite the partial structural damages.

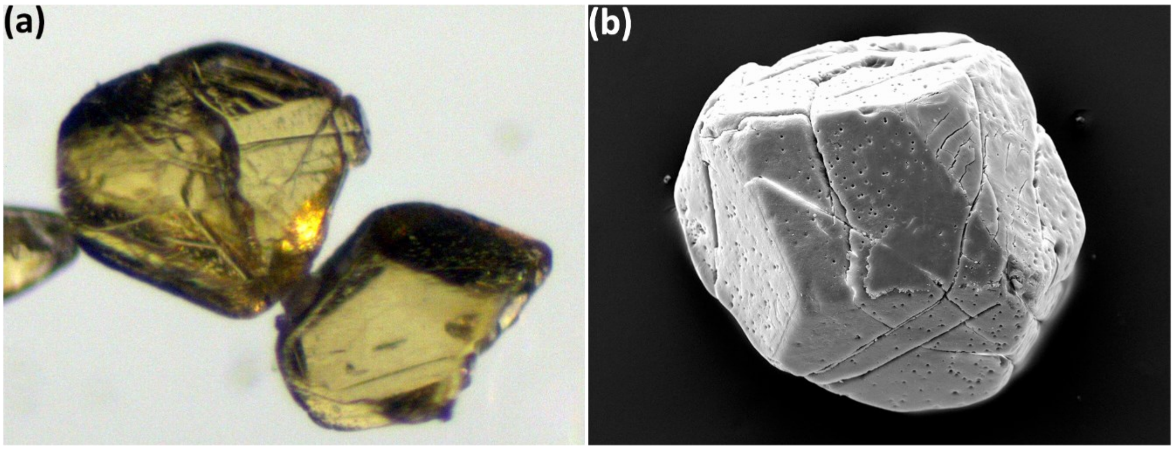

Figure 6-23. (a) Optical microscopy image and (b) SEM image of MUF-80ec. Cracks and holes were noted, indicating the stress during the click reaction.

Despite the stress applied to MUF-80ec crystal samples, the collected

SCXRD data set was good enough to solve the crystal structure. The crystal structure presented a set of relatively strong electron density peaks that corresponds to the triazole rings of each linker. However, the carbon atoms linking the two triazole rings could be assigned after the solvent mask was applied due to their low electron density.

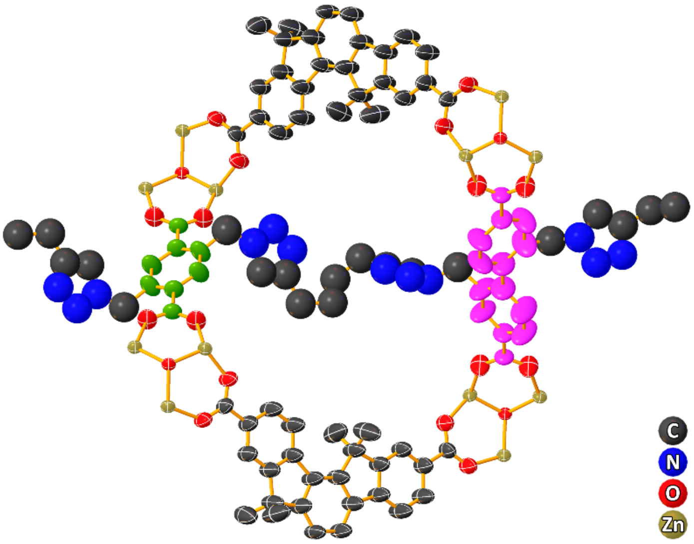

Figure 6-24. The crystal structure of MUF-80ec.

The gas physisorption results well illustrate both physical and chemical changes after the azide-alkyne click reaction. The total N_2 uptake (77 K, 1 bar) was significantly dropped (approximately from 1000 to 700 cc/g) after the guest-mediated click reaction. Consequently, a reduction of both the BET surface area and total pore volume was followed (Figure 6-25a). Although the partial structural damage could cause such reductions, it is reasonable that the pore volume in MUF-80e was reduced by the covalently added dioctyne guest.

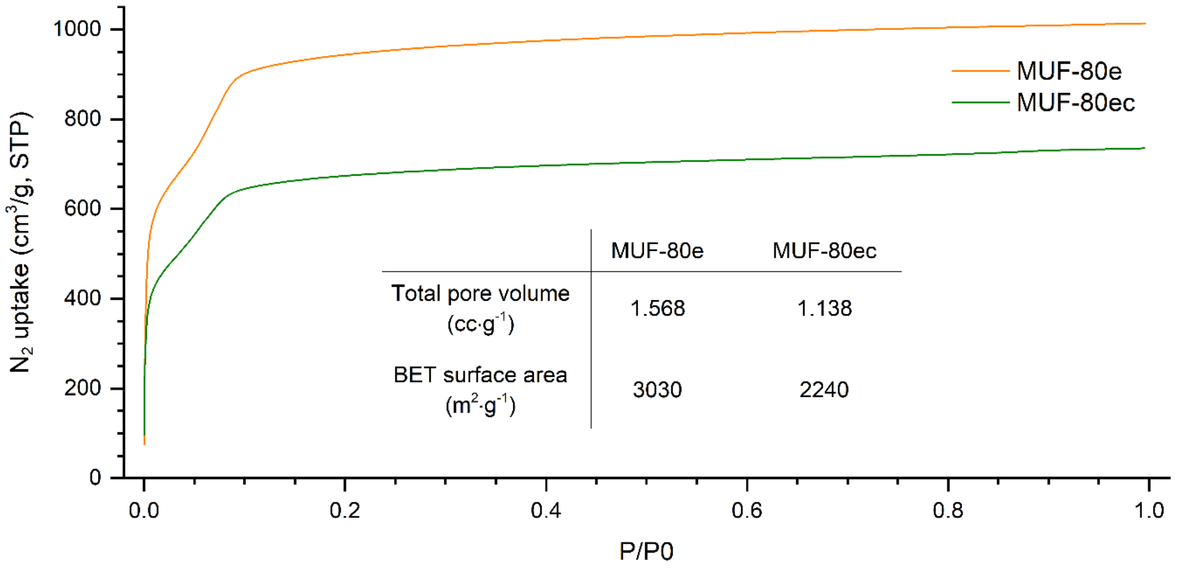

	MUF-80e	MUF-80ec
Total pore volume (cc·g^{-1})	1.568	1.138
BET surface area (m^2·g^{-1})	3030	2240

Figure 6-25. (a) N_2 adsorption isotherm at 77K and the total pore volume and BET surface area of MUF-80e and MUF-80ec;(b) the pore size distributions of pore-C in each framework; (c) The isosteric heats of adsorption of CH_4, CO_2, C_2H_4 and C_2H_6 at zero loading in kJ·mol^{-1}.

The pore size distributions of MUF-80e and MUF-80ec also agree with such reasoning. As depicted in Figure 6-26, notable changes were observed with the pore size distribution of the two frameworks. The first peak shown around 8 – 12 Å represents the PSD of pore-C, and a significant change is shown after the guest-mediated click reaction. According to the peak shape, the average pore size decreased (the peak was shifted to the left), and the peak width got narrow, indicating that the size of pore-C became uniform. The statistics (the table in Figure 6-26) induced from the Gaussian fit of the PSD curve for pore-C in each framework are also coincident with the observation above. The PSD change after the click reaction

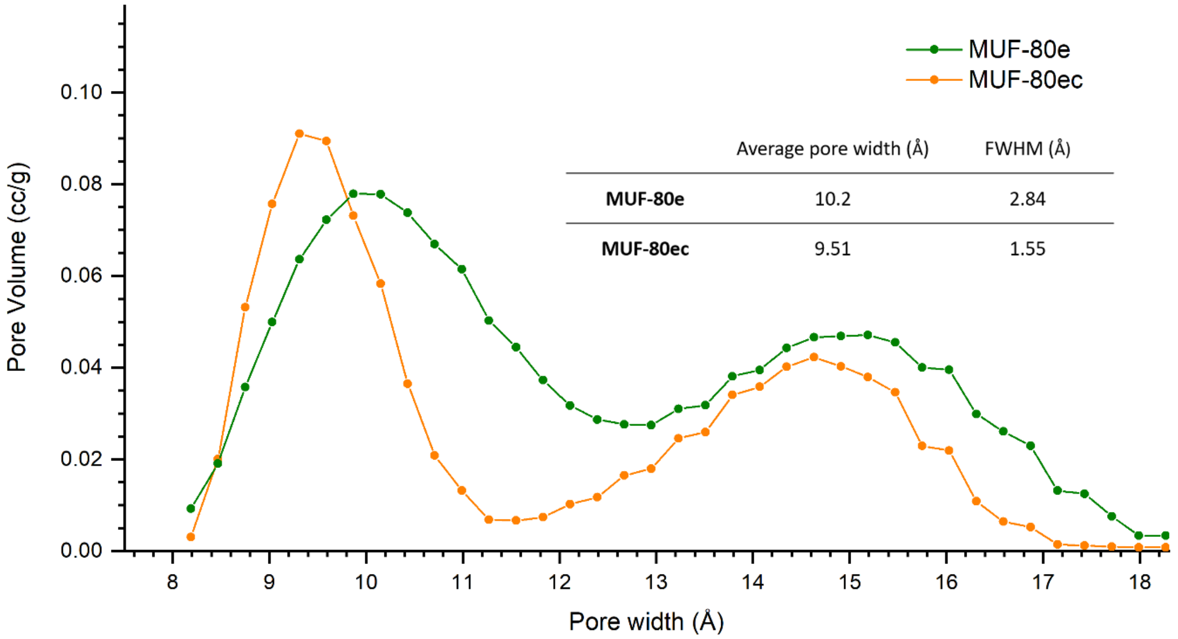

	Average pore width (Å)	FWHM (Å)
MUF-80e	10.2	2.84
MUF-80ec	9.51	1.55

Figure 6-26. The poresize distribution of MUF-80e and MUF-80ec. The statistics from the Gaussian fit for pore-C were also presented.

indicates that the two dangling azide moieties placed in pore-C are tied with dioctyne guest, resulting in a reduced pore volume with little variation. However, the pore size reduction also appears in pore-A and -B, and it could be caused by the half-clicked flexible dioctyne chain that can freely rotate around the linear linker backbone.

The isosteric heats of adsorption (Q_{st}) for CH_4, CO_2, C_2H_4 and C_2H_6 were calculated for MUF-80e and MUF-80ec based on the two different adsorption measurements at 273K and 293K. The Q_{st} values illustrate that the affinity toward the adsorbates, CO_2, C_2H_4 and C_2H_6, were notably increased. The newly introduced triazole rings are the main cause of this.

Table 6-1. The isosteric heats of adsorption of CH_4, CO_2, C_2H_4 and C_2H_6 at zero loading in kJ·mol^{-1}. Two adsorption measurements at two different temperatures, 273 K and 293 K, were used for the calculation.

	CH_4 (kJ·mol^{-1})	CO_2 (kJ·mol^{-1})	C_2H_4 (kJ·mol^{-1})	C_2H_6 (kJ·mol^{-1})
MUF-80e	5.00	14.3	16.2	17.7
MUF-80ec	4.79	17.3	20.2	20.1

6.3. Conclusion

In this chapter, three different postsynthetic coupling reactions between the two different linear ligands were introduced to synthesise sequence-specific polymers. Since the two monomers (linear linkers) are functionalised with the same chemical pendent, their sequence will be random in a homogeneous polymerisation reaction. However, a novel strategy of using a MOF scaffold to arrange the two monomers in a controlled manner make such challenging polymer synthesis an achievable target.

Unfortunately, the polymerisation using alkene-alkene coupling reaction did not show much progress. Nevertheless, in the other two cases, utilising alkyne-alkyne coupling reaction or guest-mediated azide-alkyne click reaction, some degree of polymerisation reaction was proved by various characterisation methods. However, more analyses, such as mass spectrometry or gel permeation chromatography, need to be conducted to confirm whether the polymerisation reaction occurred and determine the chain length of the polymers.

6.4. Experimental section

Syntheses, gas physorption and ^{1}H NMR data are presented in Appendix D.

6.4.1. General procedures

All starting materials and solvents were used as received from commercial sources without further purification unless otherwise noted. H_2L7 (2,5-bis(azidomethyl)terephthalic acid) was prepared with the known procedure.[163]

Column chromatography was carried out on silica gel (grade 60, mesh size 230-400, Scharlau).

The IR spectroscopy data were collected using ThermoFisher Nicolet 5700 equipped with Smart iTR™ Attenuated Total Reflectance (ATR) Sampling Accessory and processed with OMNIC™ Specta Software.

NMR spectra were recorded at room temperature (unless otherwise noted) on Bruker-500 Avance instruments, with the use of the solvent proton as an internal standard.

All powder X-ray diffraction measurements were carried out on either Rigaku Spider or Bruker D8 Venture. Rigaku Spider X-ray diffractometer is equipped with CuKα radiation (Rigaku MM007 microfocus rotating-anode generator), monochromated and focused with high-flux Osmic multilayer mirror optics and a curved image plate detector. Bruker D8 Venture diffractometer is equipped with CuKα radiation with a diamond microfocus X-ray source and a Photon III 28 detector. The samples were solvated with DMF prior to and during measurements. The two-dimensional images of the Debye rings were integrated with 2DP or Diffract Eva to give 2θ vs I diffractograms. Predicted powder patterns were generated from single-crystal structures using Mercury.

All single-crystal X-ray diffraction measurements were carried out on Bruker D8 Venture, and the measurement temperature was controlled using Oxford Cryostream if required. Bruker APEX 3 was used to collect and process data, and the structure was solved and refined using the Shelx package[107,119] under Olex2[120]. The crystal samples were solvated in n-octane and mounted on a nylon loop using Fomblin oil in most cases. Alternatively, if moisture sensitive, a single crystal was completely sealed in a glass capillary during the measurement.

Thermogravimetric analyses were performed on a TA Instruments Q50 instrument.

6.4.2. Post-synthetic coupling reactions

6.4.2.1. Alkene-alkene coupling reaction

6.4.2.1.1. Test reaction with styrene

Grubbs 2nd generation catalyst (6.2 mg, 7.3 μmol) (Figure 6-8) was introduced to styrene (1 ml, 8.7 mmol) in 4 ml vial, and then the mixture was kept at 30 °C for an hour. The ^{1}H NMR spectrum of the solidified material confirmed diphenylethylene.

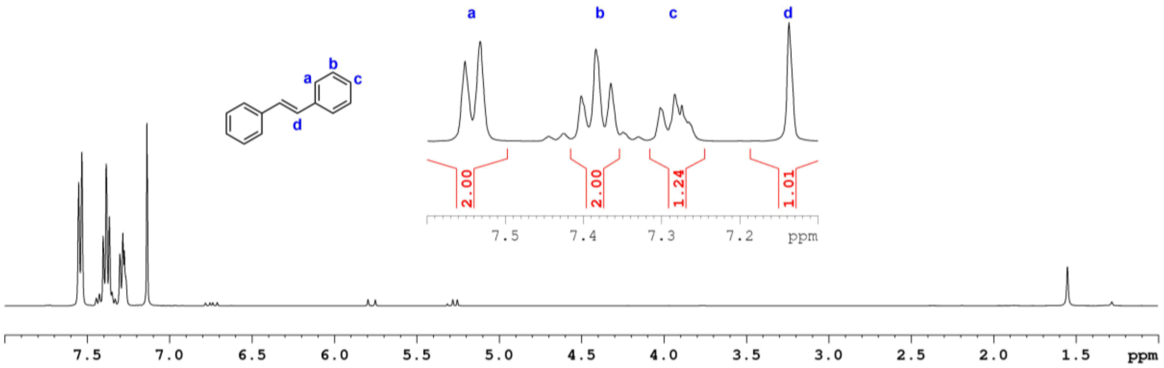

6.4.2.1.2. Post-synthetic alkene metathesis with G2C

MUF-80c (~ 3 mg) was placed in a 10 mL microwave vial, and THF (1 mL) and G2C (5.0 mg, 0.8 equivalent with respect to the alkenes in MUF-80c) was added to the vial, and the vial was heated to 80 °C for 18 hours with a microwave.

6.4.2.1.3. Post-synthetic alkene metathesis with $W(CO)_6$

MUF-80c (~ 3 mg), $W(CO)_6$ (various amount, 4–15 mg) and CCl_4 (1.7 mL) was placed in a vial, and the mixture was irradiated with light (360 nm, UV torch) overnight.

6.4.2.1.4. Post-synthetic dimerisation of alkene with zirconocene

MUF-80c (~ 3 mg) and catalyst solution[e] (various amount, 10–100 μL) was added to solvent (1 mL of toluene, THF or DEF) and heated with an isothermal oven or microwave (at a various temperature between 50 °C and 200 °C for a various amount of time).

---

[e] To a solution of pre-dried zirconocene dichloride (290 mg, 1.0 mmol, 2.0 eq.) in toluene (10 mL), was added trimethylaluminum (1.5 mL, 2.0 M solution in toluene, 3. 0 mmol, 6. 0 eq.). The solution was stirred for 15 min, and then cooled to 0 °C, and DI water (9 μL, 0.5 mmol, 1.0 eq.) was carefully added. The pale-yellow solution was allowed to stir for 0.5 h at 0 °C.

6.4.2.2. **Glaser-Hay coupling**

6.4.2.2.1. Test reaction with phenylacetylene

Phenylacetylene (0.1 mL, 0.91 mmol) and CuI·P(OEt)$_3$ (16.2 mg, 45 μmol, 5 mol %) dissolved in acetone (2 mL) and DMEDA (4.9 μL, 45 μmol, 5 mol %) was added to the mixture. The reaction mixture was kept at room temperature for five hours, and the product was extracted with EtOAc and dried. The ^{1}H NMR spectrum of the dried material indicates that more than 90 % of phenylacetylene was dimerised.

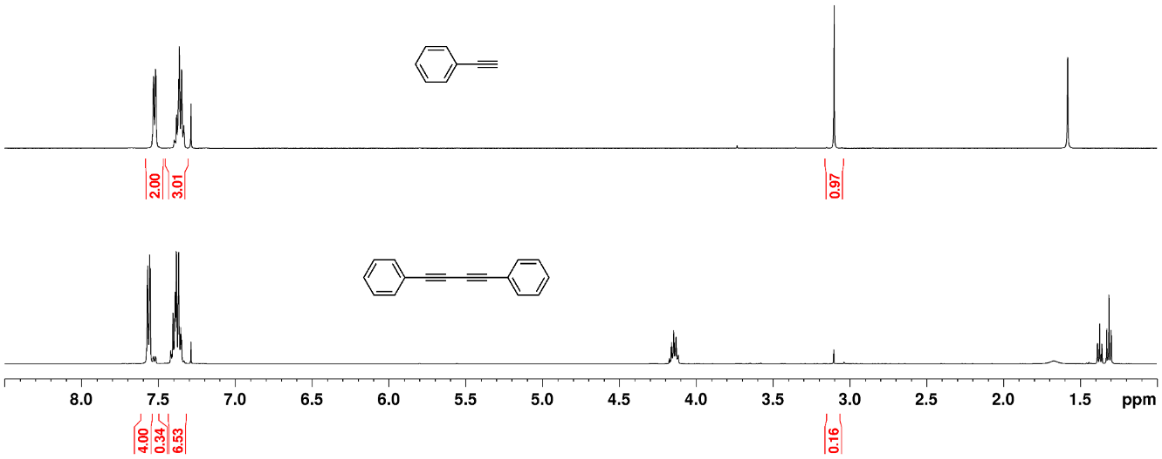

6.4.2.2.2. MUF-80dc-c

MUF-80d (~ 5 mg), the catalyst stock solution[f] (20 μL) and DEF (0.5 mL) was placed in a microwave vessel (10 mL), and O2 gas was briefly bubbled before capping. The reaction mixture was heated with a microwave (300 W) for three hours. The crystal sample was washed with DMF and CH$_2$Cl$_2$ several times for analyses.

6.4.2.3. **Guest-mediated azide-alkyne click reaction**

MUF-80e (~ 40 mg) was soaked in the 10-fold dilute 1,7-octadiyne solution in DMF (1 mL) at 60 °C for 30 minutes. After cooling down to room temperature, the solvent was removed by decanting, and the crystal sample was briefly rinsed with DMF. Then, the catalyst solution[g] (1 mL) was added to the crystal sample, and the mixture was kept in an isothermal oven at 100 °C overnight. After determining the completion of the reaction with IR spectroscopy, the crystal sample was washed with DMF several times with brief sonication to remove precipitate formed from the copper catalyst, followed by washing with CH$_2$Cl$_2$ and n-hexane. The crystal was kept in n-hexane for further analysis.

---

[f] Two separate solutions of CuI·P(OEt)$_3$ (35.6 mg, 0.1 mmol) in DEF (1 mL) and DMEDA (10.8 μL, 0.1 mmol) in DEF (1 mL) were mixed with 1:1 ratio just before use.

[g] CuI·P(OEt)$_3$ (50 mg, 140 μmol) was dissolved in DMF (1 mL).

6.4.3. Analyses

6.4.3.1. PXRDs

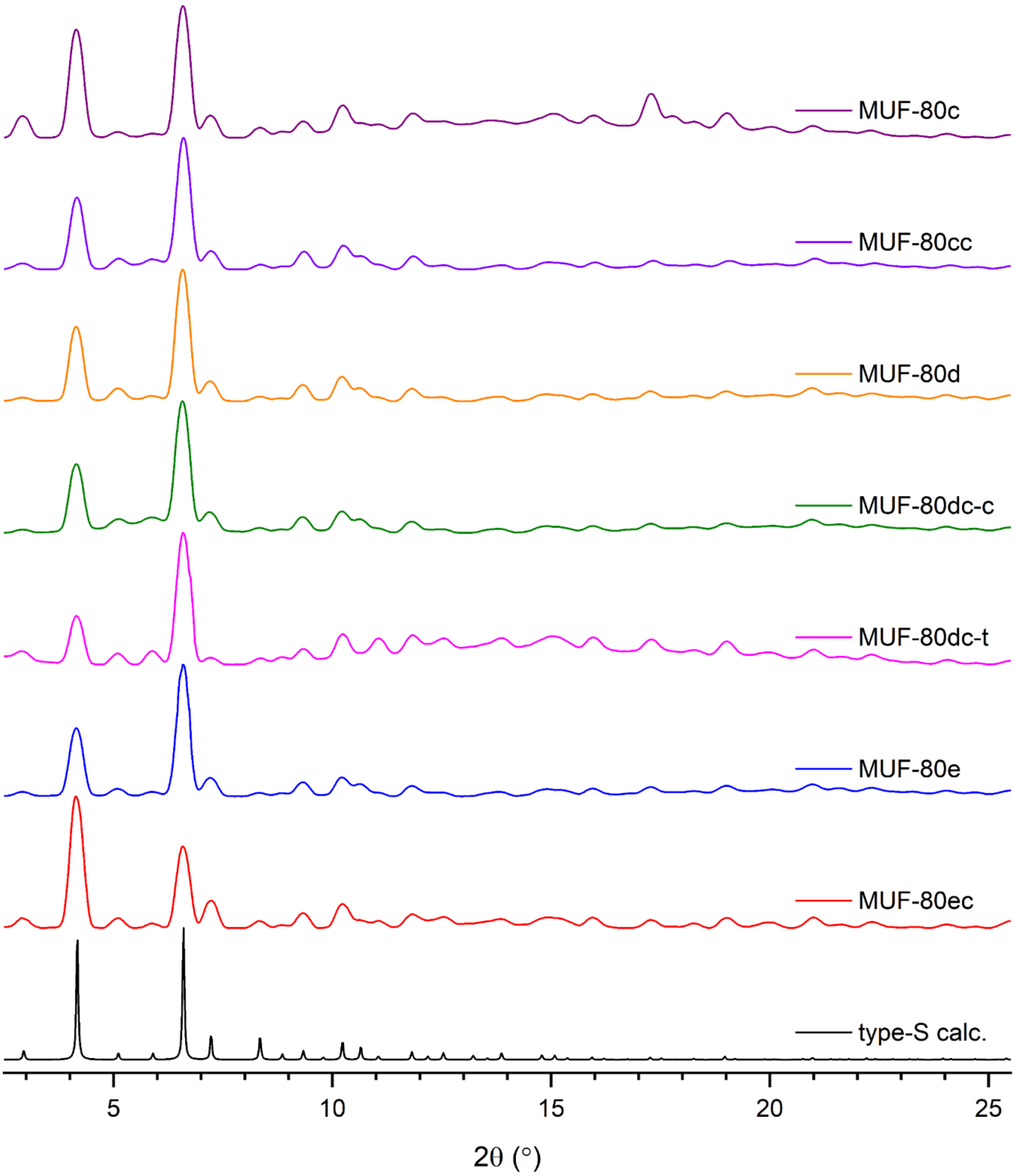

Figure 6-27. PXRD patterns of various MOFs before and after postsynthetic coupling reactions.

6.4.3.2. SCXRD

All cif files are available through the link provided below.

https://drive.google.com/drive/folders/1mEMRFRL3ME5N6OtzIjeEWkluLPOIArSg?usp=sharing

Table 6-2. Summary of X-ray crystallography data collection and refinement details of MUF-80c, MUF-80d, MUF-80dc-t, MUF-80e and MUF-80ec.

Identification code	MUF-80c	MUF-80d	MUF-80dc-t	MUF-80e	MUF-80ec
Empirical formula	$C_{69}H_{54}O_{15}Zn_4$	$C_{71}H_{58}O_{15}Zn_4$	$C_{71}H_{58}O_{15}Zn_4$	$C_{61}H_{44}N_6O_{13}Zn_4$	$C_{69}H_{54}N_6O_{13}Zn_4$
Formula weight	1384.6	1412.65	1412.65	1330.5	1436.66
Temperature/K	273	103	293.15	293.15	298
Crystal system	cubic	cubic	cubic	cubic	cubic
Space group	Pm-3	Pm-3	Pm-3	Pm-3	Pm-3
a = b = c (Å)	29.9281(3)	29.9529(5)	29.9524(18)	29.9170(9)	29.8569(3)
α = β = γ (°)	90	90	90	90	90
Volume (Å^3)	26806.3(8)	26873.0(13)	26872(5)	26777(2)	26615.5(8)
Z	6	6	6	6	6
ρ_{calc}g (cm^3)	0.515	0.524	0.524	0.495	0.538
μ (mm^{-1})	0.805	0.807	0.807	0.799	0.82
F(000)	4248	4344	4344	4056	4404
Crystal size (mm^3)	0.3 × 0.2 × 0.2	0.4 × 0.4 × 0.3	0.5 × 0.4 × 0.4	0.5 × 0.4 × 0.3	0.5 × 0.4 × 0.2
Radiation	CuKα (λ = 1.54178)	CuKα (λ = 1.54178)	CuKα (λ = 1.54184)	CuKα (λ = 1.54184)	CuKα (λ = 1.54178)
2Θ range for data collection (°)	4.176 to 152.49	2.95 to 152.106	4.172 to 152.132	4.176 to 152.026	4.186 to 152.782
Resolution range for refinement (Å)	0.79	0.79	0.79	0.79	0.79
Index ranges	$-30 \le h \le 36$ $-34 \le k \le 22$ $-28 \le l \le 32$	$-27 \le h \le 36$ $-37 \le k \le 31$ $-33 \le l \le 32$	$-37 \le h \le 36$ $-26 \le k \le 16$ $-24 \le l \le 37$	$-30 \le h \le 36$ $-36 \le k \le 18$ $-30 \le l \le 37$	$-36 \le h \le 22$ $-31 \le k \le 37$ $-27 \le l \le 30$
Reflections collected	76171	112551	82706	115139	76383
Tmin / Tmax	0.668 / 0.754	0.667 / 0.754	0.607 / 0.754	0.598 / 0.754	0.576 / 0.754
Independent reflections	9810 $R_{int} = 0.0359$ $R_{sigma} = 0.0255$	9750 $R_{int} = 0.0331$ $R_{sigma} = 0.0188$	9855 $R_{int} = 0.0442$ $R_{sigma} = 0.0210$	9769 $R_{int} = 0.0260$ $R_{sigma} = 0.0151$	9818 $R_{int} = 0.0308$ $R_{sigma} = 0.0149$
Data/restraints/parameters	9810/32/252	9750/33/270	9855/38/252	9769/25/240	9818/49/252
Goodness-of-fit on F^2	1.13	1.063	1.054	1.09	1.077
Data completeness	0.986	0.979	0.989	0.988	0.994
Final R indexes [I>=2σ (I)]	$R_1 = 0.0692$ $wR_2 = 0.2027$	$R_1 = 0.0435$ $wR_2 = 0.1307$	$R_1 = 0.0636$ $wR_2 = 0.2018$	$R_1 = 0.0515$ $wR_2 = 0.1703$	$R_1 = 0.0635$ $wR_2 = 0.2184$
Final R indexes [all data]	$R_1 = 0.0801$ $wR_2 = 0.2199$	$R_1 = 0.0472$ $wR_2 = 0.1346$	$R_1 = 0.0674$ $wR_2 = 0.2072$	$R_1 = 0.0541$ $wR_2 = 0.1741$	$R_1 = 0.0665$ $wR_2 = 0.2251$
Largest diff. peak/hole (e Å^{-3})	0.86/-0.92	0.53/-0.56	0.62/-0.94	0.67/-0.49	0.84/-0.75

6.4.3.3. **IR spectroscopy**

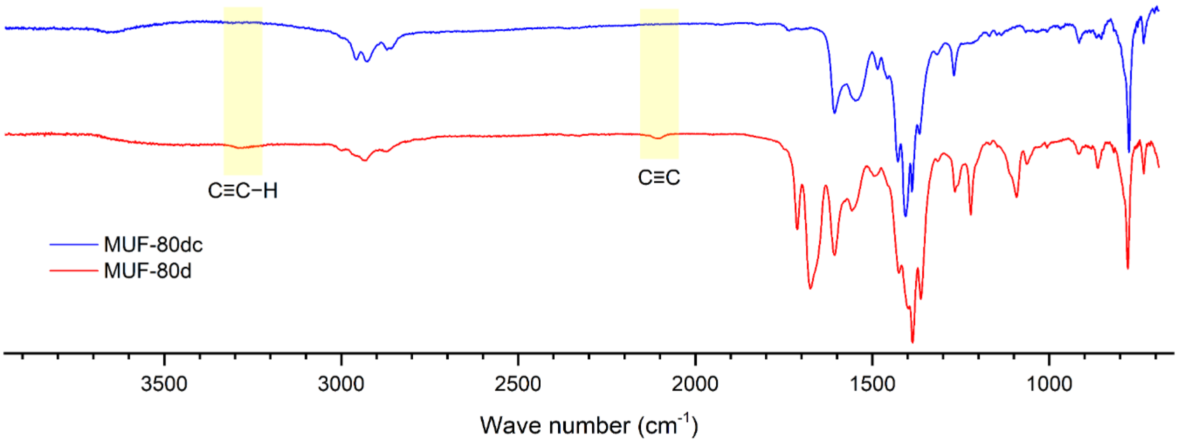

Figure 6-28. IR spectra of MUF-80d and MUF-80dc-t. The characteristic peaks belonging to the terminal alkyne were disappeared after the alkyne-alkyne thermal coupling reaction.

Chapter 7 **Summary and Perspectives**

7.1. **Thesis summary**

The studies presented in this thesis initially focussed on various applications of multi-component MOFs using MUF-77 derived materials (type-S framework). However, MUF-7 (type-L framework) was sometimes formed unexpectedly during the MOF synthesis. We found that the type-L frameworks are as useful as the type-S framework. Both frameworks, comprised of topologically different organic linkers, have unique features providing spaces where all three organic linkers interact. The applications presented here are unique and not easily replicable in other MOFs since they utilise all three linkers in the type-L or type-S frameworks.

In Chapter 2, the two sister frameworks, type-L and type-S, were introduced with their similarities and differences in details. The type-L framework had a spotlight once it was discovered because it was the first quaternary MOF built using three different organic linkers. However, it has received relatively less focus for applications due to the structural weakness induced by the btb linker, which we regarded as the key building block to form this material. In contrast, the spotlight has been moved to the type-S framework from its discovery and vigorously studied for various applications in different fields because it provides stability and robustness under various circumstances. However, during the research using the type-S framework for catalysis, it was accidentally discovered that the type-L framework could also be formed from the same building blocks as the type-S framework synthesis. This made the type-L framework as useful as the type-S framework, and it demonstrated similar or even better performances from a simple catalysis experiment.

In Chapter 3 and 4, a novel way of asymmetry induction during catalysis was introduced. Unlike the traditional asymmetric catalysts, each of the two functions, catalysis and asymmetry induction, were carried out using separate molecules within the same framework. Initially, the work was designed to implement the concept using the type-S framework, and it seemed it was successfully achieved. We could enhance the performance of the RAI catalyst by tweaking various parameters and conditions. However, the results were not consistent and were affected by some parameters which did not seem important in relation to the principal mechanism of the RAI catalyst (e.g. alkyl chain length on the truxene linker). However, it was revealed that the type-L framework was also formed unexpectedly, and the unique pore structure in the type-L framework had played a crucial role in inducing such enhanced performances. This discovery was very meaningful because it made us realise that the type-L frameworks could also do what the type-S framework does. Therefore, we can selectively use them depending on the purpose since both frameworks provide different pore environments which can fit better for a specific task. However, prior to that, we have to establish reliable synthesis methods for both frameworks with the desired functionality. In the following section (7.3), an idea to obtain the desired phase between the type-L and type-S frameworks will be introduced.

In Chapter 5, an inter-ligand PSM reaction was introduced. We have demonstrated linkage formation between the two linkers in a prebuilt framework utilising a coupling reaction between two complementary functional groups installed on each linker. The difference between this work and the other similar works reported by other studies was that it was carried out in an MC-MOF scaffold (the type-S framework). Therefore, the linkage formation between the functional groups was achieved in a regulated way. As a result of this PSM reaction, a new functional group (triazole) was introduced to the framework, and it demonstrated improved affinity towards a few selected absorbates.

In Chapter 6, a novel way of polymer synthesis using inter-ligand PSM reactions, inspired by the works presented in Chapter 5, was introduced. If two different monomers are functionalised with the same chemical group, one is unable to arrange them in a specific sequence using conventional methods. The type-S framework scaffold allowed the arrangement of the two different linkers in alternating order, and the PSM coupling reaction then connected these two linkers. Two different concepts were demonstrated in this work, one is a direct connection using homocoupling reaction, and another is an indirect connection by introducing a guest molecule. The experimental results evidenced that the desired coupling reaction occurred in both cases. However, more analyses are required to evaluate the degree of polymerisation achieved by these methods, which will be carried out with our collaborators.

7.2. Brønsted acid catalyst

The concept and system used in RAI catalyst (Chapter 3 and 4) were not known and not presented in any other studies prior to this work. This novel concept was well implemented using the guanidine moiety along with a few oxazolidinone-derived chiral modulators, and they demonstrated enantioselectivity over the Henry reaction. However, we wondered whether this system would work with other combinations of achiral catalyst and chiral modulator units. We would also like to prove that this system can be utilised as a regular approach to induce asymmetry. For this reason, other catalytic units were tested for the RAI catalyst, and promising results were obtained among a few.

The catalytic capability of a few bpdc derivatives with the nitrogen-based organic catalysts was screened over a few reactions in Chapter 3. However, not many of them showed good catalytic activity except for the guanidine for the Henry reaction. Thus, we have turned our attention to other catalytic moieties that could be incorporated into the RAI catalyst system. Using Brønsted acidity is one of the common ways to perform catalysis in MOF chemistry.[190] Sulfonic acid is widely used as a catalyst unit, and its catalytic capability in MOFs has been

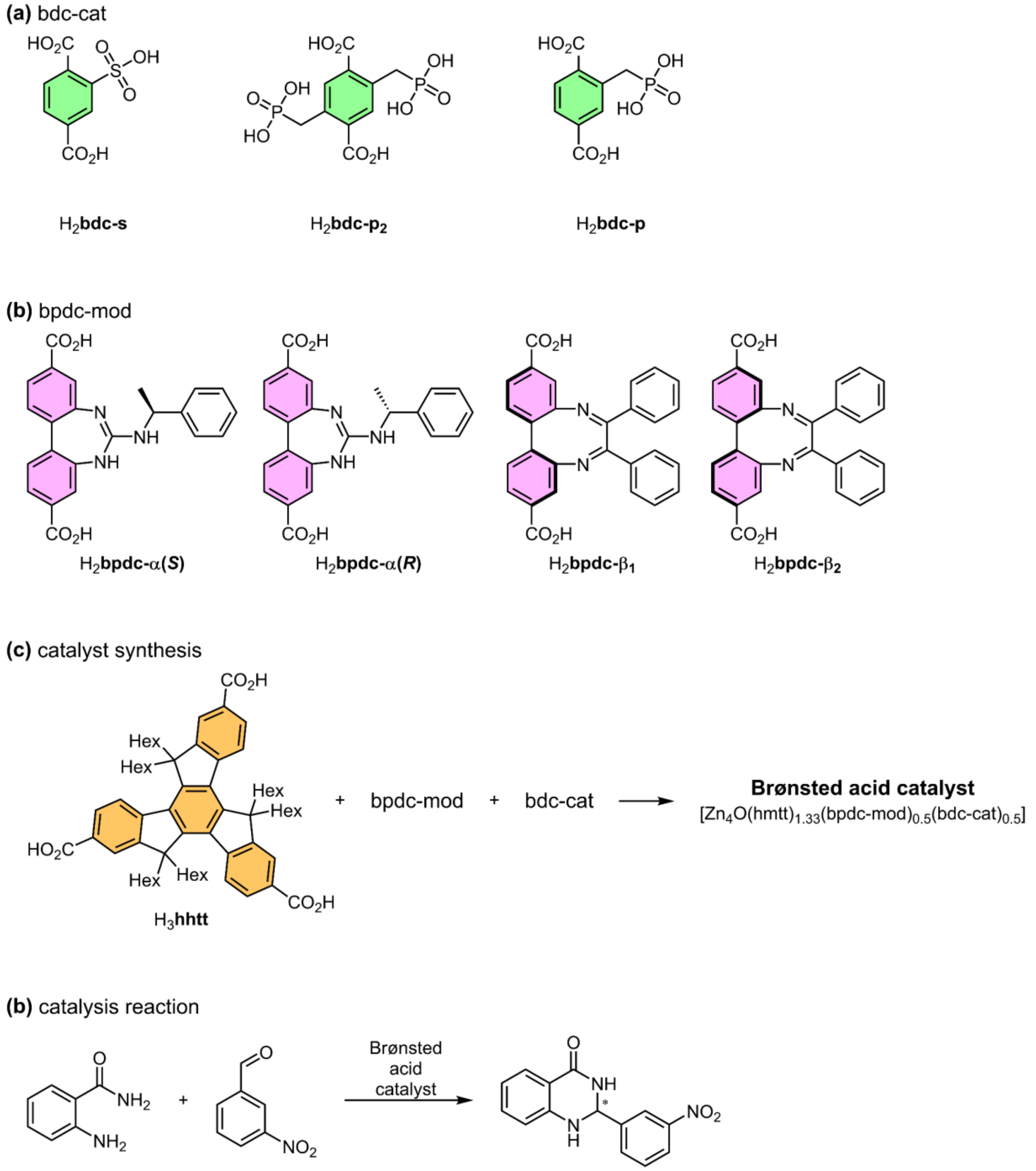

Figure 7-1. (a) bdc linkers functionalised with sulfonic or phosphonic acid; (b) bpdc derived chiral modulating groups; (c) a schematic diagram of Brønsted acid catalyst synthesis; (d) a target reaction (cyclisation of 2-aminobenzamide and 3-nitrobenzaldehyde) to test the prepared Brønsted acid catalysts.

successfully demonstrated.[97,191-192]

A sulfonic acid containing bdc linker was prepared (bdc-s in Figure 7-1a), and it was successfully incorporated into the framework along with bpdc-derived chiral modulators (Figure 7-1b and c). Additionally, two other bdc derivatives with phosphonic acid groups were also tested, but they could not form the desired framework due to strong coordinating nature of phosphonate.[193] The prepared MOFs were then tested for the cyclisation reaction of 2-aminobenzamide and 3-nitrobenzaldehyde.[194] The result showed that the principal mechanism of the RAI catalyst was working with some of the combinations. Although no catalytic activity was observed when bpdc-β was used as a modulating group, the two catalysts ($[Zn_4O(hhtt)_{1.33}(bpdc\text{-}\alpha(S))_{0.5}(bdc\text{-}s)_{0.5}]$ and $[Zn_4O(hhtt)_{1.33}(bpdc\text{-}\alpha(R))_{0.5}(bdc\text{-}s)_{0.5}]$) comprised bpdc-α produced notably different enantioselectivities (5.0 vs -4.4 %) (Figure 7-2).

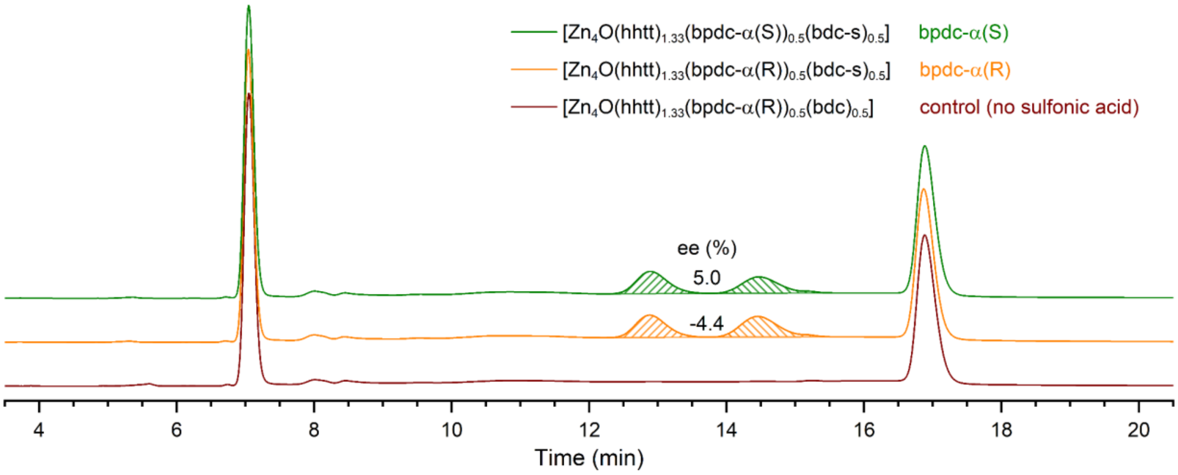

Figure 7-2. The HPLC chromatograms of some reaction mixtures for the reaction of 2-aminobenzamide and 3-nitrobenzaldehyde catalysed by selected catalysts.

These results evidence that the RAI catalyst system can be utilised as a general asymmetric catalyst. Moreover, Brønsted acids are versatile catalysts and extensively employed in many applications.[195-196] Another advantage of using bdc-s is that it allows us to install a wide range of chiral modulating group to the bpdc backbone. Installing a functionality to the bpdc backbone is usually more feasible than installing to the bdc backbone. In addition, the bpdc-

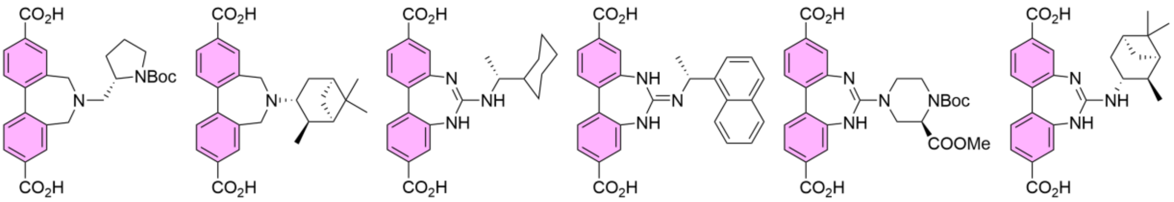

Figure 7-3. A few examples of bpdc derivatives which can be utilised as a chiral modulator in RAI catalysts together with bdc-s.

derived linkers cause a lot less trouble during MOF synthesis. Hence, we will have more options for the chiral modulators that play a crucial role in this RAI catalyst system; a few examples were illustrated in Figure 7-3.

7.3. MOF synthesis with pre-linked chains

The inter-ligand click reaction between bpdc and bdc derivatives was introduced in Chapter 5. When we initially planned the experiment, re-synthesising a framework using the polymerised linker was also planned. We can extract the linked bpdc-bdc polymer chain by digesting the framework after the click reaction, and the chain can be reused as a building block for MOF synthesis. However, this did not go well. We think that the polymer chain is probably too long, and the uneven chain length also causes a problem.

However, an interesting result was obtained from the preliminary test to estimate the feasibility of the idea. As depicted in Figure 7-4a, pre-linked bpdc-bdc dimer was prepared using the click reaction. The bpdc-bdc dimer was then used for MOF synthesis with hmtt and Zn(II), and the type-S framework was obtained (Figure 7-4b). Although some microcrystals were formed together, most of the crystals were in good shape and size (ca. 0.5 mm).

This interesting result brought us an idea to control the phase of crystal between type-L and type-S using pre-linked ligands in MOF synthesis. The issue with the crystal phase between type-L and type-S has been constantly presented in this thesis. Although we could obtain a better result due to the unexpectedly formed the type-L framework in Chapter 3 and 4, it

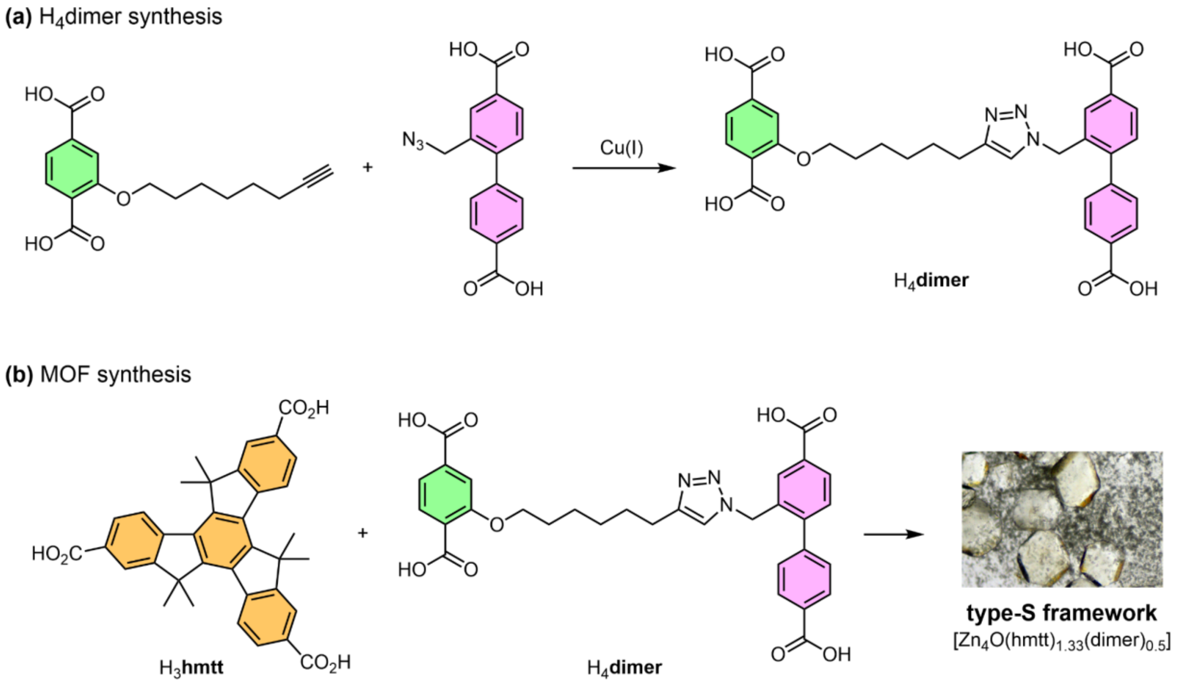

Figure 7-4. (a) A schematic diagram of a dimer synthesis comprised bdc and bpdc; (b) the type-S framewrok was formed from the dimer.

could have had the opposite effect. Unfortunately, we still have no control over this phase issue, and this will bother us as long as we continue researching these two materials.

The prominent structural difference between the two frameworks is the arrangement of the two linear linkers. As illustrated inFigure 7-5, a pair of bpdc and a pair bdc are alternating in the type-L framework, whereas bpdc and bdc are alternating in the type-S framework. Therefore, if we use the two dimers of the same kind (bpdc-bpdc and bdc-bdc) for MOF synthesis, it is expected that only the type-L framework will exclusively be formed. On the other hand, we can use equimolar ratios of the two trimers, bdc-bpdc-bdc and bpdc-bdc-bpdc, to form the type-S framework if the trimers can be integrated into the framework. Although the bpdc-bdc dimer presented above formed the type-S framework, it is not reliable since it could also form the type-L framework. Therefore, using the trimer could be a promising solution, provided that the trimers are incorporated into the MOF without any issues.

(a) type-L synthesis using dimers

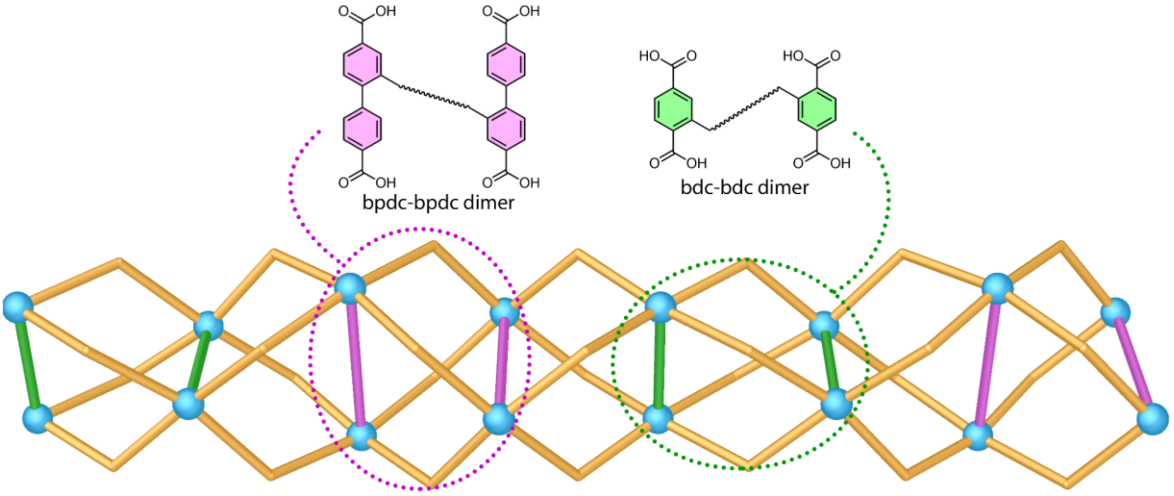

(b) type-S synthesis using trimers

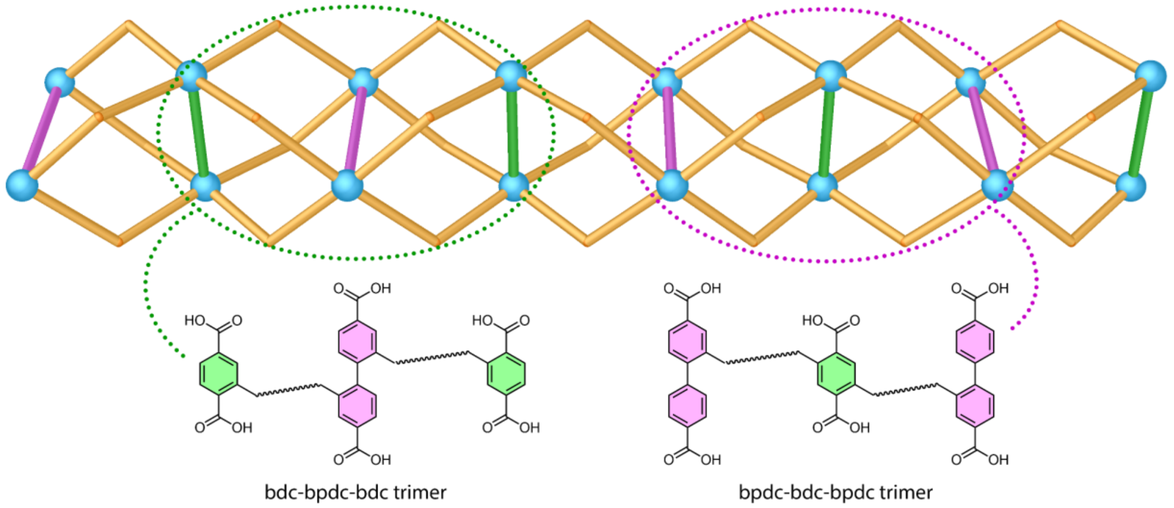

Figure 7-5. Schematic diagrams for synthesising the phase pure framework; (a) the type-L framework can be formed from the two dimers, bpdc-bpdc and bdc-bdc; (b) the type-S framework will probably be formed if the equimolar two trimers were used together.

If this method works, we can then add the desired functionality using derivatised dimers or trimers with the desired functional groups (Figure 7-6). Alternatively, only a small portion of the dimers or trimers can be mixed with the normal bpdc and bdc derived ligands in the synthesis mixture if adding functionality to the pre-linked ligands is not feasible. Once these pre-linked ligands are incorporated into the framework, they can then guide the following bpdc and bdc to coordinate in the same manner.

(a) functionalised dimers

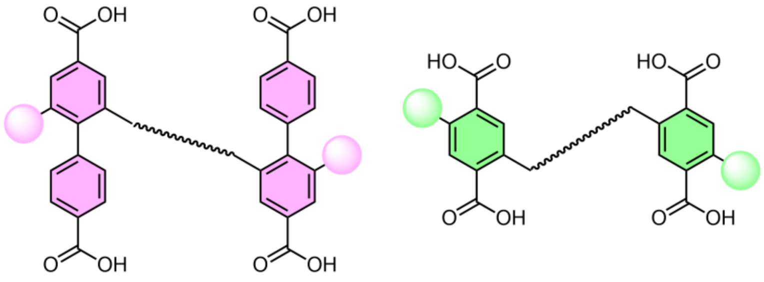

(b) functionalised trimers

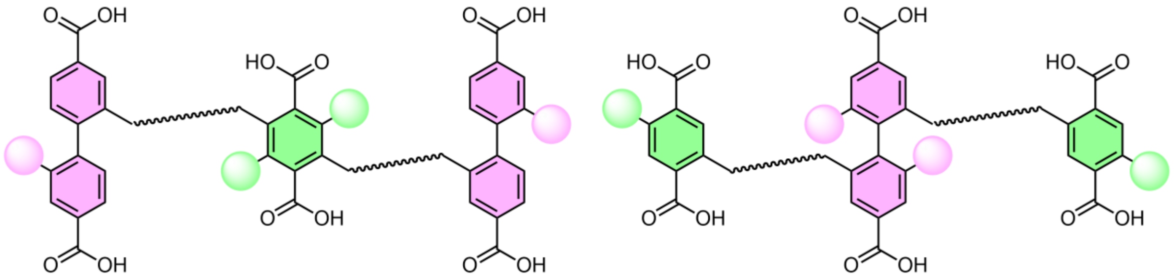

Figure 7-6. Functionalised (a)dimers and (b) trimers.

References

(1) Ockwig, N. W.; Delgado-Friedrichs, O.; O'Keeffe, M.; Yaghi, O. M. Reticular Chemistry: Occurrence and Taxonomy of Nets and Grammar for the Design of Frameworks. *Acc. Chem. Res.* **2005**, *38*, 176-182.

(2) Gropp, C.; Canossa, S.; Wuttke, S.; Gándara, F.; Li, Q.; Gagliardi, L.; Yaghi, O. M. Standard Practices of Reticular Chemistry. *ACS Cent. Sci.* **2020**, *6*, 1255-1273.

(3) Batten, S. R.; Champness, N. R.; Chen, X.-M.; Garcia-Martinez, J.; Kitagawa, S.; Öhrström, L.; O'Keeffe, M.; Paik Suh, M.; Reedijk, J. Terminology of metal–organic frameworks and coordination polymers (IUPAC Recommendations 2013). *Pure Appl. Chem.* **2013**, *85*, 1715-1724.

(4) Li, H.; Eddaoudi, M.; O'Keeffe, M.; Yaghi, M. Design and synthesis of an exceptionally stable and highly porous metal-organic framework. *Nature* **1999**, *402*, 276-279.

(5) Feng, D.; Wang, K.; Su, J.; Liu, T.-F.; Park, J.; Wei, Z.; Bosch, M.; Yakovenko, A.; Zou, X.; Zhou, H.-C. A Highly Stable Zeotype Mesoporous Zirconium Metal–Organic Framework with Ultralarge Pores. *Angew. Chem. Int. Ed.* **2015**, *54*, 149-154.

(6) Chui, S. S.-Y.; Lo, S. M.-F.; Charmant, J. P. H.; Orpen, A. G.; Williams, I. D. A Chemically Functionalizable Nanoporous Material $[Cu_3(TMA)_2(H_2O)_3]_n$. *Science* **1999**, *283*, 1148-1150.

(7) Liu, L.; Telfer, S. G. Systematic ligand modulation enhances the moisture stability and gas sorption characteristics of quaternary metal-organic frameworks. *J. Am. Chem. Soc.* **2015**, *137*, 3901-3909.

(8) Koh, K.; Wong-Foy, A. G.; Matzger, A. J. Coordination Copolymerization Mediated by $Zn_4O(CO_2R)_6$ Metal Clusters: a Balancing Act between Statistics and Geometry. *J. Am. Chem. Soc.* **2010**, *132*, 15005-15010.

(9) Hoskins, B. F.; Robson, R. Infinite polymeric frameworks consisting of three dimensionally linked rod-like segments. *J. Am. Chem. Soc.* **1989**, *111*, 5962-5964.

(10) Yaghi, O. M.; Li, H. Hydrothermal Synthesis of a Metal-Organic Framework Containing Large Rectangular Channels. *J. Am. Chem. Soc.* **1995**, *117*, 10401-10402.

(11) Suh, M. P.; Park, H. J.; Prasad, T. K.; Lim, D.-W. Hydrogen Storage in Metal–Organic Frameworks. *Chem. Rev.* **2012**, *112*, 782-835.

(12) Sumida, K.; Rogow, D. L.; Mason, J. A.; McDonald, T. M.; Bloch, E. D.; Herm, Z. R.; Bae, T.-H.; Long, J. R. Carbon Dioxide Capture in Metal–Organic Frameworks. *Chem. Rev.* **2012**, *112*, 724-781.

(13) Li, J.-R.; Sculley, J.; Zhou, H.-C. Metal–Organic Frameworks for Separations. *Chem. Rev.* **2012**, *112*, 869-932.

(14) Chughtai, A. H.; Ahmad, N.; Younus, H. A.; Laypkov, A.; Verpoort, F. Metal–organic frameworks: versatile heterogeneous catalysts for efficient catalytic organic transformations. *Chem. Soc. Rev.* **2015**, *44*, 6804-6849.

(15) Yi, F.-Y.; Chen, D.; Wu, M.-K.; Han, L.; Jiang, H.-L. Chemical Sensors Based on Metal–Organic

Frameworks. *ChemPlusChem* **2016**, *81*, 675-690.

(16) Wang, L.; Han, Y.; Feng, X.; Zhou, J.; Qi, P.; Wang, B. Metal–organic frameworks for energy storage: Batteries and supercapacitors. *Coord. Chem. Rev.* **2016**, *307*, 361-381.

(17) Kitao, T.; Zhang, Y.; Kitagawa, S.; Wang, B.; Uemura, T. Hybridization of MOFs and polymers. *Chem. Soc. Rev.* **2017**, *46*, 3108-3133.

(18) Liu, J.; Wöll, C. Surface-supported metal–organic framework thin films: fabrication methods, applications, and challenges. *Chem. Soc. Rev.* **2017**, *46*, 5730-5770.

(19) Wu, M.-X.; Yang, Y.-W. Metal–Organic Framework (MOF)-Based Drug/Cargo Delivery and Cancer Therapy. *Adv. Mater.* **2017**, *29*, 1606134.

(20) Mon, M.; Bruno, R.; Ferrando-Soria, J.; Armentano, D.; Pardo, E. Metal–organic framework technologies for water remediation: towards a sustainable ecosystem. *J. Mater. Chem. A* **2018**, *6*, 4912-4947.

(21) Lustig, W. P.; Mukherjee, S.; Rudd, N. D.; Desai, A. V.; Li, J.; Ghosh, S. K. Metal–organic frameworks: functional luminescent and photonic materials for sensing applications. *Chem. Soc. Rev.* **2017**, *46*, 3242-3285.

(22) Xu, G.; Nie, P.; Dou, H.; Ding, B.; Li, L.; Zhang, X. Exploring metal organic frameworks for energy storage in batteries and supercapacitors. *Mater. Today* **2017**, *20*, 191-209.

(23) Mehta, J.; Bhardwaj, N.; Bhardwaj, S. K.; Kim, K.-H.; Deep, A. Recent advances in enzyme immobilization techniques: Metal-organic frameworks as novel substrates. *Coord. Chem. Rev.* **2016**, *322*, 30-40.

(24) Park, K. S.; Ni, Z.; Côté, A. P.; Choi, J. Y.; Huang, R.; Uribe-Romo, F. J.; Chae, H. K.; O’Keeffe, M.; Yaghi, O. M. Exceptional chemical and thermal stability of zeolitic imidazolate frameworks. *PNAS* **2006**, *103*, 10186-10191.

(25) Lee, S. J.; Doussot, C.; Baux, A.; Liu, L.; Jameson, G. B.; Richardson, C.; Pak, J. J.; Trousselet, F.; Coudert, F.-X.; Telfer, S. G. Multicomponent Metal–Organic Frameworks as Defect-Tolerant Materials. *Chem. Mater.* **2016**, *28*, 368-375.

(26) Rosi, N. L.; Kim, J.; Eddaoudi, M.; Chen, B.; O'Keeffe, M.; Yaghi, O. M. Rod Packings and Metal-Organic Frameworks Constructed from Rod-Shaped Secondary Building Units. *J. Am. Chem. Soc.* **2005**, *127*, 1504-1518.

(27) Valvekens, P.; Vandichel, M.; Waroquier, M.; Van Speybroeck, V.; De Vos, D. Metal-dioxidoterephthalate MOFs of the MOF-74 type: Microporous basic catalysts with well-defined active sites. *J. Catal.* **2014**, *317*, 1-10.

(28) Cavka, J. H.; Jakobsen, S.; Olsbye, U.; Guillou, N.; Lamberti, C.; Bordiga, S.; Lillerud, K. P. A New Zirconium Inorganic Building Brick Forming Metal Organic Frameworks with Exceptional Stability. *J. Am. Chem. Soc.* **2008**, *130*, 13850-13851.

(29) Griffin, S. L.; Champness, N. R. A periodic table of metal-organic frameworks. *Coord. Chem. Rev.* **2020**, *414*, 213295.

(30) O’Keeffe, M.; Peskov, M. A.; Ramsden, S. J.; Yaghi, O. M. The Reticular Chemistry Structure Resource (RCSR) Database of, and Symbols for, Crystal Nets. *Acc. Chem. Res.* **2008**, *41*, 1782-1789.

(31) Blatov, V. A.; Shevchenko, A. P.; Proserpio, D. M. Applied Topological Analysis of Crystal Structures with the Program Package ToposPro. *Cryst. Growth Des.* **2014**, *14*, 3576-3586.

(32) Stock, N.; Biswas, S. Synthesis of Metal-Organic Frameworks (MOFs): Routes to Various MOF Topologies, Morphologies, and Composites. *Chem. Rev.* **2012**, *112*, 933-969.

(33) Rubio-Martinez, M.; Avci-Camur, C.; Thornton, A. W.; Imaz, I.; Maspoch, D.; Hill, M. R. New synthetic routes towards MOF production at scale. *Chem. Soc. Rev.* **2017**, *46*, 3453-3480.

(34) Guo, C.; Zhang, Y.; Guo, Y.; Zhang, L.; Zhang, Y.; Wang, J. A general and efficient approach for tuning the crystal morphology of classical MOFs. *Chem. Commun.* **2018**, *54*, 252-255.

(35) Howarth, A. J.; Peters, A. W.; Vermeulen, N. A.; Wang, T. C.; Hupp, J. T.; Farha, O. K. Best Practices for the Synthesis, Activation, and Characterization of Metal–Organic Frameworks. *Chem. Mater.* **2017**, *29*, 26-39.

(36) Ma, J.; Kalenak, A. P.; Wong-Foy, A. G.; Matzger, A. J. Rapid Guest Exchange and Ultra-Low Surface Tension Solvents Optimize Metal-Organic Framework Activation. *Angew. Chem. Int. Ed.* **2017**, *56*, 14618-14621.

(37) Dodson, R. A.; Wong-Foy, A. G.; Matzger, A. J. The Metal–Organic Framework Collapse Continuum: Insights from Two-Dimensional Powder X-ray Diffraction. *Chem. Mater.* **2018**, *30*, 6559-6565.

(38) Mondloch, J. E.; Karagiaridi, O.; Farha, O. K.; Hupp, J. T. Activation of metal–organic framework materials. *CrystEngComm* **2013**, *15*, 9258-9264.

(39) Cohen, S. M. The Postsynthetic Renaissance in Porous Solids. *J. Am. Chem. Soc.* **2017**, *139*, 2855-2863.

(40) Wu, C.-D.; Hu, A.; Zhang, L.; Lin, W. A Homochiral Porous Metal-Organic Framework for Highly Enantioselective Heterogeneous Asymmetric Catalysis. *J. Am. Chem. Soc.* **2005**, *127*, 8940-8941.

(41) Alkordi, M. H.; Liu, Y.; Larsen, R. W.; Eubank, J. F.; Eddaoudi, M. Zeolite-like Metal−Organic Frameworks as Platforms for Applications: On Metalloporphyrin-Based Catalysts. *J. Am. Chem. Soc.* **2008**, *130*, 12639-12641.

(42) Wang, C.; Xie, Z.; deKrafft, K. E.; Lin, W. Doping Metal–Organic Frameworks for Water Oxidation, Carbon Dioxide Reduction, and Organic Photocatalysis. *J. Am. Chem. Soc.* **2011**, *133*, 13445-13454.

(43) Shultz, A. M.; Sarjeant, A. A.; Farha, O. K.; Hupp, J. T.; Nguyen, S. T. Post-Synthesis Modification of a Metal–Organic Framework To Form Metallosalen-Containing MOF Materials. *J. Am. Chem. Soc.* **2011**, *133*, 13252-13255.

(44) Garibay, S. J.; Wang, Z.; Cohen, S. M. Evaluation of Heterogeneous Metal−Organic Framework Organocatalysts Prepared by Postsynthetic Modification. *Inorg. Chem.* **2010**, *49*, 8086-8091.

(45) Lun, D. J.; Waterhouse, G. I. N.; Telfer, S. G. A General Thermolabile Protecting Group Strategy for Organocatalytic Metal-Organic Frameworks. *J. Am. Chem. Soc.* **2011**, *133*, 5806-5809.

(46) Deshpande, R. K.; Minnaar, J. L.; Telfer, S. G. Thermolabile Groups in Metal–Organic

Frameworks: Suppression of Network Interpenetration, Post-Synthetic Cavity Expansion, and Protection of Reactive Functional Groups. *Angew. Chem. Int. Ed.* **2010**, *49*, 4598-4602.

(47) Song, X.; Kim, T. K.; Kim, H.; Kim, D.; Jeong, S.; Moon, H. R.; Lah, M. S. Post-Synthetic Modifications of Framework Metal Ions in Isostructural Metal–Organic Frameworks: Core–Shell Heterostructures via Selective Transmetalations. *Chem. Mater.* **2012**, *24*, 3065-3073.

(48) Kim, M.; Cahill, J. F.; Fei, H.; Prather, K. A.; Cohen, S. M. Postsynthetic Ligand and Cation Exchange in Robust Metal–Organic Frameworks. *J. Am. Chem. Soc.* **2012**, *134*, 18082-18088.

(49) Karagiaridi, O.; Bury, W.; Tylianakis, E.; Sarjeant, A. A.; Hupp, J. T.; Farha, O. K. Opening Metal–Organic Frameworks Vol. 2: Inserting Longer Pillars into Pillared-Paddlewheel Structures through Solvent-Assisted Linker Exchange. *Chem. Mater.* **2013**, *25*, 3499-3503.

(50) Eddaoudi, M.; Kim, J.; Rosi, N.; Vodak, D.; Wachter, J.; O'Keeffe, M.; Yaghi, O. M. Systematic design of pore size and functionality in isoreticular MOFs and their application in methane storage. *Science* **2002**, *295*, 469-472.

(51) Jiang, H.-L.; Makal, T. A.; Zhou, H.-C. Interpenetration control in metal–organic frameworks for functional applications. *Coord. Chem. Rev.* **2013**, *257*, 2232-2249.

(52) Deng, H.; Grunder, S.; Cordova, K. E.; Valente, C.; Furukawa, H.; Hmadeh, M.; Gándara, F.; Whalley, A. C.; Liu, Z.; Asahina, S.et al. Large-Pore Apertures in a Series of Metal-Organic Frameworks. *Science* **2012**, *336*, 1018-1023.

(53) Yuan, D.; Zhao, D.; Sun, D.; Zhou, H.-C. An Isoreticular Series of Metal–Organic Frameworks with Dendritic Hexacarboxylate Ligands and Exceptionally High Gas-Uptake Capacity. *Angew. Chem. Int. Ed.* **2010**, *49*, 5357-5361.

(54) Brunauer, S.; Emmett, P. H.; Teller, E. Adsorption of Gases in Multimolecular Layers. *J. Am. Chem. Soc.* **1938**, *60*, 309-319.

(55) Li, T.; Chen, D.-L.; Sullivan, J. E.; Kozlowski, M. T.; Johnson, J. K.; Rosi, N. L. Systematic modulation and enhancement of $CO_2 : N_2$ selectivity and water stability in an isoreticular series of bio-MOF-11 analogues. *Chem. Sci.* **2013**, *4*, 1746-1755.

(56) Liu, L.; Konstas, K.; Hill, M. R.; Telfer, S. G. Programmed Pore Architectures in Modular Quaternary Metal–Organic Frameworks. *J. Am. Chem. Soc.* **2013**, *135*, 17731-17734.

(57) Kang, I. J.; Khan, N. A.; Haque, E.; Jhung, S. H. Chemical and Thermal Stability of Isotypic Metal–Organic Frameworks: Effect of Metal Ions. *Chem. Eur. J.* **2011**, *17*, 6437-6442.

(58) Xiong, Y.; Fan, Y.-Z.; Damasceno Borges, D.; Chen, C.-X.; Wei, Z.-W.; Wang, H.-P.; Pan, M.; Jiang, J.-J.; Maurin, G.; Su, C.-Y. Ligand and Metal Effects on the Stability and Adsorption Properties of an Isoreticular Series of MOFs Based on T-Shaped Ligands and Paddle-Wheel Secondary Building Units. *Chem. Eur. J.* **2016**, *22*, 16147-16156.

(59) Furukawa, H.; Cordova, K. E.; O’Keeffe, M.; Yaghi, O. M. The Chemistry and Applications of Metal-Organic Frameworks. *Science* **2013**, *341*.

(60) Carton, A.; Mesbah, A.; Aranda, L.; Rabu, P.; François, M. New metastable hybrid phase, $Zn_2(OH)_2(C_8H_4O_4)$, exhibiting unique oxo-penta-coordinated Zn(II) atoms. *Solid State Sci.* **2009**, *11*, 818-823.

(61) Carton, A.; Abdelouhab, S.; Renaudin, G.; Rabu, P.; François, M. Structure of zinc hydroxy-

terephthalate: $Zn_3(OH)_4(C_8H_4O_4)$. *Solid State Sci.* **2006**, *8*, 958-963.

(62) Saffon-Merceron, N.; Barthélémy, M.-C.; Laurent, C.; Fabing, I.; Hoffmann, P.; Vigroux, A. Two new metal–organic framework structures derived from terephthalate and linear trimetallic zinc building units. *Inorg. Chim. Acta* **2015**, *426*, 15-19.

(63) Hawxwell, S. M.; Adams, H.; Brammer, L. Two-dimensional metal-organic frameworks containing linear dicarboxylates. *Acta Cryst. B* **2006**, *62*, 808-814.

(64) Edgar, M.; Mitchell, R.; Slawin, A. M. Z.; Lightfoot, P.; Wright, P. A. Solid-State Transformations of Zinc 1,4-Benzenedicarboxylates Mediated by Hydrogen-Bond-Forming Molecules. *Chem. Eur. J.* **2001**, *7*, 5168-5175.

(65) Loiseau, T.; Muguerra, H.; Férey, G.; Haouas, M.; Taulelle, F. Synthesis and structural characterization of a new open-framework zinc terephthalate $Zn_3(OH)_2(bdc)_2{\cdot}2DEF$, with infinite Zn–($\mu_3$-OH)–Zn chains. *J. Solid State Chem.* **2005**, *178*, 621-628.

(66) Jiang, Z.; An, Y.; Zhu, X.; Tian, C.; Bai, J.; Li, Y. Solvent-Dependent Synthesis from Layer to Microporous Pillared-Layer Framework for Selective Sorption of Gas Light Hydrocarbons. *Z. Anorg. Allg. Chem.* **2015**, *641*, 2599-2603.

(67) Lee, S. J.; Doussot, C.; Telfer, S. G. Architectural Diversity in Multicomponent Metal–Organic Frameworks Constructed from Similar Building Blocks. *Cryst. Growth Des.* **2017**, *17*, 3185-3191.

(68) Chae, H. K.; Siberio-Perez, D. Y.; Kim, J.; Go, Y. B.; Eddaoudi, M.; Matzger, A. J.; O'Keeffe, M.; Yaghi, O. M. A route to high surface area, porosity and inclusion of large molecules in crystals. *Nature* **2004**, *427*, 523-527.

(69) Yao, Q.; Su, J.; Cheung, O.; Liu, Q.; Hedin, N.; Zou, X. Interpenetrated metal–organic frameworks and their uptake of CO_2 at relatively low pressures. *J. Mater. Chem.* **2012**, *22*, 10345-10351.

(70) Pang, Q.; Tu, B.; Li, Q. Metal–organic frameworks with multicomponents in order. *Coord. Chem. Rev.* **2019**, *388*, 107-125.

(71) Tu, B.; Diestel, L.; Shi, Z.-L.; Bandara, W. R. L. N.; Chen, Y.; Lin, W.; Zhang, Y.-B.; Telfer, S. G.; Li, Q. Harnessing Bottom-Up Self-Assembly To Position Five Distinct Components in an Ordered Porous Framework. *Angew. Chem. Int. Ed.* **2019**, *58*, 5348-5353.

(72) Deng, H.; Doonan, C. J.; Furukawa, H.; Ferreira, R. B.; Towne, J.; Knobler, C. B.; Wang, B.; Yaghi, O. M. Multiple Functional Groups of Varying Ratios in Metal-Organic Frameworks. *Science* **2010**, *327*, 846-850.

(73) Wang, L. J.; Deng, H.; Furukawa, H.; Gándara, F.; Cordova, K. E.; Peri, D.; Yaghi, O. M. Synthesis and Characterization of Metal–Organic Framework-74 Containing 2, 4, 6, 8, and 10 Different Metals. *Inorg. Chem.* **2014**, *53*, 5881-5883.

(74) Osborn Popp, T. M.; Yaghi, O. M. Sequence-Dependent Materials. *Acc. Chem. Res.* **2017**, *50*, 532-534.

(75) Osborn Popp, T. M.; Plantz, A. Z.; Yaghi, O. M.; Reimer, J. A. Precise Control of Molecular Self-Diffusion in Isoreticular and Multivariate Metal-Organic Frameworks. *Chemphyschem* **2020**, *21*, 32-35.

(76) Zhou, C.; Longley, L.; Krajnc, A.; Smales, G. J.; Qiao, A.; Erucar, I.; Doherty, C. M.; Thornton, A. W.; Hill, A. J.; Ashling, C. W.et al. Metal-organic framework glasses with permanent accessible porosity. *Nat. Commun.* **2018**, *9*, 5042.

(77) Titi, H. M.; Marrett, J. M.; Dayaker, G.; Arhangelskis, M.; Mottillo, C.; Morris, A. J.; Rachiero, G. P.; Friščić, T.; Rogers, R. D. Hypergolic zeolitic imidazolate frameworks (ZIFs) as next-generation solid fuels: Unlocking the latent energetic behavior of ZIFs. *Sci. Adv.* **2019**, *5*, eaav9044.

(78) He, T.; Pachfule, P.; Wu, H.; Xu, Q.; Chen, P. Hydrogen carriers. *Nat. Rev. Mater* **2016**, *1*, 16059.

(79) Rosi, N. L.; Eckert, J.; Eddaoudi, M.; Vodak, D. T.; Kim, J.; O'Keeffe, M.; Yaghi, O. M. Hydrogen Storage in Microporous Metal-Organic Frameworks. *Science* **2003**, *300*, 1127-1130.

(80) Lin, X.; Telepeni, I.; Blake, A. J.; Dailly, A.; Brown, C. M.; Simmons, J. M.; Zoppi, M.; Walker, G. S.; Thomas, K. M.; Mays, T. J.et al. High Capacity Hydrogen Adsorption in Cu(II) Tetracarboxylate Framework Materials: The Role of Pore Size, Ligand Functionalization, and Exposed Metal Sites. *J. Am. Chem. Soc.* **2009**, *131*, 2159-2171.

(81) Ma, S.; Eckert, J.; Forster, P. M.; Yoon, J. W.; Hwang, Y. K.; Chang, J.-S.; Collier, C. D.; Parise, J. B.; Zhou, H.-C. Further Investigation of the Effect of Framework Catenation on Hydrogen Uptake in Metal−Organic Frameworks. *J. Am. Chem. Soc.* **2008**, *130*, 15896-15902.

(82) Zhou, W.; Wu, H.; Yildirim, T. Enhanced H2 Adsorption in Isostructural Metal−Organic Frameworks with Open Metal Sites: Strong Dependence of the Binding Strength on Metal Ions. *J. Am. Chem. Soc.* **2008**, *130*, 15268-15269.

(83) Lee, Y.-G.; Moon, H. R.; Cheon, Y. E.; Suh, M. P. A Comparison of the H2 Sorption Capacities of Isostructural Metal–Organic Frameworks With and Without Accessible Metal Sites: [{Zn_2(abtc)$(dmf)_2$}$_3$] and [{Cu_2(abtc)$(dmf)_2$}$_3$] versus [{Cu_2(abtc)}$_3$]. *Angew. Chem. Int. Ed.* **2008**, *47*, 7741-7745.

(84) Ding, M.; Flaig, R. W.; Jiang, H.-L.; Yaghi, O. M. Carbon capture and conversion using metal–organic frameworks and MOF-based materials. *Chem. Soc. Rev.* **2019**, *48*, 2783-2828.

(85) Liu, J.; Wei, Y.; Zhao, Y. Trace Carbon Dioxide Capture by Metal–Organic Frameworks. *ACS Sustain. Chem. Eng.* **2019**, *7*, 82-93.

(86) Olajire, A. A. Synthesis chemistry of metal-organic frameworks for CO_2 capture and conversion for sustainable energy future. *Renew. Sust. Energ. Rev.* **2018**, *92*, 570-607.

(87) Couck, S.; Denayer, J. F. M.; Baron, G. V.; Rémy, T.; Gascon, J.; Kapteijn, F. An Amine-Functionalized MIL-53 Metal−Organic Framework with Large Separation Power for CO_2 and CH_4. *J. Am. Chem. Soc.* **2009**, *131*, 6326-6327.

(88) Qazvini, O. T.; Babarao, R.; Telfer, S. G. Selective capture of carbon dioxide from hydrocarbons using a metal-organic framework. *Nat. Commun.* **2021**, *12*, 197.

(89) Park, J.; Yuan, D.; Pham, K. T.; Li, J.-R.; Yakovenko, A.; Zhou, H.-C. Reversible Alteration of CO_2 Adsorption upon Photochemical or Thermal Treatment in a Metal–Organic Framework. *J. Am. Chem. Soc.* **2012**, *134*, 99-102.

(90) Moghadam, P. Z.; Ivy, J. F.; Arvapally, R. K.; dos Santos, A. M.; Pearson, J. C.; Zhang, L.; Tylianakis, E.; Ghosh, P.; Oswald, I. W. H.; Kaipa, U.et al. Adsorption and molecular siting of

CO_2, water, and other gases in the superhydrophobic, flexible pores of FMOF-1 from experiment and simulation. *Chem. Sci.* **2017**, *8*, 3989-4000.

(91) Kökçam-Demir, Ü.; Goldman, A.; Esrafili, L.; Gharib, M.; Morsali, A.; Weingart, O.; Janiak, C. Coordinatively unsaturated metal sites (open metal sites) in metal–organic frameworks: design and applications. *Chem. Soc. Rev.* **2020**.

(92) Schlichte, K.; Kratzke, T.; Kaskel, S. Improved synthesis, thermal stability and catalytic properties of the metal-organic framework compound $Cu_3(BTC)_2$. *Microporous Mesoporous Mater.* **2004**, *73*, 81-88.

(93) Corma, A.; Iglesias, M.; Llabrés i Xamena, F. X.; Sánchez, F. Cu and Au Metal–Organic Frameworks Bridge the Gap between Homogeneous and Heterogeneous Catalysts for Alkene Cyclopropanation Reactions. *Chem. Eur. J.* **2010**, *16*, 9789-9795.

(94) Pérez-Mayoral, E.; Čejka, J. [$Cu_3(BTC)_2$]: A Metal–Organic Framework Catalyst for the Friedländer Reaction. *ChemCatChem* **2011**, *3*, 157-159.

(95) Opanasenko, M.; Shamzhy, M.; Čejka, J. Solid Acid Catalysts for Coumarin Synthesis by the Pechmann Reaction: MOFs versus Zeolites. *ChemCatChem* **2013**, *5*, 1024-1031.

(96) Zhou, M.; El-Sayed, E.-S. M.; Ju, Z.; Wang, W.; Yuan, D. The synthesis and applications of chiral pyrrolidine functionalized metal–organic frameworks and covalent-organic frameworks. *Inorg. Chem. Front.* **2020**, *7*, 1319-1333.

(97) Zhou, Y.-X.; Chen, Y.-Z.; Hu, Y.; Huang, G.; Yu, S.-H.; Jiang, H.-L. MIL-101-SO_3H: A Highly Efficient Brønsted Acid Catalyst for Heterogeneous Alcoholysis of Epoxides under Ambient Conditions. *Chem. Eur. J.* **2014**, *20*, 14976-14980.

(98) Roberts, J. M.; Fini, B. M.; Sarjeant, A. A.; Farha, O. K.; Hupp, J. T.; Scheidt, K. A. Urea Metal–Organic Frameworks as Effective and Size-Selective Hydrogen-Bond Catalysts. *J. Am. Chem. Soc.* **2012**, *134*, 3334-3337.

(99) Schreiner, P. R.; Wittkopp, A. H-Bonding Additives Act Like Lewis Acid Catalysts. *Org. Lett.* **2002**, *4*, 217-220.

(100) Shultz, A. M.; Farha, O. K.; Hupp, J. T.; Nguyen, S. T. A Catalytically Active, Permanently Microporous MOF with Metalloporphyrin Struts. *J. Am. Chem. Soc.* **2009**, *131*, 4204-4205.

(101) Meng, L.; Cheng, Q.; Kim, C.; Gao, W.-Y.; Wojtas, L.; Chen, Y.-S.; Zaworotko, M. J.; Zhang, X. P.; Ma, S. Crystal Engineering of a Microporous, Catalytically Active fcu Topology MOF Using a Custom-Designed Metalloporphyrin Linker. *Angew. Chem. Int. Ed.* **2012**, *51*, 10082-10085.

(102) Katsuki, T. Chiral Metallosalen Complexes: Structures and Catalyst Tuning for Asymmetric Epoxidation and Cyclopropanation. *Adv. Synth. Catal.* **2002**, *344*, 131-147.

(103) Zhang, W.; Loebach, J. L.; Wilson, S. R.; Jacobsen, E. N. Enantioselective epoxidation of unfunctionalized olefins catalyzed by salen manganese complexes. *J. Am. Chem. Soc.* **1990**, *112*, 2801-2803.

(104) Cho, S.-H.; Ma, B.; Nguyen, S. T.; Hupp, J. T.; Albrecht-Schmitt, T. E. A metal-organic framework material that functions as an enantioselective catalyst for olefin epoxidation. *Chem. Commun.* **2006**, 2563-2565.

(105) Yang, Z.; Zhu, C.; Li, Z.; Liu, Y.; Liu, G.; Cui, Y. Engineering chiral Fe(salen)-based metal-organic

frameworks for asymmetric sulfide oxidation. *Chem. Commun.* **2014**, *50*, 8775-8778.

(106) Walton, K. S.; Snurr, R. Q. Applicability of the BET Method for Determining Surface Areas of Microporous Metal−Organic Frameworks. *J. Am. Chem. Soc.* **2007**, *129*, 8552-8556.

(107) Sheldrick, G. A short history of SHELX. *Acta Cryst. A* **2008**, *64*, 112-122.

(108) Shi-Yao Yang; La-Sheng Long; Rong-Bin Huang; Lan-Sun Zheng. Crystal Structure of a 3D Coordination Polymer: Zinc Terephthalate Hydrate. *Main Group Met. Chem.* **2002**, *25*, 329.

(109) Liu, L.; Zhou, T.-Y.; Telfer, S. G. Modulating the Performance of an Asymmetric Organocatalyst by Tuning Its Spatial Environment in a Metal-Organic Framework. *J. Am. Chem. Soc.* **2017**, *139*, 13936-13943.

(110) Cornelio, J.; Zhou, T.-Y.; Alkaş, A.; Telfer, S. G. Systematic Tuning of the Luminescence Output of Multicomponent Metal–Organic Frameworks. *J. Am. Chem. Soc.* **2018**, *140*, 15470-15476.

(111) Zhou, T.-Y.; Auer, B.; Lee, S. J.; Telfer, S. G. Catalysts Confined in Programmed Framework Pores Enable New Transformations and Tune Reaction Efficiency and Selectivity. *J. Am. Chem. Soc.* **2019**, *141*, 1577-1582.

(112) Gardarsson, H.; Schweizer, W. B.; Trapp, N.; Diederich, F. Structures and Properties of Molecular Torsion Balances to Decipher the Nature of Substituent Effects on the Aromatic Edge-to-Face Interaction. *Chem. Eur. J.* **2014**, *20*, 4608-4616.

(113) Alkaş, A.; Friche, L. E. S.; Harris, S. N.; Telfer, S. G. Thermal Elimination of Ethylene from Cyclobutyl Groups Characterized by X-ray Crystallography in a Metal–Organic Framework Matrix. *Chem. Eur. J.* **2020**, *26*, 10321-10329.

(114) Forster, P. M.; Burbank, A. R.; Livage, C.; Férey, G.; Cheetham, A. K. The role of temperature in the synthesis of hybrid inorganic–organic materials: the example of cobalt succinates. *Chem. Commun.* **2004**, 368-369.

(115) Sun, Y.-X.; Sun, W.-Y. Influence of temperature on metal-organic frameworks. *Chin. Chem. Lett.* **2014**, *25*, 823-828.

(116) Sorrenti, A.; Jones, L.; Sevim, S.; Cao, X.; deMello, A. J.; Martí-Gastaldo, C.; Puigmartí-Luis, J. Growing and Shaping Metal–Organic Framework Single Crystals at the Millimeter Scale. *J. Am. Chem. Soc.* **2020**, *142*, 9372-9381.

(117) Kwon, O.; Kim, J. Y.; Park, S.; Lee, J. H.; Ha, J.; Park, H.; Moon, H. R.; Kim, J. Computer-aided discovery of connected metal-organic frameworks. *Nat. Commun.* **2019**, *10*, 3620.

(118) Deria, P.; Gómez-Gualdrón, D. A.; Hod, I.; Snurr, R. Q.; Hupp, J. T.; Farha, O. K. Framework-Topology-Dependent Catalytic Activity of Zirconium-Based (Porphinato)zinc(II) MOFs. *J. Am. Chem. Soc.* **2016**, *138*, 14449-14457.

(119) Sheldrick, G. SHELXT - Integrated space-group and crystal-structure determination. *Acta Cryst. A* **2015**, *71*, 3-8.

(120) Dolomanov, O. V.; Bourhis, L. J.; Gildea, R. J.; Howard, J. A. K.; Puschmann, H. OLEX2: a complete structure solution, refinement and analysis program. *J. Appl. Crystallogr.* **2009**, *42*, 339-341.

(121) Inaki, M.; Liu, J.; Matsuno, K. Cell chirality: its origin and roles in left-right asymmetric development. *Philos. Trans. R. Soc. B* **2016**, *371*, 20150403.

(122) Blaschke, G.; Kraft, H. P.; Fickentscher, K.; Kohler, F. Chromatographic separation of racemic thalidomide and teratogenic activity of its enantiomers (author's transl). *Arzneimittelforschung* **1979**, *29*, 1640-1642.

(123) Halpern, J.; Trost, B. M. Asymmetric Catalysis. *Proc. Natl. Acad. Sci. U.S.A.* **2004**, *101*, 5347-5347.

(124) Cerqueira, N.; Moorthy, H.; Fernandes, P. A.; Ramos, M. J. The mechanism of the Ser-(cis)Ser-Lys catalytic triad of peptide amidases. *Phys. Chem. Chem. Phys.* **2017**, *19*, 12343-12354.

(125) Xue, Y. P.; Cao, C. H.; Zheng, Y. G. Enzymatic asymmetric synthesis of chiral amino acids. *Chem. Soc. Rev.* **2018**, *47*, 1516-1561.

(126) Shugrue, C. R.; Miller, S. J. Applications of Nonenzymatic Catalysts to the Alteration of Natural Products. *Chem Rev* **2017**, *117*, 11894-11951.

(127) Metrano, A. J.; Miller, S. J. Peptide-Based Catalysts Reach the Outer Sphere through Remote Desymmetrization and Atroposelectivity. *Acc. Chem. Res.* **2019**, *52*, 199-215.

(128) Toste, F. D.; Sigman, M. S.; Miller, S. J. Pursuit of Noncovalent Interactions for Strategic Site-Selective Catalysis. *Acc. Chem. Res.* **2017**, *50*, 609-615.

(129) Wu, X.; He, C.; Wu, X.; Qu, S.; Duan, C. An l-proline functionalized metallo-organic triangle as size-selective homogeneous catalyst for asymmetry catalyzing aldol reactions. *Chem. Commun.* **2011**, *47*, 8415-8417.

(130) Song, F.; Wang, C.; Falkowski, J. M.; Ma, L.; Lin, W. Isoreticular Chiral Metal-Organic Frameworks for Asymmetric Alkene Epoxidation: Tuning Catalytic Activity by Controlling Framework Catenation and Varying Open Channel Sizes. *J. Am. Chem. Soc.* **2010**, *132*, 15390-15398.

(131) Dang, D.; Wu, P.; He, C.; Xie, Z.; Duan, C. Homochiral Metal-Organic Frameworks for Heterogeneous Asymmetric Catalysis. *J. Am. Chem. Soc.* **2010**, *132*, 14321-14323.

(132) Jing, X.; He, C.; Dong, D.; Yang, L.; Duan, C. Homochiral Crystallization of Metal-Organic Silver Frameworks: Asymmetric [3+2] Cycloaddition of an Azomethine Ylide. *Angew. Chem. Int. Ed.* **2012**, *51*, 10127-10131.

(133) Xia, Z.; Jing, X.; He, C.; Wang, X.; Duan, C. Coordinative Alignment of Chiral Molecules to Control over the Chirality Transfer in Spontaneous Resolution and Asymmetric Catalysis. *Sci. Rep.* **2017**, *7*, 15418.

(134) Shi, H.; Herron, A. N.; Shao, Y.; Shao, Q.; Yu, J.-Q. Enantioselective remote meta-C–H arylation and alkylation via a chiral transient mediator. *Nature* **2018**, *558*, 581-585.

(135) Lewis, C. A.; Gustafson, J. L.; Chiu, A.; Balsells, J.; Pollard, D.; Murry, J.; Reamer, R. A.; Hansen, K. B.; Miller, S. J. A Case of Remote Asymmetric Induction in the Peptide-Catalyzed Desymmetrization of a Bis(phenol). *J. Am. Chem. Soc.* **2008**, *130*, 16358-16365.

(136) Damron, J. T.; Ma, J.; Kurz, R.; Saalwachter, K.; Matzger, A. J.; Ramamoorthy, A. The Influence of Chemical Modification on Linker Rotational Dynamics in Metal-Organic

Frameworks. *Angew. Chem. Int. Ed.* **2018**, *57*, 8678-8681.

(137) Pakhira, S.; Takayanagi, M.; Nagaoka, M. Diverse Rotational Flexibility of Substituted Dicarboxylate Ligands in Functional Porous Coordination Polymers. *J. Phys. Chem. C* **2015**, *119*, 28789-28799.

(138) Sinha, N.; Deshpande, I.; Pakhira, S. Substituents Effects of Organic Linkers on Rotational Energy Barriers in Metal-Organic Frameworks. *ChemistrySelect* **2019**, *4*, 8584-8592.

(139) Ali Akbar Razavi, S.; Morsali, A. Linker functionalized metal-organic frameworks. *Coord. Chem. Rev.* **2019**, *399*, 213023.

(140) Yoshihiro, S.; Yuichi, H.; Kazuo, N. Guanidine-Thiourea Bifunctional Organocatalyst for the Asymmetric Henry (Nitroaldol) Reaction. *Adv. Synth. Catal.* **2005**, *347*, 1643-1648.

(141) Otevrel, J.; Bobal, P. Diamine-Tethered Bis(thiourea) Organocatalyst for Asymmetric Henry Reaction. *J. Org. Chem* **2017**, *82*, 8342-8358.

(142) Padmanaban, M.; Müller, P.; Lieder, C.; Gedrich, K.; Grünker, R.; Bon, V.; Senkovska, I.; Baumgärtner, S.; Opelt, S.; Paasch, S.et al. Application of a chiral metal-organic framework in enantioselective separation. *Chem. Commun.* **2011**, *47*, 12089-12091.

(143) Hoffmann, H. C.; Paasch, S.; Müller, P.; Senkovska, I.; Padmanaban, M.; Glorius, F.; Kaskel, S.; Brunner, E. Chiral recognition in metal-organic frameworks studied by solid-state NMR spectroscopy using chiral solvating agents. *Chem. Commun.* **2012**, *48*, 10484-10486.

(144) Dyson, P. J.; Jessop, P. G. Solvent effects in catalysis: rational improvements of catalysts via manipulation of solvent interactions. *Catal. Sci. Technol.* **2016**, *6*, 3302-3316.

(145) Wang, Z.; Cohen, S. M. Postsynthetic modification of metal-organic frameworks. *Chem. Soc. Rev.* **2009**, *38*, 1315-1329.

(146) Kolb, H. C.; Finn, M. G.; Sharpless, K. B. Click Chemistry: Diverse Chemical Function from a Few Good Reactions. *Angew. Chem. Int. Ed.* **2001**, *40*, 2004-2021.

(147) Wang, Z.; Liu, J.; Arslan, H. K.; Grosjean, S.; Hagendorn, T.; Gliemann, H.; Brase, S.; Woll, C. Post-synthetic modification of metal-organic framework thin films using click chemistry: the importance of strained C-C triple bonds. *Langmuir* **2013**, *29*, 15958-15964.

(148) Li, B.; Gui, B.; Hu, G.; Yuan, D.; Wang, C. Postsynthetic Modification of an Alkyne-Tagged Zirconium Metal-Organic Framework via a "Click" Reaction. *Inorg. Chem.* **2015**, *54*, 5139-5141.

(149) Goto, Y.; Sato, H.; Shinkai, S.; Sada, K. "Clickable" Metal-Organic Framework. *J. Am. Chem. Soc.* **2008**, *130*, 14354-14355.

(150) Feng, L.; Lv, X.-L.; Yan, T.-H.; Zhou, H.-C. Modular Programming of Hierarchy and Diversity in Multivariate Polymer/Metal-Organic Framework Hybrid Composites. *J. Am. Chem. Soc.* **2019**, *141*, 10342-10349.

(151) Ishiwata, T.; Furukawa, Y.; Sugikawa, K.; Kokado, K.; Sada, K. Transformation of Metal–Organic Framework to Polymer Gel by Cross-Linking the Organic Ligands Preorganized in Metal–Organic Framework. *J. Am. Chem. Soc.* **2013**, *135*, 5427-5432.

(152) Fluch, U.; McCarthy, B. D.; Ott, S. Post synthetic exchange enables orthogonal click

chemistry in a metal organic framework. *Dalton Trans.* **2019**, *48*, 45-49.

(153) Hema, K.; Gonnade, R. G.; Sureshan, K. M. Crystal-to-Crystal Synthesis of Helically Ordered Polymers of Trehalose by Topochemical Polymerization. *Angew. Chem. Int. Ed.* **2020**, *59*, 2897-2903.

(154) Pathigoolla, A.; Gonnade, R. G.; Sureshan, K. M. Topochemical Click Reaction: Spontaneous Self-Stitching of a Monosaccharide to Linear Oligomers through Lattice-Controlled Azide–Alkyne Cycloaddition. *Angew. Chem. Int. Ed.* **2012**, *51*, 4362-4366.

(155) Fishburn, M. G.; Skelton, D. R.; Telfer, S. G.; Wagner, P.; Richardson, C. Second-order programming the synthesis of metal–organic frameworks. *Chem. Commun.* **2020**, *56*, 12355-12358.

(156) Ishiwata, T.; Furukawa, Y.; Sugikawa, K.; Kokado, K.; Sada, K. Transformation of metal-organic framework to polymer gel by cross-linking the organic ligands preorganized in metal-organic framework. *J. Am. Chem. Soc.* **2013**, *135*, 5427-5432.

(157) Furukawa, Y.; Ishiwata, T.; Sugikawa, K.; Kokado, K.; Sada, K. Nano- and Microsized Cubic Gel Particles from Cyclodextrin Metal–Organic Frameworks. *Angew. Chem. Int. Ed.* **2012**, *51*, 10566-10569.

(158) Nagata, S.; Sato, H.; Sugikawa, K.; Kokado, K.; Sada, K. Conversion of azide to primary amine via Staudinger reaction in metal-organic frameworks. *CrystEngComm* **2012**, *14*, 4137-4141.

(159) Ding, J.; Zhou, C.; Li, K.; Zhang, A.; Yao, F.; Xu, L.; Fu, G. Preparation of well-defined fibrous hydrogels via electrospinning and in situ “click chemistry”. *RSC Advances* **2016**, *6*, 27871-27878.

(160) L'Abbe, G. Decomposition and addition reactions of organic azides. *Chem. Rev.* **1969**, *69*, 345-363.

(161) Thommes, M.; Kaneko, K.; Neimark, A. V.; Olivier, J. P.; Rodriguez-Reinoso, F.; Rouquerol, J.; Sing, K. S. W. Physisorption of gases, with special reference to the evaluation of surface area and pore size distribution (IUPAC Technical Report). *Pure Appl. Chem.* **2015**, *87*, 1051-1069.

(162) Nuhnen, A.; Janiak, C. A practical guide to calculate the isosteric heat/enthalpy of adsorption via adsorption isotherms in metal–organic frameworks, MOFs. *Dalton Trans.* **2020**, *49*, 10295-10307.

(163) Steemers, L.; Wanner, M. J.; van Leeuwen, B. R. C.; Hiemstra, H.; van Maarseveen, J. H. Attempted [2]Catenane Synthesis via a Quasi[1]catenane by a Templated Backfolding Strategy. *Eur. J. Org. Chem.* **2018**, *2018*, 874-878.

(164) Dincă, M.; Dailly, A.; Liu, Y.; Brown, C. M.; Neumann, D. A.; Long, J. R. Hydrogen Storage in a Microporous Metal–Organic Framework with Exposed Mn2+ Coordination Sites. *J. Am. Chem. Soc.* **2006**, *128*, 16876-16883.

(165) Britovsek, G. J. P.; Gibson, V. C.; Wass, D. F. The Search for New-Generation Olefin Polymerization Catalysts: Life beyond Metallocenes. *Angew. Chem. Int. Ed.* **1999**, *38*, 428-447.

(166) Brintzinger, H. H.; Fischer, D.; Mülhaupt, R.; Rieger, B.; Waymouth, R. M. Stereospecific Olefin Polymerization with Chiral Metallocene Catalysts. *Angew. Chem. Int. Ed.* **1995**, *34*, 1143-1170.

(167) Trnka, T. M.; Grubbs, R. H. The Development of L2X2RuCHR Olefin Metathesis Catalysts: An Organometallic Success Story. *Acc. Chem. Res.* **2001**, *34*, 18-29.

(168) Grubbs, R. H. Olefin metathesis. *Tetrahedron* **2004**, *60*, 7117-7140.

(169) Janiak, C. Metallocene and related catalysts for olefin, alkyne and silane dimerization and oligomerization. *Coord. Chem. Rev.* **2006**, *250*, 66-94.

(170) Sarkar, D.; Bera, N.; Ghosh, S. [2+2] Photochemical Cycloaddition in Organic Synthesis. *Eur. J. Org. Chem.* **2020**, *2020*, 1310-1326.

(171) Grubbs, R. H.; Trnka, T. M. (2005). Ruthenium-Catalyzed Olefin Metathesis. In *Ruthenium in Organic Synthesis* (pp. 153-177). Wiley-VCH Verlag GmbH & Co. KGaA. doi: 10.1002/3527603832.ch6

(172) Schrodi, Y.; Pederson, R. *Evolution and applications of second-generation ruthenium olefin metathesis catalysts*, 2007.

(173) Vermeulen, N. A.; Karagiaridi, O.; Sarjeant, A. A.; Stern, C. L.; Hupp, J. T.; Farha, O. K.; Stoddart, J. F. Aromatizing Olefin Metathesis by Ligand Isolation inside a Metal– Organic Framework. *J. Am. Chem. Soc.* **2013**, *135*, 14916-14919.

(174) Poater, A.; Ragone, F.; Correa, A.; Szadkowska, A.; Barbasiewicz, M.; Grela, K.; Cavallo, L. Mechanistic Insights into the cis–trans Isomerization of Ruthenium Complexes Relevant to Catalysis of Olefin Metathesis. *Chem. Eur. J.* **2010**, *16*, 14354-14364.

(175) Benitez, D.; Goddard, W. A. The Isomerization Equilibrium between Cis and Trans Chloride Ruthenium Olefin Metathesis Catalysts from Quantum Mechanics Calculations. *J. Am. Chem. Soc.* **2005**, *127*, 12218-12219.

(176) Karan, B.; İmamoğlu, Y. (1989). On the Presence of Dichloro-W-Carbenes in Photocatalytic Olefin Metathesis Reactions. In Schubert, U. (ed.) *Advances in Metal Carbene Chemistry* (pp. 347-349). Dordrecht: Springer Netherlands. doi: 10.1007/978-94-009-2317-1_37

(177) Vidavsky, Y.; Lemcoff, N. G. Light-induced olefin metathesis. *Beilstein J. Org. Chem.* **2010**, *6*, 1106-1119.

(178) Kissin, Y. V.; Goldman, A. S. Chemistry and Mechanism of Alkene Polymerization Reactions with Metallocene Catalysts. *Macromol. Chem. Phys.* **2009**, *210*, 1942-1956.

(179) Collins, R. A.; Russell, A. F.; Mountford, P. Group 4 metal complexes for homogeneous olefin polymerisation: a short tutorial review. *Appl. Petrochem. Res.* **2015**, *5*, 153-171.

(180) Claassens, I. E.; Nikolayenko, V. I.; Haynes, D. A.; Barbour, L. J. Solvent-Mediated Synthesis of Cyclobutane Isomers in a Photoactive Cadmium(II) Porous Coordination Polymer. *Angew. Chem. Int. Ed.* **2018**, *57*, 15563-15566.

(181) Glaser, C. Beiträge zur Kenntniss des Acetenylbenzols. *Berichte der deutschen chemischen Gesellschaft* **1869**, *2*, 422-424.

(182) Glaser, C. Untersuchungen über einige Derivate der Zimmtsäure. *Justus Liebigs Ann. Chem.* **1870**, *154*, 137-171.

(183) Siemsen, P.; Livingston, R. C.; Diederich, F. Acetylenic Coupling: A Powerful Tool in Molecular Construction. *Angew. Chem. Int. Ed.* **2000**, *39*, 2632-2657.

(184) Hua, R. (2013). Copper-Catalyzed Alkynylation and Alkenylation Reactions of Alkynyl Derivatives: New Access to Diynes and Enynes. In *Copper-Mediated Cross-Coupling Reactions* (pp. 455-483). doi: https://doi.org/10.1002/9781118690659.ch12

(185) Vilhelmsen, M. H.; Jensen, J.; Tortzen, C. G.; Nielsen, M. B. The Glaser–Hay Reaction: Optimization and Scope Based on 13C NMR Kinetics Experiments. *Eur. J. Org. Chem.* **2013**, 701-711.

(186) Su, L.; Dong, J.; Liu, L.; Sun, M.; Qiu, R.; Zhou, Y.; Yin, S.-F. Copper Catalysis for Selective Heterocoupling of Terminal Alkynes. *J. Am. Chem. Soc.* **2016**, *138*, 12348-12351.

(187) Lee, C.-C.; Leung, M.-k.; Lee, G.-H.; Liu, Y.-H.; Peng, S.-M. Revisit of the Dessy−White Intramolecular Acetylene−Acetylene [2 + 2] Cycloadditions. *J. Org. Chem* **2006**, *71*, 8417-8423.

(188) Maitra, U. Molecule of the month. *Resonance* **1996**, *1*, 90-91.

(189) Maier, G. Tetrahedrane and Cyclobutadiene. *Angew. Chem. Int. Ed. Engl.* **1988**, *27*, 309-332.

(190) Jiang, J.; Yaghi, O. M. Bronsted acidity in metal-organic frameworks. *Chem. Rev.* **2015**, *115*, 6966-6997.

(191) Juan-Alcañiz, J.; Gielisse, R.; Lago, A. B.; Ramos-Fernandez, E. V.; Serra-Crespo, P.; Devic, T.; Guillou, N.; Serre, C.; Kapteijn, F.; Gascon, J. Towards acid MOFs – catalytic performance of sulfonic acid functionalized architectures. *Catal. Sci. Technol.* **2013**, *3*, 2311-2318.

(192) Zang, Y.; Shi, J.; Zhang, F.; Zhong, Y.; Zhu, W. Sulfonic acid-functionalized MIL-101 as a highly recyclable catalyst for esterification. *Catal. Sci. Technol.* **2013**, *3*, 2044-2049.

(193) Gagnon, K. J.; Perry, H. P.; Clearfield, A. Conventional and Unconventional Metal–Organic Frameworks Based on Phosphonate Ligands: MOFs and UMOFs. *Chem. Rev.* **2012**, *112*, 1034-1054.

(194) Zheng, Y.; Bian, M.; Deng, X.-Q.; Wang, S.-B.; Quan, Z.-S. Synthesis and Anticonvulsant Activity Evaluation of 5-Phenyl-[1,2,4]triazolo[4,3-c]quinazolin-3-amines. *Arch. Pharm.* **2013**, *346*, 119-126.

(195) Merad, J.; Lalli, C.; Bernadat, G.; Maury, J.; Masson, G. Enantioselective Brønsted Acid Catalysis as a Tool for the Synthesis of Natural Products and Pharmaceuticals. *Chem. Eur. J.* **2018**, *24*, 3925-3943.

(196) Shagufta; Ahmad, I.; Dhar, R. Sulfonic Acid-Functionalized Solid Acid Catalyst in Esterification and Transesterification Reactions. *Catal. Surv. from Asia.* **2017**, *21*, 53-69.

DRC 16

MASSEY UNIVERSITY
TE KUNENGA KI PŪREHUROA
UNIVERSITY OF NEW ZEALAND

GRADUATE
RESEARCH
SCHOOL

STATEMENT OF CONTRIBUTION
DOCTORATE WITH PUBLICATIONS/MANUSCRIPTS

We, the candidate and the candidate's Primary Supervisor, certify that all co-authors have consented to their work being included in the thesis and they have accepted the candidate's contribution as indicated below in the *Statement of Originality*.

Name of candidate:	Seok June Lee
Name/title of Primary Supervisor:	Professor Shane Telfer
In which chapter is the manuscript /published work:	Chapter 5

Please select one of the following three options:

○ The manuscript/published work is published or in press

- Please provide the full reference of the Research Output:

○ The manuscript is currently under review for publication – please indicate:

- The name of the journal:
- The percentage of the manuscript/published work that was contributed by the candidate:
- Describe the contribution that the candidate has made to the manuscript/published work:

● It is intended that the manuscript will be published, but it has not yet been submitted to a journal

Candidate's Signature:	Digitally signed by Seok June Lee Date: 2021.02.22 12:26:42 +13'00'
Date:	22-Feb-2021
Primary Supervisor's Signature:	SGTelfer Digitally signed by Shane Telfer DN: cn=Shane Telfer, c=NZ, o=Massey University, email=s.telfer@massey.ac.nz Date: 2021.02.22 12:43:10 +13'00'
Date:	22-Feb-2021

This form should appear at the end of each thesis chapter/section/appendix submitted as a manuscript/publication or collected as an appendix at the end of the thesis.

GRS Version 5 – 13 December 2019
DRC 19/09/10

MASSEY UNIVERSITY
TE KUNENGA KI PŪREHUROA
UNIVERSITY OF NEW ZEALAND

GRADUATE RESEARCH SCHOOL

STATEMENT OF CONTRIBUTION
DOCTORATE WITH PUBLICATIONS/MANUSCRIPTS

We, the candidate and the candidate's Primary Supervisor, certify that all co-authors have consented to their work being included in the thesis and they have accepted the candidate's contribution as indicated below in the *Statement of Originality*.

Name of candidate:	Seok June Lee
Name/title of Primary Supervisor:	Professor Shane Telfer
In which chapter is the manuscript /published work:	Chapter 6

Please select one of the following three options:

○ The manuscript/published work is published or in press

- Please provide the full reference of the Research Output:

○ The manuscript is currently under review for publication – please indicate:

- The name of the journal:
- The percentage of the manuscript/published work that was contributed by the candidate:
- Describe the contribution that the candidate has made to the manuscript/published work:

● It is intended that the manuscript will be published, but it has not yet been submitted to a journal

Candidate's Signature:	Digitally signed by Seok June Lee Date: 2021.02.22 12:27:07 +13'00'
Date:	22-Feb-2021
Primary Supervisor's Signature:	Digitally signed by Shane Telfer DN: cn=Shane Telfer, c=NZ, o=Massey University, email=s.telfer@massey.ac.nz Date: 2021.02.22 12:42:39 +13'00'
Date:	22-Feb-2021

This form should appear at the end of each thesis chapter/section/appendix submitted as a manuscript/ publication or collected as an appendix at the end of the thesis.

GRS Version 5 – 13 December 2019
DRC 19/09/10

Appendix A. For Chapter 2

A.1. Phase determination of co-crystal

A.1.1. Procedure

Three other type-L frameworks were chosen whose organic linkers consist of light atoms (C, H, O and N) and are not much different from the ones of co-crystal in terms of electron density (Figure A-1). The four hkl files from the SCXRD data of each framework were used to determine whether the co-crystal is a mixture of type-L and type-S frameworks.

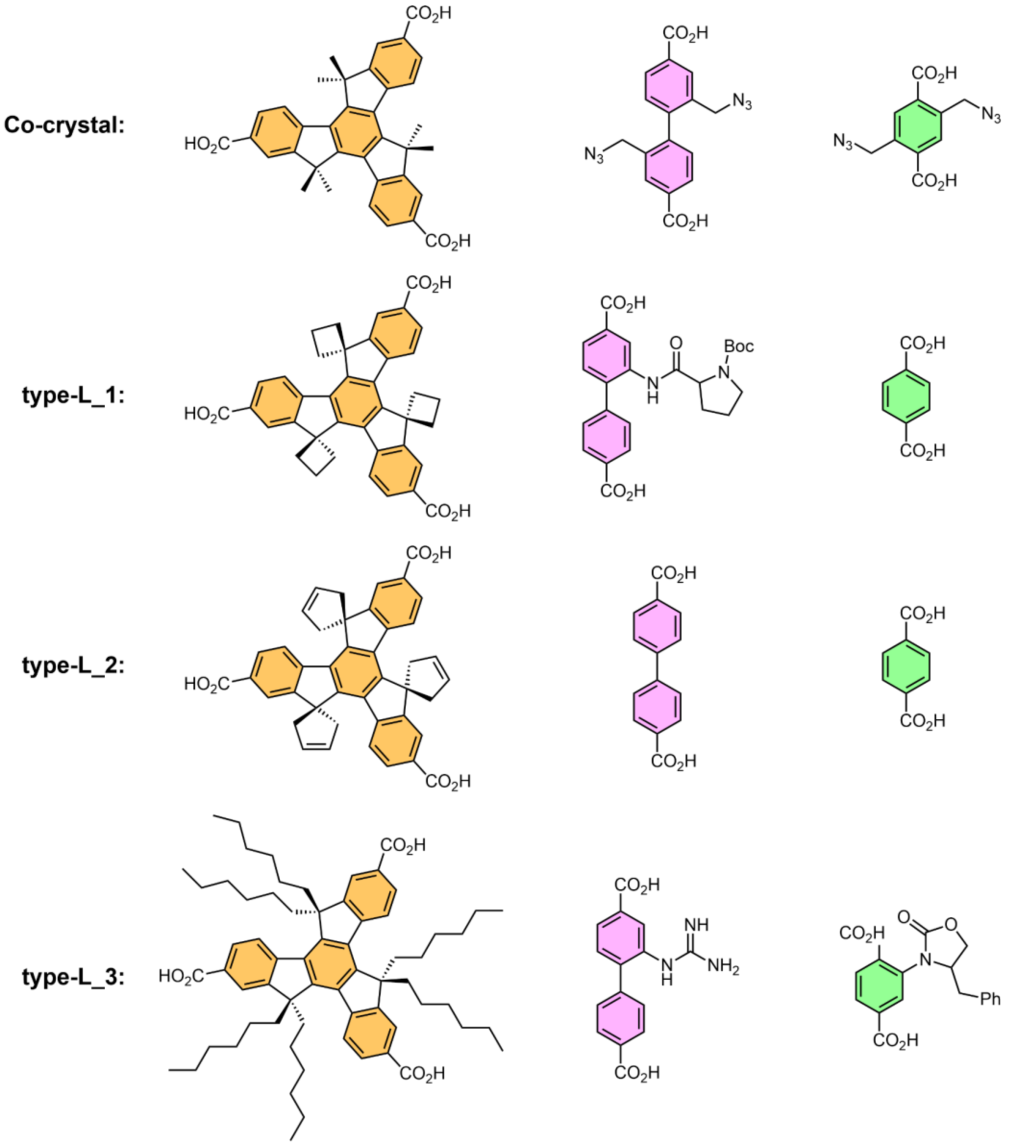

Figure A-1. The linker combinations which used to synthesise the co-crystal (irregularly shaped crystal) and three type-L frameworks.

Each diffraction spot is generally collected multiple times over the number of frames during data collection to increase the reliability of the data. Once data collection is finished, the intensity of each diffraction spot on each frame will be calculated during the integration process. Then each frame will be scaled by comparing the identical diffraction spots appearing over the different frames since the incident X-ray beam intensity may vary for each frame, or the crystal orientation may affect the diffraction spot intensity. After scaling the frames, each diffraction spot's Miller indices, scaled intensity (I) and error for the intensity (σ(I)) are recorded in a text file referred to as HKL file. An example of HKL file content is illustrated in Figure A-2. The file contents were borrowed from one of the type-L frameworks, and in this case, all the entry containing the same numbers for HKL indices considered as the same regardless of the appearing order or their sign due to the symmetry of the cubical lattice of the type-L framework.

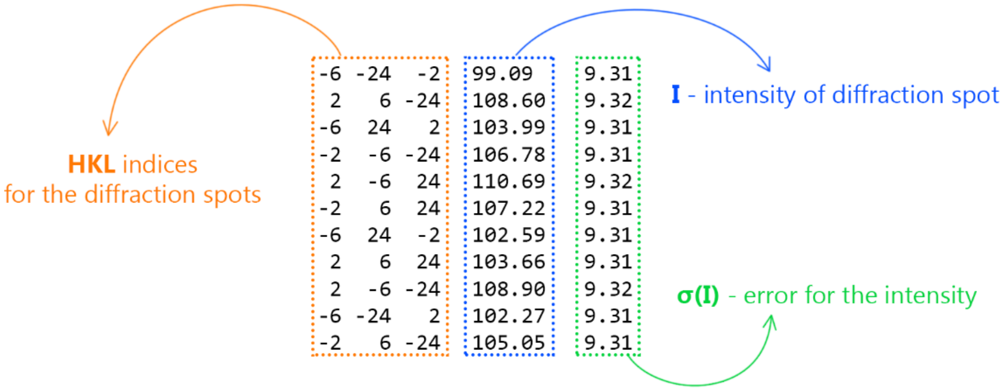

```
-6 -24  -2  99.09  9.31
 2   6 -24 108.60  9.32
-6  24   2 103.99  9.31
-2  -6 -24 106.78  9.31
 2  -6  24 110.69  9.32
-2   6  24 107.22  9.31
-6  24  -2 102.59  9.31
 2   6  24 103.66  9.31
 2  -6 -24 108.90  9.32
-6 -24   2 102.27  9.31
-2   6 -24 105.05  9.31
```

Figure A-2. An example of HKL file content for the diffraction spots belong to the same lattice plane (35 42 1). The intensity for the spot collected several times at different orientation angles with respect to the incident ray during the measurement, and scaled intensity of the diffraction spots and corresponding errors are recorded along with the HKL indices.

In order to compare the intensities of the diffraction spots which diffracted from the co-crystal and other type-L frameworks, ten spots were judiciously chosen from each group, having a wide range of spot intensities. The diffraction image presented in Figure 2-15 is used to select those two groups of spots, and the chosen spots are shown in Figure A-3. The spots denoted with a# (#: 0 – 9) are the ones that do not superimpose with the calculated type-S diffraction spots, and the ones labelled with b# were enclosed in the predicted diffraction spots of the type-S framework. Hence, the intensities belonging to spot a#s (group a) are contributed by only the type-L framework, whereas those of spot b#s (group b) are added up from both type-L and type-S frameworks. The method to compare diffraction spot intensities of the selected two groups of spots are described below.

- The Miller indices for all twenty spots were searched from the diffraction image (Figure A-3) and recorded.
- All the entries corresponding to each Miller index were searched from the HKL file of the co-crystal, and the intensities belonging to the same Miller index were averaged.
- The same procedure was carried on with the other known type-L frameworks (Figure A-1), which are composed of similar organic linkers.
- Compare the averaged spot intensities belonging to the same Miller index between the ones of the co-crystal and those of the other type-L frameworks.

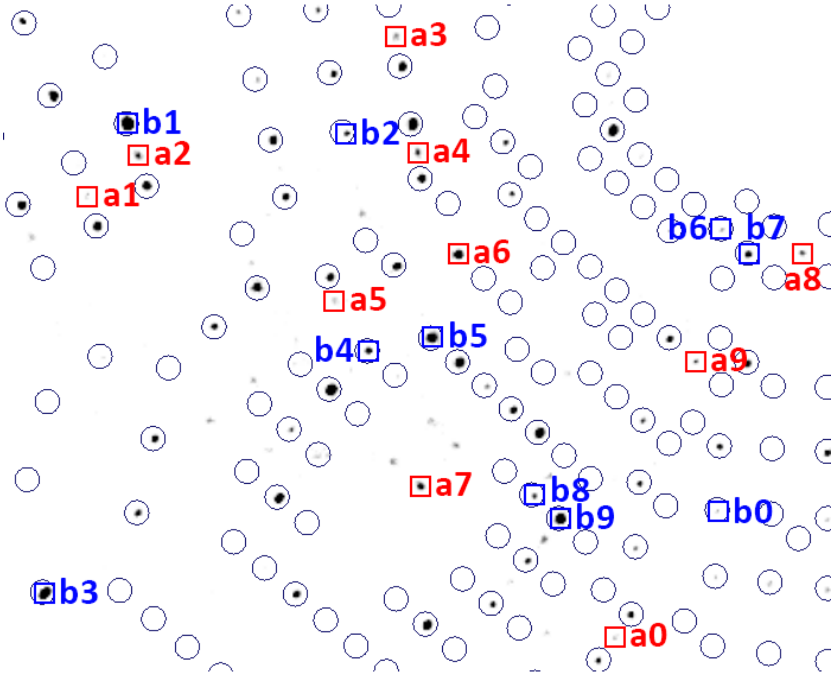

Figure A-3. The circles are the predicted diffraction spot positions based on the calculations with the type-S framework. Two groups of spots, which do not superimpose with the predicted spots of the type-S framework (group a) or which are enclosed in the predicted type-S spots (group b), were carefully chosen to sample various intensities of the spots.

The averaged spot intensities for all twenty spots of each framework are shown in Figure 2-16 (refer to A.1.2 for the detailed HKL file contents). The plots are normalised for a better comparison because the absolute intensity values largely depend on many parameters for data collection, such as exposure time for each frame image. As seen in Figure 2-16, there is an evident intensity difference between the co-crystal and the other type-L frameworks. Most of all, the overall intensity of the diffraction spots in the group a# is generally much lower than the ones belonging to the group b# in the case of the co-crystal. On the other hand, the intensities for both groups lay in a comparable range for all three type-L frameworks. Moreover, the trend in relative spot intensities in all three type-L derivatives is pretty much alike to each other. The three type-L frameworks are built from various ligand combinations as shown on Figure A-1, and there is not much difference in terms of the number of atoms on the ligands or electron density compared to the ones of the co-crystal. Therefore, if co-crystal were a pure type-L framework, it would also show a similar intensity trend to those of type-L frameworks.

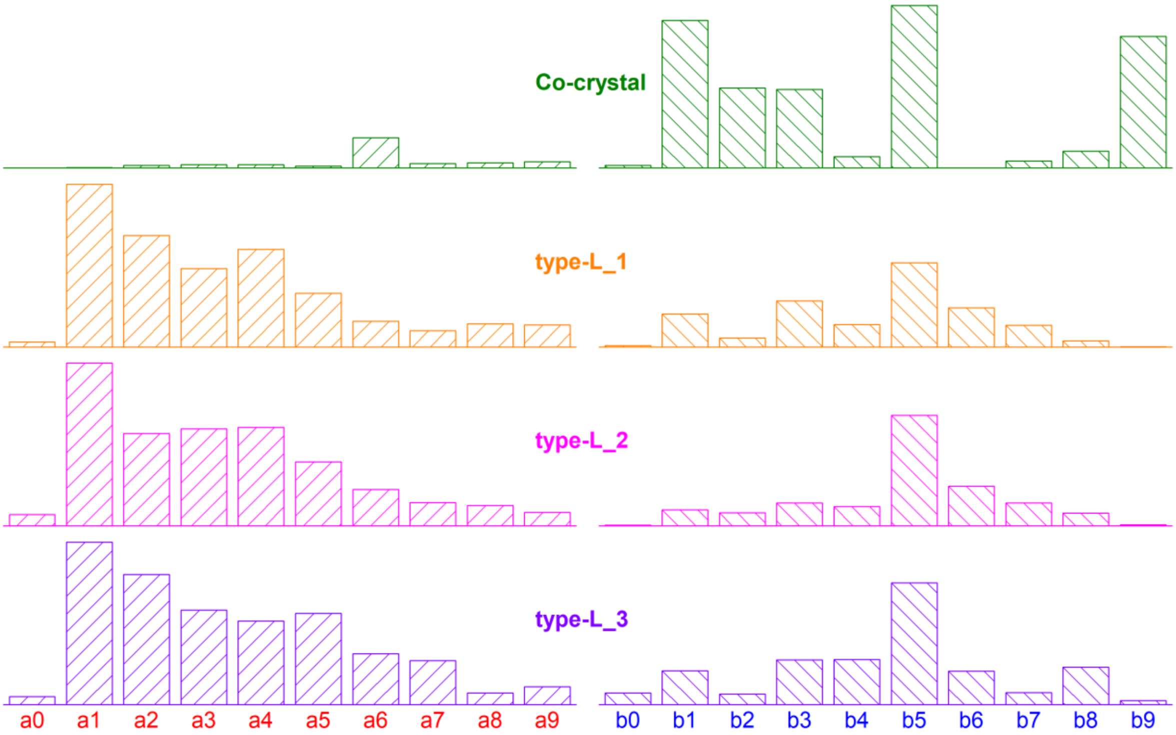

Figure A-4. The comparison of relative spot intensities between two groups, a and b in each framework. There is a notable difference in the trends of spot intensities between co-crystal and the other three MUF-7 structures.

A.1.2. **HKL data**

Table A-1. The HKL index and corresponding intensity data retrieved from the HKL files of the selected frameworks.

	Co-crystal	type-L_1	type-L_2	type-L_3
a0	1 -42 35 -0.27 0.41 1 -42 35 -0.18 0.29 35 -1 42 0.1 0.33 35 -1 42 0.18 0.26 -35 1 42 -0.16 0.21 -1 42 35 0.03 0.49 35 1 42 0.05 0.25 -1 -42 35 -0.26 0.41 1 42 35 0.36 0.49 42 35 1 -0.22 0.27 -1 -42 35 -0.54 0.29 35 1 42 -0.09 0.32 -35 -1 42 0.19 0.23	-1 42 -35 2.01 0.32 35 42 -1 1.84 0.36 -1 42 -35 1.99 0.34 1 42 35 1.62 0.36 42 35 1 1.3 0.35 1 35 -42 1.35 0.27 35 42 -1 1.46 0.35 -1 42 35 1.4 0.35 1 42 -35 1.73 0.33 1 42 -35 1.12 0.28 35 42 1 1.73 0.34 42 35 -1 2.08 0.38 35 42 1 1.96 0.36	1 -35 42 0.6 0.04 42 1 -35 0.61 0.06 -1 -35 -42 0.63 0.06 -42 -1 -35 0.59 0.05 1 35 -42 0.55 0.05 -42 1 35 0.53 0.05 -35 42 1 0.69 0.05 -42 1 35 0.63 0.05 -35 42 1 0.63 0.05 -35 42 -1 0.6 0.05 -42 -1 35 0.67 0.05 1 -35 -42 0.59 0.06 -42 1 -35 0.55 0.05 42 -1 -35 0.62 0.06 -42 -1 35 0.61 0.05 -1 35 -42 0.57 0.05 -35 42 -1 0.53 0.05 -1 -35 42 0.59 0.05	42.00 -35.00 1.00 0.36 0.07 35.00 -1.00 42.00 0.34 0.06 35.00 1.00 -42.00 0.33 0.07 35.00 1.00 -42.00 0.38 0.1 42.00 35.00 -1.00 0.49 0.08 1.00 -42.00 35.00 0.41 0.07 -1.00 -42.00 -35.00 0.35 0.07 1.00 -42.00 35.00 0.39 0.07 -1.00 -42.00 35.00 0.38 0.07 35.00 1.00 42.00 0.34 0.06 1.00 -42.00 -35.00 0.32 0.07 42.00 -35.00 -1.00 0.43 0.07 42.00 35.00 1.00 0.35 0.06 35.00 -1.00 -42.00 0.35 0.07 35.00 -1.00 -42.00 0.48 0.11 -1.00 -42.00 35.00 0.39 0.07
a1	9 -1 32 0.75 0.16 -1 32 9 0.74 0.26 1 32 -9 0.62 0.32 32 9 -1 0.76 0.21 9 -1 32 0.73 0.21 1 -32 9 1.12 0.21 32 9 -1 1.36 0.23 1 -32 9 1.02 0.26 -1 32 -9 0.44 0.34 32 9 1 0.8 0.16 -1 -32 9 0.88 0.2 1 32 9 0.75 0.29 32 9 1 0.81 0.2 32 9 1 0.71 0.23 9 1 32 0.74 0.18	1 32 9 53.99 1.35 -1 32 -9 54.05 1.3 1 32 9 51.85 1.25 -9 32 1 54.82 1.29 9 32 -1 55.22 1.33 -9 32 1 55.04 1.34 1 9 -32 53.18 1.24 9 32 -1 53.19 1.36 -1 32 -9 55.31 1.36 -9 32 -1 54.86 1.33 9 32 1 55.14 1.32 9 32 1 52.1 1.35 1 32 -9 54.21 1.48 -1 9 -32 52.6 1.23 -9 32 -1 55.07 1.28 -1 32 9 54.3 1.38 1 32 -9 54.63 1.31	1 32 9 53.99 1.35 -1 32 -9 54.05 1.3 1 32 9 51.85 1.25 -9 32 1 54.82 1.29 9 32 -1 55.22 1.33 -9 32 1 55.04 1.34 1 9 -32 53.18 1.24 9 32 -1 53.19 1.36 -1 32 -9 55.31 1.36 -9 32 -1 54.86 1.33 9 32 1 55.14 1.32 9 32 1 52.1 1.35 1 32 -9 54.21 1.48 -1 9 -32 52.6 1.23 -9 32 -1 55.07 1.28 -1 32 9 54.3 1.38 1 32 -9 54.63 1.31 -1 32 -9 8.86 0.3 -32 9 -1 8.81 0.31	9.00 1.00 -32.00 7.58 0.56 1.00 32.00 -9.00 8.14 0.56 9.00 -1.00 32.00 7.57 0.56 -1.00 -32.00 -9.00 7.77 0.56 -1.00 32.00 9.00 8.12 0.56 1.00 -32.00 9.00 7.49 0.57 1.00 -32.00 9.00 7.91 0.56 -9.00 1.00 32.00 7.74 0.56 9.00 1.00 32.00 7.58 0.56 -1.00 -32.00 9.00 7.89 0.56 -9.00 -1.00 32.00 7.80 0.56 1.00 -32.00 -9.00 7.23 0.57 -1.00 32.00 -9.00 8.00 0.56 9.00 -1.00 -32.00 7.44 0.56 -1.00 -32.00 9.00 7.24 0.57 1.00 32.00 9.00 8.33 0.56
a2	3 34 -9 2.19 0.43 -3 34 9 3.77 0.46 9 -3 34 2.98 0.35 3 -34 9 4.12 0.35 3 -34 9 3.42 0.38 9 -3 34 2.64 0.28 34 9 3 3.67 0.44 3 34 9 3.8 0.59 34 9 3 3.9 0.32 34 9 3 3.63 0.36 -3 34 -9 2.16 0.44 9 3 34 2.69 0.33 -3 -34 9 3.32 0.42	-3 34 -9 37.57 1.04 34 3 -9 36.55 1.02 -3 34 -9 36.53 0.99 9 34 -3 37.41 1.01 9 34 -3 35.7 1.04 -9 34 3 38.11 0.96 -9 34 3 36.79 1.14 3 34 9 38.08 1.06 3 34 9 36.32 0.95 3 34 -9 36.97 1 9 34 3 36.9 1.05 -9 34 -3 38.01 1.03 -3 34 9 37.43 1.03 34 9 -3 37.01 1.04 -9 34 -3 37.4 0.98 3 34 -9 35.6 1.03	-3 34 9 5.12 0.18 -9 -3 -34 4.78 0.18 -3 34 9 4.59 0.18 -34 9 3 5.02 0.18 -34 9 3 4.97 0.19 3 34 -9 4.89 0.18 -34 -9 -3 4.94 0.19 9 3 -34 5.08 0.19 -34 9 -3 4.87 0.19 9 -3 -34 4.87 0.18 -9 3 -34 4.68 0.18 -34 9 -3 5 0.19 3 34 9 4.88 0.18 -34 -9 3 4.95 0.18 -3 34 -9 4.95 0.18 -34 -9 3 4.83 0.19 -3 34 -9 4.94 0.18	3.00 -34.00 9.00 5.85 0.46 -9.00 3.00 34.00 6.33 0.45 3.00 34.00 -9.00 6.61 0.46 9.00 -3.00 34.00 6.34 0.45 -3.00 34.00 9.00 6.14 0.45 3.00 -34.00 9.00 6.08 0.45 9.00 3.00 -34.00 6.15 0.45 -3.00 -34.00 -9.00 5.98 0.46 9.00 3.00 34.00 5.95 0.45 -9.00 -3.00 34.00 6.03 0.45 9.00 -3.00 -34.00 6.20 0.45 -3.00 34.00 -9.00 6.22 0.45 3.00 -34.00 -9.00 6.23 0.46 -3.00 -34.00 9.00 5.97 0.46 3.00 34.00 9.00 6.61 0.46 -3.00 -34.00 9.00 6.32 0.45
a3	13 -13 42 4.07 0.42 -13 42 13 4.52 0.65 13 -42 13 4.45 0.46 13 -13 42 3.67 0.45 42 -13 13 4.08 0.42 -13 -13 42 3.42 0.44 -13 -42 13 5.21 0.53 -13 -42 13 4.96 0.51 13 13 42 4.05 0.51 42 13 13 4.14 0.49 42 13 13 4.42 0.61 -13 -13 42 4.44 0.41 42 13 13 4.69 0.44	-13 42 13 25.7 0.88 13 42 -13 24.88 0.91 -13 42 -13 27.97 0.89 13 42 -13 25.86 0.87 42 13 -13 25.06 0.91 13 42 13 26.02 0.97 42 13 13 26.63 0.95	13 42 -13 5.02 0.2 -42 13 13 5.16 0.2 13 13 -42 5.36 0.21 -13 -13 -42 5.23 0.2 -42 -13 -13 5.11 0.21 -42 13 13 5.03 0.2 -13 42 13 5.59 0.19 42 13 -13 5.36 0.2 -42 -13 13 5.31 0.21 13 -13 -42 5.23 0.2 -42 -13 13 5.05 0.2 -42 13 -13 5.14 0.21 -13 -13 42 5.13 0.19 -13 42 -13 4.95 0.2 -13 42 -13 5.04 0.2 -13 -42 13 4.94 0.2 -42 13 -13 4.82 0.21	13.00 42.00 -13.00 4.59 0.34 13.00 -42.00 13.00 4.24 0.34 -13.00 -42.00 -13.00 4.33 0.35 13.00 13.00 -42.00 4.91 0.38 13.00 -13.00 42.00 4.54 0.34 13.00 13.00 -42.00 4.35 0.34 13.00 -42.00 13.00 4.47 0.35 -13.00 -42.00 13.00 4.57 0.34 13.00 -13.00 -42.00 4.55 0.34 -13.00 -13.00 42.00 4.20 0.34 13.00 42.00 13.00 4.55 0.34 13.00 -42.00 -13.00 4.46 0.35 -13.00 13.00 -42.00 4.55 0.38 -13.00 -42.00 13.00 4.68 0.35
a4	17 -9 42 4.82 0.43 -9 42 17 4.39 0.68 9 -42 17 4.37 0.44 9 -42 17 4.49 0.5 17 -9 42 4.28 0.46 17 9 42 4.3 0.48 -17 -9 42 3.6 0.39 -9 -42 17 5.33 0.54 -9 -42 17 4.58 0.57 42 17 9 4.42 0.62 9 42 17 2.56 0.57 42 17 9 3.55 0.49	-9 42 -17 31.36 0.98 42 9 -17 32.55 1.03 -17 42 9 32.72 1 17 42 -9 31.71 1.06 42 17 9 32.09 1.07 -9 42 -17 34.89 1.03 17 42 -9 32.17 1.01 9 42 17 32.29 1.08 42 -9 -17 31.66 0.98 9 42 -17 33.24 1.06 9 42 -17 31.07 0.99 -9 42 17 33.77 1.05 17 42 9 32.93 0.98 17 42 9 32.09 1.08 42 17 -9 32.35 1.07	9 42 -17 5.16 0.2 -42 17 9 5.13 0.2 -9 42 17 5.08 0.19 17 9 -42 5.17 0.21 -42 17 9 5.18 0.21 -42 -17 -9 5.2 0.21 -42 -17 9 5.29 0.2 -9 42 -17 5.18 0.2 -42 17 -9 5.28 0.22 17 -9 -42 5.37 0.21 -42 17 -9 5.26 0.22 -17 -9 42 5.37 0.2 -9 -42 17 5.29 0.2 -42 -17 9 5.17 0.21	-9.00 -42.00 -17.00 3.38 0.31 9.00 42.00 -17.00 4.48 0.31 9.00 -42.00 17.00 3.83 0.32 17.00 -9.00 42.00 4.43 0.31 9.00 -42.00 17.00 4.21 0.31 17.00 9.00 -42.00 3.28 0.34 17.00 9.00 -42.00 4.02 0.31 9.00 42.00 17.00 4.61 0.31 17.00 -9.00 -42.00 3.79 0.3 -9.00 -42.00 17.00 3.99 0.32 17.00 9.00 42.00 4.18 0.31 9.00 -42.00 -17.00 3.40 0.31 -9.00 -42.00 17.00 4.15 0.31

	Co-crystal					type-L_1					type-L_2					type-L_3				
a5	-19	1	38	2.17	0.24	19	38	-1	18.78	0.71	-38	-19	-1	3.51	0.14	1.00	-38.00	19.00	4.70	0.33
	19	-1	38	3.04	0.35	19	38	-1	17.83	0.74	-19	1	38	3.28	0.13	1.00	-38.00	19.00	4.07	0.34
	1	-38	19	3.08	0.41	-1	38	-19	17.07	0.66	-38	-19	-1	2.89	0.16	19.00	-1.00	38.00	4.39	0.33
	1	-38	19	3.02	0.5	1	19	-38	18.01	0.62	1	38	-19	3.39	0.14	19.00	1.00	-38.00	4.48	0.33
	-1	38	19	1.77	0.47	-1	38	-19	17.46	0.71	19	1	-38	3.57	0.15	1.00	38.00	-19.00	4.31	0.33
	1	38	19	1.82	0.48	1	38	19	18.59	0.74	-38	19	1	3.37	0.15	-1.00	-38.00	19.00	4.93	0.35
	38	19	1	3.65	0.58	38	1	-19	17.56	0.67	-38	19	1	3.42	0.15	19.00	-1.00	-38.00	4.11	0.33
	-19	-1	38	2.12	0.25	38	19	1	17.34	0.73	-38	-19	1	3.54	0.14	1.00	-38.00	-19.00	3.65	0.33
	38	19	1	3.49	0.53	1	38	-19	18.01	0.72	19	-1	-38	3.65	0.15	-1.00	-38.00	19.00	3.97	0.34
	19	1	38	2.68	0.44	19	38	1	16.85	0.73	1	38	19	3.49	0.13	19.00	1.00	38.00	4.64	0.33
	-1	-38	19	1.8	0.36	38	-1	-19	17.36	0.67	-19	-1	38	3.35	0.13	-1.00	38.00	-19.00	4.60	0.34
	-1	-38	19	1.76	0.41	-1	38	19	17.81	0.73	-38	19	-1	3.46	0.15					
						1	38	-19	17.14	0.67	-38	19	-1	3.25	0.16					
						38	19	-1	18.17	0.74	-1	38	-19	3.47	0.14					
						19	38	1	19.07	0.71										
						-1	19	-38	18.56	0.63										
a6	-6	42	22	40.84	2.38	42	6	-22	8.18	0.52	-42	22	6	1.89	0.1	22.00	6.00	-42.00	2.41	0.2
	22	-6	42	39.1	2.22	6	22	-42	8.84	0.46	-22	6	42	1.96	0.08	6.00	-42.00	22.00	2.33	0.2
	6	-42	22	42.01	2.21	22	42	-6	7.99	0.53	22	6	-42	1.9	0.1	22.00	6.00	-42.00	2.52	0.25
	6	-42	22	40.34	2.24	42	22	6	9.25	0.6	-42	-22	-6	1.82	0.1	42.00	22.00	-6.00	2.29	0.19
	22	-6	42	40.11	2.19	-6	42	-22	9.06	0.54	-42	22	6	1.94	0.1	22.00	-6.00	42.00	2.51	0.2
	-22	-6	42	39.61	2.18	6	42	22	8.39	0.58	6	42	-22	1.97	0.1	6.00	-42.00	22.00	2.57	0.22
	6	42	22	38.62	2.42	-6	42	-22	8.22	0.5	-42	22	-6	1.83	0.11	6.00	42.00	-22.00	2.42	0.21
	22	6	42	37.79	2.3	22	42	-6	8.48	0.57	-22	-6	42	1.98	0.09	-6.00	-42.00	-22.00	2.20	0.2
	42	22	6	42.55	2.33	42	22	-6	8.04	0.57	-42	-22	6	1.9	0.1	6.00	-42.00	-22.00	2.63	0.21
	-6	-42	22	40.27	2.27	-6	42	22	8.91	0.57	-6	42	-22	1.88	0.1	6.00	42.00	22.00	2.44	0.2
	42	22	6	43.41	2.23	6	42	-22	8.55	0.52	-42	-22	6	1.94	0.1	-6.00	-42.00	22.00	2.38	0.21
	-6	-42	22	34.31	2.22	22	42	6	7.79	0.57	22	-6	-42	2.06	0.1	42.00	22.00	6.00	2.51	0.19
	22	6	42	41.65	2.21	22	42	6	9.05	0.54	-42	22	-6	1.95	0.11	-6.00	-42.00	22.00	2.34	0.2
						6	42	-22	8.55	0.56						22.00	-6.00	-42.00	2.41	0.2
																22.00	6.00	42.00	2.42	0.2
a7	29	-3	36	6.84	0.53	29	36	-3	5.91	0.52	-36	-29	-3	1.25	0.08	3.00	36.00	-29.00	2.06	0.18
	36	29	-3	5.71	0.65	3	36	29	5.5	0.52	29	3	-36	1.23	0.08	36.00	29.00	-3.00	2.49	0.18
	29	-3	36	5.73	0.56	3	29	-36	5.21	0.42	-36	29	3	1.25	0.08	-3.00	-36.00	-29.00	1.84	0.18
	-3	36	29	5.49	0.69	36	29	3	5.34	0.51	-36	29	3	1.18	0.07	36.00	-29.00	3.00	1.72	0.18
	-29	-3	36	5.3	0.49	-3	36	-29	5.45	0.43	-29	3	36	1.25	0.06	29.00	-3.00	36.00	2.19	0.18
	-29	-3	36	4.74	0.55	36	29	3	5.79	0.47	3	36	-29	1.27	0.07	3.00	-36.00	29.00	2.23	0.18
	3	36	29	6.18	0.8	29	36	-3	5.07	0.49	-29	3	36	1.14	0.09	3.00	-36.00	29.00	2.30	0.19
	36	29	3	4.5	0.71	3	29	-36	5.45	0.46	-3	36	-29	1.09	0.07	29.00	3.00	-36.00	2.07	0.18
	29	3	36	4.26	0.57	-3	36	-29	4.62	0.45	3	-36	-29	1.28	0.08	-3.00	-36.00	29.00	2.12	0.18
	-3	-36	29	6.71	0.64	-3	29	-36	5.31	0.45	-29	-3	36	1.22	0.06	-3.00	-36.00	29.00	2.00	0.19
	-3	-36	29	7	0.56	-3	36	29	6.17	0.51	-36	29	-3	1.32	0.08	36.00	29.00	3.00	2.38	0.17
	29	3	36	6.93	0.53	36	29	-3	4.93	0.5	-36	29	-3	1.28	0.08	3.00	-36.00	-29.00	1.99	0.18
	29	3	36	5.13	0.62	36	29	-3	5.59	0.46	29	-3	-36	1.27	0.08	36.00	-29.00	-3.00	1.88	0.18
						29	36	3	5.38	0.5	-36	-29	3	1.27	0.08	29.00	-3.00	-36.00	1.97	0.18
						3	36	-29	5.09	0.46						29.00	3.00	36.00	2.24	0.18
						-3	29	-36	5.32	0.42										
						3	36	-29	4.83	0.43										
						29	36	3	5.51	0.51										
a8	18	-46	36	6.07	0.6	36	46	-18	7.98	0.55	-46	36	18	1.11	0.07	46.00	36.00	-18.00	0.63	0.09
	-18	46	36	5.66	0.86	36	46	-18	8.35	0.57	18	46	-36	1.08	0.07	18.00	-46.00	36.00	0.54	0.09
	36	-18	46	7.15	0.59	46	36	18	8.5	0.58	46	36	-18	1.17	0.08	36.00	18.00	-46.00	0.55	0.1
	36	-18	46	6.69	0.67	-18	36	46	6.5	0.55	36	18	-46	1.09	0.08	46.00	-36.00	18.00	0.55	0.08
	18	-46	36	6.33	0.57	18	36	-46	6.85	0.65	-36	-18	46	1.05	0.07	36.00	-18.00	46.00	0.58	0.08
	18	46	36	7.58	1	18	46	36	7.57	0.63	-18	-46	36	1.08	0.07	18.00	46.00	-36.00	0.54	0.09
	46	36	18	7.27	0.76	-18	46	36	7.28	0.59	-36	-18	46	1.1	0.07	18.00	-46.00	-36.00	0.55	0.08
	36	18	46	6.64	0.72	18	46	-36	7.34	0.51	-46	36	-18	1.06	0.07	36.00	-18.00	-46.00	0.54	0.08
	-36	-18	46	7.51	0.62	18	46	-36	8.5	0.57	-46	-36	18	1.06	0.07	46.00	-36.00	-18.00	0.55	0.08
	-18	-46	36	7.35	0.71	46	36	-18	8.87	0.6	-46	36	-18	1.11	0.07	46.00	36.00	18.00	0.55	0.08
	36	18	46	7.13	0.65	36	46	18	7.74	0.74	36	-18	-46	1.02	0.07	18.00	46.00	36.00	0.53	0.08
	36	18	46	6.27	0.69	18	36	46	7.54	0.6	-18	46	-36	1.09	0.07					
	46	36	18	6.74	0.62															
	-18	-46	36	6.81	0.66															
a9	-10	44	36	6.28	0.96	36	44	-10	6.35	0.56	36	-10	44	0.75	0.05	36.00	44.00	-10.00	1.02	0.12
	10	-44	36	7.16	0.67	44	36	10	7	0.58	-44	36	10	0.68	0.05	44.00	-10.00	36.00	0.86	0.09
	36	-10	44	9.01	0.66	36	44	-10	7.16	0.58	36	10	-44	0.74	0.07	44.00	10.00	-36.00	0.95	0.16
	36	-10	44	7.94	0.71	10	44	36	7.81	0.64	10	44	-36	0.71	0.05	-10.00	-36.00	-44.00	0.62	0.11
	10	-44	36	6.96	0.73	10	36	-44	7.11	0.47	-44	36	10	0.73	0.06	10.00	-36.00	44.00	0.89	0.11
	-36	-10	44	8.64	0.66	-10	44	36	7.81	0.6	-36	10	44	0.73	0.05	36.00	44.00	10.00	0.97	0.11
	36	10	44	8.74	0.7	36	44	10	7.69	0.56	-36	-10	44	0.77	0.06	44.00	-10.00	-36.00	0.87	0.14
	-10	-44	36	7.13	0.8	36	44	10	6.91	0.56	-44	36	-10	0.65	0.06	-10.00	-36.00	44.00	0.86	0.11
	44	36	10	9.6	0.82	10	44	-36	7.76	0.52	-44	36	-10	0.73	0.06	10.00	-36.00	-44.00	0.62	0.13
	-10	-44	36	7.55	0.74	10	36	44	6.55	0.59	-36	-10	44	0.75	0.05					
	36	10	44	8.2	0.76	10	44	-36	7.63	0.57	36	-10	-44	0.65	0.09					
	10	44	36	9.34	1.05	44	36	-10	7.9	0.62	-10	44	-36	0.64	0.06					
	36	10	44	8.53	0.72						-44	-36	10	0.67	0.06					

	Co-crystal					type-L_1					type-L_2					type-L_3				
b0	-6	42	40	3.18	0.62	-6	40	42	0.47	0.33	-40	42	6	0.04	0.02	-6.00	-42.00	-40.00	0.56	0.09
	6	-42	40	4.29	0.59	40	42	-6	0.34	0.3	-42	6	40	0.03	0.02	42.00	-40.00	6.00	0.50	0.08
	40	-6	42	2.76	0.45	6	42	40	0.49	0.32	-40	42	6	0.03	0.02	6.00	-42.00	40.00	0.46	0.08
	6	-42	40	3.13	0.44	6	40	-42	0.41	0.24	42	6	-40	0.02	0.03	40.00	-6.00	42.00	0.70	0.08
	40	-6	42	3.54	0.56	42	40	6	-0.17	0.28	-42	-6	40	0.03	0.02	40.00	6.00	-42.00	0.41	0.07
	-6	-42	40	3.13	0.45	40	42	-6	0.25	0.28	-40	42	-6	0.03	0.02	42.00	40.00	-6.00	0.67	0.09
	-6	-42	40	3.37	0.58	6	40	-42	0.7	0.3	-40	42	-6	0.03	0.02	40.00	6.00	-42.00	0.43	0.09
	42	40	6	4.09	0.74	40	42	6	0.51	0.3	-40	-42	6	0.03	0.02	6.00	-42.00	40.00	0.61	0.09
	-40	-6	42	3.02	0.4	42	40	-6	-0.02	0.27	42	-6	-40	0.04	0.03	40.00	-6.00	-42.00	0.64	0.09
	40	6	42	2.84	0.5	6	40	42	0.77	0.34	-6	40	-42	0.03	0.03	42.00	-40.00	-6.00	0.37	0.07
	6	42	40	3.43	0.65	6	42	-40	0.4	0.25	-42	-6	40	0.06	0.02	6.00	-42.00	-40.00	0.47	0.08
	40	6	42	3.41	0.42	6	42	-40	0.28	0.27						-6.00	-42.00	40.00	0.69	0.09
						40	42	6	0.57	0.3						-6.00	-42.00	40.00	0.72	0.09
						-6	42	40	0.36	0.3						42.00	40.00	6.00	0.64	0.09
						42	40	-6	0.69	0.34						40.00	-6.00	-42.00	0.47	0.1
b1	4	-34	8	205.61	10.19	8	34	-4	10.87	0.49	-34	-8	-4	0.86	0.06	8.00	-4.00	34.00	1.47	0.13
	34	-8	4	198.86	10.18	-4	34	-8	11.36	0.52	-4	34	8	0.83	0.04	4.00	-34.00	8.00	1.56	0.13
	4	34	-8	195.91	10.29	34	4	-8	10.8	0.51	-34	8	4	0.89	0.05	4.00	-34.00	8.00	1.67	0.14
	-4	34	8	189.89	10.22	4	34	8	11.21	0.53	-4	34	8	0.91	0.05	-4.00	-34.00	-8.00	1.93	0.14
	8	-4	34	194.45	10.17	-8	34	4	10.89	0.45	-8	-4	-34	0.84	0.05	-4.00	34.00	8.00	1.48	0.14
	34	8	4	193.22	10.17	-8	34	4	11.58	0.61	8	4	-34	0.85	0.05	-8.00	4.00	34.00	1.70	0.13
	-4	-34	8	199.34	10.22	8	34	-4	10.83	0.52	4	34	-8	0.9	0.05	4.00	34.00	-8.00	1.56	0.14
	8	4	34	188.88	10.17	-4	34	-8	11.27	0.48	-34	8	4	0.8	0.05	8.00	4.00	-34.00	1.64	0.14
	-4	-34	8	194.66	10.19	4	34	8	10.35	0.45	-34	8	-4	0.84	0.06	-8.00	-4.00	34.00	1.64	0.14
	-8	-4	34	192.93	10.12	8	34	4	10.62	0.48	-34	-8	4	0.85	0.05	4.00	34.00	8.00	1.49	0.13
	-4	34	-8	196.14	10.31	8	34	4	11.26	0.53	8	-4	-34	0.88	0.05	8.00	4.00	34.00	1.58	0.13
	34	8	4	195.13	10.24	-4	34	8	11.22	0.52	4	34	8	0.81	0.05	-4.00	-34.00	8.00	1.57	0.13
	4	34	8	196.7	10.28	4	34	-8	10.36	0.48	-8	4	-34	0.84	0.05	4.00	-34.00	-8.00	1.68	0.14
	34	8	4	196.47	10.2	4	34	-8	11.03	0.52	-34	-8	4	0.89	0.06	-4.00	34.00	-8.00	1.57	0.14
						-8	34	-4	10.5	0.46	-34	8	-4	0.84	0.06	-4.00	-34.00	8.00	1.70	0.15
						34	8	-4	10.48	0.51	-4	34	-8	0.86	0.05	8.00	-4.00	-34.00	1.62	0.14
						-8	34	-4	10.8	0.51	-4	34	-8	0.84	0.05					
						-4	34	8	11.59	0.44										
b2	8	-40	14	105.19	5.59	-8	40	-14	2.89	0.34	-14	-8	-40	0.61	0.04	8.00	-40.00	14.00	0.45	0.08
	14	-8	40	106.34	5.66	40	8	-14	2.32	0.32	8	40	-14	0.69	0.05	14.00	-8.00	40.00	0.50	0.08
	-8	40	14	109.17	5.67	8	40	14	2.89	0.36	14	8	-40	0.78	0.06	14.00	8.00	-40.00	0.41	0.1
	14	-8	40	102.02	5.57	14	40	-8	2.82	0.35	-40	-14	-8	0.73	0.06	8.00	-40.00	14.00	0.53	0.07
	8	-40	14	109.41	5.61	14	40	-8	2.59	0.32	-40	14	8	0.64	0.05	14.00	8.00	-40.00	0.58	0.08
	-8	-40	14	106.28	5.62	40	14	8	2.73	0.34	-8	40	14	0.66	0.05	8.00	40.00	-14.00	0.49	0.08
	14	8	40	103.3	5.62	-8	40	-14	2.88	0.31	-8	40	14	0.66	0.04	-8.00	-40.00	-14.00	0.43	0.08
	40	14	8	102.21	5.58	-8	40	14	2.95	0.35	-40	14	8	0.75	0.05	14.00	-8.00	-40.00	0.53	0.08
	-8	-40	14	104.91	5.64	8	40	-14	2.62	0.3	-40	-14	-8	0.74	0.06	8.00	40.00	14.00	0.64	0.08
	40	14	8	107.39	5.68	8	40	-14	2.96	0.35	-40	-14	8	0.62	0.05	8.00	-40.00	-14.00	0.47	0.07
	8	40	14	108.52	5.74	14	40	8	3.84	0.52	14	-8	-40	0.6	0.05	14.00	8.00	40.00	0.42	0.06
	40	14	8	108.44	5.61	-14	40	-8	3.53	0.34	-8	40	-14	0.72	0.05	-8.00	-40.00	14.00	0.54	0.08
	-14	-8	40	107.04	5.55	14	40	8	2.89	0.36	-14	-8	40	0.73	0.05	-14.00	8.00	-40.00	0.50	0.1
						40	14	-8	3.16	0.36	-40	14	-8	0.73	0.06	-14.00	-8.00	40.00	0.52	0.07
											-40	14	-8	0.65	0.06					
											-40	-14	8	0.67	0.05					
											-8	40	-14	0.68	0.05					
											-8	-40	14	0.68	0.05					
											8	40	14	0.71	0.04					
b3	-20	10	24	97.77	5.42	24	20	10	15.27	0.58	20	10	-24	1.17	0.06	10.00	20.00	-24.00	2.12	0.18
	24	-20	10	105.35	5.46	20	24	-10	15.21	0.59	-24	20	10	1.15	0.06	20.00	24.00	-10.00	1.93	0.16
	20	-10	24	102.8	5.45	24	20	10	14.94	0.57	10	24	-20	1.39	0.06	24.00	10.00	-20.00	2.36	0.18
	10	-24	20	99.02	5.46	20	24	-10	14.85	0.58	-24	-20	-10	1.25	0.06	-10.00	-20.00	-24.00	2.44	0.17
	20	-10	24	103.8	5.48	24	10	-20	15.57	0.58	10	-24	20	1.28	0.06	20.00	-24.00	10.00	2.15	0.17
	24	-20	10	108.3	5.45	24	10	-20	15.66	0.55	-10	-24	-20	1.27	0.07	24.00	-10.00	20.00	2.05	0.17
	24	20	-10	103.81	5.49	-10	24	-20	15.82	0.55	-20	-10	24	1.18	0.06	24.00	10.00	-20.00	1.97	0.16
	10	-24	20	105.02	5.45	10	20	-24	15.82	0.56	-24	-20	10	1.19	0.06	10.00	20.00	-24.00	2.27	0.19
	20	10	24	107.83	5.51	-10	24	-20	14.53	0.53	-10	24	-20	1.19	0.06	20.00	-24.00	10.00	2.02	0.17
	-20	-10	24	105.52	5.45	10	20	-24	15.21	0.58	-10	24	-20	1.08	0.06	10.00	-20.00	24.00	1.98	0.2
	-24	-20	10	106.43	5.49	20	24	10	15.44	0.59	10	-24	-20	1.19	0.06	-24.00	-10.00	20.00	2.25	0.16
	24	20	10	103.48	5.52	20	24	10	15.43	0.58	20	-10	-24	1.13	0.06	-10.00	-20.00	24.00	2.07	0.17
	-10	-24	20	107.41	5.46	20	10	-24	15.22	0.55	-20	10	-24	1.24	0.06	24.00	-10.00	-20.00	2.15	0.16
	-10	-24	20	103.61	5.48	24	20	-10	14.66	0.59	-20	10	-24	1.14	0.07	20.00	-24.00	-10.00	2.25	0.17
	-20	-10	24	99.16	5.47	10	24	-20	15.65	0.59	-24	20	-10	1.24	0.07	10.00	-20.00	-24.00	2.06	0.18
	10	24	20	109.07	5.53	10	24	-20	14.28	0.7	24	-20	-10	1.19	0.06	24.00	10.00	20.00	2.09	0.16
	-24	-20	10	103.84	5.47	20	10	-24	16.03	0.56	-10	-24	20	1.22	0.06	-20.00	-24.00	10.00	1.87	0.16
						-10	20	-24	15.59	0.53	-24	20	-10	1.25	0.07	-10.00	-20.00	24.00	2.19	0.17
						-10	20	-24	15.41	0.54	-24	-20	10	1.24	0.06					
						24	20	-10	15.64	0.58										
b4	-22	0	38	15.06	0.87	0	38	-22	7.02	0.5	22	0	-38	1.02	0.07	0.00	38.00	-22.00	2.19	0.19
	0	-38	22	14.37	0.98	0	38	22	7.8	0.53	-38	-22	0	0.98	0.06	0.00	-38.00	22.00	2.09	0.18
	0	-38	22	14.65	0.94	22	38	0	7.77	0.51	-22	0	38	1.09	0.05	38.00	22.00	0.00	2.51	0.17
	0	38	22	14.31	1.14	38	22	0	6.88	0.52	-38	22	0	1.02	0.07	22.00	0.00	-38.00	2.01	0.18
	22	0	38	14.94	0.95	0	38	-22	7.05	0.47	0	38	-22	1.02	0.06	22.00	0.00	38.00	2.10	0.18
	38	22	0	15.16	1.05	0	22	-38	8.42	0.45	-38	22	0	0.97	0.07	0.00	38.00	22.00	2.27	0.2
	22	0	38	15.53	0.91	22	38	0	7.58	0.54	-38	-22	0	1.01	0.07	0.00	-38.00	22.00	1.88	0.19
	22	0	38	14.36	0.97															

	Co-crystal					type-L_1					type-L_2					type-L_3				
b5	24	-2	40	202.81	11.22	2	24	-40	27.32	0.85	-40	24	2	5.6	0.23	24.00	2.00	-40.00	6.11	0.43
	-24	2	40	205.4	11.21	40	2	-24	26.95	0.89	-40	24	2	5.59	0.23	24.00	-2.00	40.00	5.39	0.43
	24	-2	40	211.31	11.26	40	24	2	27.81	1	2	40	-24	5.89	0.23	2.00	-40.00	24.00	5.99	0.44
	40	24	-2	231.64	11.35	2	40	24	29.39	1.02	-24	2	40	5.78	0.21	2.00	40.00	-24.00	5.91	0.43
	2	-40	24	221.62	11.27	-2	40	-24	29.86	0.97	-40	-24	-2	5.84	0.23	2.00	-40.00	24.00	5.44	0.43
	-2	40	24	216.78	11.37	-2	40	-24	27.62	0.91	24	2	-40	5.83	0.23	24.00	2.00	40.00	5.83	0.43
	2	-40	24	221.4	11.24	24	40	-2	27.99	0.95	-40	-24	2	6.01	0.23	-2.00	-40.00	24.00	6.05	0.44
	24	-2	40	200.14	11.27	40	24	-2	29.3	1	-40	-24	2	6.04	0.23	-2.00	-40.00	24.00	5.60	0.43
	-2	-40	24	221.14	11.27	24	40	2	28.79	1	-24	-2	40	5.89	0.21					
	24	2	40	218.04	11.27	-2	40	24	27.78	0.98	-40	24	-2	5.99	0.24					
	24	2	40	215.34	11.33	2	40	-24	28.64	0.91	-40	24	-2	5.94	0.23					
	-24	-2	40	203.21	11.21	24	40	2	28.24	0.96	-2	40	-24	6	0.23					
	40	24	2	225.82	11.34	2	40	-24	26.93	0.94	24	-2	-40	5.9	0.23					
	24	2	40	212.25	11.23	-2	24	-40	26	0.85										
	2	40	24	218.8	11.4	40	-2	-24	27.68	0.89										
	-2	-40	24	221.49	11.25															
b6	-16	46	30	0.03	0.45	46	16	-32	13.16	0.62	-46	32	16	2.03	0.11	16.00	-46.00	30.00	1.59	0.15
	16	-46	30	-0.23	0.22	16	46	32	12.32	0.74	16	46	-32	2.24	0.11	30.00	-16.00	46.00	1.50	0.14
	30	-16	46	-0.08	0.25	46	32	16	12.8	0.68	32	16	-46	2.2	0.12	30.00	16.00	-46.00	1.48	0.15
	30	-16	46	-0.11	0.34	16	32	-46	12.75	0.57	32	-16	46	2.11	0.09	30.00	16.00	-46.00	1.23	0.18
	16	-46	30	-0.32	0.32	32	46	-16	11.79	0.67	-16	-46	32	2.12	0.11	46.00	30.00	-16.00	1.62	0.15
	46	30	16	-0.24	0.28	32	46	-16	11.88	0.66	-46	32	-16	2.1	0.11	16.00	-46.00	30.00	1.56	0.16
	-16	-46	30	-0.04	0.4	-16	46	32	13.27	0.68	-46	-32	16	1.99	0.11	16.00	46.00	30.00	1.46	0.18
	-16	-46	30	-0.12	0.31	16	32	46	13.81	0.73	-16	46	-32	2.01	0.11	30.00	-16.00	-46.00	1.29	0.14
	-30	-16	46	0.44	0.37	32	46	16	14.11	0.73	-32	-16	46	2.1	0.11	-16.00	-46.00	30.00	1.52	0.17
	30	16	46	0.04	0.27	46	16	32	14.07	0.68	32	-16	-46	2.19	0.11	-30.00	-16.00	46.00	1.49	0.14
	30	16	46	0.05	0.27	16	46	-32	13.66	0.7	-46	32	-16	2.07	0.1	46.00	30.00	16.00	1.73	0.14
	16	46	30	-0.24	0.54	46	32	-16	13.75	0.73	-32	-16	46	2.09	0.1	16.00	-46.00	-30.00	1.44	0.15
	46	30	16	-0.01	0.32	16	46	-32	12.32	0.64						16.00	-46.00	32.00	1.96	0.17
	-30	-16	46	-0.33	0.25											16.00	46.00	-32.00	1.72	0.16
																32.00	-16.00	46.00	1.67	0.16
																16.00	-46.00	32.00	1.70	0.17
																46.00	32.00	-16.00	1.74	0.16
																32.00	16.00	-46.00	1.61	0.16
																-16.00	-46.00	32.00	1.89	0.16
																46.00	32.00	16.00	1.89	0.15
																16.00	-46.00	-32.00	1.52	0.16
																16.00	46.00	32.00	1.68	0.15
																32.00	-16.00	-46.00	1.54	0.15
b7	16	-46	34	8.52	0.68	34	46	-16	6.76	0.54	16	46	-34	1.17	0.08	46.00	34.00	-16.00	0.65	0.1
	16	-46	34	7.79	0.71	16	46	34	8.19	0.63	34	16	-46	1.24	0.08	34.00	16.00	-46.00	0.58	0.1
	34	-16	46	9.53	0.73	46	34	16	7.73	0.56	-46	34	16	1.18	0.08	16.00	-46.00	34.00	0.58	0.09
	-16	46	34	7.24	0.95	16	34	-46	7.54	0.46	-34	-16	46	1.42	0.08	46.00	-34.00	16.00	0.56	0.09
	34	-16	46	9.79	0.77	34	46	-16	6.83	0.55	-16	-46	34	1.23	0.08	34.00	-16.00	46.00	0.54	0.08
	16	46	34	9.76	1.1	-16	46	34	6.37	0.55	-46	-34	16	1.08	0.08	16.00	-46.00	34.00	0.57	0.09
	-16	-46	34	8.8	0.83	34	46	16	7.56	0.58	-46	34	-16	1.25	0.08	16.00	46.00	-34.00	0.55	0.09
	34	16	46	9.25	0.78	16	34	46	7.04	0.61	-16	46	-34	1.31	0.08	46.00	34.00	16.00	0.60	0.08
	-34	-16	46	9.11	0.74	16	46	-34	6.76	0.51	-34	-16	46	1.02	0.1	34.00	-16.00	-46.00	0.52	0.09
	34	16	46	9.62	0.74	16	46	-34	6.3	0.53	34	-16	-46	1.25	0.08	16.00	46.00	34.00	0.54	0.08
	46	34	16	9.67	0.73	46	34	-16	7.7	0.6						-16.00	-46.00	34.00	0.57	0.09
	46	34	16	9.21	0.85											16.00	-46.00	-34.00	0.59	0.1
	34	16	46	9.09	0.81															
b8	34	0	38	23.73	1.33	0	34	-38	1.55	0.3	-34	0	38	0.73	0.05	0.00	-34.00	38.00	1.99	0.17
	-34	0	38	19.52	1.3	34	38	0	2.61	0.39	-38	-34	0	0.6	0.06	34.00	-38.00	0.00	1.40	0.16
	0	-38	34	24.74	1.41	0	38	34	2.02	0.38	-38	34	0	0.69	0.06	38.00	0.00	-34.00	1.87	0.16
	38	34	0	21.66	1.46	0	38	-34	2.21	0.33	-34	0	38	0.66	0.05	38.00	0.00	34.00	1.91	0.16
	0	-38	34	23.48	1.35	38	34	0	1.9	0.38	0	38	-34	0.76	0.06					
	34	0	38	21.1	1.36	0	38	-34	1.78	0.32	-38	34	0	0.63	0.06					
	0	38	34	21.31	1.55	38	34	0	2.58	0.36	34	0	-38	0.62	0.06					
						0	34	-38	1.79	0.32										
						34	38	0	1.91	0.36										
b9	0	-38	36	175.98	9.16	0	36	-38	-0.25	0.23	-38	36	0	0.06	0.03	0.00	-36.00	-38.00	0.29	0.06
	36	0	38	167.82	9.14	0	38	36	0.23	0.3	-38	-36	0	0.04	0.03	38.00	0.00	36.00	0.10	0.05
	38	36	0	174.95	9.24	0	38	-36	0.09	0.23	-38	36	0	0.08	0.03	36.00	-38.00	0.00	0.29	0.06
	36	0	38	173.33	9.12	0	38	-36	0.23	0.26	-36	0	38	0.03	0.03	38.00	0.00	-36.00	0.15	0.06
	0	-38	36	178.68	9.14	38	36	0	0.16	0.26	-36	0	38	0.05	0.02	0.00	-36.00	38.00	0.22	0.06
						38	36	0	0	0.28	0	38	-36	0.06	0.02	0.00	-36.00	38.00	0.11	0.06
						36	38	0	0.12	0.28	36	0	-38	0.01	0.03	36.00	38.00	0.00	0.09	0.05
						36	38	0	-0.06	0.27						38.00	0.00	-36.00	0.25	0.08
						0	36	-38	0	0.23										

A.2. Ligand combination vs Phase

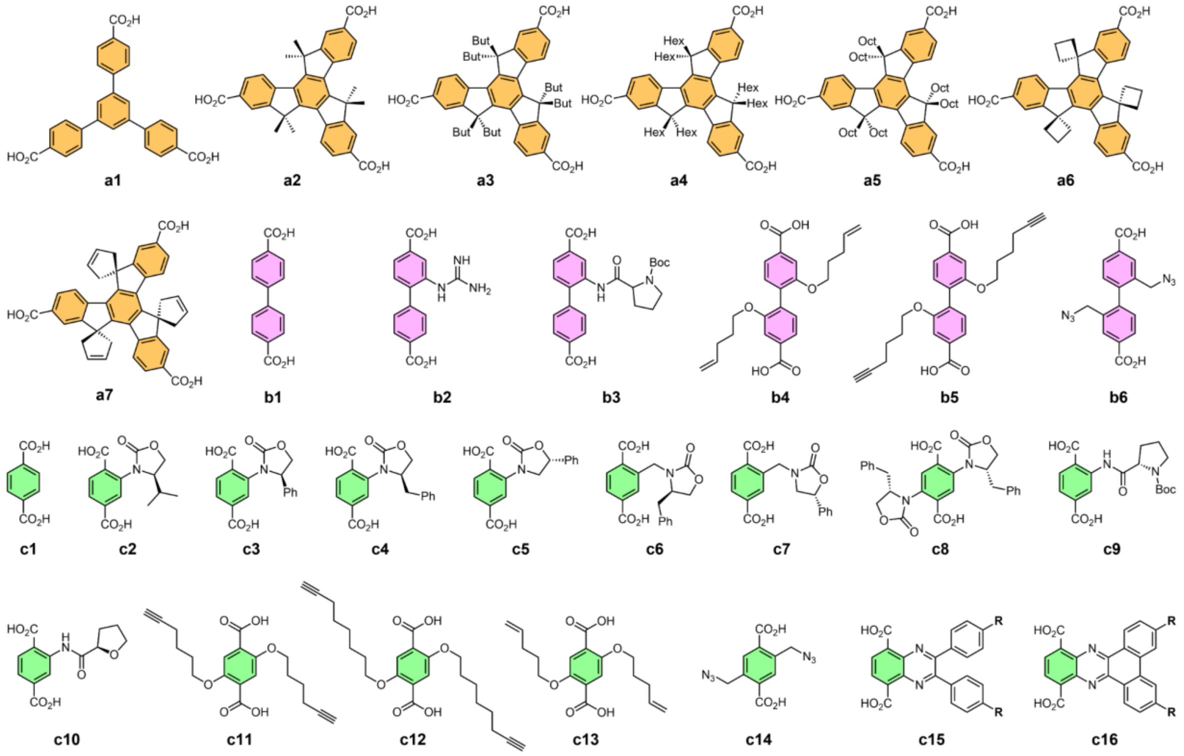

Figure A-5. A list of all the ligands used for this thesis.

Table A-2. The ligand combinations and the resulting phase of the corresponding framework. L and S represent type-L and type-S, respectively.

Tritopic	bpdc	bdc	Phase	SCXRD	Tritopic	bpdc	bdc	Phase	SCXRD
a1	b1	c1	L	Y	a4	b2	c4	L	Y
a2	b1	c1	S	Y	a4	b2	c5	L	N
a2	b1	c15	L	Y	a4	b2	c6	S	N
a2	b1	c16	S	Y	a4	b2	c7	M	N
a6	b1	c1	L	Y	a4	b2	c8	L	N
c6	b3	c1	L	Y	a4	b2	c9	S	N
a7	b1	c1	L	Y	a4	b2	c10	M	N
a2	b2	c1	S	N	a3	b2	c4	S	N
a2	b1	c4	S	N	a5	b2	c4	S	N
a2	b2	c4	M	N	a2	b6	c11	S	Y
a2	b2	c2	M	N	a2	b6	c12	S	Y
a4	b2	c1	S	N	a2	b4	c13	S	Y
a4	b2	c2	L	N	a2	b5	c11	S	Y
a4	b2	c3	M	N	a2	b6	c6	S	Y

A.3. HPLC precision determination

To determine the precision of the enantiomeric excess (ee) using HPLC, a prepared asymmetric reaction solution was analysed. Ten HPCL chromatograms were successively collected from the same reaction mixture after removing catalyst (Figure A-6). The peak area of the two enantiomeric product peaks (Peak_A and Peak_B) was used; the peak area was calculated by the software (Thermofisher Chromeleon 7) and used without any modification. The results are presented in Table A-3. According to the calculated standard error, the ee values using HPLC is reliable to two decimal places.

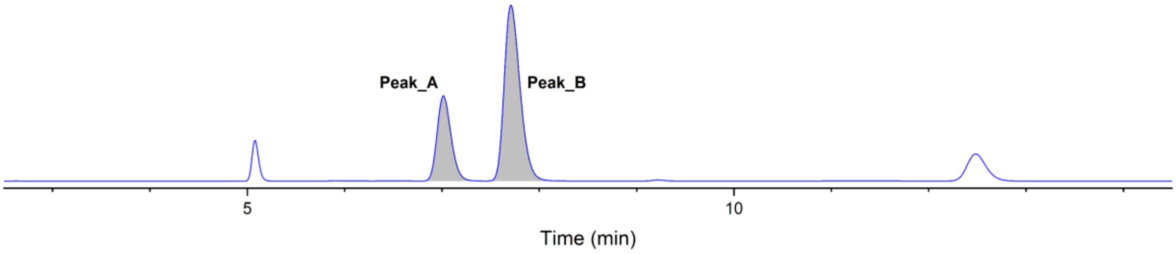

Figure A-6. The chromatogram for determining the precision of ee calculation. The two enantiomeric product peaks were labelled with Peak_A and Peak_B.

Table A-3. The peak areas of Peak_A and Peak_b and calculated ees for each HPLC chromatogram are tabulated and the calculated mean and standard values were also presented.

	Peak_A	Peak_B	ee (%)
1	168.270	393.736	-40.118
2	166.814	390.145	-40.098
3	167.545	391.654	-40.077
4	167.178	390.883	-40.086
5	167.998	392.991	-40.106
6	168.609	394.160	-40.079
7	167.674	392.170	-40.100
8	168.346	393.551	-40.079
9	167.548	391.642	-40.075
10	167.092	390.520	-40.069

$$\text{ee}\ (\%) = \frac{\text{Peak\_A} - \text{Peak\_B}}{\text{Peak\_A} + \text{Peak\_B}} \times 100$$

mean: -40.089
standard error: 0.005077
ee (%) -40.09 ± 0.05

A.4. ^{1}H NMR

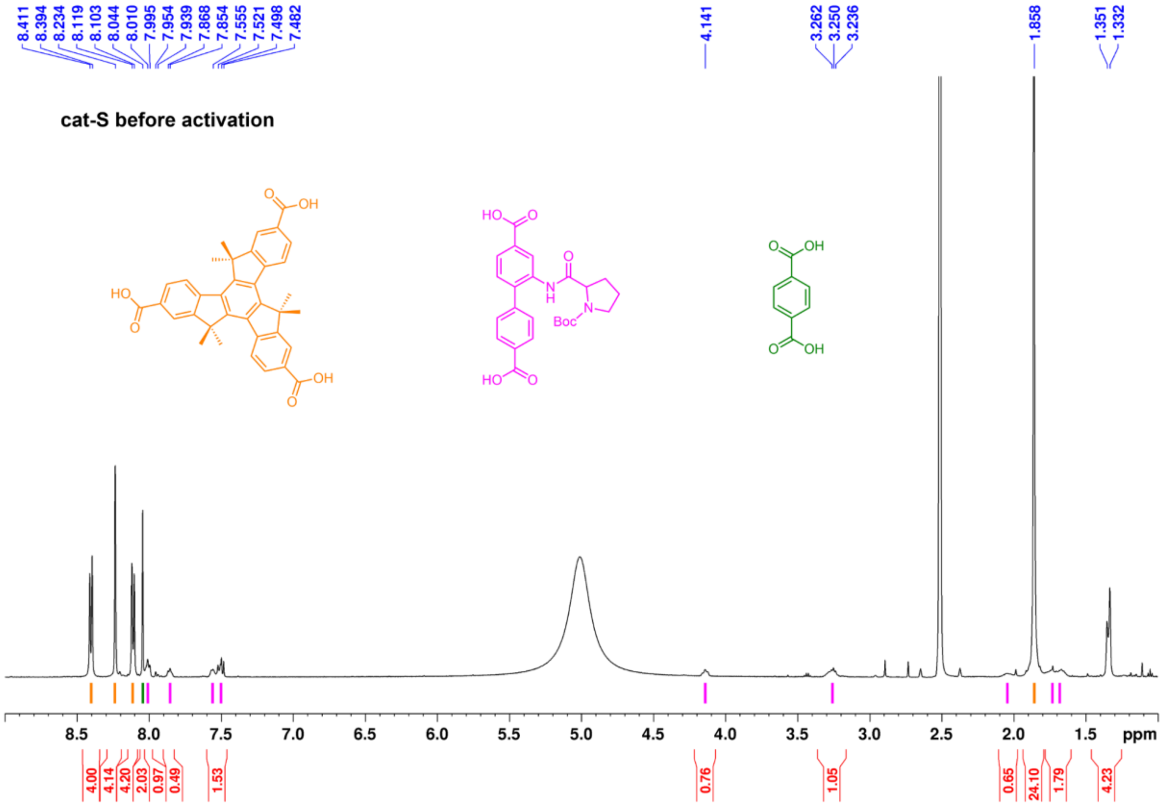

Figure A-7. ^{1}H NMR of cat-S before thermolysis. The Boc protecting group is presented at 1.3 ppm.

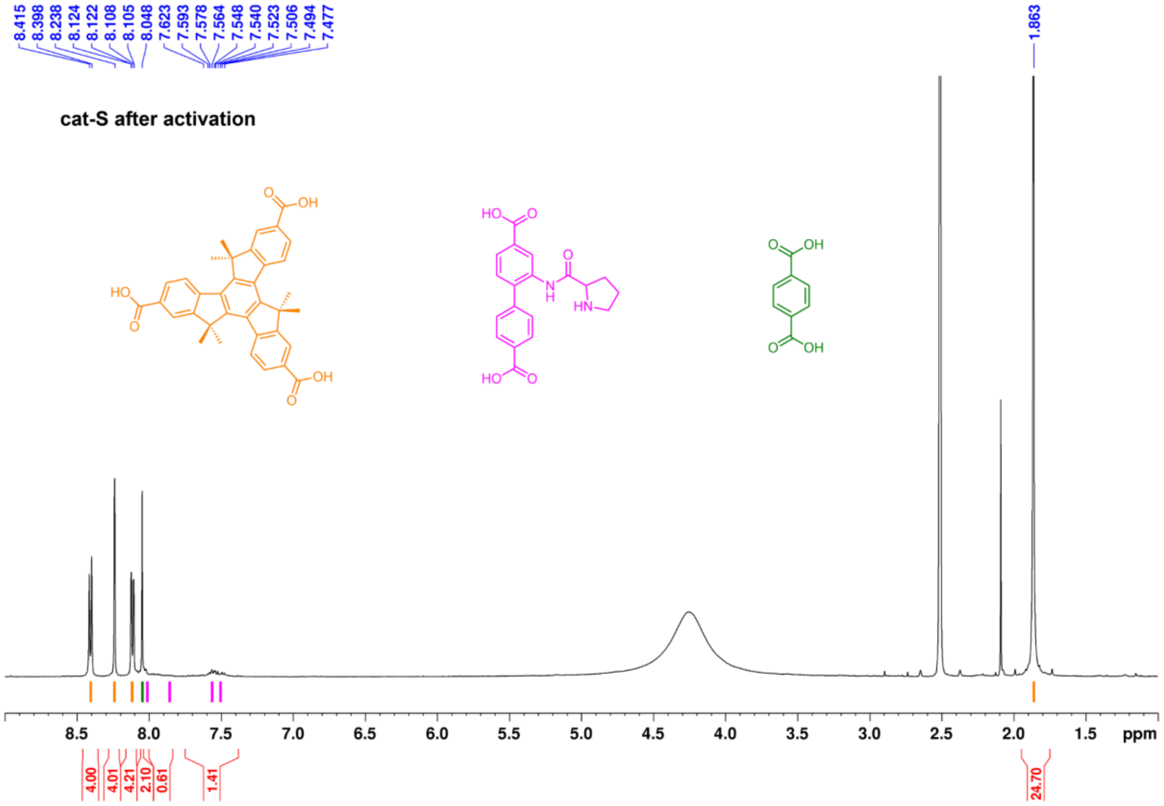

Figure A-8. ^{1}H NMR of cat-S before thermolysis. The peak of Boc protecting group is disappeared.

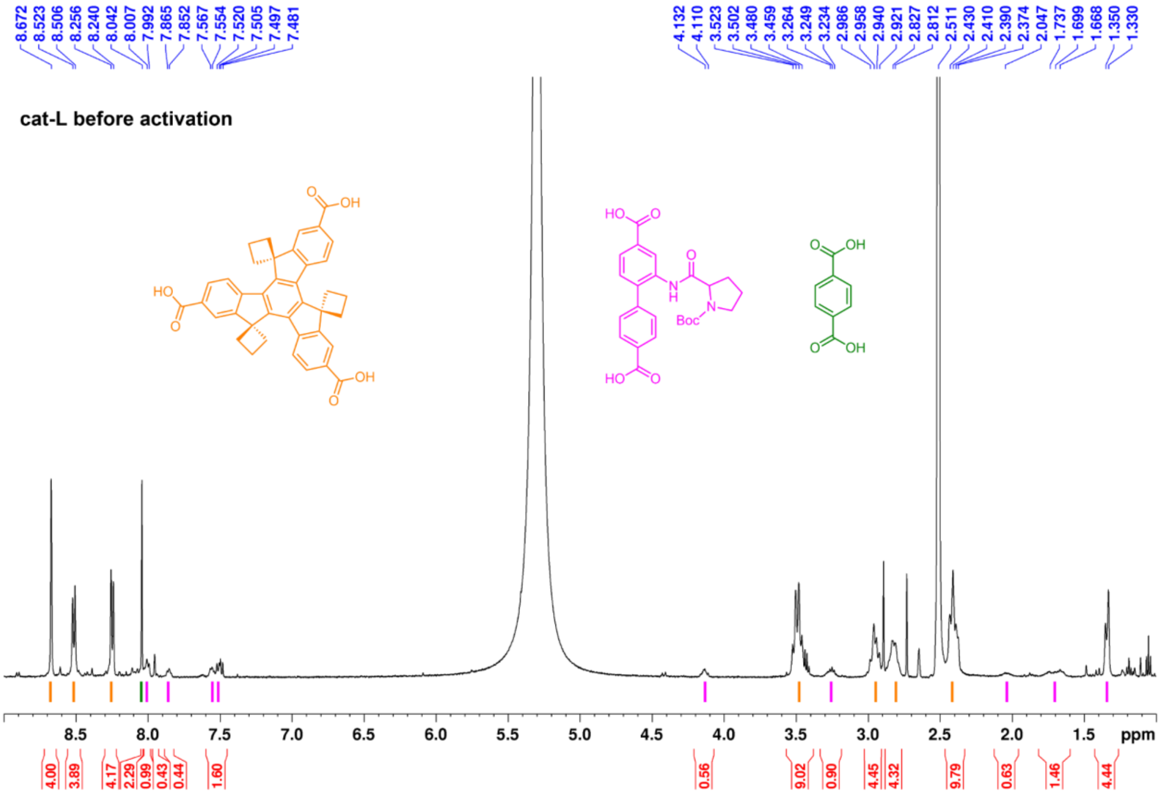

Figure A-9. ^{1}H NMR of cat-L before thermolysis. The Boc protecting group is presented at 1.3 ppm.

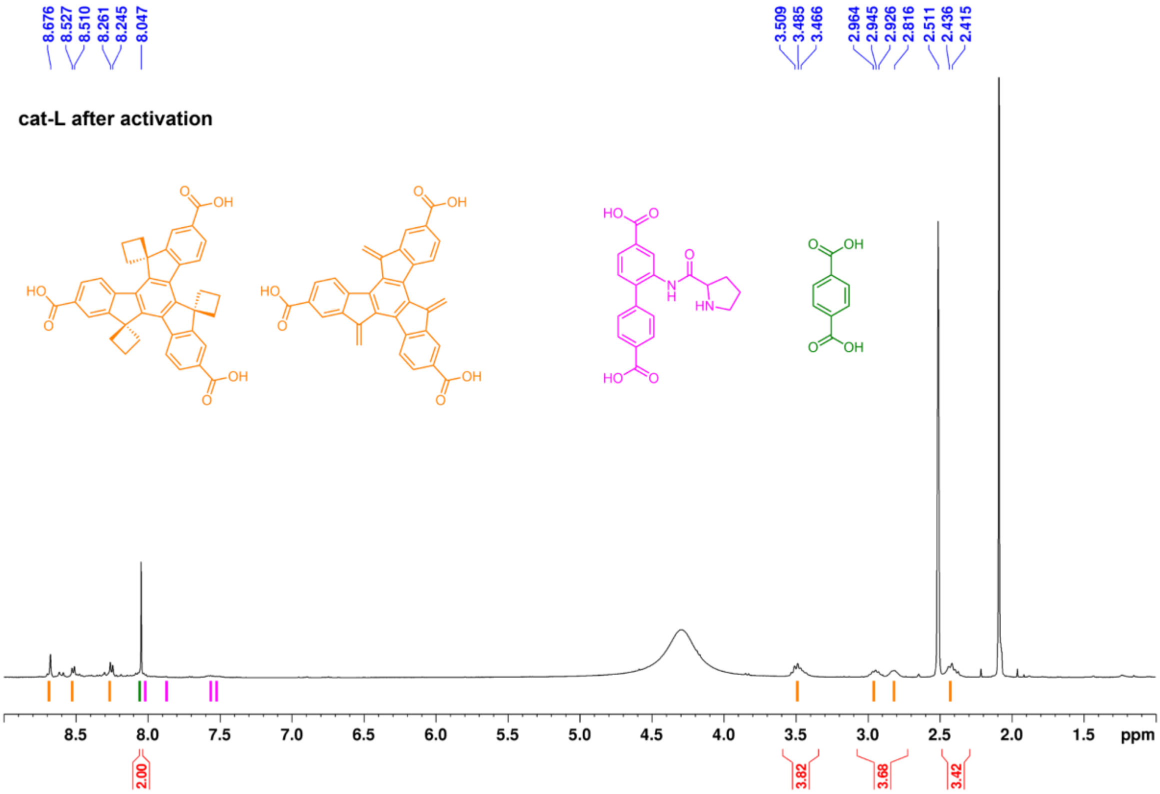

Figure A-10. ^{1}H NMR of cat-S before thermolysis. Due to the partial thermolysis of the cyclobutyl group, peaks were broadened. Approximately 50 % of cbtt was decomposed based on the integrals comparing with bdc.

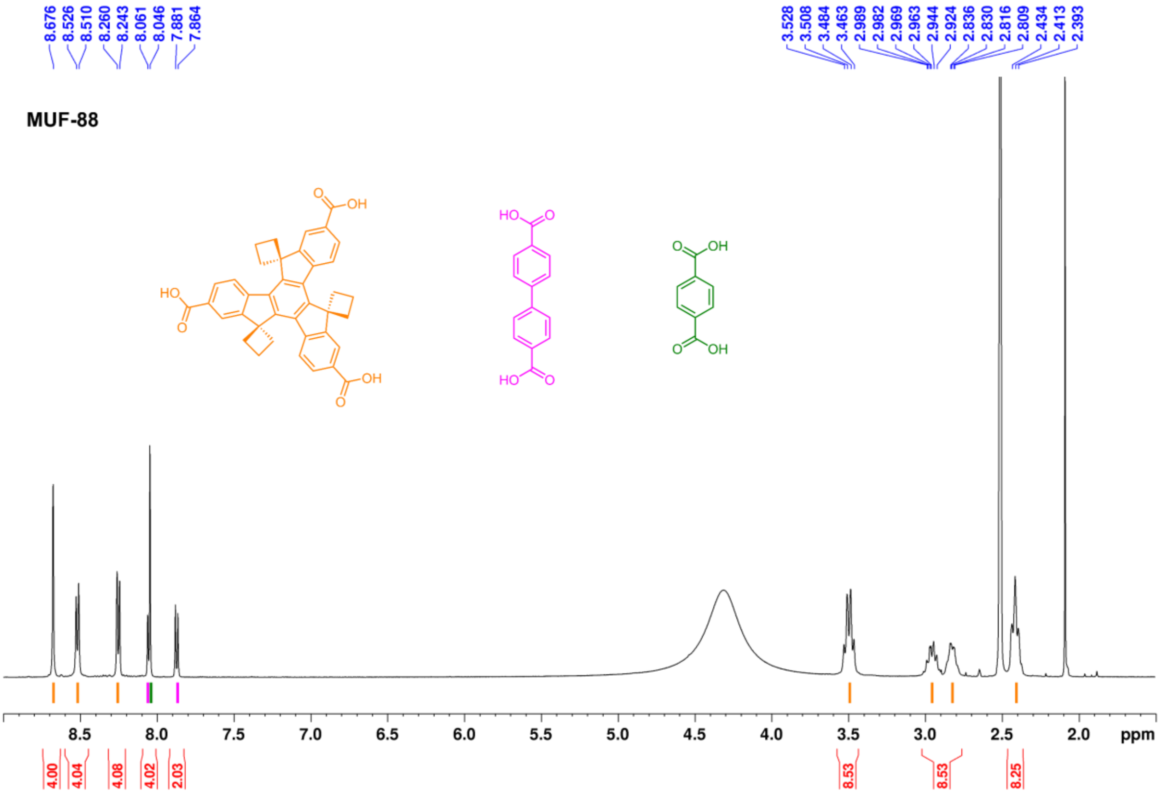

Figure A-11. ^{1}H NMR of MUF-88 before thermolysis.

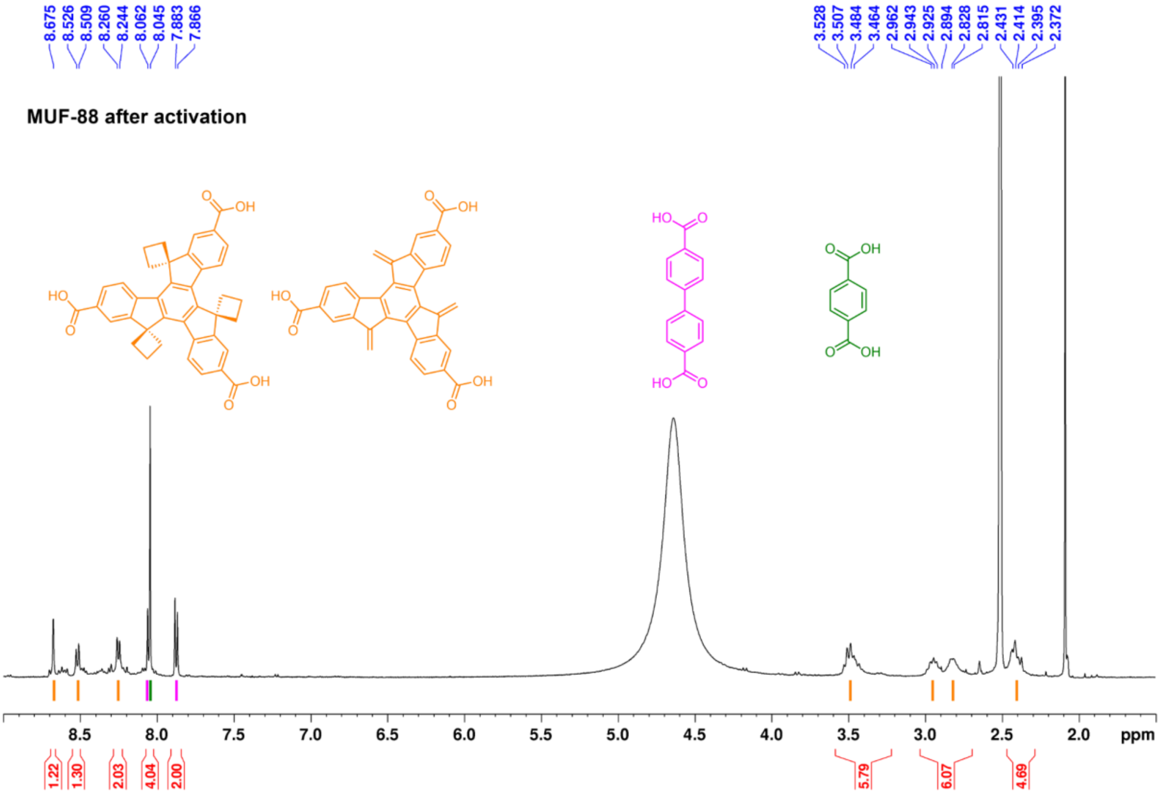

Figure A-12. ^{1}H NMR of MUF-88 before thermolysis. Due to the partial thermolysis of the cyclobutyl group, cbtt peaks were broadened. Approximately 40 % of cbtt was decomposed based on the integrals comparing with bdc.

Appendix B. For Chapter 3

B.1. Ligand synthesis and characterisation

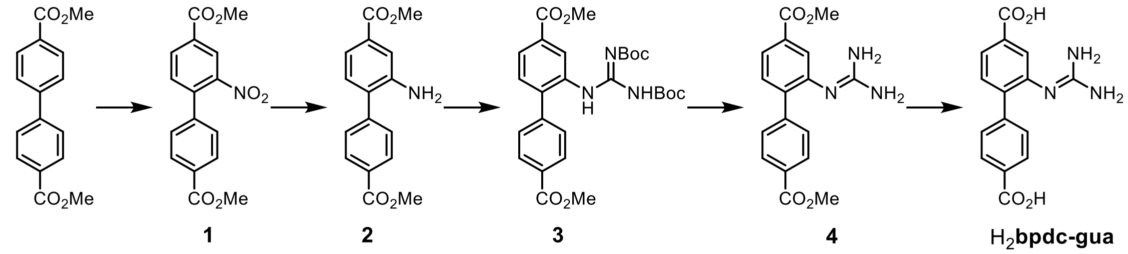

1 Me_2bpdc (20.0 g, 74.0 mmol) was dissolved in conc. H_2SO_4 (98 %, 100 mL) in an ice bath. Then the diluted nitric acid (69 wt%, 5.3 mL, 1.1 eq.) in conc. H_2SO_4 (98 %, 30 mL) was added to the above solution dropwisely over a period of 1 hour while the temperature was kept between 0-5 °C. After the addition, the reaction mixture was kept in an ice bath for 1 hour and then slowly warmed up to RT for another 1 hour. The reaction mixture was poured into an ice/water mixture, and the white sticky material was extracted with EtOAc, and the extraction was washed with water and dried over Na_2SO_4. The yellow solid material was then purified by silica column chromatogram (eluent: ~25 % EtOAc/n-hexane) to yield a pure white powder of 1 (15.3 g, 65.5 % yield).

^{1}H NMR (500 MHz, Chloroform-*d*) δ 8.59 (d, *J* = 1.7 Hz, 1H), 8.32 (dd, *J* = 8.0, 1.7 Hz, 1H), 8.18 – 8.12 (m, 2H), 7.57 (d, *J* = 7.9 Hz, 1H), 7.46 – 7.41 (m, 2H), 4.03 (s, 3H), 3.98 (s, 3H).

2 1 (15.3 g, 48.5 mmol) was dissolved in 100 mL DCM/Methanol (40:60), and then Pd on activated carbon (10 wt%, 0.3 g) was added to the above solution. The system was tumbled in hydrogenator under H_2 for a day. A dark solution was filtered off through a celite pad with hot EtOAc, and the solvent was removed from the filtrate to produce a yellow solid of 2 (13.3 g, 96 % yield).

^{1}H NMR (500 MHz, Chloroform-*d*) δ 8.16 (dd, *J* = 8.2, 3.0 Hz, 1H), 7.58 (dd, *J* = 8.0, 2.5 Hz, 1H), 7.54 – 7.45 (m, 1H), 3.98 (t, *J* = 2.5 Hz, 1H), 3.94 (d, *J* = 2.8 Hz, 1H), 3.89 (s, 1H), 1.63 – 1.59 (m, 1H).

3 *N,N'*-Bis(tert-butoxycarbonyl)-S-methylisothiourea (6.84 g, 1.2 eq.), $HgCl_2$ (6.4 g, 1.2 eq.) and triethylamine (10 mL, 3.6 eq.) was mixed with DMF (100 mL), and the mixture was cooled down in an ice bath stirring, then 2 (5.6 g, 19.6 mmol) was added. The mixture was stirred overnight while the temperature was slowly increasing to RT. The light yellow mixture was poured into water and extracted by EtOAc, and washed with brine and water. The crude product was recrystallised from MeOH to yield a pure product of 3 (6.16 g, 59.5 % yield).

^{1}H NMR (500 MHz, Chloroform-*d*) δ 11.44 (s, 1H), 10.06 (s, 1H), 8.62 (d, *J* = 1.7 Hz, 1H), 8.11 – 8.06 (m, 2H), 7.91 (dd, *J* = 8.0, 1.7 Hz, 1H), 7.47 – 7.42 (m, 2H), 7.35 (d, *J* = 8.0 Hz, 1H), 7.26 (s, 2H), 3.94 (d, *J* = 1.1 Hz, 6H), 1.46 (s, 9H), 1.41 (s, 9H).

4 To a colourless solution of 3 (5.16 g, 10.5 mmol) in DCM (40 mL) was added TFA (40 mL) dropwisely at ice bath. After the addition, the solution was gradually warmed up to room temperature overnight. To the acidic solution were added saturated K_2CO_3 aqueous solution and K_2CO_3 powder until no bubble was produced while the solution was kept in on ice bath. Then the product was extracted with DCM, and DCM was removed under reduced pressure to yield the pure product of 4 (2.64 g, 77 % yield).

^{1}H NMR (500 MHz, Chloroform-*d*) δ 8.08 – 8.03 (m, 2H), 7.99 (dd, *J* = 8.0, 1.8 Hz, 1H), 7.89 (d, *J* = 1.7 Hz, 1H), 7.55 – 7.47 (m, 3H), 3.97 (s, 3H), 3.93 (s, 3H).

H_2**bpdc-gua** 4 (2.6 g, 7.9 mmol) was dissolved in THF (30 mL), aqueous NaOH solution (1 M, 30 mL) was added, and the mixture was stirred at 50 °C overnight. After cooling down to RT, THF was removed, the aqueous solution was acidified with HCl (1 M) to ~ pH 6, and the white precipitate was filtered off and dried to yield the pure product of 5 (1.62 g, 68 % yield).

^{1}H NMR (500 MHz, DMSO-*d*$_6$) δ 7.95 (d, *J* = 8.1 Hz, 1H), 7.88 (d, *J* = 7.8 Hz, 2H), 7.82 (s, 1H), 7.48 (t, *J* = 9.6 Hz, 3H).

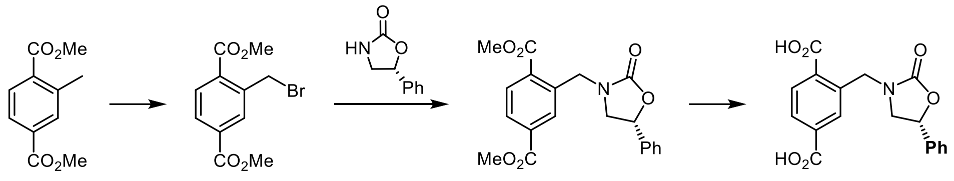

5 6 H_2**bdc-mephox**

5 A mixture of Me_2bdc-Me (0.50 g, 2.40 mmol), NBS (513 mg, 1.2 eq.), and AIBN (40 mg, 0.1 eq.) was placed in a 50 mL round bottom flask with dry benzene (15 mL), and the flask was vacuumed and purged with N_2 gas several times. Then, the mixture was heated to 60 °C with stirring overnight under an N_2 atmosphere. After cooling down to RT, the solvent was reduced under vacuum, and the crude product was purified by silica column (eluent: 10 % EtOAc/cyclohexane). The solvent was removed under reduced pressure to yield a clear oily product of 5 (0.5g, 70 % yield).

^{1}H NMR (400 MHz, Chloroform-*d*) δ 8.22 (ddd, *J* = 8.0, 1.4, 0.8 Hz, 1H), 8.22 – 8.16 (m, 1H), 8.03 – 7.96 (m, 1H), 5.40 – 5.35 (m, 2H), 3.99 (d, *J* = 1.0 Hz, 0H), 3.98 (s, 3H).

6 The reaction was conducted under the inert condition. The mixture of oxazolidinone derivative (0.55 mmol) and potassium tert-butoxide (69 mg, 1.1 eq.) in DMF (5 mL) was stirred for 30 mins at room temperature. Then the premixed solution of 5 (160 mg, 1 eq.) in DMF (5 mL) was added dropwise to the reaction mixture, and the mixture was stirred overnight at RT. The reaction mixture was diluted with EtOAc and washed with an excess amount of water to remove residual DMF, the organic layer was dried over $MgSO_4$, and the organic solvent was removed under reduced pressure. The crude material was purified with a silica column (eluent: 30 % EtOAc/n-hexane) to yield the light yellow oily product.

^{1}H NMR (500 MHz, Chloroform-*d*) δ 8.12 (d, *J* = 1.6 Hz, 1H), 8.08 – 7.99 (m, 2H), 7.46 – 7.34 (m, 5H), 5.54 (t, *J* = 8.2 Hz, 1H), 5.01 (d, *J* = 15.8 Hz, 1H), 4.86 (d, *J* = 15.8 Hz, 1H), 3.96 (d, *J* = 8.2 Hz, 6H), 3.88 (t, *J* = 8.8 Hz, 1H), 3.43 (dd, *J* = 9.0, 7.7 Hz, 1H), 1.28 (t, *J* = 7.1 Hz, 1H).

H_2**bdc-mephox** 6 was stirred overnight in a mixture of THF (5 mL) and 1 M NaOH (5 mL), then it was acidified with 2 M HCl to ~pH 4. The product was extracted with EtOAc and washed with H_2O, and the organic layer was dried over $MgSO_4$. The organic solvent was removed under reduced pressure to yield light yellow powder material (overall yield ~40 %).

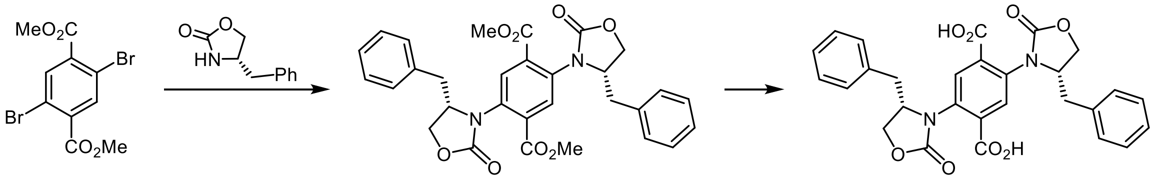

8

H2bdc-(bnox(S))2

8 To a stirring mixture of dimethyl-2,5-dibromoterephthalate (1.00 g, 2.84 mmol), (S)-4-benzyloxazolidin-2-one (1.11 g, 2.2 eq.), CuI (1.08 g, 2 eq.) and K_2CO_3 (2.36 g, 6 eq.) in toluene (30 mL), was added N,N-Dimethylethylenediamine (1.22 mL, 4 eq.), and the reaction mixture refluxed for 2 days under N_2 atmosphere. After cooling down to RT, the reaction mixture was diluted with water, and the organic was extracted with EtOAc, washed with water (200 mL × 3), and dried over $MgSO_4$. The crude product was then purified by silica column chromatography (eluent: EtOAc/Hexane=1:2-1:1). The desired product was obtained as a light brown solid (0.52 g, 33 % yield).

^1H NMR (500 MHz, Chloroform-*d*) δ 7.86 (s, 2H), 7.33 – 7.23 (m, 10H), 4.71 – 4.58 (m, 2H), 4.50 (t, *J* = 8.6 Hz, 2H), 4.30 (dd, *J* = 8.8, 6.5 Hz, 2H), 3.97 (s, 6H), 3.18 (dd, *J* = 13.6, 4.8 Hz, 2H), 2.94 (dd, *J* = 13.5, 9.6 Hz, 2H).

H_2**bdc-(bnox(S))$_2$** 8 (100 mg, 184 μmol) was stirred in THF (1 mL) in an ice bath, and aqueous KOH solution (1 M, 0.55 mL, 3 eq.) was added to the mixture, then the mixture was stirred overnight while the temperature gradually increased to RT. The cloudy mixture turned into a clear yellow solution after overnight stirring. The reaction mixture was then acidified to ~pH 4 with dilute HCl (1 M), and the organic was extracted with EtOAc and washed with H_2O and dried to yield the brownish solid product (94 mg, 94 % yield).

^1H NMR (500 MHz, DMSO-d_6) δ 13.40 (s, 2H), 7.77 (s, 2H), 7.23 – 7.15 (m, 8H), 7.11 (t, *J* = 7.0 Hz, 2H), 4.79 (p, *J* = 7.3 Hz, 2H), 4.45 (t, *J* = 8.5 Hz, 2H), 4.19 (t, *J* = 7.5 Hz, 2H), 2.91 (h, *J* = 8.1 Hz, 4H). ^{13}C NMR (126 MHz, DMSO) δ 165.69, 155.81, 136.28, 134.17, 132.68, 130.32, 128.97, 128.37, 126.51, 67.60, 58.39, 38.61. ES-MS (negative mode, CH_3OH): m/z = 515.145 ($[C_{28}H_{23}N_2O_8]^-$, calcd. 515.145).

B.1.1. MOF synthesis

H_3hxtt (4 μmol), H_2bpdc derivatives (4.8 μmol), H_2bdc derivatives (8.0 μmol), benzoic acid[8], and $Zn(NO_3)_2{\cdot}4H_2O$ (16.5 mg) were placed in a 4 mL vial, and DEF (1 mL) and H_2O (50 μL) was added. The mixture was briefly sonicated, and the vial was placed in an isothermal oven at 85 °C for a day, and approximately 15 mg of crystal was obtained. The mother liquor was decanted off, and the crystals were washed with fresh DMF (×2) to remove residual organics and kept in DMF until use.

(a) MOF synthesis (1 mL scale)

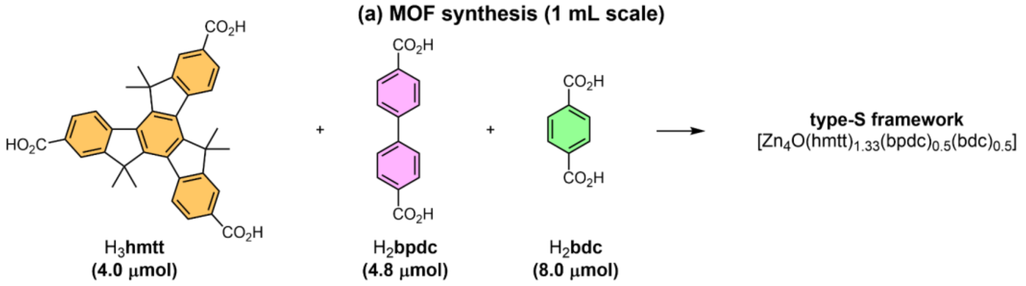

(b) Amount of ligand for synthesis

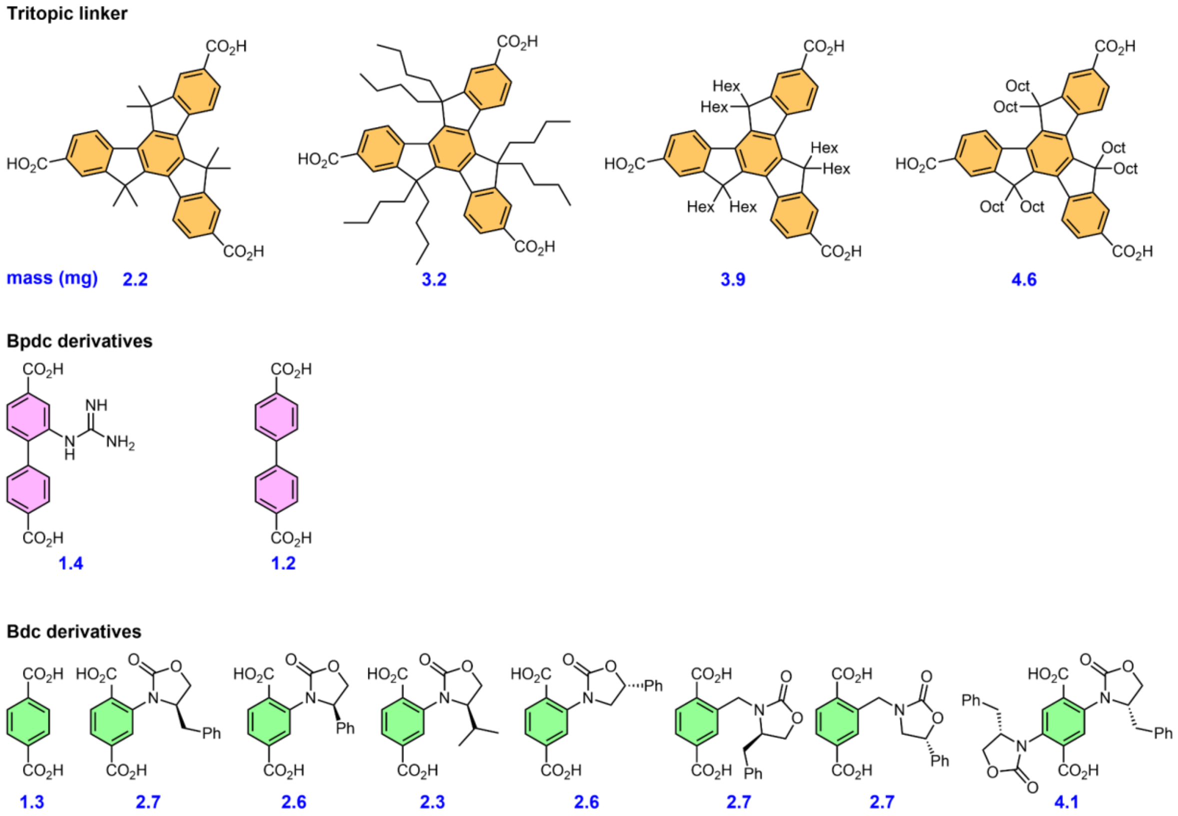

Figure B-1. (a) A schematic diagram of MOF synthesis; (b) the required amout (indicated with blue numbers) of each ligand for 1 mL scale synthesis.

---

[8] 8 mg of benzoic acid was added to the synthesis mixture if hmtt was used for the tritopic linker, otherwise 14 mg of benzoic acid was used.

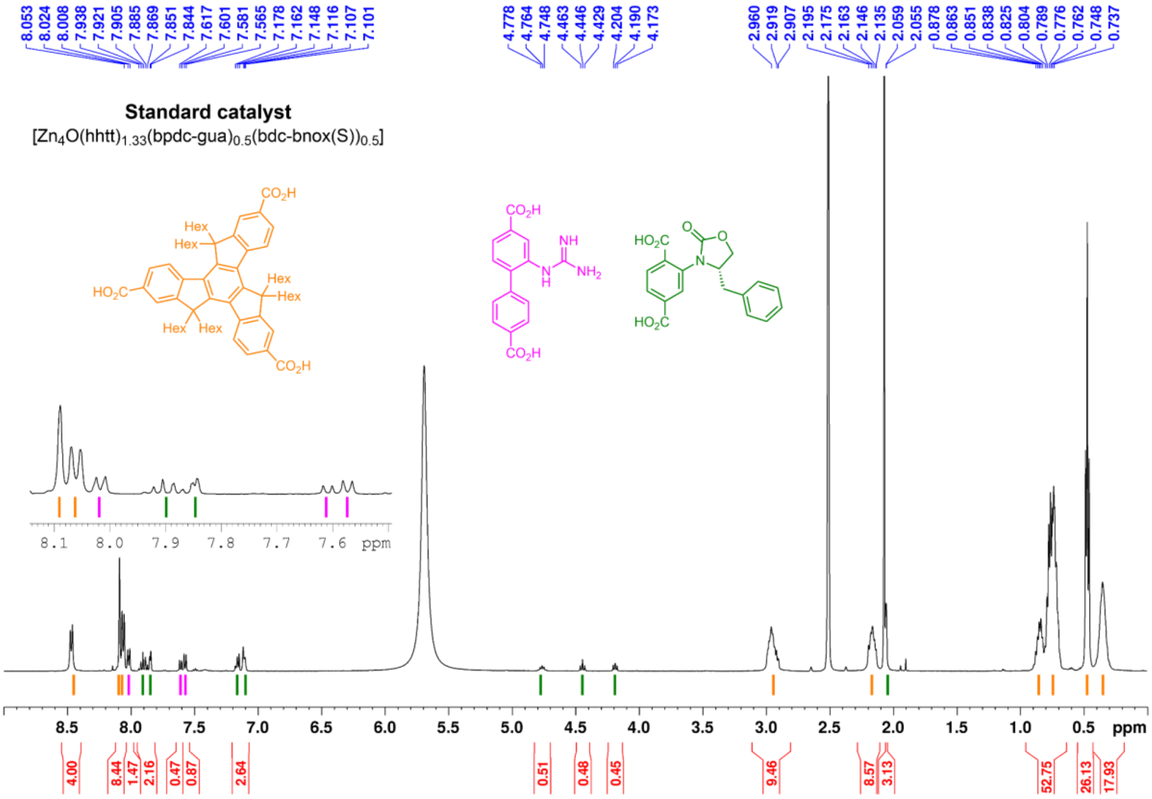

Figure B-2. A digested standard catalyst ([$Zn_4O(hhtt)_{1.33}(bpdc\text{-}gua)_{0.5}(bdc\text{-}bnox(S))_{0.5}$]) in DMSO-d6 (0.6 mL) and DCl (10 µL)

Appendix C. For chapter 5

C.1. Ligand Synthesis

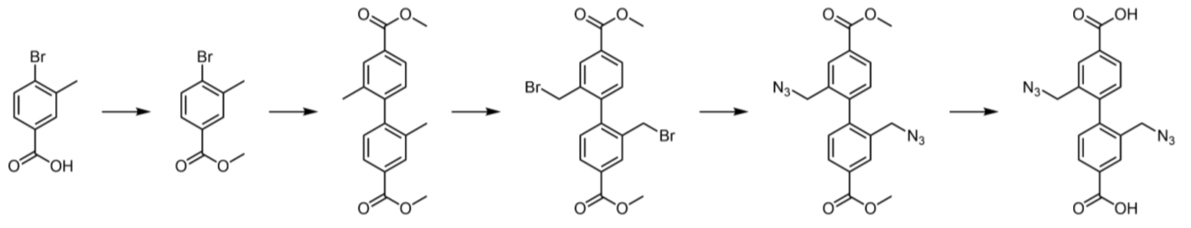

1a 1b 1c 1d H_2**L1**

Figure C-1. A schematic diagram of the synthesis of L1.

1a 4-Bromo-3-methylbenzoic acid (10.0 g, 46.5 mmol) was dissolved in MeOH (100 mL) and conc. H_2SO_4 (98 %, 2 mL) was added, then the reaction mixture was refluxed with stirring overnight. The volume was reduced under reduced pressure, and the solid material was precipitated by the addition of water, washed with water, and dried to yield the pure product as a pink solid (10.6 g, 46.3 mmol, 99 % yield).

^{1}H NMR (500 MHz, $CDCl_3$) δ 7.90 (d, *J* = 2.2 Hz, 1H), 7.70 (dd, *J* = 8.3, 2.1 Hz, 1H), 7.60 (d, *J* = 8.2 Hz, 1H), 3.91 (s, 3H), 2.45 (s, 3H).

1b A mixture of 1a (5.35 g, 23.4 mmol, 1 eq.), bis(pinacolato)diboron (6.52 g, 1.1 eq), KOAc (6.88 g, 3 eq.), and $Pd(OAc)_2$ (0.157 g, 0.03 eq.) in DMF (100 mL) was stirred at 90 °C under N_2 atmosphere overnight. After cooling down to room temperature, 1a (5.0 g, 0.93 eq.), K_2CO_3 (4.7 g, 1.46 eq.) and $Pd(PPh_3)_4$ (0.81 g, 0.03 eq.) were added to the reaction mixture, and the reaction mixture was refluxed under N_2 atmosphere overnight. After cooling down to room temperature, the reaction mixture diluted with H_2O/EtOAc (400 mL, 1:1), then filtered through a celite pad. The organic layer was washed with brine (100 mL × 3) and dried over $MgSO_4$, and the solvent was evaporated under vacuum. The crude product was purified with a silica column chromatogram (eluent: 20 % EtOAc/n-hexane) to yield 3b (5.6 g, 80 % yield).

^{1}H NMR (500 MHz, $CDCl_3$) δ 8.01 – 7.95 (m, 1H), 7.91 (dd, *J* = 7.9, 1.8 Hz, 1H), 7.16 (d, *J* = 7.9 Hz, 1H), 3.94 (s, 3H), 2.08 (s, 3H).

1c 1b (5.45 g, 18.3 mmol, 1 eq.), N-bromosuccinimide (6.50 g, 2.0 eq.) and azobisisobutyronitrile (0.30 g, 0.10 eq.) were stirred in dry benzene (100 mL) at 85 °C under N_2 atmosphere for three hours. The solvent was removed under reduced pressure, and the residue dissolved in EtOAc (50 mL) and washed with brine and water. The organic layer was dried over $MgSO_4$, and the solvent was removed under vacuum to yield a brown oily crude product (7.9 g, 95 % yield).

^{1}H NMR (500 MHz, Chloroform-*d*) δ 8.24 (d, *J* = 1.7 Hz, 1H), 8.06 (dd, *J* = 7.9, 1.8 Hz, 1H), 7.36 (d, *J* = 7.9 Hz, 1H), 4.33 (d, *J* = 10.2 Hz, 1H), 4.17 (d, *J* = 10.3 Hz, 1H), 3.97 (s, 3H).

1d To a mixture of 1c (7.9 g, 17.3 mmol, 1 eq.) in CH_2Cl_2 (60 mL) and MeOH (80 mL), was slowly added the premixed solution of NaN_3 (5.3 g, 4.5 eq.) in CH_3OH (100 mL), then the reaction mixture was stirred under N_2 atmosphere for two days at ambient temperature. The reaction mixture was diluted with water (200 mL), and the organic was extracted with CH_2Cl_2 and dried over $MgSO_4$, and the solvent was removed to afford a light brown/yellow oily product. The crude product was purified by a silica column chromatogram (eluent: 20 % EtOAc/n-hexane), and a beige solid (4.2 g, 60 % yield) was obtained after removing the solvent.

^{1}H NMR (500 MHz, $CDCl_3$) δ 8.17 (d, *J* = 1.7 Hz, 1H), 8.09 (dd, *J* = 7.9, 1.8 Hz, 1H), 7.30 (d, *J* = 7.9 Hz, 1H), 4.17 (d, *J* = 13.8 Hz, 1H), 4.11 (d, *J* = 13.7 Hz, 1H), 3.98 (s, 3H).

H_2**L1** 1d (4.0 g, 10.5 mmol, 1.0 eq.) was stirred in THF (25 mL) and aqueous KOH solution (2 M, 25 mL) at 60 °C overnight. After cooling down to room temperature, the THF was removed under reduced pressure, and the reaction mixture was acidified to pH 2 with dilute HCl (1 M) to form a white precipitate. The white solid was filtered, washed with water, and dried to yield the light beige product (3.5 g, 95 % yield).

^{1}H NMR (500 MHz, DMSO-*d*$_6$) δ 13.21 (s, 1H), 8.13 (d, *J* = 1.7 Hz, 1H), 8.00 (dd, *J* = 7.9, 1.8 Hz, 1H), 7.37 (d, *J* = 7.9 Hz, 1H), 4.33 (d, *J* = 13.9 Hz, 1H), 4.21 (d, *J* = 13.9 Hz, 1H).

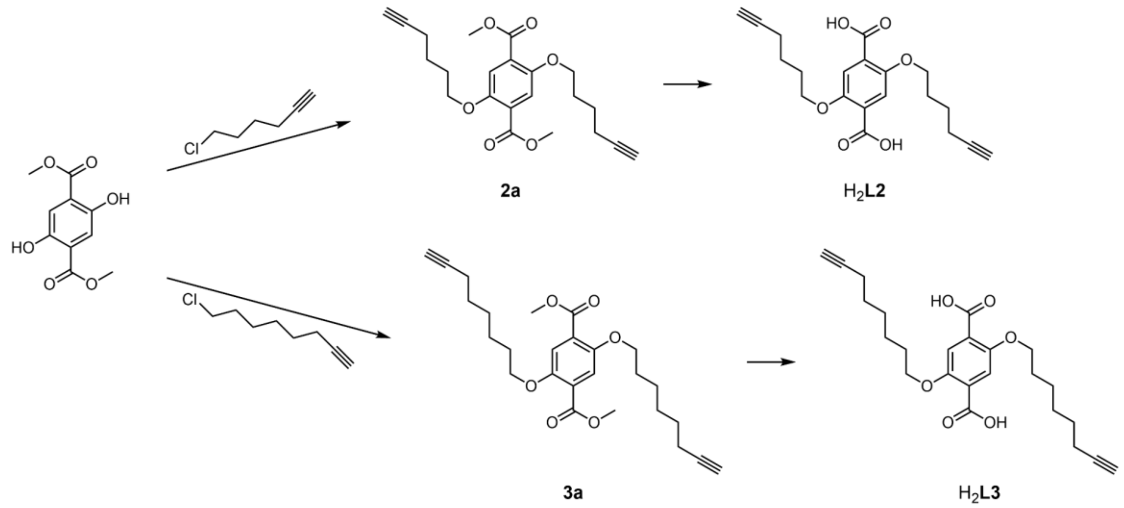

Figure C-2. A schematic diagram of the syntheses of H_2L2 and H_2L3.

2a Dimethyl-2,5-dihydroxyterephthalate (1.0 g, 4.4 mmol, 1 eq.), KI (110 mg, 0.15 eq.), and K_2CO_3 (1.8 g, 3.0 eq.) were stirred in DMF (10 mL), then 1-chloro-hex-5-yne (1.55 g, 3.0 eq.) in 10 mL DMF was added dropwise under a nitrogen atmosphere. The reaction mixture was then stirred overnight at 100 °C. After cooling down to room temperature, an excess amount of water was added to the reaction mixture, and the mixture was kept at a low temperature to yield a brown precipitate, and then the precipitate was washed with water and dried. The crude product (1.2 g, 70 % yield) was used for the next step without further purification.

^{1}H NMR (400 MHz, $CDCl_3$) δ 7.36 (s, 1H), 4.05 (t, *J* = 6.2 Hz, 2H), 3.93 (s, 3H), 2.29 (td, *J* = 7.0, 2.6 Hz, 2H), 1.98 (q, *J* = 3.1 Hz, 1H), 1.93 (dd, *J* = 10.3, 4.6 Hz, 2H), 1.76 (p, *J* = 7.1 Hz, 2H).

H_2**L2** 2a (1.2 g, 3.1 mmol) was stirred in THF (10 mL) and aqueous KOH solution (1 M, 10 mL) at 60 °C overnight. After cooling to room temperature, THF was removed under reduced pressure, and the solution was acidified with dilute HCl (1 M) to pH 2. The precipitate was filtered, washed with water, and dried to yield light yellow powder (1.06 g, 95 % yield).

^{1}H NMR (500 MHz, DMSO-*d*$_6$) δ 12.93 (s, 1H), 7.28 (s, 1H), 4.01 (t, *J* = 6.2 Hz, 2H), 2.77 (t, *J* = 2.7 Hz, 1H), 2.23 (td, *J* = 7.1, 2.6 Hz, 2H), 1.85 – 1.71 (m, 2H), 1.71 – 1.55 (m, 2H). ^{13}C NMR (126 MHz, DMSO) δ 167.28, 150.88, 125.93, 115.98, 84.88, 71.76, 69.10, 28.33, 25.01, 17.88. ESI (negative mode, CH_3OH): m/z = 357.1345 ($[C_{20}H_{22}O_6]^-$, calc. 357.1333).

3a Dimethyl-2,5-dihydroxyterephthalate (500 mg, 2.21 mmol, 1eq.), KI (55 mg, 0.15 eq.), and K_2CO_3 (920 mg, 3.0 eq.) were stirred in DMF (8mL), then, 8-chloro-1-octyne (1.03 mL, 3.0 eq.) in 5 mL DMF was added dropwise under a nitrogen atmosphere. The reaction mixture was stirred at 100 °C overnight. After cooling down to room temperature, the reaction mixture was diluted with water, and the organic was extracted with EtOAc. The crude material was then purified by silica column chromatography (eluent: 10 % EtOAc/n-hexane). A beige solid was deposited after removing the solvent (0.40 g, 41 % yield).

^{1}H NMR (500 MHz, $CDCl_3$) δ 7.38 (s, 2H), 4.03 (t, *J* = 6.4 Hz, 4H), 3.93 (s, 6H), 2.23 (td, *J* = 7.0, 2.6 Hz, 4H), 1.96 (t, *J* = 2.6 Hz, 2H), 1.89 – 1.78 (m, 4H), 1.65 – 1.43 (m, 12H).

H_2**L3** 3a (0.4 g, 0.9 mmol) was stirred in THF (5 mL) and aqueous KOH solution (2 M, 5 mL) at 60 °C overnight. After cooling down to room temperature, THF was removed under reduced pressure, and the solution was acidified to pH 2 with aqueous HCl solution (1 M). The precipitate was filtered, washed with an excess amount of water, and dried under vacuum to yield a light yellow powder (0.37 g, 100 % yield).

^{1}H NMR (500 MHz, DMSO-d_6) δ 13.19 – 12.58 (s, 1H), 7.27 (s, 2H), 3.98 (t, *J* = 6.4 Hz, 4H), 2.73 (t, *J* = 2.7 Hz, 2H), 2.16 (td, *J* = 6.9, 2.6 Hz, 4H), 1.68 (p, *J* = 6.5 Hz, 4H), 1.53 – 1.33 (m, 12H). ^{13}C NMR (126 MHz, DMSO) δ 167.28, 150.93, 125.96, 116.03, 85.04, 71.58, 69.57, 40.59, 40.50, 40.42, 40.33, 40.25, 40.16, 40.09, 39.99, 39.92, 39.83, 39.66, 39.49, 29.04, 28.41, 28.25, 25.26, 18.07.

C.2. MOF synthesis

MUF-80a [$Zn_4O(hmtt)_{4/3}$ $(L1)_{1/2}(L2)_{1/2}$] $Zn(NO_3)_2{\cdot}4H_2O$ (16.5 mg, 6.3 µmol), H_2L1 (1.6 mg, 4.6 µmol), H_2L2 (2.9 mg, 8.0 µmol), H_3hmtt (2.2 mg, 4.0 µmol), benzoic acid (8.0 mg, 65 µmol), H_2O (50 µL), diethylformamide (1 mL) was mixed in a 4 mL vial, and briefly sonicated. The reaction mixture was placed in an isothermal oven at 85 °C for a day. The resulting colourless crystals were washed with DMF several times and kept in fresh DMF for further analysis.

MUF-80a-1 [$Zn_4O(hmtt)_{4/3}$ $(L1)_{1/2}(bdc)_{1/2}$] $Zn(NO_3)_2{\cdot}4H_2O$ (16.5 mg, 6.3 µmol), H_2L1 (1.6 mg, 4.6 µmol), bdc (1.3 mg, 8.0 µmol), H_3hmtt (2.2 mg, 4.0 µmol), benzoic acid (8.0 mg, 65 µmol), H_2O (50 µL), diethylformamide (1 mL) was mixed in a 4 mL vial, and briefly sonicated. The reaction mixture was placed in an isothermal oven at 85 °C for a day. The resulting colourless crystals were washed with DMF several times and kept in fresh DMF for further analysis.

MUF-80a-2 [$Zn_4O(hmtt)_{4/3}(bpdc)_{1/2}(L2)_{1/2}$] $Zn(NO_3)_2{\cdot}4H_2O$ (16.5 mg, 6.3 µmol), bpdc (1.1 mg, 4.6 µmol), H_2L2 (2.9 mg, 8.0 µmol), H_3hmtt (2.2 mg, 4.0 µmol), benzoic acid (8.0 mg, 65 µmol), H_2O (50 µL), diethylformamide (1 mL) was mixed in a 4 mL vial, and briefly sonicated. The reaction mixture was placed in an isothermal oven at 85 °C for a day. The resulting colourless crystals were washed with DMF several times and kept in fresh DMF for further analysis.

MUF-80b [$Zn_4O(hmtt)_{4/3}(L1)_{1/2}(L3)_{1/2}$] $Zn(NO_3)_2{\cdot}4H_2O$ (16.5 mg, 6.3 µmol), H_2L1 (1.6 mg, 4.6 µmol), H_2L3 (3.3 mg, 8.0 µmol), H_3hmtt (2.2 mg, 4.0 µmol), benzoic acid (8.0 mg, 65 µmol), H_2O (50 µL), diethylformamide (1 mL) was mixed in a 4 mL vial, and briefly sonicated. The reaction mixture was placed in an isothermal oven at 85 °C for a day. The resulting colourless crystals were washed with DMF several times and kept in fresh DMF for further analysis.

C.3. ^{1}H NMR spectrum

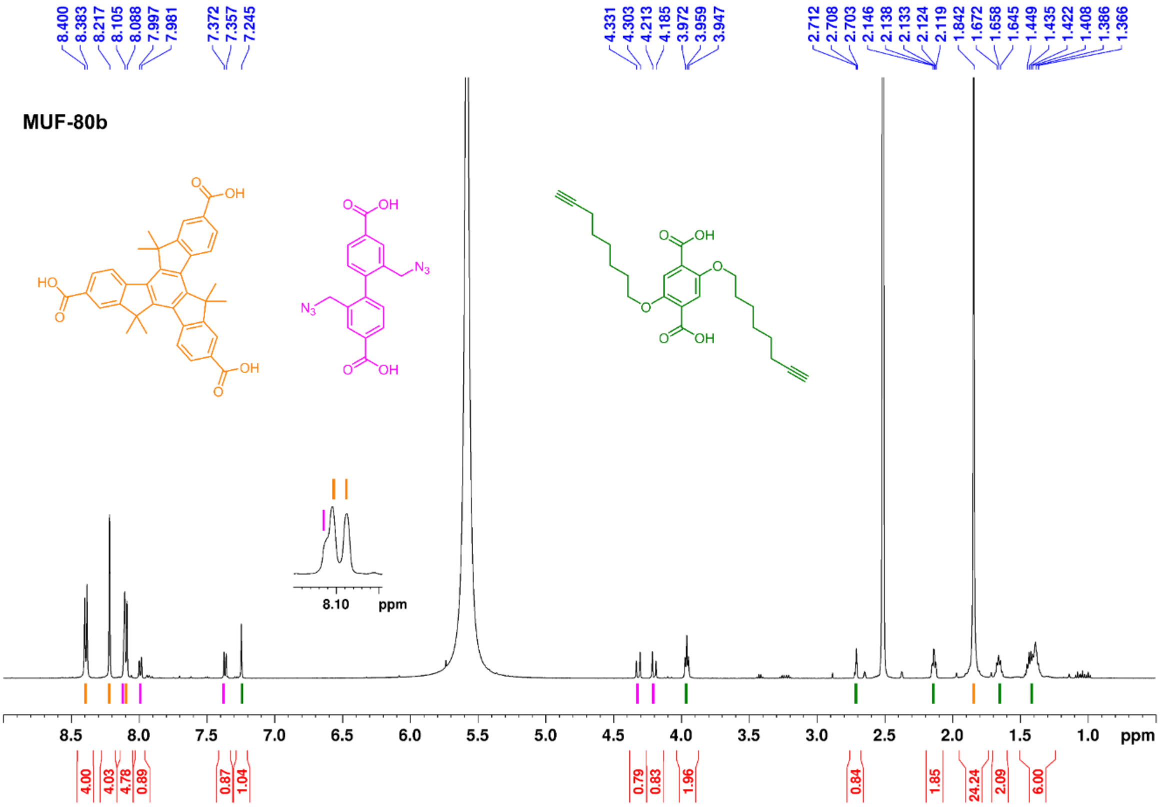

Figure C-3. ^{1}H NMR of digested MUF-80b in DMSO-d_6 and DCl mixture

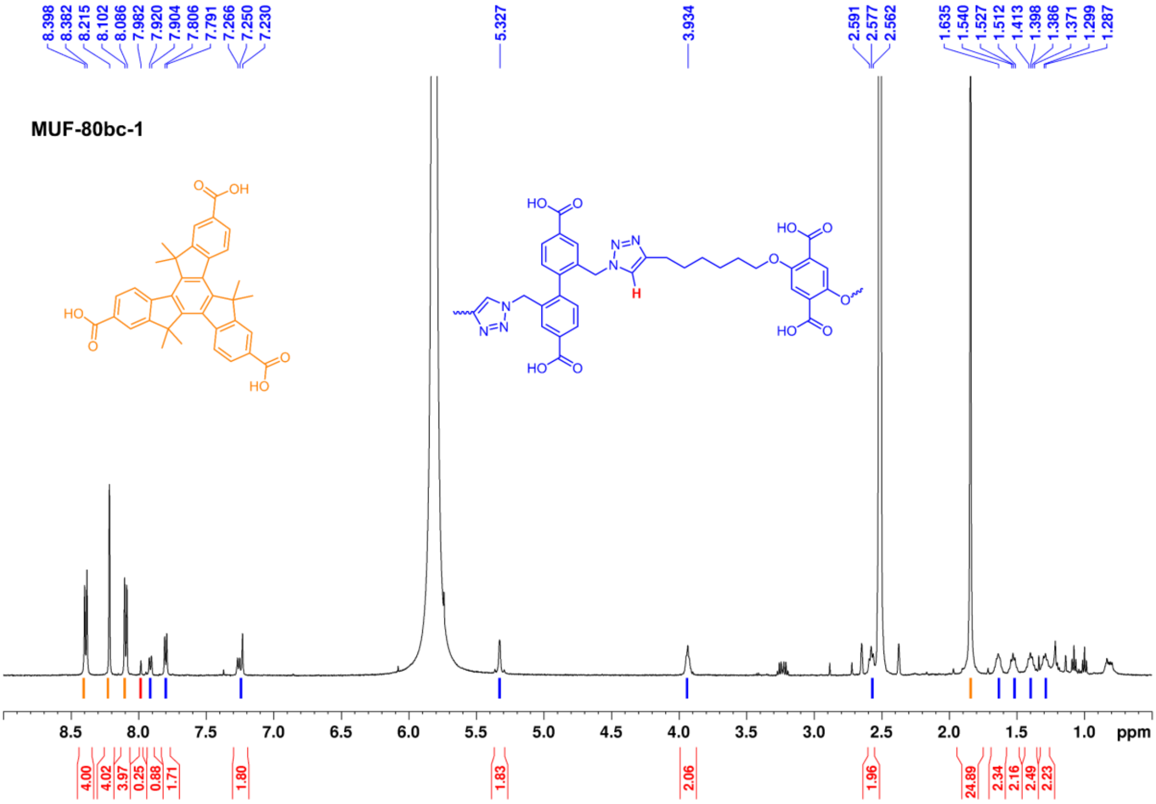

Figure C-4. ^{1}H NMR of digested MUF-80bc-1 in DMSO-d_6 and DCl mixture

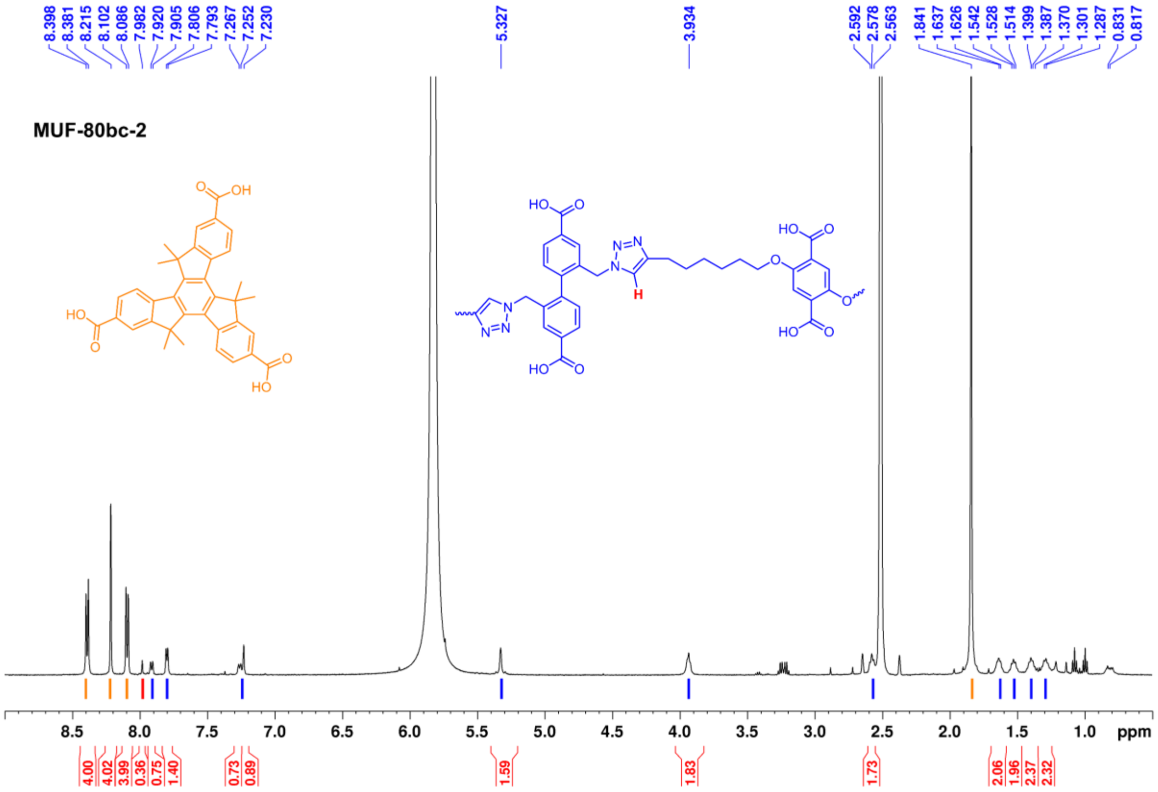

Figure C-5. ^{1}H NMR of digested MUF-80bc-2 in DMSO-d_6 and DCl mixture

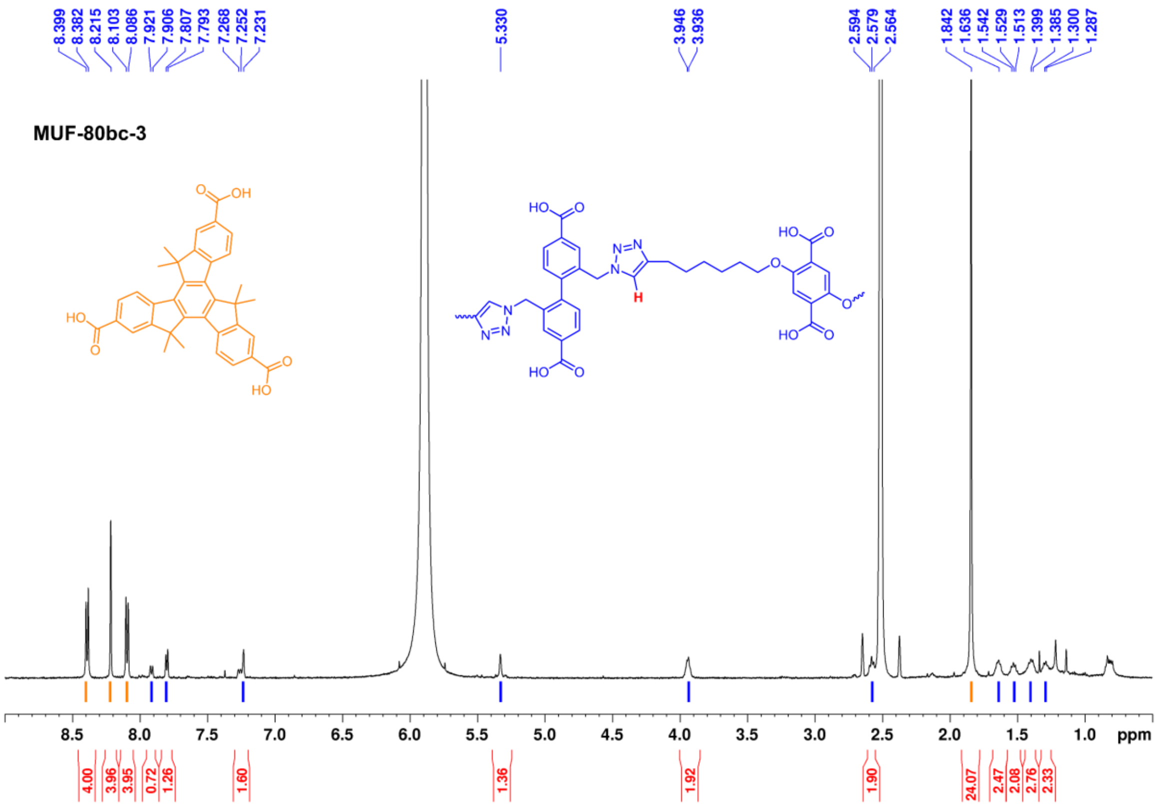

Figure C-6. ^{1}H NMR of digested MUF-80bc-3 in DMSO-d_6 and DCl mixture

C.4. Gas adsorption

C.4.1. N_2 adsoprtion at 77 K and BET plots

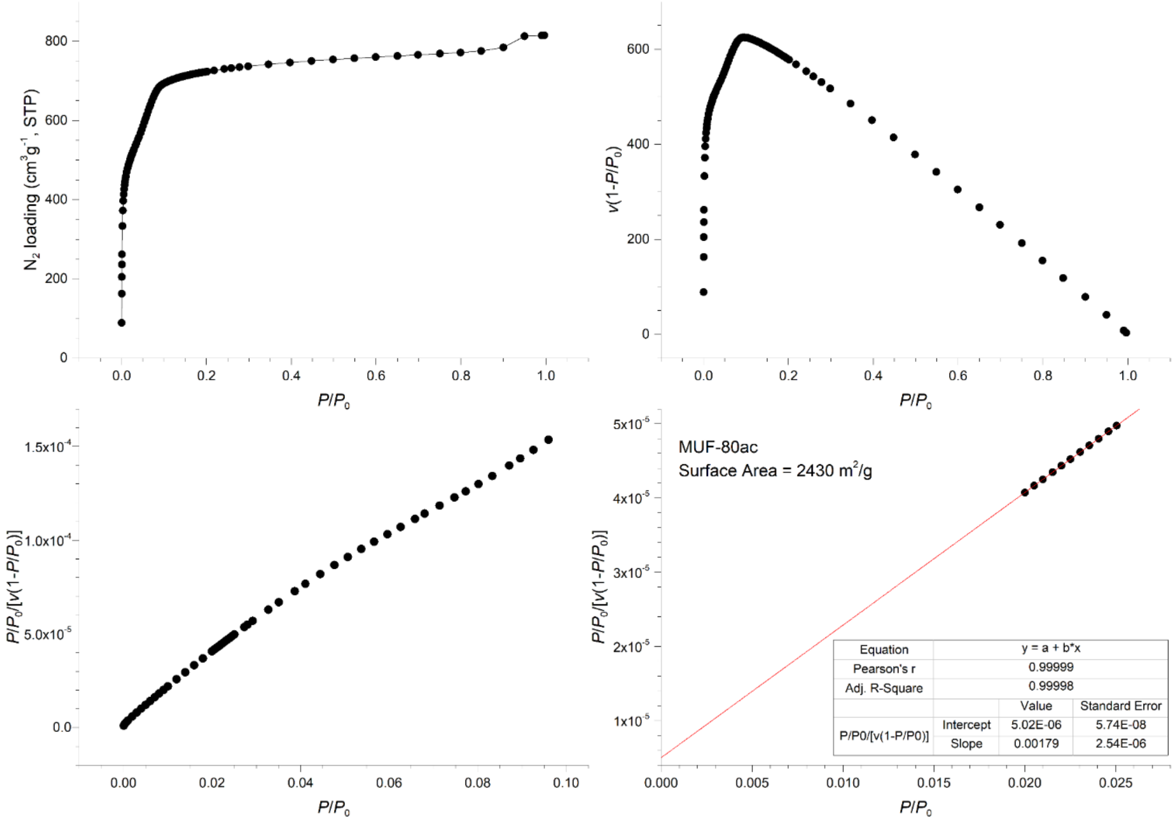

Figure C-7. N_2 adsorption isotherm at 77 K and BET surface area plots for MUF-80ac.

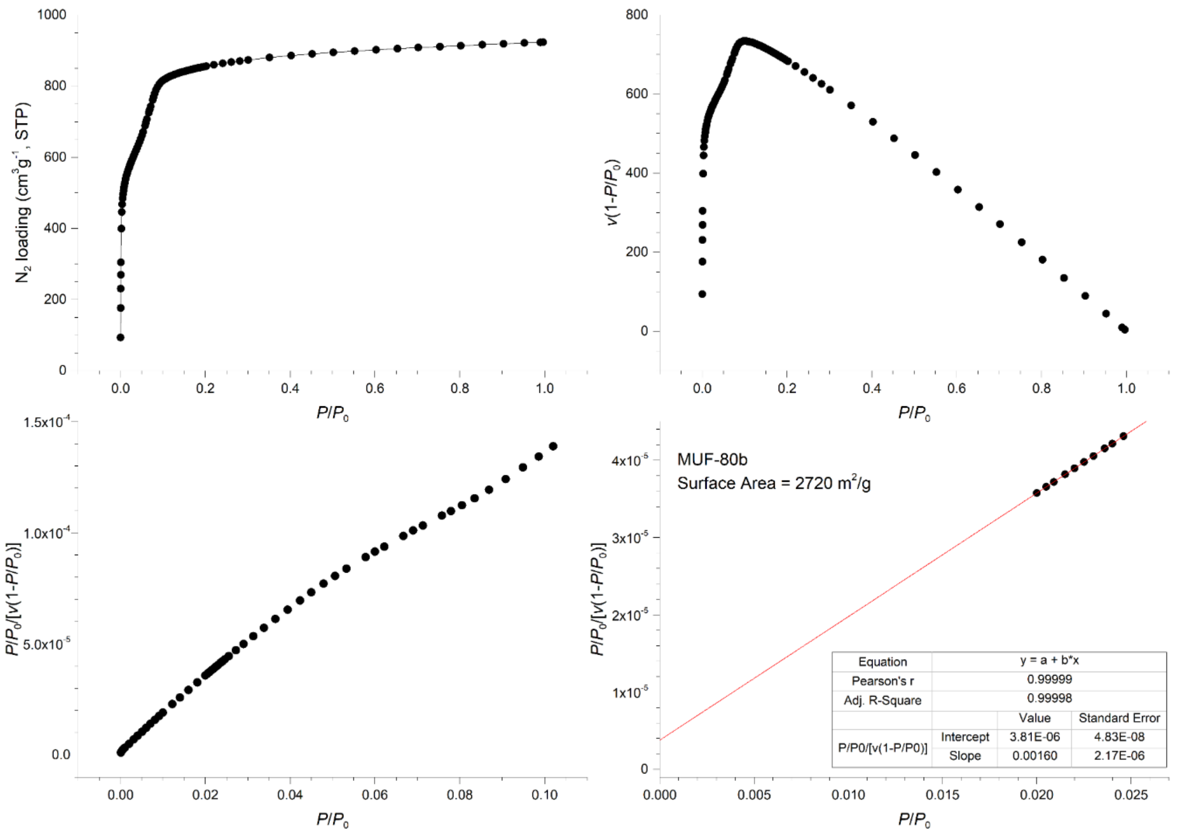

Equation		y = a + b*x	
Pearson's r		0.99999	
Adj. R-Square		0.99998	
		Value	Standard Error
P/P0/[v(1-P/P0)]	Intercept	3.81E-06	4.83E-08
	Slope	0.00160	2.17E-06

Figure C-8. N_2 adsorption isotherm at 77 K and BET surface area plots for MUF-80b.

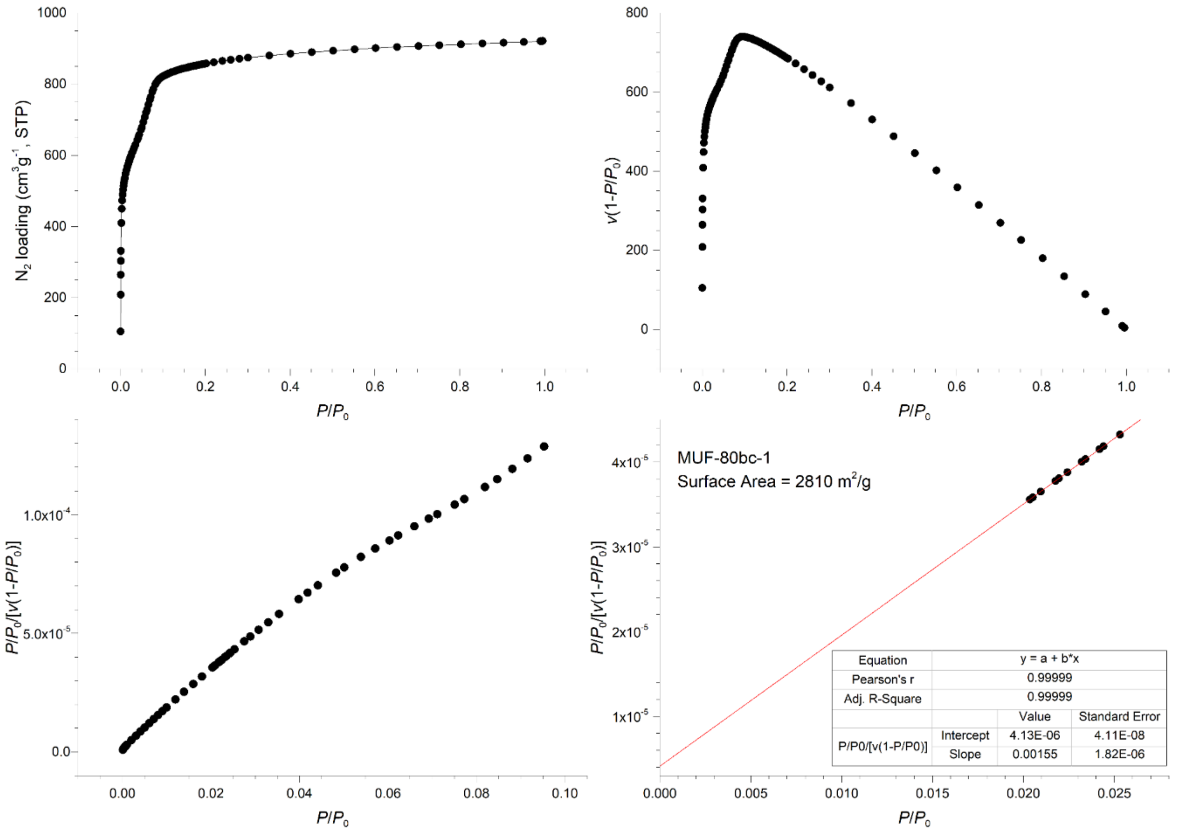

Equation		y = a + b*x	
Pearson's r		0.99999	
Adj. R-Square		0.99999	
		Value	Standard Error
P/P0/[v(1-P/P0)]	Intercept	4.13E-06	4.11E-08
	Slope	0.00155	1.82E-06

Figure C-9. N_2 adsorption isotherm at 77 K and BET surface area plots for MUF-80bc-1.

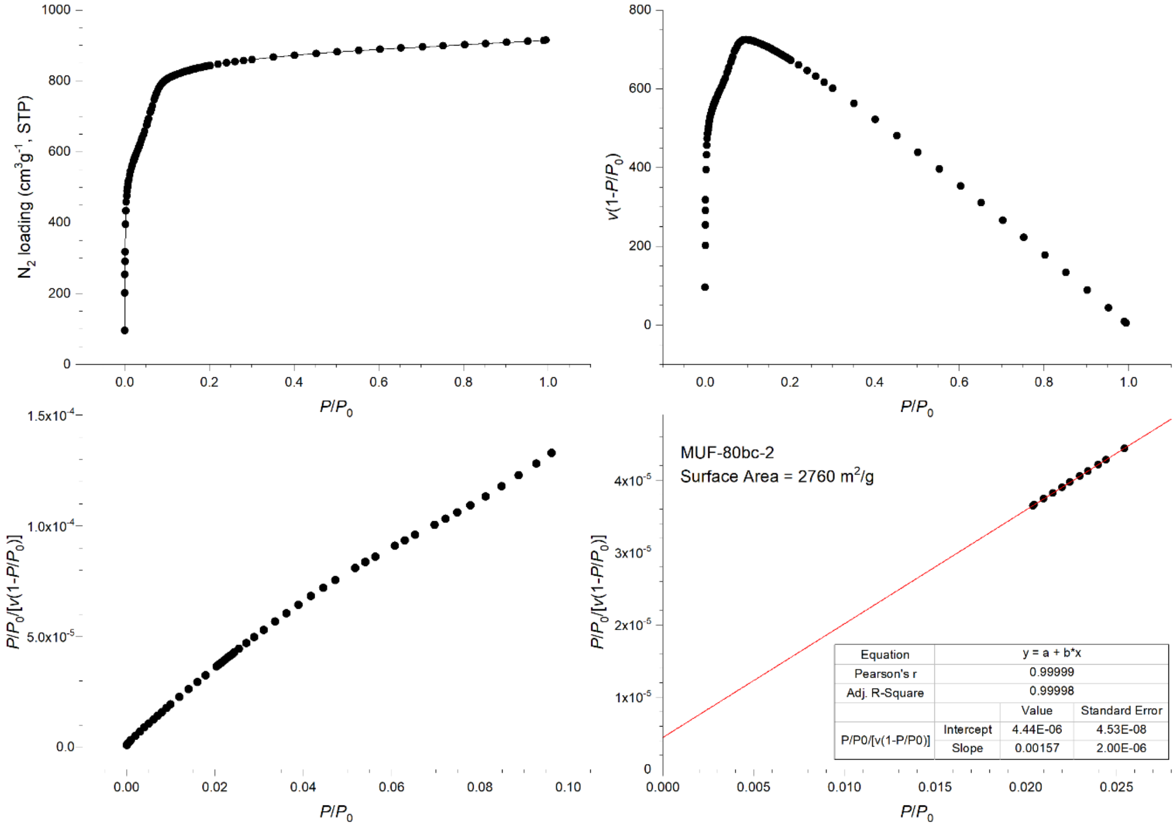

Equation		y = a + b*x	
Pearson's r		0.99999	
Adj. R-Square		0.99998	
		Value	Standard Error
P/P0/[v(1-P/P0)]	Intercept	4.44E-06	4.53E-08
	Slope	0.00157	2.00E-06

Figure C-10. N_2 adsorption isotherm at 77 K and BET surface area plots for MUF-80bc-2.

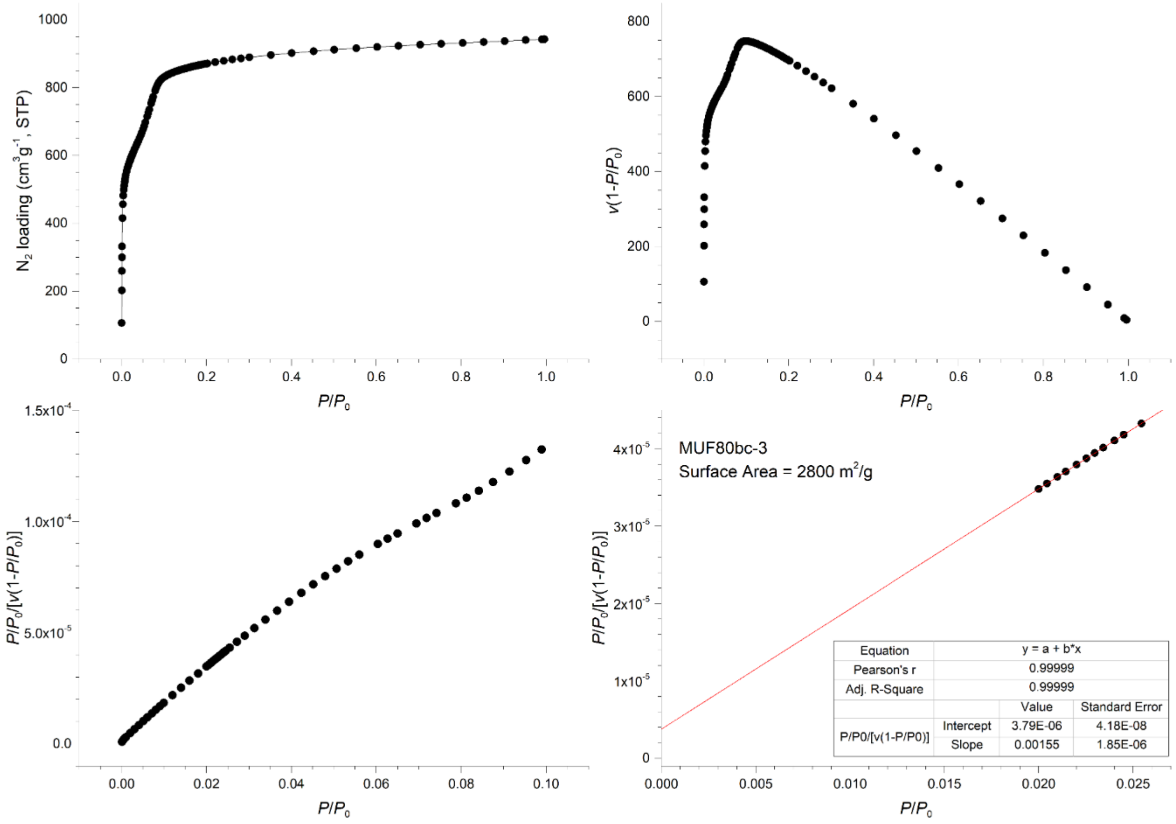

Equation		y = a + b*x	
Pearson's r		0.99999	
Adj. R-Square		0.99999	
		Value	Standard Error
P/P0/[v(1-P/P0)]	Intercept	3.79E-06	4.18E-08
	Slope	0.00155	1.85E-06

Figure C-11. N_2 adsorption isotherm at 77 K and BET surface area plots for MUF-80bc-3.

C.4.2. **Selected gas physorption at 273 K and 293K**

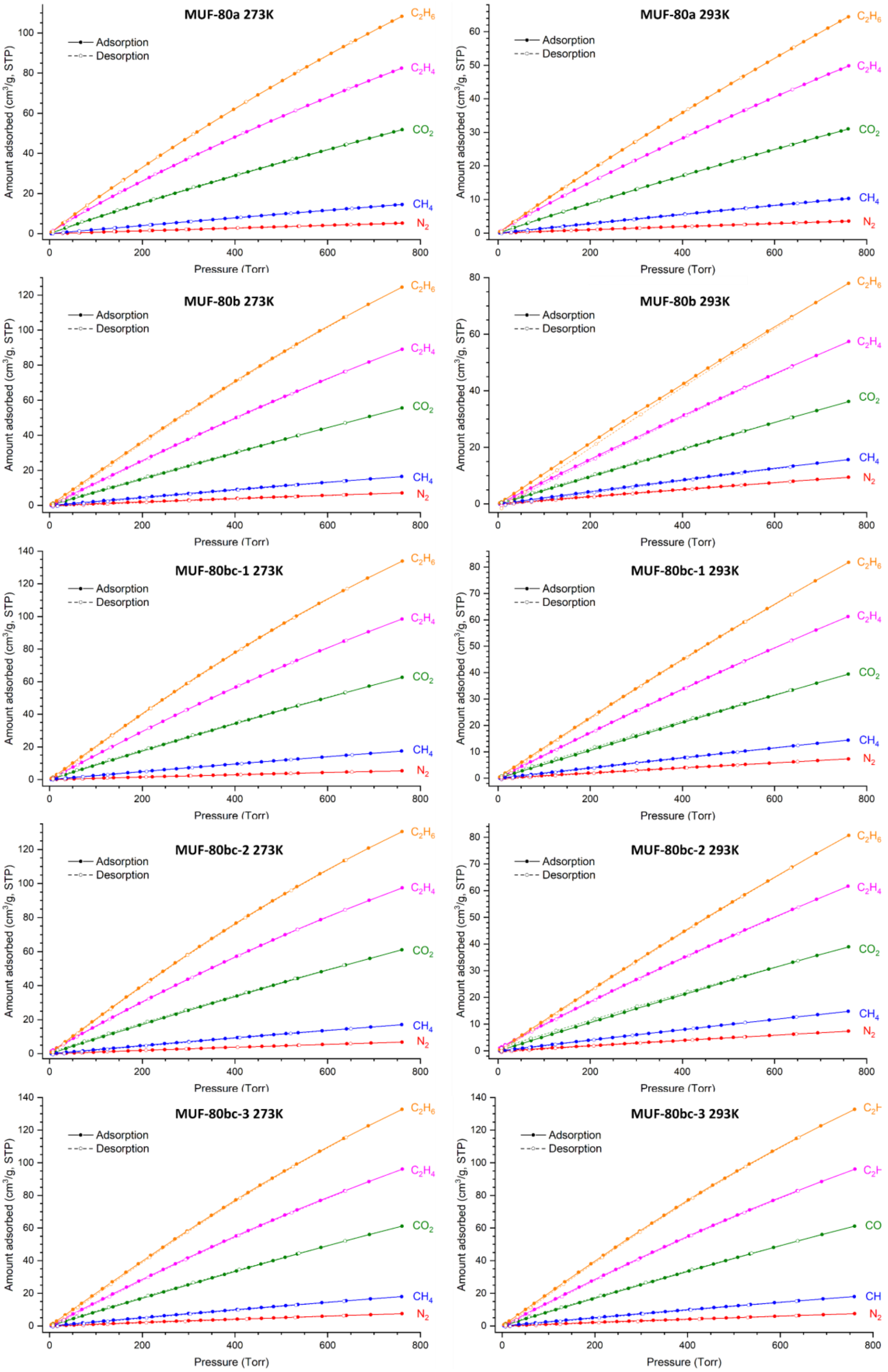

Figure C-12. Gas physorption of selected gases at 273 K and 293 K for the selected frameworks.

C.4.3. Heats of adsorption for slelcted gases

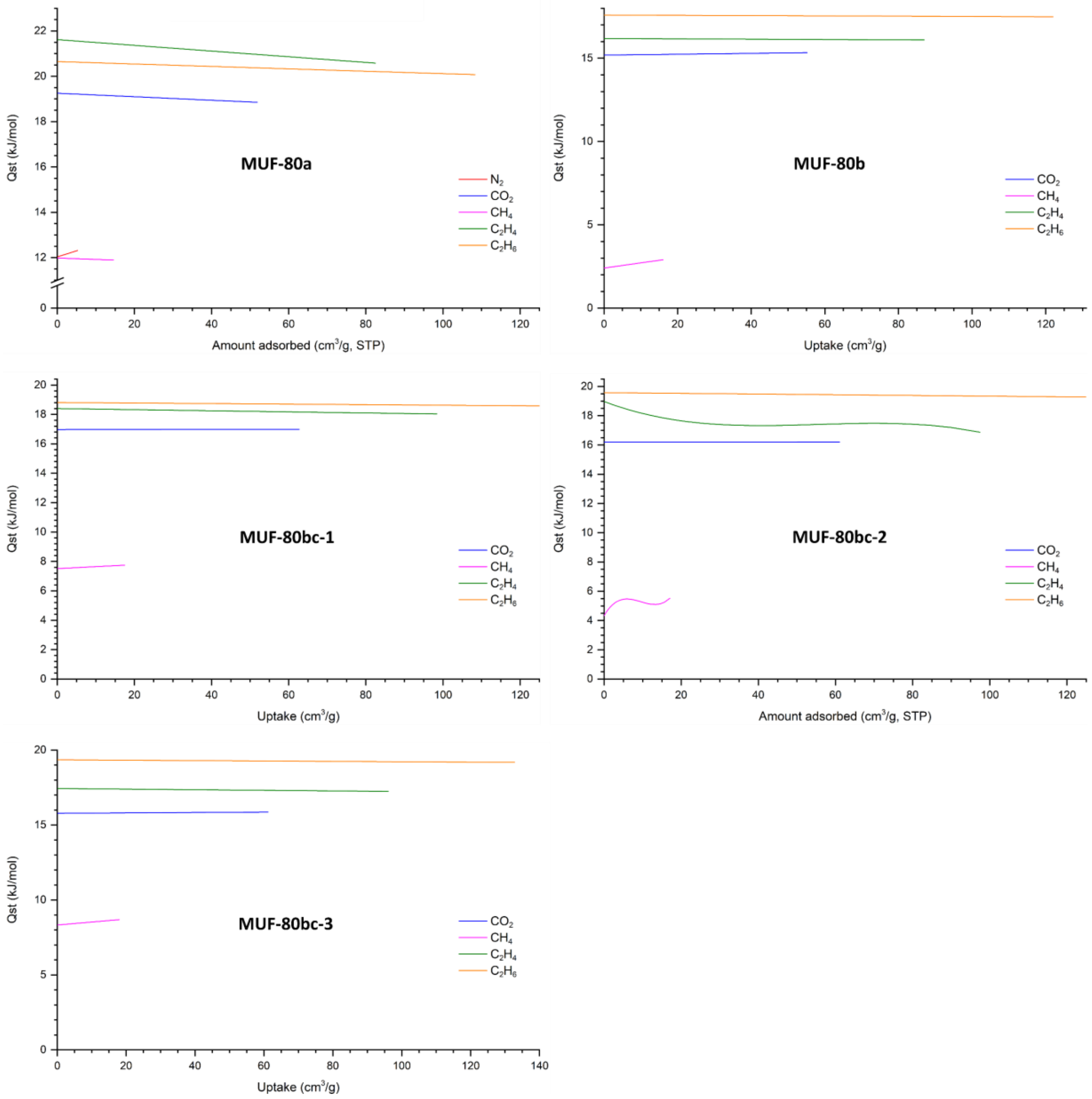

Figure C-13. Isosteric heat of adsorptions of selected gases for the selected frameworks as a function of uptake.

C.4.4. **Virial fits**

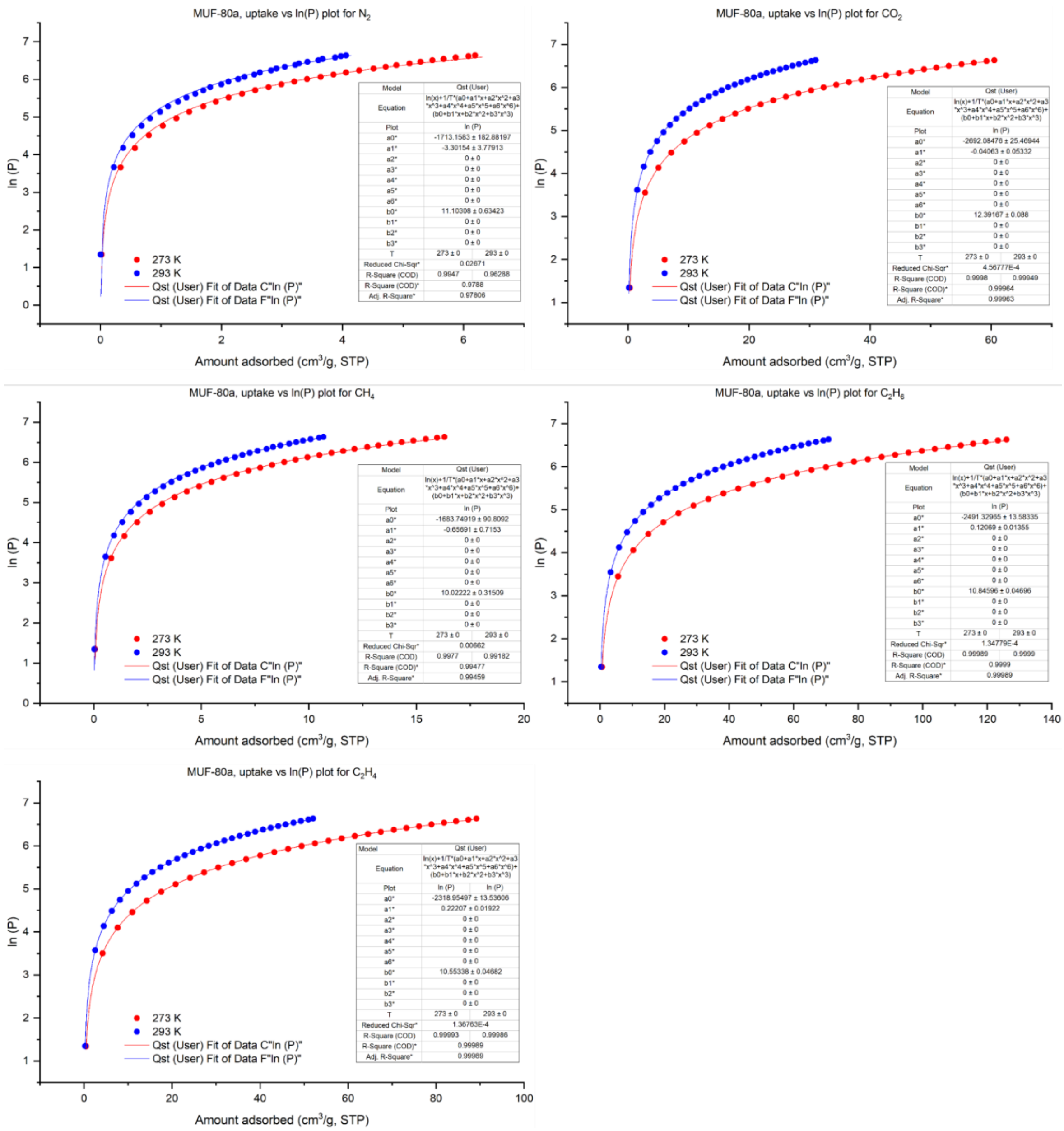

Model	Qst (User)	
Equation	ln(x)+1/T*(a0+a1*x+a2*x^2+a3*x^3+a4*x^4+a5*x^5+a6*x^6)+(b0+b1*x+b2*x^2+b3*x^3)	
Plot	ln (P)	
a0*	-1713.1583 ± 182.88197	
a1*	-3.30154 ± 3.77913	
a2*	0 ± 0	
a3*	0 ± 0	
a4*	0 ± 0	
a5*	0 ± 0	
a6*	0 ± 0	
b0*	11.10308 ± 0.63423	
b1*	0 ± 0	
b2*	0 ± 0	
b3*	0 ± 0	
T	273 ± 0	293 ± 0
Reduced Chi-Sqr*	0.02671	
R-Square (COD)	0.9947	0.96288
R-Square (COD)*	0.9788	
Adj. R-Square*	0.97806	

Model	Qst (User)	
Equation	ln(x)+1/T*(a0+a1*x+a2*x^2+a3*x^3+a4*x^4+a5*x^5+a6*x^6)+(b0+b1*x+b2*x^2+b3*x^3)	
Plot	ln (P)	
a0*	-2692.08476 ± 25.46944	
a1*	-0.04063 ± 0.05332	
a2*	0 ± 0	
a3*	0 ± 0	
a4*	0 ± 0	
a5*	0 ± 0	
a6*	0 ± 0	
b0*	12.39167 ± 0.088	
b1*	0 ± 0	
b2*	0 ± 0	
b3*	0 ± 0	
T	273 ± 0	293 ± 0
Reduced Chi-Sqr*	4.56777E-4	
R-Square (COD)	0.9998	0.99949
R-Square (COD)*	0.99964	
Adj. R-Square*	0.99963	

Model	Qst (User)	
Equation	ln(x)+1/T*(a0+a1*x+a2*x^2+a3*x^3+a4*x^4+a5*x^5+a6*x^6)+(b0+b1*x+b2*x^2+b3*x^3)	
Plot	ln (P)	
a0*	-1683.74919 ± 90.8092	
a1*	-0.65691 ± 0.7153	
a2*	0 ± 0	
a3*	0 ± 0	
a4*	0 ± 0	
a5*	0 ± 0	
a6*	0 ± 0	
b0*	10.02222 ± 0.31509	
b1*	0 ± 0	
b2*	0 ± 0	
b3*	0 ± 0	
T	273 ± 0	293 ± 0
Reduced Chi-Sqr*	0.00662	
R-Square (COD)	0.9977	0.99182
R-Square (COD)*	0.99477	
Adj. R-Square*	0.99459	

Model	Qst (User)	
Equation	ln(x)+1/T*(a0+a1*x+a2*x^2+a3*x^3+a4*x^4+a5*x^5+a6*x^6)+(b0+b1*x+b2*x^2+b3*x^3)	
Plot	ln (P)	
a0*	-2491.32965 ± 13.58335	
a1*	0.12069 ± 0.01355	
a2*	0 ± 0	
a3*	0 ± 0	
a4*	0 ± 0	
a5*	0 ± 0	
a6*	0 ± 0	
b0*	10.84596 ± 0.04696	
b1*	0 ± 0	
b2*	0 ± 0	
b3*	0 ± 0	
T	273 ± 0	293 ± 0
Reduced Chi-Sqr*	1.34779E-4	
R-Square (COD)	0.99989	0.9999
R-Square (COD)*	0.9999	
Adj. R-Square*	0.99989	

Model	Qst (User)	
Equation	ln(x)+1/T*(a0+a1*x+a2*x^2+a3*x^3+a4*x^4+a5*x^5+a6*x^6)+(b0+b1*x+b2*x^2+b3*x^3)	
Plot	ln (P)	ln (P)
a0*	-2318.95497 ± 13.53606	
a1*	0.22207 ± 0.01922	
a2*	0 ± 0	
a3*	0 ± 0	
a4*	0 ± 0	
a5*	0 ± 0	
a6*	0 ± 0	
b0*	10.55338 ± 0.04682	
b1*	0 ± 0	
b2*	0 ± 0	
b3*	0 ± 0	
T	273 ± 0	293 ± 0
Reduced Chi-Sqr*	1.36763E-4	
R-Square (COD)	0.99993	0.99986
R-Square (COD)*	0.99989	
Adj. R-Square*	0.99989	

Figure C-14. Virial fits of selected gases for MUF-80a.

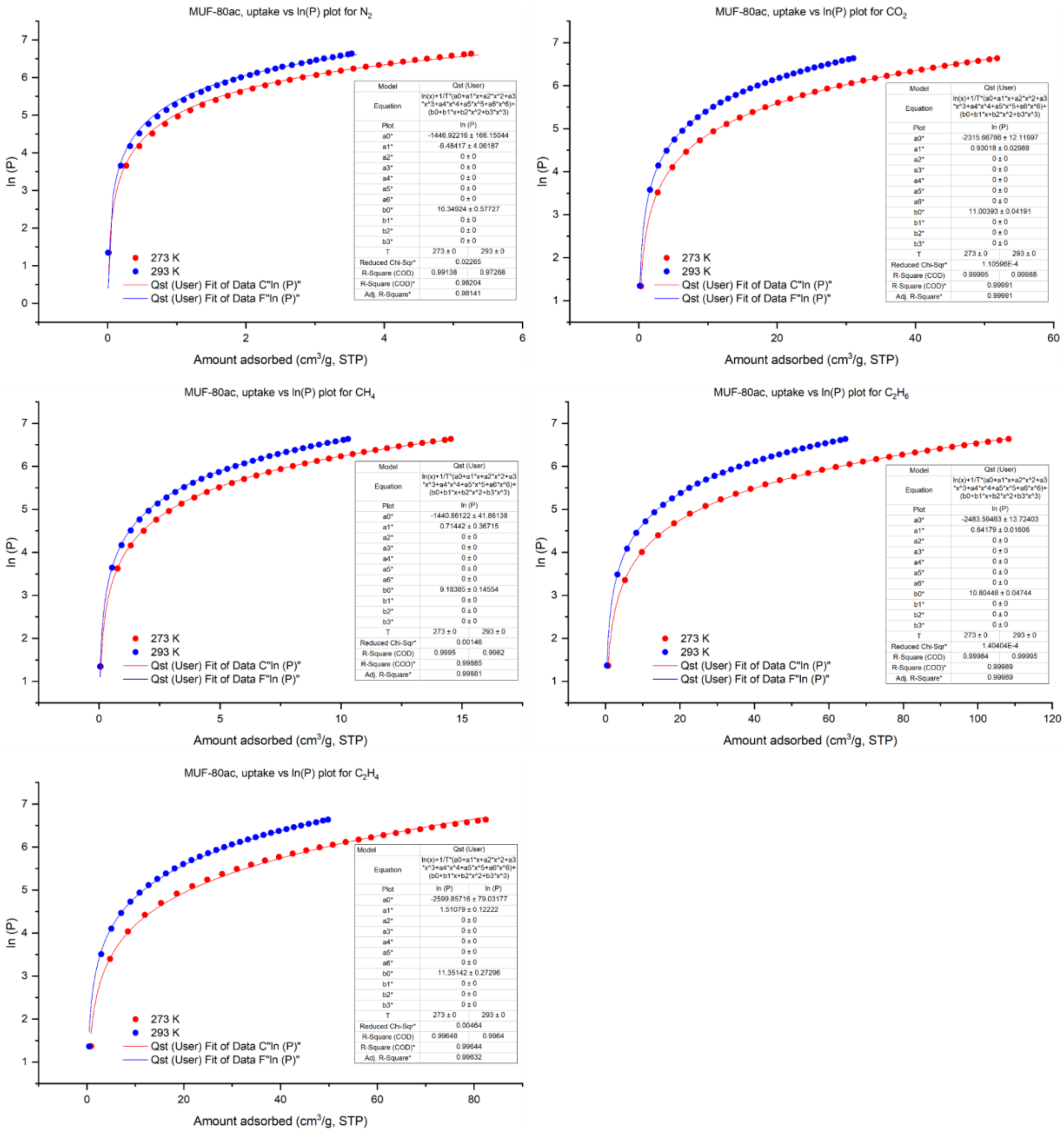

Model	Qst (User)	
Equation	ln(x)+1/T*(a0+a1*x+a2*x^2+a3*x^3+a4*x^4+a5*x^5+a6*x^6)+(b0+b1*x+b2*x^2+b3*x^3)	
Plot	ln (P)	
a0*	-1446.92216 ± 166.15044	
a1*	-6.48417 ± 4.06187	
a2*	0 ± 0	
a3*	0 ± 0	
a4*	0 ± 0	
a5*	0 ± 0	
a6*	0 ± 0	
b0*	10.34924 ± 0.57727	
b1*	0 ± 0	
b2*	0 ± 0	
b3*	0 ± 0	
T	273 ± 0	293 ± 0
Reduced Chi-Sqr*	0.02265	
R-Square (COD)	0.99138	0.97268
R-Square (COD)*	0.98204	
Adj. R-Square*	0.98141	

Model	Qst (User)	
Equation	ln(x)+1/T*(a0+a1*x+a2*x^2+a3*x^3+a4*x^4+a5*x^5+a6*x^6)+(b0+b1*x+b2*x^2+b3*x^3)	
Plot	ln (P)	
a0*	-2315.66786 ± 12.11997	
a1*	0.93018 ± 0.02988	
a2*	0 ± 0	
a3*	0 ± 0	
a4*	0 ± 0	
a5*	0 ± 0	
a6*	0 ± 0	
b0*	11.00393 ± 0.04191	
b1*	0 ± 0	
b2*	0 ± 0	
b3*	0 ± 0	
T	273 ± 0	293 ± 0
Reduced Chi-Sqr*	1.10596E-4	
R-Square (COD)	0.99995	0.99988
R-Square (COD)*	0.99991	
Adj. R-Square*	0.99991	

Model	Qst (User)	
Equation	ln(x)+1/T*(a0+a1*x+a2*x^2+a3*x^3+a4*x^4+a5*x^5+a6*x^6)+(b0+b1*x+b2*x^2+b3*x^3)	
Plot	ln (P)	
a0*	-1440.86122 ± 41.86138	
a1*	0.71442 ± 0.36715	
a2*	0 ± 0	
a3*	0 ± 0	
a4*	0 ± 0	
a5*	0 ± 0	
a6*	0 ± 0	
b0*	9.18385 ± 0.14554	
b1*	0 ± 0	
b2*	0 ± 0	
b3*	0 ± 0	
T	273 ± 0	293 ± 0
Reduced Chi-Sqr*	0.00146	
R-Square (COD)	0.9995	0.9982
R-Square (COD)*	0.99885	
Adj. R-Square*	0.99881	

Model	Qst (User)	
Equation	ln(x)+1/T*(a0+a1*x+a2*x^2+a3*x^3+a4*x^4+a5*x^5+a6*x^6)+(b0+b1*x+b2*x^2+b3*x^3)	
Plot	ln (P)	
a0*	-2483.59463 ± 13.72403	
a1*	0.84179 ± 0.01606	
a2*	0 ± 0	
a3*	0 ± 0	
a4*	0 ± 0	
a5*	0 ± 0	
a6*	0 ± 0	
b0*	10.80448 ± 0.04744	
b1*	0 ± 0	
b2*	0 ± 0	
b3*	0 ± 0	
T	273 ± 0	293 ± 0
Reduced Chi-Sqr*	1.40404E-4	
R-Square (COD)	0.99984	0.99995
R-Square (COD)*	0.99989	
Adj. R-Square*	0.99989	

Model	Qst (User)	
Equation	ln(x)+1/T*(a0+a1*x+a2*x^2+a3*x^3+a4*x^4+a5*x^5+a6*x^6)+(b0+b1*x+b2*x^2+b3*x^3)	
Plot	ln (P)	ln (P)
a0*	-2599.85716 ± 79.03177	
a1*	1.51079 ± 0.12222	
a2*	0 ± 0	
a3*	0 ± 0	
a4*	0 ± 0	
a5*	0 ± 0	
a6*	0 ± 0	
b0*	11.35142 ± 0.27296	
b1*	0 ± 0	
b2*	0 ± 0	
b3*	0 ± 0	
T	273 ± 0	293 ± 0
Reduced Chi-Sqr*	0.00464	
R-Square (COD)	0.99648	0.9964
R-Square (COD)*	0.99644	
Adj. R-Square*	0.99632	

Figure C-15. Virial fits of selected gases for MUF-80ac.

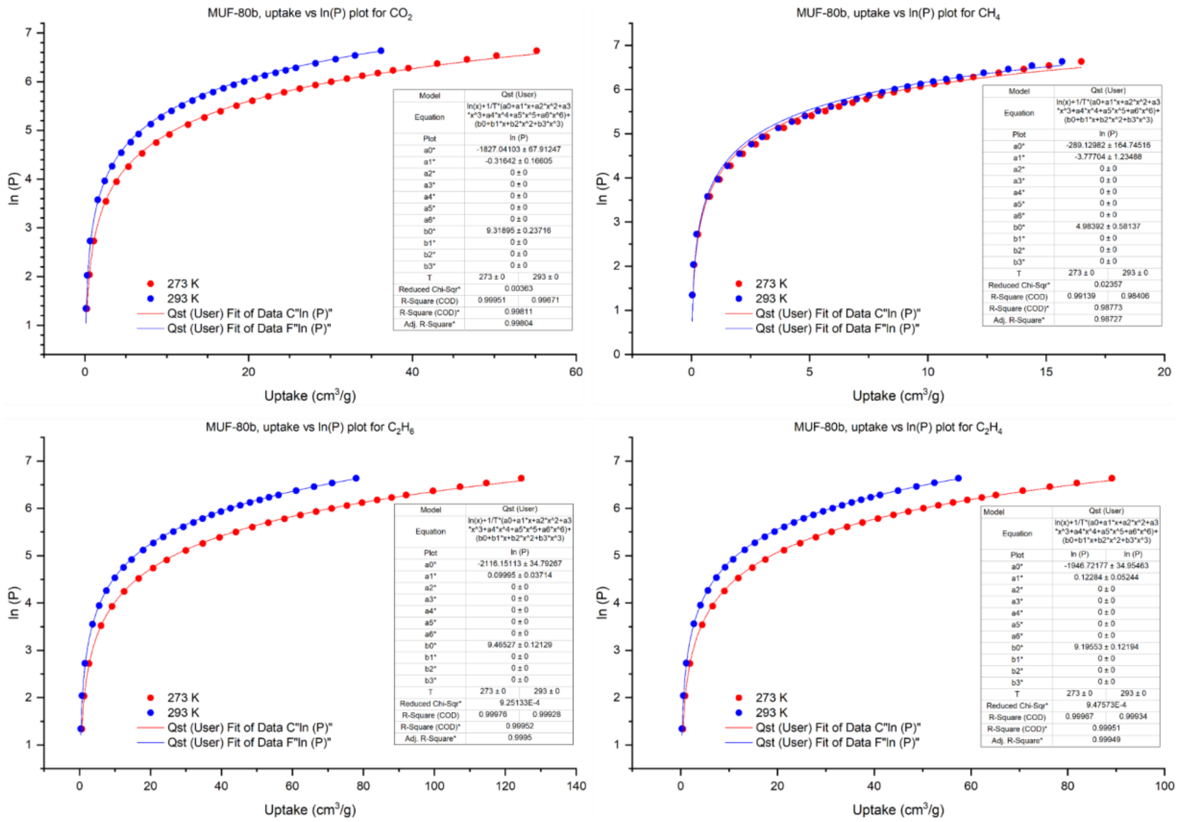

Model	Qst (User)	
Equation	ln(x)+1/T*(a0+a1*x+a2*x^2+a3*x^3+a4*x^4+a5*x^5+a6*x^6)+(b0+b1*x+b2*x^2+b3*x^3)	
Plot	ln (P)	
a0*	-1827.04103 ± 67.91247	
a1*	-0.31642 ± 0.16605	
a2*	0 ± 0	
a3*	0 ± 0	
a4*	0 ± 0	
a5*	0 ± 0	
a6*	0 ± 0	
b0*	9.31895 ± 0.23716	
b1*	0 ± 0	
b2*	0 ± 0	
b3*	0 ± 0	
T	273 ± 0	293 ± 0
Reduced Chi-Sqr*	0.00363	
R-Square (COD)	0.99951	0.99671
R-Square (COD)*	0.99811	
Adj. R-Square*	0.99804	

Model	Qst (User)	
Equation	ln(x)+1/T*(a0+a1*x+a2*x^2+a3*x^3+a4*x^4+a5*x^5+a6*x^6)+(b0+b1*x+b2*x^2+b3*x^3)	
Plot	ln (P)	
a0*	-289.12982 ± 164.74516	
a1*	-3.77704 ± 1.23488	
a2*	0 ± 0	
a3*	0 ± 0	
a4*	0 ± 0	
a5*	0 ± 0	
a6*	0 ± 0	
b0*	4.98392 ± 0.58137	
b1*	0 ± 0	
b2*	0 ± 0	
b3*	0 ± 0	
T	273 ± 0	293 ± 0
Reduced Chi-Sqr*	0.02357	
R-Square (COD)	0.99139	0.98406
R-Square (COD)*	0.98773	
Adj. R-Square*	0.98727	

Model	Qst (User)	
Equation	ln(x)+1/T*(a0+a1*x+a2*x^2+a3*x^3+a4*x^4+a5*x^5+a6*x^6)+(b0+b1*x+b2*x^2+b3*x^3)	
Plot	ln (P)	
a0*	-2116.15113 ± 34.79267	
a1*	0.09995 ± 0.03714	
a2*	0 ± 0	
a3*	0 ± 0	
a4*	0 ± 0	
a5*	0 ± 0	
a6*	0 ± 0	
b0*	9.46527 ± 0.12129	
b1*	0 ± 0	
b2*	0 ± 0	
b3*	0 ± 0	
T	273 ± 0	293 ± 0
Reduced Chi-Sqr*	9.25133E-4	
R-Square (COD)	0.99976	0.99928
R-Square (COD)*	0.99952	
Adj. R-Square*	0.9995	

Model	Qst (User)	
Equation	ln(x)+1/T*(a0+a1*x+a2*x^2+a3*x^3+a4*x^4+a5*x^5+a6*x^6)+(b0+b1*x+b2*x^2+b3*x^3)	
Plot	ln (P)	ln (P)
a0*	-1946.72177 ± 34.95463	
a1*	0.12284 ± 0.05244	
a2*	0 ± 0	
a3*	0 ± 0	
a4*	0 ± 0	
a5*	0 ± 0	
a6*	0 ± 0	
b0*	9.19553 ± 0.12194	
b1*	0 ± 0	
b2*	0 ± 0	
b3*	0 ± 0	
T	273 ± 0	293 ± 0
Reduced Chi-Sqr*	9.47573E-4	
R-Square (COD)	0.99967	0.99934
R-Square (COD)*	0.99951	
Adj. R-Square*	0.99949	

Figure C-16. Virial fits of selected gases for MUF-80b.

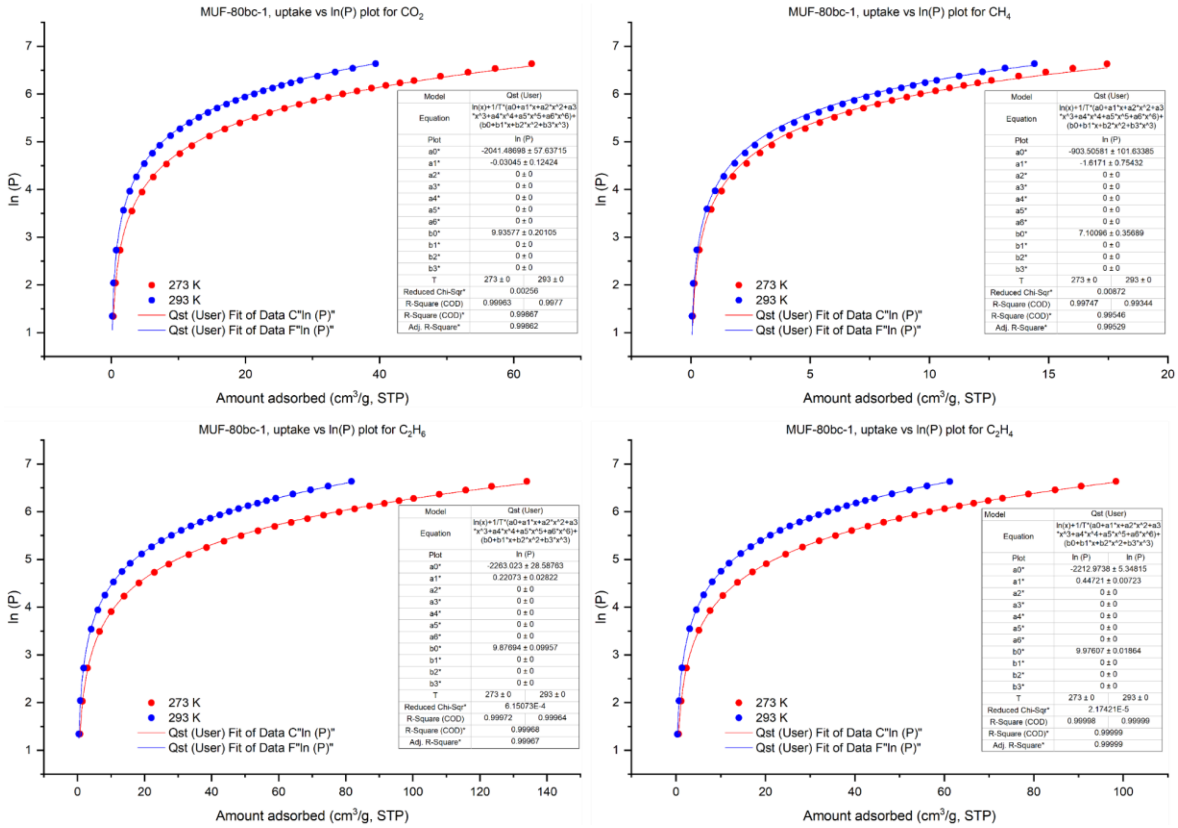

Model	Qst (User)	
Equation	ln(x)+1/T*(a0+a1*x+a2*x^2+a3*x^3+a4*x^4+a5*x^5+a6*x^6)+(b0+b1*x+b2*x^2+b3*x^3)	
Plot	ln (P)	
a0*	-2041.48698 ± 57.63715	
a1*	-0.03045 ± 0.12424	
a2*	0 ± 0	
a3*	0 ± 0	
a4*	0 ± 0	
a5*	0 ± 0	
a6*	0 ± 0	
b0*	9.93577 ± 0.20105	
b1*	0 ± 0	
b2*	0 ± 0	
b3*	0 ± 0	
T	273 ± 0	293 ± 0
Reduced Chi-Sqr*	0.00256	
R-Square (COD)	0.99963	0.9977
R-Square (COD)*	0.99867	
Adj. R-Square*	0.99862	

Model	Qst (User)	
Equation	ln(x)+1/T*(a0+a1*x+a2*x^2+a3*x^3+a4*x^4+a5*x^5+a6*x^6)+(b0+b1*x+b2*x^2+b3*x^3)	
Plot	ln (P)	
a0*	-903.50581 ± 101.63385	
a1*	-1.6171 ± 0.75432	
a2*	0 ± 0	
a3*	0 ± 0	
a4*	0 ± 0	
a5*	0 ± 0	
a6*	0 ± 0	
b0*	7.10096 ± 0.35689	
b1*	0 ± 0	
b2*	0 ± 0	
b3*	0 ± 0	
T	273 ± 0	293 ± 0
Reduced Chi-Sqr*	0.00872	
R-Square (COD)	0.99747	0.99344
R-Square (COD)*	0.99546	
Adj. R-Square*	0.99529	

Model	Qst (User)	
Equation	ln(x)+1/T*(a0+a1*x+a2*x^2+a3*x^3+a4*x^4+a5*x^5+a6*x^6)+(b0+b1*x+b2*x^2+b3*x^3)	
Plot	ln (P)	
a0*	-2263.023 ± 28.58763	
a1*	0.22073 ± 0.02822	
a2*	0 ± 0	
a3*	0 ± 0	
a4*	0 ± 0	
a5*	0 ± 0	
a6*	0 ± 0	
b0*	9.87694 ± 0.09957	
b1*	0 ± 0	
b2*	0 ± 0	
b3*	0 ± 0	
T	273 ± 0	293 ± 0
Reduced Chi-Sqr*	6.15073E-4	
R-Square (COD)	0.99972	0.99964
R-Square (COD)*	0.99968	
Adj. R-Square*	0.99967	

Model	Qst (User)	
Equation	ln(x)+1/T*(a0+a1*x+a2*x^2+a3*x^3+a4*x^4+a5*x^5+a6*x^6)+(b0+b1*x+b2*x^2+b3*x^3)	
Plot	ln (P)	ln (P)
a0*	-2212.9738 ± 5.34815	
a1*	0.44721 ± 0.00723	
a2*	0 ± 0	
a3*	0 ± 0	
a4*	0 ± 0	
a5*	0 ± 0	
a6*	0 ± 0	
b0*	9.97607 ± 0.01864	
b1*	0 ± 0	
b2*	0 ± 0	
b3*	0 ± 0	
T	273 ± 0	293 ± 0
Reduced Chi-Sqr*	2.17421E-5	
R-Square (COD)	0.99998	0.99999
R-Square (COD)*	0.99999	
Adj. R-Square*	0.99999	

Figure C-17. Virial fits of selected gases for MUF-80bc-1.

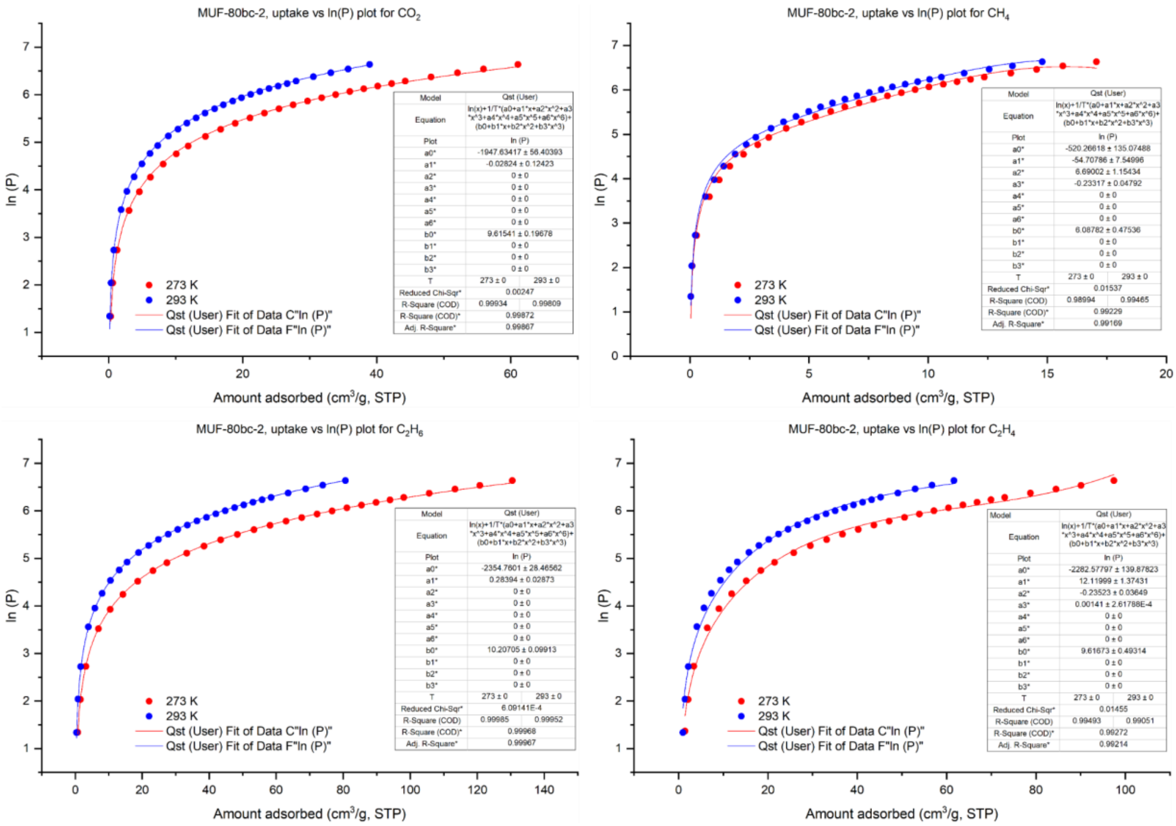

Model	Qst (User)	
Equation	ln(x)+1/T*(a0+a1*x+a2*x^2+a3*x^3+a4*x^4+a5*x^5+a6*x^6)+(b0+b1*x+b2*x^2+b3*x^3)	
Plot	ln (P)	
a0*	-1947.63417 ± 56.40393	
a1*	-0.02824 ± 0.12423	
a2*	0 ± 0	
a3*	0 ± 0	
a4*	0 ± 0	
a5*	0 ± 0	
a6*	0 ± 0	
b0*	9.61541 ± 0.19678	
b1*	0 ± 0	
b2*	0 ± 0	
b3*	0 ± 0	
T	273 ± 0	293 ± 0
Reduced Chi-Sqr*	0.00247	
R-Square (COD)	0.99934	0.99809
R-Square (COD)*	0.99872	
Adj. R-Square*	0.99867	

Model	Qst (User)	
Equation	ln(x)+1/T*(a0+a1*x+a2*x^2+a3*x^3+a4*x^4+a5*x^5+a6*x^6)+(b0+b1*x+b2*x^2+b3*x^3)	
Plot	ln (P)	
a0*	-520.26618 ± 135.07488	
a1*	-54.70786 ± 7.54996	
a2*	6.69002 ± 1.15434	
a3*	-0.23317 ± 0.04792	
a4*	0 ± 0	
a5*	0 ± 0	
a6*	0 ± 0	
b0*	6.08782 ± 0.47536	
b1*	0 ± 0	
b2*	0 ± 0	
b3*	0 ± 0	
T	273 ± 0	293 ± 0
Reduced Chi-Sqr*	0.01537	
R-Square (COD)	0.98994	0.99465
R-Square (COD)*	0.99229	
Adj. R-Square*	0.99169	

Model	Qst (User)	
Equation	ln(x)+1/T*(a0+a1*x+a2*x^2+a3*x^3+a4*x^4+a5*x^5+a6*x^6)+(b0+b1*x+b2*x^2+b3*x^3)	
Plot	ln (P)	
a0*	-2354.7601 ± 28.46562	
a1*	0.28394 ± 0.02873	
a2*	0 ± 0	
a3*	0 ± 0	
a4*	0 ± 0	
a5*	0 ± 0	
a6*	0 ± 0	
b0*	10.20705 ± 0.09913	
b1*	0 ± 0	
b2*	0 ± 0	
b3*	0 ± 0	
T	273 ± 0	293 ± 0
Reduced Chi-Sqr*	6.09141E-4	
R-Square (COD)	0.99985	0.99952
R-Square (COD)*	0.99968	
Adj. R-Square*	0.99967	

Model	Qst (User)	
Equation	ln(x)+1/T*(a0+a1*x+a2*x^2+a3*x^3+a4*x^4+a5*x^5+a6*x^6)+(b0+b1*x+b2*x^2+b3*x^3)	
Plot	ln (P)	
a0*	-2282.57797 ± 139.87823	
a1*	12.11999 ± 1.37431	
a2*	-0.23523 ± 0.03649	
a3*	0.00141 ± 2.61788E-4	
a4*	0 ± 0	
a5*	0 ± 0	
a6*	0 ± 0	
b0*	9.61673 ± 0.49314	
b1*	0 ± 0	
b2*	0 ± 0	
b3*	0 ± 0	
T	273 ± 0	293 ± 0
Reduced Chi-Sqr*	0.01455	
R-Square (COD)	0.99493	0.99051
R-Square (COD)*	0.99272	
Adj. R-Square*	0.99214	

Figure C-18. Virial fits of selected gases for MUF-80bc-2.

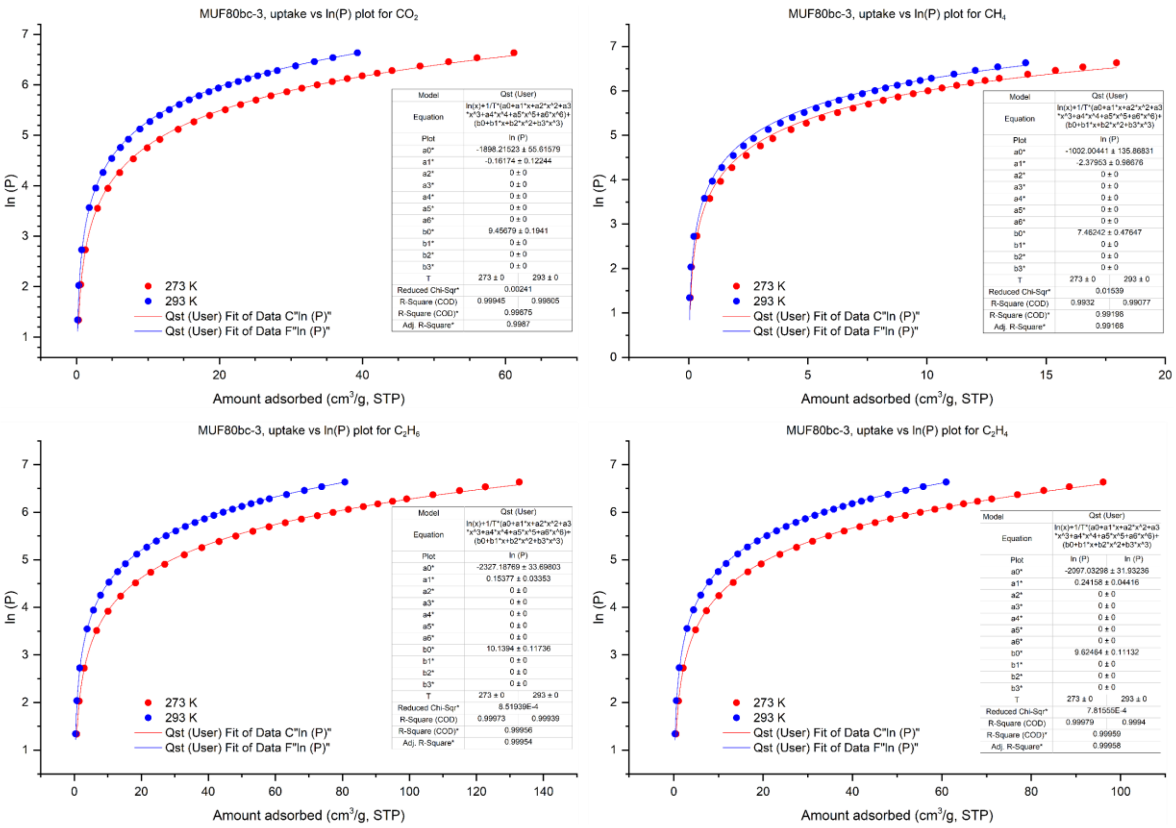

Model	Qst (User)	
Equation	ln(x)+1/T*(a0+a1*x+a2*x^2+a3*x^3+a4*x^4+a5*x^5+a6*x^6)+(b0+b1*x+b2*x^2+b3*x^3)	
Plot	ln (P)	
a0*	-1898.21523 ± 55.61579	
a1*	-0.16174 ± 0.12244	
a2*	0 ± 0	
a3*	0 ± 0	
a4*	0 ± 0	
a5*	0 ± 0	
a6*	0 ± 0	
b0*	9.45679 ± 0.1941	
b1*	0 ± 0	
b2*	0 ± 0	
b3*	0 ± 0	
T	273 ± 0	293 ± 0
Reduced Chi-Sqr*	0.00241	
R-Square (COD)	0.99945	0.99805
R-Square (COD)*	0.99875	
Adj. R-Square*	0.9987	

Model	Qst (User)	
Equation	ln(x)+1/T*(a0+a1*x+a2*x^2+a3*x^3+a4*x^4+a5*x^5+a6*x^6)+(b0+b1*x+b2*x^2+b3*x^3)	
Plot	ln (P)	
a0*	-1002.00441 ± 135.86831	
a1*	-2.37953 ± 0.98676	
a2*	0 ± 0	
a3*	0 ± 0	
a4*	0 ± 0	
a5*	0 ± 0	
a6*	0 ± 0	
b0*	7.48242 ± 0.47647	
b1*	0 ± 0	
b2*	0 ± 0	
b3*	0 ± 0	
T	273 ± 0	293 ± 0
Reduced Chi-Sqr*	0.01539	
R-Square (COD)	0.9932	0.99077
R-Square (COD)*	0.99198	
Adj. R-Square*	0.99168	

Model	Qst (User)	
Equation	ln(x)+1/T*(a0+a1*x+a2*x^2+a3*x^3+a4*x^4+a5*x^5+a6*x^6)+(b0+b1*x+b2*x^2+b3*x^3)	
Plot	ln (P)	
a0*	-2327.18769 ± 33.69803	
a1*	0.15377 ± 0.03353	
a2*	0 ± 0	
a3*	0 ± 0	
a4*	0 ± 0	
a5*	0 ± 0	
a6*	0 ± 0	
b0*	10.1394 ± 0.11736	
b1*	0 ± 0	
b2*	0 ± 0	
b3*	0 ± 0	
T	273 ± 0	293 ± 0
Reduced Chi-Sqr*	8.51939E-4	
R-Square (COD)	0.99973	0.99939
R-Square (COD)*	0.99956	
Adj. R-Square*	0.99954	

Model	Qst (User)	
Equation	ln(x)+1/T*(a0+a1*x+a2*x^2+a3*x^3+a4*x^4+a5*x^5+a6*x^6)+(b0+b1*x+b2*x^2+b3*x^3)	
Plot	ln (P)	ln (P)
a0*	-2097.03298 ± 31.93236	
a1*	0.24158 ± 0.04416	
a2*	0 ± 0	
a3*	0 ± 0	
a4*	0 ± 0	
a5*	0 ± 0	
a6*	0 ± 0	
b0*	9.62464 ± 0.11132	
b1*	0 ± 0	
b2*	0 ± 0	
b3*	0 ± 0	
T	273 ± 0	293 ± 0
Reduced Chi-Sqr*	7.81555E-4	
R-Square (COD)	0.99979	0.9994
R-Square (COD)*	0.99959	
Adj. R-Square*	0.99958	

Figure C-19. Virial fits of selected gases for MUF-80bc-3.

C.4.5. Pore size distribution

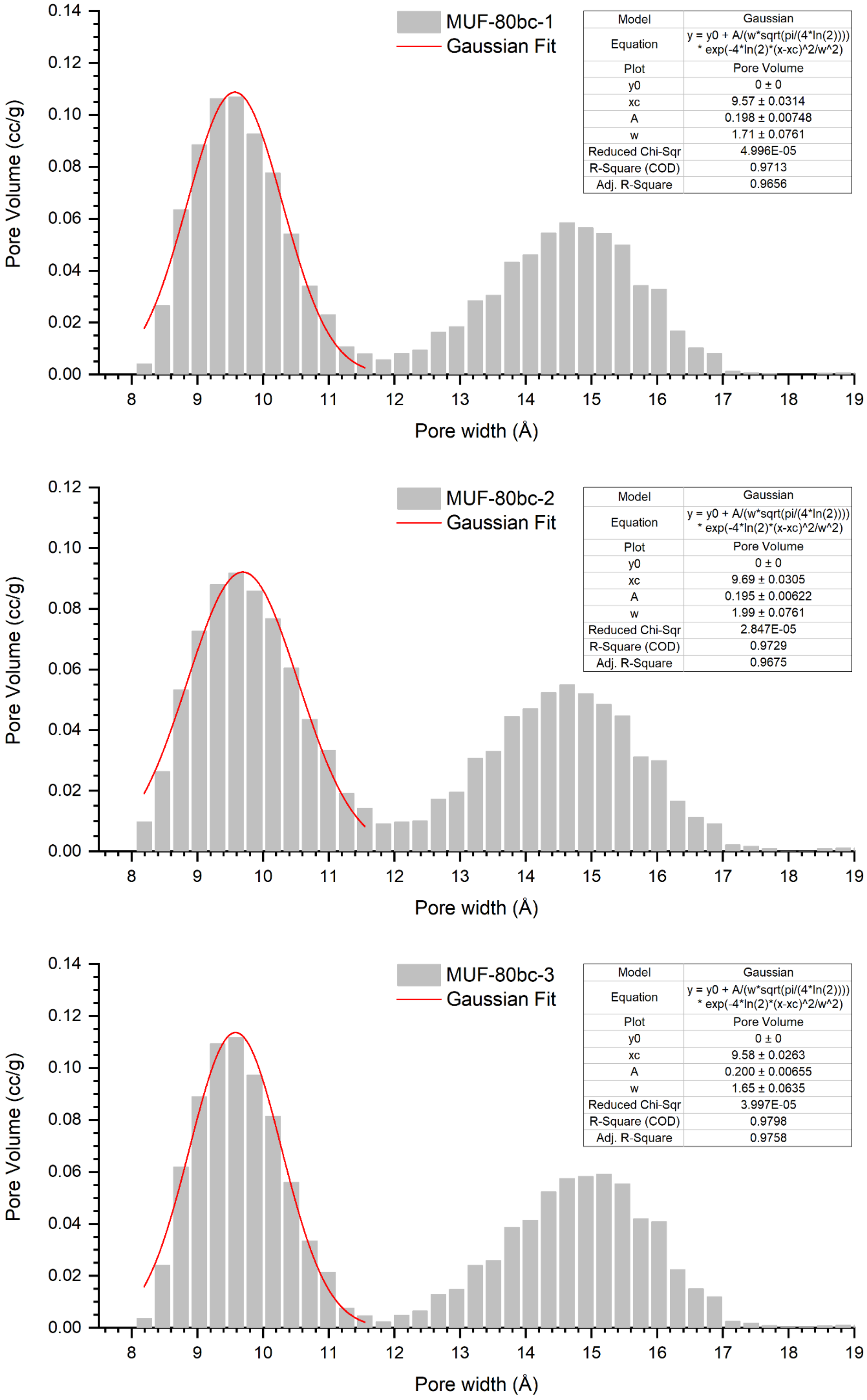

Model	Gaussian
Equation	y = y0 + A/(w*sqrt(pi/(4*ln(2)))) * exp(-4*ln(2)*(x-xc)^2/w^2)
Plot	Pore Volume
y0	0 ± 0
xc	9.57 ± 0.0314
A	0.198 ± 0.00748
w	1.71 ± 0.0761
Reduced Chi-Sqr	4.996E-05
R-Square (COD)	0.9713
Adj. R-Square	0.9656

Model	Gaussian
Equation	y = y0 + A/(w*sqrt(pi/(4*ln(2)))) * exp(-4*ln(2)*(x-xc)^2/w^2)
Plot	Pore Volume
y0	0 ± 0
xc	9.69 ± 0.0305
A	0.195 ± 0.00622
w	1.99 ± 0.0761
Reduced Chi-Sqr	2.847E-05
R-Square (COD)	0.9729
Adj. R-Square	0.9675

Model	Gaussian
Equation	y = y0 + A/(w*sqrt(pi/(4*ln(2)))) * exp(-4*ln(2)*(x-xc)^2/w^2)
Plot	Pore Volume
y0	0 ± 0
xc	9.58 ± 0.0263
A	0.200 ± 0.00655
w	1.65 ± 0.0635
Reduced Chi-Sqr	3.997E-05
R-Square (COD)	0.9798
Adj. R-Square	0.9758

Figure C-20. Pore volume distribution plots and the Gaussian fits for pore-C for the selected frameworks.

Appendix D. For Chapter 6

D.1. Organic ligands syntheses

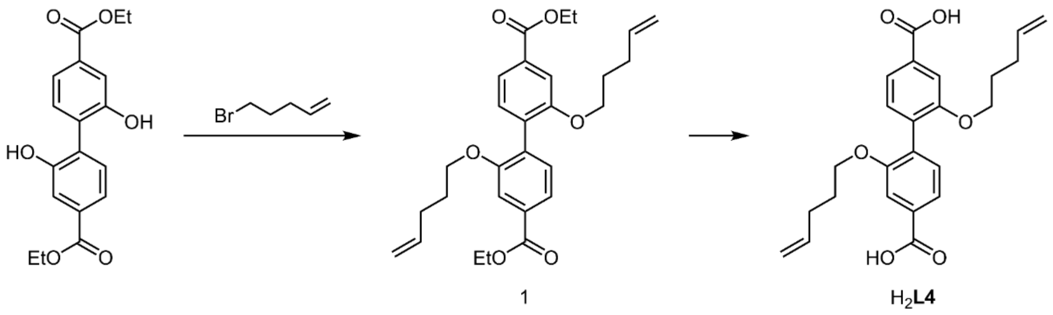

1 To a stirred mixture of diethyl 2,2'-dihydroxy-[1,1'-biphenyl]-4,4'-dicarboxylate (0.5 g, 1.51 mmol, 1 eq.), KI (38 mg, 0.15 eq.), and K_2CO_3 (0.63 g, 3 eq.) in DMF (15 mL), was added 5-bromo-pent-1-ene (0.72 mL, 4 eq.), and then the reaction mixture was stirred at 100 °C overnight under a N_2 atmosphere. After cooling down to RT, water (~ 100 mL) was added, and the organic was extracted with CH_2Cl_2 (20 mL × 3). The organic extract was then washed with brine and water several times and dried over $MgSO_4$. After removing the solvent under vacuum, the brown oily product (590 mg, 84 % yield) was obtained.

^{1}H NMR (500 MHz, $CDCl_3$) **δ 7.69 (dd, J = 7.8, 1.5 Hz, 1H), 7.62 (d, J = 1.5 Hz, 1H), 7.31 (d, J = 7.8 Hz, 1H), 5.74 (ddt, J = 16.9, 10.2, 6.7 Hz, 1H), 4.99 – 4.93 (m, 1H), 4.96 – 4.91 (m, 1H), 4.42 (q, J = 7.1 Hz, 2H), 4.01 (t, J = 6.4 Hz, 2H), 2.09 – 2.01 (m, 2H), 1.77 – 1.70 (m, 2H), 1.43 (t, J = 7.1 Hz, 3H).**

H$_2$**L4** **1** (590 mg, 1.26 mmol) was stirred in a mixture of THF and 2 M aqueous KOH (30 mL, 1:1 v/v) at 60 °C overnight. After cooling down to room temperature, the organic solvent was dried under vacuum, and the aqueous solution was acidified with 1 M HCl to pH 2. The precipitate was filtered, washed with water and dried under vacuum to yield the beige powdery product (0.51 g, 98 % yield).

^{1}H NMR (500 MHz, DMSO-d_6) δ 13.03 (s, 2H), 7.59 (dd, J = 7.8, 1.5 Hz, 2H), 7.55 (d, J = 1.6 Hz, 2H), 7.32 (d, J = 7.7 Hz, 2H), 5.75 (ddt, J = 16.9, 10.2, 6.6 Hz, 2H), 5.09 – 4.72 (m, 4H), 3.99 (t, J = 6.4 Hz, 4H), 2.00 (q, J = 7.2 Hz, 4H), 1.66 (p, J = 6.6 Hz, 4H). ^{13}C NMR (126 MHz, DMSO) δ 167.60, 156.37, 138.40, 131.96, 131.86, 131.49, 121.66, 115.52, 112.68, 67.72, 40.59, 40.49, 40.42, 40.33, 40.25, 40.16, 40.09, 39.99, 39.83, 39.66, 39.49, 29.93, 28.23. ESI (negative mode, CH_3OH): m/z = 409.1648 ($[C_{24}H_{25}O_6]^-$, calc. 409.1646).

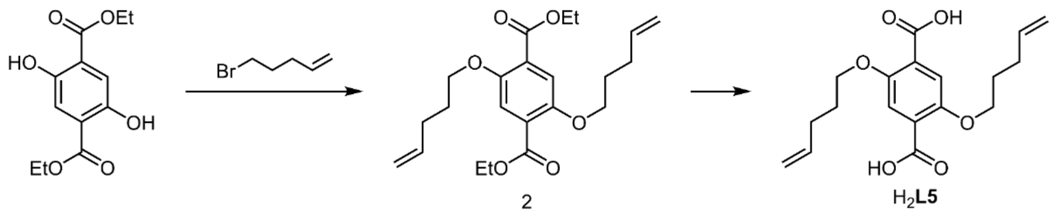

2 To a mixture of dimethyl 2,5-dihydroxyterephthalate (200 mg, 0.79 mmol, 1 eq.), KI (20 mg, 0.12 mmol, 0.15 eq.), and K_2CO_3 (330 mg, 2.39 mmol, 3.0 eq.) in DMF (7 mL) was added 5-bromo-1-pentene (0.37 mL, 3.12 mmol, 4.0 eq.), and then the mixture was stirred overnight at 100 °C under N_2 atmosphere. After cooling down to room temperature, the product was precipitated out by the addition of water (~ 50 mL). The solid was then filtered, washed with water and dried to yield the solid beige product (0.25 g, 0.64 mmol, 81 % yield).

^{1}H NMR (500 MHz, $CDCl_3$) δ 5.85 (ddt, J = 16.9, 10.1, 6.6 Hz, 1H), 5.06 (dq, J = 17.2, 1.7 Hz, 1H), 5.00 (ddt, J = 10.2, 2.2, 1.3 Hz, 1H), 4.38 (q, J = 7.1 Hz, 2H), 4.02 (t, J = 6.3 Hz, 2H), 2.31 – 2.22 (m, 2H), 1.95 – 1.86 (m, 2H), 1.39 (t, J = 7.1 Hz, 3H).

H_2L5 **2** (0.25 g, 0.64 mmol) was dissolved in a mixture of THF (10 mL) and aqueous KOH solution (1 M, 10 mL), and then the reaction mixture was stirred at 60 °C overnight. After cooling down to room temperature, the solution was acidified with 1 M HCl to pH 2. The beige precipitate was filtered, washed with water and dried under vacuum to yield the beige powder (0.21 g, 0.63 mmol, 98 % yield).

^{1}H NMR (500 MHz, $CDCl_3$) δ 11.40 – 10.55 (m, 1H), 7.87 (s, 1H), 5.82 (ddt, J = 17.0, 10.3, 6.7 Hz, 1H), 5.09 (t, J = 14.3 Hz, 2H), 4.32 (t, J = 6.5 Hz, 2H), 2.27 (dt, J = 7.1 Hz, 2H), 2.03 (tt, J = 6.9 Hz, 2H). ^{13}C NMR (126 MHz, $CDCl_3$) δ 163.90, 151.68, 136.28, 122.76, 117.56, 116.54, 77.28, 77.02, 76.77, 70.51, 29.80, 27.94. ESI (negative mode, CH_3OH): m/z = 333.1344 ($[C_{18}H_{21}O_6]^-$, calc. 333.1333).

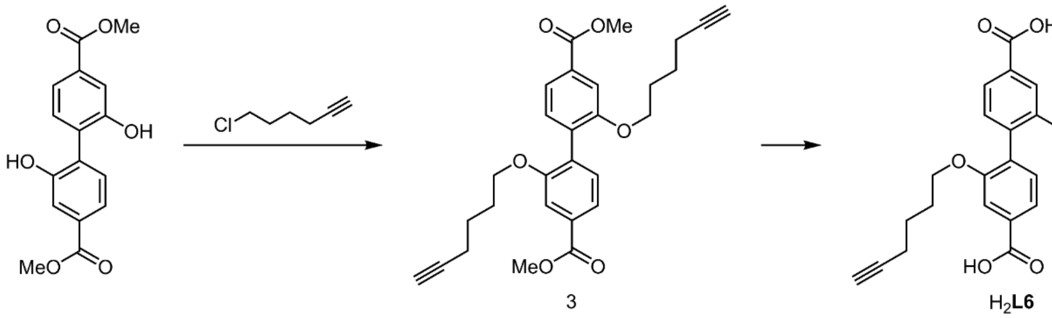

3 To the stirring mixture of dimethyl 2,2'-dihydroxy-[1,1'-biphenyl]-4,4'-dicarboxylate (0.56 g, 1.85 mmol), KI (46 mg, 0.15 eq.) and K_2CO_3 (770 mg, 3 eq.) in DMF 6 mL was added 6-chloro-1-octyne (0.9 mL, 4 eq.), and then the mixture was stirred at 120 °C for two days under N_2 atmosphere. After cooling down to room temperature, the reaction mixture was diluted with EtOAc and washed with brine and water, and then the volume was reduced under vacuum to yield the product as a brown oil (830 mg, 97 % yield).

^{1}H NMR (500 MHz, $CDCl_3$) δ 7.70 (dd, *J* = 7.8, 1.5 Hz, 2H), 7.62 (d, *J* = 1.5 Hz, 2H), 7.31 (d, *J* = 7.8 Hz, 2H), 4.03 (t, *J* = 6.2 Hz, 4H), 3.97 (s, 6H), 2.14 (td, *J* = 7.1, 2.7 Hz, 4H), 1.94 (t, *J* = 2.6 Hz, 2H), 1.78 (dq, *J* = 8.1, 6.3 Hz, 4H), 1.58 – 1.50 (m, 4H).

H_2L6 3 was stirred in a mixture of THF (10 mL) and aqueous NaOH solution (1 M, 10 mL) at 60 °C overnight. After cooling down to RT, THF was removed under vacuum, and the aqueous residue was acidified with 1 M HCl to pH 2. The beige precipitate was then filtered, washed with water and dried to yield a beige solid (0.77 g, 99 % yield).

^{1}H NMR (500 MHz, D_2O) δ 7.50 – 7.46 (m, 2H), 7.46 – 7.41 (m, 2H), 7.17 (d, *J* = 7.7 Hz, 2H), 3.95 (t, *J* = 6.2 Hz, 4H), 1.94 (t, *J* = 7.2 Hz, 4H), 1.58 (p, *J* = 6.6 Hz, 4H), 1.31 (p, *J* = 7.3 Hz, 4H).

D.2. MOF synthesis

MUF-80c ([$Zn_4O(hmtt)_{1.33}(L_4)_{0.5}(L_5)_{0.5}$])

H_3hmtt (11.0 mg, 20 µmol), H_2L4 (9.4 mg, 23 µmol), H_2L5 (13.4 mg, 40 µmol), Benzoic acid (40 mg, 330 µmol), $Zn(NO_3)_2{\cdot}4H_2O$ (83 mg, 300 µmol) was dissolved in a mixture of DEF (5 mL) and water (0.25 mL) in a 20 mL vial. The vial was briefly sonicated and then kept at an isothermal oven at 85 °C for 20 hours. The resulting colourless crystals were washed with DMF several times and kept in fresh DMF for further analysis.

MUF-80d ([$Zn_4O(hmtt)_{1.33}(L_6)_{0.5}(L_2)_{0.5}$])

H_3hmtt (11.0 mg, 20 µmol), H_2L6 (10.0 mg, 23 µmol), H_2L2 (14.3 mg, 40 µmol), Benzoic acid (40 mg, 330 µmol), $Zn(NO_3)_2{\cdot}4H_2O$ (83 mg, 300 µmol) was dissolved in a mixture of DEF (5 mL) and water (0.25 mL) in a 20 mL vial. The vial was briefly sonicated and then kept at an isothermal oven at 85 °C for 20 hours. The resulting colourless crystals were washed with DMF several times and kept in fresh DMF for further analysis.

MUF-80e ([$Zn_4O(hmtt)_{1.33}(L_1)_{0.5}(L_7)_{0.5}$])

H_3hmtt (11.0 mg, 20 µmol), H_2L1 (7.7 mg, 22 µmol), H_2L7 (11.0 mg, 40 µmol), Benzoic acid (40 mg, 330 µmol), $Zn(NO_3)_2{\cdot}4H_2O$ (83 mg, 300 µmol) was dissolved in a mixture of DEF (5 mL) and water (0.25 mL) in a 20 mL vial. The vial was briefly sonicated and then kept at an isothermal oven at 85 °C for 20 hours. The resulting colourless crystals were washed with DMF several times and kept in fresh DMF for further analysis.

D.3. ^{1}H NMR spectroscopy

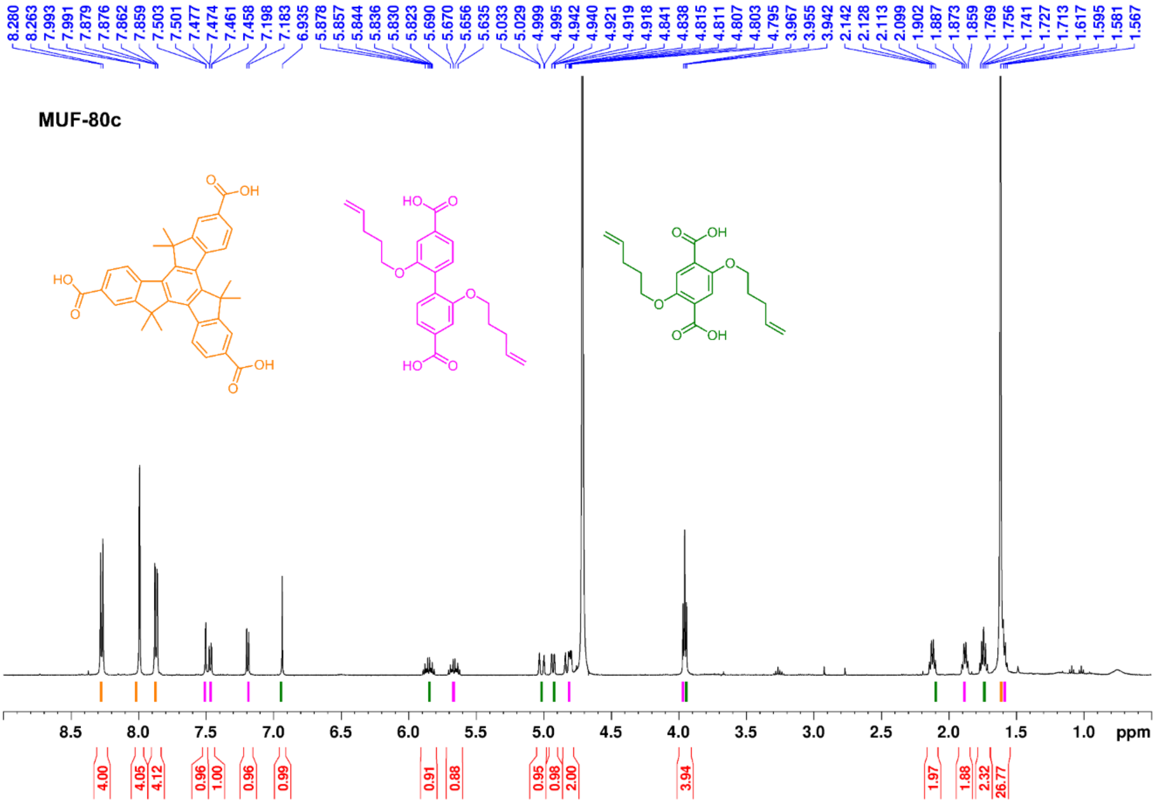

Figure D-1. ^{1}H NMR of digested MUF-80c in DMSO-d_6 and DCl mixture.

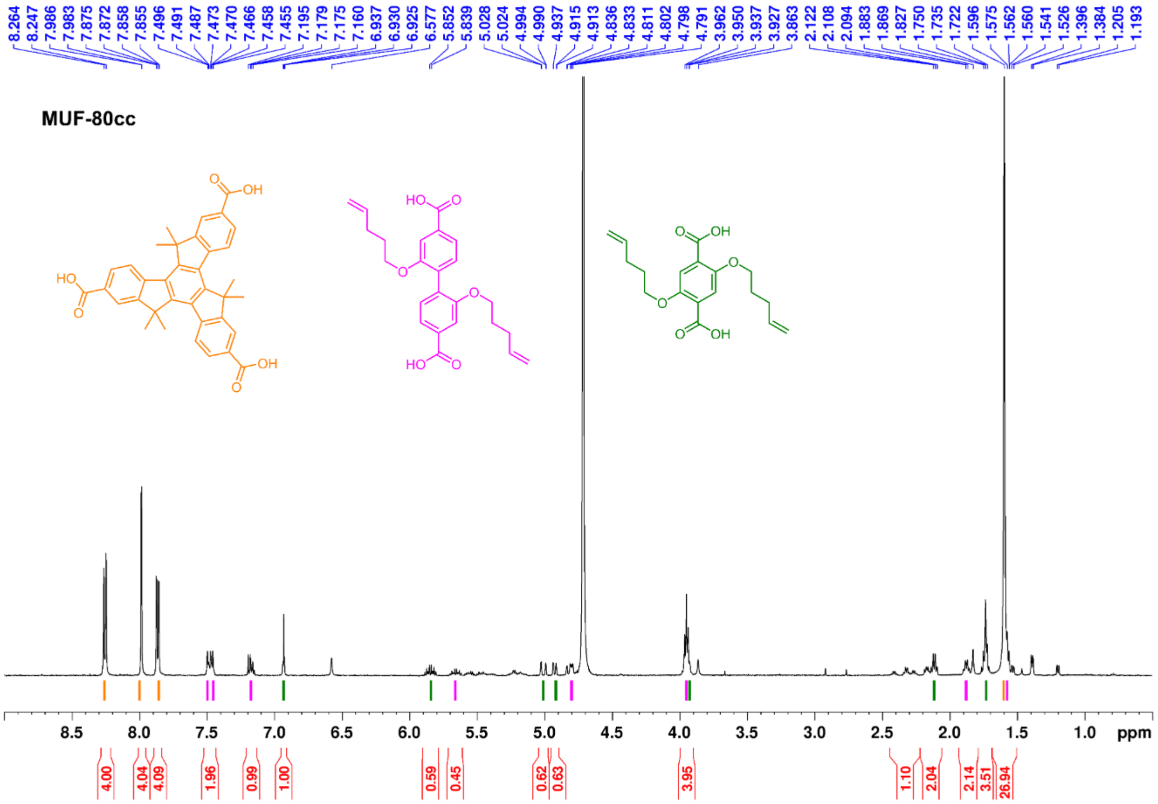

Figure D-2. ^{1}H NMR of digested MUF-80cc in NaOD and D_2O mixture.

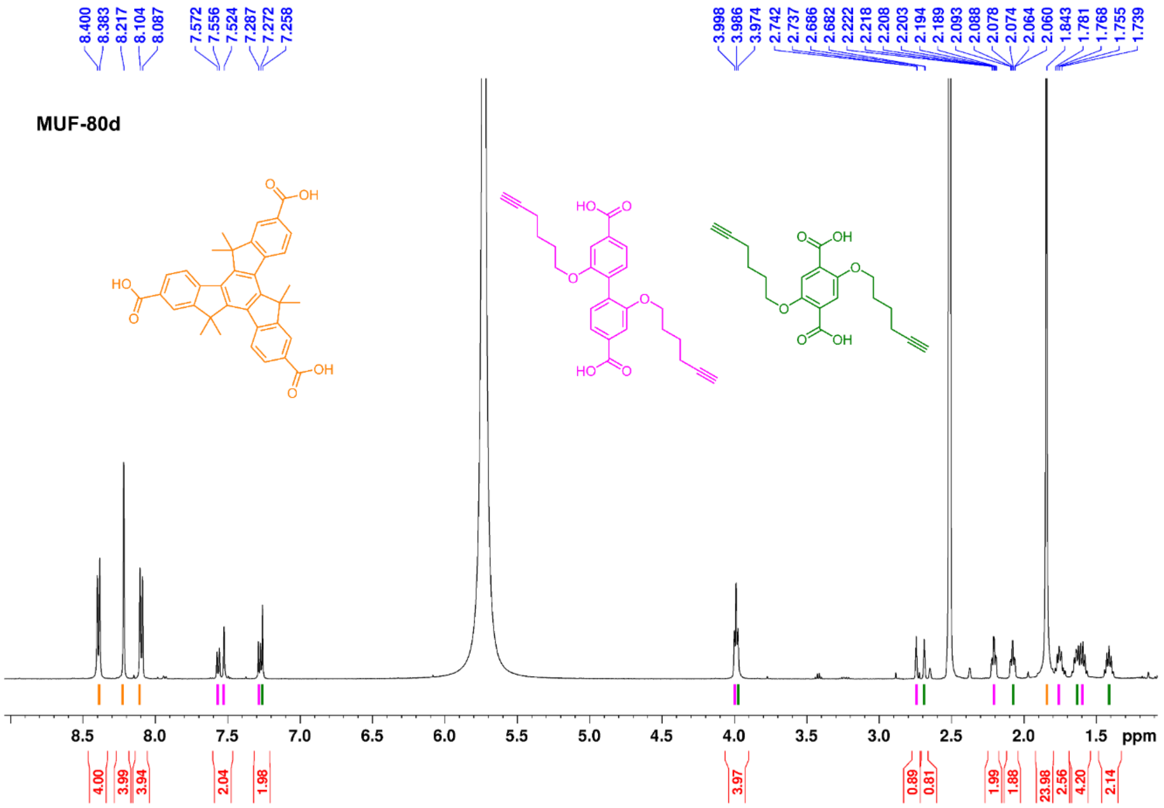

Figure D-3. ^{1}H NMR of digested MUF-80d in DMSO-d_6 and DCl mixture.

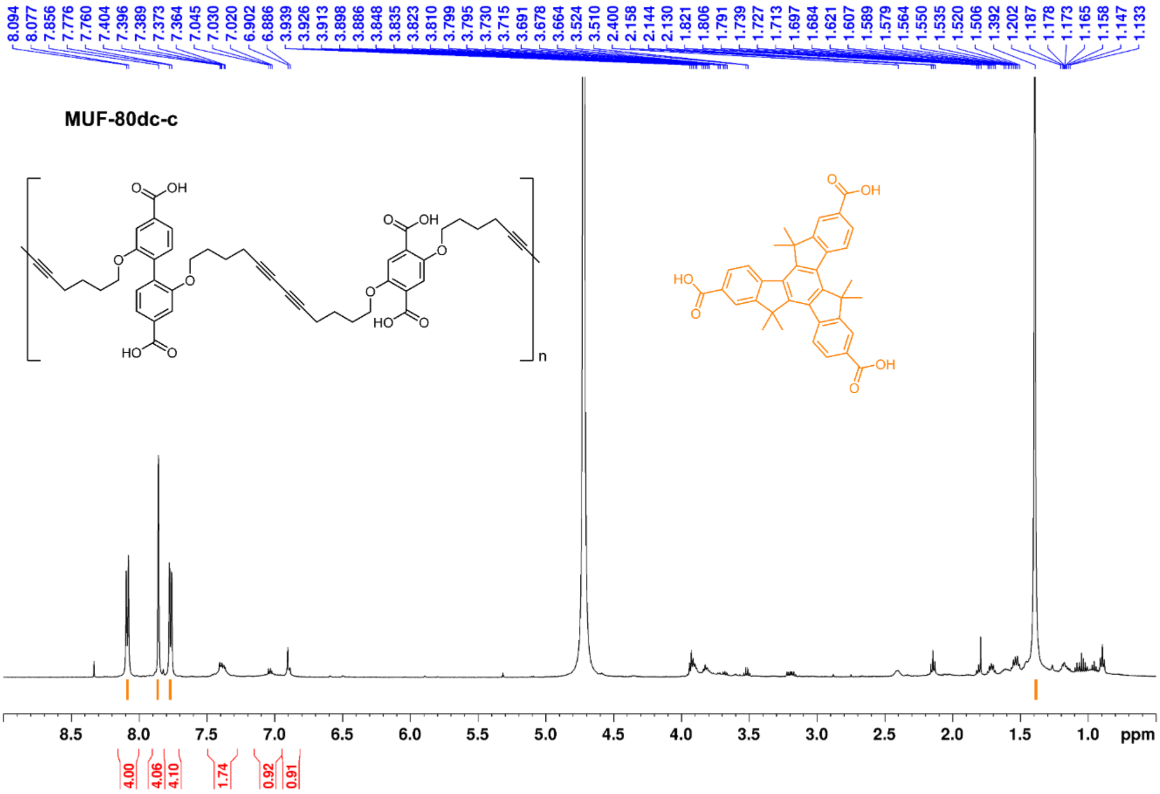

Figure D-4. ^{1}H NMR of digested MUF-80dc-c in DMSO-d_6 and DCl mixture.

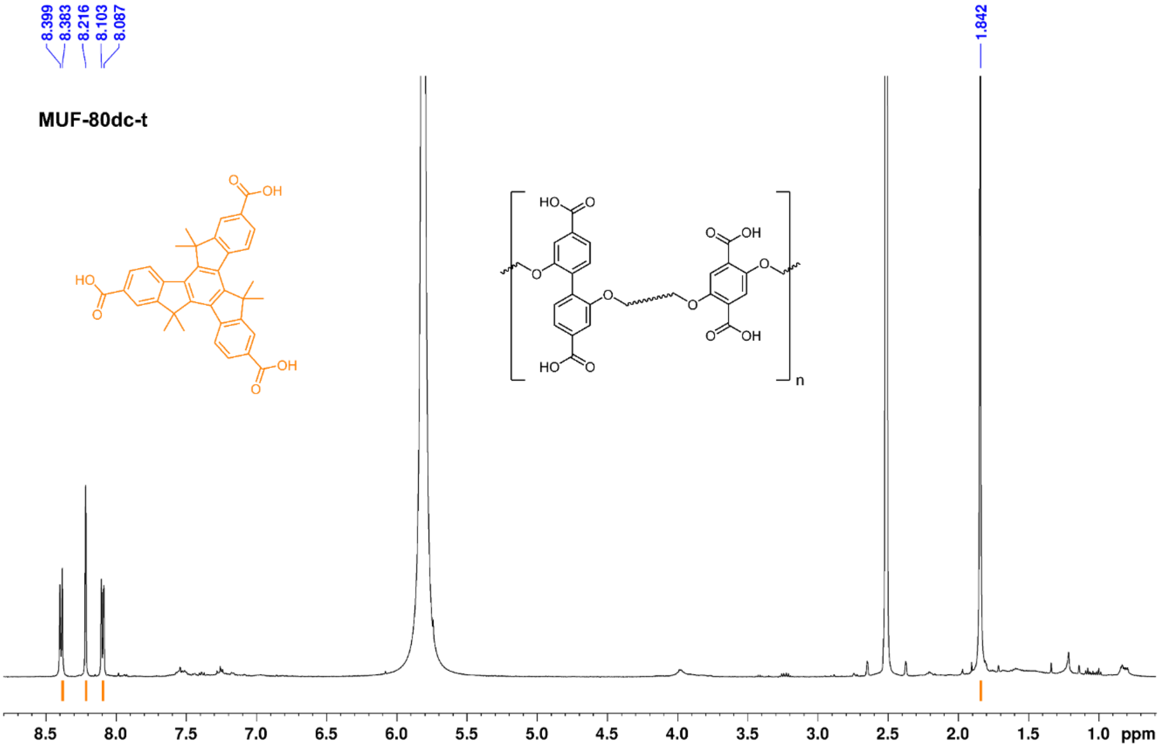

Figure D-5. ^{1}H NMR of digested MUF-80dc-t in DMSO-d_6 and DCl mixture.

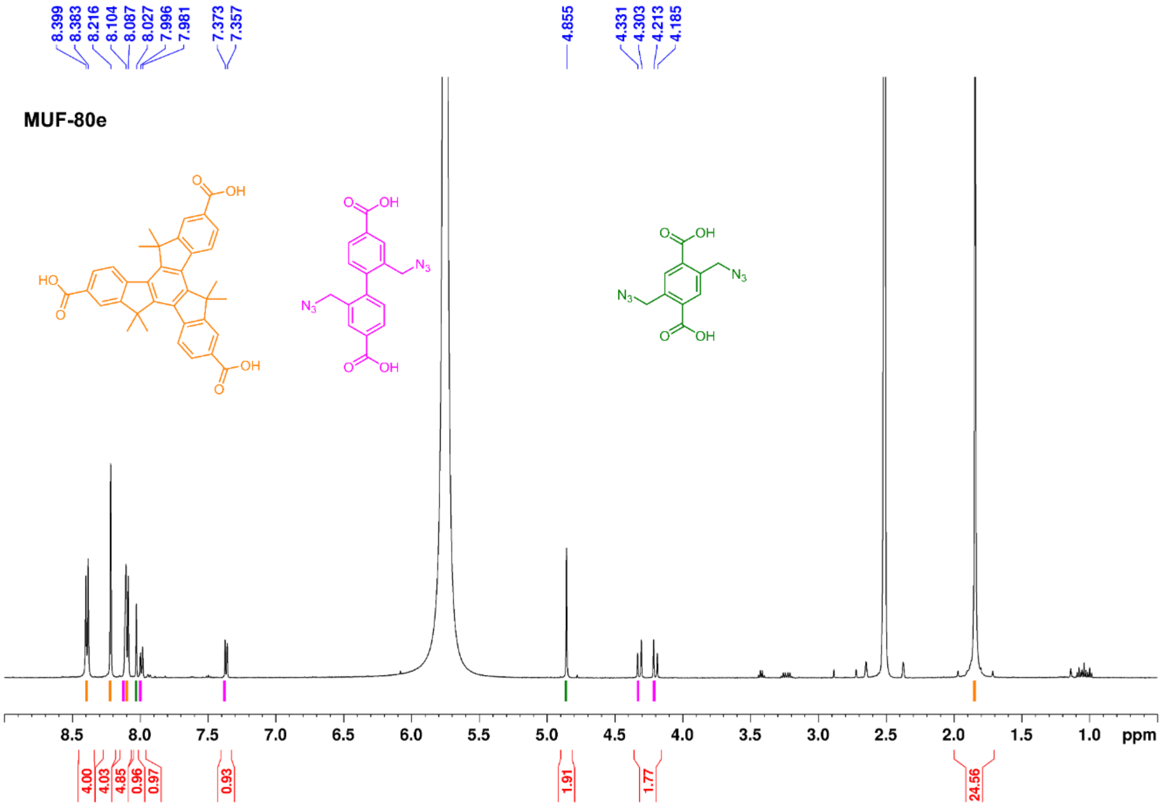

Figure D-6. ^{1}H NMR of digested MUF-80e in DMSO-d_6 and DCl mixture.

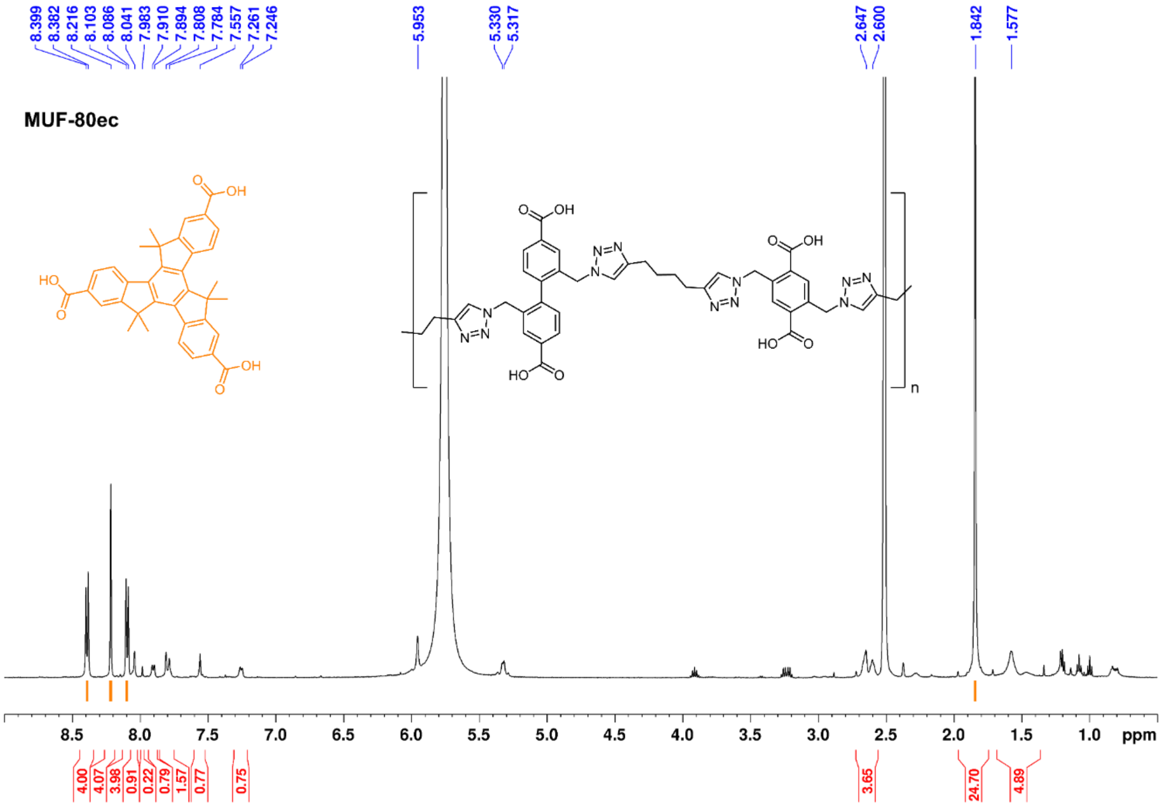

Figure D-7. ^{1}H NMR of digested MUF-80ec in DMSO-d_6 and DCl mixture.

D.4. Gas physorption

D.4.1. N_2 adsoprtion at 77 K and BET plots

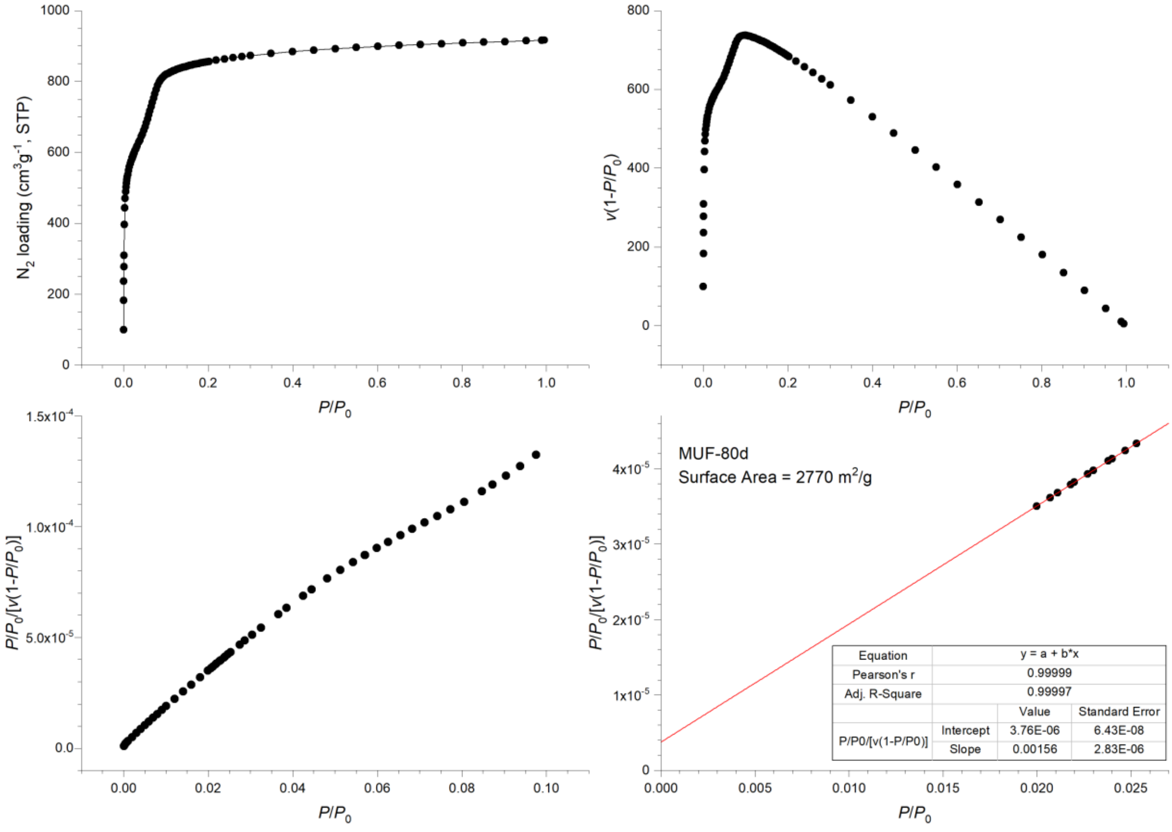

Equation		y = a + b*x	
Pearson's r		0.99999	
Adj. R-Square		0.99997	
		Value	Standard Error
P/P0/[v(1-P/P0)]	Intercept	3.76E-06	6.43E-08
	Slope	0.00156	2.83E-06

Figure D-8. N_2 adsorption isotherm at 77 K and BET surface area plots for MUF-80d.

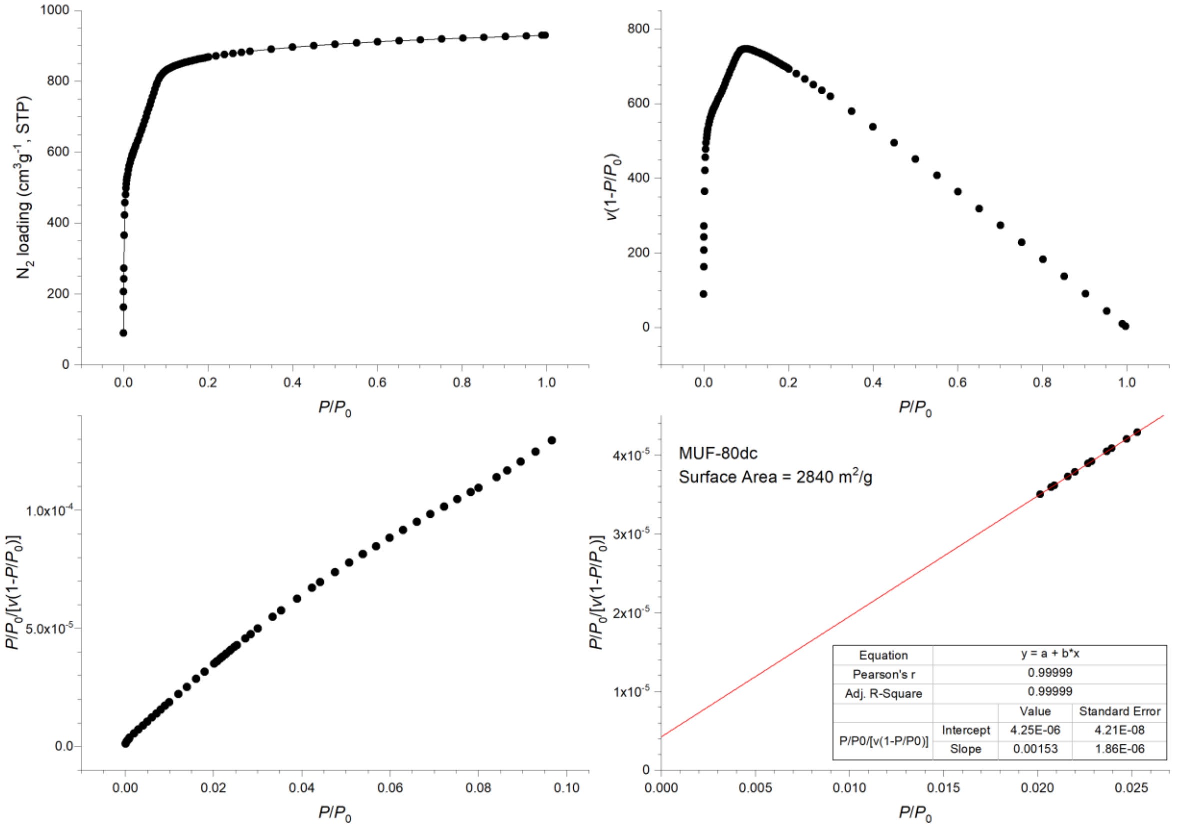

Equation		y = a + b*x	
Pearson's r		0.99999	
Adj. R-Square		0.99999	
		Value	Standard Error
P/P0/[v(1-P/P0)]	Intercept	4.25E-06	4.21E-08
	Slope	0.00153	1.86E-06

Figure D-9. N$_2$ adsorption isotherm at 77 K and BET surface area plots for MUF-80dc.

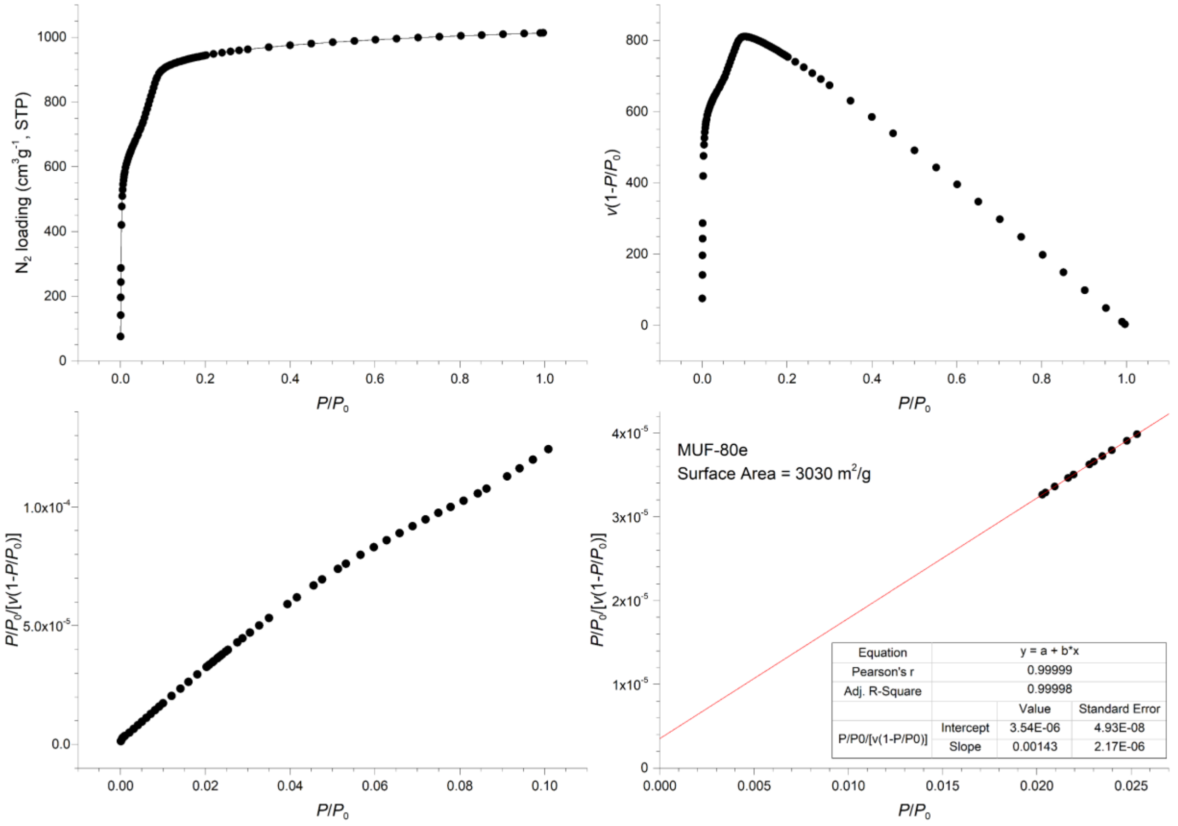

Equation		y = a + b*x	
Pearson's r		0.99999	
Adj. R-Square		0.99998	
		Value	Standard Error
P/P0/[v(1-P/P0)]	Intercept	3.54E-06	4.93E-08
	Slope	0.00143	2.17E-06

Figure D-10. N$_2$ adsorption isotherm at 77 K and BET surface area plots for MUF-80e.

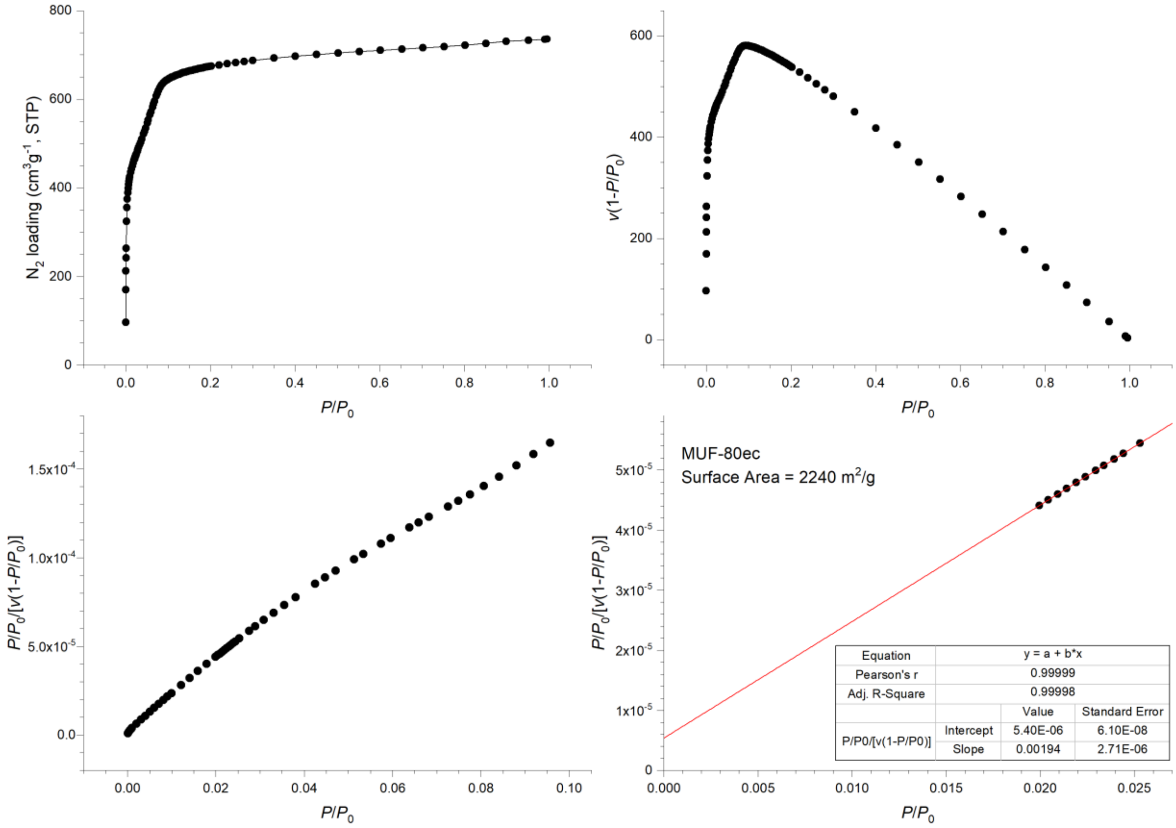

Equation		y = a + b*x	
Pearson's r		0.99999	
Adj. R-Square		0.99998	
		Value	Standard Error
P/P0/[v(1-P/P0)]	Intercept	5.40E-06	6.10E-08
	Slope	0.00194	2.71E-06

Figure D-11. N_2 adsorption isotherm at 77 K and BET surface area plots for MUF-80ec.

D.4.2. Selected gas physorption at 273 K and 293 K

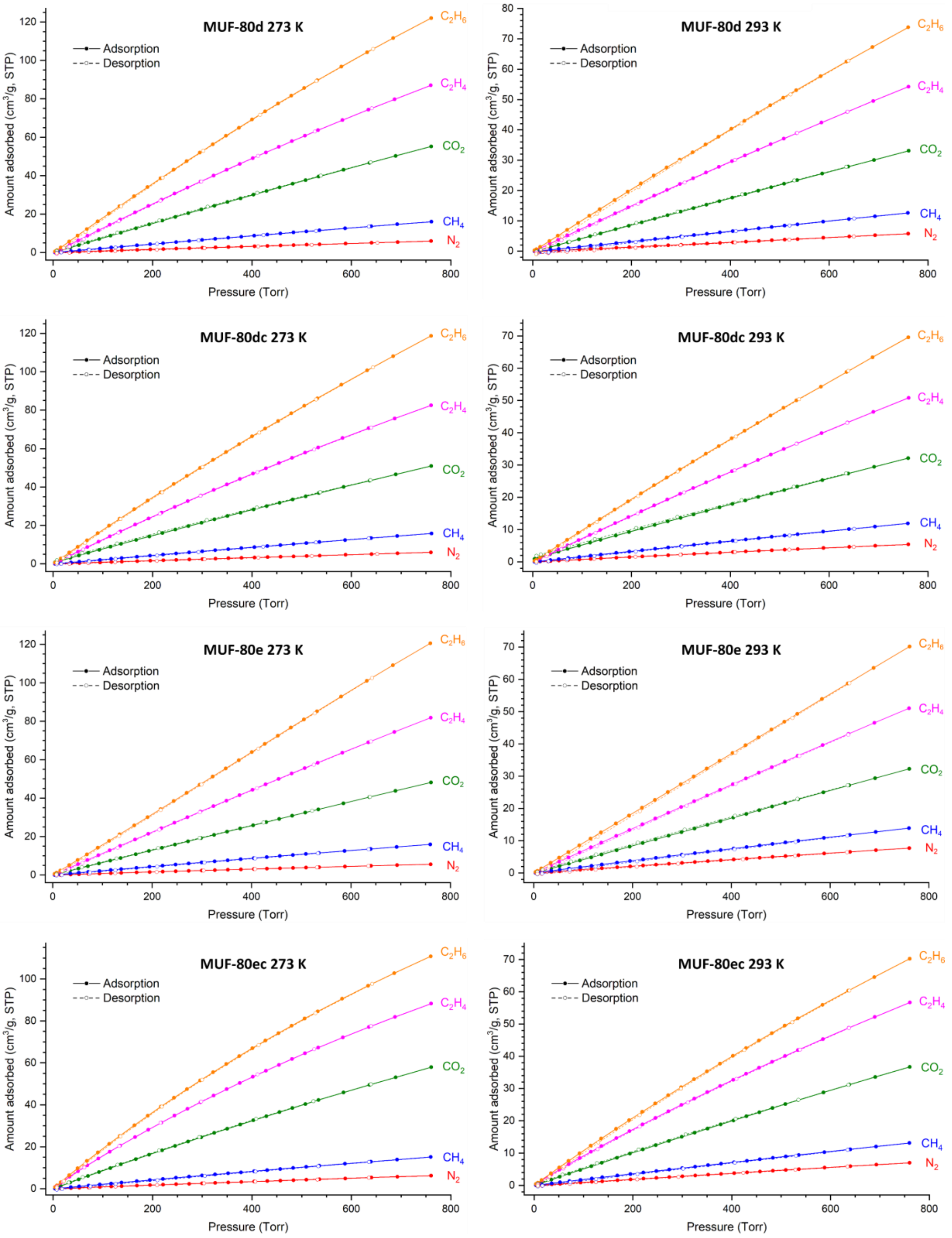

Figure D-12. Gas physorption of selected gases at 273 K and 293 K for the selected frameworks.

D.4.3. Heats of adsorption for slelcted gases

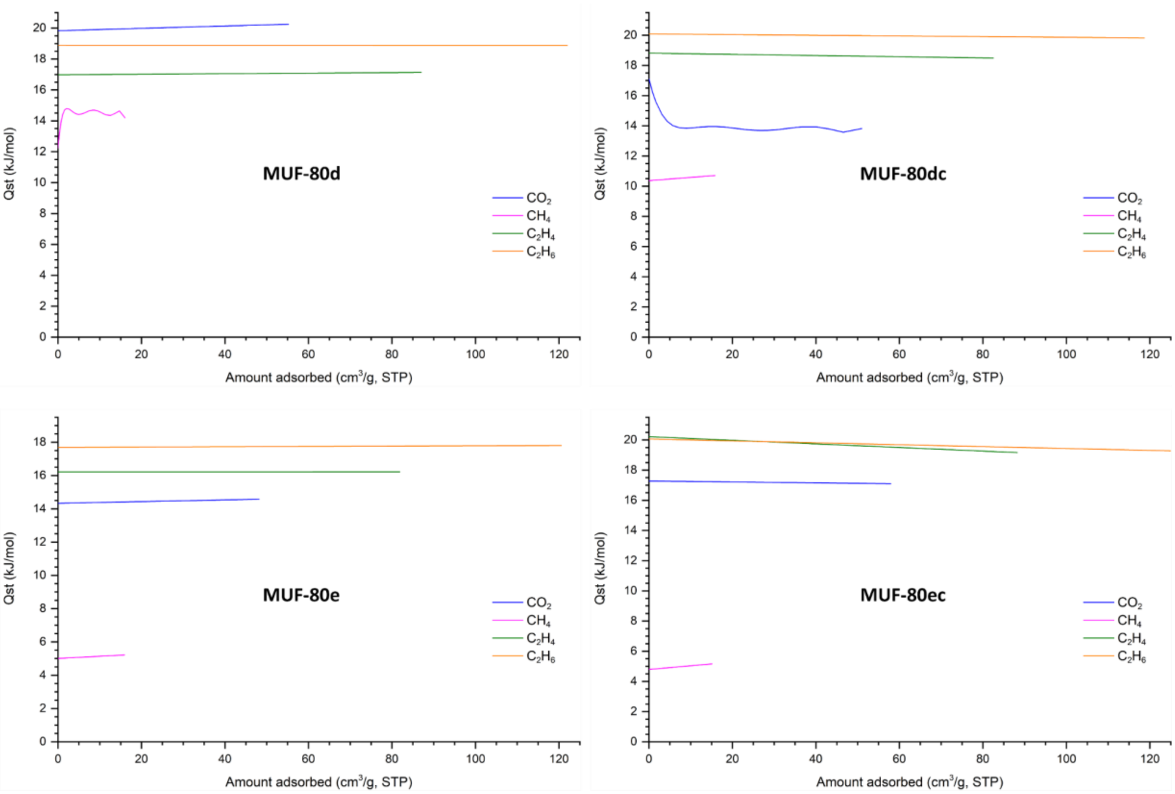

Figure D-13. Isosteric heat of adsorptions of selected gases for the selected frameworks as a function of uptake.

D.4.4. **Virial fits**

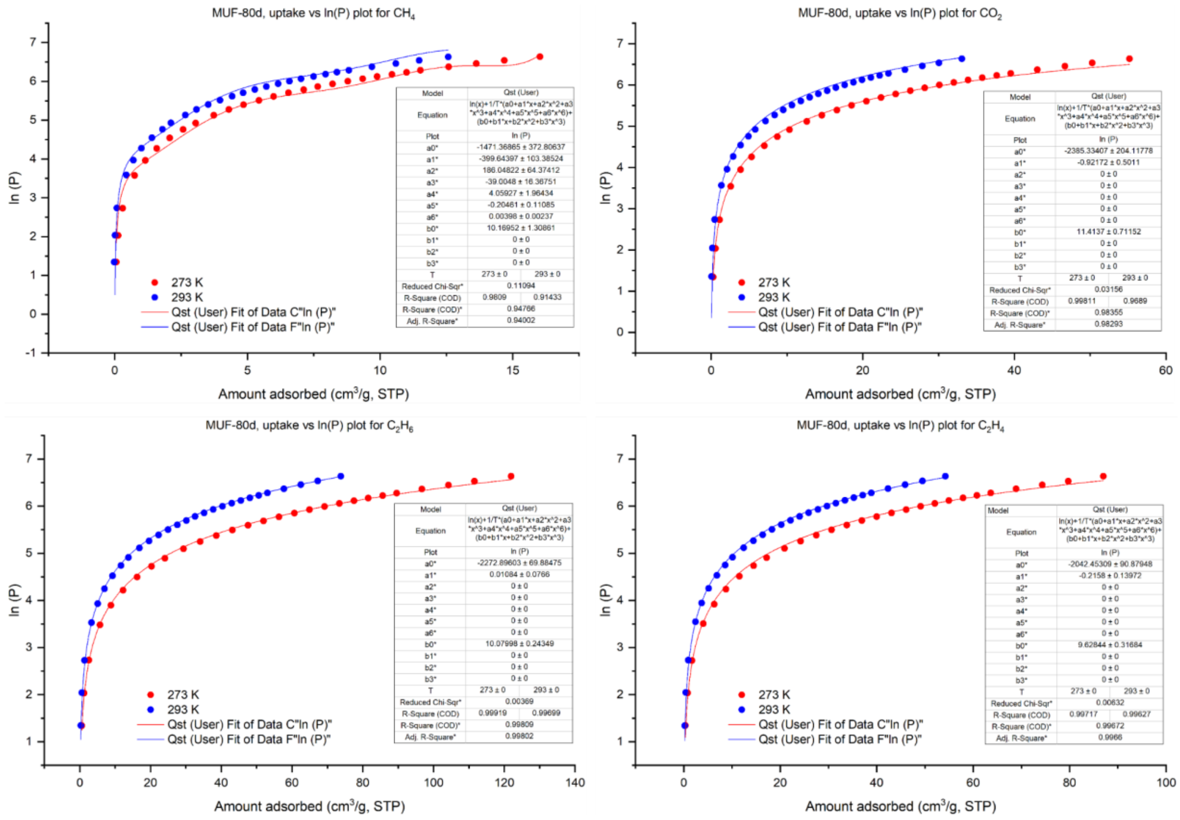

MUF-80d, uptake vs ln(P) plot for CH_4

Model	Qst (User)	
Equation	ln(x)+1/T*(a0+a1*x+a2*x^2+a3*x^3+a4*x^4+a5*x^5+a6*x^6)+(b0+b1*x+b2*x^2+b3*x^3)	
Plot	ln (P)	
a0*	-1471.36865 ± 372.80637	
a1*	-399.64397 ± 103.38524	
a2*	186.04822 ± 64.37412	
a3*	-39.0048 ± 16.36751	
a4*	4.05927 ± 1.96434	
a5*	-0.20461 ± 0.11085	
a6*	0.00398 ± 0.00237	
b0*	10.16952 ± 1.30861	
b1*	0 ± 0	
b2*	0 ± 0	
b3*	0 ± 0	
T	273 ± 0	293 ± 0
Reduced Chi-Sqr*	0.11094	
R-Square (COD)	0.9809	0.91433
R-Square (COD)*	0.94766	
Adj. R-Square*	0.94002	

MUF-80d, uptake vs ln(P) plot for CO_2

Model	Qst (User)	
Equation	ln(x)+1/T*(a0+a1*x+a2*x^2+a3*x^3+a4*x^4+a5*x^5+a6*x^6)+(b0+b1*x+b2*x^2+b3*x^3)	
Plot	ln (P)	
a0*	-2385.33407 ± 204.11778	
a1*	-0.92172 ± 0.5011	
a2*	0 ± 0	
a3*	0 ± 0	
a4*	0 ± 0	
a5*	0 ± 0	
a6*	0 ± 0	
b0*	11.4137 ± 0.71152	
b1*	0 ± 0	
b2*	0 ± 0	
b3*	0 ± 0	
T	273 ± 0	293 ± 0
Reduced Chi-Sqr*	0.03156	
R-Square (COD)	0.99811	0.9689
R-Square (COD)*	0.98355	
Adj. R-Square*	0.98293	

MUF-80d, uptake vs ln(P) plot for C_2H_6

Model	Qst (User)	
Equation	ln(x)+1/T*(a0+a1*x+a2*x^2+a3*x^3+a4*x^4+a5*x^5+a6*x^6)+(b0+b1*x+b2*x^2+b3*x^3)	
Plot	ln (P)	
a0*	-2272.89603 ± 69.88475	
a1*	0.01084 ± 0.0766	
a2*	0 ± 0	
a3*	0 ± 0	
a4*	0 ± 0	
a5*	0 ± 0	
a6*	0 ± 0	
b0*	10.07998 ± 0.24349	
b1*	0 ± 0	
b2*	0 ± 0	
b3*	0 ± 0	
T	273 ± 0	293 ± 0
Reduced Chi-Sqr*	0.00369	
R-Square (COD)	0.99919	0.99699
R-Square (COD)*	0.99809	
Adj. R-Square*	0.99802	

MUF-80d, uptake vs ln(P) plot for C_2H_4

Model	Qst (User)	
Equation	ln(x)+1/T*(a0+a1*x+a2*x^2+a3*x^3+a4*x^4+a5*x^5+a6*x^6)+(b0+b1*x+b2*x^2+b3*x^3)	
Plot	ln (P)	
a0*	-2042.45309 ± 90.87948	
a1*	-0.2158 ± 0.13972	
a2*	0 ± 0	
a3*	0 ± 0	
a4*	0 ± 0	
a5*	0 ± 0	
a6*	0 ± 0	
b0*	9.62844 ± 0.31684	
b1*	0 ± 0	
b2*	0 ± 0	
b3*	0 ± 0	
T	273 ± 0	293 ± 0
Reduced Chi-Sqr*	0.00632	
R-Square (COD)	0.99717	0.99627
R-Square (COD)*	0.99672	
Adj. R-Square*	0.9966	

Figure D-14. Virial fits of selected gases for MUF-80d.

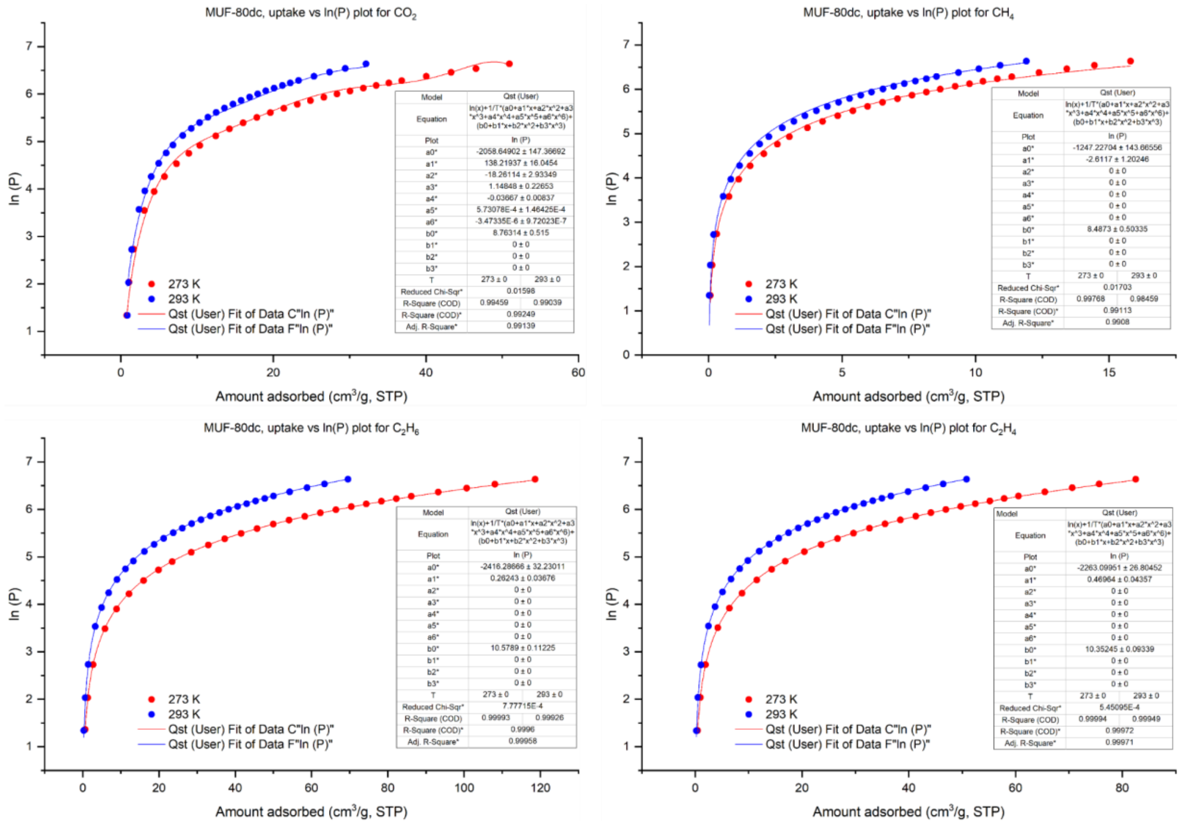

MUF-80dc, uptake vs ln(P) plot for CO_2

Model	Qst (User)	
Equation	ln(x)+1/T*(a0+a1*x+a2*x^2+a3*x^3+a4*x^4+a5*x^5+a6*x^6)+(b0+b1*x+b2*x^2+b3*x^3)	
Plot	ln (P)	
a0*	-2058.64902 ± 147.36692	
a1*	138.21937 ± 16.0454	
a2*	-18.26114 ± 2.93349	
a3*	1.14848 ± 0.22653	
a4*	-0.03667 ± 0.00837	
a5*	5.73078E-4 ± 1.46425E-4	
a6*	-3.47335E-6 ± 9.72023E-7	
b0*	8.76314 ± 0.515	
b1*	0 ± 0	
b2*	0 ± 0	
b3*	0 ± 0	
T	273 ± 0	293 ± 0
Reduced Chi-Sqr*	0.01598	
R-Square (COD)	0.99459	0.99039
R-Square (COD)*	0.99249	
Adj. R-Square*	0.99139	

MUF-80dc, uptake vs ln(P) plot for CH_4

Model	Qst (User)	
Equation	ln(x)+1/T*(a0+a1*x+a2*x^2+a3*x^3+a4*x^4+a5*x^5+a6*x^6)+(b0+b1*x+b2*x^2+b3*x^3)	
Plot	ln (P)	
a0*	-1247.22704 ± 143.66556	
a1*	-2.6117 ± 1.20246	
a2*	0 ± 0	
a3*	0 ± 0	
a4*	0 ± 0	
a5*	0 ± 0	
a6*	0 ± 0	
b0*	8.4873 ± 0.50335	
b1*	0 ± 0	
b2*	0 ± 0	
b3*	0 ± 0	
T	273 ± 0	293 ± 0
Reduced Chi-Sqr*	0.01703	
R-Square (COD)	0.99768	0.98459
R-Square (COD)*	0.99113	
Adj. R-Square*	0.9908	

MUF-80dc, uptake vs ln(P) plot for C_2H_6

Model	Qst (User)	
Equation	ln(x)+1/T*(a0+a1*x+a2*x^2+a3*x^3+a4*x^4+a5*x^5+a6*x^6)+(b0+b1*x+b2*x^2+b3*x^3)	
Plot	ln (P)	
a0*	-2416.28666 ± 32.23011	
a1*	0.26243 ± 0.03676	
a2*	0 ± 0	
a3*	0 ± 0	
a4*	0 ± 0	
a5*	0 ± 0	
a6*	0 ± 0	
b0*	10.5789 ± 0.11225	
b1*	0 ± 0	
b2*	0 ± 0	
b3*	0 ± 0	
T	273 ± 0	293 ± 0
Reduced Chi-Sqr*	7.77715E-4	
R-Square (COD)	0.99993	0.99926
R-Square (COD)*	0.9996	
Adj. R-Square*	0.99958	

MUF-80dc, uptake vs ln(P) plot for C_2H_4

Model	Qst (User)	
Equation	ln(x)+1/T*(a0+a1*x+a2*x^2+a3*x^3+a4*x^4+a5*x^5+a6*x^6)+(b0+b1*x+b2*x^2+b3*x^3)	
Plot	ln (P)	
a0*	-2263.09951 ± 26.80452	
a1*	0.46964 ± 0.04357	
a2*	0 ± 0	
a3*	0 ± 0	
a4*	0 ± 0	
a5*	0 ± 0	
a6*	0 ± 0	
b0*	10.35245 ± 0.09339	
b1*	0 ± 0	
b2*	0 ± 0	
b3*	0 ± 0	
T	273 ± 0	293 ± 0
Reduced Chi-Sqr*	5.45095E-4	
R-Square (COD)	0.99994	0.99949
R-Square (COD)*	0.99972	
Adj. R-Square*	0.99971	

Figure D-15. Virial fits of selected gases for MUF-80dc.

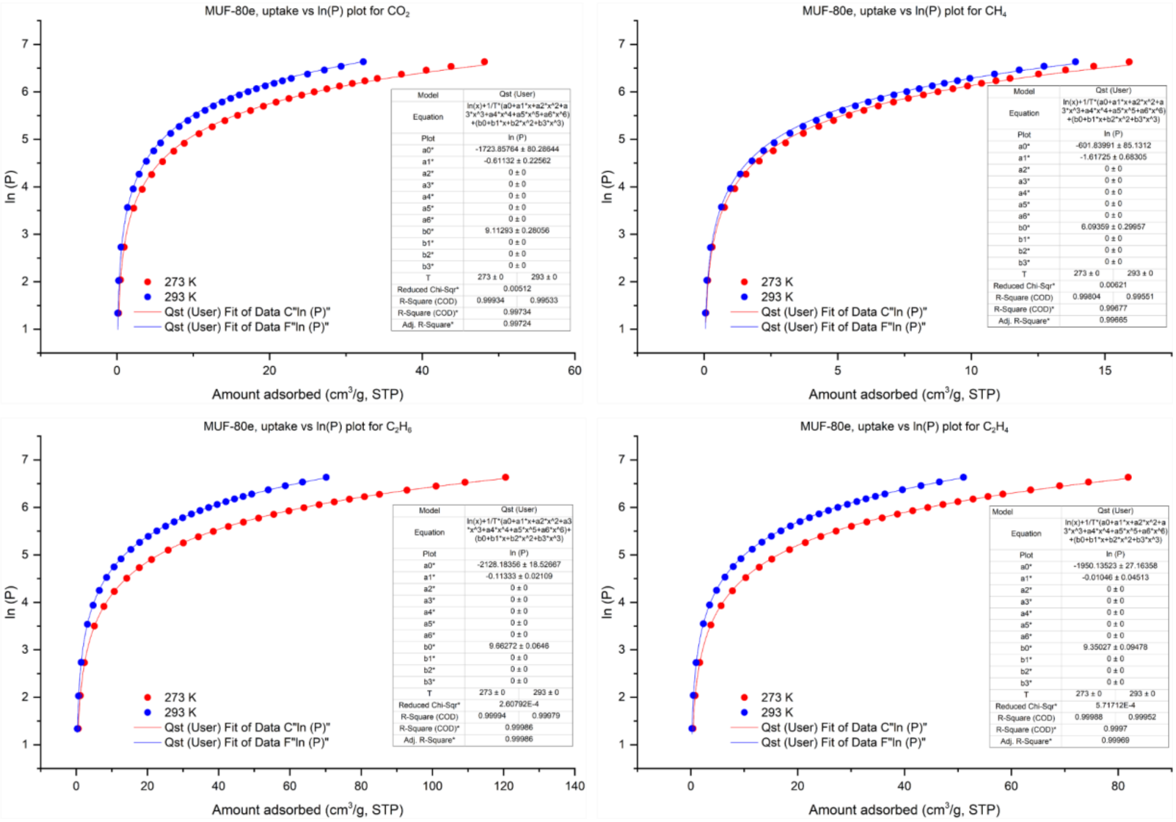

Model	Qst (User)	
Equation	ln(x)+1/T*(a0+a1*x+a2*x^2+a3*x^3+a4*x^4+a5*x^5+a6*x^6)+(b0+b1*x+b2*x^2+b3*x^3)	
Plot	ln (P)	
a0*	-1723.85764 ± 80.28644	
a1*	-0.61132 ± 0.22562	
a2*	0 ± 0	
a3*	0 ± 0	
a4*	0 ± 0	
a5*	0 ± 0	
a6*	0 ± 0	
b0*	9.11293 ± 0.28056	
b1*	0 ± 0	
b2*	0 ± 0	
b3*	0 ± 0	
T	273 ± 0	293 ± 0
Reduced Chi-Sqr*	0.00512	
R-Square (COD)	0.99934	0.99533
R-Square (COD)*	0.99734	
Adj. R-Square*	0.99724	

Model	Qst (User)	
Equation	ln(x)+1/T*(a0+a1*x+a2*x^2+a3*x^3+a4*x^4+a5*x^5+a6*x^6)+(b0+b1*x+b2*x^2+b3*x^3)	
Plot	ln (P)	
a0*	-601.83991 ± 85.1312	
a1*	-1.61725 ± 0.68305	
a2*	0 ± 0	
a3*	0 ± 0	
a4*	0 ± 0	
a5*	0 ± 0	
a6*	0 ± 0	
b0*	6.09359 ± 0.29957	
b1*	0 ± 0	
b2*	0 ± 0	
b3*	0 ± 0	
T	273 ± 0	293 ± 0
Reduced Chi-Sqr*	0.00621	
R-Square (COD)	0.99804	0.99551
R-Square (COD)*	0.99677	
Adj. R-Square*	0.99665	

Model	Qst (User)	
Equation	ln(x)+1/T*(a0+a1*x+a2*x^2+a3*x^3+a4*x^4+a5*x^5+a6*x^6)+(b0+b1*x+b2*x^2+b3*x^3)	
Plot	ln (P)	
a0*	-2128.18356 ± 18.52667	
a1*	-0.11333 ± 0.02109	
a2*	0 ± 0	
a3*	0 ± 0	
a4*	0 ± 0	
a5*	0 ± 0	
a6*	0 ± 0	
b0*	9.66272 ± 0.0646	
b1*	0 ± 0	
b2*	0 ± 0	
b3*	0 ± 0	
T	273 ± 0	293 ± 0
Reduced Chi-Sqr*	2.60792E-4	
R-Square (COD)	0.99994	0.99979
R-Square (COD)*	0.99986	
Adj. R-Square*	0.99986	

Model	Qst (User)	
Equation	ln(x)+1/T*(a0+a1*x+a2*x^2+a3*x^3+a4*x^4+a5*x^5+a6*x^6)+(b0+b1*x+b2*x^2+b3*x^3)	
Plot	ln (P)	
a0*	-1950.13523 ± 27.16358	
a1*	-0.01046 ± 0.04513	
a2*	0 ± 0	
a3*	0 ± 0	
a4*	0 ± 0	
a5*	0 ± 0	
a6*	0 ± 0	
b0*	9.35027 ± 0.09478	
b1*	0 ± 0	
b2*	0 ± 0	
b3*	0 ± 0	
T	273 ± 0	293 ± 0
Reduced Chi-Sqr*	5.71712E-4	
R-Square (COD)	0.99988	0.99952
R-Square (COD)*	0.9997	
Adj. R-Square*	0.99969	

Figure D-16, Virial fits of selected gases for MUF-80e.

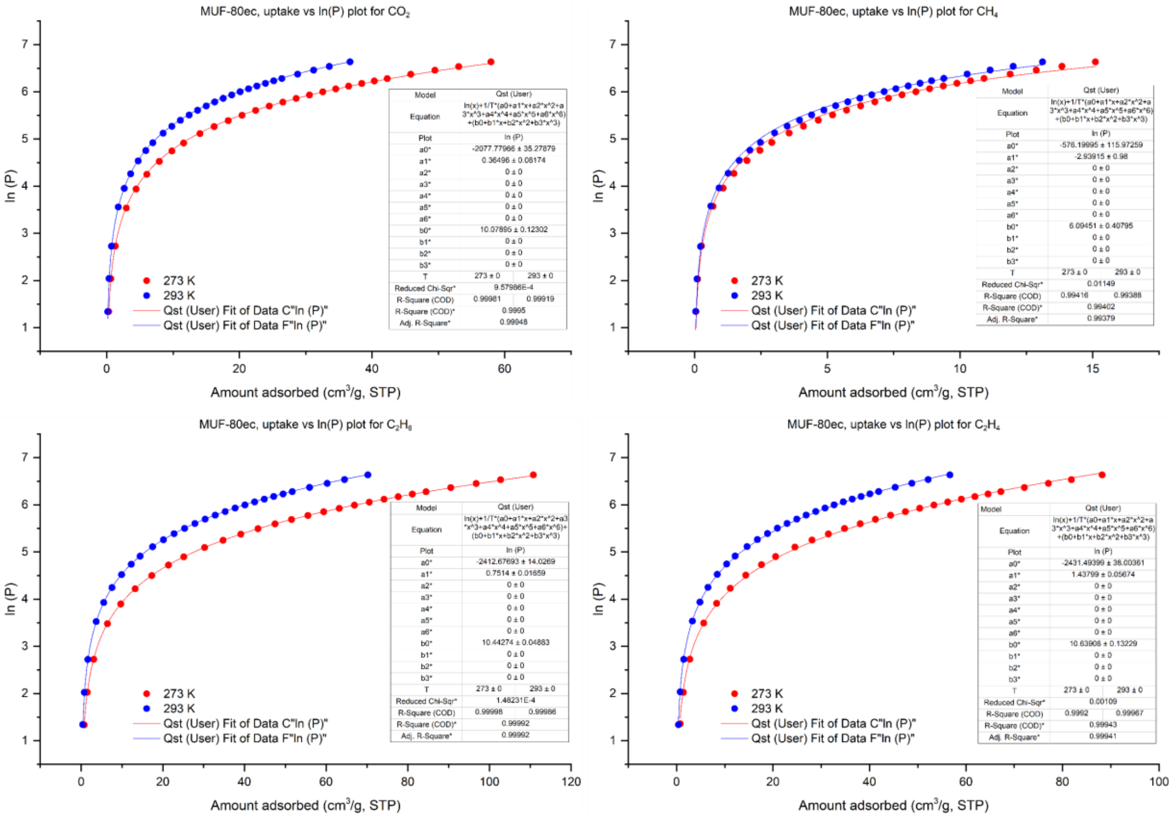

Model	Qst (User)	
Equation	ln(x)+1/T*(a0+a1*x+a2*x^2+a3*x^3+a4*x^4+a5*x^5+a6*x^6)+(b0+b1*x+b2*x^2+b3*x^3)	
Plot	ln (P)	
a0*	-2077.77966 ± 35.27879	
a1*	0.36496 ± 0.08174	
a2*	0 ± 0	
a3*	0 ± 0	
a4*	0 ± 0	
a5*	0 ± 0	
a6*	0 ± 0	
b0*	10.07895 ± 0.12302	
b1*	0 ± 0	
b2*	0 ± 0	
b3*	0 ± 0	
T	273 ± 0	293 ± 0
Reduced Chi-Sqr*	9.57986E-4	
R-Square (COD)	0.99981	0.99919
R-Square (COD)*	0.9995	
Adj. R-Square*	0.99948	

Model	Qst (User)	
Equation	ln(x)+1/T*(a0+a1*x+a2*x^2+a3*x^3+a4*x^4+a5*x^5+a6*x^6)+(b0+b1*x+b2*x^2+b3*x^3)	
Plot	ln (P)	
a0*	-576.19995 ± 115.97259	
a1*	-2.93915 ± 0.98	
a2*	0 ± 0	
a3*	0 ± 0	
a4*	0 ± 0	
a5*	0 ± 0	
a6*	0 ± 0	
b0*	6.09451 ± 0.40795	
b1*	0 ± 0	
b2*	0 ± 0	
b3*	0 ± 0	
T	273 ± 0	293 ± 0
Reduced Chi-Sqr*	0.01149	
R-Square (COD)	0.99416	0.99388
R-Square (COD)*	0.99402	
Adj. R-Square*	0.99379	

Model	Qst (User)	
Equation	ln(x)+1/T*(a0+a1*x+a2*x^2+a3*x^3+a4*x^4+a5*x^5+a6*x^6)+(b0+b1*x+b2*x^2+b3*x^3)	
Plot	ln (P)	
a0*	-2412.67693 ± 14.0269	
a1*	0.7514 ± 0.01659	
a2*	0 ± 0	
a3*	0 ± 0	
a4*	0 ± 0	
a5*	0 ± 0	
a6*	0 ± 0	
b0*	10.44274 ± 0.04883	
b1*	0 ± 0	
b2*	0 ± 0	
b3*	0 ± 0	
T	273 ± 0	293 ± 0
Reduced Chi-Sqr*	1.48231E-4	
R-Square (COD)	0.99998	0.99986
R-Square (COD)*	0.99992	
Adj. R-Square*	0.99992	

Model	Qst (User)	
Equation	ln(x)+1/T*(a0+a1*x+a2*x^2+a3*x^3+a4*x^4+a5*x^5+a6*x^6)+(b0+b1*x+b2*x^2+b3*x^3)	
Plot	ln (P)	
a0*	-2431.49399 ± 38.00361	
a1*	1.43799 ± 0.05674	
a2*	0 ± 0	
a3*	0 ± 0	
a4*	0 ± 0	
a5*	0 ± 0	
a6*	0 ± 0	
b0*	10.63908 ± 0.13229	
b1*	0 ± 0	
b2*	0 ± 0	
b3*	0 ± 0	
T	273 ± 0	293 ± 0
Reduced Chi-Sqr*	0.00109	
R-Square (COD)	0.9992	0.99967
R-Square (COD)*	0.99943	
Adj. R-Square*	0.99941	

Figure D-17. Virial fits of selected gases for MUF-80ec.

D.4.5. Pore size distribution

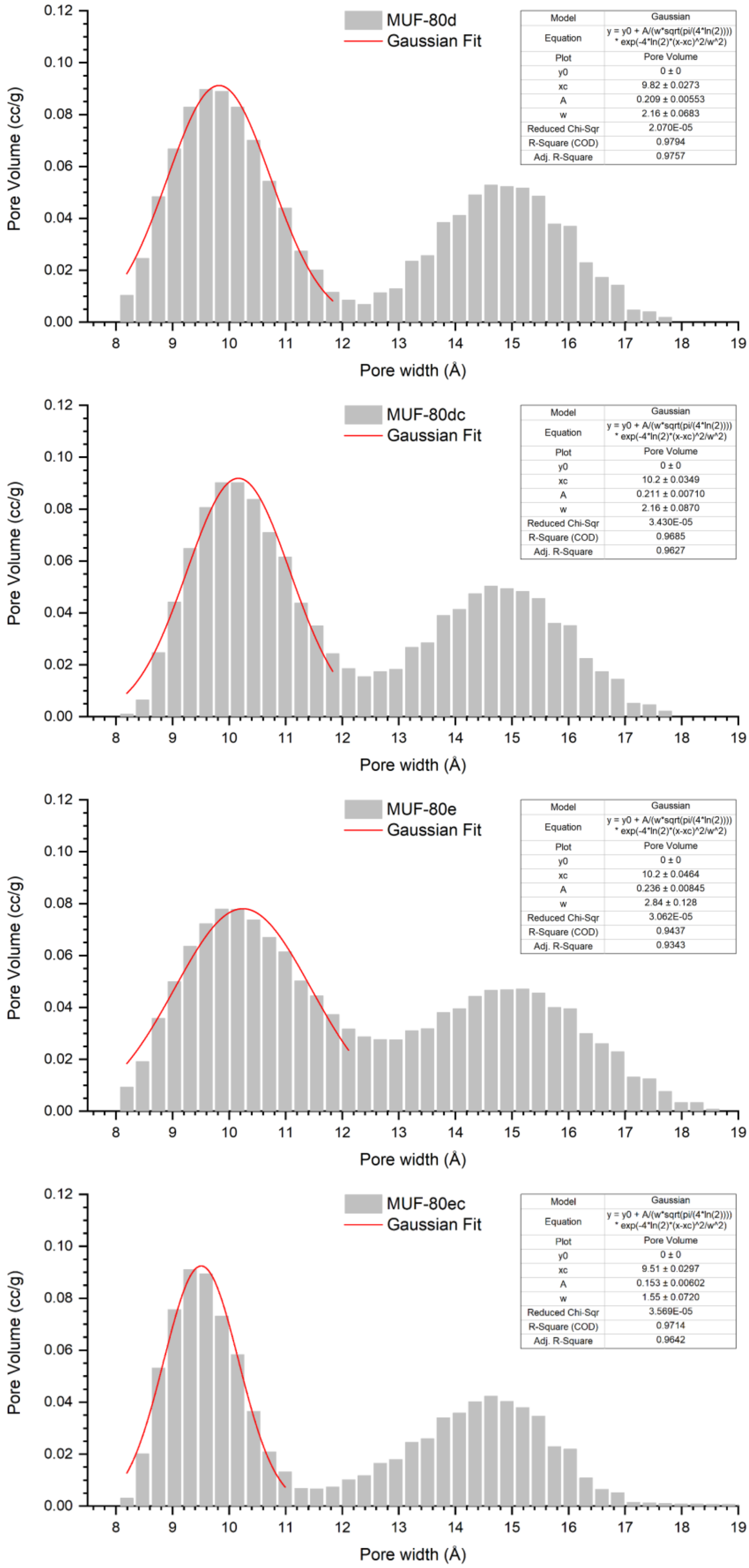

Model	Gaussian
Equation	y = y0 + A/(w*sqrt(pi/(4*ln(2)))) * exp(-4*ln(2)*(x-xc)^2/w^2)
Plot	Pore Volume
y0	0 ± 0
xc	9.82 ± 0.0273
A	0.209 ± 0.00553
w	2.16 ± 0.0683
Reduced Chi-Sqr	2.070E-05
R-Square (COD)	0.9794
Adj. R-Square	0.9757

Model	Gaussian
Equation	y = y0 + A/(w*sqrt(pi/(4*ln(2)))) * exp(-4*ln(2)*(x-xc)^2/w^2)
Plot	Pore Volume
y0	0 ± 0
xc	10.2 ± 0.0349
A	0.211 ± 0.00710
w	2.16 ± 0.0870
Reduced Chi-Sqr	3.430E-05
R-Square (COD)	0.9685
Adj. R-Square	0.9627

Model	Gaussian
Equation	y = y0 + A/(w*sqrt(pi/(4*ln(2)))) * exp(-4*ln(2)*(x-xc)^2/w^2)
Plot	Pore Volume
y0	0 ± 0
xc	10.2 ± 0.0464
A	0.236 ± 0.00845
w	2.84 ± 0.128
Reduced Chi-Sqr	3.062E-05
R-Square (COD)	0.9437
Adj. R-Square	0.9343

Model	Gaussian
Equation	y = y0 + A/(w*sqrt(pi/(4*ln(2)))) * exp(-4*ln(2)*(x-xc)^2/w^2)
Plot	Pore Volume
y0	0 ± 0
xc	9.51 ± 0.0297
A	0.153 ± 0.00602
w	1.55 ± 0.0720
Reduced Chi-Sqr	3.569E-05
R-Square (COD)	0.9714
Adj. R-Square	0.9642

Figure D-18. Pore volume distribution plots and the Gaussian fits for the selected frameworks.

D.4.6. **Optical microscope images**

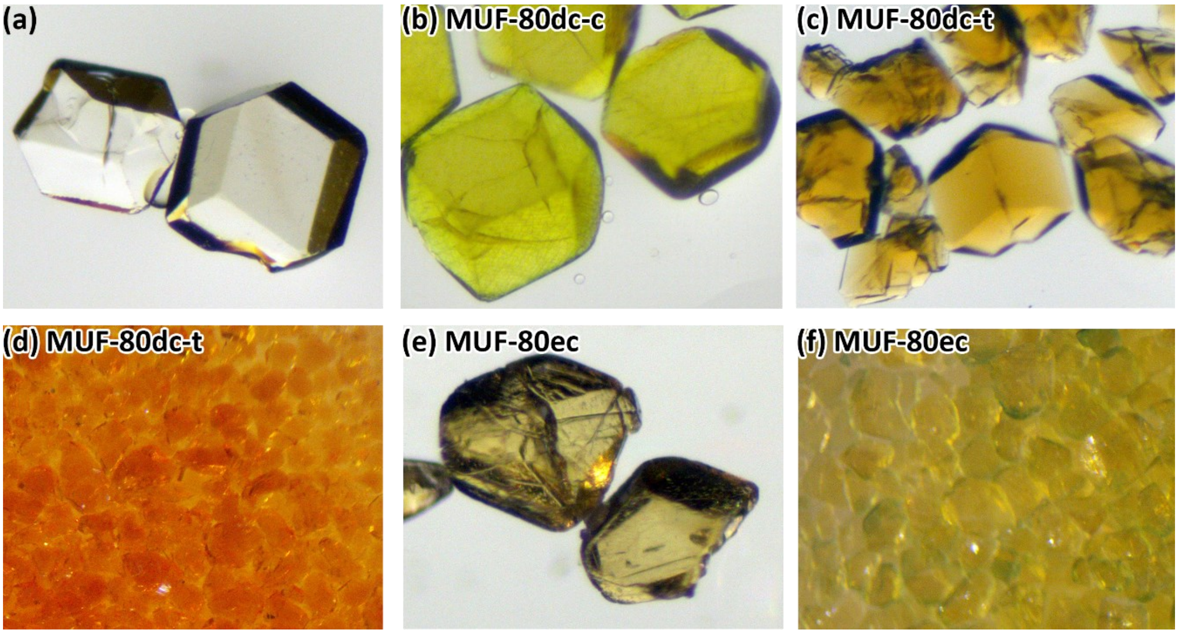

Figure D-19. Optical microscope images of crystal samples; (a) a general figure of MUF-80c, d, and e; (b) greenish MUF-80dc-c crystals due to transmetallation with copper; (c)(d) intense orange MUF-80dc-t after thermal coupling reaction; (e) greenish yellow MUF-80ec crystals; (f) cracked MUF-80ec due to the stress during click reaction.

D.4.7. SEM images

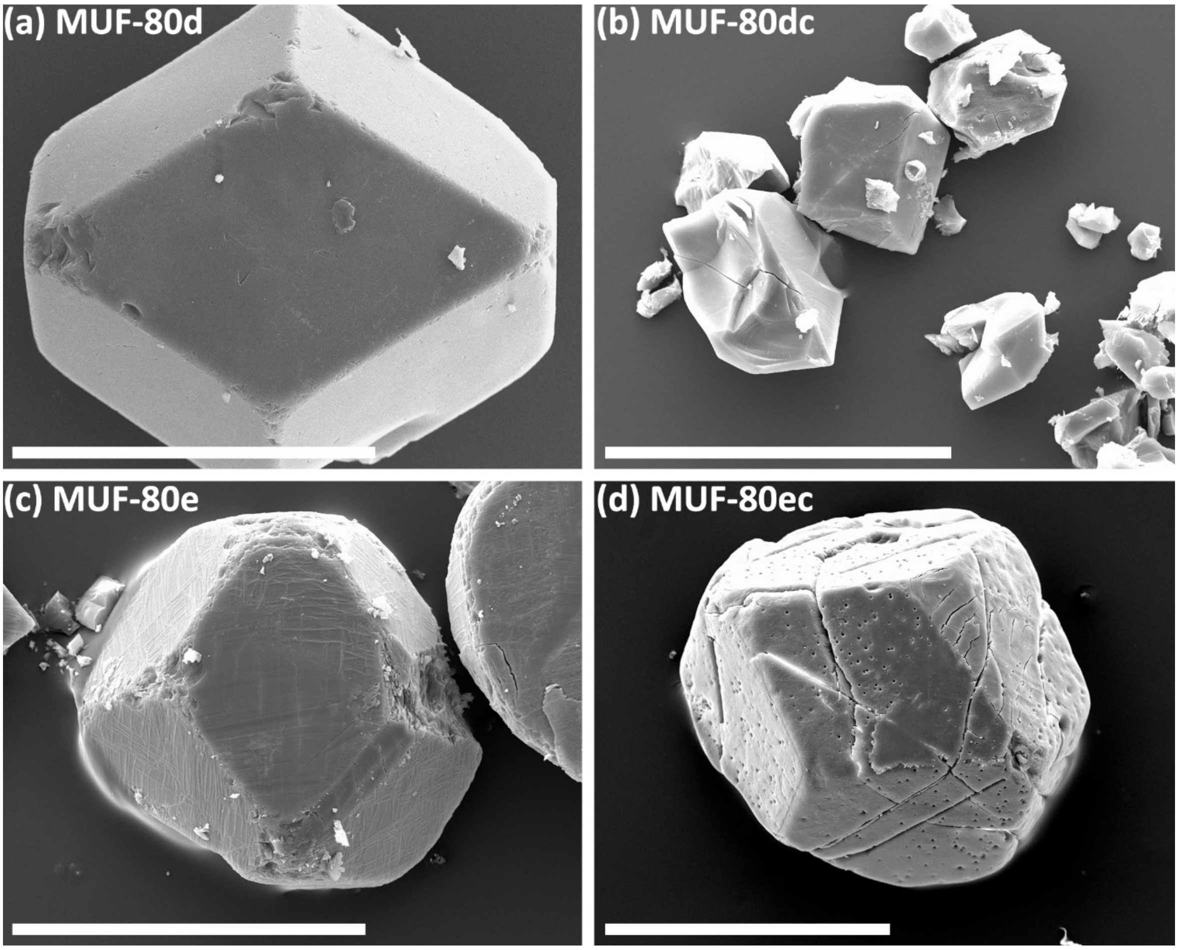

Figure D-20. SEM images of MUF-80d, MUF-80dc, MUF-80e and MUF-80ec; the scale bar is equivalent to 400 µm.